Конденсированные среды и межфазные границы

РЕЦЕНЗИРУЕМЫЙ НАУЧНЫЙ ЖУРНАЛ

Condensed Matter and Interphases

Kondensirovannye Sredy i Mezhfaznye Granitsy
PEER-REVIEWED SCIENTIFIC JOURNAL

Том 23, № 4
Vol. 23, No. 4
2021

Condensed Matter and Interphases

Kondensirovannye sredy i mezhfaznye granitsy

Peer-reviewed scientific journal

Published since January 1999

Periodicity: Quarterly

Volume 23, No. 4, 2021

Full-text version is available in the Russian language on the website: https://journals.vsu.ru/kcmf

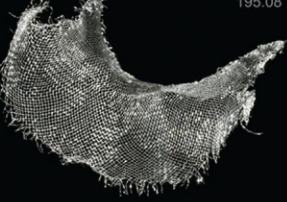**Condensed Matter and Interphases** (Kondensirovannye Sredy i Mezhfaznye Granitsy) publishes articles in Russian and English dedicated to key issues of condensed matter and physicochemical processes at interfaces and in volumes.

The mission of the journal is to provide open access to the results of original research (theoretical and experimental) at the intersection of contemporary condensed matter physics and chemistry, material science and nanoindustry, solid state chemistry, inorganic chemistry, and physical chemistry, and to share scientific data in the **following sections**: atomic, electron, and cluster structure of solids, liquids, and interphase boundaries; phase equilibria and defect formation processes; structure and physical and chemical properties of interphases; laser thermochemistry and photostimulated processes on solid surfaces; physics and chemistry of surface, thin films and heterostructures; kinetics and mechanism of formation of film structures; electrophysical processes in interphase boundaries; chemistry of surface phenomena in sorbents; devices and new research methods.

The journal accepts for publication: reviews, original articles, short communications by leading Russian scientists, foreign researchers, lecturers, postgraduate and undergraduate students.

CONTENTS

Original articles

Kinetic regularities of electrochemical oxidation of the methionine anion on platinated platinum

E. V. Bobrinskaya✉, A. V. Vvedenskii, E. Yu. Sheremetova, A. I. Frolova

Voronezh State University,
1 Universitetskaya pl., Voronezh 394018, Russian Federation

Abstract

The purpose of this study was the determination of the kinetic regularities of the methionine electrooxidation process on the Pt(Pt) electrode in an aqueous-alkaline medium.

The main kinetic regularities of the methionine anion electrooxidation process were determined using by the methods of cyclic voltammetry, coulometry, and electrochemical impedance spectroscopy. The concentration of methionine in the alkaline solution before and after anodic oxidation was determined spectrophotometrically using spectrophotometer UNICO 2800. The measurements were carried out at room temperature both in an argon atmosphere and in an aerated aqueous solution. The results of voltammetric measurements were adjusted for the limiting oxygen recovery current and the charging current of the double electric layer.

The range of potentials of the electrochemical activity of the methionine anion on the Pt(Pt) electrode, the number of electrons involved in the anode process, and its kinetic scheme were determined. The main product of the electrooxidation of methionine in an alkaline medium on Pt(Pt) was the methionine sulfoxide anion. It was shown that the electrooxidation of the methionine anion on Pt (Pt) was carried out from the adsorbed state and was irreversible.

Keywords: Amino acid, Methionine, Platinum, Voltammetry, Electrooxidation, Anodic process

✉ Elena V. Bobrinskaya, e-mail: elena173.68@mail.ru

Condensed Matter and Interphases / Конденсированные среды и межфазные границы   2021;23(4): 459–467

E. V. Bobrinskaya et al.   Kinetic regularities of electrochemical oxidation of the methionine anion...

1. Introduction

For many years, special attention has been paid to methods for extracting platinum metals from ore-forming minerals. In particular, biotechnological methods based on the dissolution of platinoids by the metabolic products of heterotrophic metallophilic microorganisms. Amino acids and peptides are widely used for this purpose [1, 2]. It should be noted that amino acids are promising solvents in the process of microbiological leaching of gold-bearing raw materials; it is possible that this is also characteristic of platinum. This fact necessitates a more detailed study of the process of interaction of platinum with protein residues (in particular, with amino acids and short peptides), as well as clarification of the fundamental possibility of using substances of a protein nature as solvents of platinum. It is known that some amino acids affect the anodic dissolution of platinum, accelerating or slowing it down, but, in addition, the amino acid itself can be oxidized in the anodic process. Accordingly, it is important to take into account not only the direct anodic behaviour of platinum in alkaline solutions, but also specify the processes occurring with the amino acid.

Usually, the role of two functional groups $-NH_2$ and $-COOH$ is primarily studied during investigation of the electrooxidation process and adsorption of various amino acids on a platinum electrode [3–12]. Less information is available about the electrochemical and adsorption activity of amino acids containing other functional groups, for example, $-OH$ or $-S-CH$ [13–21]. On the other hand, studies [15, 19, 21] demonstrated that the presence of the $-S-CH$ group in the methionine molecule affects the regularities of its adsorption behaviour. Since during the electrooxidation of organic substances there is a correlation between adsorption and kinetic regularities of electrode processes, the purpose of this study was the determination of the kinetic regularities of the methionine electrooxidation process on the Pt(Pt) electrode in an aqueous-alkaline medium.

2. Experimental

The measurements were carried out at room temperature both in an argon atmosphere (chemically pure grade) and in an aerated aqueous solution by the cyclic voltammetry methods using a computerized potentiostatic complex IPC-Compact; frequency impedance spectra were obtained using the IPC Compact – FRA1 complex.

The methionine concentration in the alkaline solution before and after anodic oxidation was determined spectrophotometrically using a UNIKO 2800 spectrophotometer at wavelengths of 190–450 nm in quartz cuvettes with a thickness of 10 mm.

Potentiodynamic I,E-curves were obtained in a glass three-electrode cell with undivided cathode and anode spaces. It was preliminarily established that the separation of the spaces of the working and auxiliary electrodes practically does not affect the measurement results, however, it decreases the speed of the potentiostatic complex. The working electrode was platinum in the form of a grid, on which platinum black was electrolytically deposited. The auxiliary electrode was a smooth platinum mesh. The potential of the working electrode was measured relative to a saturated silver chloride reference electrode.

Before the experiment, the working electrode was treated with concentrated nitric acid for three minutes, washed repeatedly with bidistilled water, and then with a background 0.1 M NaOH solution.

Methionine solutions ($5·10^{-3} \div 0.1$ M) was prepared from a weighed portion of a crystalline amino acid (Merck) in a background solution of sodium hydroxide (chemically pure grade) in bidistilled water. The fact that the introduction of an amino acid into the background solution is accompanied by a change in its acidity due to the occurrence of protonation/deprotonation reactions, changing the ratio between the main ionic forms of the amino acid was taken into account [22].

For the removal of possible electroactive impurities, before each measurement, the working electrode was treated with concentrated nitric acid (reagent grade), then repeatedly washed with distilled and rinsed with bidistilled water, and then subjected to potentiostatic anodic-cathodic activation in the background solution, changing the activation potential from +1.0 to −1.0 V, receiving 50 activation cycles.

The peak potential E_{max} of voltammetric $I,E(t)$-curve and the faradaic current at I_{max} are the main values experimentally measured

Condensed Matter and Interphases / Конденсированные среды и межфазные границы   2021;23(4): 459–467

E. V. Bobrinskaya et al.   Kinetic regularities of electrochemical oxidation of the methionine anion...

by linear voltammetry method. The results of voltammetric measurements were corrected for both the maximum current of oxygen reduction and the double layer charging current $I_{dl} = C_{dl}v$, where v is the potential scanning speed. Capacity value C_{dl} of the working electrode was evaluated by electrochemical impedance spectroscopy.

3. Results and discussion

For the determination of the potential range of the electrochemical activity of the methionine anion (Met⁻) on the Pt(Pt)-electrode, cyclic voltammograms were obtained both in the background solution and in the presence of Met⁻ both in aerated and deaerated solutions (Fig. 1).

In the absence of an amino acid on the Pt-electrode, three characteristic regions can be distinguished. In the hydrogen region (from −1.20 to −0.50 V) the processes of formation and ionization of adsorbed atomic hydrogen take place. Beyond the area of potentials from −0.50 to −0.20 V, in which only the currents of charging the double layer and the reduction of molecular oxygen were recorded, there was a region of oxygen adsorption, which began at $E > -0.20$ V. Processes with the participation of atomic oxygen are characterized by noticeable irreversibility: desorption of oxygen (for recoil curve) occurs at potentials corresponding to the charge of the double layer on the anodic branch of the voltammogram. Intensive release of molecular oxygen on the Pt-electrode started at $E > 0.6$ V.

The introduction of the methionine additive led to a noticeable increase in the current on the anodic branch of the cyclogram and the appearance of a peak at a potential of 0.60 V for aerated solution and 0.70 V for a deaerated solution, which was probably due to the electrooxidation of the amino acid. It should be noted that the change in the peak potential of electrooxidation with a change in the concentration of dissolved oxygen at a qualitative level indicates the involvement of oxygen-containing particles in the anodic process.

For the conformation of methionine electrooxidation in the range of the anodic peak potentials and for the determination of the number of electrons involved in this process, coulometric measurements were carried out, followed by spectrophotometric determination of the Met⁻ concentration in solution. It was found that the anodic peak potentials actually correspond to the process of electrooxidation of Met⁻, and two electrons take part in the anodic reaction (based on a current efficiency close to 100 %). Taking into account the results of coulometry, the total process of electrooxidation can be represented as follows:

$$2C_5H_{10}NSO_2^- + 2OH^- \rightarrow 2C_5H_{10}NSO_3^- + H_2O + 2\bar{e}.$$
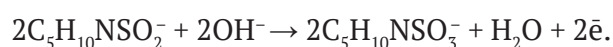
In this case, the main product of electrooxidation is methionine sulfoxide anion.

The identification of the kinetic limitations of the electrooxidation process requires diagnostic criteria allowing to detect the nature of the limiting stage of the electrochemical reaction, complicated by the adsorption of the reagent or product(s), and to establish the reversibility of
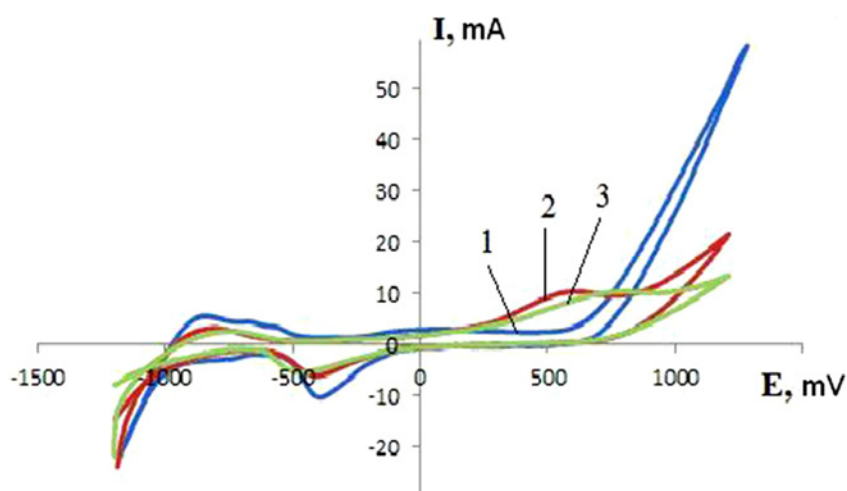
Fig. 1. Cyclic voltammograms obtained on a Pt-electrode at v = 0.005 V/s in an aqueous solution of 0.1 M NaOH (*1*) and 0.1 M NaOH + 0.01 M methionine without deaeration (*2*) and after deaeration of the solution (*3*)

Condensed Matter and Interphases / Конденсированные среды и межфазные границы   2021;23(4): 459–467

E. V. Bobrinskaya et al.   Kinetic regularities of electrochemical oxidation of the methionine anion...

the process. The method of linear voltammetry usually uses the current I_{max} in peak on the anodic branch $I,E(t)$-dependencies and the corresponding potential E_{max} as such criteria. Both parameters depend on the concentration of the amino acid, the pH of the background solution, and the potential scan rate.

The analysis of the experimental data shows that with an increase in the potential scanning rate, the current on both branches of the voltammogram increased. In this case, the anodic peak potential was noticeably improved, both under deaeration conditions and in an aerated solution. The decrease in the height of the oxygen desorption peak, as well as the shift towards the anodic side of the cathodic peak potentials, observed on the recoil curves, were most probably associated with the adsorption of the amino acid and (or) its oxidation products on the electrode. An increase in the concentration of the methionine anion led to a similar result. At the same time, the value of the current at the

peak and its position were practically invariant in relation to a change in the rotational speed of the platinum disk electrode (Fig. 2).

The obtained result indicates that the anodic peak current at $I,E(t)$-dependence was not associated with liquid-phase diffusion of reagents or products. It probably reflected the features of their adsorption accumulation on the electrode, which can be confirmed by analysing the diagnostic criteria of the linear voltammetry method [23–25].

The current and the anodic peak potential depend on the potential scan rate (v), the concentration of the methionine anion and the pH value, both in a previously deaerated solution and in a solution in equilibrium with the atmosphere. It was established that dependencies $I_{max} = f(v)$ are linear and, after correcting for the oxygen reduction current and the charging current of the electric double layer, they are extrapolated to the origin of coordinates (Fig. 3). This fact and the slope of this dependence close to one, indicate that the methionine electrooxidation
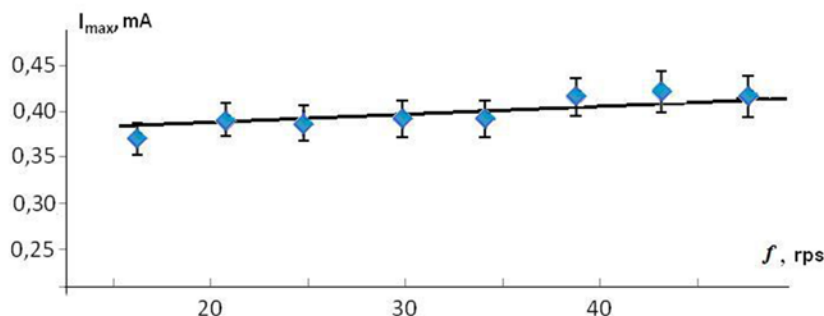
Fig. 2. The dependence of the peak current of electrooxidation in 0.10 M NaOH + 0.03 M Met⁻ solution, on the number of revolutions Pt of the rotating disk electrode; v = 0.10 V/s
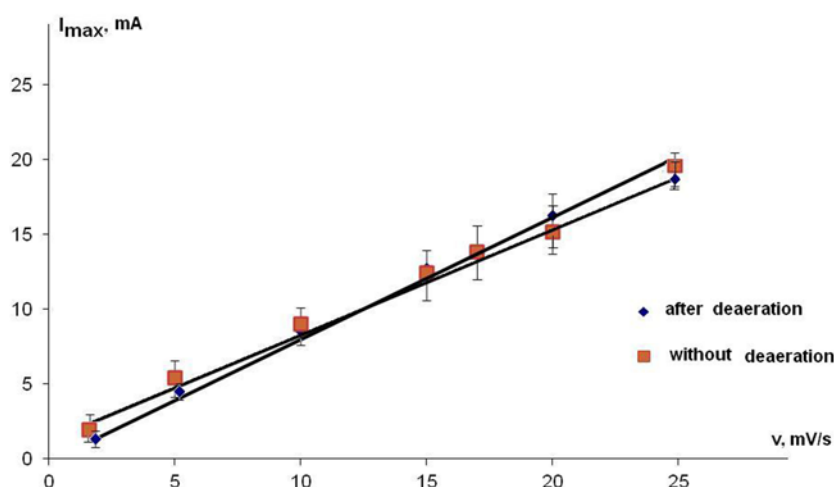
Fig. 3. Effect of the potential scanning rate on the value of the anodic peak current in a 0.10 M NaOH solution containing 0.01 M Met⁻

Condensed Matter and Interphases / Конденсированные среды и межфазные границы   2021;23(4): 459–467

E. V. Bobrinskaya et al.   Kinetic regularities of electrochemical oxidation of the methionine anion...

process is limited by the charge transfer stage and is irreversible. At the same time, the adsorbed particles are involved in the electrochemical reaction.

It can be assumed that the two-electron net process of methionine electrooxidation is a stepwise process. Considering that the dependencies $E_{max} - \lg v$ and $E_{max} - \lg I_{max}$ are linear (Fig. 4), and the value of $d\lg I_{max}/d\lg v$ parameter equals 0.21±0.052 (without deaeration of the solution) and 0.12±0.014 (after deaeration), then the stage of abstraction of the first electron is most likely the limiting stage of the anodic reaction of methionine electrooxidation. It should be noted that if the stage of transition of the second electron is taken as the limiting stage, then the slope of the corresponding dependence would be much smaller. In addition, the amplitude of the current on the voltammogram is affected

by both the concentration of the methionine anion and the concentration of OH⁻ ions. With an increase in the concentration of the methionine anion, the amplitude of the anodic peak current increases (Fig. 5), and the peak potential becomes more positive.

In this case, the value of the parameter $\dfrac{d\lg I_{max}}{d\lg C_{Met^-}} < 1$ and is 0.22 (after deaeration) and 0.27 (without deaeration). The latter means that the adsorbed particles are involved in the process of electrooxidation, as we assumed above. Another confirmation of this fact is the voltammograms obtained in the background electrolyte after washing the working electrode. The adsorption accumulation of methionine anions was carried out at potentials of 0.00; 0.20 and –0.25 V for 10 minutes. The obtained anodic
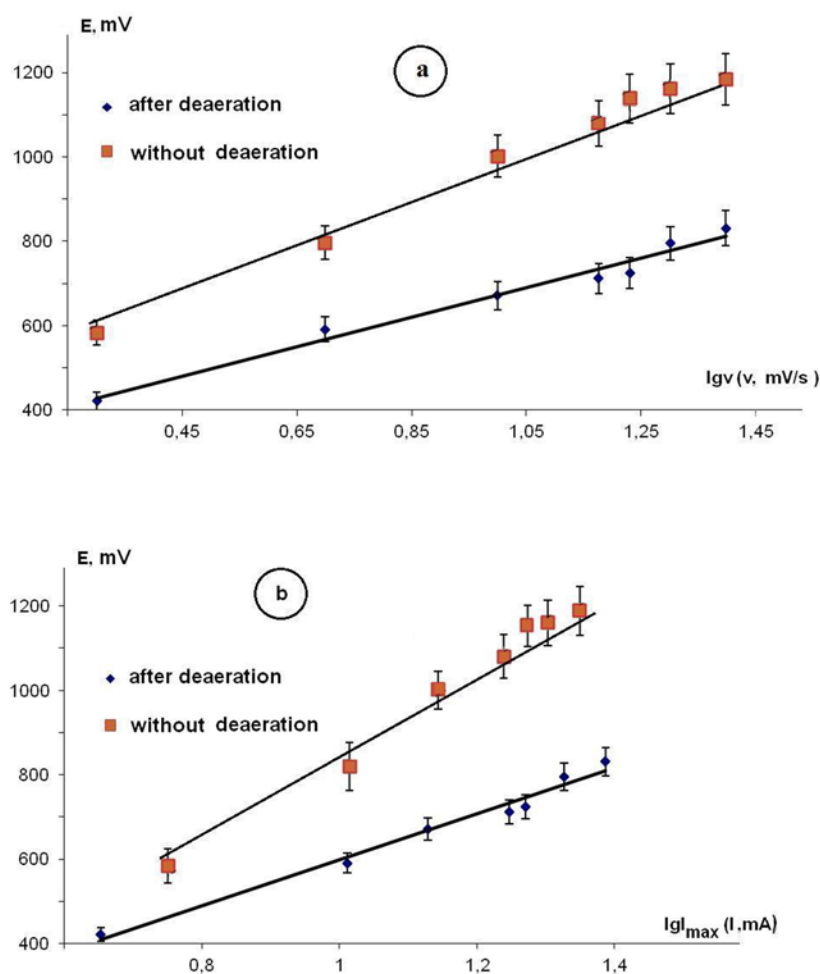
Fig. 4. Effect of the potential scanning speed (a) and the logarithm of the anodic peak current (b) on the position of the peak of electrooxidation in solutions containing 0.10 M NaOH+ 0.01 M Met⁻

Condensed Matter and Interphases / Конденсированные среды и межфазные границы   2021;23(4): 459–467

E. V. Bobrinskaya et al.   Kinetic regularities of electrochemical oxidation of the methionine anion...
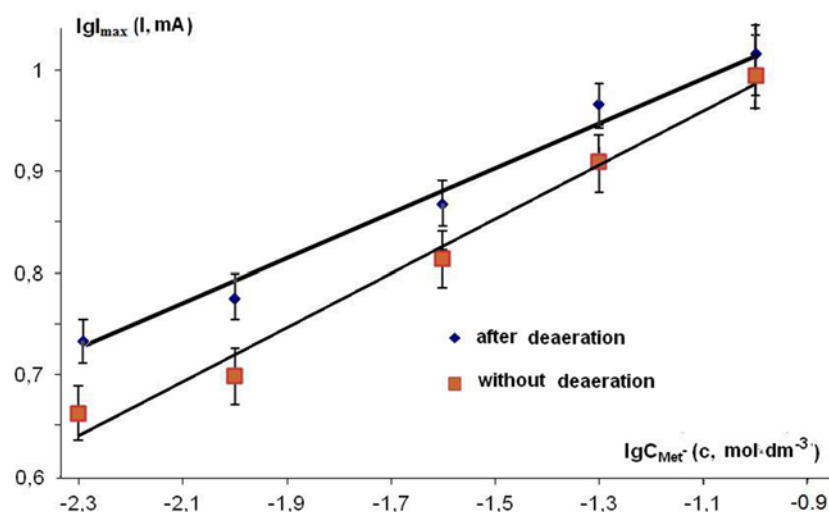
Fig. 5. The dependence of the maximum current of electrooxidation on the concentration of Met⁻ anions at $v = 0.10$ V/s

voltammograms in a 0.1 M NaOH solution before the adsorption accumulation of the amino acid (1) and after washing the electrode (2–4) are shown in Fig. 6.

The peaks of the amino acid electrooxidation were still registered on voltammograms obtained in the solution of the background electrolyte after washing the electrode. This indicates that the electrooxidation of Met⁻ on the Pt-electrode is carried out from the adsorbed state and represents the so-called "surface" electrochemical reaction. In addition, the adsorption of methionine on platinum is most likely irreversible.

Since hydroxyl ions are also involved in the process of electrooxidation of methionine anions, data on the effect of their concentration (at a constant concentration of Met⁻) on the rate of the anodic process were obtained. An increase in pH led to an increase in the amplitude of the maximum of electrooxidation and a shift in its potential in the cathodic direction, regardless of the degree of aeration of the working solution (Fig. 7). The value of the $d\lg I_{max}/d\lg C_{OH^-}$ parameter is not zero, but noticeably less than one, and in both cases amounts to 0.10 ± 0.03 (Fig.7a), which means that adsorbed OH⁻-ions were involved in the anodic process.
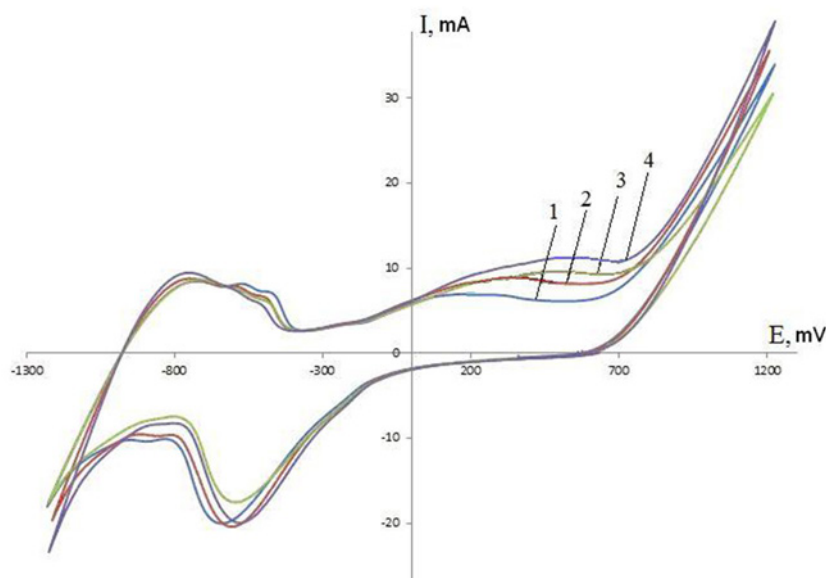
Fig. 6. Cyclic voltammograms obtained on Pt electrode at $v = 0.01$ V/s in an aqueous solution of 0.1 M NaOH before (*1*) and after adsorption accumulation and electrode washing: (*2*) – 0.00 V; (*3*) – −0.25 V; (*4*) – 0.20 V

Condensed Matter and Interphases / Конденсированные среды и межфазные границы   2021;23(4): 459–467

E. V. Bobrinskaya et al.   Kinetic regularities of electrochemical oxidation of the methionine anion...
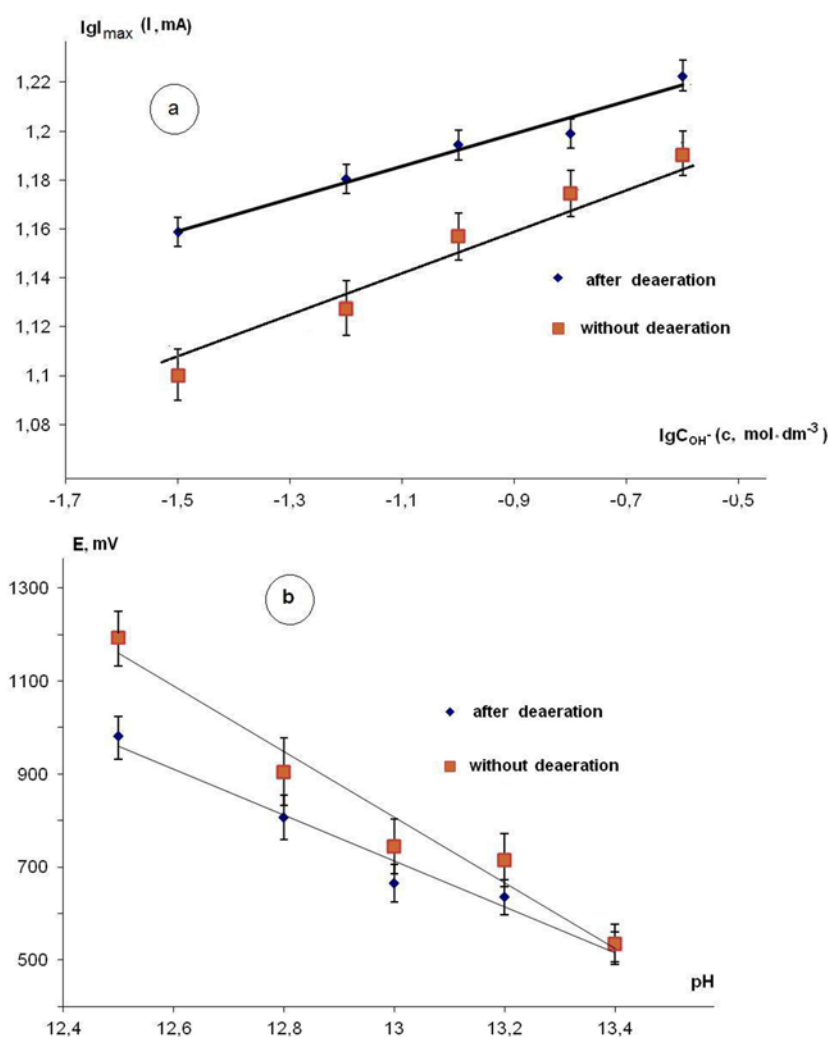
Fig. 7. Change of the current (a) and peak potential (b) of electrooxidation depending on the pH of the solution containing 0.01 M Met⁻ at $v = 0.10$ V/s

Finally, since the kinetic parameter $\dfrac{d\lg I_{max}}{d\lg C_{Met^-}} > 0$, and with an increase in pH, the potential of the anodic maximum shifts to the negative values, it can be assumed that the dominant adsorbed form is the Red-form, which means that the methionine anion exhibits higher surface activity on platinum than the products of its electrooxidation.

4. Conclusions

The methionine anion exhibits significant electrochemical activity at the Pt(Pt) electrode. Two electrons are involved in the anodic process of electrooxidation, according to coulometric analysis with subsequent spectrophotometric determination of the methionine content in the solution. The most probable product of electrooxidation is methionine sulfoxide. The results of linear voltammetry indicate that, regardless of the degree of aeration of the working solution, charge transfer is the limiting stage of the methionine electrooxidation process. The process of methionine electrooxidation is kinetically irreversible and proceeds with the participation of adsorbed Met⁻ and OH⁻ ions. The Red-form, i.e., methionine anions, is the dominant adsorptive form in the electrooxidation reaction.

Authors contributions

A. V. Vvedenskii – scientific leadership, research concept, development of methodology, final conclusions. E. V. Bobrinskaya – conducting research, writing an article, editing the text.

Condensed Matter and Interphases / Конденсированные среды и межфазные границы   2021;23(4): 459–467

E. V. Bobrinskaya et al.   Kinetic regularities of electrochemical oxidation of the methionine anion...

Sheremetova E. Yu., Frolova A. I. – conducting research.

Conflict of interests

The authors declare that they have no known competing financial interests or personal relationships that could have influenced the work reported in this paper.

References

1. Arens V. I., Chernyak A. S. Khimiya i microbiologiya v sfere gornogo dela [Mining chemistry and microbiology]. *Mining informational and analytical bulletin (scientific and technical journal)*. 2006:8: 304–313. Available at: https://elibrary.ru/item.asp?id=9496289 (In Russ.)

2. Tumanova E. A., Lozhkin V. I., Chebykin E. P., Korolev S. A., Safonov A. Yu. Electrochemical dissolution of platinum in the presence of some amino acids. *Russian Journal of Electrochemistry*. 1999;35(12): 1327–1330. Available at: https://elibrary.ru/item.asp?id=13330275

3. Huerta F., Morallón E., Quijada C., Vázquez J. L., Berlouis L. E. A. Potential modulated reflectance study of the electrooxidation of simple amino acids on Pt (111) in acidic media. *Journal of Electroanalytical Chemistry*. 2000;489(1-2): 92–95. https://doi.org/10.1016/s0022-0728(00)00202-3

4. Huerta F., Morallon E., Cases F., Rodes A., Va´zqueza J. L., Aldaz A. Electrochemical behaviour of amino acids on Pt (h,k,l). A voltammetric and in situ FTIR study. Part. 2. Serine and alanine on Pt (111). *Journal of Electroanalytical Chemistry*. 1997;431(2): 269–275. https://doi.org/10.1016/S0022-0728(97)00212-X

5. Marangoni D. G., Wylie I. G. N., Roscoe S. G. Surface electrochemistry of the oxidation reactions of a- and b-alanine at a platinum electrode. *Bioelectrochemistry and Bioenergetics*. 1991;25(2): 269–277. https://doi.org/10.1016/0302-4598(91)87008-5

6. Horányi G., Rizmayer E. M. Study of the adsorption of glycine on platinized platinum electrodes by tracer methods. *Journal of Electroanalytical Chemistry and Interfacial Electrochemistry*. 1975;64(1): 15–19. https://doi.org/10.1016/s0022-0728(75)80275-0

7. Ogura K., Kobayashi, M., Nakayama, M., Miho M. Electrochemical and in situ FTIR studies on the adsorption and oxidation of glycine and lysine in alkaline medium. *Journal of Electroanalytical Chemistry*. 1998;449(1-2): 101–109. https://doi.org/10.1016/s0022-0728(98)00015-1

8. Xiao, Sun S.-G., Yao J.-L., Wu Q.-H., Tian Z.-Q. Surface-enhanced Raman spectroscopic studies of dissociative adsorption of amino acids on platinum and gold electrodes in alkaline solutions. *Langmuir*. 2002;18(16): 6274–6249. https://doi.org/10.1021/la025817f

9. Vvedenskii A. V., Bobrinskaya E. V., Kraschenko T. G., Vitnova O. A., Kuleshova N. E. Kinetics of anodic oxidation of anions of mono-and dicarboxylic aminoacids on Pt. *Proceedings of Voronezh State University. Series: Chemistry. Biology. Pharmacy*. 2013;2: 19–25. Available at: https://elibrary.ru/item.asp?id=20400913 (In Russ., abstract in Eng.)

10. Kraschenko T. G., Vvedenskii A. V., Bobrinskaya E. V., Kuleshova N. E. Kinetics of electrochemical oxidation of anion glycine on gold. *Kondensirovannye sredy i mezhfaznye granitsy = Condensed Matter and Interphases*. 2014;16(1): 42-49. Available at: https://elibrary.ru/item.asp?id=21490889 (In Russ., abstract in Eng.)

11. Tumanova E. A., Safonov A. Yu. Adsorption of some amino acids and dipeptides on the platinum electrode. *Russian Journal of Electrochemistry*. 1998;34(2): 153–159. Available at: https://elibrary.ru/item.asp?id=13289291

12. Bakanina U. N., Zhukova E. A., Abdullin I. F., Turova E. H., Budnikov G. K. Voltammetric study of some amino acids on platinum, gold, copper, and nickel electrodes. *Russian Journal of General Chemistry*. 2000;70(6): 837–840. Available at: https://elibrary.ru/item.asp?id=13360186

13. Huerta F., Morallón E., Vázquez J. L., Aldaz A. Electrochemical behaviour of amino acids on Pt(hkl). A voltammetric and in situ FTIR study: Part IV. Serine and alanine on Pt(100) and Pt(110). Journal of Electroanalytical Chemistry. 1999;475(1): 38–45. https://doi.org/10.1016/S0022-0728(99)00337-X

14. Kong D.-W., Zhu T.-W., Zeng D.-M., Zhen C.-H., Chen S.-P. In- situ FTIR spectroscopic studies of adsorption and oxidation of L- serine on Pt electrodes in neutral solutions. *Chemical Journal of Chinese Universities*. 2009;30(10): 2040–2044. Available at: http://www.cjcu.jlu.edu.cn/EN/Y2009/V30/I10/2040

15. Reynaud J. A., Malfoy B., Canesson P. Electrochemical investigations of amino acids at solid electrodes. *Journal of Electroanalytical Chemistry and Interfacial Electrochemistry*. 1980;114(2): 195–211. https://doi.org/10.1016/s0022-0728(80)80447-5

16. Horányi G. A direct and indirect radiotracer study of the adsorption of serine at a platinized platinum electrode. *Journal of Electroanalytical Chemistry and Interfacial Electrochemistry*. 1991;304(1-2): 211–217. https://doi.org/10.1016/0022-0728(91)85503-h

17. Mescheryakov V. V., Popova S. S., Raspopova G. A., Bobrova V. A. Eleceokhimicheskoe povedenie aminokislot na Pt-electrode [Electrochemical behavior of amino acids on the Pt electrode]. In: *Actual problems of electrochemical technology: Collection of*

Condensed Matter and Interphases / Конденсированные среды и межфазные границы   2021;23(4): 459–467

E. V. Bobrinskaya et al.   Kinetic regularities of electrochemical oxidation of the methionine anion...

articles by young scientists. Saratov: Sarat. state tech. un-t Publ.; 2000. pp. 244–249. (In Russ.)

18. Gu Y.-J., Sun S.-G., Chen S.-P., Zhen C.-H., Zhou Z.-Y. Adsorption of Serine on Pt single-crystal electrodes in sulfuric acid solutions. *Langmuir.* 2003;23(19): 9823–9830. https://doi.org/10.1021/la034758i

19. Popova S. S., Okisheva N. A., Ryabukhova T. O. Adsorbtsionno-elektrokhimicheskoe povedenie aminokislot na grafitirovannom mednom Cu(C)-elektrode [Adsorption-electrochemical behavior of amino acids on graphitized copper Cu (C)-electrode]. *Bulletin of the Technological University.* 2016;19(9): 155–157. Available at: https://www.elibrary.ru/item.asp?id=25948195 (In Russ.)

20. Shaidarova L. G., Ziganshina S. A., Budnikov G. K. Electrocatalytic Oxidation of cysteine and cystine at a carbon-paste electrode modified with ruthenium(IV) oxide. *Journal of Analytical Chemistry.* 2003;58(6): 577–582. https://doi.org/10.1023/a:1024124421268

21. Reynaud J. A., Malfoy B., Canesson P. Electrochemical investigations of amino acids at solid electrodes. *Journal of Electroanalytical Chemistry and Interfacial Electrochemistry.* 1980;114(2): 195–211. https://doi.org/10.1016/s0022-0728(80)80447-5

22. Tukavkina N. A. *Bioorganicheskaya khimiya* [Bioorganic chemistry: textbook for universities]. Moscow: Drofa Publ.; 2005. 542 p. (In Russ.)

23. Galus V. *Teoreticheskie osnovy elektrokhimicheskogo analisa* [Theoretical Foundations of Electrochemical Analysis]. Moscow: Mir Publ., 1974. 552 p. (In Russ.)

24. Bard A. J., Faulkner L. R. Electrochemical methods: fundamentals and applications. New York: John Wiley & Sons; 2001. 833 p.

25. Laviron E. The use of polarography and cyclic voltammetry for the study of redox systems with adsorption of the reactants. Heterogeneous vs. surface path. *J. Electroanal. Chem.* 1995;382(1-2): 111–127.

Information about the authors

Vvedenskii Alexander Viktorovich, DSc in Chemistry, Professor, Professor at the Department of Physical Chemistry, Voronezh State University, Voronezh, Russian Federation; e-mail alvved@chem.vsu.ru. ORCID iD: https://orcid.org/ 0000-0003-2210-5543.

Elena V. Bobrinskaya, PhD in Chemistry, Associate Professor at the Department of Physical Chemistry, Voronezh State University, Voronezh, Russian Federation; e-mail: elena173.68@mail.ru. ORCID iD: https://orcid.org/0000-0001-7123-4224.

Elena Yu. Sheremetova, second year master's student, Faculty of Chemistry, Voronezh State University, Voronezh, Russian Federation.

Angelina I. Frolova, fifth year student, Faculty of Chemistry, Voronezh State University, Voronezh, Russian Federation.

Translated by Valentina Mittova
Edited and proofread by Simon Cox

Original articles

Entropy features of the PeTa effect during phase transformations of water

G. S. Bordonskiy✉

Institute of Natural Resources, Ecology, and Cryology of the Siberian Branch of the Russian Academy of Sciences,
16 a Nedorezova ul., Chita 672014, Russian Federation

Abstract

The article discusses a hypothesis put forward by V. A. Tatarchenko and M. E. Perelman. According to it, the first order phase transition during vapour condensation or melt crystallisation (PeTa effect) is accompanied by the appearance of nonthermal radiation of the media. The generally accepted point of view is that the latent heat of phase transformation can only be released in the form of heat. When the authors of the hypothesis tried to prove the existence of the effect of nonthermal radiation and considered the facts confirming it, they did not take into account the peculiarities of the initial and final states of the medium (i.e. their entropy). To clarify the physics of the process of liquid crystallisation and to consider the possibility of nonthermal radiation, we studied the peculiarities of water crystallisation and the formation of ice. This is the process the authors referred to in order to prove their hypothesis. It was shown that in various experiments, it is necessary to consider both the state (structure) of the initial water samples and the formed ice, which can consist of various crystalline modifications with chaotic packing. These features of initial and final states, i.e. the entropy of water and ice samples in real experiments and under observed natural phenomena, make it more difficult to assess the characteristics of a possible radiation. The entropy of the initial and final states was determined by the procedure of the system preparation and the peculiarities of the phase transition dynamics. Its values depend on macroscopic parameters, as well as on the microstructure of the media, the determination of which is a very challenging task in each specific case. In addition, in many cases, we have to deal with metastable media, for which it is necessary to take into account the influence of fluctuations on the process of the phase transition. Therefore, the concepts of equilibrium thermodynamics are not applicable to them. However, these are the media where non-heat radiations may occur in accordance with the laws of self-organisation in nonlinear weakly nonequilibrium objects. This work shows a method for preparing low-entropy medium with its subsequent phase transformation into ice. To do so we conducted an experiment which involved freezing concentrated alcohol in order to obtain deeply supercooled water. It appears that to find the characteristics of the PeTa radiation it is necessary to take into account the entropy constraints for each specific case, which will allow assessing the spectrum of possible non-heated radiations and their characteristics.

Keywords: Phase transition, Non-heat radiation, Supercooled water, Entropy

✉ Georgy S. Bordonskiy, e-mail: lgc255@mail.ru

1. Introduction

It is known that the behaviour of chemical reactions is determined by their energy characteristics and the entropy of the reaction products. In particular, the direction of isothermal processes, close to equilibrium, is determined by the Gibbs energy. Energy and entropy constraints also apply to the phase transitions of matter in isolated and closed systems.

A number of works [1–3] detected non-heat radiation during phase transitions of the first kind. This effect was called the PeTa effect after the names of the researchers who described the phenomenon in detail (M. E. Perelman and V. A. Tatarchenko). Phenomena experimentally similar to the PeTa effect were found to enhance microwave radiation during the deformation of ice crystals [4], during phase transformations in ferromagnetic alloys [5], and during sonoluminescence [6].

For example, in terms of energy relations, during the phase transition of a substance from the liquid state into the solid state, the estimated energy of the radiation quanta for a mole of matter according to [1–3] is calculated from the equality: $h\nu = \dfrac{\lambda}{N_A}$, where h is the Planck's constant, ν is the frequency of electromagnetic radiation, N_A is Avogadro number, and λ is the specific heat of the phase transition. A multiphoton radiation process is also possible: $h\nu = n\dfrac{\lambda}{N_A}$, where n is the number of photons in an individual act of radiation. According to the estimates, in most cases the energy quanta are within the infra-red range. Since the explanation of the effect has caused an ambiguous assessment, as was noted in [2], it is of interest to consider other aspects of the issue.

In particular, [1–3] first of all took into account the energy and quantum-mechanical features of the PeTa effect. At the same time, there is a challenging issue regarding the probability of the considered events. It appears that the solution of this issue requires a careful consideration of the initial and final states of the system in terms of changing entropy, i.e. the implementation of the second law of thermodynamics. The entropy of the system is determined by very diverse structural characteristics of the medium and electromagnetic radiation (the volume of the components; the spectrum, polarisation, and the direction of the radiation; the shape of the parts of the system; their mutual arrangement in space, etc.).

The purpose of this work was to use the example of freezing water to consider at a qualitative level the entropy features of the PeTa effect which have not been previously taken into account by researchers.

Problem statement. When considering the PeTa effect, a number of issues arise. 1. It is not clear what proportion of energy can be converted into monochromatic radiation or other types of non-thermal radiation and what their characteristics are (degree of coherence, spectrum, etc.). 2. In what type of processes PeTa and PeTa related radiations can occur (for example, during cavitation, supercooling with a subsequent phase transition, pressure pulses, etc.). It seems that to answer these questions, it is necessary to take into account entropy constraints alongside with the law of conservation of energy and the concept of quantum mechanics about the probability of radiative transitions. It is known that in isolated systems, entropy cannot decrease spontaneously (i.e. the energy of the system cannot be effectively transformed into the energy of monochromatic radiation, which has a lower entropy).

2. Theoretical consideration

As follows from [3], A. D Sakharov (in a private communication) drew attention to the process of freezing supercooled water, which can be accompanied by an energy discharge from the sample by means of radiation resulting in non-thermal radiation. Its registration could serve as an experimental confirmation of the existence of the PeTa effect. This follows from the fact that the relatively fast transition from the liquid to the solid state of bulk water observed in some experiments is impossible since it is not provided for by the process of thermal conductivity.

Let us consider this process of phase transformation in terms of the second law of thermodynamics. Let us denote S_0 as the entropy of the initial state (for a mole of liquid water), S_L as the entropy of the formed ice, and S_E as the entropy of the released energy equal to the

latent heat of the phase transition. Then, S_E will be represented as the sum of two components: $S_E = S_E' + S_E''$, where S_E' is associated with thermal energy, and S_E'' is associated with non-thermal radiation. Then, from the second law of thermodynamics:

$$S_E' + S_E'' + S_L \geq S_0, \text{ or } (S_E' + S_E'') \geq (S_0 - S_L) \qquad (1).$$

If the entire process of phase transition is accompanied by a release of heat (in quasi-static processes), it means that for one mole of a substance $(S_0 - S_L) = \dfrac{\lambda}{T_0}$, where T_0 is the temperature of the phase transition (it is assumed that liquid water is initially at T_0, the same is true for the formed solid fraction).

In case of the PeTa effect and a release of part of the energy (E'') in the form of radiation during transformations with one mole of water, relation (1) is represented as:

$$(S_0 - S_L) \leq \left(\frac{\alpha\lambda}{T_0} + S_E'' \right), \qquad (2),$$

where $\alpha = (0\ldots1)$ characterises the share of thermal energy released during the phase transformation. Full energy: $E = \alpha\lambda + E'' = \alpha\lambda + (1-\alpha)\lambda$. The relation $E''/E = (1 - \alpha)$ characterises the energy output of the PeTa effect.

For the equilibrium phase transition, the value of the difference between S_0 and S_L equals $\dfrac{\lambda}{T_0}$. Then, it follows from (2) that if $\alpha < 1$ (i.e. in the event of radiation), S_E'' given per single unit of energy should not be lower than for the process of heat transfer by contact. This can be verified by using the equal sign in (2) and $(S_0 - S_L) = \dfrac{\lambda}{T_0}$, then

the minimum $S_E'' = \dfrac{(1-\alpha)\lambda}{T_0}$. Hence, the conclusion that there is a thermodynamic exclusion of the PeTa effect or more precisely that the radiation entropy for the equilibrium phase transition cannot be lower than the entropy accompanying the energy released in the form of heat.

This conclusion is quite obvious, since electromagnetic radiation with a narrow band has a low entropy due to its "ordering". $S_E'' \sim \Delta\nu\Delta\phi$

[7], where $\Delta\nu$ is the frequency bandwidth for the electromagnetic radiation and $\Delta\phi$ is the width of the solid angle of the radiation beam. For the case when $\Delta\nu$ or $\Delta\phi$ tend to zero, S_E'' also tends to zero, and relation (2) is not satisfied if α is less than one (for fixed values of S_0 and S_L).

At the same time, in real-life physical systems, the difference $(S_0 - S_L)$ presented in formulas (1, 2) can be reduced by preparing a special initial state leading to a decrease in this difference. To do this, S_0 should be reduced and S_L should be increased. Let us consider both cases.

2.1. Increasing S_L. This is possible if the structure of the formed ice is broken, for example, part of the ice is in an amorphous state or there are mixed structures with a chaotic arrangement of the ice crystals Ih and Ic. In recent works, the discovery of transitional forms during the phase transition of water [8, 9] in the form of the so-called stacking-disordered ice I_{SD} was reported. This is a mixture of Ih (hexagonal) ice and Ic (cubic) ice with a complex random structure. It is believed that previous reports of the experimental determination of cubic ice actually referred to stacking-disordered ice.

2.2. Decreasing S_0. S_0 can be decreased by the supercooling of water. Supercooling in the natural environment was observed for cloudy aerosol down to –37.5 °C [10]. In this case, the entropy of supercooled metastable water S_{0S} is below the initial state S_0 by the value of

$$\Delta S = \int\limits_{T_0}^{T_x} \frac{\delta Q}{T}, \text{ where } \delta Q \text{ is a variation of thermal}$$

energy and T_x is the supercooling temperature. The lower T_x is, the smaller the new value of S_{0S} is. In addition, a reduced entropy can occur due to its decrease determined by the geometry of parts of the system if the water volume is divided into separate small fragments (in the case of hydrosol or films on the surface of pores or small particles).

The integral for ΔS significantly depends on the value of T_x. However, there are additional complications in the case of water. According to numerous studies, the heat capacity of supercooled water at constant pressure tends to soar when approaching –45 °C (at normal atmospheric pressure) [11]. This feature is determined by the influence of the second critical

point of water and the appearance of the Widom line, the locus of increased density and entropy fluctuations of liquid bulk water [11, 12]. Although reaching –45 °C without water crystallisation is very difficult in practice, a decrease in entropy during supercooling is possible, for example, in porous media with nanosized pores, where the supercooling of bulk water to –70 °C was observed [13]. Due to an increase in heat capacity during the supercooling of liquid water, the entropy decreases nonlinearly with the temperature and it plummets near –45 °C. It might be for this reason that the temperature of homogeneous nucleation (i.e. below which there is only crystalline ice) is considered to be approximately –41 °C, i.e. it corresponds to a higher value than the temperature on the Widom line.

In graphical form, the section of the process where the PeTa radiation might occur during the supercooling of water is shown in Fig. 1. The graph has a starting point A. Point 1 corresponds to temperature T_0, at which ice formation for bulk water is observed experimentally. Up to point 2, under certain conditions, there is a possibility of liquid water supercooling with the formation of metastable water with reduced entropy. Region 2–2′ is the area where the PeTa effect might appear, where a nonequilibrium phase transition is observed. 2′–3 is the area of "normal", i.e. equilibrium phase transformation of a liquid into a crystalline body with a release of heat. In other words, compared to area 2′–3, in region 2–2′, more thermal energy is released per unit mass of the formed ice, since the medium is heated from T_x to T_0. Moreover, the heat takes more entropy than for section 2′–3 where the temperature is constant. However, some of the energy may have reduced entropy.

3. Experimental

We studied the freezing of an associated liquid (concentrated ethyl alcohol containing a small amount of water) as an example explicitly demonstrating the peculiarities of the initial state. In this experiment, it was expected to achieve extreme supercooling of water released as a result of the decomposition of the associates during the phase transition of alcohol and, thus, its special initial state with a low entropy. This technique was used for the supercooling of
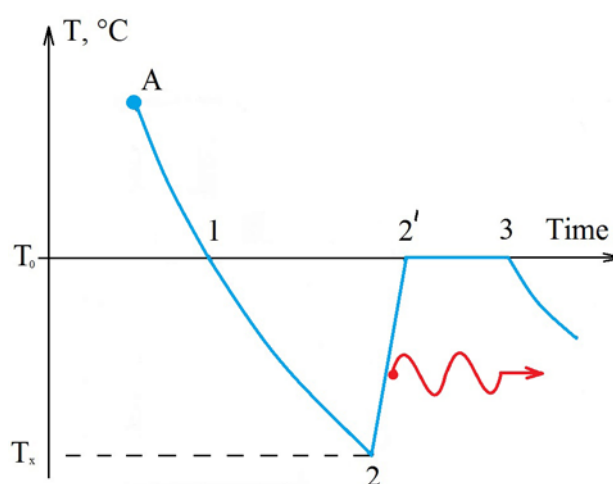
Fig. 1 Graphical representation of water cooling over time and the area where there is a possibility of PeTa radiation during the process of supercooling of a certain volume of water. The wavy arrow marks radiation from region 2–2′ on the temperature versus time graph (non-thermal radiation)

water for the first time. To register the moment of the phase transition and its features, a non-contact method was used. It recorded the electromagnetic radiation passing through the sample in the microwave range. The change in the transmitted power depending on the medium temperature allowed determining the onset of the phase transformation, the rate of the thermal energy release, and the variations of the sample temperature.

During the experiment, a sample of a nanoporous sorbent saturated with alcohol was exposed to radiation in the microwave range at a frequency of 34 GHz and was placed in a waveguide section. The experimental installation included a low-power Gunn diode generator and a crystal detector. The waveguide in which the sample was placed had a rectangular section of 3.4 mm by 7.2 mm. A sample in a 5 mm thick plate-like cuvette with sorbent powder was placed in the waveguide at an angle of ~ 45 degrees to the waveguide axis to eliminate interference effects. The power of the transmitted radiation and the temperature of the medium were measured as a function of time while cooling the sample with cold nitrogen vapour. To prepare the sample, ethyl alcohol and silica gel KSKG were kept in a desiccator to saturate the sorbent. The average size of the KSKG pores was 8 nm.

Ethyl alcohol with a concentration of 95% was used in the experiment. The alcohol contained 5% of water. As a result, its freezing point was about −114 °C. At the moment of the phase transition, a release of deeply supercooled water was expected. Its freezing proceeded according to a scheme similar to that shown in Fig. 1 for area 2–2′. The temperature of the medium was measured using a thermocouple. The temperature accuracy was within several degrees. The time constant of the thermocouple was about 0.1 s. Signals were recorded by an Agilent data acquisition system at a rate of two measurements per second. The measurement results of the transmitted power of microwave radiation depending on the temperature of the medium are shown in Fig. 2.
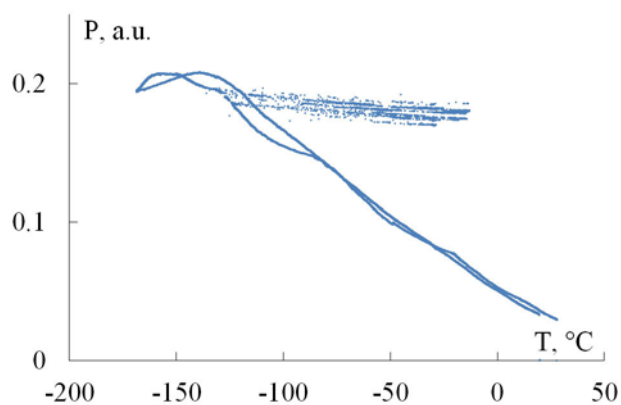
Fig. 2 A change in the power of microwave radiation (*P*) (in relative units) transmitted through the wave-guide section with silica gel saturated with 95% ethyl alcohol depending on the temperature of the medium

When the sample was cooled, multiple temperature jumps were observed during the alcohol crystallisation within a certain time interval when the temperature was below −114 °C. This was accompanied by a rapid heating of the medium. This phenomenon is well known in cryology and is explained by the freezing of nonequilibrium supercooled water. Multiple jumps can be explained by the inhomogeneity of the temperature distribution in the sample volume and by the variations in the parameters of the sorbent with alcohol and the pore space. Since the measurement time between individual points was 0.5 s, it was possible to use points of the graphs to estimate the time of a temperature jump when the released volumes of water were frozen. It was about one minute. The temperature

increment during the jump approached 0 °C (the graphs showed a value equal to approximately −10 °C, this can be explained by the thermal inertia of the medium and the thermocouple, as well as the spatial separation of the thermocouple and active regions where the heat was released). It is obvious that the heat emissions were accompanied by the formation of ice from the state of water with a reduced entropy. Currently, there are no data regarding the entropy of the formed stacking-disordered ice that would allow estimating this value. It was reported that the proportion of cubic ice in the I_{SD} ice can reach 70% [8].

The obtained results confirmed the hypothesis regarding the release of heat by supercooled metastable water with a low initial entropy at temperatures well below the point of the equilibrium phase transition, which creates the preconditions for the appearance of nonthermal radiation.

4. Discussion

There is an additional challenge with regard to the discussed process owing to a hindered emission of quanta into the external medium due to their absorption in the bulk of the liquid and solid phases. Therefore, the PeTa effect can only be observed on the surface layer with the thickness of a skin layer of water. For the thermal infra-red region, the skin layer value for water and ice is about 10 μm. As a result, the equal sign will not work in relation (1). Thus, only sign ">" remains, which complicates the analysis of the system. In this case, nonthermal radiation may not be registered in the experiment.

It is possible that when using porous, weakly moistened sorbents, the radiation emerging from the medium in the IR region may not be significantly attenuated if the matrix material is sufficiently transparent within this wavelength range.

The experiment with concentrated ethyl alcohol showed the possibility of deep supercooling of water that is formed as a result of alcohol freezing and that at the initial moment has a temperature of its phase transformation of −114 °C. In the case of such deep supercooling, water has an extremely low entropy. It is interesting to note that below this temperature, a glass transition of water occurs (at approximately

–130 °C), which is presented in a form of amorphous (disordered) ice.

To perform a similar experiment in order to detect non-thermal electromagnetic radiation, sufficiently fast measuring instruments are required to register electromagnetic fields. In the performed experiment that involved alcohol freezing in a porous medium, temperature jumps were observed over a time of about tens of seconds and the intensity of microwave radiation did not change significantly. This is owing to the thermal inertia of the sorbent matrix and the applied measuring devices: a microwave detector and a thermocouple. The proposed technique can also be used to search lower frequency radiations that penetrate well the medium than radiations in the IR range considered in [1–3], for example, at frequencies below 1 GHz.

As an example of using the entropy approach, let us estimate the energy of nonthermal radiation during the crystallisation of supercooled water in a cloudy aerosol, for example, at a temperature of -10 °C. Let us accept a number of assumptions that simplify the assessment. Let us assume that no stacking-disordered ice is formed and let us not take into account the change in the entropy of water upon its crushing into droplets in aerosol. We also assume that the value of the water heat capacity is invariable at constant pressure (C_p) within the range of 0 to –10 °C. During the process of water supercooling, its entropy decreases by

$$\Delta S = C_p \int_{T_0}^{T_x} \frac{dT}{T}, \text{ where } T_0 = 273 \text{ °C, } T_\text{X} = 263 \text{ °C,}$$

C_P = 4.2 J/(g deg). As a result of calculations, we get ΔS = 0.15 J/(g deg). For an equilibrium process for 1 gram of water, this change will be $S' = \lambda/T_0 \approx 1.2$ J/(g deg), here λ = 333 J/g. The entropy difference ($S_0 - S_\text{L}$) is provided by the outflow of thermal energy. If this difference decreases with the same outflow of energy, part of the energy (i.e. E'') may have zero entropy in the limiting case. This means the PeTa effect is possible.

Relative fraction of non-thermal radiation energy is $E''/\lambda = \Delta S/(S_0 - S_\text{L})$, hence $E'' = T_0\Delta S$. The ratio, i.e. the fraction of the radiation energy per unit mass of matter, will be 0.12 in this example. However, it should be taken into account that in the process of phase transformation, the temperature of the medium rises and its effective temperature will be above –10 °C. If this process is considered to be linear, the effective ΔS will be twice as low. Consequently, the final estimate of the fraction of the energy of nonthermal radiation in the overall balance of the released energy will be 0.06.

It should be noted that low-frequency electromagnetic fields during water freezing at frequencies below 1 MHz were previously recorded, for example in [14], however, their occurrence was interpreted as associated with the relaxation of spatial or surface charges. In addition, at the beginning of the supercooled water freezing, there is a sharp increase in the entropy production (entropy derivative with respect to time) due to a rapid release of energy. According to the thermodynamics of irreversible processes, in this case, ordered structures might appear [15], therefore, the electromagnetic radiation can be studied using these concepts. The same applies to the study of radiation during cavitation [2] and other weakly nonequilibrium processes [6].

5. Conclusions

1. The example of water crystallisation was used to show that the PeTa effect associated with the appearance of nonthermal radiation during the first-order phase transition is only possible in specially prepared systems. Due to a lowered value of entropy (and in the case of decreased energy barrier for the formation of solid phase nuclei), such systems should be in a metastable state. Upon the initiation of a phase transition, a nonequilibrium phase transition will occur in the system, during which nonthermal radiation may appear.

2. It was shown that in the specific case of the phase transition of deeply supercooled water, it is necessary to carefully study the issue regarding the generation of electromagnetic nonthermal radiations, whose characteristics depend on the entropy of the initial and final states. The same applies to any other media with their own unique properties. The entropy of the initial and final states is determined by the sample preparation procedure, the features of the phase transition, and the macro and micro structure of the medium in the initial and final states. These

features will determine a wide range of radiation characteristics (intensity, frequency spectrum, coherence, direction, and polarisation).

Conflict of interests

The author declares that they have no known competing financial interests or personal relationships that could have appeared to influence the work reported in this paper.

References

1. Perelman M. E., Tatartchenko V. A. Phase transition of the first kind as radiation processes. *Physics Letters A*. 2008;372(12): 2480–2483. https://doi.org/10.1016/j.physleta.2007.11.056

2. Tatartchenko V. A., Smirnov P. V., Wu Y. First order phase transitions as radiation processes. *Optics and Photonics Journal*. 2013;3: 1–12. https://doi.org/10.4236/opj.2013.38A001

3. Tatartchenko V. A. Sonoluminescence as the PeTa radiation. *Optics and Photonics Journal*. 2017;7: 27–55. https://doi.org/10.4236/opj.2017.72004

4. Bordonsky G. S., Gurulev A. A., Orlov A. O., Tsyrenzhapov S. V Amplification of microwave radiation in ice upon pressure-induced phase transition. *Technical Physics Letters*. 2012;38(10): 884–886. https://doi.org/10.1134/S1063785012100045

5. Bychkov I.V., Golunov V.A., Kalenov D.S., Kamancev A.P., Kuchin D.S., Koledov V.V., Kuzmin D.A., Meriakri V.V., fon Gratovski S.V., Parhomenko M.P., Mashirov A.V., SHavrov V.G. Sobstvennoe izluchenie i koefficient otrazheniya EMV v diapazone 8 mm splavov $Ni_{2,14}Mn_{0,81}GaFe_{0,05}$ i TiNi v temperaturnom intervale vblizi fazovfh perekhodov 1-go i 2-go roda [The intrinsic radiation and electromagnetic wave reflection coefficient in the range of 8 mm of $Ni_{2,14}Mn_{0,81}GaFe_{0,05}$ and Ti-Ni alloys in the temperature interval near the phase transitions of the 1st and 2nd order]. *Zhurnal radioelektroniki = Journal of Radio Electronics*. 2014;(12): 1–20. Available at: https://elibrary.ru/item.asp?id=23206423 (In Russ.)

6. Tatartchenko V. A. Bubble glow at hydrothermal vents as the PeTa radiation. *Optics and Photonics Journal*. 2019;9(11): 189–217. https://doi.org/10.4236/opj.2019.911017

7. Petrushkin S. V., Samarcev V. V. *Lazernoe ohlazhdenie tverdyh tel* [Laser cooling of solids]. Moscow: Fizmatlit. Publ.; 2004. 224 p. (In Russ.)

8. Salzmann C. G. Advances in the experimental exploration of water's phase diagram. *The Journal of Chemical Physics*. 2019;150(6): 060901. https://doi.org/10.1063/1.5085163

9. Leoni P., Russo J. Non-classical nucleation pathway in stacking-disordered crystals. *Physical Review X*. 2021;11(3). https://doi.org/10.1103/physrevx.11.031006

10. Rosenfeld D., Woodley W. L. Deep convective clouds with sustained supercooled liquid water down to –37.5 °C. *Nature*. 2000;405(6785): 440–442. https://doi.org/10.1038/35013030

11. Gallo P., Amann-Vinkel K., Angell C. A., Anisimov M. A., Caupin F., Chakravarty C., Lascaris E., Loerting T., Panagiotopoulos A. Z., Russo J., Sellberg J. A., Stanley H. E., Tanaka H., Vega C., Xu L., Petterson L. G. M. Water: a tail of two liquids. *Chemical Review*. 2016;116(13): 7463–7500. https://doi.org/10.1021/acs.chemrev.5b00750

12. Bordonskiy G. S., Gurulev A. A. Regarding physical and chemical transformations with the involvement of water near –45 °C. *Kondensirovannye sredy i mezhfaznye granitsy = Condensed Matter and Interphases*. 2019;21(4): 478–489. https://doi.org/10.17308/kcmf.2019.21/2359

13. Limmer D. T, Chandler D., Phase diagram of supercooled water confined to hydrophilic nanopores. *Journal of Chemical Physics*. 2012;137(4): 044509/11. https://doi.org/10.1063/1.4737907

14. Shibkov A. A. Intrinsic electromagnetic radiation of growing ice. *Vestnik Tambovskogo Universiteta = Tambov University Reports. Series Natural and Technical Sciences*. 2009;14(6): 1192–1195. Available at: https://elibrary.ru/item.asp?id=13067701 (In Russ., abstract in Eng.)

15. Prigozhin I. *Introduction to thermodynamics of irreversible processes*. New York: Interscience Publishers; 1961. 119 p.

Information about the authors

Georgy S. Bordonskiy, DSc in Physics and Mathematics, Professor, Chief Researcher of the Laboratory of Geophysics of Cryogenesis, Institute of Natural Resources, Ecology, and Cryology of the Siberian Branch of the Russian Academy of Sciences; Chita, Russian Federation; e-mail: lgc255@mail.ru. ORCID iD: https://orcid.org/0000-0002-0009-0822.

Translated by Irina Charychanskaya
Edited and proofread by Simon Cox

Condensed Matter and Interphases

Original articles

Cylindrical model of electrochromic colouration of hydrated vanadium pentoxide thin films with point contacts

P. P. Boriskov[1✉], S. V. Burdyukh[1,2], O. Ya. Berezina[1]

[1]*Petrozavodsk State University,
33 Lenina prospekt, Petrozavodsk 185910, Russian Federation*

[2]*Institute of Geology of the Karelian Research Centre of the Russian Academy of Sciences
11 Pushkinskaya ul., Petrozavodsk 185910, Russian Federation*

Abstract

This article analyses experiments on the kinetics of the internal electrochromism of thin (micron) films of hydrated vanadium pentoxide xerogel with point contacts. It describes a cylindrical model of electrochromic colouration, which was used to evaluate the concentration of the colour centres in the initial film and after additional hydrogenation of this film by plasma-immersion ion implantation.

When we compared the calculated values of the concentration of colour centres with the equilibrium concentration of protons in the xerogel, we saw that the mobility of the protons migrating from the depth of the film to the cathode region, which are involved in the electrochemical reaction, was not a determinant of the electrochromism kinetics.

The rate of electrochromic colouration could be increased by the formation of layered film structures based on hydrated vanadium pentoxide, which have increased overall electron conductivity and, as a consequence, low faradaic resistance of the electrochromic cathodic reaction.

Keywords: Electrochromism, Hydrated vanadium pentoxide, Plasma-immersion ion implantation, Ion current kinetics

✉ Petr P. Boriskov, e-mail: boriskov@petrsu.ru

Condensed Matter and Interphases / Конденсированные среды и межфазные границы   2021;23(4): 475–481

P. P. Boriskov et al.   Cylindrical model of electrochromic colouration of hydrated vanadium pentoxide thin...

1. Introduction

Electrochromism is a reversible change in the optical properties of a material (light transmission and colour) under the influence of an electric field, as a result of the injection/extraction of hydrogen or alkali metal ions [1]. In most cases, the effect takes place in the presence of an external electrolyte, which acts as one of the electrodes (anode) and injects ions into the electrochromic material. This type of electrochromism is used in electrochromic indicators and gas sensors [1–3].

Previously we have discovered and described [4, 5] internal electrochromism (IEC) without contact with the electrolyte in thin films of hydrated vanadium pentoxide (HVP) xerogel $V_2O_5 \times nH_2O$. When a step voltage pulse is applied between two point electrodes touching the surface of the film, a coloured (red) spot is formed around the cathode (an example is given in coloured figure 3 [6]). The spot usually remains coloured for many hours, but disappears a few minutes after a back (inverse) voltage is applied. Internal electrochromism has a threshold character, i.e., it does not occur below a certain voltage level. The more the electrochromic cell voltage exceeds the threshold level, the stronger the effect becomes: the cathode spot has a deeper red colour, a larger area, and grows faster. In a fully dried HVP sample (water removed), which corresponds to the V_2O_5 structure, internal electrochromism was practically absent [4–6].

There is also no electrochromism in hydrogen vanadium bronzes, where the maximum oxidation state of vanadium is 4. On the other hand, a number of higher poly-vanadium acids (the oxidation state of vanadium is 5) are red in acid solutions. In this regard, we hypothesised [5] that the cause of electrochromism in HVP is the migration of protons to the cathode region, followed by the formation of higher poly-vanadium acid fragments, as colour centres of the type:

$$n\text{H}^+ + \left[\text{polyvanadat groups}\right] + ne^- \rightarrow$$
$$\rightarrow \left[\text{polyvanadat acids}\right]. \tag{1}$$
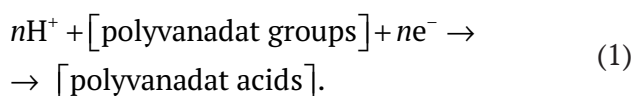
Defects containing fragment ions of, for example, hexavanadate $V_6O_{17}^{-4}$, which form molecules (clusters) of hexavanadic acid ($H_4V_6O_{17}$)

under reaction (1), can act as poly-vanadate groups.

X-ray studies of HVP show [7] that the material has a quasi-one-dimensional layered structure, where crossed fibres, predominantly oriented along the substrate, are connected by water molecules. If we compare the ion and electron components of the conductivity of HVP, we can see that this material exhibits mixed ion-electron charge transfer [8–10]. The electron conductivity of HVP has a pronounced activation character with very low mobility [9] and depends on the content of V^{4+} ions, which are found in the defects and impurities. The ion component of conductivity, in turn, depends on the water content in HVP, it decreases sharply with a decrease in the water concentration [9]. The migration of protons through ordered hydrogen-bonded water molecules is thought to be the mechanism of ion conductivity. However, there are suggestions [10] that protons can also exhibit a hopping migration through the vanadium-oxygen (V_2O_5) HVP layers.

In this article, we analysed our experiments [6, 11] on the kinetics of internal electrochromism and on the passing current in a thin-film HVP structure with point contacts upon additional (homogeneous and inhomogeneous) hydrogenation of the xerogel by plasma-immersion ion implantation (PIII). Using a cylindrical model of electrochromic colouration of the film, we estimated the concentration of electrochromism colour centres in HVP.

2. Experimental

The HVP films were synthesised by the liquid-phase sol-gel method [1–3, 5]. In our experiments, vanadium pentoxide gel with a thickness of $h \sim 1$ μm was applied onto a glass substrate. Then, the samples were dried for a day at room temperature, so that their composition with partially removed water, according to the results of X-ray analysis, corresponded to the $V_2O_5 \times 1.8H_2O$ phase [6].

The samples were hydrogenated (doped with hydrogen) in a hydrogen plasma by PIII [6]. The PIII unit (Fig. 1) consists of a chamber with a sample holder inside, a vacuum system, a plasma generator, a high-voltage pulse system, and a gas supply system. A plasma source with a heated

Condensed Matter and Interphases / Конденсированные среды и межфазные границы   2021;23(4): 475–481

P. P. Boriskov et al.   Cylindrical model of electrochromic colouration of hydrated vanadium pentoxide thin...
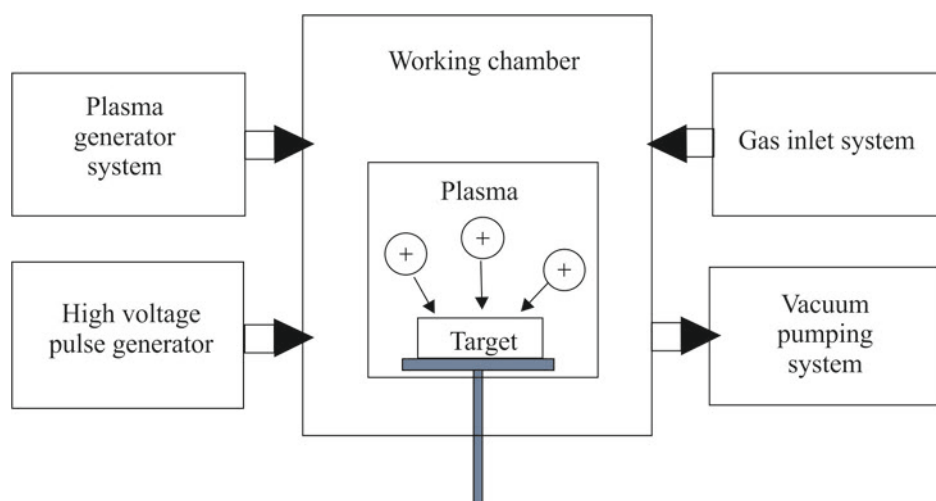
Fig. 1. The PIII unit layout

cathode was attached to one of the flanges of the chamber to produce an electric arc in the chamber. A vacuum system based on the NVR-16D fore-vacuum pump and the 01 AB-1500-004 turbomolecular pump allowed the pressure in the chamber to be reduced to 10^{-4} Pa. Voltage pulses were applied to the sample holder through the HVS-10-10 solid-state switch. Gas was injected into the chamber using a gas supply system of two FC-260 regulators.

Ions were implanted from plasma (at 4 Pa), when negative high-voltage pulses (2 kV) with a frequency of 1.7 kHz were applied to the sample for 5 µs. The current pulse amplitude was 50 mA and the total treatment time was 30 min. The implantation dose was approximately $\sim 3.5 \cdot 10^{17}$ cm^{-2}. During hydrogenation, part of the sample could be covered by a rectangular mask to avoid protons entering that area. The area of the film implanted with hydrogen changed colour from grey-green to dark green. The colour change was due to a partial modification of HVP under the PIII treatment. As determined by nuclear magnetic resonance, it caused the increase in the concentration of V^{+4} [6].

We recorded the growth rate of the cathode spot area (Fig. 2) and the kinetics of the current (Fig. 3) between the clamping point contacts with radii of $r_o \sim 0.1$ mm and distance $d = 3$ mm at voltage $U_o = 30$ V in three variants of experiments: (I) – the original HVP film, (II) – the film where the cathode region is the original HVP and the anode region is the hydrogenated HVP, and (III) – the fully hydrogenated film. Note that the area

of the electrochromic colouration over time was determined using the images made by a digital camera with a 1 s sweep length; the current was recorded using a Keithley 2400 source measure unit.

At the beginning of the electrochromic colouration process, a red spot was formed very quickly (in a few seconds) around the cathode (see coloured Fig. 3 in [6]). The spot was perfectly round with a radius of ~ 0.4–0.5 mm. Then it slowly increased, reaching its final size (~ 2 mm) 5–6 minutes after the voltage was turned on. The colouration rate and the depth of red differed significantly between the experimental variants. Internal electrochromism was most pronounced in the mixed variant (II): it had the maximum
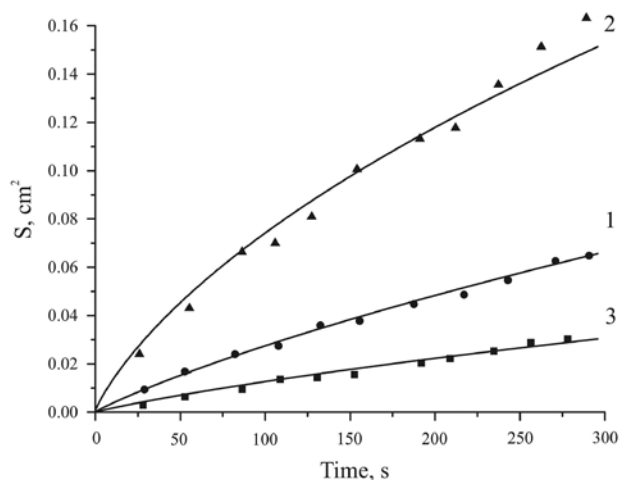
Fig. 2. The growth of the electrochromic spot area over time. *1* – initial film (experiment I), *2* – mixed film (experiment II), and *3* – fully hydrogenated film (experiment III)

Condensed Matter and Interphases / Конденсированные среды и межфазные границы   2021;23(4): 475–481

P. P. Boriskov et al.   Cylindrical model of electrochromic colouration of hydrated vanadium pentoxide thin...
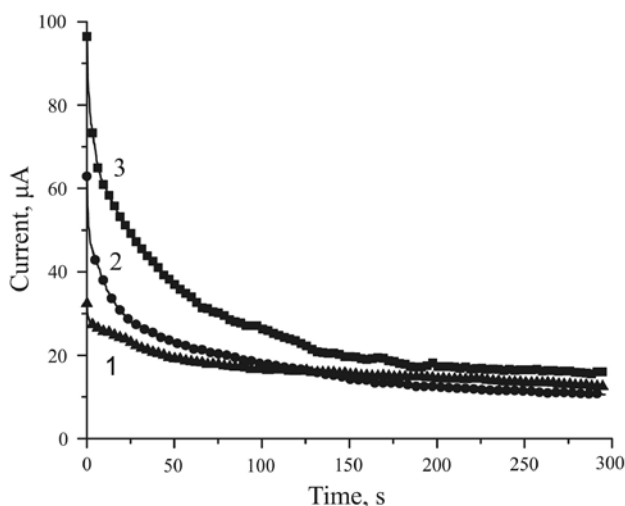
Fig. 3. Kinetics of the current passing through the HVP films: *1* – initial film (experiment I), *2* – mixed sample (experiment II), and *3* – fully hydrogenated film (experiment III)

growth rate of the spot area (Fig. 2, curve *2*), the colour of the spot was bright red. The effect was weaker in the original film (Fig. 2, curve *1*) and even less pronounced in the fully hydrogenated film (Fig. 2, curve *3*).

The currents recorded (Fig. 3) in all variants of the experiments (I–III) first increased sharply (in a few µs) to a maximum. Then they almost exponentially decreased to their stationary values. The largest current peak was recorded in the fully hydrogenated film (Fig. 3, curve *3*), and the smallest one was registered in the original film (Fig. 3, curve *1*).

3. The model of electrochromic colouration

The total recorded current $I(t)$ (Fig. 3) in HVP, as in a material with mixed electron-ion conductivity, consists of a purely electron current passing through the film, which we regard as constant, and of an ion current $I_p(t)$ changing over time. The ion current involves additional electrons from the external circuit in charge transfer. These electrons are involved in the IEC electrochemical reaction (1), in the charging of the double layer at the interface of the electrodes, and, possibly, in the process of partial adsorption of hydrogen at the cathode. Since the last two processes can be neglected for a point contact with a very small area (~0.03 mm²), the ion current is determined exclusively by the electrochemical

reaction (1). This reaction gradually slows down, and with bigger time values (actually more than 300 s) the electrochromic colouration (Fig. 2) stops. Then we can assume that the purely electronic component $I(t)$ should be equal to the stationary current $I(t \rightarrow \infty) \equiv I_{st}$, when the ionic current disappears, that is, $I_p(t) = I(t) - I_{st}$. In turn, at any given point of time the area of the coloured spot $S(t)$ must be proportional to the proton charge $Q(t)$ involved in the IEC reaction, and its growth rate must be proportional to the ionic current:

$$\frac{dS(t)}{dt} = \alpha \frac{dQ(t)}{dt} = \alpha I_p(t), \qquad (2)$$

where the proportionality coefficient α is the electrochromism efficiency parameter [11].

The electrochromic spot is almost circular in shape, centred on the cathode. This indicates that colour centres are formed under the influence of the field in the region around the cathode, which has almost a cylindrical shape (Fig. 4). Indeed, the distance between the contacts is much greater than the film thickness (d = 3 mm $\gg$ h = 1 µm). This is the condition for the cylindrical geometry of current distribution from point electrodes. It can be observed, for example, in experiments on probe measurement of thin film conductivity on dielectric substrates [12].

Then we assumed a simplified model for the electrochromic colouration region in the form of a cylinder around the cathode with a radius
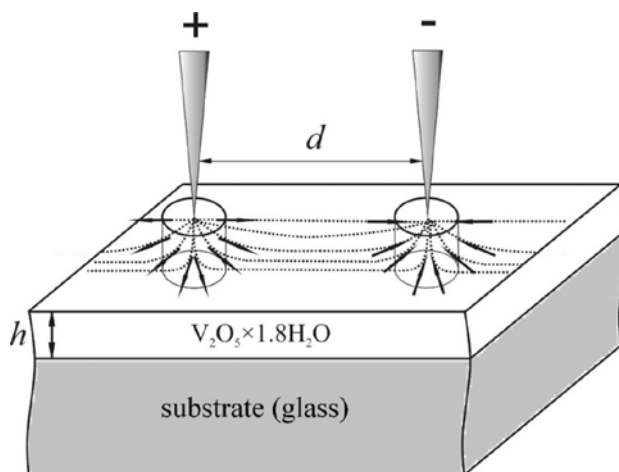
Fig. 4. Layout of an HVP-based electrochromic film on a dielectric substrate (glass) with point (probe) contacts. Around electrodes of cylindrical geometry, the current lines are shown

Condensed Matter and Interphases / Конденсированные среды и межфазные границы   2021;23(4): 475–481

P. P. Boriskov et al.   Cylindrical model of electrochromic colouration of hydrated vanadium pentoxide thin...

$R(t)$ and a height equal to the film thickness h. The growth of the observed spot is the internal electrochromism reaction (1) process with a moving boundary, which is the lateral surface of this cylinder with an area $S_L(t) = 2\pi R(t)h$. We believe that at any given time the concentration of the resulting colour centres inside the cylinder is N_s and outside the cylinder it is zero. Then the ion current is:

$$I_p(t) = J_p(t) \cdot S_L(t) = qN_s \frac{dR(t)}{dt} \cdot 2\pi R(t)h, \qquad (3)$$

where the ion current density $J_p(t)$ is the product of the ion charge concentration qN_s (q is the elementary charge) inside the cylinder by the velocity of its boundary motion ($dR(t)/dt$).

The second equality in (3) can be expressed as:

$$qN_s \frac{dR(t)}{dt} \cdot 2\pi R(t)h = qN_s \frac{dS(t)}{dt}h, \qquad (4)$$

which establishes a direct relationship between the ion current and the growth rate of the area of the electrochromic spot (the area of the upper base of the cylinder) $S(t) = \pi R^2(t)$:

$$I_p(t) = I(t) - I_{st} = qN_s h \frac{dS(t)}{dt}. \qquad (5)$$

We compared (2) and (5) and determined that the electrochromism efficiency parameter was inversely related to the concentration of the formed colour centres N_s:

$$\alpha = \frac{1}{qN_s h}. \qquad (6)$$

Thus, having determined the growth rate of the spot area from the curves in Fig. 2, and the corresponding ion currents by the experiments described in Fig. 3, we obtained the electrochromism efficiency parameters and the concentration of the formed colour centres from relations (5) and (6). The results from the calculation are shown in Table 1. The N_s values are also compared with the estimated values of

the equilibrium concentration of HVP protons (N_o) for all variants of experiments (I–III).

We calculated the N_o value for the original film (experiment I) based on the HVP chemical formula ($V_2O_5 \times 1.8H_2O$), obtained using X-ray diffraction [5]. Since the volume of the tetragonal unit cell of HVP is $V_e = a \times b \times c = 1.118 \cdot 10^{-24}$ cm^3 ($a = 11.5$ Å, $b = 3.6$ Å, $c = 27$ Å), and the number of hydrogen atoms is 18 [10], then N_o is approximately equal to $1.6 \cdot 10^{22}$ per 1 cm^3. According to the data of thermogravimetric analysis [6], for the fully hydrogenated film (experiment III) with an implantation dose of $3.5 \cdot 10^{17}$ cm^{-2}, this value decreases by ~ 2.6 times. Apparently, this is due to the partial evaporation of interlayer water when the film is heated (to about 100 °C [6]) during hydrogenation.

The sample in experiment II is inhomogeneous: the cathode region is the initial HVP film, and the anode region is the hydrogenated HVP film. Both parts of the film, as determined above, have different concentrations of protons. Inevitably, there must be a diffusion flux near their boundaries to equalize these concentrations. If we take into account the time between the PIII treatment and experiment II (dozens of minutes), as well as the heating of the film subjected to PIII, which also affects the cathode (untreated) region, it becomes clear that such a redistribution of hydrogen is bound to occur. Then, we assumed the average of the concentrations estimated above for variants I and III to be the equilibrium concentration of protons in experiment II.

As can be seen from Table 1, the values obtained for the concentration of the formed colour centres N_s in all experiments are more than one order of magnitude lower than the equilibrium concentration of HVP protons N_o. Thus, there are more than enough protons for the IEC reaction (1) even within the cylindrical region of electrochromic spot. It can then be assumed that the mobility of the protons migrating into

Table 1. Parameters for electrochromism efficiency and concentration of colouring centres and HVP protons

Parameters	Experiment I	Experiment II	Experiment III
α, cm^2/C	130	320	610
N_s, cm^{-3}	$3 \cdot 10^{20}$	$7.4 \cdot 10^{20}$	$1.4 \cdot 10^{20}$
N_o, cm^{-3}	$1.6 \cdot 10^{22}$	$1.1 \cdot 10^{22}$	$6.2 \cdot 10^{21}$

Condensed Matter and Interphases / Конденсированные среды и межфазные границы   2021;23(4): 475–481

P. P. Boriskov et al.   Cylindrical model of electrochromic colouration of hydrated vanadium pentoxide thin…

the cathode region from the depth of the film is not essential for the kinetics of electrochromism. The factor determining the IEC rate should be the faradaic contact resistance of electrons [13] involved in the electrochemical reaction.

Thus, for the initial and inhomogeneously hydrogenated films (experiments I and II), the concentration of potential colour centres should be the same, since the cathode region in experiment II is not subjected to PIII and is identical to the initial film. However, in variant II, a significantly (almost 2.5 times) higher growth rate and concentration of the colour centres are observed (Table 1). As pointed out in [11], the reason for the increased efficiency of electrochromism after heterogeneous hydrogenation is the decrease in the electron resistance of the anode region of the film subjected to PIII. Consequently, the faradaic conductivity of the IEC reaction increases.

On the other hand, in a film fully treated with PIII (experiment III), internal electrochromism is very weak, with a low concentration of colour centres (Table 1). In our opinion, this is due to the plasma-ion modification of the material, when the action of the proton flux on the film partially restores V^{+5} to V^{+4} in HVP. This leads to an increase in the electron (hopping) conductivity of HVP (an increase in the V^{+4} concentration) and an increase in the total current (see Fig. 3, curve *3*). At the same time, the concentration of poly-vanadate colour centres, in which vanadium should be pentavalent, decreases [5].

4. Conclusions

Having analysed the internal electrochromism in HVP, we made the following conclusions

1. A thin-film electrochemical cell with point (probe) contacts can be represented by a simple cylindrical model of ion current distribution. Based on this model, we can assess the reaction rate through the visualisation of the electrochemical reaction, as is the case with electrochromism in HVP. The concentration of the forming reagents (colour centres) can be estimated from the current kinetics. The concentration of colour centres in the HVP xerogel films generally corresponds to a highly disordered material structure with a large number of defects, which can be poly-vanadate group fragments (the oxidation state of vanadium is +5).

2. The determining factor in the kinetics of electrochromism in HVP is not the mobility and concentration of protons migrating from the depth of the film to the cathode region, but the rate of the IEC reaction, which depends on the faradaic contact resistance. Therefore, additional hydrogenation of HVP alone cannot enhance electrochromism, even if we reduce the role of negative PIII factors, such as through the intense heating of the films with partial evaporation of water and reduction of V^{+5} to V^{+4}. In our opinion, the IEC rate in HVP could be increased by forming electrochromic cells with increased electronic conductivity. For example, they could have alternating layers of initial HVP and PIII-treated films, as well as other hydrogenated materials with mobile protons and high electron conductivity.

Author contributions

P. P. Boriskov – research concept, methodology development, text writing, and final conclusions. S. V. Burdyukh – research concept and experiment. O. Ya. Berezina – scientific leadership, sample synthesis, and text editing.

Conflict of interests

The authors declare that they have no known competing financial interests or personal relationships that could have influenced the work reported in this paper.

References

1. Monk P. M. S., Mortimer R. J., Rosseinsky D. R. *Electrochromism and electrochromic devices.* Cambridge University Press; 2007. 512 p. https://doi.org/10.1017/cbo9780511550959

2. Chernova N. A., Roppolo M., Dillonb A. C, Whittingham M. S. Layered vanadium and molybdenum oxides: batteries and electrochromics. *Journal of Materials Chemistry.* 2009;19(17) 2526–2552. https://doi.org/10.1039/B819629J

3. Schneider K., Lubecka M., Czapla A. V_2O_5 thin films for gas sensor applications. *Sensors and Actuators B: Chemical.* 2016;236: 970–977. https://doi.org/10.1016/j.snb.2016.04.059

4. Yakovleva D. S., Malinenko V. P., Pergament A. L., Stefanovich G. B. Electrical and optical properties of thin films of hydrated vanadium pentoxide featuring electrochromic effect. *Technical Physics Letters.* 2007;33(12): 1022–1024. https://doi.org/10.1134/S1063785007120115

Condensed Matter and Interphases / Конденсированные среды и межфазные границы   2021;23(4): 475–481

P. P. Boriskov et al.   Cylindrical model of electrochromic colouration of hydrated vanadium pentoxide thin...

5. Yakovleva D. S., Pergament A. L., Berezina O. Ya., Boriskov P. P., Kirienko D. A., Pikulev V. B. Internal electrochromism in vanadium pentoxide xerogel films. *Materials Science in Semiconductor Processing.* 2016;44: 78–84. https://doi.org/10.1016/j.mssp.2016.01.003

6. Burdyukh S. V., Berezina O. Ya., Pergament A. L., Lugovskaya L. A., Kolyagin Yu. G. Effect of hydrogenation on the optical properties and internal electrochromism in vanadium pentoxide xerogel films. *Thin Solid Films*. 2018; 656: 22–29. https://doi.org/10.1016/j. tsf.2018.04.026

7. Livage J. Vanadium pentoxide gels. *Chemistry of Materials...* 1991;3(4): 578–593. https://doi. org/10.1021/cm00016a006

8. Bullot J., Gourier D., Gallais O., et al. Thin layers deposited from V_2O_5 gels. l. A conductivity study. *J. Non-Cryst. Solids*. 1984;68(1): 123–134.

9. Barboux P., Baffier N., Morineau R., Livage J. Diffusion protonique dans les xerogels de pentoxyde de vanadium. *Solid State Ionics*. 1983, v. 9-10, 1073–1080. https://doi.org/10.1016/0167-2738(83)90133-9

10. Sanchez C., Bobonneau F., Morineau R., Livage J. Semiconducting properties of V_2O_5 gels. *Philosophical Magazine B*. 1983;47(3): 279–290. https://doi.org/10.1080/13642812.1983.9728310

11. Burdyukh S. V., Berezina O. Y., Boriskov P. P., Pergament A. L., Yakovleva D. S. Kinetics of coloration in hydrogenated vanadium pentoxide films under an internal electrochromic effect. *Technical Physics Letters*. 2018;44(9): 779–782. https://doi. org/10.1134/S1063785018090043

12. Mazda F. F. *Electronic instruments and measurement techniques*. New York: Cambridge University Press; 1987., 312 p.]

13. Bard A. J., Faulkner L. R. *Electrochemical methods: fundamentals and applications*. Toronto: John Wiley & Sons, Inc.; 2001. 833 p.

Information about the authors

Petr P. Boriskov, PhD in Physics and Mathematics, leading engineer, Institute of Physics and Technology, Petrozavodsk State University, Petrozavodsk, Russian Federation; e-mail: boriskov@petrsu.ru, ORCID iD: https://orcid.org/ 0000-0002-2904-9612.

Olga Ya. Berezina, PhD in Physics and Mathematics, Assistant Professor at the Department of General Physics, Petrozavodsk State University, Petrozavodsk, Russian Federation; e-mail: berezina@petrsu.ru, ORCID, iD: https://orcid.org/ 0000-0003-4055-5759.

Sergei V. Burdyukh, PhD in Physics and Mathematics, research fellow, Institute of Geology of the Karelian Research Centre of the Russian Academy of Sciences, Petrozavodsk, Russian Federation; e-mail: burduch@gmail.com. ORCID, iD: https://orcid.org/0000-0002-1954-7300.

Condensed Matter and Interphases

Original articles

High-temperature spectrophotometry of indium chloride vapours as a method of study of the In – Se system

N. Yu. Brezhnev, A. V. Kosyakov, A. V. Steich, A. Yu. Zavrazhnov⊠

Voronezh State University,
1 Universitetskaya pl., Voronezh 394018, Russian Federation

Abstract

The goals of this work are as follows: (a) searching for a method of study of the In – Se system taking into account the specified problems and difficulties, (*b*) choosing a way for the instrumental implementation of this method, and (*c*) obtaining experimental evidence that this method and its implementation are promising.

The choice of the In – Se system is related to the fact that indium selenides, layered structures and semiconductor phases with stoichiometric vacancies, are promising from the point of view of materials science. This choice is also related to the use of binary precursors for the synthesis of heterostructures based on CIS compounds.

We studied the possibility of applying the auxiliary component method using the equilibrium with the participation of indium chloride vapours which were made to contact the condensed phases of the In – Se system. Equilibrium was achieved using high-temperature spectrophotometry of the vapour phase. The experiment had two stages. During the first stage we determined the absorption characteristics of the $InCl_3$ vapour. During the second stage we studied the heterogeneous equilibrium of the unsaturated indium chloride vapour with several phases of the In – Se system. Over the course of the study, we determined the molar attenuation coefficients of the $InCl_3$ vapour and plotted the temperature dependences of the value $K_P^{\#}$.

It was found that the phase composition of the alloys significantly influences the position of the corresponding lines on the $K_P^{\#}$–T diagram, which proves the possibility of using the suggested auxiliary component method in its specific instrumental (spectrophotometric) implementation in order to study the In – Se system. We also showed the additional possibilities of using this method for plotting *T-x* diagrams of binary systems in such high-temperature areas where the binary solid phase is in equilibrium with the melt. This application of the method is related to the solubility of a vapour of an auxiliary component (chlorine in the form of indium chlorides) in the melts of binary phases (indium selenides).

Keywords: High-temperature spectrophotometry, In – Se system, Phase diagram, Heterogeneous equilibria, Indium chlorides

⊠ Alexander Yu. Zavrazhnov, e-mail: alzavr08@rambler.ru

Condensed Matter and Interphases / Конденсированные среды и межфазные границы   2021;23(4): 482–495

N. Yu. Brezhnev et al.   High-temperature spectrophotometry of indium chloride vapours…

1. Introduction

The systems where non-equilibrium and/or metastable states easily emerge but are hard to eliminate cause most difficulties in the studies of phase diagrams. Among the examples of them are A(III) – B(VI) systems. For instance, metastable states (and a corresponding metastable *T-x* diagram) were observed at heating rates over ~10 K/min during the study of the In – S system using differential thermal analysis (DTA). The elimination of non-equilibrium states in this system required thorough dispersion and extensive annealing of the samples. This problem is even more serious for a similar chalcogenide In – Se system studied in this article. This was also proved by the results of our preliminary DTA experiments. The data on the system are incomplete and controversial, which indirectly indicates the same problem. The existence of In_4Se_3, $InSe$, In_6Se_7, and $In_{2.66}Se_4$ (or β-In_2Se_3) and various polymorphic forms of In_2Se_3 of almost stoichiometric composition is obvious [1–7]. Several contemporary studies also justify the existence of two more selenides on the phase diagram, In_9Se_{11} and In_5Se_7 [3–6] (Fig. 1). At the same time, we found no data on the assignment of these phases to certain structures (in [5, p. 459] they only mention the In_5Se_7 phase as a cubic one but without any argumention or details). In calculations performed in 2020 [7] the *T-x*

diagram of the In – Se system was presented without these two phases. The situation with the extent of the homogeneity ranges and, particularly, with the limits of the temperature stability of indium selenides seems even more confusing [5, 6].

Such disagreement in the published data is not unexpected if we take into account the fact that non-equilibrium and metastable states emerge easily. The reasonable approach for this system is the following: the study of phase equilibria must be preceded by the development of appropriate methods and methodologies. The goals of this work are the following:

(*a*) searching for a method of study of the In – Se system taking into account the specified problems and difficulties, (*b*) choosing a way for the instrumental implementation of this method, and (*c*) obtaining experimental evidence that this method and its implementation are promising. The goals were considered to be achieved only in case the reproducibility was proved and the results were internally consistent.

The In – Se system was not chosen randomly but due to the expected high materials science prospects of:

– Layered phases (InSe and some modifications of In_2Se_3) as 2D materials.

– Semiconductor compounds with the so-called stoichiometric vacancies.
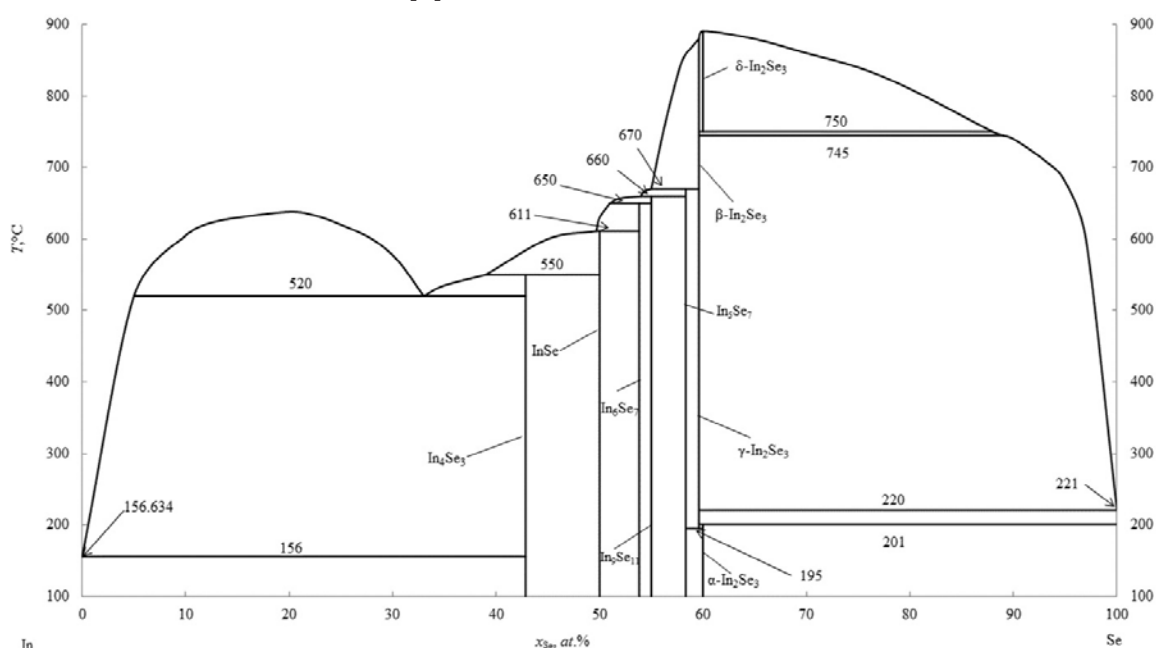
Fig. 1. *T-x* diagram of the In –Se system according to the review article [1]

Condensed Matter and Interphases / Конденсированные среды и межфазные границы   2021;23(4): 482–495

N. Yu. Brezhnev et al.   High-temperature spectrophotometry of indium chloride vapours...

– Binary precursors for the synthesis of heterostructures based on CIS compounds.

1.1. The applied method

The auxiliary component method and the choice of the component. As for the systems where it is difficult to eliminate non-equilibrium states, we can use the *auxiliary component method* [8, 9], the idea of which is to bypass the equilibrium that is hard to achieve with the participation of the components of the initial system (in this case In – Se) and replace it with an equilibrium with the participation of an auxiliary component introduced to the system. Chlorine in the form of indium chlorides was chosen as this component.

Such an experiment, where indium chlorides in the state of unsaturated vapour would interact with the studied indium selenides, can be organised in a closed isothermal system. Based on the data from [9, 10], it was assumed and then confirmed that such an interaction leads to a heterogeneous equilibrium

$$2In'' + InCl_3' \rightleftarrows 3InCl', \qquad (1)$$

$$K_P^\# = \frac{(p_{InCl})^3}{p_{InCl_3}}. \qquad (2)$$

In (1) the "″" symbol stands for the condensed state of the substance, while "′" stands for the vapour; so In″ corresponds to indium in the composition of condensed phases of the In – Se system. Selenium (Se″) chemically bound by indium must be inert with respect to the vapour of indium chlorides. Such inertness was expected due to the fact that the vapours of indium chlorides dissociate considerably at high temperatures [11] so we did not record them on the spectra, while ternary phases in the In – Se – C system were formed only in an oxidising environment (the interaction of In_2Se_3 + $InCl_3$ with an excess of selenium [12]).

The exchange of substance between various condensed phases of the In – Se system can be achieved if the reaction (1) proceeds mainly in the forward or backward direction. The state of equilibrium is achieved as a result of the transfer of chemical substances. This allows obtaining a sample of the studied binary system (in this case In – Se) that is internally in equilibrium, while the correct determination of temperature dependences of the $K_P^\#$ values for the series of various compositions in the state of equilibrium

allows extracting the information on the phase diagram of this system. The $K_P^\#$ value links the partial pressures of vapours in equilibrium (1) according to the expression (2), that is similar to the "classic" equilibrium constant K_p. However, unlike the latter, the "pseudoconstant" $K_P^\#$ depends not only on the temperature (T) but also on the composition (x) of the condensed phase that is in equilibrium with the vapour. (Also, $K_P^\#$ depends on pressure P, although this dependence is usually insignificant.) The thermodynamic meaning of the $K_P^\#$ value and its connection with the chemical potential of indium participating in reaction (1) were analysed in more detail in [8, 10, 13]. In these works it was also stated that $K_P^\#–T$ diagrams look very similar to classic $P–T$ diagrams obtained without the introduction of an auxiliary component. The analysis of $K_P^\#–T$ diagrams, in particular, can help to identify phase relations in the studied binary system.

The experiments were performed at temperatures of 400–700 °C for the compositions with the selenium content not extending 60 mol%. Under these conditions, the selected method is also convenient due to the fact that the pressure of their "own" vapours (In_2Se, Se_2) on indium selenides is low (P <1 Pa) [5] and does not hinder the registration of partial pressures of molecular forms created by the auxiliary component. Chlorine was chosen as the auxiliary component due to the following:

a) Low solubility of chlorine in indium selenides, according to indirect data [14], which makes it unlikely that there is a significant distortion of information on the phase diagram due to the solution with a foreign impurity (chlorine atoms) in the binary phase.

b) Possibility of obtaining vapours of indium chlorides with a concentration appropriate for correct spectrophotometric measurement [15, 16].

c) Various ratios of the components in the molecules of indium chloride present in the vapour (In_2Cl_6, $InCl_3$, In_2Cl_4, and $InCl$ [15, 17]). Due to the differences in these ratios, in other words, in the oxidation states of indium, reaction (1) and similar independent reactions become possible.

d) Expectation, similar to the Ga – Se – Cl and In – S – Cl systems, of a *selective* interaction between indium chloride vapours and the condensed selenides, where only indium participates in a reversible reaction [10, 13].

Condensed Matter and Interphases / Конденсированные среды и межфазные границы   2021;23(4): 482–495

N. Yu. Brezhnev et al.   High-temperature spectrophotometry of indium chloride vapours...

As this work is focused on the determination of the $K_P^{\#}$ value at different temperatures and the compositions of the In – Se system, high-temperature spectrophotometry was chosen for the instrumental implementation of the auxiliary component method. High-temperature spectrophotometry allowed obtaining absorption UV spectra of indium chloride vapours that were in equilibrium with the condensed sample of the In – Se system of the set composition. Processing these spectra, we found the values of concentrations and partial pressures of the InCl and $InCl_3$ vapours, and then we substituted them in expression (2) and calculated the $K_P^{\#}$ values.

2. Experimental

Taking into account the aforementioned, we decided that the main goal of the work to be achieved should consist in the determination of the temperature dependences of the $K_P^{\#}$ value for various compositions of indium selenides that are in equilibrium with the unsaturated vapour of indium chlorides (see formula 1). This problem was solved in two stages: During the **first stage** we determined the molar attenuation coefficients of indium trichloride $\varepsilon_{\lambda}(InCl_3)$ where λ is the wavelength for the typical absorption band. As for indium monochloride, similar values $\varepsilon_{\lambda}(InCl)$ were determined for several typical peaks in the previous work [16]. After that, we moved to the **second stage** and studied the equilibria of indium selenides with indium chloride vapours. During this stage, we obtained the absorption spectra of the equilibrium vapour of indium chloride at various temperatures. Based on these spectra and taking into account the molar attenuation coefficients, we calculated the values of partial pressures of the p_{InCl3} and p_{InCl} vapours and then the value of $K_P^{\#}$. Finally, we analysed the temperature dependences of the $K_P^{\#}$ values obtained for the In – Se alloys of various compositions.

2.1. Stage 1. Spectrophotometric study of $InCl_3$ vapours

For this study we used a methodology similar to the one described in our previous works [16, 18]. Indium trichloride was synthesised from simple substances [15]. The studied equilibrium was implemented in a sealed optical quartz cuvette ($\sim 25 \times 10 \times 10$ mm³) with the optical path of 10.0 mm inside the cuvette. Very small quantities of indium trichloride were introduced to the cuvette in such a way so that at temperatures of 400–450 °C solid $InCl_3$ would completely sublime and form an unsaturated vapour. During one of the two experiments, a small amount of chlorine gas was also introduced to the system in order to suppress the thermal dissociation of $InCl_3$. The methods of the synthesis and introduction of small amounts of indium trichloride and chlorine into the cuvette are described in [15].

The sealed-off cuvette was placed in a resistance heating furnace. The furnace had small openings (windows) for the transmission of light through it. Absorption spectra were obtained in the range of 200–400 nm using an array based on an MDR-41 monochromator. The furnace with the cuvette inside it was mounted in the array. Typical spectra obtained during the experiment with the excess of chlorine are presented in Fig. 2. As can be seen from Fig. 2, the only broad absorption band with the maximum absorption at 210–215 nm can be observed in the specified spectral range.

This band was also observed in [15] where it was associated with indium trichloride. Fig. 2 also shows that typical light absorption grows with increasing temperature (t): it grows sharply at $t \leqslant 425$ °C and gradually at higher temperatures. We associated this change in the temperature course of absorption with the "Saturated vapour ↔ Unsaturated vapour" transition as the amount of $InCl_3$ in the experiment and the cuvette volume were chosen so that such transition would be observed in the temperature range of 400–450 °C.

A similar change in this spectral band with the temperature was observed in a similar experiment where indium trichloride was used, but chlorine was not added. A series of sharp peaks (in the ranges of 260–290 and 337–363 nm) typical for indium *monochloride* InCl were also seen on the spectra. However, the content of InCl in the vapour calculated using the values of the molar attenuation coefficients did not exceed 2% of the content of $InCl_3$. Also, neither in this experiment, nor in any other experiments we saw any noticeable bands with a wavelength of about 320 nm, which is typical for indium (II) chloride In_2Cl_4. Taking this into account, the data of the experiment conducted without the addition of chlorine was also used to determine the absorption properties of indium trichloride, ignoring its insignificant degradation in this experiment.

Condensed Matter and Interphases / Конденсированные среды и межфазные границы   2021;23(4): 482–495

N. Yu. Brezhnev et al.   High-temperature spectrophotometry of indium chloride vapours...
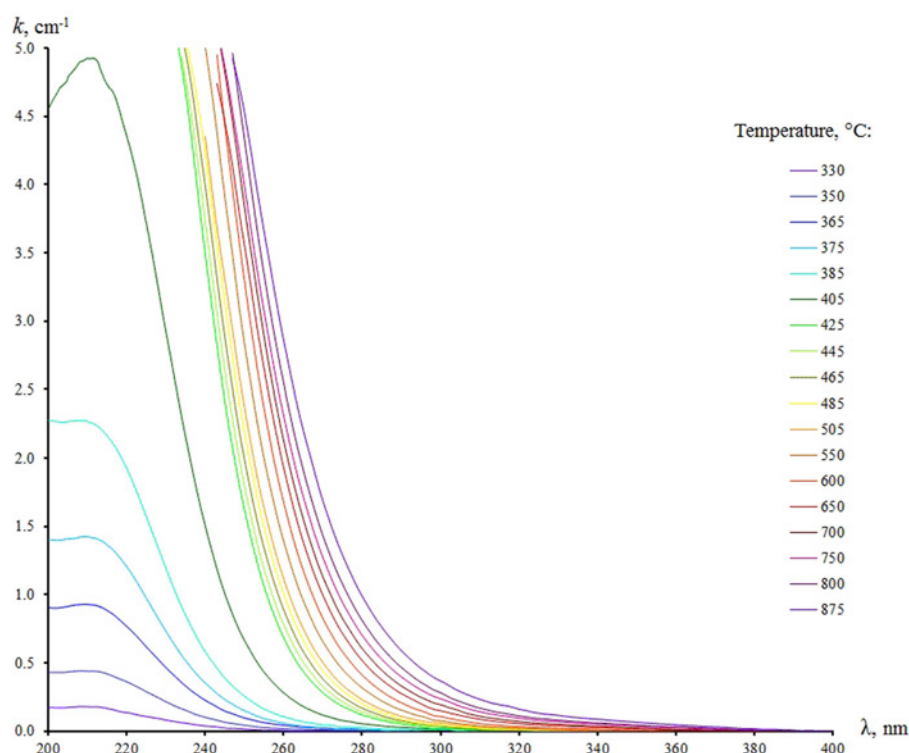
Fig. 2. UV absorption spectra of saturated and unsaturated (over 425 °C) vapours of InCl$_3$ at various temperatures specified in the legend

The *optical absorption coefficient* ($k_\lambda(i)$) was the basic value measured in our spectrophotometric experiments. Each specific value of $k_\lambda(i)$ was determined for the specific wavelength at which the light absorption of the *i*-th substance takes place*. To calculate the values of the *molar attenuation coefficients* ($\varepsilon_\lambda(InCl_3)$), we extracted $k_\lambda(InCl_3)$ from the registered spectra in those temperature ranges that corresponded to the *saturated* vapour of InCl$_3$. The measurements were performed for the wavelengths of 240, 245, and 250 nm. These values correspond to the InCl$_3$ absorption band but they are situated on its wavelength edge in relation to the <u>absorption maximum</u>. This choice is explained

* In these and other spectrophotometric experiments performed in this work, the measurement error for the intensity of radiation ($\Delta I°$) passing through an empty cuvette did not exceed 0.5% of the measured value ($I°$). The calculation by the error accumulation method showed that the error for the determination of the optical absorption coefficient was minimal for k_λ = 1.3 cm^{-1} and was about 1.8 % of the measured value. The error increased in case of the increase or decrease in the optical absorption coefficient. For the further calculations in this work we used the values of k_λ in the range from 0.1 to 4.5 cm^{-1} with the error not exceeding 10 %. When calculating the errors of other values ($C(i), p(i), K_P^{\#}$), it was assumed that only the discussed value made significant contribution to random errors.

by the fact that the applied array provided a radiation intensity which was too low for the wavelengths of up to 240 nm, and the quantitative determination of absorption was performed with poor accuracy. Moreover, as many substances have great attenuation in the short-wave region of the UV spectrum (up to 240 nm), as a result, the quantitative determination of InCl$_3$ in this spectral region can be distorted even by the presence of impurity traces in vapour.

To obtain the required values ($\varepsilon_\lambda(InCl_3)$), we used the correlation (3) between the partial vapour pressure ($pInCl_3$) and the optical absorption coefficient $k_\lambda(InCl_3)$, which was obvious from Beer's law and the ideal gas law.

$$k_{\lambda\,(InCl_3)} \cdot R \cdot T = p_{(InCl_3)} \cdot \varepsilon_{\lambda\,(InCl_3)} \cdot \ln(10) \qquad (3)$$

This expression was primarily used to assess the validity of the obtained results. To do that, we compared the dependence of the $\ln(k_\lambda(InCl_3) \cdot R \cdot T)$ value on the reciprocal temperature obtained from the experimental data with a similar dependence of $\ln(pInCl_3)$ on T^{-1} according to the <u>data from [19]**</u> (Fig. 3).

** There are significant discrepancies in the published data on the temperature dependence of the saturated vapour pressure of InCl$_3$ over solid indium trichloride, which is

Condensed Matter and Interphases / Конденсированные среды и межфазные границы   2021;23(4): 482–495

N. Yu. Brezhnev et al.   High-temperature spectrophotometry of indium chloride vapours...
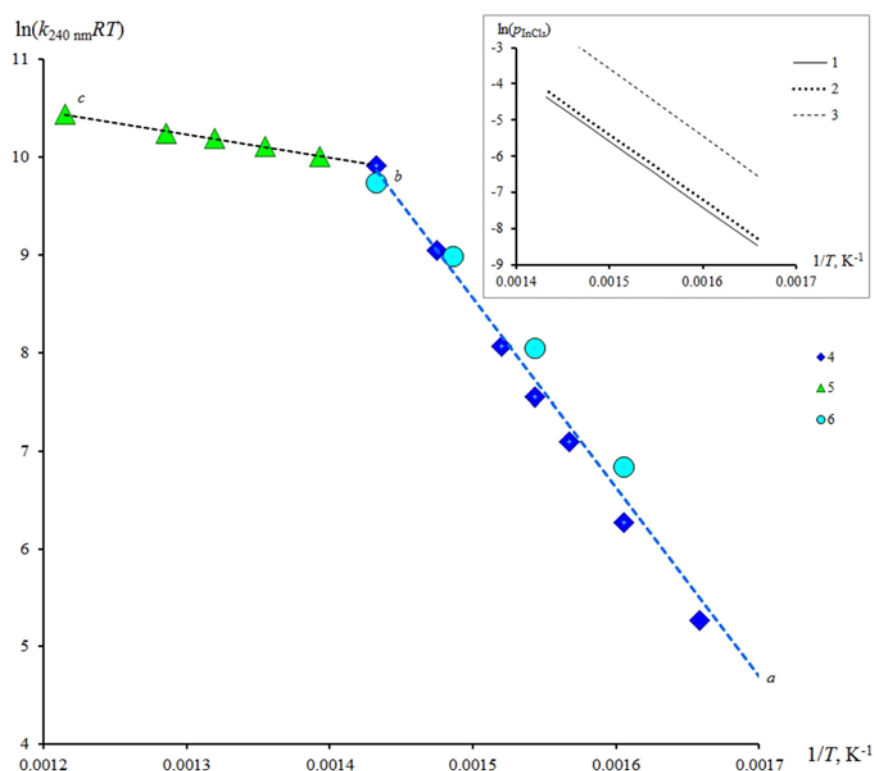
Fig. 3. The data on the temperature dependences of the value $k_{240\,nm}$ (InCl$_3$)·R·T (our experiment) and pressures of the InCl$_3$ saturated vapour (inset in the right upper corner; published data) presented in Arrhenius coordinates. **Legend:** *1*, *2*, and *3* are published data of [19], [20], and [21] respectively. *4* and *5* are the experiment with an excess of chlorine and areas of saturated and unsaturated steam, respectively; *6* is the experiment without an excess of chlorine and saturated vapour. Errors in the determination of the ln(k_λ(InCl$_3$)·R·T) value do not exceed the sized of experimental dots

Taking into account the Clausius–Clapeyron relation for small temperature ranges and assuming that the temperature dependence of the attenuation coefficient is insignificant, both dependences must be almost linear for the *saturated vapour area*. In addition, both lines must have the same angular coefficient that corresponds to the enthalpy of sublimation of ($\Delta_S H(T$av.).) of indium trichloride with a precision of up to the *R* factor. It should be stressed that the $\Delta_S H(T$cp.) value calculated for the average temperature of the study area (325–425 °C) refers to the sublimation of solid indium trichloride with the formation of vapours of a certain molecular form, which is InCl$_3$.

Indeed, the dependence of ln(k_λ(InCl$_3$)·R·T) on the reciprocal temperature turned out to be

close to linear (line |*ab*| Fig. 3). Calculated for the temperature range of 325–425 °C, the value of enthalpy of sublimation of indium trichloride was 161±3.0 kJ/mol, which within the range of 4–6 % corresponds with the results in [15], [19], and [20] (156, 152, and 151 kJ/mol, respectively). Therefore, the obtained data are internally consistent and correlate with the published data.

This allowed us to assume that the values of the molar attenuation coefficients calculated from expression (3) were correct. To make calculations from (3), we evaluated ε_λ(InCl$_3$) and substituted the experimental values of k_λ(InCl$_3$), temperature *T*, and the values of p(InCl$_3$) from the published data on the saturated vapour of InCl$_3$ into the obtained expression. The values of p(InCl$_3$) were obtained for specific temperatures based on the temperature dependences [19]. The obtained averaged values of ε_λ(InCl$_3$) are presented in Table 1.

Therefore, we obtained all the required data in order to proceed to the second and final stage of

selectively presented on the inset in Fig. 3. In our opinion, it is difficult to determine this dependence correctly because of the complex composition of the saturated vapour with a commensurable presence of InCl$_3$ and In$_2$Cl$_6$ molecules, and because of the possible thermal dissociation of InCl$_3$ into InCl and Cl$_2$. In this work, we used the data from a detailed work [19], which correlate well with the results of [20].

Condensed Matter and Interphases / Конденсированные среды и межфазные границы   2021;23(4): 482–495

N. Yu. Brezhnev et al.   High-temperature spectrophotometry of indium chloride vapours...

Table 1. Values of the molar attenuation coefficients of the InCl and InCl$_3$ vapours

Molecular shape for which the calculation is performed	Wavelengths corresponding to the calculated values ε_λ λ, nm	Molar attenuation coefficient ε_λ, cm^2/mol	Source
InCl$_3$		$(6.1 \pm 0.6) \cdot 10^6$	This work
InCl$_3$		$(4.1 \pm 0.5) \cdot 10^6$	This work
InCl$_3$		$(2.7 \pm 0.4) \cdot 10^6$	This work
InCl	267.0	$1.167 \cdot 10^8$	[16]
InCl	270.4	$3.822 \cdot 10^7$	[16]
InCl	342.4	$5.240 \cdot 10^5$	[16]
	Wavelength range $\lambda_1 - \lambda_2$ (nm), corresponding to the values $\varepsilon_{\lambda_1 - \lambda_2}$ for the calculations by the peak area	$\varepsilon_{\lambda_1 - \lambda_2}$, cm^3/mol	
InCl	337–365	$2.283 \cdot 10^6$	[16]

Notes to Table 2. 1 and 2 are the calculations of the the partial pressure of InCl vapours by the absorption with the wavelengths of 342.4 and 270.9 nm respectively; 3 is the calculation of the the partial pressure of InCl$_3$ vapours by the absorption with the wavelength of 240.0 nm, 4 is the mole fraction of indium monochloride in vapour calculated to the approximation of the presence of only two forms, InCl and InCl$_3$, in the vapour.

the work. Before we describe this stage, it should be added that the specific features of the changes in light absorption in the *unsaturated* vapour of InCl$_3$ are not directly related to the goal and purpose of the work, so they are analysed in the APPENDIX.

2.2. Stage 2. Spectrophotometric study of the equilibrium of vapours of indium chlorides with some condensed phases of the In – Se system

In this part of the study, we introduced crushed powder of an alloy of the In – Se system to the point of equilibrium with the vapour of indium chlorides. It was important to show that alloys with different phase compositions provide noticeably different quantitative characteristics of equilibrium with the vapour of the auxiliary component. We used two alloys to identify these differences: one with the selenium content of 49.9 mol% Se (alloy 1) and another with the selenium content of 58.5 mol% Se (alloy 2). The poorest phases were to be contained in the first one and the phases rich in selenium in the second one. However, polymorphic modifications of the most selenium-rich phases that almost corresponded to the stoichiometry of In$_2$Se$_3$ were not used in this work as these substances may have noticeable values of vapour pressures of their own components (In$_2$Se, Se$_x$) at temperatures of the planned experiments (400–800 °C). Molecular forms of selenium (Se$_x$; x =1, 2, 3, 4...8) and diindium selenide (In$_2$Se), in their turn, would be seen on the spectra and would make it difficult to analyse them.

Both alloys were synthesised during the interaction of stoichiometric amounts of simple substances (In-00, high purity Se, double distilled) in the evacuated quartz ampoules at 900 °C. The melts were stirred and the ampoules were occasionally shaken within two hours, then cooled down to 600 °C, and after that the samples were kept at this temperature for 24 hours. The annealing was finished by quenching the ampoules in iced water. The quartz ampoules were opened, and the ingots weighing 2–3 g were extracted from them.

The DTA and XRD data showed that both alloy 1 (49.9 mol% Se) and alloy 2 (58.5 mol% Se) are heterogeneous: the first one is almost exclusively presented by the hexagonal phase of InSe-2H with a negligible impurity of In$_4$Se$_3$, while alloy 2 contained β-In$_2$Se$_3$ and In$_6$Se$_7$ phases.

To conduct a spectrophotometric experiment, we placed a weighed portion of the alloy ground into powder on the bottom of the cuvette and then introduced a certain amount of an auxiliary component into the cuvette. As for the auxiliary component, at this stage of work it was more convenient to initially introduce indium *monochloride* into the cuvette since it is not important which initial phase of indium chloride is introduced into the system to achieve heterogeneous equilibrium. The amount of InCl was selected on the condition that *unsaturated* vapour must be formed in the system

Condensed Matter and Interphases / Конденсированные среды и межфазные границы   2021;23(4): 482–495

N. Yu. Brezhnev et al.   High-temperature spectrophotometry of indium chloride vapours...

at temperatures over 400 °C. Taking into account the small volume of the cuvette and the high absorption of indium chlorides, we are referring to the introduction of a very small amount (~10^5 g), which cannot be measured directly using analytical scales. A special methodology described in [16] was developed for the synthesis and transfer of such small amounts into the cuvette. Once the defined microquantity of InCl was transferred into the cuvette, it was evacuated, sealed off, and placed as necessary in the furnace of the spectrophotometric unit. It should be noted that as the total amount of the In – Se alloy exceeds the amount of halides in vapour

by 4–5 orders of magnitude, the change of the composition of liquid (molten) indium selenides must be negligibly small in case of any deviations in the equilibrium (1) during the experiment.

3. Results and Discussion

Typical absorption spectra of indium chloride vapours that are in equilibrium with alloy 1 at temperatures from 410 to 610 °C are presented in Fig. 4. At a temperature of 400 °C, a typical series of sharp peaks are observed in the wavelength ranges of 260–290 and 337–362 nm on these spectra indicate the appearance of noticeable concentrations of indium *monochloride* in the
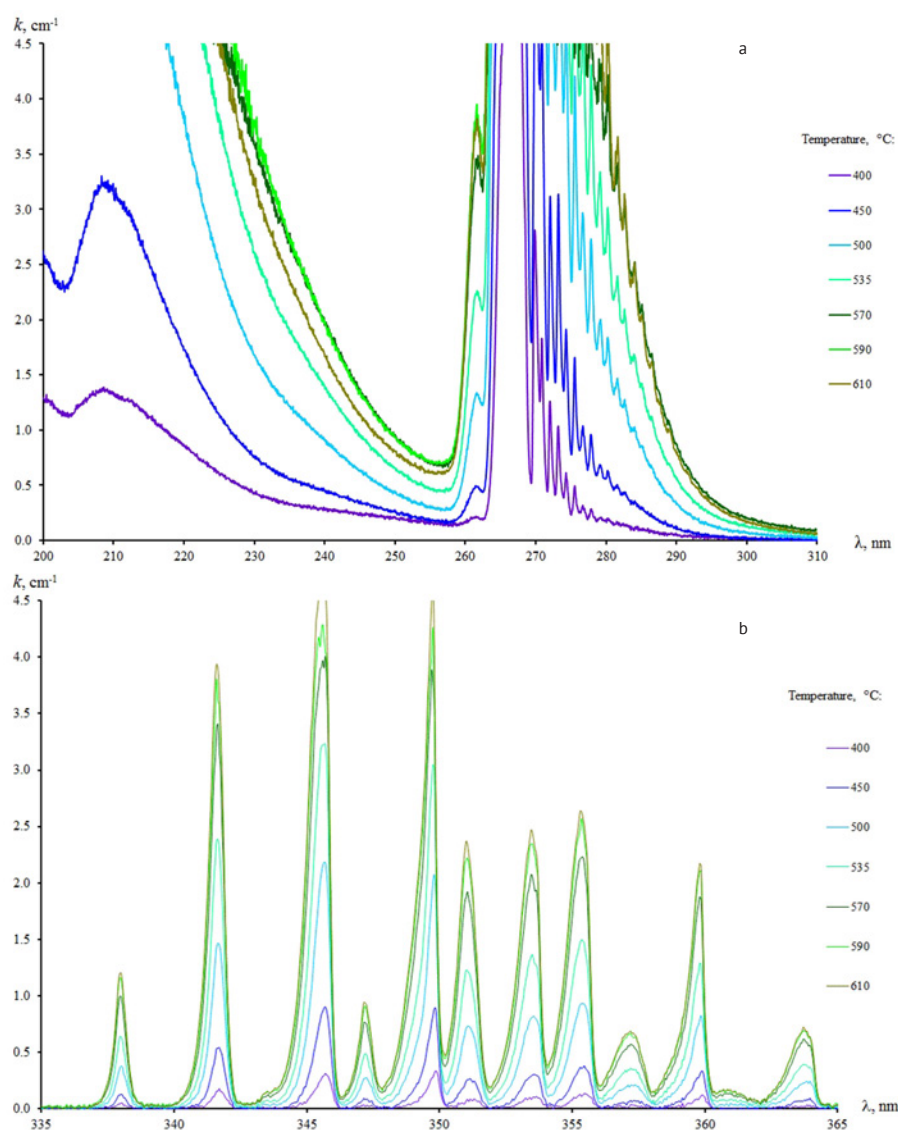
Fig. 4. UV absorption spectra of indium chloride vapours obtained at temperatures from 410 to 610 °C and being in equilibrium with alloy 1 (phase 2H-InSe and traces of In_4Se_3): *a*) spectral area of 200–310 nm where a wide absorption band of $InCl_3$ (shortwave part of the spectrum ~up to 250 nm) and a series of peaks of InCl (~260–300 nm) appear; *b*) spectral area of 335–365 nm where InCl absorption peaks appear

Condensed Matter and Interphases / Конденсированные среды и межфазные границы   2021;23(4): 482–495

N. Yu. Brezhnev et al.   High-temperature spectrophotometry of indium chloride vapours...

vapour. As for the specified temperature range, the intensities of the characteristic peaks of InCl significantly increased together with the temperature, which is indicative of a strong deviation of equilibrium (1) to the right. Similarly, at temperatures from 400 to 650 °C, the shape of spectral curves for the experiment with alloy 2 also changed due to a higher content of selenium (58.5 mol%).

The known values of the molar attenuation coefficients of InCl and $InCl_3$ (Table 1) allowed determining the equilibrium concentrations of these molecular forms in the vapour and then determining the values of partial pressures $p(InCl)$ and $p(InCl_3)$ and, finally, the $K_P^{\#}$ value (2). Table 2 and Fig. 5 show these results referring to the temperatures at which alloys 1 and 2 remain crystalline (there are no melts or their fraction is negligibly small).

The data provided in this table indicate a clear deviation of equilibrium (1) to the right with an increase in the temperature (see the columns with the $K_P^{\#}$ values). As for alloy 2 with a relatively low content of indium (41.5 mol%), the $K_P^{\#}$ values were several orders of magnitude smaller than the ones for alloy 1 (50.1 mol % In) which contained indium-rich phases. This was indicative of a great increase in the affinity of indium to selenium in the transition from lower to higher selenides.

However, despite a significant difference between the $K_P^{\#}$ values for the equilibria with alloys of various compositions (including phase composition), noticeable concentrations of $InCl_3$ and InCl always remained in the vapour.

Their joint presence should accelerate the achievement of the equilibrium state and the obtaining of samples of indium selenides with internal equilibrium upon their contact with the vapour of these halides under the conditions of a spectrophotometric experiment. It should be noted that in a number of cases the contact of condensed phases with vapour contributes not only to the achievement of the equilibrium position but also to the elimination of metastable states. For instance, [22] showed that marcasite (α-FeS_2) is a metastable phase in relation to pyrite (β-FeS_2). It was proved by a monotropic transformation of marcasite to pyrite, which occurred only upon the contact with a liquid phase, specifically an iron carrier ($FeCl_2$). In [23], metastable inclusions of γ-GaSe in ε-GaSe were eliminated upon annealing of gallium monoselenide crystals with an excess of gallium in the presence of GaI and GaI_3 iodide vapours that ensured the transfer of gallium between the solid phases and the vapour.

Going back to Fig. 5, it should be noted that $K_P^{\#}$ temperature dependences in Arrhenius coordinates are a) similar to linear ones and b) are very different both in the absolute values of $K_P^{\#}$ and in the slope. Greater $K_P^{\#}$ values correspond to the equilibrium with the alloy with a greater indium content (alloy 1), while the temperature dependence of this value presented in Arrhenius coordinates has smaller slope.

The identified features on Fig. 5 corresponded to those expected and showed quality analogy between $K_P^{\#} - T$ and $p_i - T$ diagrams. For instance,

Table 2. Partial pressures of the $InCl_3$ and InCl vapours in equilibrium with the alloys of the In – Se system with a selenium content of 49.9 and 58.5 mol %

Equilibrium with the In – Se alloy; 49.9 mol% Se					Equilibrium with the In – Se alloy; 58.5 mol% Se				
t, °C	p_{InCl} [1]	p_{InCl3} [3]	$K_P^{\#}$	x_{InCl}, % [4]	t, °C	p_{InCl} [2]	p_{InCl3} [3]	$K_P^{\#}$	x_{InCl}, % [4]
400	0.006	0.003	7E-05	68.9	400	1.1E-04	4.7E-02	5.6E-12	0.2
450	0.020	0.004	0.002	82.5	425	1.9E-04	4.6E-02	2.1E-11	0.4
500	0.060	0.009	0.023	86.5	450	2.6E-04	4.3E-02	3.0E-10	0.6
535	0.10	0.015	0.07	87.2	475	2.9E-04	3.6E-02	7.5E-10	0.8
570	0.15	0.022	0.15	87.2	500	4.6E-04	3.2E-02	3.6E-09	1.4
590	0.17	0.023	0.22	88.2	525	4.9E-04	2.8E-02	6.4E-09	1.7
610	0.19	0.020	0.32	90.3	550	7.8E-04	2.0E-02	3.2E-08	3.7
					575	1.1E-03	1.4E-02	1.0E-07	7.0
					600	1.5E-03	1.2E-02	2.4E-07	11.0
					625	1.7E-03	6.7E-03	6.2E-07	20.3
					650	2.3E-03	4.4E-03	1.7E-06	34.6

Condensed Matter and Interphases / Конденсированные среды и межфазные границы   2021;23(4): 482–495

N. Yu. Brezhnev et al.   High-temperature spectrophotometry of indium chloride vapours...
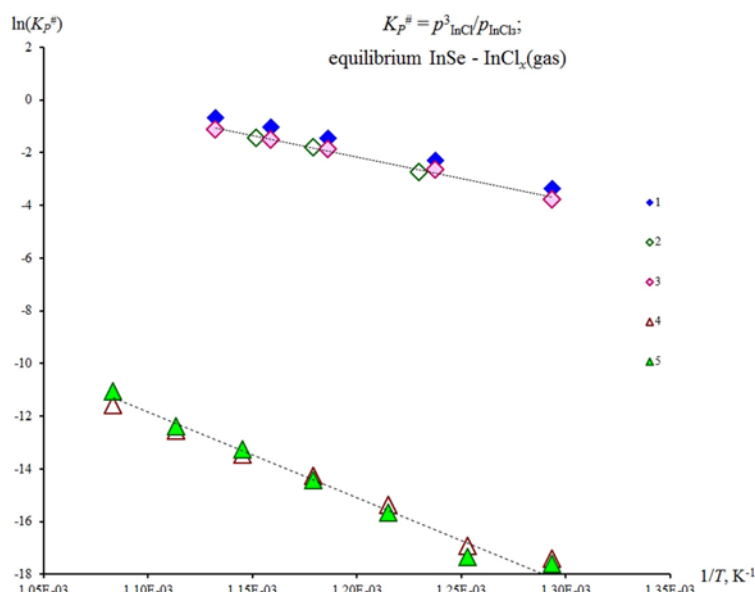
Fig. 5. Temperature dependences of the $K_P^{\#}$ value for equilibrium (1): indium chlorides in the vapour phase, alloys of the In – Se system in the condensed phase. Line $|cd|$ is an alloy of the 49.9 mol% Se composition, line $|ef|$ is an alloy of the 58.5 mol% Se composition. **Legend:** *1 – 3* are data of two experiments with the In – Se alloy of the 50.0 mol% composition Se, *1*, and *2* are the calculation of p(InCl) by the absorption coefficient with the wavelength of 342.4 nm; *3* is the calculation by the peak area within the wavelength range of 337-362 nm. *4* and *5* are the experiment with an alloy of the 50.0 mol% composition % Se; calculations of p(InCl) by the absorption coefficient with the wavelengths of 267.5 and 270.9 nm respectively

if the temperature dependence of the partial pressure of indium vapors p_{In} over heterogeneous samples of alloy 1 and alloy 2 were studied directly in the In – Se system (without an auxiliary component), we should have observed the dependences of $\ln(p_{In})$ on T^{-1} similar to the ones shown in Fig. 5. Such behaviour stems from the connection (4), shown in [8], between the chemical potential of indium (μ_{In}) in the condensed phase of the In – Se system and the $K_P^{\#}$ value for equilibria of type (1).

$$\mu_{In} = 0.5 \cdot RT \cdot \ln(K_P^{\#}) + F(T), \qquad (4)$$

where $F(T)$ is the element depending only on the temperature.

3.1. Additional possibilities of spectrophotometry with the vapours of the auxiliary component when studying T – x diagrams of the In – Se system

The analysis of the behaviour of absorption spectra at temperatures over 610 °C for alloy 1 and over 665 °C for alloy 2 allowed identifying unexpected features. Under these conditions, at first a sharp decrease and then a smooth increase of the intensities of InCl peaks was observed on the spectra upon the increase of temperature (Fig. 6 and Fig. 7). It is obvious that the *concentration* of indium monochloride in the vapour changed in the same way. Similar changes were observed also in the concentration of indium *trichloride* in the vapour.

We associated such an unusual course of the temperature dependence of the InCl and InCl₃ concentration in the vapour with a noticeable solubility of indium chlorides in the melt of indium selenides. Since alloy 1 consisted practically of the InSe phase (the fraction of the In₄Se₃ phase was very small), the appearance of the first noticeable amounts of the melt must correspond to the incongruent melting temperature of InSe.

Then, practically, the beginning of the reduction in the concentration of halides in the vapour must correspond to this temperature* on the corresponding temperature dependence.

---

* It was already noted that the total amount of the In – Se alloy exceeds the amount of halides in vapour by 4 – 5 orders of magnitude. As a result, the cryoscopic effect, a reduction of the temperature of phase melting due to the solubility in the melt of halides, must be much smaller than the error in the determination of the temperature using a thermocouple (2 K).

Condensed Matter and Interphases / Конденсированные среды и межфазные границы   2021;23(4): 482–495

N. Yu. Brezhnev et al.   High-temperature spectrophotometry of indium chloride vapours...
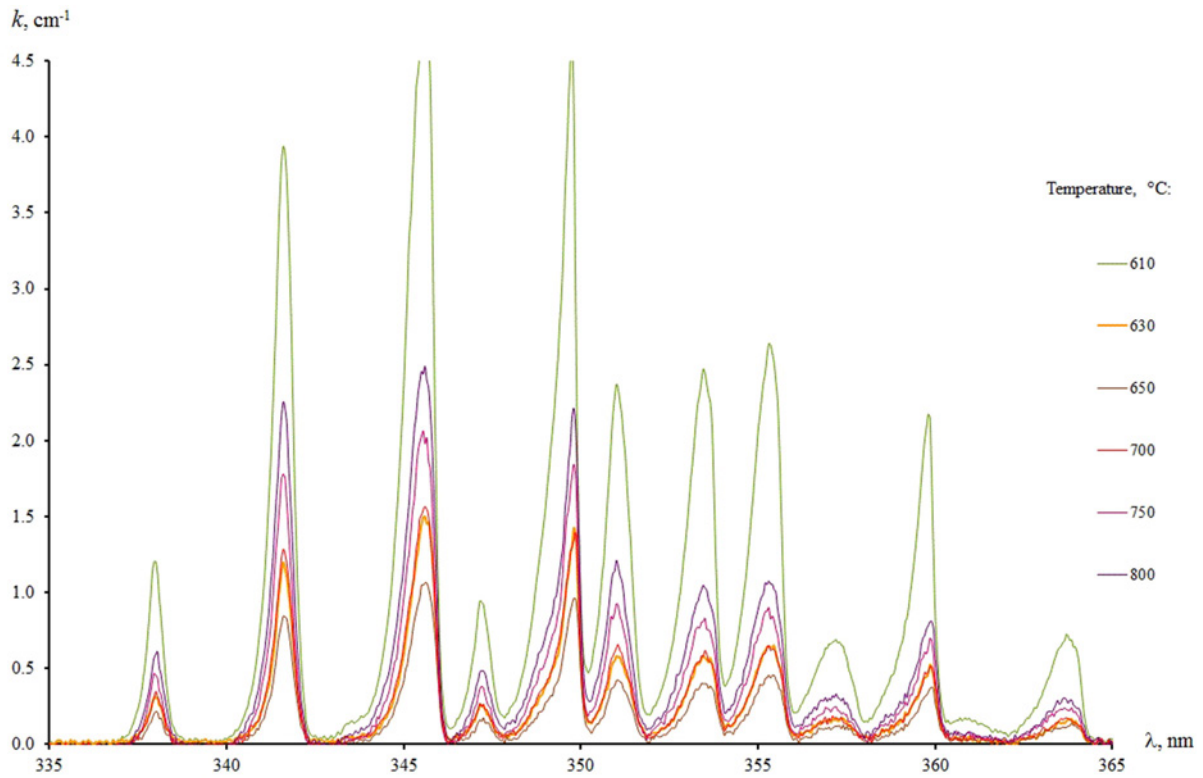
Fig. 6. UV absorption spectra of indium chloride vapours obtained at temperatures from 610 to 800 °C and being in equilibrium with alloy 1 (phase 2H-InSe and traces of In_4Se_3) Spectral area of 335 – 365 nm where InCl absorption peaks appear
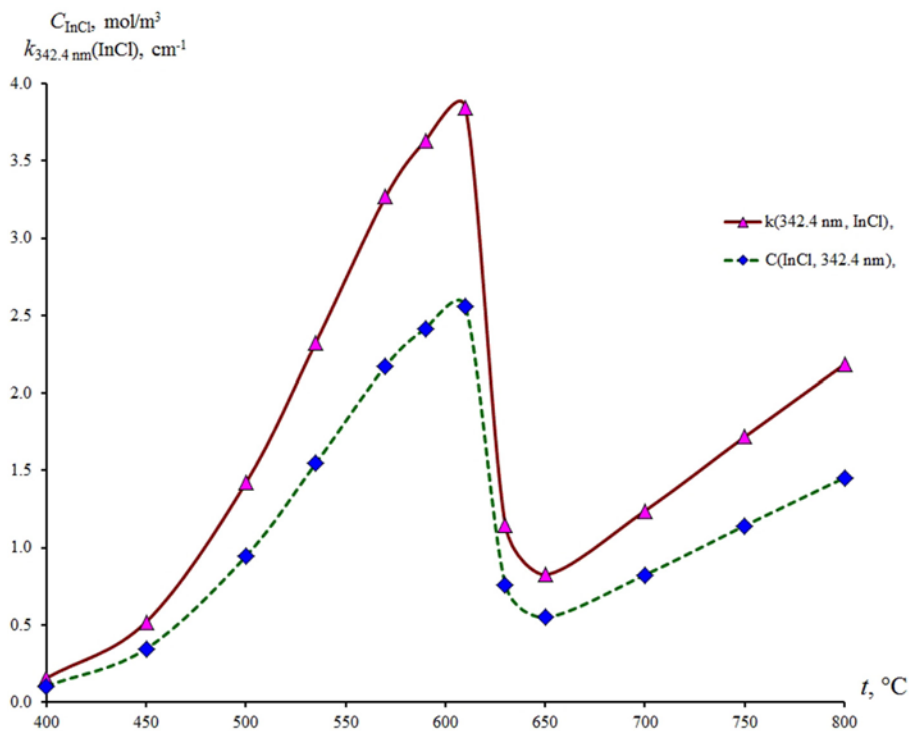
Fig. 7. Temperature dependences of the optical absorption coefficient of the InCl vapour for the wavelength of 342.4 nm (curve *1*) and concentrations of InCl in vapour (curve *2*) over the whole studied temperature range (400 – 800 °C). Equilibrium of the unsaturated indium chloride vapour with alloy 1 (49.9 mol% Se composition, phase 2H-InSe, and traces of In_4Se_3)

Condensed Matter and Interphases / Конденсированные среды и межфазные границы   2021;23(4): 482–495

N. Yu. Brezhnev et al.   High-temperature spectrophotometry of indium chloride vapours...

Taking into account the incongruent melting of the studied sample, a further increase in temperature should obviously result in the increased amount of melt in the system. Then the amount of vapour absorbed by the melt may increase with the temperature, and the concentration of chlorides remaining in the vapour may decrease within the range from the temperature of incongruent melting to the temperature corresponding (for this alloy composition) to the liquidus line.

This reduction should stop at a temperature similar to liquidus as the selenide sample becomes a homogeneous alloy under these conditions, while the solubility of gas a homogeneous liquid should decrease when the temperature increases. Indeed, as for alloy 1, the reduction of light absorption characteristic for InCl with an increase of temperature coincided with the melting temperature of InSe (610 °C according to the data from [24]) and stopped at about 650 °C, which also corresponded well with the value of the temperature for the point on the liquidus line corresponding to the composition of this alloy.

The same reasoning can also be used for the equilibria of chloride vapour with any other samples of the In – Se system. Indeed, in the experiment with alloy 2 the temperature of the beginning of the reduction of absorption (and, correspondingly, concentration) of InCl in the vapour (665 °C) correlated well with the incongruent phase melting temperature of In_6Se_7 (663 °C according to the data from [24]).

Therefore, the obtained effect allows constructing a phase diagram of the In – Se system in the region of coexistence of the liquid and solid phases and identifying the solidus and liquidus lines using an independent static method (Fig. 8). It should be noted that a similar method has already been used by one of the authors of this work for the construction of the *T-x* diagram of the Ga – Se system [25].

3. Conclusions

It can be concluded that the spectrophotometric study of a set of alloys of the In – Se system with various compositions conducted using indium chlorides will allow clarifying the issue of phase relationships in the studied system. However, such a study goes beyond the goals and objectives of this work. Our experiments based on the example of a specific system showed that it is possible to use the promising auxiliary component method and high-temperature spectrophotometry as an instrumental basis for this method. We also showed additional possibilities of this method for plotting *T-x* diagrams of binary systems in such high-temperature areas where the binary solid phase is in equilibrium with the melt. This application of the method is related to the solubility of vapour of an auxiliary component (chlorine in the form of indium chlorides) in the melts of binary phases (indium selenides).

APPENDIX

Let us analyse the data on the **unsaturated** vapour of $InCl_3$. Fig. 2 shows the change in the nature of the temperature dependence related to the "saturated vapour – unsaturated vapour" transition, and this transition becomes even more evident in Fig. 3 in the form of a fracture in point b on the dependence of the $\ln(k_{240\,nm}(InCl_3) \cdot R \cdot T)$ value on reciprocal temperature. In the area
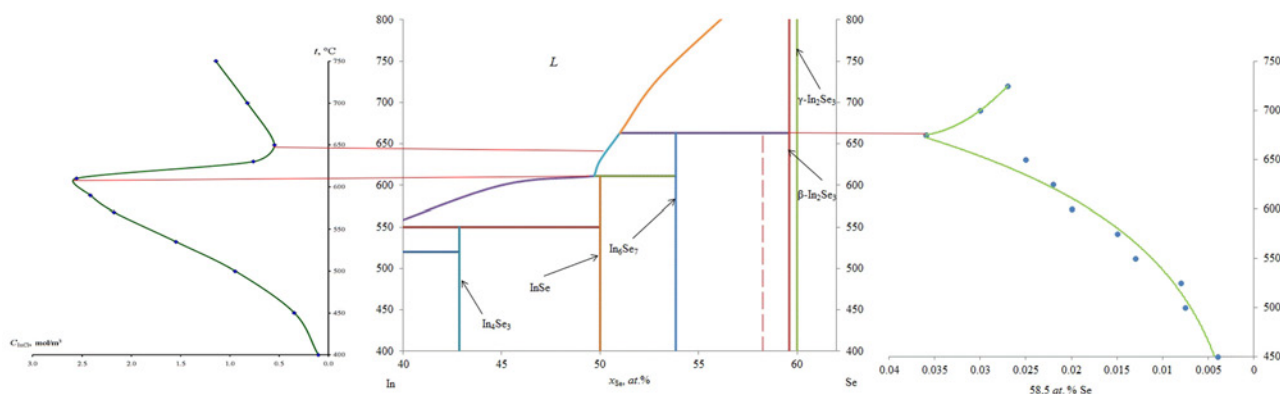
Fig. 8. Fragment of a *T – x* diagram of the In – Se system according to the data from [24] and temperature dependences of the concentration of InCl vapour that is in equilibrium with the alloys of the In – Se system with selenium content of 49.9 mol% (on the left) and 58.5 mol% (on the right)

Condensed Matter and Interphases / Конденсированные среды и межфазные границы   2021;23(4): 482–495

N. Yu. Brezhnev et al.   High-temperature spectrophotometry of indium chloride vapours...

of **un**saturated vapour (line |*bc*| Fig. 3), we should pay attention to the ongoing increase of characteristic absorption of $InCl_3$ together with the temperature (Fig. 2, spectra at $t \geqslant 425\ °C$). We associated this phenomenon with the increase of the concentration of $InCl_3$ molecules in the vapour, which is explained by the following. According to [15, 17], both monomer ($InCl_3$) and dimer molecules (In_2Cl_6) must be present in the indium trichloride vapours under the conditions similar to our experiment, while dimer molecules do not appear in the studied spectral area [15]. Increased temperature shifts the equilibrium in the unsaturated vapour towards the monomer [17]. In its turn, this should lead to an increase in the concentration of indium trichloride in unsaturated vapour when temperature increases.

Author contributions

All authors made an equivalent contribution to the preparation of the publication.

Conflict of interests

The authors declare that they have no known competing financial interests or personal relationships that could have influenced the work reported in this paper.

References

1. Okamoto H. In-Se (Indium-Selenium). *Journal of Phase Equilibria and Diffusion*. 2004;25(2): 201. https://doi.org/10.1007/s11669-004-0031-y

2. Tedenac J.-C., Vassilev G. P., Daouchi B., Rachidi J., Brun G. Low-temperature region of the In-Se system. *Crystal Research and Technology*. 1997; 32(4): 605–616. https://doi.org/10.1002/crat.2170320417

3. Li J. B., Record M. C., Tedenac J. C. A thermodynamic assessment of the In-Se system. *Zeitschrift für Metallkunde*. 2003;94(4): 381–389. https://doi.org/10.3139/146.030381

4. Gödecke T., Haalboom T., Sommer F. Stable and metastable phase equilibria of the In-Se system. *Journal of Phase Equilibria*. 1998;19(6): 572–578. https://doi.org/10.1007/bf02701021

5. Barker M. G. *Inorganic chemistry of the main-group elements*. Volume 3. C. C. Addison (ed.). Royal Society of Chemistry, UK; 2007. 550 p. https://doi.org/10.1039/9781847556400

6. Chi Y., Sun Z.-D., Xu Q.-T. Hexagonal In_2Se_3: A defect wurtzite-type infrared nonlinear optical material with moderate birefringence contributed by unique $InSe_5$ Unit. *ACS Applied Materials & Interfaces.* 2020;12(15): 17699–17705. https://doi.org/10.1021/acsami.9b23085

7. Chen S., Hutabalian Y., Gierlotka W., Wang C., Lu S. Phase diagram of Bi–In–Se ternary system. *Calphad*. 2020;68: 101744. https://doi.org/10.1016/j.calphad.2020.101744

8. Zavrazhnov A. Yu. Design of *P-T-x* diagrams for gallium chalcogenides with the use of an ancillary component. *Russian Journal of Inorganic Chemistry*. 2003;48(10): 1577–1590. Available at: https://elibrary.ru/item.asp?id=13439652

9. Zavrazhnov A. Yu. Upravlyaemyi sintez nestekhiometricheskikh soedinenii i issledovanie fazovykh ravnovesii pri pomoshchi vspomogatel'nogo komponenta [Guided synthesis of nonstoichiometric compounds and phase equilibrium studies using an auxiliary component]. *Diss. ... DSc in Chemistry*. Voronezh; 2004. 340 p. Available at: https://www.dissercat.com/content/upravlyaemyi-sintez-nestekhiometricheskikh-soedinenii-i-issledovanie-fazovykh-ravnovesii-s-p

10. Zavrazhnov A. Y., Naumov A. V., Sergeeva A. V., Sidei V. I. Selective chemical vapor transport as a means of varying the composition of nonstoichiometric indium sulfides. *Inorganic Materials*. 2007;43: 1167–1178. https://doi.org/10.1134/S0020168507110039

11. Lamoureux M., Milne J. The disproportionation of diselenium dichloride, Se_2Cl_2, and diselenium dibromide, Se_2Br_2. *Canadian Journal of Chemistry*. 1989;67(11): 1936–1941. https://doi.org/10.1139/v89-301

12. Hahn H., Nickels W. Uber sulfid-, selenid- und telluridhalogenide des indiums. *Zeitschrift for anorganische und allgemeine Chemie*. 1960;304(1-2): 100–108. https://doi.org/10.1002/zaac.19603040112

13. Kosyakov A. V., Zavrazhnov A. Y., Naumov A. V. Refinement of the In-S phase diagram using spectrophotometric characterization of equilibria between hydrogen and indium sulfides. *Inorganic Materials*. 2010;46: 343–345. https://doi.org/10.1134/S0020168510040035

14. Ashok A., Regmi G., Velumani S. Growth of In_2Se_3 thin films prepared by the pneumatic spray pyrolysis method for thin film solar cells applications. In: *17th International Conference on Electrical Engineering, Computing Science and Automatic Control (CCE)*. 2020; 1–6. https://doi.org/10.1109/cce50788.2020.9299133

15. Kunia Y., Hosada S., Hosuka M. Studies on the vapor phase reactions in the system In–Cl_2. *Denki Kagaku oyobi Kogyo Butsuri Kagaku*. 1974;42(1): 20–25. https://doi.org/10.5796/kogyobutsurikagaku.42.20

16. Zavrazhnov A. Y., Naumov A. V., Malygina E. N., Kosyakov A. V. Indium monochloride vapor pressure: the vapor-gauge and spectrophotometric experimaental data. *Kondensirovannye Sredy i*

Condensed Matter and Interphases / Конденсированные среды и межфазные границы 2021;23(4): 482–495

N. Yu. Brezhnev et al. High-temperature spectrophotometry of indium chloride vapours...

Mezhfaznye Granitsy = Condensed Matter and Interphases. 2019;21(1): 60–71. https://doi.org/10.17308/kcmf.2019.21/717

17. Fedorov P. I. *Indii* [Indium]. Moscow: Nauka Publ.; 2000. 276 p. (In Russ.)

18. Zavrazhnov A. Yu., Kosyakov A. V., Sergeeva A. V., Berezin S. S., Chernenko K. K. High-temperature in situ vapor spectrophotometry as a static variant of tensimetric method equilibria in the Ga-I system. *Kondensirovannye sredy i mezhfaznye granitsy = Condensed Matter and Interphases*. 2015;17(4): 417–436. https://elibrary.ru/item.asp?id=25946578

19. Brunetti B., Piacente V., Scardala P. A torsion study on the sublimation process of InCl₃. *Journal of Chemical & Engineering Data*. 1998;43(1): 101–104. https://doi.org/10.1021/je970188a

20. Oppermann H., Krausze R., Bruhn U., Balarin M. Zurn sattigungsdruck von GaCl₃, und InCl₃. *Zeitschrift for anorganische und allgemeine Chemie*. 1994;620(6): 1110-1114. https://doi.org/10.1002/zaac.19946200627

21. Polyachenok O. G.; Komshilova O. N. Vapor-pressure of indium chloride. *Izv. Akad. Nauk BSSR. Ser. Fiz.-Energ*. 1970;2: 90-94.

22. Zavrazhnov A., Naumov A., Kosyakov A., Berezin S., Volkov V., Sergeeva A. The iron sulfides crystal growth from the halide melts. *Material Research*. 2018;21(4): 20170648. https://doi.org/10.1590/1980-5373-mr-2017-0648

23. Zavrazhnov A. Y., Naumov A. V., Sidey V. I., Pervov V. S. Composition control of low-volatile solids through chemical vapor transport reactions. III. The example of gallium monoselenide: Control of the polytypic structure, non-stoichiometry and properties. *Thermochimica Acta*. 2012;527(1): 118–124. https://doi.org/10.1016/j.tca.2011.10.012

24. Daouchi B., Record M. C., Tedenac J. C., Vassilev G. Phase diagram investigation of the indium-selenium system. *Zeitschrift fuer Metallkunde.*. 1998;89(9): 612–617. Available at: https://elibrary.ru/item.asp?id=27948695

25. Turchen D. N., Zavrazhnov A. Yu., Goncharov E. G. Issledovanie nestekhiometrii faz s nizkoi letuchest'yu. Oblast' gomogennosti GaSe [Investigation of nonstoichiometry of phases with low volatility. GaSe homogeneity region]. *Russian Journal of General Chemistry*. 1998:68(6): 920–925. Available at: https://elibrary.ru/item.asp?id=29113194 (In Russ.)

Information about the authors

Nikolay Yu. Brezhnev, Junior Researcher in Chemistry, PhD student, Department of General and Inorganic Chemistry, Voronezh State University; Voronezh, Russian Federation; e-mail: brezhnevnick@gmail.com. ORCID iD: https://orcid.org/0000-0002-3287-8614.

Andrey V. Kosyakov, PhD in Chemistry, Assistant Professor, Department of General and Inorganic Chemistry, Voronezh State University, Voronezh, Russian Federation; e-mail: lavchukb@mail.ru. ORCID iD: https://orcid.org/0000-0001-9662-7091.

Anastasia V. Steich, Student, Department of General and Inorganic Chemistry, Voronezh State University, Voronezh, Russian Federation; e-mail: Nastya.steitch@yandex.ru. ORCID iD: https://orcid.org/ 0000-0003-3945-896X.

Alexander Yu. Zavrazhnov, DSc in Chemistry, Professor at the Department of General and Inorganic Chemistry, Voronezh State University, Voronezh, Russian Federation; e-mail: alzavr08@rambler.ru. ORCID iD: https://orcid.org/ 0000-0003-0241-834X.

Original articles

Nonlinear optical properties of single-walled carbon nanotubes/water dispersed media exposed to laser radiation with nano- and femtosecond pulse durations

P. N. Vasilevsky[1,2✉], M. S. Savelyev[1,2,3], S. A. Tereshchenko[1,2],
S. V. Selishchev[1], A. Yu. Gerasimenko[1,2,3]

[1]National Research University of Electronic Technology,
1 Shokina pl., Zelenograd, Moscow 124498, Russian Federation

[2]Institute of Nanotechnology of Microelectronics of the Russian Academy of Sciences,
32a Leninsky pr., Moscow 119991, Russian Federation

[3]I. M. Sechenov First Moscow State Medical University,
8-2 Trubetskaya ul., Moscow 119991, Russian Federation

Abstract

The constant increase in the power of laser systems and the growth of potential fields for the application of lasers make the problem of protecting sensitive elements of electro-optical systems and visual organs from high-intensity radiation an urgent issue. Modern systems are capable of generating laser radiation in a wide range of wavelengths, durations, and pulse repetition rates. High-quality protection requires the use of a universal limiter capable of attenuating laser radiation, not causing colour distortion, and having a high transmission value when exposed to low-power radiation. For this, dispersed media based on carbon nanotubes with unique physicochemical properties can be used. Such media have constant values of their absorption coefficient and refractive index when exposed to low-intensity laser radiation and change their properties only when the threshold value is reached.

The aim of this work was the study of the nonlinear optical properties of an aqueous dispersion of single-walled carbon nanotubes exposed to nano- and femtosecond radiation. For the characterization of the studied medium, Z-scan and fixed sample location experiments were used. The optical parameters were calculated using a threshold model based on the radiation transfer equation.

As a result of the experiments, it was shown that the aqueous dispersion of single-walled carbon nanotubes is capable of limiting radiation with wavelengths from the visible and near-IR ranges: nano- (532, 1064 nm) and femtosecond (810 nm). A description of nonlinear optical effects was proposed for when a medium is exposed to radiation with a nanosecond duration due to reverse saturable absorption and two-photon absorption. When the sample exposed for a femtosecond duration the main limiting effect is spatial self-phase modulation. The calculated optical parameters can be used to describe the behaviour of dispersions of carbon nanotubes when exposed to radiation with different intensities. The demonstrated effects allow us to conclude that it is promising to use the investigated media as limiters of high-intensity laser radiation in optical systems to protect light-sensitive elements.

Keywords: Laser radiation Limiters, Nano- and femtosecond radiation, Carbon nanotubes, Reverse saturable absorption, Spatial self-phase modulation, Z-scan, Radiation transfer equation

✉ Pavel N. Vasilevsky, e-mail: pavelvasilevs@yandex.ru

Condensed Matter and Interphases / Конденсированные среды и межфазные границы   2021;23(4): 496–506

P. N. Vasilevsky et al.   Nonlinear optical properties of single-walled carbon nanotubes/water dispersed media...

1. Introduction

Since the invention of the laser in the 50s, laser radiation has been widely used in various fields [1–3]. Devices for laser welding and cutting [4], photolithography systems [5], laser surgical and vision correction complexes [6], spectrometers for determining the chemical composition of substances [7], laser designators and range finders [8] have been actively used for several decades. Recently, laser scanning using lidars and laser communication systems has been under development [9, 10].

Most of the laser systems operate in the visible and near IR regions of radiation. This is explained by the simplicity of implementation of both the laser system (for example, Nd:YAG lasers with the generation of additional harmonics) and the photodetector equipment for detecting radiation. Silicon photodiodes are sensitive in the range from 200 nm to 1100 nm, which corresponds well to the generation wavelengths of the Nd:YAG laser (1064, 532, 355 nm, etc.) [11]. Also, laser radiation in the range of 350–1100 nm is weakly absorbed by water, which makes it possible to use lidars with these wavelengths for scanning in rainy weather and for bathymetry [12].

The development of laser technology is accompanied by an increase in the power of the used systems. High-intensity radiation can interfere with the operation of light-sensitive detectors and damage the eyes. In accordance with the ANSI Z136 international standards, radiation with a power of less than 5 mW is considered safe for the human eye if the exposure time is no more than 0.25 s. When working with more powerful radiation, protective equipment must be used.

In the case of laser scanning and ranging systems, the range of measured distances is limited by the fact that the use of high-power laser pulses can overload the photodetector in the near field. This is due to the fact that as the distance to the measured object decreases, the energy of the echo pulse increases. In such cases, optical limiters of laser radiation are used to protect the photodetector equipment. However, limiters with a constant transmission value (such as absorption and interference filters), while protecting against strong echo pulses, attenuate the "useful" signal to the same extent, i.e. decrease the upper limit of the operating range. In addition, absorption filters have spectral selectivity, i.e. their attenuation coefficient depends on the wavelength of the incident radiation.

Chromogenic materials are able to change their optical density depending on external parameters (temperature, applied voltage, etc.), but their response rate does not ensure the limitation of nanosecond pulses or less [13–15]. Therefore, potentially the most suitable media for limiting laser radiation are nonlinear optical materials.

Nonlinear optical media are those media, the optical properties of which depend on the intensity of the incident laser radiation. Such substances are used for laser three-dimensional printing [16], nonlinear optical switches [17], and can also be used to limit the intensity of laser radiation [18]. With a low intensity of I they have high transmittance (more than 70%) and constant optical parameters, such as absorption coefficient and refractive index, and upon reaching the threshold intensity of I_{th}, they start to change their transmission due to nonlinear optical effects (Fig. 1) [19].

The nonlinear optical medium exhibits different properties depending on the type of laser radiation. When exposed to pulsed nanosecond radiation with an intensity above the threshold value, nonlinear absorption occurs in the medium [20]. This property of nonlinear optical media, in addition to limiting laser radiation, can be used in optical switches to control the signal [21], as well as to create three-dimensional biocompatible structures for the restoration of damaged tissues [22]. In the case of prolonged exposure to continuous or femtosecond radiation with a high pulse repetition rate, a change in the refractive index occurs. This change causes a change in the beam's shape due to self-focusing or self-defocusing [23].

Condensed Matter and Interphases / Конденсированные среды и межфазные границы   2021;23(4): 496–506

P. N. Vasilevsky et al.   Nonlinear optical properties of single-walled carbon nanotubes/water dispersed media...
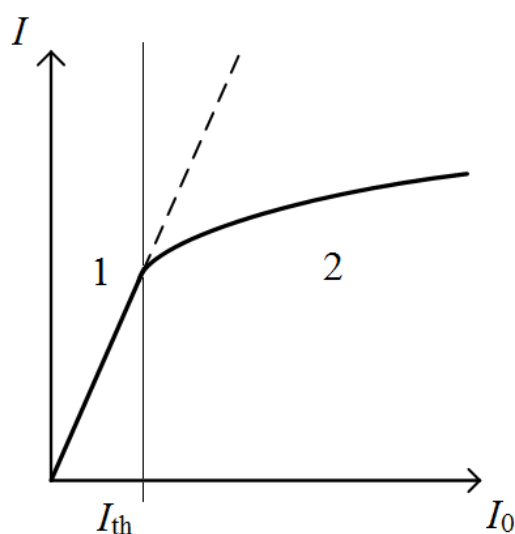
Fig. 1. Typical form of the dependence of the transmitted radiation intensity on the intensity of the incident radiation. Area *1* – linear transmission, Area *2* – nonlinear transmission

A large number of materials such as quantum dots [24], metal nanoparticles [25], organic dyes [26] and carbon nanoparticles [27] have nonlinear optical properties. Carbon nanomaterials, in contrast to dyes and metals, are colour neutral, i.e. their transmission spectrum does not have pronounced absorption peaks. By adjusting the concentration, high linear transmittance in the visible and near IR ranges can be achieved. Such a limiter can be used in tunable wavelength systems. One of the promising carbon nanomaterials are carbon nanotubes, which, in addition to optical properties exhibit unique mechanical and electrically conductive properties [28, 29].

The aim of this work was the study of the nonlinear optical properties of an aqueous dispersion of single-walled carbon nanotubes exposed to nano- and femtosecond radiation.

Samples of single-walled carbon nanotubes/ water dispersion (SWCNTs) were created and experimental studies were carried out using Z-scanning methods and fixed sample location experiment. Calculations of nonlinear optical parameters, such as nonlinear absorption coefficient, nonlinear refractive index and the corresponding threshold values, allow assessing the prospects for using the investigated media as a nonlinear optical limiter.

2. Experimental

1.1. Preparation of liquid dispersions

For the production of the investigated sample, SWCNT with a purity of 95% were used. The nanotube diameter varied over the range of 1–2 nm. Distilled water with pH = 6 was used as a solvent. SWCNT were mixed with water in a way that the mass fraction of SWCNT in the initial solution did not exceed 0.005 wt%. The original solution was placed in an ultrasonic homogenizer Sonicator Q700 (Qsonica, USA), where it was stirred for 1 hour under the influence of a powerful ultrasonic field with an amplitude of 45 W. Then the aqueous dispersion was stirred on a magnetic stirrer for 1 hour.

1.2. Methods for determining the linear and nonlinear absorption

For the determination of the linear absorption coefficient, a Genesys 10S Uv-Vis single-beam spectrophotometer (Thermo Fisher Scientific, USA) was used. A xenon lamp, allowing a spectrum in the near UV, visible, and near IR ranges was used as a radiation source.

For the determination of the nonlinear absorption coefficient, an experimental system based on an LS-2147 Nd: YAG laser (LOTIS TII, Belarus) was constructed (Fig. 2). For the research the fundamental (1064 nm) and second harmonics (532 nm) were used. Irradiation was performed with single pulses. The pulse duration was 16 ns. The radiation generated by the laser (*1*), was passed through a set of neutral light filters (*2*), which was necessary for the control of the radiation energy on the sample. The use of neutral light filters allowed more precise selection of the input energy ranges required for various experimental conditions. A Glan prism (*3*) was necessary for the fixed sample location experiment. It was used for the adjustment of
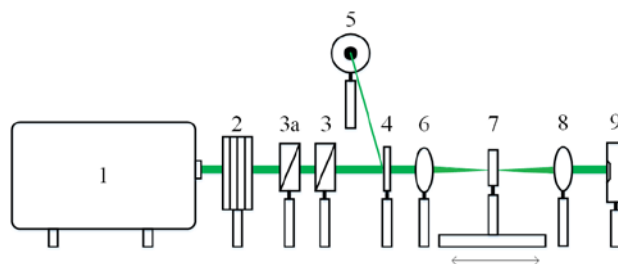
Fig. 2. Optical scheme of the experiment for detecting nonlinear optical absorption

Condensed Matter and Interphases / Конденсированные среды и межфазные границы   2021;23(4): 496–506

P. N. Vasilevsky et al.   Nonlinear optical properties of single-walled carbon nanotubes/water dispersed media...

laser radiation energy in ranges set by neutral light filters (*2*). Adjusting the energy values by rotating the Glan prism (*3*) can be carried out only when using polarized laser radiation, therefore, when working with a wavelength of 1064 nm, in front of the Glan control prism (*3*). A Glan polarizing prism (*3a*), transmitting only the linear polarization component, was additionally installed. When using radiation with a wavelength of 532 nm, polarization occurs in the laser during the generation of the second harmonic on a nonlinear crystal, therefore polarizing the Glan prism (*3a*) is not required.

Then the beam reached the beam splitter plate (*4*). It reflects ~ 5% of the original beam to the sensor (*5*), recording the input energy values. Lenses (*6*) and (*8*) have the same focal length L = 10 cm and are located confocal, at a distance of $2L$ = 20 cm. Due to this, the beam focused on the sample (*7*) by the lens (*6*), after passing through the lens (*8*) acquires the same shape as before focusing. The beam radius at the waist is 25 μm. A sample in a quartz cell with a thickness of 2 mm was placed on a motorized ruler, with which a Z-scan experiment was performed. Then the beam reached the sensor (*9*), which measured the values of the output energy, i.e. the energy after the passage of the beam through the sample.

Research was performed using Z-scan techniques and experiments with a fixed sample position. The radiation intensity was determined as:

$$I = \frac{2U}{\tau w^2 \pi^{3/2}}, \tag{1}$$

where U – pulse energy, τ – pulse duration, w – the radius of the beam. In the case of a Z-scan, the intensity of the incident radiation changes by changing the radius of the beam. The radiation energy remains constant. For experiments with a fixed position of the sample, the investigated medium was placed in focus and the energy of the incident radiation changed.

1.3. Methods for determining nonlinear optical refraction

The study of the nonlinear refractive index was performed based on a femtosecond Ti:Sapphire laser Chameleon Ultra (Coherent, USA). The pulse generation frequency was 80 MHz, the pulse duration was 140 fs, and the wavelength was 800 nm. The lens focused the laser beam onto the studied sample. The focal length of the lens is 10 cm, the radius of the beam at the focus of the lens is 100 μm. For the reordering of the interference pattern obtained by spatial self-phase modulation, an SP620U CCD camera (Ophir, Israel) was placed behind the sample at a distance of 4 cm. For the limitation of the high-intensity laser radiation, a slit was used, which cut off part of the radiation with an increase in the beam radius. The experimental technique is similar to the experiment with a fixed position of the sample exposed to nanosecond radiation. The size of the slit was chosen in a way that the laser beam completely entered the hole in the absence of a sample. Irradiation was carried out when the cell was positioned vertically. The design of the experiment was similar to the experiment with a nanosecond laser, except for the presence of a slit and the absence of a second lens for collecting radiation.

3. Results and discussion

3.1. Linear and nonlinear optical properties under nanosecond radiation

The optical linear transmission spectrum of SWCNT/water dispersion in the range from 300 to 1100 nm is shown in Fig. 3. There were no pronounced peaks in the spectrum, with the exception of the water absorption peak in the wavelength range from 950 to 980 nm. The transmission at 532 and 1064 nm was 70%. In experiments with a nanosecond laser, the transmission of the medium with low radiation intensity, when nonlinear effects were not recorded, was also 70%. This suggests that the studied medium does not have colour selectivity, and the limiters created on the basis of such a medium will not cause colour discomfort during use. The linear absorption coefficient α was determined as:

$$\alpha(\lambda) = -\frac{\lg\left(T_{\text{lin}}(\lambda)\right)}{d} \tag{2}$$

where $T_{\text{lin}}(\lambda)$ – linear transmission at a certain wavelength, d – the thickness of the sample. In this study, a 2 mm thick cell was used in all experiments. For the 532 and 1064 nm wavelengths, the linear absorption coefficient α is 1.78.

Condensed Matter and Interphases / Конденсированные среды и межфазные границы   2021;23(4): 496–506

P. N. Vasilevsky et al.   Nonlinear optical properties of single-walled carbon nanotubes/water dispersed media…
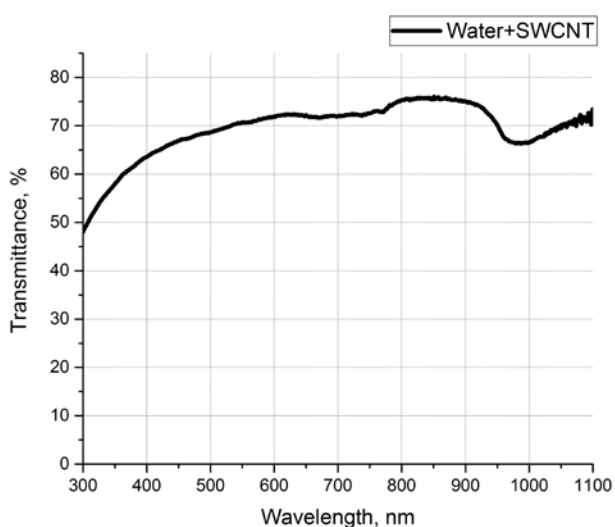
Fig. 3. Optical transmission spectrum of SWCNT/water dispersion

For the investigation of the nonlinear optical parameters of the studied medium interacting with pulsed nanosecond radiation, a cell with SWCNT/water dispersion was placed on a motorized linear positioner at a distance of 6 cm from the lens focus. A Z-scan experiment was then performed. The cell was moved along the optical axis of laser beam propagation and irradiated with single nanosecond pulse every 3 mm. The incident radiation energy remained unchanged and amounted to 550 mJ. Thus, we have obtained the dependence of the normalized transmission $T_{norm}(z)$ on the position of the test sample relative to the focus of the lens z, where $T_{norm}(z)$ is defined as:

$$T_{norm}(z) = \frac{T(z)}{T_{lin}}, \tag{3}$$

where $T(z)$ – the transmission value at each point z, T_{lin} – the value of linear transmission, i.e. transmission in the absence of nonlinear effects.

Then the cell was placed in the focus of the lens, and the fixed sample location experiment was performed. Based on the results, the dependence of the energy of laser radiation transmitted through the sample on the energy of the radiation incident on the sample was obtained.

In Fig. 4 the experimental and theoretically calculated dependences for SWCNT/water dispersion at wavelengths of 532 nm (Fig. 4a, b) and 1064 nm (Fig. 4c, d). In Fig. 4a, it can be seen

that the decrease in the normalized transmission begins almost immediately after the start of the experiment. This indicates a low value of the threshold intensity for the studied medium at a wavelength of 532 nm. This also causes a narrow linear absorption zone in Fig. 4b. It can also be noted that in the presented dependencies there are no knock-out points that do not correspond to the general dependency. This indicates the high stability of the dispersion, i.e. the absence of large SWCNT agglomerates in it, which could contribute to a sharp change in the energy of the transmitted radiation and cause the limiter to malfunction. Also, post-focus transmittances correspond to pre-focus transmittances at similar distances. This shows that there were no changes in the medium (welding of individual nanotubes and precipitation, sublimation of SWCNT, formation of solvent microbubbles, etc.) when passing through the focus of the lens, i.e., through a region of high intensity.

A similar picture was observed upon pulsed irradiation of SWCNT/water dispersion at a wavelength of 1064 nm. As the cell approached the focus of the lens, a decrease in the normalized transmission and then the restoration of the optical properties the further from the focus were observed. In Fig. 4c, the linear absorption, region when the transmission of the medium did not change is clearly visible.

The onset of nonlinear absorption and the corresponding change in the characteristics of the medium can be described using the reverse saturable absorption mechanism and the Jablonski diagram [30]. With low laser radiation intensity, the absorption of photons causes the excitation of molecules from the ground state to the first excited state and is described by the Beer-Lamber-Bouguer law. As the intensity increases, the first excited state becomes almost completely occupied, and then the absorption is described by a transition from the first to the second excited state, i.e., it acquires a nonlinear character.

According to the results of experiments, the nonlinear optical parameters were calculated for SWCNT/water dispersion. The calculation of nonlinear optical parameters was carried out using a threshold model based on the radiation transfer equation [31]. This model allows taking into account the fact that changes

Condensed Matter and Interphases / Конденсированные среды и межфазные границы   2021;23(4): 496–506

P. N. Vasilevsky et al.   Nonlinear optical properties of single-walled carbon nanotubes/water dispersed media...
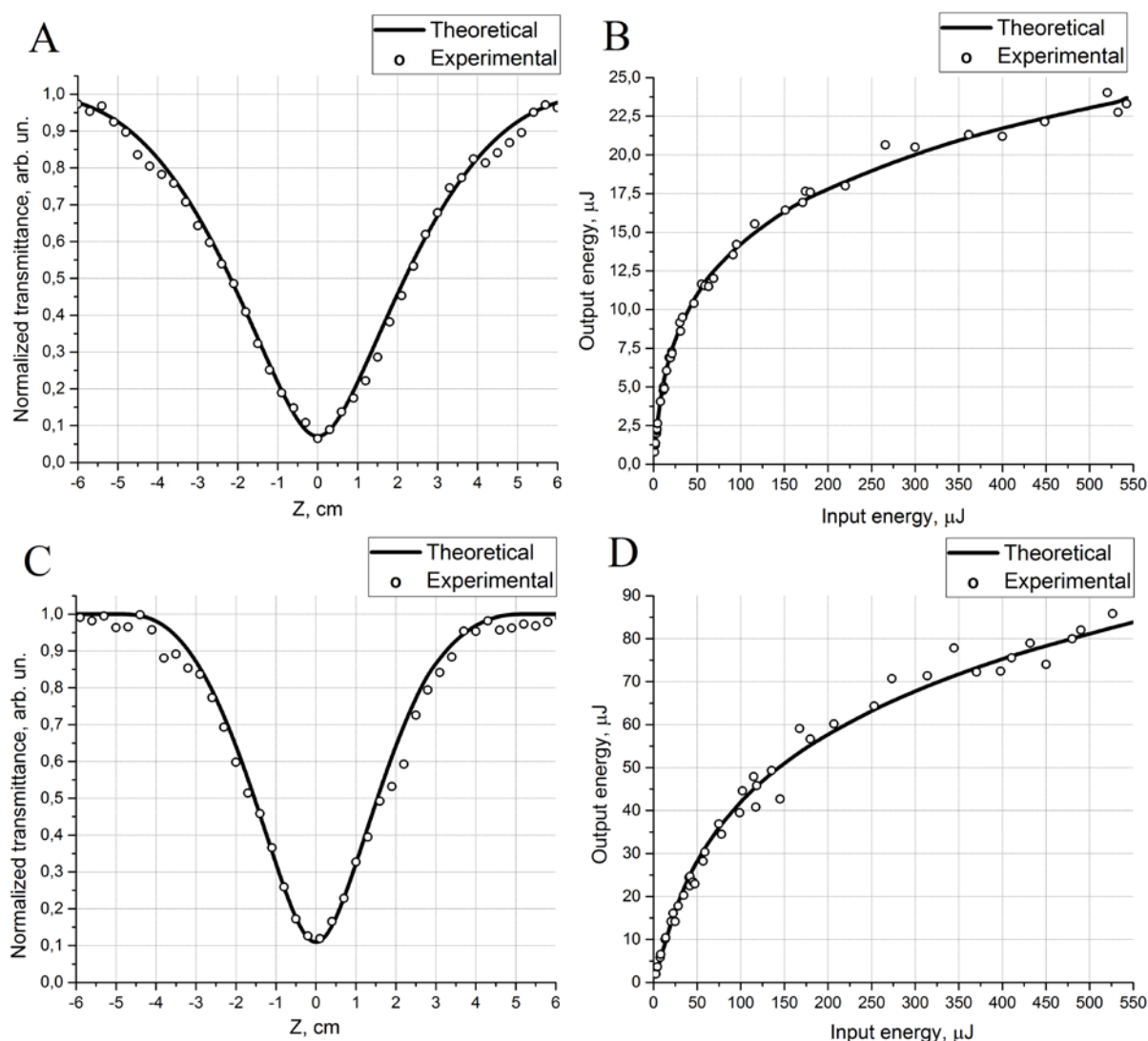
Fig. 4. Curves of dependences obtained from the results of Z-scanning and experiments with a fixed position of the sample for wavelengths of 532 (a, b) and 1064 nm (c, d)

in the parameters of the medium do not occur immediately, but only when a certain intensity value was reached:

$$\mu(I) = \alpha + \beta \cdot (I - I_{th}) \cdot \eta(I - I_{th}) \qquad (4)$$

where $\mu(I)$ - the total absorption coefficient, β – the nonlinear absorption coefficient, $\eta(I - I_{th})$ – Heaviside step function. Thus, after the calculation of the optical parameters presented in formula (4), it is possible to predict the behaviour of the medium under different intensities. The threshold model is described in detail in [32].

The calculation results are presented in Table 1. The difference in the threshold intensity can be explained by two-photon absorption. Although this effect is nonthreshold, it affects the degree of radiation absorption in addition to linear absorption. For this reason, gas formation can occur at the interface between the solid and liquid phases much earlier, which manifests as the formation of microbubbles and, accordingly, in an increase in absorption with an increase in the optical path of the laser beam due to multiple scattering [33]. Despite the higher nonlinear absorption coefficient, the attenuation coefficient at a wavelength of 1064 nm was lower than at a wavelength of 532 nm. This was due to the later occurrence of nonlinear absorption due to the higher threshold intensity. The values of the nonlinear absorption coefficient for SWCNT/water dispersion were much higher than the values for the graphene and graphene

Condensed Matter and Interphases / Конденсированные среды и межфазные границы   2021;23(4): 496–506

P. N. Vasilevsky et al.   Nonlinear optical properties of single-walled carbon nanotubes/water dispersed media...

Table 1. Optical parameters of SWCNT/water dispersion at different wavelengths

Wavelength, nm	Linear absorption coefficient, 1/cm	Nonlinear absorption coefficient, cm/GW	Threshold intensity, MW/cm²	Attenuation coefficient
532	1.78	1111	5.5	15.3
1064	1.78	2010	18	9.7

oxide particles dispersions (3 and 45 cm/GW, respectively) presented in [34, 35]. This can be explained by the fact that carbon nanotubes increase multiple scattering more strongly, increasing the optical path inside the sample. Due to the increase in the optical path, more photons are absorbed, which causes more excitation in the molecules and, accordingly, stronger nonlinear properties.

3.2. Linear and nonlinear optical properties under femtosecond radiation

Irradiation with femtosecond radiation was performed in a frequency mode with a pulse repetition rate of 80 MHz. The cell was placed at the focus of the lens. Images from a CCD camera at different power of laser radiation are shown in Table 2. With low radiation power, the transmitted beam corresponds to the Gaussian shape of the incident beam. It can be seen that at the radiation power $P \approx 100$ mW the laser beam starts to expand significantly. The increase in power leads to the further expansion of the beam with the formation of a ring-shaped structure. The radius of the outer ring was taken as the beam size upon the formation of rings. It should be noted that the transmission of the sample in this case did not change with increasing power.

The emergence of such diffraction pattern is a consequence of spatial self-phase modulation [36]. The refractive index n starts to change due to the thermal effects in the medium, under the action of laser radiation above a certain threshold. In this case, due to the Gaussian shape of the incident radiation at different points of the medium, the change in the refractive index will be different, forming a gradient in the refractive index. This leads to the appearance of the self-defocusing effect, i.e., the divergence of the beam and an increase in its radius.

Together with this, a change in the phase of coherent laser radiation occurs in the medium, since a gradient change in the refractive index

leads to a change in the propagation rate of the beam in the medium υ:
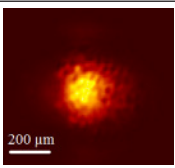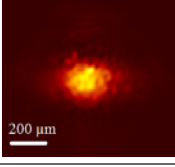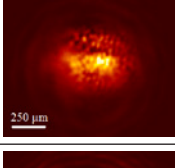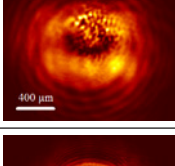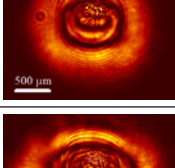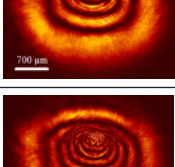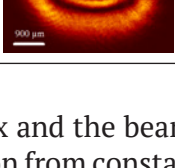
$$\upsilon = \frac{c}{n} \tag{5}$$

where c – the propagation rate of the beam in a vacuum. Thus, different parts of the transmitted radiation have different phases, which leads to the appearance of an interference pattern on the screen. Dark areas correspond to radiation in opposite phase, and light areas correspond to interference maxima.

The thermal nature of this effect was confirmed by the distortion of the interference pattern in the images. The rings above the centre of the irradiation site narrow, forming an asymmetry along the Y axis. This is due to the appearance of thermal convection determined by the vertical position of the cell. When the liquid is heated, the heat goes up, and the temperature gradient and the gradient of the refractive index, become smaller in the upper part of the irradiated zone. This leads to the approximately the same rate of beam propagation above the centre of irradiation and the phase shift becomes much lower the lower the centre of irradiation is or at the edges.

In our study, we propose to use the effect of spatial self-phase modulation to attenuate the power of radiation transmitted through the studied medium. For this, a system with a slit which cuts off part of the radiation at the expansion of beam was proposed. The dependence of the transmitted laser power on the incident power is shown in Fig. 5. It can be seen that when the power reached $P = 150$ mW, a sharp drop in the transmitted power occurred. This was due to the fact that the size of the beam becomes larger than the size of the slit, and part of the beam is cut off. With a further increase in the power, the transmitted power stops to decrease and again starts to increase slowly, but this increase was much less than in the linear case, i.e. before the appearance of a gradient in the

Condensed Matter and Interphases / Конденсированные среды и межфазные границы   2021;23(4): 496–506

P. N. Vasilevsky et al.   Nonlinear optical properties of single-walled carbon nanotubes/water dispersed media...

Table 2. The shape and size of the beam after passing through the sample at different powers

No.	Beam visualization from CCD camera	Power, mW	Beam size X, µm	Beam size Y, µm
1	200 µm	10	280	280
2	200 µm	45	270	220
3	250 µm	100	500	300
4	400 µm	160	1020	700
5	500 µm	330	1880	1450
6	700 µm	520	2700	2050
7	900 µm	710	3600	2700

refractive index and the beam's expansion. Due to this transition from constant transmittance to nonlinear transmittance, the effect of limiting the power of laser radiation occurs. This effect can be used both for the protection of photosensitive elements and control of the signal in optical switches.

The value of linear refractive index n_0 was obtained using a portable refractometer. For the studied dispersion it was 1.33 and it was equal to the refractive index of water. This finding suggests that the addition of carbon nanotubes does not lead to a change in the refractive index of the solvent.

Based on the results of the experiment, the nonlinear refractive index n_2 was determined according to the formula:

$$n_2 = \frac{\lambda N}{2n_0 dI} = \frac{\lambda N w_0^2 \pi}{4n_0 dP}, \tag{6}$$

where N - the number of rings. For the calculation, the number of rings was considered below the centre of irradiation. It was found that for the studied SWCNT/water dispersion sample, the nonlinear refractive index was 0.16 cm²/MW, which is several orders of magnitude higher than the nonlinear refractive index of graphene dispersion (0.0025 cm²/MW) obtained in [37]. A stronger non-linear

Condensed Matter and Interphases / Конденсированные среды и межфазные границы   2021;23(4): 496–506

P. N. Vasilevsky et al.   Nonlinear optical properties of single-walled carbon nanotubes/water dispersed media...
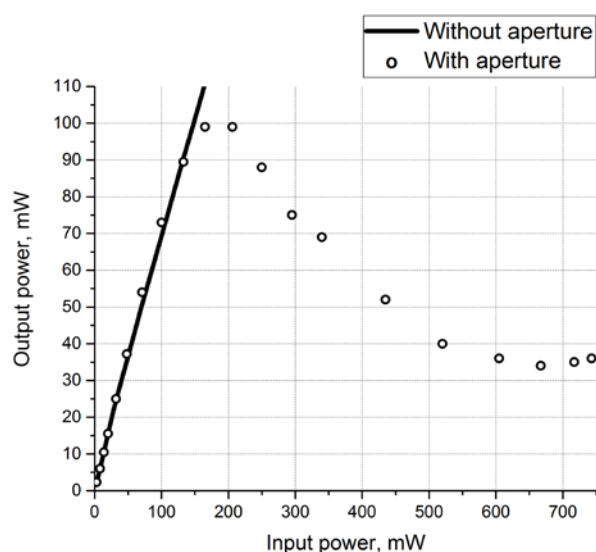
Fig. 5. Curve of the dependence of the transmitted power on the incident power when exposed to femtosecond radiation

response potentially leads to a larger increase in the radius of the rings, and thus a sharper decrease in transmission when using the slit.

4. Conclusions

As a result of the performed studies, the linear and nonlinear optical parameters for SWCNT/water dispersion at different wavelengths were determined. The obtained values can be used to characterize the investigated medium exposed to radiation of different intensities. The conditions for the occurrence of nonlinear absorption and refraction effects in a medium, leading to a change in the corresponding optical characteristics, were determined. The high stability of the investigated medium to the action of high-intensity laser radiation was shown. The effects of nonlinear absorption (reverse saturable absorption and two-photon absorption) and nonlinear refraction (spatial self-phase modulation) appear in the studied medium exposed to laser radiation with nano- and femtosecond pulse durations. The high linear transmission and the calculated nonlinear optical parameters allowed to conclude that SWCNT/water dispersion can be used for the limitation of both single pulses and radiation with a high pulse repetition rate in the visible and near IR ranges. Thus, single-walled carbon nanotubes have the potential to be used as an active medium of laser radiation limiters for the protection of light-sensitive sensors and visual organs.

Authors contributions

Vasilevsky P. N. – writing text, obtaining data for analysis, final conclusions. Savelyev M. S. – analysis of experimental data, development of methodology, text editing. Tereshchenko S. A. – creation of a theoretical model, text editing. Selishchev S.V. – research concept, text editing. Gerasimenko A. Yu. – scientific guidance, text editing.

Conflict of interests

The authors declare that they have no known competing financial interests or personal relationships that could have influenced the work reported in this paper.

References

1. Shin Y. C., Wu B., Lei S., Cheng G. J., Lawrence Yao Y. Overview of laser applications in manufacturing and materials processing in recent years. *Journal of Manufacturing Science and Engineering*. 2020;142(11): 110818. https://doi.org/10.1115/1.4048397

2. Kalisky Y. Y., Kalisky O. The status of high-power lasers and their applications in the battlefield. *Optical Engineering*. 2010;49(9): 091003. https://doi.org/10.1117/1.3484954

3. Nishizawa N. Ultrashort pulse fiber lasers and their applications. *Japanese Journal of Applied Physics*. 2014;53(9): 090101. http://dx.doi.org/10.7567/JJAP.53.090101

4. Kashaev N., Ventzke V., Çam G. Prospects of laser beam welding and friction stir welding processes for aluminum airframe structural applications. *Journal of Manufacturing Processes*. 2018;36: 571–600. https://doi.org/10.1016/j.jmapro.2018.10.005

5. Liaros N., Fourkas J. T. Ten years of two-color photolithography. *Optical Materials Express*. 2019;9(7): 3006–3020. https://doi.org/10.1364/OME.9.003006

6. Roberts H. W., Day A. C., O'Brart D. P. S. Femtosecond laser–assisted cataract surgery: a review. *European Journal of Ophthalmology*. 2020;30(3): 417–429. https://doi.org/10.1177/1120672119893291

7. Campbell P., Moore I. D., Pearson M. R. Laser spectroscopy for nuclear structure physics. *Progress in Particle and Nuclear Physics*. 2016;86: 127–180. https://doi.org/10.1016/j.ppnp.2015.09.003

8. Dekan M., František D., Andrej B., Jozef R., Dávid R., Josip M. Moving obstacles detection based on laser range finder measurements. *International Journal of Advanced Robotic Systems*. 2018;15(1): 1–18. https://doi.org/10.1177/1729881417748132

9. Bukin O. A., Babii M. Yu., Golik S. S., Il'in A. A., Kabanov A. M., Kolesnikov A. V., Kulchin Yu. N., Lisitsa V. V., Matvienko G. G., Oshlakov V. K.,

Condensed Matter and Interphases / Конденсированные среды и межфазные границы   2021;23(4): 496–506

P. N. Vasilevsky et al.   Nonlinear optical properties of single-walled carbon nanotubes/water dispersed media...

Shmirko K. A. Lidar sensing of the atmosphere with gigawatt laser pulses of femtosecond duration. *Quantum Electronics*. 2014;44(6): 563–569. https://doi.org/10.1070/QE2014v044n06ABEH015431

10. Goodin C., Carruth D., Doude M., Hudson C. Predicting the influence of rain on LIDAR in ADAS. *Electronics*. 2019;8(1): 89. https://doi.org/10.3390/electronics8010089

11. Farid N., Li C., Wang H., Ding H. Laser-induced breakdown spectroscopic characterization of tungsten plasma using the first, second, and third harmonics of an Nd: YAG laser. *Journal of Nuclear Materials*. 2013;433(1-3): 80–85. https://doi.org/10.1016/j.jnucmat.2012.09.002

12. Saylam K., Hupp J. R., Averett A. R., Gutelius W. F., Gelhar B. W. Airborne lidar bathymetry: assessing quality assurance and quality control methods with Leica Chiroptera examples. *International Journal of Remote Sensing*. 2018;39(8): 2518–2542. https://doi.org/10.1080/01431161.2018.1430916

13. Chomicki D., Kharchenko O., Skowronski L., Kowalonek J., Smokal V., Krupka O., Derkowska-Zielinska B. Influence of methyl group in a quinoline moiety on optical and light-induced properties of side-chain azo-polymers. *Applied Nanoscience*. 2021: 1–9. https://doi.org/10.1007/s13204-021-01764-0

14. Büyükekşi S. I., Karatay A., Orman E. B., Selçuki N. A., Özkaya A. R., Salih B., Elmali A., Şengül A. A novel AB 3-type trimeric zinc (ii)-phthalocyanine as an electrochromic and optical limiting material. *Dalton Transactions*. 2020;49(40): 14068–14080. https://doi.org/10.1039/D0DT02460K

15. Beverina L., Pagani G. A., Sassi M. Multichromophoric electrochromic polymers: colour tuning of conjugated polymers through the side chain functionalization approach. *Chemical Communications*. 2014;50(41): 5413–5430. https://doi.org/10.1039/C4CC00163J

16. Savelyev M. S., Gerasimenko A. Y., Vasilevsky P. N., Fedorova Y. O., Groth T., Ten G. N., Telyshev D. V. Spectral analysis combined with nonlinear optical measurement of laser printed biopolymer composites comprising chitosan/SWCNT. *Analytical biochemistry*. 2020;598: 113710. https://doi.org/10.1016/j.ab.2020.113710

17. Eevon C., Halimah M. K., Zakaria A., Azurahanim C. A. C., Azlan M. N., Faznny M. F. Linear and nonlinear optical properties of Gd^{3+} doped zinc borotellurite glasses for all-optical switching applications. *Results in Physics*. 2016;6: 761–766. https://doi.org/10.1016/j.rinp.2016.10.010

18. Varma S. J., Kumar, J., Liu, Y., Layne, K., Wu, J., Liang, C., Nakanishi Y., Aliyan A. Yang W. Ajayan P. M., Thomas J. 2D TiS$_2$ layers: a superior nonlinear optical limiting material. *Advanced Optical Materials*. 2017;5(24): 1700713. https://doi.org/10.1002/adom.201700713

19. Tutt L. W., Boggess T. F. A review of optical limiting mechanisms and devices using organics, fullerenes, semiconductors and other materials. *Progress in Quantum Electronics*. 1993;17(4): 299–338. https://doi.org/10.1016/0079-6727(93)90004-S

20. Li R., Dong N., Ren F., Amekura H., Wang J., Chen F. Nonlinear absorption response correlated to embedded Ag nanoparticles in BGO single crystal: from two-photon to three-photon absorption. *Scientific Reports*. 2018;8(1): 1–8. https://doi.org/10.1038/s41598-018-20446-6

21. Miao R., Hu Y., Ouyang H., Tang Y., Zhang C., You J., Zheng X., Xu Z., Cheng X., Jiang T. A polarized nonlinear optical response in a topological insulator Bi$_2$Se$_3$–Au nanoantenna hybrid-structure for all-optical switching. *Nanoscale*. 2019;11(31): 14598–14606. https://doi.org/10.1039/C9NR02616A

22. Savelyev M. S., Vasilevsky P. N., Gerasimenko A. Y., Ichkitidze L. P., Podgaetsky V. M., Selishchev S. V. Nonlinear optical characteristics of albumin and collagen dispersions with single-walled carbon nanotubes. *Materials Physics and Mechanics*. 2018;37(2): 133–139. https://doi.org/10.18720/mpm.3722018_4

23. Savotchenko S. E. Periodic states near the plane defect with non-linear response separating non-linear self-focusing and linear crystals. *Kondensirovannye Sredy I Mezhfaznye Granitsy = Condensed Matter and Interphases*. 2020;20(2): 255–262. https://doi.org/10.17308/kcmf.2018.20/517

24. Valligatla S., Haldar K. K., Patra A., Desai N. R. Nonlinear optical switching and optical limiting in colloidal CdSe quantum dots investigated by nanosecond Z-scan measurement. *Optics & Laser Technology*. 2016;84: 87–93. https://doi.org/10.1016/j.optlastec.2016.05.009

25. Zhang Y., Wang Y. Nonlinear optical properties of metal nanoparticles: a review. *RSC Advances*. 2017;7(71); 45129–45144. https://doi.org/10.1039/C7RA07551K

26. Kuzmina E. A., Dubinina T. V., Vasilevsky P. N., Saveliev M. S., Gerasimenko A. Y., Borisova N. E., Tomilova L. G. Novel octabromo-substituted lanthanide (III) phthalocyanines–Prospective compounds for nonlinear optics. *Dyes and Pigments*. 2021;185: 108871. https://doi.org/10.1016/j.dyepig.2020.108871

27. Papagiannouli I., Bourlinos A. B., Bakandritsos A., Couris S. Nonlinear optical properties of colloidal carbon nanoparticles: nanodiamonds and carbon dots. *RSC Advances*. 2014;4(76): 40152–40160. https://doi.org/10.1039/C4RA04714A

28. Gerasimenko A. Yu. Laser structuring of the carbon nanotubes ensemble intended to form biocompatible ordered composite materials. *Kondensirovannye Sredy I Mezhfaznye Granitsy = Condensed Matter and Interphases*. 2017;19(4): 489–

Condensed Matter and Interphases / Конденсированные среды и межфазные границы   2021;23(4): 496–506

P. N. Vasilevsky et al.   Nonlinear optical properties of single-walled carbon nanotubes/water dispersed media...

501. https://doi.org/10.17308/kcmf.2017.19/227 (In Russ., absract in Eng.)

29. Atlukhanova L. B., Dolbin I. V., Kozlov G. V. The Physics of Interfacial Adhesion between a Polymer Matrix and Carbon Nanotubes (Nanofibers) in Nanocomposites. *Kondensirovannye Sredy I Mezhfaznye Granitsy = Condensed Matter and Interphases*. 2020;22(2): 190–196. https://doi.org/10.17308/kcmf.2020.22/2822

30. Maurya S. K., Rout A., Ganeev R. A., Guo C. Effect of size on the saturable absorption and reverse saturable absorption in silver nanoparticle and ultrafast dynamics at 400 nm. *Journal of Nanomaterials*. 2019;2019: 1–13. https://doi.org/10.1155/2019/9686913

31. Tereshchenko S. A., Podgaetskii V. M., Gerasimenko A. Yu., Savel'ev M. S. Threshold effect under nonlinear limitation of the intensity of high-power light. *Quantum Electronics*. 2015;45(4): 315–320. https://doi.org/10.1070/QE2015v045n04ABEH015569

32. Tereshchenko S. A., Savelyev M. S., Podgaetsky V. M., Gerasimenko A. Yu., Selishchev S. V. Nonlinear threshold effect in the Z-scan method of characterizing limiters for high-intensity laser light. *Journal of Applied Physics*. 2016;120(9): 093109. https://doi.org/10.1063/1.4962199

33. Savelyev M. S., Gerasimenko A. Y., Podgaetskii V. M., Tereshchenko S. A., Selishchev S. V., Tolbin A. Y. Conjugates of thermally stable phthalocyanine J-type dimers with single-walled carbon nanotubes for enhanced optical limiting applications. *Optics & Laser Technology*. 2019;117: 272–279. https://doi.org/10.1016/j.optlastec.2019.04.036

34. Tong Q., Wang Y. H., Yu X. X., Wang B., Liang Z., Tang M., Wu A. S., Zhang H. J., Liang F., Xie Y. F. Nonlinear optical and multi-photon absorption properties in graphene–ZnO nanocomposites. *Nanotechnology*. 2018;29(16): 165706. https://doi.org/10.1088/1361-6528/aaac13

35. Wang S., Dong Y., He C., Gao Y., Jia N., Chen Z., Song W. The role of sp 2/sp 3 hybrid carbon regulation in the nonlinear optical properties of graphene oxide materials. *RSC Advances*. 2017;7(84): 53643–53652. https://doi.org/10.1039/C7RA10505C

36. Li J., Zhang Z., Yi J., Miao L., Huang J., Zhang J., He Y., Huang B., Zhao C., Zou Y., Wen S. Broadband spatial self-phase modulation and ultrafast response of MXene $Ti_3C_2T_x$ (T= O, OH or F). *Nanophotonics*. 2020;9(8): 2415–2424. https://doi.org/10.1515/nanoph-2019-0469

37. Stavrou M., Dalamaras I., Karampitsos N., Couris S. Determination of the nonlinear optical properties of single-and few-layered graphene dispersions under femtosecond laser excitation: electronic and thermal origin contributions. *The Journal of Physical Chemistry C*. 2020;124(49): 27241–27249. https://doi.org/10.1021/acs.jpcc.0c09959

Information about the authors

Pavel N. Vasilevsky, Postgraduate Student, Engineer in Institute of Biomedical Systems, National Research University of Electronic Technology – MIET, Zelenograd, Moscow, Russian Federation; Junior Research Fellow, Institute of Nanotechnology of Microelectronics of the Russian Academy of Sciences, Moscow, Russian Federation; e-mail: pavelvasilevs@yandex.ru. ORCID iD: https://orcid.org/0000-0002-5733-8497.

Mikhail S. Savelyev, PhD in Physics and Mathematics, Assistant Professor in Institute of Biomedical Systems, National Research University of Electronic Technology – MIET, Zelenograd, Moscow, Russian Federation; Research Fellow, Institute of Nanotechnology of Microelectronics of the Russian Academy of Sciences, Moscow, Russian Federation; Research Fellow, I. M. Sechenov First Moscow State Medical University, Moscow, Russian Federation; e-mail: savelyev@bms.zone. ORCID iD: https://orcid.org/0000-0003-1255-0686.

Sergey A. Tereshchenko, DSc in Physics and Mathematics, Professor in Institute of Biomedical Systems, National Research University of Electronic Technology – MIET, Zelenograd, Moscow, Russian Federation; Research Fellow, Institute of Nanotechnology of Microelectronics of the Russian Academy of Sciences, Moscow, Russian Federation; e-mail: tsa@miee.ru. https://orcid.org/0000-0002-3163-5741.

Sergey V. Selishchev, DSc in Physics and Mathematics, Director of Institute of Biomedical Systems, National Research University of Electronic Technology – MIET, Zelenograd, Moscow, Russian Federation; e-mail: selishchev@bms.zone. ORCID: https://orcid.org/0000-0002-5589-7068.

Alexander Yu. Gerasimenko, Dsc in Physics and Mathematics, Assistant Professor in Institute of Biomedical Systems, National Research University of Electronic Technology – MIET, Zelenograd, Moscow, Russian Federation; Research Fellow, Institute of Nanotechnology of Microelectronics of the Russian Academy of Sciences, Moscow, Russian Federation; Head of the Laboratory of Biomedical Nanotechnology, I. M. Sechenov First Moscow State Medical University, Moscow, Russian Federation; e-mail: gerasimenko@bms.zone. https://orcid.org/0000-0001-6514-2411.

Original articles

Formation of a quasi-equilibrium domain structure of crystals of the TGS group near T_C

O. M. Golitsyna, S. N. Drozhdin✉

Voronezh State University,
1 Universitetskaya pl., Voronezh 394018, Russian Federation

Abstract

In the temperature range $\Delta T \approx 321\ K \div 322\ K$, the kinetics of the nonequilibrium domain structure of triglycine sulphate crystals, both pure and with specially introduced defects, has been studied by means of piezoresponse force microscopy technique. The temporal change in the domain structure as a set of regions with a scalar order parameter of $P(r, t) = +1$ and -1 for oppositely polarized domains was analysed by the behaviour of the space-time correlation function $C(r,t) = \langle P(r,t)P(0,t) \rangle$. At different distances from the Curie point T_c, the characteristic length L_c, as a scale measure of the average domain size, increases with time according to the power law $L_c(t) \sim (t-t_0)^\alpha$. A decrease of the exponent α with distance from T_c can be a consequence of the transition of the domain structure of TGS crystals from a non-conservative state to a conservative one.

Keywords: Piezoresponse atomic force microscopy, Triglycine sulfate, space-time correlation function, Characteristic length, Time dependences, Power law

✉ Sergey N. Drozhdin, e-mail: drozhdin@phys.vsu.ru

Condensed Matter and Interphases / Конденсированные среды и межфазные границы   2021;23(4): 507–517

O. M. Golitsyna, S. N. Drozhdin   Formation of a quasi-equilibrium domain structure of crystals...

1. Introduction

Triglycine sulphate $(NH_2CH_2COOH)_3 \cdot H_2SO_4$ – TGS, its isomorphs (triglycine selenate, triglycine fluoroberyllate), their deuterated analogues, as well as their modifications doped with various impurities, are some of the best materials for pyroelectric applications. But they are of no less interest as convenient model objects for studying structural phase transitions [1–3], the domain structure [4–14], the influence of a weak magnetic field on non-magnetic ferroelectric materials [15–18], the manifestation of ferroelectric properties under conditions of limited geometry [19–22], etc.

The study of any physical properties of ferroelectrics and, in particular, these crystals is impossible without a detailed analysis of the role of the domain structure in the behaviour of these properties, especially near T_c, where it is anomalous. Therefore, in this work, the kinetics of the formation of a domain structure (DS) of several crystals of the TGS group was studied at an insignificant (no more than 1 K), distance from the phase transition temperature T_c, at which point this structure occurs, being in a significantly non-equilibrium state during the initial moments of time.

The choice of the temperature range was also dictated by the fact that in this critical region, which is quite close to the point of phase transition, where fluctuation effects can still be noticeable, and the thickness of the domain walls can be comparable to the width of the domains, such studies were practically not carried out. Earlier [7–10], the behaviour of DS of only nominally pure TGS crystals was studied after their exposure in the paraelectric phase followed by a rapid cooling into the ferroelectric phase to temperatures spaced from the Curie point by $\Delta T_c > 2$ K. At temperatures closer to the phase transition, the formation of a quasi-equilibrium DS was studied only in [6] and [11, 12] during its visualization, respectively, by the method of nematic liquid crystals and atomic force microscopy. There are no data on such studies of TGS crystals with defects of a known type in the literature.

The objectives of this work were to find out: 1) whether the behaviour of the studied crystals near T_c is consistent with that established for TGS crystals at a significant distance from T_c [7–10];

2) to what extent this behaviour corresponds to the general regularities of the ordering processes of various two-phase systems [23] after their transition from an disordered high-symmetric phase to an ordered low-symmetric one.

Obtaining objective results in the studies of crystals of the TGS group is not an easy task, since not only crystals grown under different conditions and having different post-growth history, but even samples from different growth pyramids of the same crystal have different domain structures. The static and dynamic properties of the domain structure of TGS crystals also significantly depend on the presence of any defects in them [5]. And if an impurity (such as L,α-alanine) enters non-uniformly into the volume of the growing crystal, then the DS can be different even within the same growth pyramid [24]. Differences in the experimental techniques used and in the measurement conditions also play a significant role.

The symmetry of the ferroelectric phase of the TGS crystal is simple (the space group $P2_1$ of the monoclinic syngony), but its 180° domain structure is diverse and geometrically complex. Five typical configurations of antiparallel domains can be observed in nominally pure TGS crystals [25]. Four of them are characteristic of freshly grown crystals, and the fifth, the most typical striped (lamellar) domain structure (type E, according to [25]), studied in this paper, occurs in an aged TGS crystal after its annealing in the paraelectric phase and subsequent transfer to the ferroelectric phase. At the same time, small lenticular domains of the opposite sign can be incorporated into the lamellae, fully or partially growing along the polar direction. These are type A and type B according to the classification [25] (Fig. 1).

After holding an electrically free TGS crystal in the paraelectric phase ($T > T_c = 322$ K) and its subsequent cooling into the ferroelectric phase, a nonequilibrium DS as a set of very small domains occurs in it. For energy reasons [4], such a domain structure gradually enlarges over time [5]. This process can be studied within the framework of phase ordering kinetics [23], an approach used to describe the behaviour of various systems subjected to quenching (rapid cooling) from a homogeneous phase to a phase with broken symmetry. Here 180° ferroelectric

Condensed Matter and Interphases / Конденсированные среды и межфазные границы   2021;23(4): 507–517

O. M. Golitsyna, S. N. Drozhdin   Formation of a quasi-equilibrium domain structure of crystals...
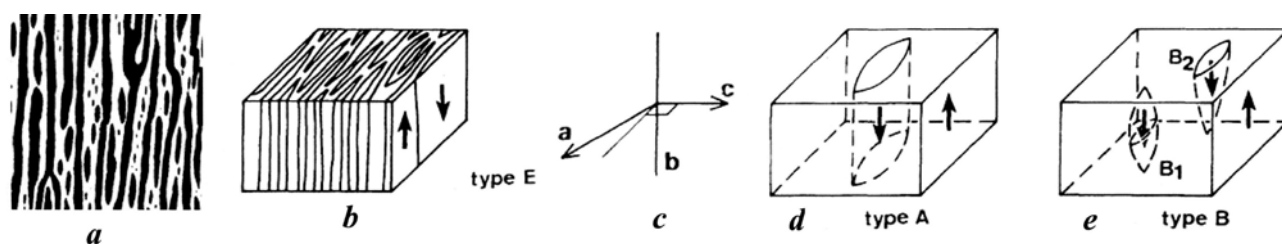
Fig. 1. The real lamellous domain structure of the TGS crystal – a; types of the domain structure of TGS according to the classification [25]: E – b, A – d, B – e; the coordinate axes of the unit cell of the TGS – c

DS is considered as a two-phase system described by the scalar long-range order parameter P (r,t) [26], which takes values "+1" and "–1" in antiparallel domains. Its evolution at T = const can be analysed using the space-time correlation functions $C(r, t) = \langle P(r,t)P(0,t)\rangle$ [6–9].

In this work, the functions $C(r,t)$ were calculated for domain patterns visualized by means of piezoresponse force microscopy technique during the evolution of the DS of TGS crystals in the temperature range 321 K $\leq T < T_c$ = 322 K. The main questions were the following: 1) the time dependence and the equilibrium value of the characteristic scale length L_c of the average domain size, 2) the features of the order parameter $P(r,t)$, which determine the form of the dependence $L_c(t)$, 3) the scaling of the correlation function, 4) the effect of defects on the quantitative parameters of the evolution of the domain structure.

2. Experimental

Crystals of pure TGS (crystal growth conditions and its properties are described in articles [12, 27]), as well as TGS with impurity (L,α-alanine – ATGS, chromium – TGS-Cr, phosphorus – TGSP) and radiation (X-ray irradiation – XR-TGS) defects were studied. All doped crystals were grown at temperatures below T_c. The TGS crystal was grown from a solution with the concentration of L,α-alanine in it of 10 mol%. The TGS-Cr crystal was grown from a solution containing 1 mol% salt of $Cr_2(SO_4)_3 6H_2O$. The TGSP crystal was grown from a solution of a mixture of triglycine sulphate and triglycine phosphate salts taken in a ratio of 1:1 [28]. Radiation defects were generated by irradiation of nominally pure TGS with CuKα X-rays (quantum energy of 30 keV, total dose of 240 kR). High concentrations of L,α-alanine, and chromium impurities, as well as high X-ray

radiation doses, can suppress the dynamics of domains in TGS, which was unacceptable for the purposes of this work. Therefore, relatively "soft" samples were selected from these crystals with a dielectric constant at the Curie point $\varepsilon_{max} \geq 1\cdot10^3$ and with an internal bias field $E_b \leq 500$ Vcm^{-1}, which made it possible to observe the evolution of the emerging DS in them.

The samples of the studied crystals were polar b-cleavages with an average size of 5×5×1 mm. Domain images were recorded in the contact mode of piezoelectric force microscopy (PFM) using a Solver P47 Pro microscope by applying an alternating electric field with an amplitude of 1 V and a frequency of 150 kHz to a NSG11/TiN cantilever (tip curvature radius 35 nm, force constant 11.5 N·m^{-1}, resonance frequency 255 kHz). The measurements were carried out in air at constant parameters (temperature, humidity, pressure) of the environment. The temperature of a specimen was regulated and monitored using a homemade controller mounted on the head of the microscope. The samples were preheated from T_1 = 293 K to T_2 = 333 K and, after holding for half an hour at T_2, they were cooled at a rate of 1 K min^{-1} to T_3 = 324 K. Then, the cooling rate was decreased to 0.1÷0.2 K·min^{-1} in order to minimize the time required for the stabilization of the temperature of observation (T_{ob}) with an accuracy of about ± 0.05 K. Each scan at a fixed T_{ob} was carried out on the same area of the sample surface. The recording of images of the domain structure ended when the lateral displacement of the domain walls did not exceed the measurement error of the domain size (2%).

In our measurements, the cooling of the samples into the ferroelectric phase was not a real quenching, as, for example, in [7], but, nevertheless, both the phase transition and the initial state of the crystals were obviously not

Condensed Matter and Interphases / Конденсированные среды и межфазные границы   2021;23(4): 507–517

O. M. Golitsyna, S. N. Drozhdin   Formation of a quasi-equilibrium domain structure of crystals...

equilibrium. The amplitude PSM images of the DS were converted into a digital format for further calculations in a program specially compiled in the MATHCAD package. The obtained domain images, as well as the calculated graphs of the correlation functions $C(r,t)$, were not subjected to any additional processing, the expediency of which was discussed in [29].

3. Results and discussion

Figures 2–4 show the correlation functions $C(r)$ and the corresponding images (50×50 µm) of domains of TGS, LATGS, and XR-TGS crystals during the initial and final stages of the evolution of their domain structures at two temperatures below T_c. Correlation functions were calculated for directions close to [001] and [100].

For comparison, Figures 5–7 show similar information for TGS, TGSF, and TGS-Cr crystals, but at a distance from the phase transition point $\Delta T_c = 4.0$ K, since, as shown in [13, 14], the evolutionary kinetics of the domain structure should depend on the depth of cooling into the ferroelectric phase.

The initial domain structures, especially near T_c, are ensembles of many small irregularly shaped domains, which are predominantly elongated in a direction close to [100]. In pure TGS, the domain structure is lamellar, while in doped and irradiated crystals it is more complex, with more rugged domain boundaries. Over time, the domain structures of all the crystals under study become larger, but their main topographic features are preserved, and the question is, how statistically similar are they to the original ones? The domain enlargement in all crystals includes: 1) the disappearance of small domains located inside large domains of the opposite sign; 2) the contraction and disappearance of the protrusions along ~[100] direction; 3) contraction of large domains in the longitudinal (~[100]) direction. As a result, domains expand along the lateral (~[001]) direction, and their boundaries become smoother and less curved. These features of the evolution of the domain structure of pure TGS, noted earlier in [8–10], are more pronounced with distance from T_c, where the domains are larger. In crystals with defects (especially with radiation ones),
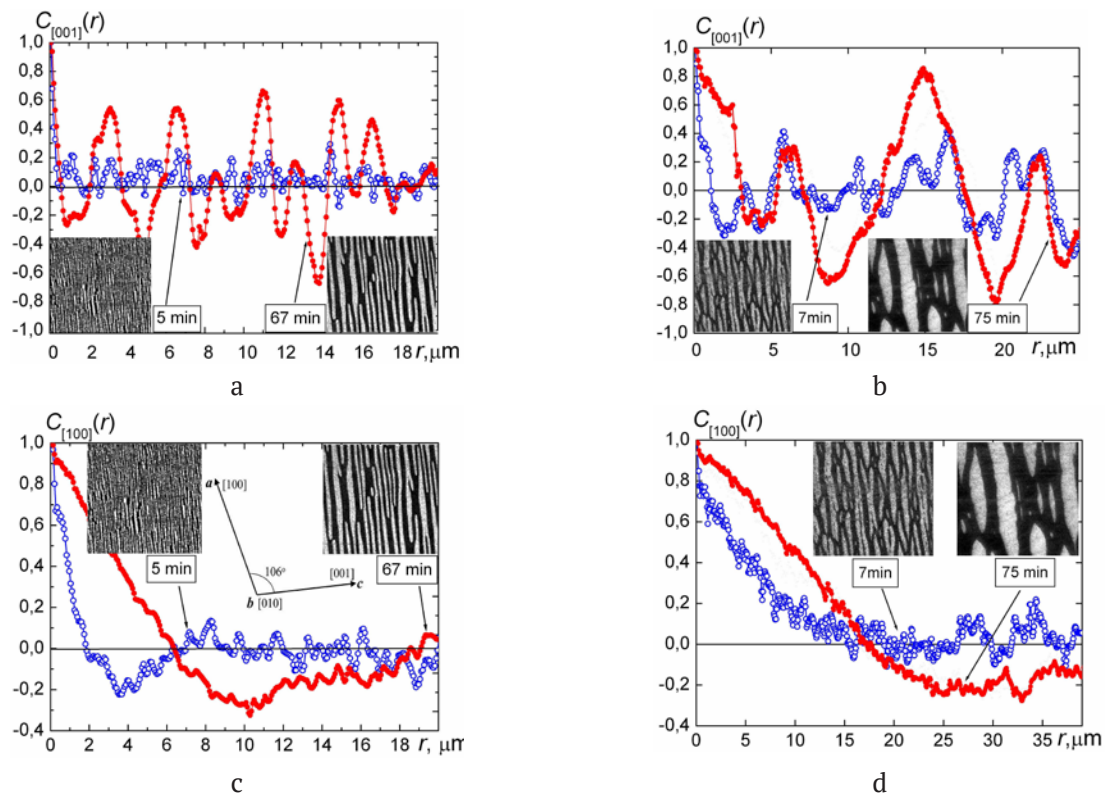
Fig. 2. The correlation functions $C(r)$ and correspondent domain pictures for a pure TGS crystal at $\Delta T_c = 0.1$ K (a, c) and $\Delta T_c = 1.0$ K (b, d) for two time moments after phase transition, and for directions [001] (a, b) and [100] (c, d)

Condensed Matter and Interphases / Конденсированные среды и межфазные границы   2021;23(4): 507–517

O. M. Golitsyna, S. N. Drozhdin   Formation of a quasi-equilibrium domain structure of crystals...
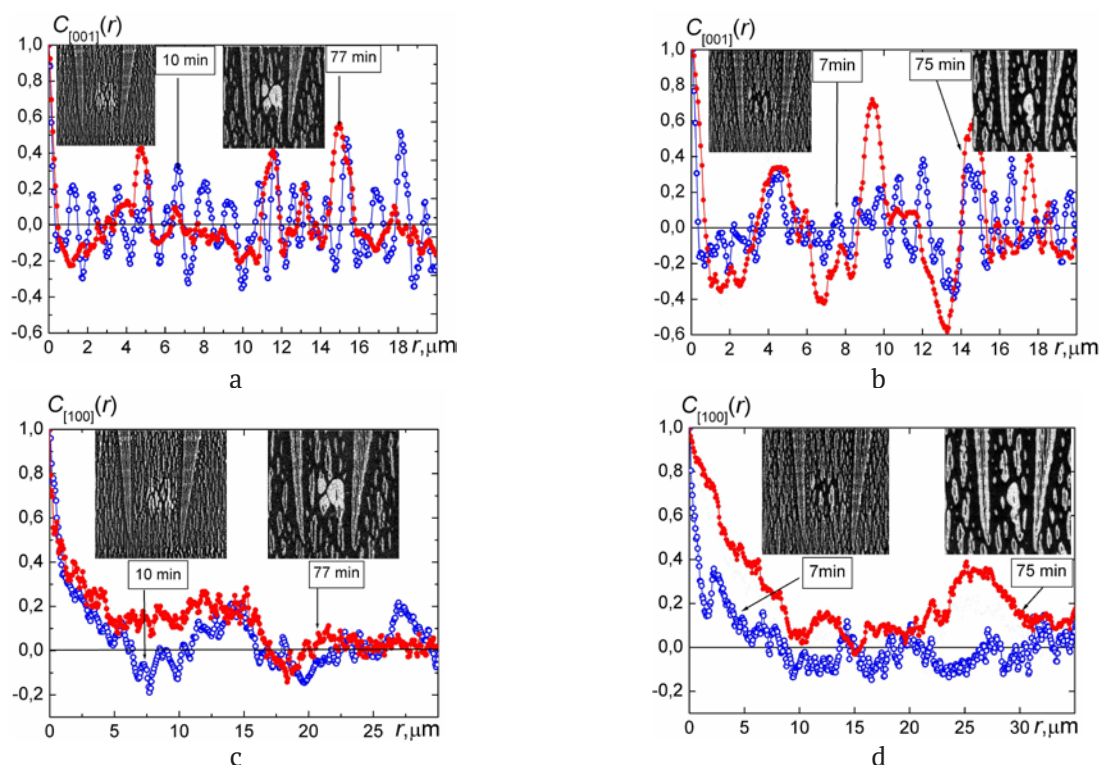
Fig. 3. The correlation functions $C(r)$ and correspondent domain pictures for a LATGS crystal at $\Delta T_c = 0.3$ K (a, c) and $\Delta T_c = 0.8$ K (b, d) for two time moments after phase transition, and for directions [001] (a, b) and [100] (c, d)
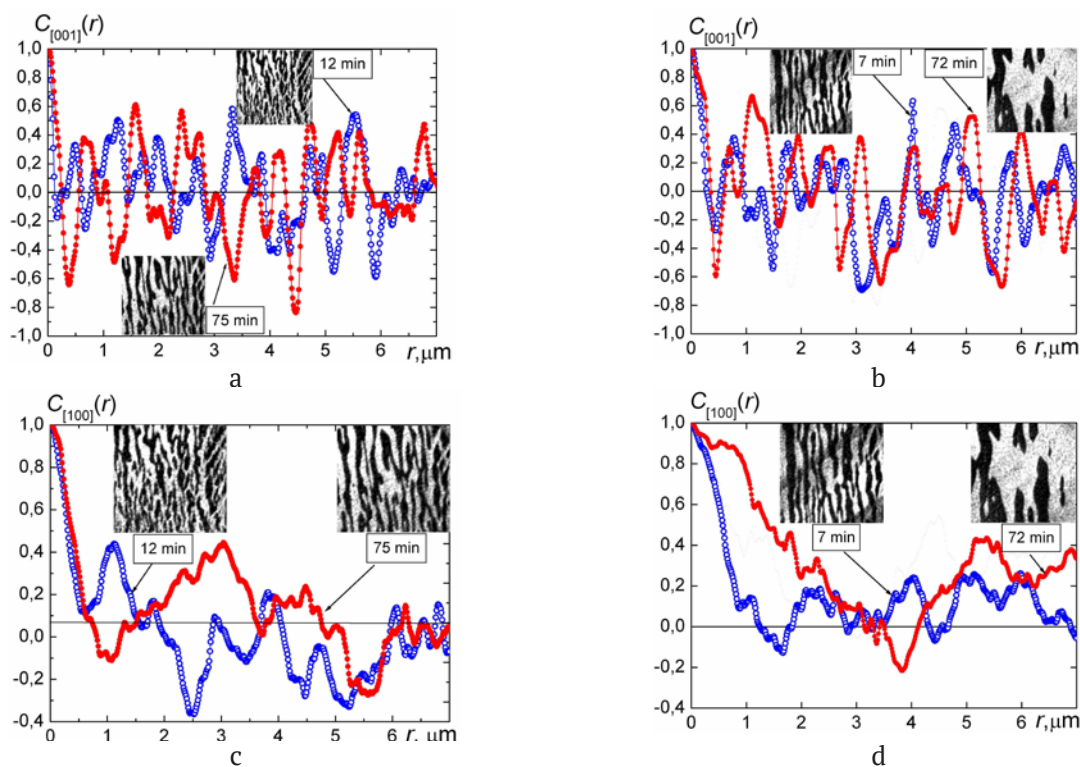
Fig. 4. The correlation functions $C(r)$ and correspondent domain pictures for a XR-TGS crystal at $\Delta T_c = 0.3$ K (a, c) and $\Delta T_c = 0.8$ K (b, d) for two time moments after phase transition, and for directions [001] (a, b) and [100] (c, d)

Condensed Matter and Interphases / Конденсированные среды и межфазные границы   2021;23(4): 507–517

O. M. Golitsyna, S. N. Drozhdin   Formation of a quasi-equilibrium domain structure of crystals...
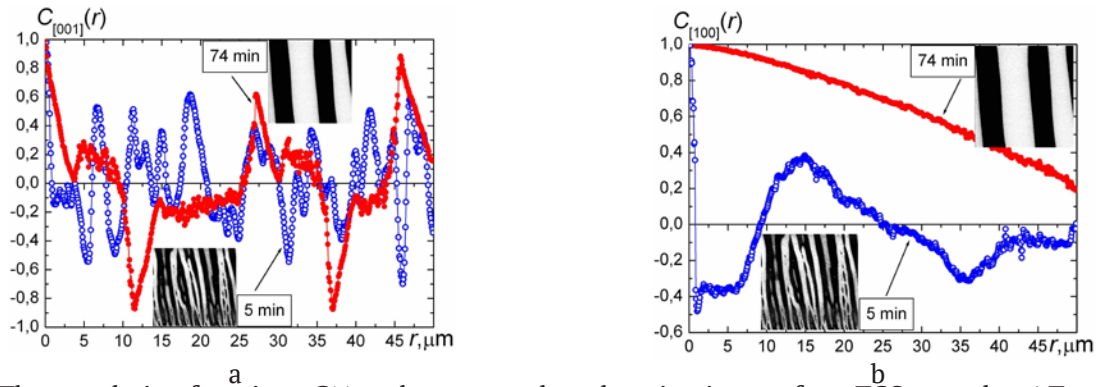
Fig. 5. The correlation functions $C(r)$ and correspondent domain pictures for a TGS crystal at $\Delta T_c = 4.0$ K for two time moments after phase transition and for directions [001] (a) and [100] (b)
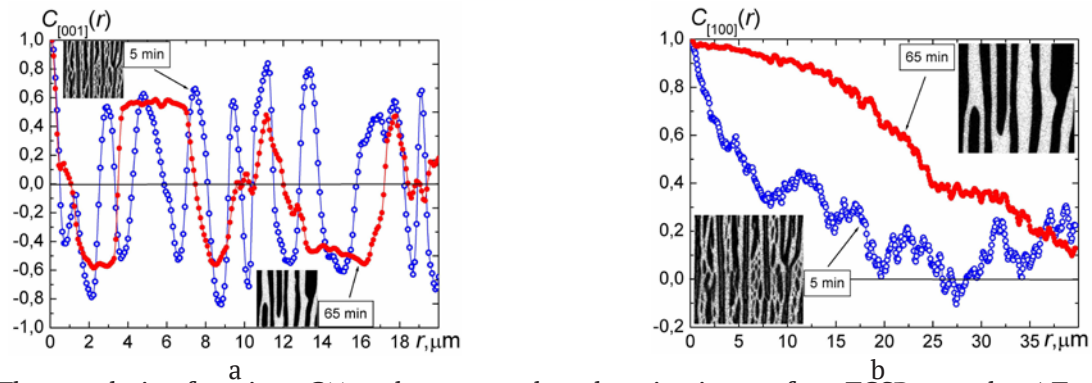
Fig. 6. The correlation functions $C(r)$ and correspondent domain pictures for a TGSP crystal at $\Delta T_c = 4.0$ K for two time moments after phase transition and for directions [001] (a) and [100] (b)
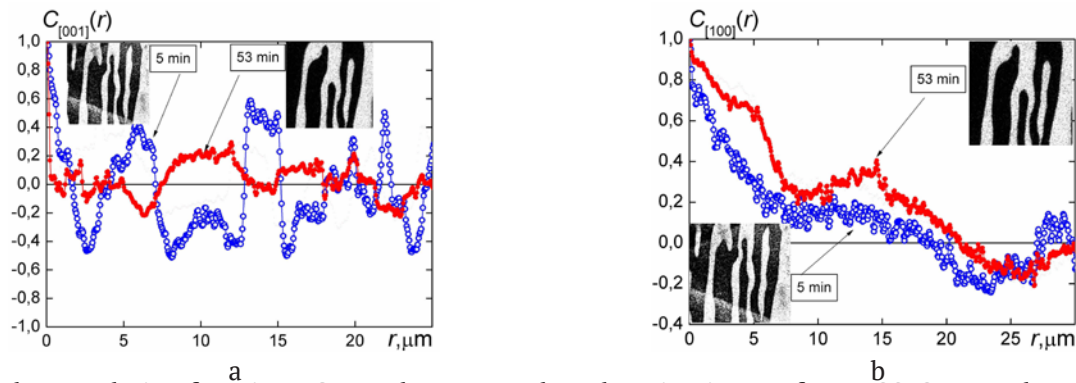
Fig. 7. The correlation functions $C(r)$ and correspondent domain pictures for a TGS-Cr crystal at $\Delta T_c = 4.0$ K for two time moments after phase transition and for directions [001] (a) and [100] (b)

these regularities are less pronounced, since the defects, pinning the domain walls, impede their "spontaneous" displacements.

The mechanism of the observed temporal change of domains is formally explained by the action of electric field forces equivalent to the surface tension forces, the value of which is determined in our case by the curvature of the domain walls [23, 30]. The relaxation kinetics of the already existing domain structure is effected by the movement of the domain walls due to near-wall nucleation and the subsequent two-dimensional growth of nuclei whose sizes are larger than a critical one [31]. The initial nucleation that leads to the appearance of new domains is most likely insignificant in the absence of an external electric field. However, any displacement of the domain wall leading to local switching of polarization in any way must be caused by the action of a local electric field $\vec{E}_{loc}$, which in the general case is the sum of the external electric field $\vec{E}_{ext}$, the depolarizing field $\vec{E}_{dep}$ and the screening field $\vec{E}_{scr}$: $\vec{E}_{loc} = \vec{E}_{ext} + \vec{E}_{dep} + \vec{E}_{scr}$ [14] and in absence of an external field $\vec{E}_{loc} = \vec{E}_{dep} + \vec{E}_{scr}$.

Condensed Matter and Interphases / Конденсированные среды и межфазные границы   2021;23(4): 507–517

O. M. Golitsyna, S. N. Drozhdin   Formation of a quasi-equilibrium domain structure of crystals...

The depolarizing field $\vec{E}_{dep}$ is the field of bound charges of spontaneous polarization, and the field $\vec{E}_{scr}$ is created as a result of either external or internal (bulk) screening. The external screening field arises as a result of the adsorption of charged particles on the surface of a ferroelectric crystal and their redistribution in the external medium. The volume screening is a result of the redistribution of charge carriers in the bulk of the ferroelectric and of the reorientation of dipole defects. The depolarizing field can be compensated completely only by volume screening, the delay of which is the cause of the jump-like motion of DWs [31, 32]. For a real ferroelectric, under the conditions of a real experiment, there is no reason to believe that the local fields are the same in the neighbouring domains, and it can be assumed that it is their difference that triggers the processes of motion of DWs, i.e. near-wall polarization reversal. The defects, pinning the domain walls, firstly, cause non-monotonicity of their displacements and, secondly, determine, along with the temperature [13, 14], the average speed of their movement that leads to a reduction in the duration of the process of changing the domain structure of the ferroelectric.

The time transformation of the obtained images of the domain structure, which to a certain extent reflect its evolution towards equilibrium, can be considered as the transition of the system from a disordered to an ordered state and analysed using the space-time correlation function $C(r, t) = \langle P(r,t)\, P(0,t)\rangle$ [7–9, 23], which is the average product of the values of the scalar order parameter $P(r) = \pm 1$ (where $+1$ corresponds to $+\boldsymbol{P}_S$ and -1 to $-\boldsymbol{P}_S$) for two fragments of the image, shifted by r relative to each other. The equal-time function $C(r, t = \text{const})$ indicates the degree of similarity between these fragments at a given time. The similarity of one and the same fragment taken at various moments in time can in principle also be detected using the correlation function. Thus, it is possible to investigate both spatial and temporal correlations of DS during its evolution.

The dependences of the function $C(r,t)$ upon r both for initial and final times of domain pictures recording, shown in Figures 2a,b–4a,b and 5a–7a, indicate to quasiperiodicity of domain patterns along ~[001] direction. As for the ~[100] direction (Figures 2c,d–4c,d and 5b–7b) the clear oscillations of $[C(r)]_{[100]}$ curves take place mostly in the vicinity of T_c, as well during the initial stage of evolution when there is a sufficient number of domains which dimensions along this direction not exceed the size of the scanned area. Absolute values of the correlation function show that during evolution the spatial correlation of domain configurations increases with time, as well as when moving away from T_c towards lower temperatures. In the crystals with defects in which the domain walls are less mobile, the absolute values of $C(r,t)$ and, consequently, the spatial correlation of domain patterns do not significantly change both upon time and temperature.

Earlier in [12], for the temperature range 321 K $\leqslant T < T_c$ = 322 K, the time dependences of some parameters of the domain structure of a pure TGS crystal during its evolution after the phase transition were found from domain pictures. It was shown, particularly, that the average linear dimensions of domains along the [001] and ~[100] directions obey the power law: $\langle w \rangle \sim t^{\alpha}$, where the exponent α varies upon temperature from 0.45 to 0.93. Here for all TGS crystals under investigation the time dependences (Figures 8 a–d) for the characteristic scale length L_c (t) were found, i.e. the distance at which the absolute value of the correlation function $C(r = L_c, t) = 0.5$ occurred. These dependences also obey the power law $L_c(t) \sim (t - t_0)^{\alpha}$, known from [23] for various thermodynamic systems undergoing phase ordering. The values of exponent α are in good agreement with those from [12].

For a nominally pure TGS, the exponent $\alpha \approx 0.5$ at a distance from T_c by 0.3–0.5 K (in Fig. 9 this region is highlighted by a dotted oval), showing that under these conditions the crystal behaves like a system with a non-conservative macroscopic order parameter [23]. This result is in good agreement with the result of [13], where it was shown within the framework of the Ginzburg–Landau theory, that near the critical point the evolution of the non-equilibrium 180° domain structure to thermodynamic equilibrium occurs in such a way that the correlation radius and, consequently, the sizes of domains of the ferroelectric grow according to the law: ~ $t^{0.5}$.

Condensed Matter and Interphases / Конденсированные среды и межфазные границы   2021;23(4): 507–517

O. M. Golitsyna, S. N. Drozhdin   Formation of a quasi-equilibrium domain structure of crystals...
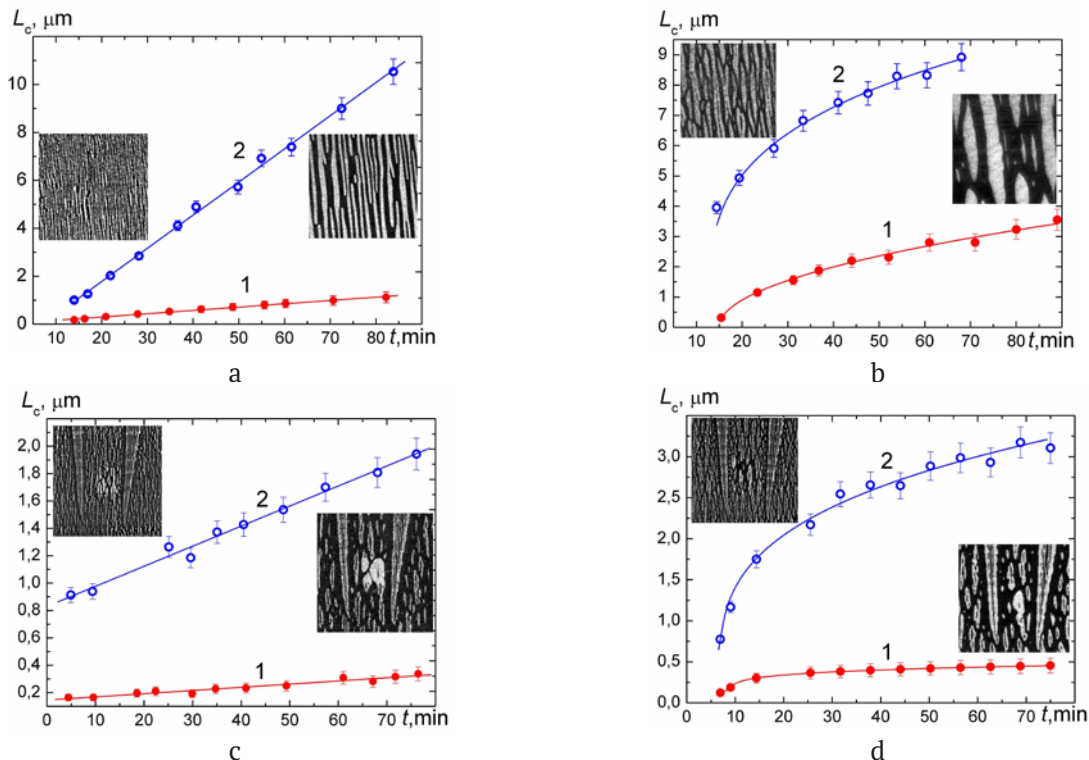
Fig. 8. Time dependences of the characteristic length L_c for pure TGS: $\Delta T_c = 0.1$ K (a); $\Delta T_c = 1.0$ K (b) and for LATGS: $\Delta T_c = 0.3$ K (c); $\Delta T_c = 0.6$ K (d). Curves *1* – [001] and *2* – [100] directions
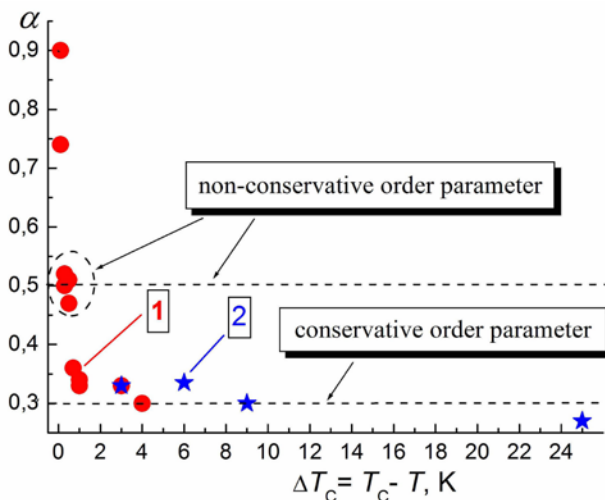
Fig. 9. The values of the exponent α in the dependence $L_c(t) \sim (t - t_0)^{\alpha}$ at different distances from T_c: according to the data of this work – *1*, according to the data of [8, 9] – *2*

Near the Curie point ($\Delta T_c \approx 0.1$–0.2 K), the exponent α for TGS is close to 1 and the same values of $\alpha \approx 1$ are demonstrated by LATGS and XR-TGS crystals, but in the range $\Delta T_c \approx 0.3$ K. The reason for such a strong discrepancy between the experimental and model behaviour of α [8, 9, 23] may be due to the fact that in the immediate vicinity of the transition point, the volumes of the polar medium components (the domains themselves and the regions separating them, interpreted as domain walls) are close in size [6, 11, 35], and between two phases of the system (domains of different signs) there are no sharp boundaries, whose existence is an obligatory element of the model approach [23]. It can be assumed that the kinetics of not only the enlargement of the domain structures of the studied crystals, but probably also of other two-phase systems in the immediate vicinity of the phase transition point is not described by existing theoretical models [23] and requires additional research.

The values of α decrease upon a decrease in temperature: for LATGS at $\Delta T_c = 0.5$ K and for XR-TGS at $\Delta T_c = 0.6$ K, they are close to the value of 0.33, which is characteristic for the evolution of systems with a conservative order parameter [6]. For pure TGS, α decreases slower and its "conservative" value of $\alpha \approx 0.3$ can presumably be achieved at $\Delta T_c \sim 2$–3 K, which, however, should depend on the quality, that is the degree of defectiveness of the crystal. Figure 9 shows the temperature dependence of the exponent α obtained for nominally pure TGS in this work, as well as its values according to the data of [8,

Condensed Matter and Interphases / Конденсированные среды и межфазные границы   2021;23(4): 507–517

O. M. Golitsyna, S. N. Drozhdin   Formation of a quasi-equilibrium domain structure of crystals...

9]. All experimental points, as can be seen from the figure, fit well on one curve, which probably indicates the objectivity of the results obtained. In the crystals with defects (LATGS, XR-TGS, TGSP, TGS-Cr) at a greater distance from T_c (3÷4 K) exponent α tends towards a value of 0.2, which is characteristic for the evolution of inhomogeneous structures with defects during spinodal decay [17].

Theoretical and experimental studies of phase ordering in various systems give grounds to describe the development of the domain structure within the framework of the scaling hypothesis [8, 23]. The essence of this approach is that the domain structure (in a statistical sense) does not depend on time, when all lengths are scaled using the characteristic length $L_c(t)$. It was shown [23] that the scaling properties of the growth kinetics of the emerged phases depend only on the spatial dimensionality of the system and are the same for systems either with defects or without them. In the present work, the scaling forms of the correlation functions $C(r, t) = f(r/L_c(t))$ were tested for all the crystals under study near the phase transition point. The examples of functions $C(r,t) = f(r/L_c(t))$, are shown in Fig. 10.

It can be seen that the scaled correlation functions for different time points on the initial section ($0 \leqslant r/L_c \leqslant 2$) of the graph decrease linearly according to the law $f(r/L_c(t)) = 1 - k(r/L_c)$ with coefficients $k = 0.54$ for TGS and $k = 0.57$ for LATGS, close to the value 1/2, where 2 is the dimensionality of the system, and then begin to gradually dissipate. This behaviour is interpreted as Porod's law [8, 23], which is characteristic for the field of both conservative and non-conservative scalar order parameters.

4. Conclusion

As a result of studying the formation of a quasi-equilibrium domain structure of ferroelectric crystals of the TGS group in a temperature range with the width of $\Delta T_c = 1$ K the following conclusions can be drawn:

1. During evolution of the DS the spatial correlation of domain configurations increases with time, as well as when moving away from T_c towards lower temperatures. In the crystals with defects in which the domain walls are less mobile, the absolute values of $C(r,t)$ and, consequently, the spatial correlation of domain patterns do not significantly change both in time and temperature.

2. The characteristic length increases over time according to a power law with an exponent that is similar for the studied crystals. The decrease of the absolute values of the exponent, when moving away from the Curie point in the studied temperature range, is a consequence of the transition of the domain structure of TGS crystals during its evolution from a non-conservative state to a conservative one [18].

3. The correlation functions of domain patterns of all studied TGS crystals, presented at different times in a scaled form $C(r, t) = f(r/L_c(t)) \equiv f(x)$, in the initial region $0 \leqslant x \leqslant 2$ and near the temperature of the ferroelectric phase transition have a universal scaling form for the ordering kinetics of two-phase systems with a scalar order parameter: $f(x) = 1 - 0.5x$.

4. The spontaneous evolution of the domain structure of crystals of the TGS group obeys the general laws of the ordering kinetics of two-phase systems of different nature not far but also near the phase transition temperature, that
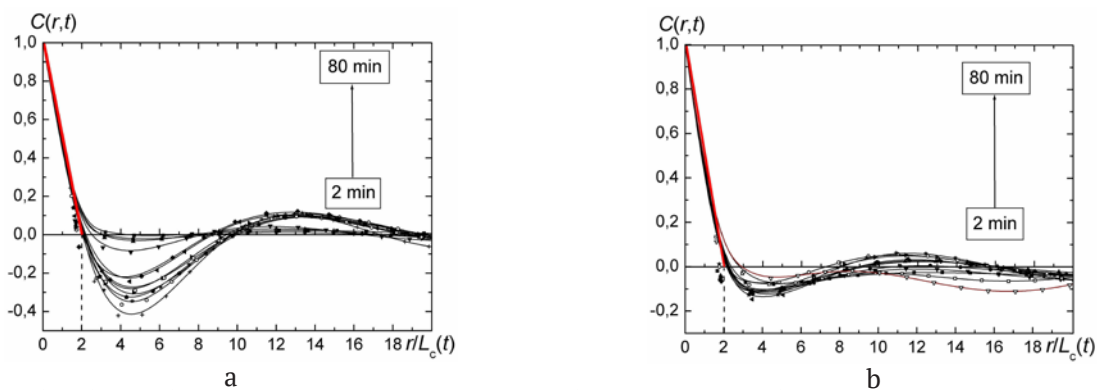
Fig. 10. The dependencies $C(r,t) = f(r/L_c(t))$ over the time interval 2 ÷ 80 min at $\Delta T_C = 0.1$ K: TGS crystal, direction [001] (a); LATGS crystal, direction [001] (b)

Condensed Matter and Interphases / Конденсированные среды и межфазные границы   2021;23(4): 507–517

O. M. Golitsyna, S. N. Drozhdin   Formation of a quasi-equilibrium domain structure of crystals...

is confirmed by the power-law time dependences of the characteristic sizes of the regions of two phases (domains) $L_c(t)$, and the scaling behaviour of the domain structure.

Authors contributions

All authors made an equivalent contribution to the preparation of the publication.

Conflict of interests

The authors declare that they have no known competing financial interests or personal relationships that could have influenced the work reported in this paper.

References

1. Choudhury R R., Chitra R., Ramanadham M., Effect of isotope substitution and pressure on the phase transition in triglycine sulphate. *Physica B: Condensed Matter.* 2005;36691-4): 116–121. https://doi.org/10.1016/j.physb.2005.05.034

2. Bdikin I. K., Wojtas M., Kiselev D., Isakov D., Kholkin A. L. Ferroelectric-paraelectric phase transition in triglycine sulphate via piezoresponse force microscopy. *Ferroelectrics*. 2012;426(1): 215–222. https://doi.org/10.1080/00150193.2012.671742

3. Hudspeth J. M., Goossens D. J., Wellbery T. R., Gutmann M. J., Diffuse scattering and the mechanism for the phase transition in triglycine sulphate. *Journal of Materials Science*. 2013;48(19): 6605–6612. https://doi.org/10.1007/s10853-013-7457-8

4. Sidorkin A. S., *Domain structure in ferroelectrics and related materials*. Cambridge International Science Publising; 2006. 240 p.

5. Tagantsev A. K., Cross L. E., Fousek J. *Domains in ferroic crystals and thin films*. New York: Springer; 2010. 830 p. https://doi.org/10.1007/978-1-4419-1417-0

6. Nakatani N., Ferroelectric domain structure in TGS just below the Curie point after heat treatment. *Japanese Journal of Applied Physics*. 1985;24(Part 2, No. 7): L528–L530. https://doi.org/10.1143/JJAP.24.L528

7. Tomita N., Orihara H., Ishibashi Y. Ferroelectric domain pattern evolution in quenched triglycine sulphate. *Journal of the Physical Society of Japan*. 1989;58(4): 1190–1196. https://doi.org/10.1143/JPSJ.58.1190

8. Likodimos V., Labardi V., Allegrini M. Kinetics of ferroelectric domains investigated by scanning force microscopy. *Physical Review B*. 2000;61(21): 14440–14447. https://doi.org/10.1103/physrevb.61.14440

9. Likodimos V., Labardi M., Orlik X. K., Pardi L., Allegrini M., Thermally activated ferroelectric domain growth due to random defects. *Physical Review B*. 2001;63(6): 064104–064107. https://doi.org/10.1103/physrevb.63.064104

10. Shin S., Baek J., Hong J. W., Khim Z. G. Deterministic domain formation observed in ferroelectrics by electrostatic forse microscopy. *Journal of Applied Physics*. 2004;96(8): 4372–4377. https://doi.org/10.1063/1.1781760

11. Tolstikhina A. L., Gainutdinov R. V., Belugina N. V., Lashkova A. K., Kalinin A. S., Atepalikhin V. V., ... Bykov V. A. Study of the quasi-periodic one dimensional domain structure near T_c of TGS crystal by PFM and hybrid PFM methods. *Physica B: Condensed Matter.* 2018;550: 332–339. https://doi.org/10.1016/j.physb.2018.09.025

12. Golitsyna O. M., Drozhdin S. N., Grechkina M. N. Evolution of the domain structure of triglycine sulphate single crystal in the vicinity of phase transition. *Ferroelectrics*. 2017;506(1): 127–135. https://doi.org/10.1080/00150193.2017.1282286

13. Mazur O. Yu., Stefanovich L. I., Yurchenko V. M. Influence of quenching conditions on the kinetics of formation of a domain structure of ferroelectrics. *Physics of the Solid State*, 2015;57(3): 576–580. https://doi.org/10.1134/S1063783415030142

14. Mazur O. U., Stefanovich L. I. Effect of the degree of overcooling on relaxation of the domain structure of triglycine sulphate. *Physics of the Solid State*. 2019;61(8): 1420–1424. https://doi.org/10.1134/s1063783419080183

15. Yakushkin E. D. Dielectric response of a uniaxial ferroelectric in a magnetic field. *JETP Letters*. 2014;99(7): 415–418. https://doi.org/10.1134/S00021364014070133

16. Ivanova E. S., Rumyantsev I. D., Petrzhik E. A., Change in dielectric properties of triglycine sulfate in a constant magnetic field. *Physics of the Solid State*. 2016:58(1): 127–133. https://doi.org/10.1134/S1063783416010157

17. Gainutdinov R. V., Ivanova E. S., Petrzhik E. A., Lashkova A. K., Volk T. R. Magnetic memory effects in triglycine sulfate ferroelectric crystals. *JETP Letters*. 2017;106(2): 97–102. https://doi.org/10.1134/S00021364017140053

18. Golitsyna O. M., Drozhdin S. N. Influence of a static magnetic field on the dielectric properties of triglycine sulfate. *Ferroelectrics*. 2020;567(1): 244-263. https://doi.org/10.1080/00150193.2020.1791610

19. Baryshnikov S. V., Charnaya E. V., Shatskaya Y. A., Milinskiy A. Yu., Samoilovich M. I., Michel D., Tien C. Effect of confined geometry on linear and nonlinear dielectric properties of triglycine sulfate near the phase transition. *Physics of the Solid State*. 2011;53(6): 1212–1216. https://doi.org/10.1134/S1063783411060059

20. Golitsyna O. M., Drozhdin S. N., Nechaev V. N., Viskovatykh A. V., Kashkarov V. M., Gridnev A. E., Chernyshev V. V. Dielectric properties of porous aluminum and silicon oxides with inclusions of

Condensed Matter and Interphases / Конденсированные среды и межфазные границы   2021;23(4): 507–517

O. M. Golitsyna, S. N. Drozhdin   Formation of a quasi-equilibrium domain structure of crystals...

triglycine sulfate and its modified analogs. *Physics of the Solid State*. 2013;55(3): 529–535. https://doi.org/10.1134/s1063783413030128

21. Golitsyna O. M., Drozhdin S. N., Kashkarov V. M., Chulakova V. O. Dielectric properties of porous silicon with inclusions of triglycinesulphate. *Kondensirovannye sredy i mezhfaznye granitsy = Condensed Matter and Interphases*. 2015;17(2): 153–159. Available at: https://www.elibrary.ru/item.asp?id=23816615 (In Russ., abstract in Eng.)

22. Mai B. D., Nguyen H. T., Ta D. H., Sidorkin A. S., Milovidova S. D. Preparation and dielectric properties of a mixed ferroelectric composite from nanoparticles of cellulose and triglycine sulfate. *Ferroelectrics*. 2019;543(1): 175–183. https://doi.org/10.1080/00150193.2019.1592431

23. Bray A. J., Theory of phase-ordering kinetics. *Advances in Physics*. 1994;43: 357–459. https://doi.org/10.1080/00018739400101505

24. Dontzova L. I., Tikhomirova N. A., Shuvalov L. A. Investigation of domain structure and switching processes in ferroelectrics by the liquid crystal method. *Ferroelectrics*. 1989;97(1): 87–124. https://doi.org/10.1080/00150198908018085

25. Takahashi K., Takagi M. Topographic study on domain boundaries in TGS. I. *Journal of the Physical Society of Japan*. 1978;44(4): 1266–1274. https://doi.org/10.1143/JPSJ.44.1266

26. Mitsui T., Tatsuzaki I., Nakamura E. *An introduction to the physics of ferroelectrics*. London: Gordon and Breach; 1976. 443 p.

27. Golitsyna O. M., Grechkina M. V., Drozhdin S. N., Chulakova V. O. Time dependencies of the domain structure parameters of TGS crystal near the phase transition temperature. *Condensed Matter and Interphases*. 2016;18(4): 494–504. Available at: https://www.elibrary.ru/item.asp?id=27474850 (In Russ., abstract in Eng.)

28. Drozhdin S. N., Golitsyna O. M., Nikishina A. I., Kostsov A. M. Pyroelectric and dielectric properties of triglycine sulphate with an impurity of phosphorus (TGSP). *Ferroelectrics*. 2008;373(1): 93–98. https://doi.org/10.1080/00150190802408804

29. Golitsyna O. M., Drozhdin S. N., Korobova A. D., Lesnikova V. O. Analysis of model and real 1800 domain picturesby means of space-time correlation functions. *OAJ Materials and Devices*. 2019;4(1): 1506.

30. Tikhomirova N. A., Pikin S. A., Shuvalov L. A., Dontsova L. I., et al., Visualization of static and the dynamics of domain structure in triglycine sulfate by liquid crystals, *Ferroelectrics*. 1980;29(1): 145–156. https://doi.org/10.1080/00150198008008470

31. Shur V. Ya., Correlated nucleation and self-organized kinetics of ferroelectric domains. In: *Nucleation Theory and Applications*. J.W.P. Schmelzer (ed.). Wiley-VCH Verlag; 2005. pp. 178–214. https://doi.org/10.1002/3527604790.ch6

32. Dolbilov M. A., Shur V. Y., Shishkina E. V., Angudovich E. S., Ushakov A. D., Baldi P., de Micheli M. P.Formation of nanodomain structure in front of the moving domain wall in lithium niobate single crystal modified by proton exchange. *Ferroelectrics*. 2013;442(1): 82–91. https://doi.org/10.1080/10584587.2013.776408

33. Vasilevskaya T. N., Andreev N. S. Experimental small-angle X-ray scattering investigation of initial stages the spinodal decomposition in model sodium silicate glasses. *Physics of the Solid State*. 2011;53: 2250–2256. https://doi.org/10.1134/S106378341111031X

34. Golitsyna O. M., Drozhdin S. N., Lesnikova V. O. Effect of L,α-alanine impurity on the spontaneous evolution of the domain structure of triglicine sulphate near the Curie point. *Kondensirovannye sredy i mezhfaznye granitsy = Condensed Matter and Interphases*. 2018;20(4): 564–573. Available at: https://www.elibrary.ru/item.asp?id=36653678 (In Russ., abstract in Eng.)

35. Novik V. K., Lotonov A. M., Gavrilova N. D. Dielectric loss as an indication of the kinetics of the ferroelectric phase transition. *Physics of the Solid State*. 2009;51: 1414–1419. https://doi.org/10.1134/s1063783409070221

Information about the authors

Olga M. Golitsyna, PhD in Physics and Mathematics, Assistant Professor, Voronezh State University, Voronezh, Russian Federation; e-mail: golitsynaom@yandex.ru. ORCID iD: https://orcid.org/0000-0003-0821-1382.

Sergey N. Drozhdin, DSc in Physics and Mathematics, Professor, Head of Department, Voronezh State University, Voronezh State University, Voronezh, Russian Federation; e-mail: drozhdin@phys.vsu.ru. ORCID iD: https://orcid.org/0000-0001-8157-365X.

Original articles

Electrodialysis of a sodium sulphate solution with experimental bentonite-modified bipolar membranes

O. A. Kozaderova[1], K. B. Kim[1✉], P. E. Belousov[2], A. V. Timkova[1], S. I. Niftaliev[1]

[1]*Voronezh State University of Engineering Technologies,
19 Revolutsii pr., Voronezh 394036, Russian Federation*

[2]*Institute of Geology of Ore Deposits, Petrography, Mineralogy, and Geochemistry of the Russian Academy of Sciences
35 Staromonetny pereulok, Moscow 119017, Russian Federation*

Abstract

The aim of this work is to study the characteristics of the electrodialysis of a sodium sulphate solution with experimental bipolar membranes based on the MA-41 anion exchange membrane and a liquid sulphonated cation-exchanger modified with bentonite clays. The conversion of sodium sulphate was conducted by electrodialysis with bipolar membranes obtained by applying a liquid sulphonated cation-exchanger containing particles of bentonite clay to the MA-41 anion-exchange membrane.

To increase the performance of membranes in terms of hydrogen and hydroxyl ions, we carried out organomodifications of bentonite with alkyldimethylbenzylammonium chloride and stearic acid at various concentrations. The bipolar membrane with the addition of bentonite modified with alkyldimethylbenzylammonium chloride (2 wt%) showed a higher performance in terms of H⁺-ions. The bipolar membrane with bentonite modified with stearic acid (3 wt%) added to its cation-exchange layer is the most effective in terms of obtaining a flux of OH⁻-ions. It was shown that a combination of alkyldimethylbenzylammonium chloride (2 wt%) and stearic acid (3 wt%) used to modify bentonite can increase the performance of the bipolar membrane during the conversion of sodium sulphate, both in terms of the acid and alkali.

Keywords: electrodialysis, bipolar membrane, modification, bentonite, organobentonite, sodium sulphate, acid, alkali

✉ Ksenia B. Kim, e-mail: kmkseniya@yandex.ru

Condensed Matter and Interphases / Конденсированные среды и межфазные границы   2021;23(4): 518–528

O. A. Kozaderova et al.   Electrodialysis of a sodium sulphate solution with experimental...

1. Introduction

The efficiency of electrodialysis used for the conversion of salt solutions largely depends on the properties of the membranes applied in the process [1]. Existing commercial ion-exchange membranes do not always meet industrial and scientific needs. Advances in membrane technology, especially in the field of new materials, can make electrodialysis even more competitive compared to traditional energy-intensive, environmentally unsafe, and expensive processes.

The analysis of reported data showed that the following studies aimed at improving ion-exchange membranes are currently important: changing the type of functional groups, choosing different polymer matrices, mixing polymers, changing crosslinking density, adding inorganic and organic fillers, modifying membrane surfaces, and introducing catalytic additives [2–11]. It is known that the introduction of various nanoparticles into the bipolar region of the ion-exchange membrane leads to an increase in the rate of dissociation of water molecules [12–21], and thus, to an increase in the performance and efficiency of the membranes.

Relatively inexpensive and accessible clay materials with a charged structure are also used to modify membranes. The use of clays for polyvinylidene fluoride (PVDF) membranes has been studied [22–32]. For example, adding cloisite and palygorskite improves the mechanical properties of such membranes and increases their resistance to surface abrasion. PVDF membranes modified with montmorillonite (MMT) have been developed. They have a higher degree of selectivity in dye filtration [33].

An increased efficiency in the waste water ultrafiltration process in the dairy industry is achieved due to the inclusion of bentonite polymer membranes in the matrix [34]. In order to increase the thermal stability of membranes, it has been proposed to modify the surface of bentonite particles with N-isopropylacrylamide [35]. As a result of ultrafiltration of solutions containing humic acid [36], modified bentonite clay significantly improves the hydrophilic properties, porosity, and water absorption of membranes. The composites obtained in this way can be used to remove heavy metal ions.

To modify Nafion membranes, the application of montmorillonite has been proposed [37]. The compatibility of inorganic clay and organic polymer can be improved by modifying the nanoclay surface by ionic, covalent, and plasma methods [38–39]. However, the addition of clay to a polymer decreases its proton conductivity [40]. This can be avoided by adding a silane agent [41], by grafting sulpho groups into the silicate layer or by organic modification of clay [42–43]. The organomodification process involves the introduction of organic molecules, usually alkylammonium salts, into the interlayer space of montmorillonite. Positively charged organic molecules replace sodium, magnesium, and calcium cations and serve as a kind of buffer between the mineral substance and the polymer, which allows creating a homogeneous system (Fig. 1) [44].

Membranes containing montmorillonite with grafted groups of organic sulphonic acids have shown better characteristics compared to the membrane made of unmodified montmorillonite and the original Nafion [45]. The high efficiency of montmorillonite modified with methylalkylbis (2-hydroxyethyl) ammonium chloride (Cloisite 30B) has been proved by adding 0.5 wt% of it to the polymer matrix [46]. The effectiveness of
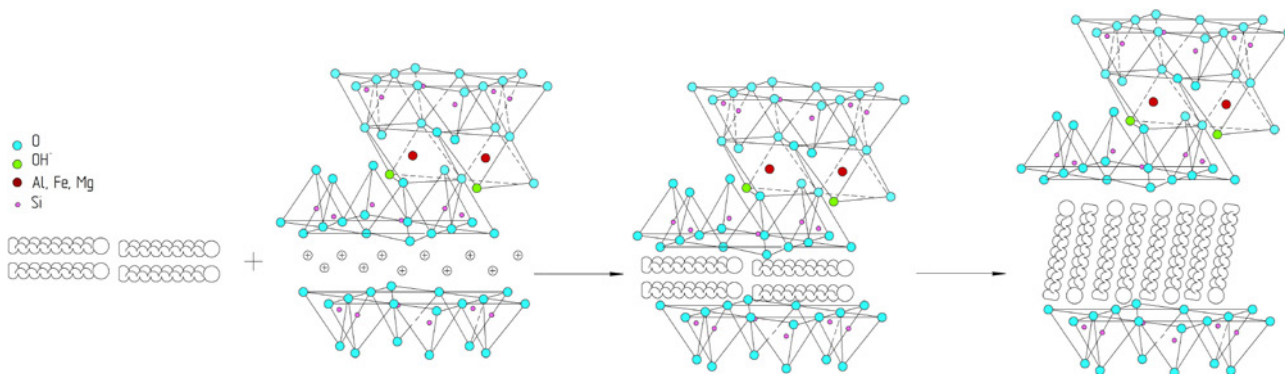
Fig. 1. Scheme of the organomodification of montmorillonite [44]

Condensed Matter and Interphases / Конденсированные среды и межфазные границы   2021;23(4): 518–528

O. A. Kozaderova et al.   Electrodialysis of a sodium sulphate solution with experimental...

Cloisite-15A, montmorillonite modified with a quaternary ammonium salt, in reverse osmosis membranes has been confirmed [47]. It has been found that the addition of the organoclay Cloisite-15A significantly improves both the water and salt permeability of the membrane by 60.5 and 44.3%, respectively [48].

The efficiency of the electrodialysis of solutions of zinc salts on new synthesised polymer membranes based on polyethersulphone (PES) and organomodified MMT has been shown [49]. For the electrodialysis, the researchers used membranes obtained by casting from a solution with the addition of cloisite nanoclay particles to a PVC matrix, which are characterised by their lower permeability and flux of divalent ions compared to monovalent ions. This quality can be used for their selective separation [50].

Heterogeneous cation exchange membranes based on polyethersulphone and cation exchange resins modified with OH-MMT and HSO_3-MMT are characterised by a more uniform distribution of the ion-exchange resin in the polymer matrix and better membrane characteristics: lower surface resistance, high permeability, and the ability to transfer ions during electrodialysis [51].

Clay materials can be successfully used to modify bipolar membranes [52] since the silicates and hydroxide ions in their composition are catalysts for the dissociation of water molecules.

The aim of this work is to study the characteristics of the electrodialysis of sodium sulphate solution with experimental bipolar membranes based on the MA-41 anion exchange membrane and a liquid sulphonated cation-exchanger modified with bentonite clays.

2. Experimental

We used alkaline bentonites from the Dash-Salakhlinsk field (Azerbaijan) with a montmorillonite content of more than 70% (introduced into the cation-exchange layer in an unchanged form and after its modification with stearic acid) and the Tikhmenevsk field on the island of Sakhalin (Russia) [53] (introduced into the cation-exchange layer of an experimental membrane after its modification with alkyl-dimethylbenzylammonium chloride). The process of organomodification involved several stages. During the first stage, a 1% suspension of bentonite clay was prepared. Further, using a laboratory centrifuge (OS-6MT "Dastan"), an enriched fraction of bentonite was obtained with a particle size of no more than 1 μm containing more than 95% of montmorillonite. A 3% aqueous suspension was prepared from the obtained enriched fraction. The modification was carried out with constant stirring at a temperature of 70 °C. A solution of alkyldimethylbenzylammonium chloride and stearic acid were used as modifiers. The characteristics of both are given in Table 1. The modification lasted 2 hours. The resulting organoclay was separated from the suspension, washed with water until there was no excess of unreacted modifier, dried, and milled in a ball mill to a fraction with a particle size of no more than 60 μm [54].

The prepared natural and modified bentonite samples were used to obtain a bipolar ion-exchange membrane. It was made using a standard anion-exchange membrane with quaternary ammonium groups (MA-41) [55] and a liquid sulphonic cation exchanger, LF-4-SK, an analogue of a perfluorinated sulphonic cation exchanger (MF-4SK) [56] (Table 2). To fix the cation-exchanger film, the surface of the MA-41 anion-exchange membrane was preliminarily degreased, roughened, and treated with acetic acid [57]. A suspension of a liquid cation exchanger with bentonite clay particles (1, 2, and 3 wt%) was

Table 1. Characteristics of substances used to modify bentonite

	Alkyldimethylbenzylammonium chloride (SAS)	Stearic acid
Appearance	light yellow powder	colourless crystals
Modifier concentration	60 mg/100 g montmorillonite	5 g/100 g bentonite
Structural formula	$\left[R-\overset{CH_3}{\underset{CH_3}{N}}-CH_3-\langle\rangle \right]^+ Cl^-$, $R-C_{12}-C_{18}$	$CH_3-(CH_2)_{16}-C\overset{O}{\underset{OH}{}}$

Condensed Matter and Interphases / Конденсированные среды и межфазные границы   2021;23(4): 518–528

O. A. Kozaderova et al.   Electrodialysis of a sodium sulphate solution with experimental…

Table 2. Characteristics of monopolar layers forming a modified bipolar membrane

Properties	Cation exchange layer	Anion exchange layer
Membrane	MF-4SK	MA-41
Polymer matrix	Polytetrafluoroethylene	Divinylbenzene cross-linked polystyrene
Elementary link		
Inert binder	–	Polyethylene
Reinforcing mesh	–	Polyamide
Swollen thickness (cm)	0.07	0.53

applied to the prepared substrate membrane (Fig. 2). To improve the dispersion of bentonite particles in the LF-4SK solution, the mixture was treated in an ultrasonic bath (VU-09-Ya-FP-01) for 20 minutes. After that, the membrane was dried for 24 hours at a temperature of 25 °C.

In order to study the effect of the modifier on the properties of the obtained bipolar membrane, sodium sulphate was converted (solution, 0.5 mol/dm^3) in an electrodialyser containing a cation-exchange (RalexCMH-PP) and anion-exchange (Ralex AMH-PP) membranes (produced by MEGA, Czech Republic [58]), and one of the bipolar membranes under study (Fig. 3).

In this work, we investigated bipolar membranes obtained by applying on the anion-exchange membrane a liquid cation exchanger that did not contain bentonite (MB$_{ex}$), as well as a cation exchanger with the addition of the following amount of bentonite (% to the mass of the cation exchanger): 1 (MB$_{BT1}$), 2 (MB$_{BT2}$), and 3 (MB$_{BT3}$). Similar experiments were carried out for membranes with the addition of bentonite modified with SAS and stearic acid in the following amount, respectively (% to the mass of the cation exchanger): 1 (MB$_{SAS1}$), 2 (MB$_{SAS2}$), 3 (MB$_{SAS3}$) and 1 (MB$_{St1}$), 2 (MB$_{St2}$), 3 (MB$_{St3}$).

Based on the experimental data, we calculated the current efficiency (η,%), specific energy consumption for the production of the target product (W, kW/kg), and the fluxes of hydrogen and hydroxyl ions generated in the bipolar membrane (J, mol/(cm^2 s)) according to the formulas:
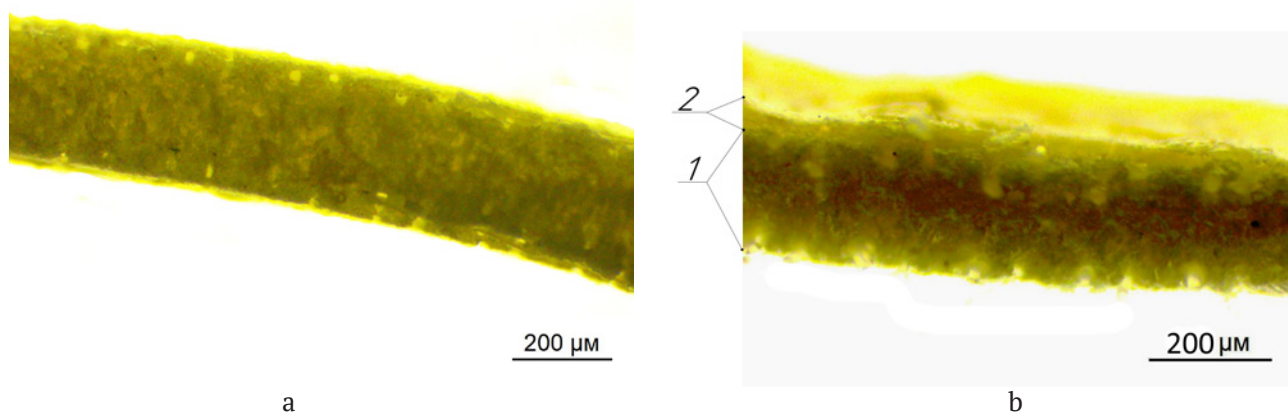
Fig. 2. Photographs of membranes (Levenhuk 625 optical microscope with M1400 Plus camera, magnification 10x0.25): (a) MA-41 monopolar membrane (substrate membrane) onto which a cation exchanger was cast, (b) experimental sample of bipolar membrane (*1* substrate membrane, *2* cation exchange layer with bentonite particles)

Condensed Matter and Interphases / Конденсированные среды и межфазные границы   2021;23(4): 518–528

O. A. Kozaderova et al.   Electrodialysis of a sodium sulphate solution with experimental...
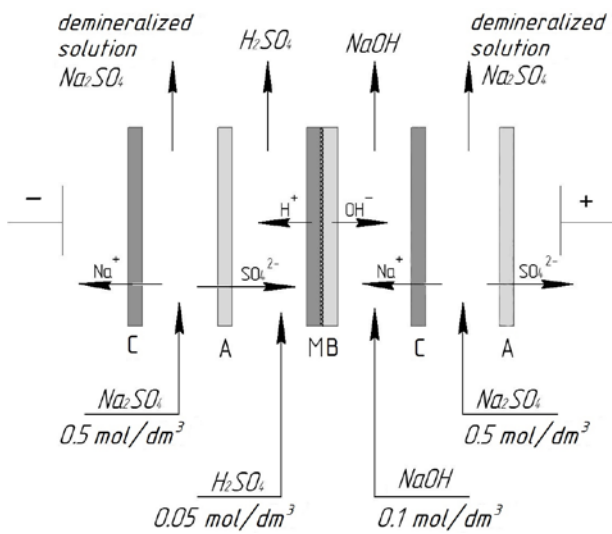
Fig. 3. Scheme of sodium sulphate conversion by electrodialysis with bipolar membranes: (K) cation exchange membrane, (A) anion exchange membrane, (MB) bipolar membrane

$$\eta = \frac{(C_0 - C_i) \cdot V \cdot F}{\tau \cdot I} \cdot 100, \qquad (1)$$

$$W = \frac{I \cdot U \cdot \tau}{m}, \qquad (2)$$

$$J_i = \frac{(C_0 - C_i) \cdot V}{\tau \cdot S}, \qquad (3)$$

where C_0 is concentration of ions in the initial solution, mol/dm³; C_i is the concentration of ions in the investigated section, mol/dm³; is the solution volume, dm³; F is Faraday constant, A·s/mol; is time, s; I is current, A; U is voltage, V; S is the area of the membrane, cm²; m is the mass of the product, kg.

3. Results and discussion

The results of the sodium sulphate conversion with a membrane obtained by applying a thin layer of a liquid cation exchanger that did not contain bentonite (MB_{ex}) on MA-41 are shown in Fig. 4. The resulting sample had the properties of a bipolar membrane and showed comparable fluxes of hydrogen and hydroxyl ions. The results of the experiment aimed at the conversion of the studied salt with the MB_{BT1}, MB_{BT2}, and MB_{BT3} membranes showed a decrease in both alkali and acid fluxes compared to the MB_{ex} membrane (Fig. 4). Hence, further studies were aimed at studying the possibility of improving the characteristics of experimental membrane samples by changing the properties of bentonite by the organomodification of SAS (MB_{SAS1}, MB_{SAS2}, MB_{SAS3}) and stearic acid (MB_{St1}, MB_{St2}, MB_{St3}).

The results of studying the dependence of membrane performance on the amount of bentonite treated with SAS are shown in Fig. 5. With an increase in SAS content, the performance in terms of medium ions did not
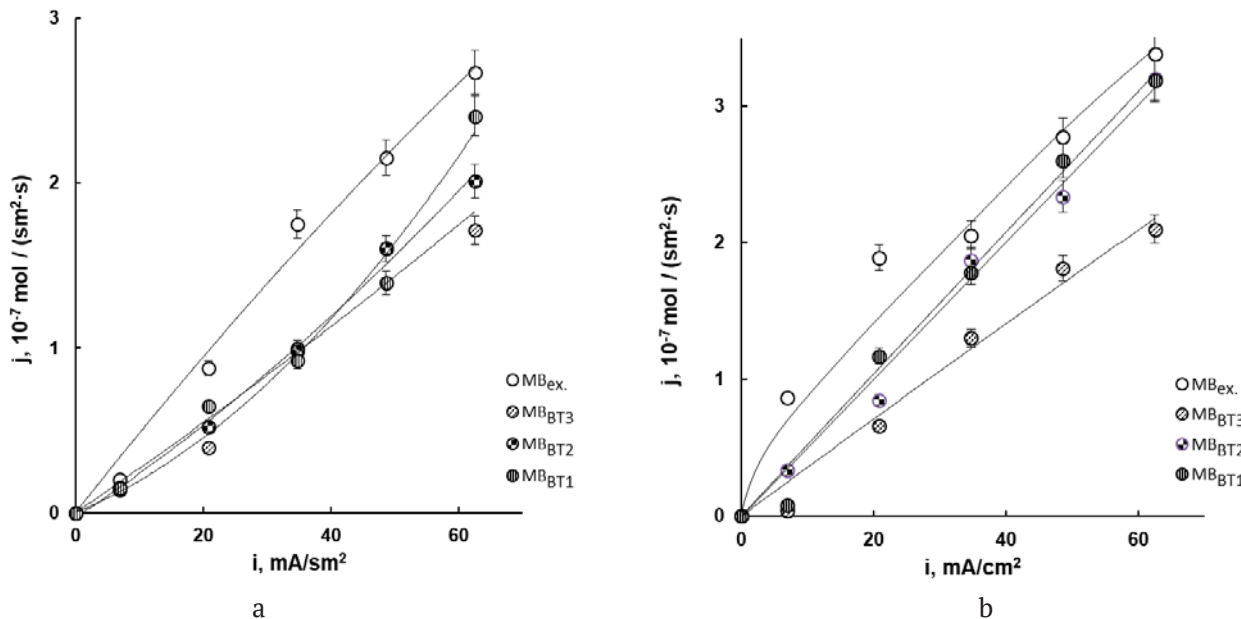
Fig. 4. Dependence of the fluxes of H⁺ (a) and OH⁻ (b) ions generated in the bipolar membrane on the current density for the experimental samples without the addition of bentonite to the cation-exchange layer and with the addition of unmodified bentonite

Condensed Matter and Interphases / Конденсированные среды и межфазные границы   2021;23(4): 518–528

O. A. Kozaderova et al.   Electrodialysis of a sodium sulphate solution with experimental...

change monotonically: the introduction of 2 wt% of organoclay (MB_{SAS2}) was optimal. The effect of bentonite treated with stearic acid on the membrane's performance is shown in Fig. 6. According to the figure, such membranes are more efficient for the production of alkalis. Maximum fluxes of OH^- ions generated in the bipolar membrane were observed when using 3% of bentonite modified with stearic acid (MB_{St3}).

The combination of bentonite (2 wt%) treated with alkyldimethylbenzylammonium chloride and bentonite (3 wt%) treated with stearic acid ($MB_{SAS2+St3}$ membrane, Fig. 7) in a liquid ion exchanger forming a cation-exchange layer of a bipolar membrane gave no fluxes of hydrogen ions comparable to MB_{SAS2}. However, a comparison of the intensity of ion generation in the MB_{St3} and $MB_{SAS2+St3}$ showed the advantages of the latter.
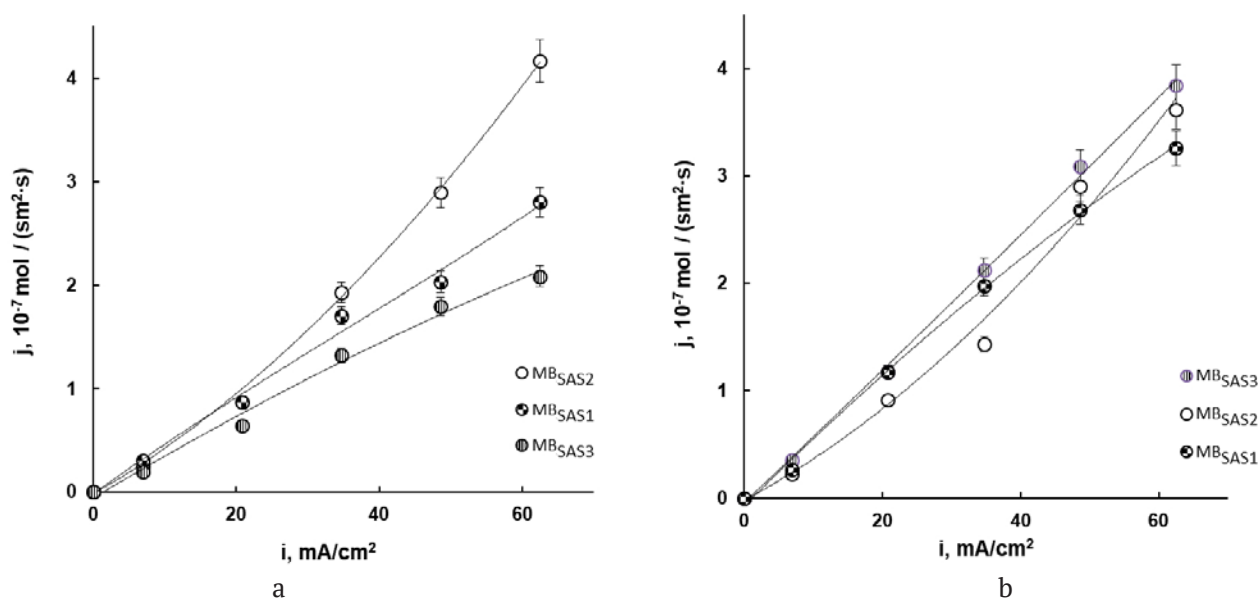
Fig. 5. Dependence of the fluxes of H^+ (a) and OH^- (b) ions generated in the bipolar membrane on the current density for the experimental samples with the addition of SAS-modified bentonite to the cation-exchange layer
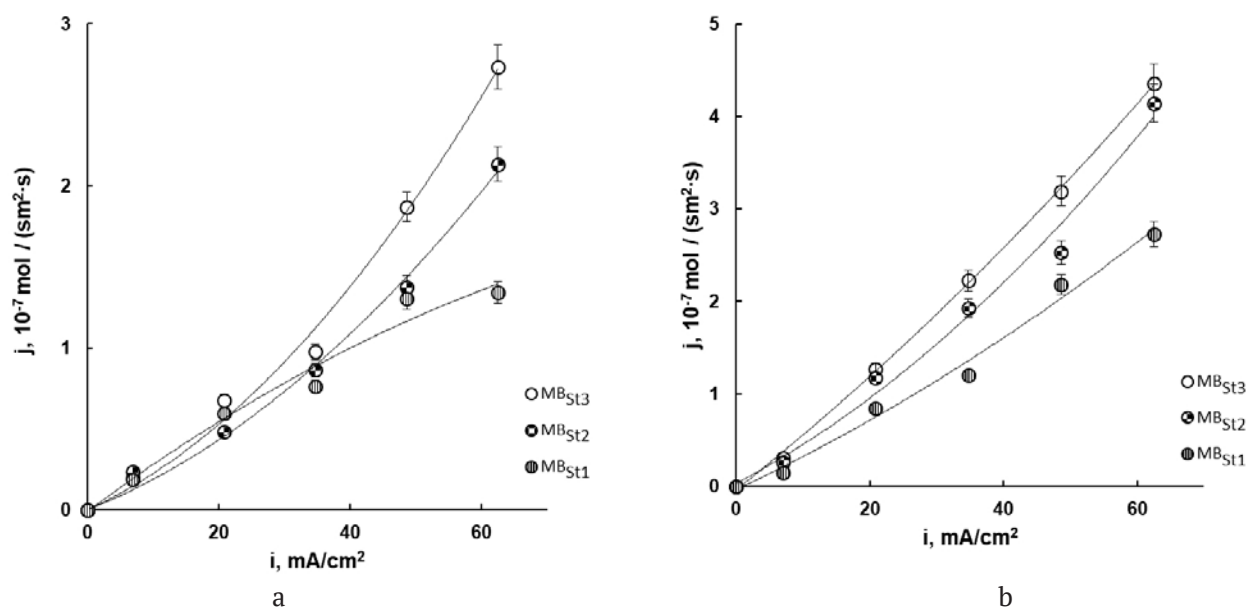
Fig. 6. Dependence of the fluxes of H^+ (a) and OH^- (b) ions generated in the bipolar membrane on the current density for the experimental samples with the addition of bentonite modified with stearic acid to the cation-exchange layer

Condensed Matter and Interphases / Конденсированные среды и межфазные границы   2021;23(4): 518–528

O. A. Kozaderova et al.   Electrodialysis of a sodium sulphate solution with experimental...
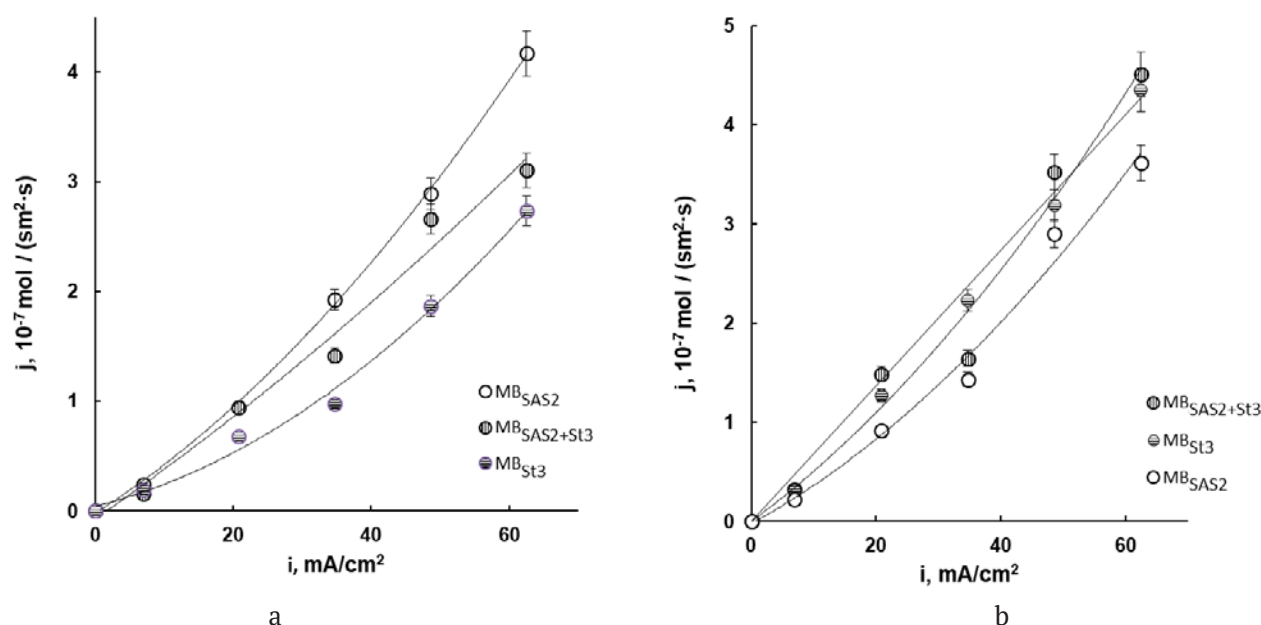
Fig. 7. Dependence of the fluxes of H^+ (a) and OH^- (b) ions generated in the bipolar membrane on the current density for the experimental samples with the addition of modified bentonite (SAS and stearic acid) to the cation-exchange layer

One of the important criteria for evaluating the efficiency of bipolar membranes is the energy consumption for obtaining a unit of the target product. These values for MB_{ex}, MB_{SAS2}, MB_{St3}, and $MB_{SAS2+St3}$ are shown in Table 3, as well as a change in the concentration of the acid and alkali in the receiving chambers, fluxes, and yields for the acid and base. It should be noted that using bipolar membranes with modified bentonite in the cation-exchange layer can significantly reduce energy consumption for the production of target products and increase the current efficiency (Table 3).

4. Conclusions

Experimental samples of bipolar membranes based on an anion-exchange membrane MA-41 and a liquid sulphonic cation exchanger with bentonite clays (natural and organomodified) were obtained. The effect of the amount and modification of bentonite (alkyldimethylbenzylammonium chloride and stearic acid) on the properties of the obtained experimental membranes was investigated. It was shown that the addition of bentonite modified with alkyldimethylbenzylammonium chloride (2 wt% of bentonite to the mass of the cation exchanger) or stearic acid (3 wt% of bentonite to the mass of the cation exchanger) into the sulphonic cation-exchange layer of the membrane leads to the maximum efficiency of bipolar electrodialysis aimed at the conversion of sodium sulphate. This effect can be achieved due to the presence of hydroxyl and silicon groups in the composition of bentonite, which are catalysts for the dissociation of water molecules [59–61]. The role of organomodifiers in bentonite clay is to change the properties of the surface of the bentonite layer, which becomes more hydrophobic and compatible

Table 3. Results of the experiment aimed at the conversion of sodium sulphate (at the current density of i = 60 mA/cm²)

Membrane	MB_{ex}		MB_{SAS2}		MB_{St3}		$MB_{SAS2+St3}$	
	H_2SO_4	NaOH	H_2SO_4	NaOH	H_2SO_4	NaOH	H_2SO_4	NaOH
ΔC, mol/dm³	0.09	0.12	0.15	0.25	0.07	0.26	0.10	0.31
J, mol/(m²·h)	9.6	12.2	15.0	13.0	9.8	15.6	11.7	16.3
W, kW·h/kg	50.8	49.2	32.5	45.8	33.9	26.1	35.4	29.8
η, %	41.3	52.2	64.3	55.8	44.2	67.2	47.9	69.7

Condensed Matter and Interphases / Конденсированные среды и межфазные границы   2021;23(4): 518–528

O. A. Kozaderova et al.   Electrodialysis of a sodium sulphate solution with experimental...

with the polymer. Using a bipolar membrane with modified bentonite allows obtaining higher concentrations of the acid and alkali during the conversion of sodium sulphate, to increase the current efficiency and performance, and to reduce energy consumption.

Authors contributions

All authors made an equivalent contribution to the preparation of the publication.

Conflict of interests

The authors declare that they have no known competing financial interests or personal relationships that could have influenced the work reported in this paper.

References

1. Strathmann H. *Ion-exchange membrane separation processes.* Elsevier; 2004. v. 43, 60 p. https://doi.org/10.1016/s0927-5193(04)80031-7

2. Fathizadeh M., Aroujalian A., Raisi A. Effect of added NaXnano-zeolite into polyamide as a top thin layer of membrane on water flux and salt rejection in a reverse osmosis process. *Journal of Membrane Science.* 2011;375(1-2): 88–95. https://doi.org/10.1016/j.memsci.2011.03.017

3. Hosseini S. M., Madaeni S. S., Zendehnam A., Moghadassi A. R., Khodabakhshi A. R., Sanaeepur H. Preparation and characterization of PVC based heterogeneous ion exchange membrane coated with Ag nanoparticles by (thermal-plasma) treatment assisted surface modification. *Journal of Industrial and Engineering Chemistry.* 2013;19(3): 854–862. https://doi.org/10.1016/j.jiec.2012.10.031

4. Zendehnam A., Arabzadegan M., Hosseini S. M., Robatmili N., Madaeni S. S. Fabrication and modification of polyvinylchloride based heterogeneous cation exchange membranes by simultaneous using Fe-Ni oxide nanoparticles and Ag nanolayer: physico-chemical and antibacterial characteristics. *Korean Journal of Chemical Engineering.* 2013;30(6): 1265–1271. https://doi.org/10.1007/s11814-013-0063-2

5. Zarrinkhameh M., Zendehnam A., Hosseini S. M. Preparation and characterization of nanocomposite heterogeneous cation exchange membranes modified by silver nanoparticles. *Korean Journal of Chemical Engineering.* 2014;31(7): 1187–1193. https://doi.org/10.1007/s11814-014-0051-1

6. Huang M., Shen Y., Cheng W., Shao Y., Sun X., Liu B., Dong S. Nanocomposite films containing Au nanoparticles formedby electrochemical reduction of metal ions in the multilayer films as electrocatalyst for dioxygenreduction. *Analytica Chimica Acta.* 2005;535(1-2): 15–22. https://doi.org/10.1016/j.aca.2004.12.006

7. Camargo P. H. C., Satyanarayana K. G., Wypych F. Nanocomposites: synthesis, structure, properties and new application opportunities. *Materials Research.* 2009;12(1): 1–39. https://doi.org/10.1590/s1516-14392009000100002

8. Yaroslavtsev A. B., Nikonenko V. V., Zabolotskiy V. I. Ion transfer in ion-exchange and membrane materials. *Russian Chemical Reviews.* 2003;72(5): 438–470. https://doi.org/10.1070/rc2003v072n05abeh000797

9. Domènech B., Bastos-Arrieta J., Alonso A., Macanás J., Muñoz M., Muraviev D. N. Bifunctional polymer-metal nanocomposite ion exchange materials. In book: *Ion exchange technologies.* 2012: 35–72. https://doi.org/10.5772/51579

10. Yaroslavtse A. B. Correlation between the properties of hybrid ion-exchange membranes and the nature and dimensions of dopant particles. *Nanotechnologies in Russia.* 2012;7(9-10): 437–451. https://doi.org/10.1134/s1995078012050175

11. Kravchenko T. A., Sakardina E. A., Kalinichev A. I., Zolotukhina E. V. Stabilization of copper nanoparticles with volume- and surface-distribution inside ion-exchange matrices. *Russian Journal of Physical Chemistry A.* 2015;89(9): 1648-1654. https://doi.org/10.7868/S0044453715080178

12. Kang M.-S., Choi Y.-J., Lee H.-J., Moon S.-H. Electrochemical characteristics of ion-exchange membranes coated with iron hydroxide/oxide and silica sol. *Journal of Colloid and Interface Science.* 2003;273(2): 523–532. https://doi.org/10.1016/j.jcis.2004.01.050

13. Sheldeshov N. V, Zabolotskiy V. I, Ganych V. V. Vliyanie nerastvorimykh gidroksidov metallov na skorost' reaktsii dissotsiatsii vody na kationoobmennoi membrane [Influence of insoluble metal hydroxides on the rate of water dissociation reaction on a cation-exchange membrane]. *Russian Journal of Electrochemistry.* 1994;30(12): 1458–1461. (In Russ.)

14. Melnikov S. S., Shapovalova O. V., Sheldeshov N. V., Zabolotsky V. I. Vliyanie gidroksidov d-metallov na dissotsiatsiyu vody v bipolyarnykh membranakh [Influence of d-metal hydroxides on water dissociation in bipolar membranes]. *Membrany i membrannye tekhnologii.* 2011;1(2): 149–156. Available at: https://elibrary.ru/item.asp?id=16316683 (In Russ.)

15. Sheldeshov N. V. Zabolotskiy V. I., Alpatova N. V. Influence of heavy metal hydroxides on water dissociation in bipolar membrane. *Polymatic online scientific journal of Kuban State Agrarian University.* 2015;114: 275–287. Available at: https://elibrary.ru/item.asp?id=25280358 (In Russ., abstract in Eng.)

16. Sheldeshov N. V., Zabolotskiy V. I. Bipolyarnye ionoobmennye membrany. Poluchenie. Svoistva.

Condensed Matter and Interphases / Конденсированные среды и межфазные границы   2021;23(4): 518–528

O. A. Kozaderova et al.   Electrodialysis of a sodium sulphate solution with experimental…

Primenenie [Bipolar ion-exchange membranes. Receiving. Properties. Application]. In book: *Membrany i membrannye tekhnologii* [Membranes and membrane technologies]. Moscow: Nauchnyi Mir Publ.; 2013. 612 p. (In Russ.)

17. Melnikov S. S., Zabolotsky V. I. Sheldeshov N. V. Electochemical properties of asymmetric bipolar membranes. *Kondensirovannye sredy i mezhfaznye granitsy = Condensed Matter and Interphases*. 2010;12(2): 143–148. Available at: https://elibrary.ru/item.asp?id=15176048 (In Russ., abstract in Eng.)

18. Jalani N. H., Dunn K., Datta R. Synthesis and characterization of Nafion(R)-MO2 (M = Zr, Si, Ti) nanocomposite membranes for higher temperature PEM fuel cells. *Electrochimica Acta.* 2005;51(3): 553–560. https://doi.org/10.1016/j.electacta.2005.05.016

19. Miyake N., Wainright J. S., Savinell R. F. Evaluation of a sol-gel derived nafion/silica hybrid membrane for polymer electrolyte membrane fuel cell applications: II. Methanol uptake and methanol permeability. *Journal of The Electrochemical Society*. 2001;148(8): 905. https://doi.org/10.1149/1.1383072

20. Balster J. H. *Membrane module and process development for monopolar and bipolar membrane electrodialysis*. Zutphen: Wöhrmann Print Service; 2006. 213 p.

21. Kozaderova O. A. Electrochemical characterization of an MB-2 bipolar membrane modified by nanosized chromium(III) hydroxide. *Nanotechnologies in Russia*. 2018;13(9-10): 508–515. https://doi.org/10.1134/S1995078018050075

22. Saccà A., Gatto I., Carbone A., Pedicini R., Passalacqua E. ZrO_2–Nafion composite membranes for polymer electrolyte fuel cells (PEFCs) at intermediate temperature. *Journal of Power Sources*. 2006;163(1) : 47–51. https://doi.org/10.1016/j.jpowsour.2005.12.062

23. Niepceron F., Lafitte B., Galiano H., Bigarré J., Nicol E., Tassin J.-F. Composite fuel cell membranes based on an inert polymer matrix and proton-conducting hybrid silica particles. *Journal of Membrane Science*. 2009;338(1-2): 100–110. https://doi.org/10.1016/j.memsci.2009.04.022

24. Novikova S., Safronova E., Lysova A., Yaroslavtsev A. Influence of incorporated nanoparticles on the ionic conductivity of MF-4SC membrane. *Mendeleev Commun.* 2010;20(3): 156–157. https://doi.org/10.1016/j.mencom.2010.05.011

25. Safronova E. Yu., Volkov V. I., Yaroslavtsev A. B. Ion mobility and conductivity of hybrid ion-exchange membranes incorporating inorganic nanoparticles. *Solid State Ionics*. 2011;188(1): 129–131. https://doi.org/10.1016/j.ssi.2010.12.006

26. Yaroslavtsev A. B., Safronova E. Yu., Lysova A. A., Novikova S. A., Stenina I. A., Volkov V. I. Ion conductivity of hybrid ion exchange membranes incorporating nanoparticles. *Desalination and Water Treatment*. 2011;35(1–3): 202–208. https://doi.org/10.5004/dwt.2011.2489

27. Gerasimova E. V., Safronova E. Yu, Volodin A. A., Ukshe A. E., Dobrovolsky Yu A., Yaroslavtsev A. B. Electrocatalytic properties of the nanostructured electrodes and membranes in hydrogen-air fuel cells. *Catalysis Today*. 2012;193(1): 81–86. https://doi.org/10.1016/j.cattod.2012.06.018

28. Safronova E. Y., Prikhno I., Yurkov G., Yaroslavtsev A. Nanocomposite membrane materials based on nafion and cesium acid salt of phosphotungstic heteropolyacid. *Chemical Engineering Transactions*. 2015;43: 679–684. https://doi.org/ 10.3303/CET1543114

29. Gerasimova E, Safronova E., Ukshe A., Dobrovolsky Yu., Yaroslavtsev A. Electrocatalytic and transport properties of hybrid Nafion® membranes doped with silica and cesium acid salt of phosphotungstic acid in hydrogen fuel cells. *Chemical Engineering Journal*. 2016;305: 121–128. https://doi.org/10.1016/j.cej.2015.11.079

30. Yaroslavtsev A. B. Correlation between the properties of hybrid ion-exchange membranes and the nature and dimensions of dopant particles. *Nanotechnologies Russ*. 2012; 7 (9–10): 437–451. https://doi.org/10.1134/S1995078012050175

31. Perepelkina A. I., Safronova E. Yu., Shalimov A. S., Yaroslavtsev A. B. Hybrid materials based on MF-4SK membranes modified with silicon carbide and carbon nanotubes. *Petroleum Chemistry*. 2012;52(7): 475–479. https://doi.org/10.1134/S0965544112070109

32. Lai C. Y., Groth A, Gray S., Duke M. Nanocomposites for improved physical durability of porous. *Membranes*. 2014;4 (57-58): 56–66. https://doi.org/10.3390/membranes4010055

33. Pramono E., Alfiansyah R., Ahdiat M., Wahyuningrum D., Radiman C. L. Hydrophilic poly(vinylidene fluoride)/bentonite hybrid membranes for microfiltration of dyes. *Materials Research Express*. 2019;6(10): 105376. https://doi.org/10.1088/2053-1591/ab42e9

34. Pagidi A., Lukka Thuyavan Y., Arthanareeswaran G., Ismail A. F., Jaafar J., Paul D. Polymeric membrane modification using SPEEK and bentonite for ultrafiltration of dairy wastewater. *Journal of Applied Polymer Science*. 2015;132(21): https://doi.org/10.1002/app.41651

35. Yaghoubi Z., & Basiri-Parsa J. Modification of ultrafiltration membrane by thermo-responsive Bentonite-poly(N-isopropylacrylamide) nanocomposite to improve its antifouling properties. *Journal of Water Process Engineering*. 2020;34: 101067. https://doi.org/10.1016/j.jwpe.2019.101067

36. Hebbar R. S., Isloor A. M., Prabhu B., Inamuddin, Asiri A. M., Ismail A. F.Removal of metal ions and humic acids through polyetherimide membrane with

Condensed Matter and Interphases / Конденсированные среды и межфазные границы   2021;23(4): 518–528

O. A. Kozaderova et al.   Electrodialysis of a sodium sulphate solution with experimental...

grafted bentonite clay. *Scientific Reports*. 2018;8(1)1665. https://doi.org/10.1038/s41598-018-22837-1

37. Pourzare K., Mansourpanah Y., Farhadi S. Advanced nanocomposite membranes for fuel cell applications: a comprehensive review. *Biofuel Research Journal*. 2016;3(4): 496–513. https://doi.org/10.18331/BRJ2016.3.4.4

38. Zhang X. Porous organic-inorganic hybrid electrolytes for high-temperature proton exchange membrane fuel cells. *Journal of the Electrochemical Society*. 2007;154(3): 322–326. https://doi.org/10.1149/1.2429045

39. Lixon Buquet C., Fatyeyeva K., Poncin-Epaillard F., Schaetzel P., Dargent E., Langevin D., Nguyen Q. T., Marais S. New hybrid membranes for fuel cells: plasma treated laponite based sulfonated polysulfone. *Journal of Membrane Science*. 2010;351(1-2): 1–10. https://doi.org/ 10.1016/j.memsci.2010.01.020

40. Fu T., Cui Z., Zhong S., Shi Y., Zhao C., Zhang G., Shao K., Na H., Xing W. Sulfonated poly(ether ether ketone)/clay–SO_3H hybrid proton exchange membranes for direct methanol fuel cells. *Journal of Power Sources*. 2008;185(1): 32–39. https://doi.org/10.1016/j.jpowsour.2008.07.004

41. Peighambardoust S. J., Rowshanzamir S., Amjadi M. Review of the proton exchange membranes for fuel cell applications. *International Journal of Hydrogen Energy*. 2010;35(17): 9349–9384. https://doi.org/10.1016/j.ijhydene.2010.05.017

42. Lee S. K., Mogi G., Li Z., Hui K. S., Lee S. K., Hui K. N, Park S. Y., Ha Y. J., Kim J. W. Measuring the relative efficiency of hydrogen energy technologies for implementing the hydrogen economy: An integrated fuzzy AHP/DEA approach. *International Journal of Hydrogen Energy*. 2011;36(20): 12655–12663. https://doi.org/10.1016/j.ijhydene.2011.06.135

43. Kakati B. K., Mohan V. Development of low-cost advanced composite bipolar Plate for proton exchange membrane fuel cell. *Fuel Cells*. 2008;8(1): 45–51. https://doi.org/10.1002/fuce.200700008

44. Nasedkin V. V., Demidenok K. V., Boeva N. M., Belousov P. E., Vasiliev A. L. Organogliny. proizvodstvo i osnovnye napravleniya ispol'zovaniya. Aktual'nye innovatsionnye issledovaniya: nauka i praktika [Organoclays. production and main directions of use]. *Actual innovative research: science and practice*. 2012;3: 1–19. Available at: https://elibrary.ru/item.asp?id=18203393 (In Russ.)

45. Zakil F. A., Kamarudin S. K., Basri S. Modified Nafion membranes for direct alcohol fuel cells: An overview. *Renewable and Sustainable Energy Reviews*. 2016;65: 841–852. https://doi.org/10.1016/j.rser.2016.07.040

46. Jung D. H., Chao S. Y., peck D. H., Kim J. S. Preparation and performance of a Nafion/montmorillonite nanocomposite membrane for direct methanol fuel cell. *Journal of Power Sources*. 2003;118(1–2): 205–211. https://doi.org/10.1016/S0378-7753(03)00095-8

47. Zaidi S., Fadhillah F., Saleem H., Hawari A., Benamor A. Organically modified nanoclay filled thin-film nanocomposite membranes for reverse osmosis application. *Materials.* 2019;12 (22): 3803. https://doi.org/10.3390/ma12223803

48. Mohamed Amin M. A., Goh P. S., Ismail A. F. Effect of organoclay on the performance of reverse osmosis membrane. *Journal of Membrane Science and Research*. 2020;6(1): 13–19. https://doi.org/ 10.22079/JMSR.2019.112286.1279

49. Caprarescu S., Ianchis R., Radu A.-L., Sarbu A., Somoghi R., Trica B., Alexandrescu E., Spataru C.-I., Fierascu R.C., Ion-Ebrasu D., Preda S., Atanase L.-I., Donescu D. Synthesis, characterization and efficiency of new organically modified montmorillonite polyethersulfone membranes for removal of zinc ions from wastewasters. *Applied Clay Science.* 2017;137(1): 135–142. https://doi.org/10.1016/j.clay.2016.12.013

50. Hosseini S. M., Seidypoor A., Nemati M., Madaeni S. S., Parvizianand F., Salehi E. Mixed matrix heterogeneous cation exchange membrane filled with clay nanoparticles: membranes' fabrication and characterization in desalination process. *Journal of Water Reuse and Desalination.* 2016;6(2): 290–300. https://doi.org/10.2166/wrd.2015.064

51. Radmanesh F., Rijnaarts T., Moheb A., Sadeghi M., de Vos W. M. Enhanced selectivity and performance of heterogeneous cation exchange membranes through addition of sulfonated and protonated. Montmorillonite. *Journal of Colloid and Interface Science*. 2019;553(1): 658–670. https://doi.org/10.1016/j.jcis.2018.08.100

52. Peng F., Peng S., Huang C., Xu T. Modifying bipolar membranes with palygorskite and $FeCl_3$. *Journal of Membrane Science*. 2008; 322(21): 122–127 https://doi.org/10.1016/j.memsci.2008.05.027

53. Belousov P. E., Krupskaya V. V. Bentonite clays of Russia and neighboring countries. *Georesursy*. 2013;21(3): 79–90. https://doi.org/10.18599/grs.2019.3.79-90

54. Boeva N. M., Bocharnikova Yu. I., Nasedkin V. V., Belousov P. E., Demidenok K. V. Thermal analysis as an express method for assessing the quality and quantity of natural and synthesized organoclays. *Nanotechnologies in Russia*. 2013;8 (3-4): 205–208. https://doi.org/10.1134/s199507801302002x

55. *Product catalog of JSC Shchekinoazot*. Available at: http://www.azotom.ru/monopolyarnye-membrany/

56. *Department of Polytetrafluoroethylene and Perfluorinated Ion Exchange Membranes*. Available at: http://www.plastpolymer.com/structure/otdel-politetraftorjetilena-i-perftorirovannyh-ionoobmennyh-membran/

527

Condensed Matter and Interphases / Конденсированные среды и межфазные границы   2021;23(4): 518–528

O. A. Kozaderova et al.   Electrodialysis of a sodium sulphate solution with experimental...

57. Zabolotskii V., Sheldeshov N., Melnikov S. Effect of cation-exchange layer thickness on electrochemical and transport characteristics of bipolar membranes. *Journal of Applied Electrochemistry*. 2013;43(11): 1117–1129. https://doi.org/10.1007/s10800-013-0560-3

58. *Membrane properties*. Available at: http://www.ralex.eu/Membrany/Uvod.aspx

59. Hanada F., Hirayama K., Ohmura N., Tanaka S. Bipolar membrane and method for its production. *US Patent*. 1993. 5, 221,455.

60. Fu R. Q., Xu T. W., Cheng Y. Y., Yang W. H., Pan Z. X. Fundamental studies on the intermediate layer of a bipolar membrane. III. Effect of starburst dendrimer (PAMAM) on water dissociation at the interface of a bipolar membrane. *Journal of Membrane Science*. 2004;240(1): 141–147. https://doi.org/10.1016/j.memsci.2004.05.002

61. Kang M. S., Choi Y. J., Lee H. J., Moon S. H. Effects of inorganic substances onwatersplitting in ion-exchangemembranes. I. Electrochemical characteristics of ion exchange membranescoated with iron hydroxide/oxide and silica sol. *Journal of Colloid and Interface Science*. 2004;273(2): 523–532. https://doi.org/10.1016/j.jcis.2004.01.050

Information about the authors

Olga A. Kozaderova, DSc in Chemistry, Professor at the Department of Inorganic Chemistry and Chemical Technology, Voronezh State University of Engineering Technologies, Voronezh, Russian Federation; e-mail: kozaderova-olga@mail.ru. ORCID iD: https://orcid.org/0000-0002-8135-5801.

Ksenia B. Kim, PhD in Chemistry, Associate Professor at the Department of Inorganic Chemistry and Chemical Technology, Voronezh State University of Engineering Technologies, Voronezh, Russian Federation; e-mail: kmkseniya@yandex.ru. ORCID iD: https://orcid.org/0000-0001-5564-8267.

Petr E. Belousov, PhD in Geology and Mineralogy, senior researcher, Institute of Geology of Ore Deposits, Petrography, Mineralogy, and Geochemistry of the Russian Academy of Sciences, Moscow, Russian Federation; e-mail: pitbl@mail.ru. ORCID iD: https://orcid.org/0000-0002-2657-5828.

Anna V. Timkova, postgraduate student, Department of Inorganic Chemistry and Chemical Technology, Voronezh State University of Engineering Technologies, Voronezh, Russian Federation, e-mail: timkova.anna@mail.ru. ORCID iD: https://orcid.org/0000-0003-0630-2993

Sabukhi I. Niftaliev, DSc in Chemistry, Professor, Head of Department of Inorganic Chemistry and Chemical Technology, Voronezh State University of Engineering Technologies, Voronezh, Russian Federation; e-mail: sabukhi@gmail.com. ORCID iD: https://orcid.org/0000-0001-7887-3061.

Original articles

Research article
https://doi.org/10.17308/kcmf.2021.23/3671

Statistical approach to the process of tunnel ionisation of impurity centres near the heterointerface

T. T. Muratov⊠

Nizami Tashkent State Pedagogical University,
27 Bunyodkor ul., Tashkent 100185, Uzbekistan

Abstract

To date, the processes of tunnel ionisation of impurities near the interface between two different semiconductors have been comprehensively studied. The most important parameters of the contact electron states of impurities have been determined. However, the calculated expressions for these parameters have been of local nature, as applied to individual impurities. Meanwhile, it is easy to understand that a number of processes, such as the flow of charge carriers and their diffusion through a heterojunction, are clearly statistical in nature. The same applies to the processes of tunnel ionisation of shallow and/or deep impurities near the interface. A statistical approach to the calculation of the parameters of tunnel ionisation of impurities broadens the opportunities for obtaining fundamental information regarding surface electron states.

The aim of this work was to use a statistical approach to study the effect of the heterointerface on the energy spectrum of shallow and deep centres. For this purpose, the expansion of the reflected quasi-classical wave function within the complete system of spherical harmonics and the subsequent extraction of the zero harmonic amplitude (*s*-component) was used to estimate the minimum distance from the impurity to the heterobarrier and to specify the limitations of the applicability of the results obtained in other works. The article analyses the conditions of the quasi-classical approximation which are used to estimate the order of the value for the minimum height of the potential barrier (pit).

This work (with due consideration given to the minimum distance estimate) presents averaged formulas obtained for the energy shift of the ground state and the lifetime of the quasi-stationary state depending on the distance from the heterobarrier. Some qualitatively new considerations can also be found in the article. The distribution of impurity centres near the heterobarrier is assumed to be uniform. The article discusses the role of electron transitions in causing the buffer field effect for both shallow and deep centres. The focus of the article is on the estimates of various physical parameters characterising electron transitions near the heterobarrier.

Keywords: Heterobarrier, Tunnelling, Shallow and deep centres, Energy shift of the ground state, Lifetime

⊠ Temur T. Muratov, e-mail: temur-muratov@yandex.ru

1. Introduction

The quasi-classical theory of tunnel ionisation of neutral impurity centres near the heterobarrier was constructed in [1–4]. However, in these studies, the calculation of the main parameters of metastable states (energy shift of the ground state and lifetime) of the impurity is of local nature and does not include many impurities concentrated near the heterojunction. To clarify the limitations of applicability of the obtained results [1], it is necessary to take into account the accumulation of shallow and/or deep neutral impurities near the heterojunction.

Various aspects of the reflection above a barrier and the tunnelling of charge carriers from the wide band-gap of the heterojunction to the narrow band-gap were considered in [2]. In this case, an electron from a donor centre located, for example, in the wide band-gap of the heterojunction, can tunnel through the potential barrier into the narrow band-gap of the heterojunction with a subsequent recombination with a hole. An excess of energy manifests itself in the bulk luminescence spectrum [5]. Taking into account the band discontinuity, an electron which was initially in a quasi-bound state changes into a quasi-free state. At the same time, the energy remains unchanged.

In [3, 4], a quasi-classical theory of ionisation of impurity centres under the action of external electric fields was constructed. The main results were obtained by the imaginary time method.

The main theoretical achievement of work [1] was the extraction of s, the component of the reflected quasi-classical wave function within the limit of a large ratio of distance L from the impurity centre to the heterobarrier to the effective Bohr radius of a shallow impurity ($L/r_B \gg 1$). As a result, the authors of [1] obtained an asymptotic formula for the energy shift of the ground state of a shallow impurity:

$$\delta E_B = -G(V_\circ)\frac{2L}{r_B}\exp\left(-\frac{2L}{r_B}\right)\cdot E_B, \qquad (1)$$

where $G(V_\circ) = \dfrac{\sqrt{E_B} - \sqrt{V_\circ + E_B}}{\sqrt{E_B} + \sqrt{V_\circ + E_B}}$ is the coefficient that determines the condition for the reflection

of the wave function, E_B is the binding energy of a shallow impurity, and $V_\circ$ is the height (depth) of the heterobarrier.

However, the procedure for the extraction of the s component given in [1] does not allow indicating the threshold distance L_{min} from the centre starting from which the asymptotic formulas obtained in [1], and formula (1) in particular, would be effective for finding the energy shift of the ground state of a shallow and/or deep impurity.

Defining the L_{min} parameter is relevant if we take into account the fact that the condition of the quasi-classical approximation can be affected near the impurity [6]. The L_{min} parameter sets the "lower limitation" of the applicability of the theory developed in [1] and consequently the optimal distance from the accumulation of neutral impurities to the heterobarrier. As a consequence, formula (1) must have the L_{min} parameter.

The purpose of this study was to find the L_{min} parameter and to use it to obtain (taking into account the results of [1]) averaged formulas for the energy shift of the impurity state and lifetime of the quasi-stationary state depending on the parameter L_{min}.

2. Calculation methodology

Mathematically correct extraction of the s component of the reflected quasi-classical wave function

$$\psi_+(\theta, L) = \frac{1}{\sqrt{\pi r_B^3}}G(V_\circ)\exp\left(-\frac{2L}{r_B\cos\theta}\right)\exp\left(\frac{L}{r_B}\right),$$
$$(0 \le \theta \le \pi/2) \qquad (2)$$

(if we expand $\cos\theta \approx 1 - \theta^2/2$ in formula (2), where θ is the angle of the wave incidence (reflection), we will end up with an approximate formula from work [1]) means the expansion of function (2) within the full system of spherical harmonics with a subsequent extraction of the zero harmonic amplitude:

$$\psi_+(\theta, L) = \sum_{l,m} a_{lm}Y_{lm}(\theta, \varphi). \qquad (3)$$

The a_{lm} coefficients are determined by the formulas:

$$a_{lm} = \int Y_{lm}^*(\theta, \varphi)\psi_+(\theta, L)d\Omega. \qquad (4)$$

For the zero harmonic coefficient:

$$a_{00} = \int Y_{00}^*(\theta,\varphi)\psi_+(\theta,L)\,d\Omega =$$

$$= \frac{1}{\sqrt{4\pi}}\frac{1}{\sqrt{\pi r_B^3}}G(V_\circ)\exp\left(\frac{L}{r_B}\right)\int_0^{2\pi}d\varphi\int_0^{\pi/2}\exp\left(-\frac{2L}{r_B\cos\theta}\right)\sin\theta\,d\theta =$$

$$= \frac{1}{\sqrt{r_B^3}}G(V_\circ)\exp\left(\frac{L}{r_B}\right)\int_0^{\pi/2}\exp\left(-\frac{2L}{r_B\cos\theta}\right)\sin\theta\,d\theta =$$

$$= \frac{1}{\sqrt{r_B^3}}G(V_\circ)\exp\left(-\frac{L}{r_B}\right)\left\{1-\frac{2L}{r_B}\exp\left(\frac{2L}{r_B}\right)\left[-Ei\left(-\frac{2L}{r_B}\right)\right]\right\}, \quad (5)$$

where $-Ei(-z)$ is integral exponent [7].

At $2L/r_B \gg 1$, from expression (5) it follows:

$$a_{00} \approx \frac{G(V_\circ)}{2L\sqrt{r_B}}\exp\left(-\frac{L}{r_B}\right). \qquad (6)$$

Substitution of (6) into expansion (3) gives the zero harmonic amplitude:

$$\psi_+(\theta,L) \approx a_{00}\cdot Y_{00} \approx \frac{G(V_\circ)}{2L\sqrt{r_B}}\exp\left(-\frac{L}{r_B}\right)\cdot\frac{1}{\sqrt{4\pi}} =$$

$$= \frac{G(V_\circ)}{4L\sqrt{\pi r_B}}\exp\left(-\frac{L}{r_B}\right). \qquad (7)$$

As can be seen from (7), the asymptotic behaviour of the *s*-component of function (2) corresponds to the asymptotic behaviour obtained in [1]. Numerical calculations of function $\Phi(z) = 1 - z\exp(z)[-Ei(-z)]$ from expression (5) show (Table) that the transition to the asymptotic formulas in [1] begins approximately from the distance $L_{\min} \approx 5r_B$ and in this context:

$$\Phi(z) = \begin{cases} 1 - z\exp(z)[-Ei(-z)], & (z<10) \\ 1/z, & (z\geq10) \end{cases}. \qquad (8)$$

At distances shorter than $L_{\min} \approx 5r_B$, the theory developed by the authors of [1] cannot properly explain the experimental results of [2, 5] and is rather a rough approximation.

To calculate the energy shift per unit of distance, for simplicity, we will assume that the distribution of impurity atoms over the matrix volume near the heterojunction is uniform and isotropic.

$$\overline{\delta E_B} = \lim_{L\to\infty}\frac{1}{\Delta L}\int_{L_{\min}}^{L}\delta E_B(x)dx = \frac{1}{\Delta L}\int_{L_{\min}}^{\infty}\delta E_B(x)dx. \quad (9)$$

By substituting formula (1) in expression (9) (we assume that the value L is a variable) we get:

Table. Values of the F(z) function

z	5	10	15	20
$\Phi(z)$	0.15	0.09	0.07	0.05

$$\overline{\delta E_B} = -G(V_\circ)\left(1+\frac{2L_{\min}}{r_B}\right)\frac{r_B}{2\Delta L}\exp\left(-\frac{2L_{\min}}{r_B}\right)\cdot E_B. \,(10)$$

Accordingly, for the average lifetime of an electron at $V_\circ < -E_B$:

$$\overline{\tau_B} = \frac{\hbar}{2E_B}\frac{|V_\circ|}{\sqrt{E_B(|V_\circ|-E_B)}}\frac{\Delta L}{r_B}\frac{\exp(2L_{\min}/r_B)}{1+2L_{\min}/r_B}. \quad (11)$$

This time is minimal if $V_\circ = -2E_B$.

Here, ΔL characterises the effective size of the impurity layer near the heterojunction (Fig. 1). As the electrons move from impurity levels to a free state, the layer becomes positively charged and acquires the character of a buffer electric field, which, however, does not have a significant effect on the tunnelling effect. The value of ΔL cannot significantly exceed r_B (~ 10 Å). At the same time, ΔL cannot be less than the critical distance between atoms ($\Delta L \geq 4r_B$) (Mott's transition) [8]. For estimates, you can assume that $\Delta L \approx L_{\min} \approx 5r_B$. For a model semiconductor with the parameters of $E_B = 0.01$ eV and $V_\circ = 0.1-1$ eV, the estimate for the lifetime of the bound electron according to formula (11) gives a value of the order of $5\cdot10^{-10}$ s. Using $L_{\min} \approx 5r_B$ the criterion of quasi-classical behaviour ($\lambda < L_{\min}$) can be determined:
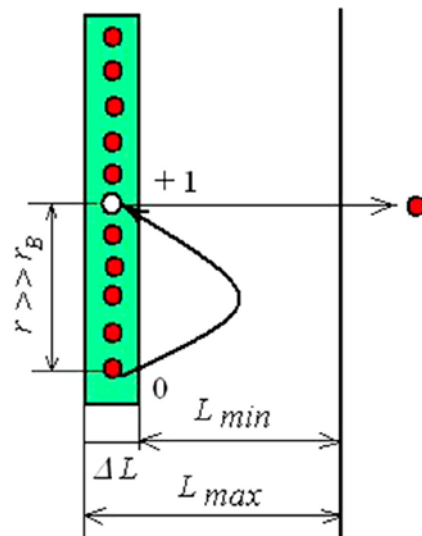
Fig. 1. Scheme of electronic transitions near the heterojunction

Condensed Matter and Interphases / Конденсированные среды и межфазные границы   2021;23(4): 529–534

T. T. Muratov   Statistical approach to the process of tunnel ionisation ...

$$|V_\circ| > 1.04 E_B \,. \quad (12)$$

Consequently, when $|V_\circ| = 1.04 E_B$, the condition of applicability of the quasi-classical approximation, i.e. the heterobarrier, must be sufficiently high (deep). By further developing this line of reasoning, it is possible to interpret $\overline{\delta E_B}$ as the average energy of shift of the ground state of impurity atoms within the effective width ΔL obtained from the beam of quasi-classical electrons. The estimation of $\overline{\delta E_B}$ by formula (10) for a model semiconductor is approximately 10^{-5} eV. The energy shift of the ground state of impurity (10) cannot be less than the value of its natural width (10^{-7} eV). This imposes certain limitations on the value of L, namely $L_{max} < 10\, r_B$. In case of great distances, formula (10) gives unrealistically low values for $\overline{\delta E_B}$. To compare, for example, the binding energy of $D^-(A^+)$ centres is of the order of meV [9].

It is interesting to compare the lifetime of a bound electron in relation to its changing into a free state with its tunnelling time between small impurities (Fig. 1). The theory provides the following formula for the tunnelling time between the centres [6]:

$$\overline{\tau_{0\to 1^+}} = \frac{\pi\hbar}{\overline{\delta E_{0\to 1^+}}}\,, \quad (13)$$

and

$$\overline{\delta E_{0\to 1^+}} \approx \frac{8r}{3r_B}\exp\left(-\frac{r}{r_B}\right)\cdot E_B\,, \quad (14)$$

where r is the average distance between the impurity atoms.

At concentrations of shallow impurities of 10^{18} cm^{-3}, formula (14) gives a value of $1.2\cdot10^{-5}$ eV, almost equal to $\overline{\delta E_B}$, i.e. $\overline{\tau_B}/\overline{\tau_{0\to 1^+}} \approx 3$. This means that for highly doped semiconductors at very low temperatures (about 2–4 K), there is hardly any effect of the buffer (quasi-electric) field and in general the impurity layer ΔL is quasi-neutral. The quasi-neutral behaviour of the layer can be disturbed by exposure to radiation, heat treatment, etching, application of an external electric field, etc. [10].

In case of the deep centre described by the "zero" radius potential [1] within the framework of this model, the bound electron has no excited states and has one single bound state. This allows considering the amplitude of the "zero harmonic" of decomposition (3), which is the only one of its kind [9]. Calculations similar to the ones used to derive formula (7) give the following formula for the amplitude of the zero harmonic of the reflected quasi-classical wave function:

$$\psi_+(\theta, L) = \frac{A(V_\circ)}{8L^2}\sqrt{\frac{a_\circ}{\pi}}\exp\left(-\frac{L}{a_\circ}\right)\;(2L/a_\circ \gg 1)\,, (15)$$

where $A(V_\circ) = \dfrac{\sqrt{E_\circ} - \sqrt{V_\circ + E_\circ}}{\sqrt{E_\circ} + \sqrt{V_\circ + E_\circ}}$, $a_\circ = \hbar / \sqrt{2m^* E_\circ}$

are the size of the wave function of the electron bound at the deep centre ($a_\circ$ usually does not exceed several constant lattice spacings [11]), m^* is the effective mass of the electron, and $E_\circ$ is the binding energy of the electron at the deep centre (of the order of eV).

Considering the fact that function (8) is universal, it is possible to immediately specify the lower limitation of the applicability of formula (15): $L_{min} \approx 5a_\circ$. By averaging the formula for the energy shift of the deep state obtained in work [1]:

$$\delta E_\circ = -A(V_\circ)\frac{a_\circ}{L}\exp\left(-\frac{2L}{a_\circ}\right)\cdot E_\circ \quad (16)$$

and using expression (9), we have:

$$\overline{\delta E_\circ} = -A(V_\circ)\frac{a_\circ}{\Delta L}\left[-\mathrm{Ei}\left(-\frac{2L_{min}}{a_\circ}\right)\right]\cdot E_\circ$$
$$(\Delta L \approx L_{min})\,. \quad (17)$$

From (17) the approximate formula follows:

$$\overline{\delta E_\circ} \approx -A(V_\circ)\frac{a_\circ}{10 L_{min}}\exp\left(-\frac{2L_{min}}{a_\circ}\right)\cdot E_\circ$$
$$(L_{min} \approx 5a_\circ)\,. \quad (18)$$

Accordingly, the average lifetime of an electron at the deep centre when $V_\circ < -E_\circ$:

$$\overline{\tau_\circ} = \frac{5\hbar}{2E_\circ}\frac{|V_\circ|}{\sqrt{E_\circ\left(|V_\circ| - E_\circ\right)}}\frac{L_{min}}{a_\circ}\exp\left(\frac{2L_{min}}{a_\circ}\right)\,. \quad (19)$$

By comparing (11) and (19) we can conclude that heterobarrier affects the position of the shallow impurity more (by about 30 times). It is clear that screening greatly reduces the probability of an electron jumping from a neutral impurity to an ionised (+1) impurity. The time required

to neutralise the deep impurity significantly exceeds the lifetime of the bound electron of the shallow impurity, and the buffer field effect will be observed for a long time. At the same time, electronic transitions between deep and shallow centres are quite possible. The corresponding calculations are described in [12–17].

3. Discussing the results with regard to the AlGaAs/GaAs heterostructure

Let us discuss the conditions for the applicability of the obtained formulas in relation to a specific AlGaAs/GaAs heterostructure with a deep centre (Fig. 2). The forbidden energy gap of gallium arsenide is 1.5 eV and in a solid solution of $Al_xGa_{1-x}As$ it increases with the growth of x. For example, at x = 1, the forbidden energy gap in the AlAs compound is 2.2 eV. As we noted above, the buffer field effect (developed within the framework of the statistical approach) will work for a long time in the case of a deep centre. Let us estimate the minimum buffer field value for the DX centre in AlGaAs. Assuming $|V_0| = 0.75$ eV, $E_0 = 0.7$ eV (Fig. 2), we will find (*e*-charge of the electron):

$$E_{buff} = \frac{|V_\circ| - E_\circ}{eL_{min}} \approx 2.4 \cdot 10^2 \text{ V/cm}$$

$$(|V_\circ| - E_\circ \ll E_{opt}). \tag{20}$$

Indeed, as we can see, the intensity of the buffer field is much less than the intensity of the optical ionisation field of the DX centre ($E_{opt} \approx 1.3$ eV) [18].

Also, we would like to note that the basic value of L_{min}, which we operated on with within the framework of the statistical approach, coincides with the critical distance from [18] ($L \approx 70$ Å). In general, all this confirms the correctness of the initial formulas (10), (11), (18), and (19).

Therefore, the statistical approach to tunnel ionisation of deep centres leads to approximately the same results as the multiphonon mechanism of ionisation of DX centre in heterostructures [18].

4. Conclusions

The content of the work can be summarised by formulas (10), (11), (18), and (19), which clarify the relevant formulas obtained in the work [1]. Numeric evaluations (Table) indicate that there is a well-defined distance from the impurity centre $L_{min} \approx 5r_B$ ($L_{min} \approx 5a_\circ$) to the heterobarrier,
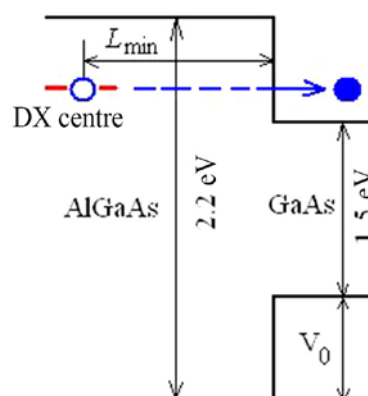
Fig. 2. First-order heterojunction (AlGaAs/GaAs). Specified tunnel transition of the electron from the DX centre

starting from which the asymptotic formulas obtained in [1] are quite accurate. This applies equally to formulas (10), (11), (18), and (19) derived from these asymptotic behaviours. After being averaged, formulas (1) and (16) of Efros et al. became a statistical average of (10) and (18). From formulas (10) and (18), it follows that the greatest contribution to the total energy shift is provided by impurity centres localised at a distance of $L = L_{min}$ from the heterointerface. This fact is not mentioned in the asymptotic formulas of Efros et al. In addition, the formulas of Efros et al. do not allow developing the idea of the "buffer field" effect, which is purely statistical in nature.

The "buffer field" effect is produced in the case of deep impurities [18]. Then, there is some similarity with quasi-electric fields in variband semiconductors. For shallow impurities, in this situation, this effect is never produced.

Conflict of interests

The author declares that they have no known competing financial interests or personal relationships that could have appeared to influence the work reported in this paper.

References

1. Ivanov M.G., Merkulov I.A., Efros Al.L. Energiya i shirina primesnogo urovnya vblizi geterogranitsy. [Energy and width of impurity level near interface]. *Physics and Technics of Semiconductor*. 1988; 22(4): 628-633. Available at: https://journals.ioffe.ru/articles/29200 (In Russ.)

2. Bresler M. S., Gusev O. B., Mikhaylova M. P., Sherstnev V. V., Yakovlev Yu. P., Yassievich I. N.

Condensed Matter and Interphases / Конденсированные среды и межфазные границы   2021;23(4): 529–534

T. T. Muratov   Statistical approach to the process of tunnel ionisation ...

Interfeysnaya lyuminessensiya, obuslovlennaya nadbar'ernym otrajeniem, v izotipnoy geterostrukture p-InAs/P-InAsPSb. [Interface luminescence appearing above barrier reflection in the isotype heterostructure p-InAs/P-InAsPSb]. *Physics and Technics of Semiconductor*. 1991;25(2): 298–306. Available at: https://journals.ioffe.ru/articles/23313 (In Russ.)

3. Kryuchkov S. V., Syroedov G. A. Ionizatsiya primesnykh centrov v uzkozonnykh poluprovodnikakh peremennym elektricheskim polem. [Ionization of impurity centers in a narrow band-gap semiconductors by ac electric field]. *Physics and Technics of Semiconductor*. 1988;22(9): 1695–1697. Available at: https://journals.ioffe.ru/articles/29445 (In Russ.)

4. Glazov S. Yu., Badikova P. V. Ionization of impurities by a constant electric field in graphene with a wide forbidden band. *Journal of Nano- and Electronic Physics*. 2018;10(2): 02020-1–02020-5. https://doi.org/10.21272/jnep.10(2).02020

5. Béranger M. Study on the use of silicon drift detector to get information on light emitted by luminescent materials. *American Journal of Physics and Applications*. 2019;7(2): 34–42. https://doi.org/10.11648/j.ajpa.20190702.11

6. Shklovskiy B. I., Efros A. L. *Elektronnye svoystva legirovannykh poluprovodnikov*. [*Electric properties of doped semiconductors*]. Moscow: Nauka Publ.; 1979. 416 p. (In Russ.)

7. Khudyaev S. I. Otsenki integralov s pomoshchyu srednikh i nekotorye ikh primeneniya. [The estimations of integrals on the base of averages and some its applications]. *Jurnal vychislitelnoy matematiki i matematicheskoy fiziki*. 1982;22(2): 280-295. (In Russ.)

8. Bychkovskiy D. N., Konstantinov O. V., Tsarenkov B. V. Fazovyi perekhod dielektrik-metall: termodinamicheskiy aspekt problemy. [Phase transition dielectric-metal: thermodynamic aspect of the problem]. *Physics and Technics of Semiconductor*. 1995;29(1): 152–161. Available at: https://journals.ioffe.ru/articles/18064 (In Russ.)

9. Imamov E. Z., Kolchanova N. M., Kreshchuk L. N., Yassievich I. N. Rol' rasseyaniya na melkikh neytralnykh centrakh v kineticheskikh yavleniyakh pri nizkoy temperature. [Role of scattering on shallow neutral centers in kinetic phenomena at low temperature]. *Solid State Physics* 1985;27(1): 69–76. (In Russ.)

10. Brudnyi V. N. Vliyanie jestkoy radiatsii na elektronnye, opticheskie i rekombinatsionnye svoystva soedineniy (Al,Ga,In)-P,(Al,Ga,)-As i ikh tverdykh rastvorov. [Influence of hard radiation on electrical, optical and recombination properties of the compositions (Al,Ga,In)-P,(Al,Ga,)-As and its solid solutions]. *Izvestiya vuzov. Fizika*. 2013;56(8): 37–39. Available at: https://www.elibrary.ru/item.asp?id=20282740 (In Russ.)

11. Mironov A. G., Serov A. S. Electron energies and states at the deep impurity level in a semiconductor. *Moscow University Physics Bulletin*. 2011;66(3): 272–277. https://doi.org/10.3103/s0027134911030143

12. Stys L.E. Mekhanizm tunnel'noy termosti-mulirovannoy relaksatsii toka. [Tunnel thermo-stimulated relaxation mechanism of a current]. *Physics and Technics of Semiconductor*. 1989;23(11): 1971–1975. Available at: https://journals.ioffe.ru/articles/29999 (In Russ.)

13. Terukov I. E., Khuzhakulov E. S. Electron exchange between neutral and ionized germanium centers in PbSe. *Semiconductors*. 2005;39(12): 1371. https://doi.org/10.1134/1.2140306

14. Muratov T. T. Recombination of mobile carriers across boron excited levels in silicon at low temperatures. *Semiconductors*. 2019;53(12): 1573–1577. https://doi.org/10.1134/s1063782619160206

15. Colston G., Myronov M. Electrical properties of n-type 3C-SiC epilayers *in situ* doped with extremely high levels of phosphorus. *Semiconductor Science and Technology*. 2018;33(10): 1–6. https://doi.org/10.1088/1361-6641/aade67

16. Ma N., Jena D. Charge scattering and mobility in atomically thin semi- conductors. *Physical Review X*. 2014;4(1): 011043-1–011043-9. https://doi.org/10.1103/physrevx.4.011043

17. Mukashev B. N., Abdullin X. A., Gorelkinskii Yu. V. Metastable and bistable defects in silicon. *Physics-Uspekhi*. 2000;43(2): 139–150. https://doi.org/10.1070/pu2000v043n02abeh000649

18. Pakhomov A. A. Termoionizatsiya glubokikh centrov vblizi interfeysa. [Thermo-ionization of deep centers near interface]. *Physics of the Solid State*. 1992; 34(11): 3417–3420. Available at: https://journals.ioffe.ru/articles/22718 (In Russ.)

Information about the author

Temur T. Muratov, PhD in Physics and Mathematics, Provisional Associate Professor at the Department of Physics and Astronomy, Nizami Tashkent State Pedagogical University, Tashkent, Uzbekistan; e-mail: temur-muratov@yandex.ru. ORCID iD: https://orcid.org/0000-0002-0905-6620.

Original articles

Research article
https://doi.org/10.17308/kcmf.2021.23/3672

Anodic behaviour of manganese germanide Mn$_5$Ge$_3$ in a sodium sulphate aqueous solution

I. L. Rakityanskaya✉, D. A. Myasnikov, A.B. Shein

Perm State National Research University,
ul. Bukireva 15, Perm, 614990 Russian Federation

Abstract

Germanides are an interesting class of two-component systems which consist of metal and germanium. They are similar in their structure with silicides but have the specific properties. The target of the investigation was finding the main anodic electrochemical behaviour mechanisms for magnesium germanide Mn$_5$Ge$_3$ in an Na$_2$SO$_4$ aqueous solution.

Electrochemical behaviour of manganese germanide obtained by Czochralski method was investigated by polarization curves and electrochemical impedance spectroscopy methods and accomplished by microscopy data. Individual manganese and germanium were investigated in the same way for comparison. It was established that in the anodic oxidation process germanium is the potential-determining component. The passivation process associated with the formation of surface oxide films was accomplished by the current density oscillations appearing due to the bad adhesion of oxide film to the surface of the sample, its imperfection and discontinuity. The nature of oxide film formed in the polarization process was partially established. The dependence of the anodic behaviour of the sample on the sulphate concentration was established: in the diluted solutions the passivation occurs at more positive potentials than in the concentrated. This phenomenon can be explained by the different mechanisms of anodic oxidation in the solutions of different concentrations.

Keywords: Manganese, Germanium, Manganese germanide, Oxide films, Anodic oxidation, Impedance spectroscopy

✉ Irina L. Rakityanskaya, e-mail: irisa@yandex.ru

Condensed Matter and Interphases / Конденсированные среды и межфазные границы   2021;23(4): 535–542

I. L. Rakityanskaya et al.   Anodic behaviour of manganese germanide Mn$_5$Ge$_3$...

1. Introduction

In the modern world, much attention is paid to the search for new materials with high corrosion resistance over a wide range of aggressive media. Such materials are transition metal silicides [1, 2]. However, the study of germanides of the same metals, which are close to silicides in structure [3] but do not have a high resistance to corrosion, may also be interesting mainly due to the elucidation of the mechanism of dissolution of systems consisting of several components, differ by their physical and chemical properties.

Manganese is a rather active element; therefore, its metal-like compounds, including silicides and germanides, have properties different from similar systems of the iron triad, studied in detail earlier [4]. There is an array of data obtained as a result of the study of electrochemical processes occurring on the silicide Mn$_5$Si$_3$ and manganese monosilicide MnSi in acidic electrolytes [5–7]. The same two-component systems in alkaline media are less studied [8, 9]. Now, data on the behaviour of manganese silicides and germanides in aqueous solutions with a pH close to 7 are limited, although majority of the electrolytes in various industries are neutral media. The publications mainly contain data on the electrochemical and corrosive behaviour of metal silicides of various compositions [10–14], while such studies for germanides are less common [15, 16].

2. Experimental

The object of the study was a double metal-like system – manganese germanide Mn$_5$Ge$_3$ obtained by the Czochralski method [1]. The germanide sample is soldered to the copper wire with a silver-containing conductive glue. The entire electrode was insulated with epoxy glue, excluding the working surface. The electroactive surface area was 0.15 cm^2.

The preparation of the electrode surface before the experiment was carried out as follows: the electrode was mechanically cleaned and polished with emery paper, successively changing its grade from 1000 to 2500. The prepared surface was degreased with 96% ethyl alcohol and rinsed with distilled and deionized water. A saturated silver chloride electrode was used as a reference electrode. The counter electrode was platinum.

Deionized water (R = 18.2 MΩ), obtained in a Milli-QAdvantage A10 water distiller (Germany), and dry sodium sulphate powder (chemically pure grade) were used for the preparation of electrolyte solutions. The studies were carried out in a standard YSE-2 electrochemical cell. Polarization and impedance measurements were performed using a Metrohm Autolab PGSTAT302N potentiostat/galvanostat. The polarisation curves were recorded in the potentiodynamic mode at the scan rate of 1 mV/s and a temperature of 20±5 °C.

The range of frequencies used in impedance measurements f (ω/2π) were from 100000 Hz to 0.05 Hz, the amplitude of the alternating signal was 10 mV. Before measuring the impedance, the electrode was kept in a solution at an appropriate potential until stable current density values were achieved. The impedance data were processed using NOVA 2.1.4 program.

The studies were carried out under natural aeration and stationary diffusion conditions. The cell was washed several times with tap, distilled, and deionized water before work. In the case of strong contamination of the cell with corrosive products, it was washed with a hot chrome mixture.

Microscopic measurements were carried out using an HITACHI S-3400N Scanning Electron Microscope with a BRUKER attachment for X-ray microanalysis.

3. Results and discussion

3.1. Polarisation measurements

When studying the electrochemical behaviour of multicomponent systems, it seems appropriate also obtain information on the analogous behaviour of simple substances which are constituents of such systems under similar conditions. A comparative study of the anodic behaviour of manganese, germanium, and manganese germanide in a 0.5 M Na$_2$SO$_4$ solution was carried out by the polarisation curve method (Fig. 1).

The dissolution of germanium in sodium sulphate occurs uniformly, without noticeable peaks in the anodic curve. With an increase in the anodic polarisation, the currents increase, but the rate of increase is not the same in different areas, which indicates a change in the dissolution mechanism and, possibly, a change

Condensed Matter and Interphases / Конденсированные среды и межфазные границы   2021;23(4): 535–542

I. L. Rakityanskaya et al.   Anodic behaviour of manganese germanide Mn₅Ge₃...
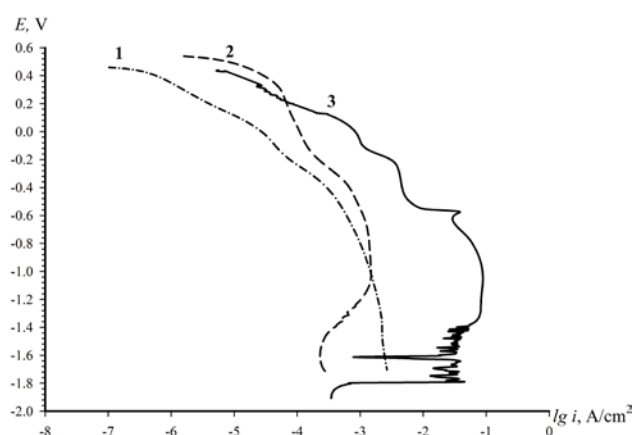
Fig. 1. Polarization curves for manganese germanide Mn5Ge3 and its individual components in 0.5 M Na$_2$SO$_4$solution: *1* – Ge; *2* – Mn; *3* – Mn$_5$Ge$_3$

in the composition of corrosion products. This is in good agreement with the literature data [4, 17], where it is stated that anodic dissolution of germanium in aqueous solutions of different compositions can form a mixture of hydrated oxides GeO and GeO$_2$ as well as metagermanic acid H$_2$GeO$_3$, which slow down the dissolution rate only in the case of accumulation of a sufficiently thick layer of phase oxide.

Manganese is an active metal, which forms many oxidized forms upon anodic polarization in aqueous media [18]. The curve of its anodic dissolution is in good agreement with the data of the Pourbaix diagram, according to which, starting from a potential of 0.1 V, Mn$_3$O$_4$ and Mn$_2$O$_3$ oxides are sequentially formed on the metal surface, and finally, MnO$_2$ is formed at a potential of 0.8 V, the accumulation of which slows down the rate of dissolution of the metal. In a 0.5 M sodium sulphate solution, the dissolution rates of pure germanium and manganese are comparable.

Upon anodic polarization manganese germanide Mn$_5$Ge$_3$demonstrates a high corrosion rate, which is 1–2 orders of magnitude higher than for its constituent pure components. Corrosion potentials for germanium and manganese were E_{cor} = −0.46V and E_{cor} = −0.56 V, respectively; for manganese germanide, E_{cor} = −0.47 V, which suggests that germanium is the potential determining component. The characteristic potentials of the anodic curve for manganese germanide, at which the Tafel slope changes, mainly coincide with the analogous potentials

for germanium polarisation curve. The latter suggests that in this situation, the features of the anodic processes on the sample are mainly due to its non-metallic component. However, with deep anodic polarisation, peaks appear at potentials +0.6 V (peak I) and +1.25 V (peak II) on Mn$_5$Ge$_3$ curve, which are not typical for both Mn and Ge. Moreover, at a potential of +1.4 V, a rather long region of current density oscillations begins, behind which a decrease in the current density was recorded, and, therefore, the dissolution processes slowed down.

The concentration of sodium sulphate affects the processes occurring during the anodic dissolution of the sample (Fig. 2). With concentrations above 0.5 M, only the dependence of the dissolution rate on the concentration is observed, the potential of all peaks of active dissolution remains constant, only its current decreases. With a decrease in the concentration of sodium sulphate to 0.25 M and below, the potentials of both peaks of active dissolution shift to the region of more positive values, which may be associated with a slowdown in the dissolution process due to a decrease in the electroconductivity of the solution. In addition, sulphates, not participating directly in the surface transformation process, can be its activators, and, thus, a decrease in their concentration can lead to diffusion limitations.

The region of anodic current density oscillations is also subjected to the influence of the electrolyte concentration: with an increase in
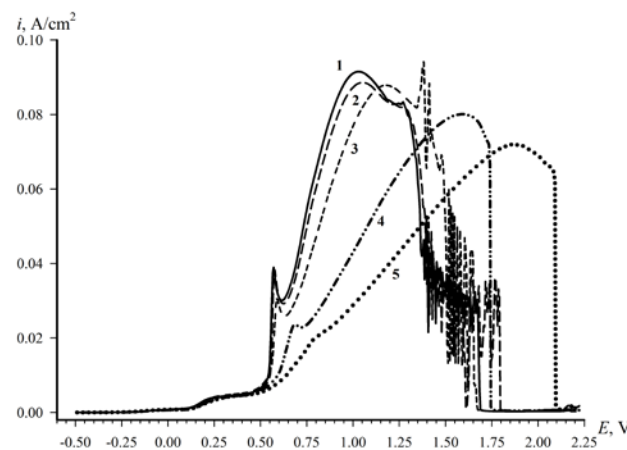
Fig. 2. Anodic polarisation curves for manganese germanide Mn$_5$Ge$_3$ obtained in Na$_2$SO$_4$ solutions of different concentrations: *1* – 1 M; *2* – 0.5 M; *3* – 0.25 M; *4* – 0.1 M; *5* – 0.05 M

Condensed Matter and Interphases / Конденсированные среды и межфазные границы   2021;23(4): 535–542

I. L. Rakityanskaya et al.   Anodic behaviour of manganese germanide Mn₅Ge₃...

the content of sulphate ions, it is observed at less and less positive potentials, and its range expands.

3.2. Impedance measurements

Nyquist plots at the corresponding potentials in a solution of 0.5 M sodium sulphate are shown in Fig. 3. As the potential shifts towards more positive values, the graph takes on the form of two clearly separated semicircles and an inductive arc.

In the potential range from –0.1 V to 0.8 V, the impedance of the system decreased, then slightly increased in the active-passive transition area. The complex nature of the curve reflects the multi-stage nature of the polarisation process: such graphs are typical for electrodes characterised by the variety of adsorbed corrosion products [19]. This confirms the earlier assumptions about the

formation of an oxide layer on the sample surface. In all spectra, the HF semicircle corresponds to the processes occurring on the hydrated oxide film and the interface between it and the electrolyte, while the LF semicircle characterizes the interface between the oxide film and the electrode surface.

The appearance of an HF pseudo-arc can be associated with several factors, first of all, with the phenomenon of capacitance dispersion, occurring due to the peculiarities of the measuring system. Often, such phenomena occur due to deficiencies in the reference electrode and the design of the cell. In this case, such part of the spectrum is an artefact; therefore, it was not taken into account when analysing the spectra [20, 21].

On all impedance spectra between two semicircles there is an inductive loop gradually
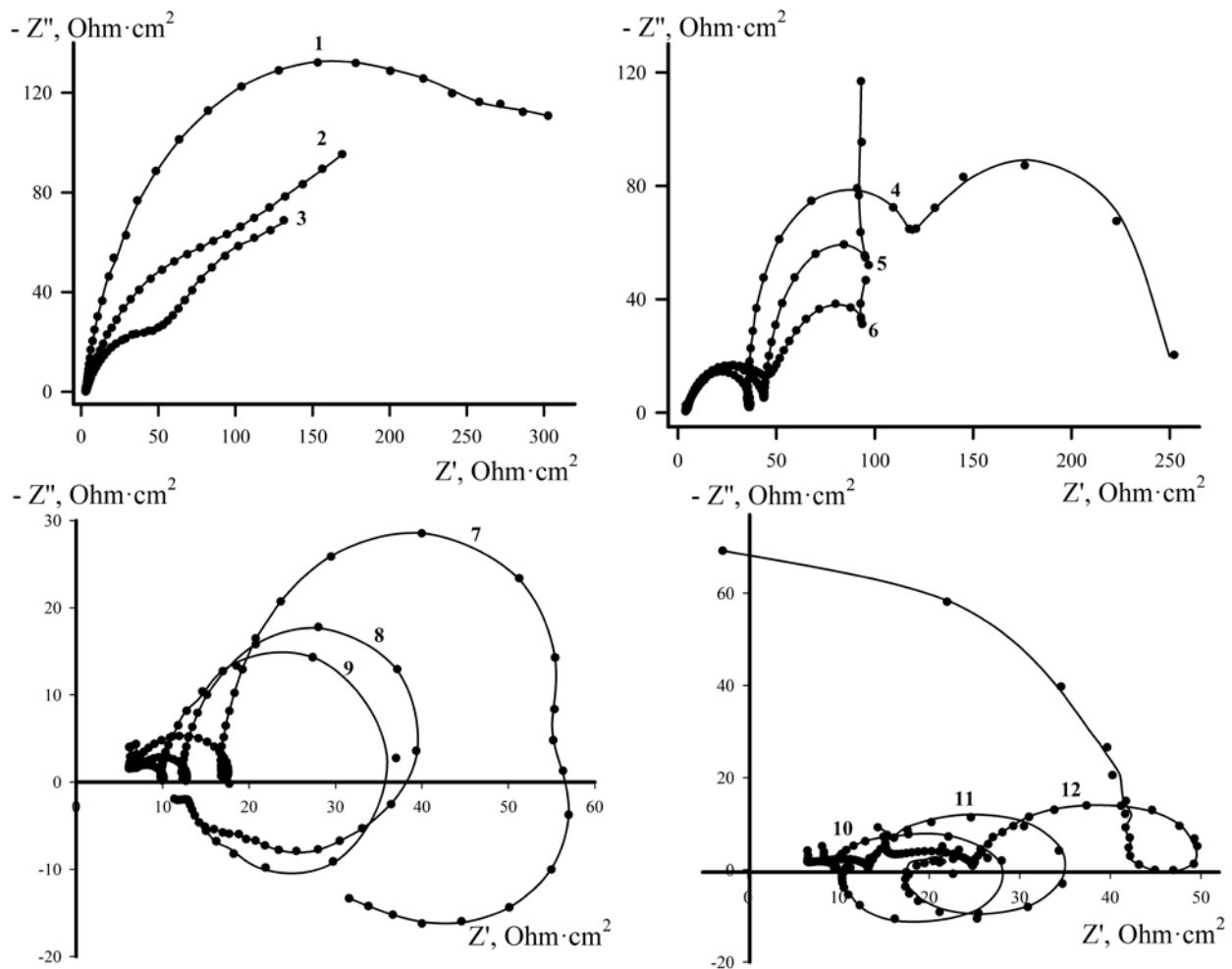
Fig. 3. Nyquist Plots for manganese germanide Mn₅Ge₃ in 0.5M Na₂SO₄ solution at the following potentials: *1* – – 0.1 V; *2* – 0 V; *3* – + 0.1 V; *4* – + 0.2 V; *5* – + 0.3 V; *6* – + 0.4 V; *7* – + 0.5 V; *8* – + 0.6 V; *9* – + 0.7 V; *10* – + 0.8 V; *11* – + 0.9 V; *12* – + 1 V

Condensed Matter and Interphases / Конденсированные среды и межфазные границы   2021;23(4): 535–542

I. L. Rakityanskaya et al.   Anodic behaviour of manganese germanide Mn$_5$Ge$_3$...

shifting to the right, which according to [22] is associated with an increase in surface roughness and stabilization of the oxide layer containing adsorbed anions. The surface roughness was presumably increased due to the formation of micropores due to the accelerated diffusion of SO$_4^{2-}$ particles in the oxide layer.

The straight line on the Nyquist plot was obtained using the Voith scheme. All spectra are characterized by two positive time constants, which can be assessed for reliability using the Kramers–Kronig relations. The inductive component of the spectrum is characterized by a negative time constant; therefore, this part of the spectrum cannot be assessed for reliability using the Kramers-Kronig relations. As the amplitude of the alternating signal changed to 5 and 3 mV, the graphs of the impedance spectra did not change.

Due to the multistage nature of the process, the impedance spectra were analysed by the characteristic frequencies f determined based on the points of inflexion on the complex plane. The dependence of the characteristic frequencies on the applied anode potential is shown in Fig. 4.

Frequency f_1, corresponding to the first semicircle and characterizing the process of charge transfer in the electrode - oxide film system, increased with increasing potential many times faster than the frequencies f_2 and f_3, which correspond to the second semicircle and the inductance loop, respectively. In turn, the frequencies f_2 and f_3 also increased with increase in potential up to 0.8 V, at which the active-passive transition area begins. The increase of these characteristics is associated with the accumulation of a thick layer of poorly soluble surface compounds, which limit the process of removing the reaction products from the electrode. With a further shift of the potential to the anodic region, these frequencies decrease due to the fact that the layer of the formed intermediates begins to crack.
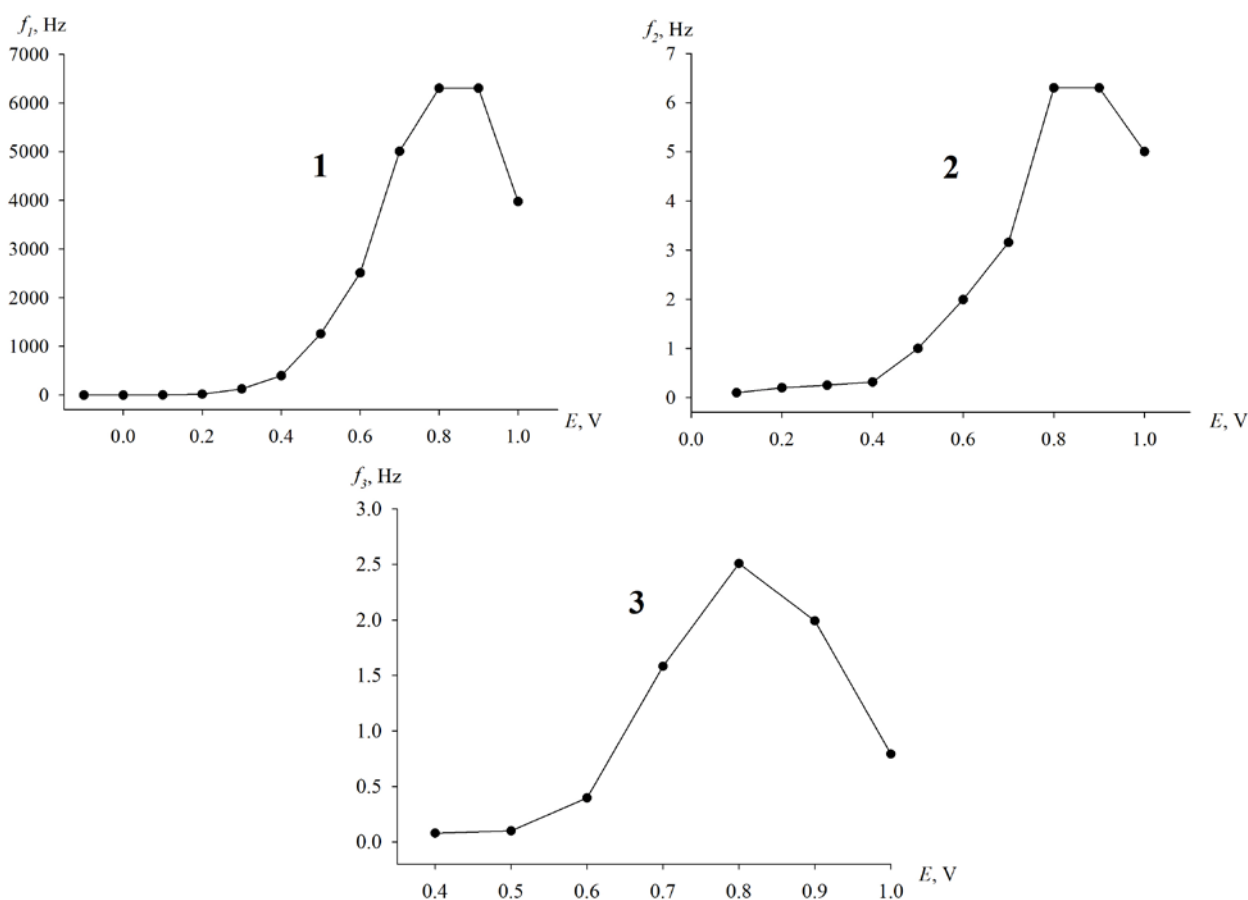
Fig. 4. Characteristic frequencies for Mn$_5$Ge$_3$-electrode in 0.5 M Na$_2$SO$_4$ solution at different anodic potentials. *1)* - HF (high frequencies) semicircle, *2)* LF (low frequencies) semicircle, *3)* LF (low frequencies) inductivity

Condensed Matter and Interphases / Конденсированные среды и межфазные границы   2021;23(4): 535–542

I. L. Rakityanskaya et al.   Anodic behaviour of manganese germanide Mn$_5$Ge$_3$...

The first time constant characterizing the HF semicircle changes most noticeably with increasing potential. The diameters of the HF and LF semicircles decrease with increasing potential, which indicates an increase in the intensity of the oxidation process. Products of $i \cdot R$ are shown in Fig. 5.

For the HF semicircle the $i \cdot R$ product increases monotonically, starting from $E = 0.4$ V. For the LF semicircle the $i \cdot R$ product also increases, but more smoothly than for the high-frequency semicircle. This means that the process of accumulation of the surface film somewhat reduced the possible rate of oxidation.

3.3. Microscopic examination of the structure

For the assessment of the composition and structure of the surface layer after polarization, micrographs of the surface were obtained and X-ray microanalysis was performed. When the electrode was kept in potentiostatic mode for ten minutes, an oxide layer was formed on its surface, which later started to exfoliate, which was especially noticeable when the electrode was removed from the electrolyte solution.

The micrograph obtained upon the potentiostatic incubation of the electrode in the region of the anodic peak at $E = 0.6$ V (Fig. 6) allowed the visualization of the morphology of the formed layer: areas free from oxidation products and areas with an exfoliating film were revealed on the electrode. X-ray spectral microanalysis of the film showed that it consists of germanium and oxygen in an atomic ratio of 1:1. The fact that the hydrated form of oxidation products in air transforms into more stable oxide forms should be taken into account. In this regard, X-ray microanalysis showed the presence of only germanium oxide and the complete absence of manganese in the composition of the film.

On the micrograph obtained upon polarization up to $E = 1.8$ V (Fig. 7), a thick oxide film is clearly visible. According to X-ray microanalysis data, it also consists only of germanium oxide, but has denser structure. Manganese oxides can be formed at high positive potentials, but they were not revealed by this method of analysis.

4. Conclusions

Manganese germanide is rather unstable to anodic oxidation in a sodium sulphate solution. The mechanism of anodic dissolution includes several stages with the adsorption of intermediates. It is most probable that in a neutral environment, a high rate of Mn$_5$Ge$_3$ oxidation is associated with the uniform dissolution of both components, but only up to a potential of -0.45 V. With a deeper anodic polarization, the surface layer is depleted of manganese due to its selective dissolution from beneath the simultaneously formed germanium oxides layer. Thus, the passivation of manganese germanide at high potentials occurs due to the non-metallic component of the sample, while the reaction is controlled by the diffusion of manganese, which
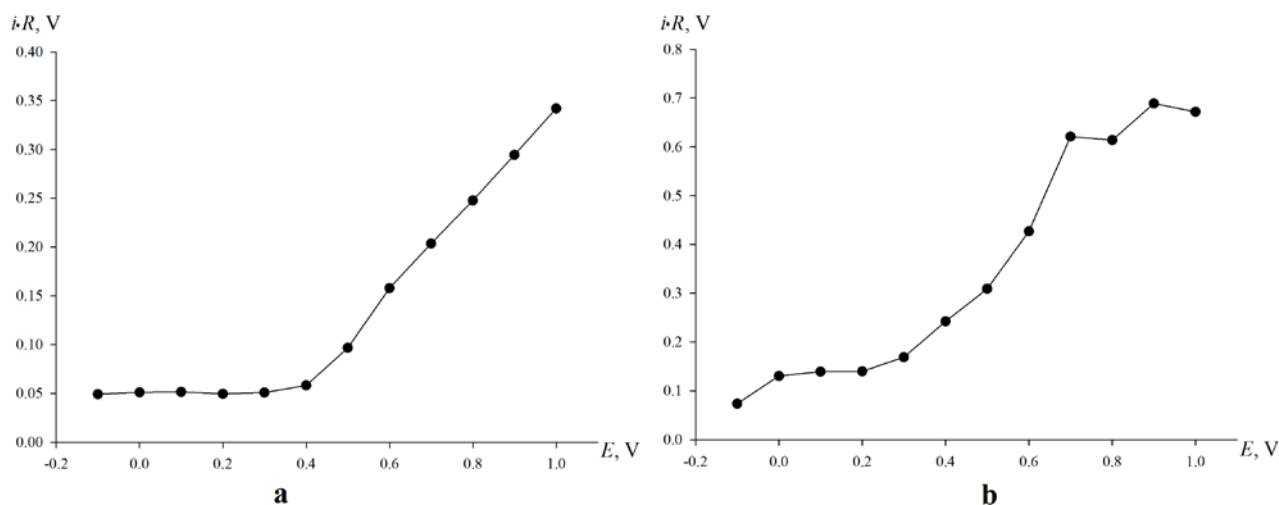
Fig. 5. Dependence of $i \cdot R$ on the potential of Mn$_5$Ge$_3$-electrode in a 0.5 M Na$_2$SO$_4$ solution: a – HF (high frequencies) semicircle, b – LF (low frequencies) semicircle

Condensed Matter and Interphases / Конденсированные среды и межфазные границы   2021;23(4): 535–542

I. L. Rakityanskaya et al.   Anodic behaviour of manganese germanide Mn₅Ge₃...

Fig. 6. Micrograph of Mn_5Ge_3 surface after 10 minutes anodic polarization at E = + 0.6V in a 0.5 M Na_2SO_4 solution
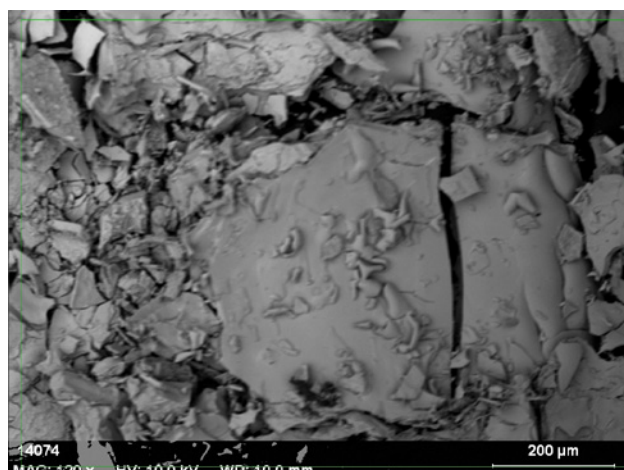
Fig. 7. Micrograph of Mn_5Ge_3 surface after 10 minutes of anodic polarization at E = + 1.8V in 0.5 M Na_2SO_4 solution

is selectively ionized through the oxidation products of germanium.

Authors contributions

Rakityanskaya I. L. – the concept of research, the choice of research methods, writing the text, the final conclusions. D. A. Myasnikov – conducting research, review and text writing. Shein A. B. – general scientific guidance, final conclusions.

Conflict of interests

The authors declare that they have no known competing financial interests or personal relationships that could have influenced the work reported in this paper.

References

1. Shein A. B. *Elektrokhimiya silitsidov i germanidov perekhodnykh metallov* [Electrochemistry of transition metals and germanides]. Perm': Perm. gos. un-t Publ.; 2009. 269 p. (In Russ.)

2. Shein A. B. Corrosion-electrochemical behavior of iron family silicides in various electrolytes. *Protection of Metals and Physical Chemistry of Surfaces.* 2010;46(4): 479–488. https://doi.org/10.1134/S2070205110040155

3. Gladyshevskii E. I. *Kristallokhimiya silitsidov i germanidov* [Crystal chemistry of silicides and germanides of transition metals]. Moscow: Metallurgiya Publ.; 1971. 296 p. (In Russ.)

4. Shein A. B., Rakityanskaya I. L., Vilesov S. P. Influence of composition of corrosive medium on anode dissolution of silicides of iron triad. *Russian Journal of Chemistry and Chemical Technology (Izvestiya Vysshikh Uchebnykh Zavedenii, Seriya Khimiya i Khimicheskaya Tekhnologiya) = ChemChemTech.* 2010;53(2): 81–83. Available at: https://elibrary.ru/item.asp?id=12973914 (In Russ., abstract in Eng.)

5. Okuneva T. G., Panteleeva V. V., Shein A. B. Anodic processes on the Mn_5Si_3 electrode in acidic media. *Kondensirovannye sredy i mezhfaznye granitsy = Condensed Matter and Interphases.* 2016;18(3): 383–393. Available at: https://journals.vsu.ru/kcmf/article/view/147 (In Russ., abstract in Eng.)

6. Shein A. B., Zubova E. N. Electrochemical behavior of manganese silicides in sulfuric acid solution. *Protection of Metals.* 2005;41(3): 234–242. https://doi.org/10.1007/s11124-005-0034-z

7. Polkovnikov I. S., Panteleeva V. V., Shein A. B. Impedance of anodic processes on Mn_5Si_3-electrode in sulfuric acid electrolyte containing fluorides. *Vestnik Permskogo universiteta. Seriya «Khimiya»* = Bulletin of Perm University. Chemistry. 2017;7(3): 250–258. Available at: http://press.psu.ru/index.php/chem/article/view/834 (In Russ., abstract in Eng.)

8. Polkovnikov I. S., Panteleeva V. V., Shein A. B. Anodic processes on Mn_5Si_3-electrode in alkaline electrolyte. *Kondensirovannye sredy i mezhfaznye granitsy = Condensed Matter and Interphases.* 2019;21(1): 26–134. https://doi.org/10.17308/kcmf.2019.21/723 (In Russ., abstract in Eng.)

9. Polkovnikov I.S., Shaydullina A.R., Panteleeva V.V., Shein A.B Anodic processes on manganese monosilicide in sodium hydroxide solutions. *Vestnik Permskogo universiteta. Seriya «Khimiya»* = Bulletin of Perm University. 2018;8(3): 325–340. DOI: http://dx.doi.org/10.17072/2223-1838-2018-3-325-341 (In Russ., abstract in Eng.)

Condensed Matter and Interphases / Конденсированные среды и межфазные границы   2021;23(4): 535–542

I. L. Rakityanskaya et al.   Anodic behaviour of manganese germanide Mn$_5$Ge$_3$...

10. Gonzalez-Rodriguez J. G., Rosales I., Casales M., Serna S., Martinez L. Corrosion performance of molybdenum silicides in acid solutions. *Materials Science and Engineering*: *A*. 2004;371(1-2): 217–221. http://doi:10.1016/j.msea.2003.11.041

11. Chen H., Ma Q., Shao X., Ma J., Huang B. X. Corrosion and microstructure of the metal silicide (Mo$_{1-x}$Nb$_x$)$_5$Si$_3$. *Corrosion Science*. 2013;70: 152–160. http://doi:10.1016/j.corsci.2013.01.024

12. Lopez-Sesenes R. Effect of crystalographic orientation on the corrosion behavior of Mo$_3$Si single crystals in NaCl solution. *International Journal of Electrochemical Science*. 2018;13(5): 4827–4840. https://doi.org/10.20964/2018.05.31

13. Pan Y., Wang P., Zhang C.-M. Structure, mechanical, electronic and thermodynamic properties of Mo$_5$Si$_3$ from first-principles calculations. *Ceramics International*. 2018;44(11): 12357–12362. https://doi.org/10.1016/j.ceramint.2018.04.023

14. Wang D., Li P., Kang K., Zhang C., Yin J., Jiang M., Zeng X. Corrosion behaviors of Cr13Ni5Si2 based composite coatings prepared by laser-induction hybrid cladding. *Surface and Coatings Technology*. 2016;300: 128–134. https://doi.org/10.1016/j.surfcoat.2016.05.040

15. Shein A. B., Aitov R. G. Electrochemical behaviour of eutectic metal-germanium alloys in sulphuric acid. *Electrochimica Acta*. 1991;36(8): 1247–1251. https://doi.org/10.1016/0013-4686(91)80002-p

16. Shein A. B. Anodic dissolution of iron and cobalt germanides in an alkaline electrolyte. *Protection of Metals*. 2000;36(4): 344–346. https://doi.org/10.1007/bf02758505

17. Tananaev I. V., Shpirt M. Ya. *Khimiya germaniya* [Chemistry of germanium]. Moscow: Khimiya Publ.; 1967. 452 p. (In Russ)

18. Rabe M., Toparli C., Chen Y.-H., Kasian O., Mayrhofer K. J. J., Erbe A. Alkaline manganese electrochemistry studied by in situ and operando spectropscopic methods - metal dissolution, oxide formation and oxygen evolution. *Physical Chemistry Chemical Physics*. 2019;21(20): 10457–10469. https://doi.org/10.1039/c9cp00911f

19. Kichigin V. I., Shein A. B. Potentiostatic and impedance spectroscopic studies of the anodic behavior of cobalt silicides in fluoride-containing acidic solutions. *Corrosion Science*. 2019;159: 108–124. https://doi.org/10.1016/j.corsci.2019.108124

20. Tran A.-T., Huet F., Ngo K., Rousseau P. Artefacts in electrochemical impedance measurement in electrolytic solutions due to the reference electrode. *Electrochimica Acta*. 2011;56(23): 8034–8039. https://doi.org/10.1016/j.electacta.2010.12.088

21. Cruz C., Lima T., Soares M., Freitas E., Fujiwara E., Garcia A., Cheung N. Effect of microstructure features on the corrosion behavior of the Sn-2.1 wt%Mg solder alloy. *Electronic Material Letters*. 2020;16: 276–292. https://doi.org/10.1007/s13391-020-00202-7

22. Cui Y.-Y., Bu R.-T., Wang D.-Y., Wang Y.-J. Effects of direct stray current on the performance of cathodic disbonding epoxy powder coatings. *Petroleum Science*. 2019;16: 1417–1429. https://doi.org/10.1007/s12182-019-00381-5

23. Rakityanskaya I. L., Mozzhegorova K. U., Erzhenkov M. V. Anodic behavior of manganese silicido-germanides of different content in 1M NaOH medium. *Vestnik Permskogo universiteta. Seriya «Khimiya»* = Bulletin of Perm University. 2018;8(3): 342–347. http://press.psu.ru/index.php/chem/article/view/1517 (In Russ., abstract in Eng.)

Information about the authors

Irina L. Rakityanskaya, PhD in Chemistry, Associate Professor at the Department of Physical Chemistry, *Perm State National Research University, Perm,* Russian Federation; e-mail: irisa@yandex.ru. ORCID iD: https://orcid.org/0000-0001-9963-2937.

Danil A. Myasnikov, Postgraduate student at the Department of Physical Chemistry, *Perm State National Research University, Perm,* Russian Federation; e-mail: bzhendzhishchchakevich@mail.ru. ORCID iD: https://orcid.org/0000-0001-8889-9580.

Anatoly B. Shein, Doctor of Chemistry, Professor, Head of the Department of Physical Chemistry, *Perm State National Research University, Perm,* Russian Federation, e-mail: ashein@psu.ru. ORCID iD: https://orcid.org/0000-0002-2102-0436.

Condensed Matter and Interphases

Original articles

Research article

Complexation processes in "PbCl$_2$-N$_2$H$_4$CS" aqueous solutions during deposition of lead sulphide films

V. N. Semenov[1✉], V. V. Volkov[2], N. V. Pereslytskikh[1]

[1]*Voronezh State University,*
1 Universitetskaya pl., Voronezh 394018, Russian Federation

[2]*Voronezh State Technical University,*
14 Moskovsky pr., Voronezh 394026, Russian Federation

Abstract

In this study, we proposed a new approach to assessing the processes of complexation in aqueous solutions using the example of the interaction of lead chloride with thiourea. The goal of this study was the investigation of processes of complexation in "PbCl$_2$-N$_2$H$_4$CS" aqueous solutions and determination of the regions of dominance of thiourea coordination compounds, which are precursors during the deposition of lead sulphide films.

Based on the diagrams and cross section lines of equal fractions constructed in three-dimensional space, the regions of dominance of all complex forms existing in the studied solution were found. Such a graphic image is the most informative, since it allows selection of the concentration ranges of the predominance of certain coordination compounds, especially thiourea complexes, which are precursors during the deposition of lead sulphide films. It was shown that an increase in the concentration of N$_2$H$_4$CS led to an increase in the total fraction of thiourea complexes: for a twofold excess of N$_2$H$_4$CS its fraction was 0.25, for a threefold excess it was 0.35, for a fourfold excess it was 0.5, for a fivefold excess it was 0.7.

Keywords: Distribution diagrams, Complexation, Thiourea, Lead chloride, Coordination compounds

✉ Victor N. Semenov, e-mail: semenov@chem.vsu.ru

Condensed Matter and Interphases / Конденсированные среды и межфазные границы   2021;23(4): 543–547

V. N. Semenov et al.   Complexation processes in "PbCl$_2$-N2H$_4$CS" aqueous solutions...

1. Introduction

Traditionally, high-temperature synthesis methods and vacuum technologies, which require complex and expensive equipment are used for obtaining photosensitive PbS layers for the near and mid-IR spectral regions. This determines the high commercial cost of thin-film detectors based on them. Therefore, the development of new cheap technologies for obtaining such photosensitive layers based on lead sulphide with unique properties [1–3] is an important task.

One such method is the method of aerosol spraying of solutions of thiourea coordination compounds (TCC) on a heated substrate [4], based on the thermal destruction of these complexes [5].

In the study [6], all ionic equilibria existing in an aqueous solution of lead chloride and thiourea (TC) were provided, and the equilibrium concentrations of [Pb^{2+}], [TC] and [Cl$^-$] for the given initial $C_{Pb^{2+}}$ and C_{TM} were calculated based on them. Further, these data were used for the determination of the equilibrium concentrations of complex ions. Using the data obtained, the fractions of these complex forms were found and distribution diagrams were plotted (about 100 variants of such diagrams were plotted). The process of plotting diagrams is very laborious and inconvenient for comparing and analysing complexation processes in different concentration ranges. For obtaining a more clearly picture, we proposed the construction of three-dimensional distribution diagrams and cross section lines of equal fractions for specific complex forms. The goal of this study was the investigation of processes of complexation in a "PbCl$_2$-N$_2$H$_4$CS" aqueous solutions and determination of the regions of dominance of TCC, which are precursors during the deposition of lead sulphide films.

2. Modelling

The construction of sections of the concentration dependences of the fractions of complex forms present in the solution was carried out using the COMSOL Multiphysics application package by the Newton–Raphson method [7]. Thus, diagrams for all 15 complex forms existing in the "PbCl$_2$-N$_2$H$_4$CS" aqueous solution were plotted. The use of initial (analytical), rather than equilibrium concentrations allowed realistic assess of the complexation process.

The concentration regions of existence of these complex forms were found by analysis of the diagrams obtained for all coordination compounds in three-dimensional space and the cross-sections plotted on their basis (Table 1).

Table 1. Fractions of complex forms prevailing in a certain concentration range in the PbCl$_2$-N$_2$H$_4$CS system

Complex form	Maximum fraction of complexes in solution	Intervals of existence for the maximum fractions of complexes, M/l	
		C_{TM}	C_{Pb}^{2+}
Pb(H$_2$O)$_n^{2+}$	1.00	$1\cdot10^{-5}-2\cdot10^{-2}$	$1\cdot10^{-5}-2\cdot10^{-3}$
PbTM^{2+}	0.08	$2\cdot10^{-2}-4\cdot10^{-2}$	$1\cdot10^{-5}-3\cdot10^{-3}$
PbTM$_2^{2+}$	0.025	$3\cdot10^{-2}-5\cdot10^{-2}$	$1\cdot10^{-5}-4\cdot10^{-3}$
PbTM$_3^{2+}$	0.06	$4\cdot10^{-2}-8\cdot10^{-2}$	$1\cdot10^{-5}-8\cdot10^{-3}$
PbTM$_4^{2+}$	1.00	$8\cdot10^{-2}-1$	$1\cdot10^{-5}-2\cdot10^{-1}$
PbCl$^+$	0.6	$1\cdot10^{-5}-8\cdot10^{-2}$	$2\cdot10^{-2}-3\cdot10^{-1}$
PbCl$_2$	0.6	$1\cdot10^{-5}-1$	$5\cdot10^{-1}-1$
PbCl$_3^-$	0.13	$7\cdot10^{-1}-1$	$8\cdot10^{-1}-1$
PbCl$_4^{2-}$	0.01	$9\cdot10^{-1}-1$	$6\cdot10^{-1}-7\cdot10^{-1}$
PbTMCl$^+$	0.07	$6\cdot10^{-2}-3\cdot10^{-1}$	$2\cdot10^{-2}-2\cdot10^{-1}$
PbTMCl$_2$	0.08	$7\cdot10^{-1}-1$	$4\cdot10^{-1}-1$
PbTMCl$_3^-$	0.04	$9\cdot10^{-1}-1$	$6\cdot10^{-1}-1$
PbTM$_2$Cl$^+$	0.04	$2\cdot10^{-1}-4\cdot10^{-1}$	$8\cdot10^{-2}-2\cdot10^{-1}$
PbTM$_3$Cl$^+$	0.3	$7\cdot10^{-1}-1$	$2\cdot10^{-1}-4\cdot10^{-1}$
PbTM$_2$Cl$_2$	0.1	$9\cdot10^{-1}-1$	$4\cdot10^{-1}-7\cdot10^{-1}$

Condensed Matter and Interphases / Конденсированные среды и межфазные границы   2021;23(4): 543–547

V. N. Semenov et al.   Complexation processes in "PbCl$_2$-N2H$_4$CS" aqueous solutions...

As can be seen from these results, in "PbCl$_2$-N$_2$H$_4$CS" aqueous solution following complexes were dominant: $Pb(H_2O)_n^{2+}$, $PbTM_4^{2+}$, $PbCl^+$, $PbCl_2$ and $PbTM_3Cl^+$. Their fractions (a) were more than 0.3. Out of the homoligand TCC, the most stable is the complex ion $PbTM_4^{2+}$. Out of the thiourea complexes, in addition to those indicated above $PbTM^{2+}$, $PbTM_3^{2+}$, $PbTMCl^+$, $PbTMCl_2$ and $PbTM_2Cl_2$ forms were relatively stable. The fraction of their presence in the solution exceeded 0.05. The maximum fraction of homoligand TCC increased in the following order: $PbTM_2^{2+} < PbTM_3^{2+} < PbTM^{2+} < PbTM_4^{2+}$, for mixed ligands: $PbTMCl_3^- \leq PbTM_2Cl^+ < PbTM_2Cl_2 < PbTM_3Cl^+$. As an illustration, diagrams and their cross sections for four TCC are shown (Figs. 1–4).

According to the study [8], the solubility of PbCl$_2$ at 25 °C is $4\,10^{-2}$ M/l. Therefore, considering the cross-section lines of equal fractions in Fig. 1 (b) – 4 (b), it can be noted that in the initial solution the fraction of complexes [PbTM$_2$Cl$_2$] is very small (Fig. 4b), while complex forms $PbTM_4^{2+}$, $PbTMCl^+$ and $PbTM_3Cl^+$ actually exist. The dependence of the fraction of formed TCC on the concentration of thiourea at a constant concentration of lead chloride ($2\cdot10^{-2}$ M/l) is shown in Table 2. The calculation was carried out based on the constructed distribution diagrams.

Data provided in Table 2 demonstrate that the total fraction of thiourea complexes, which are the supplier of lead sulphide, for a twofold excess of N$_2$H$_4$CS is 0.25, for three times excess it was 0.35,
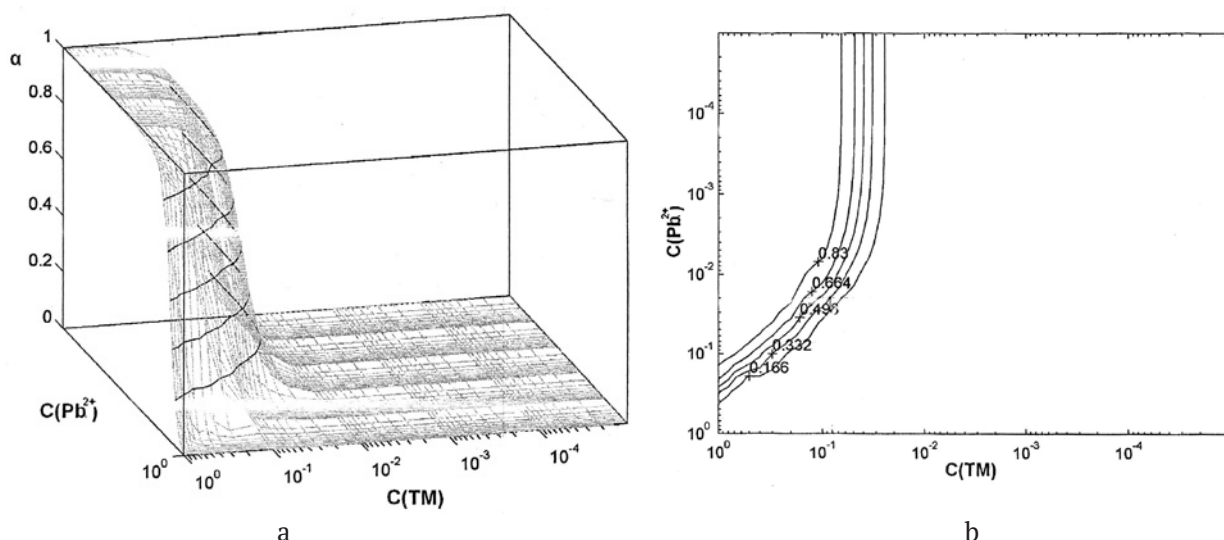
Fig. 1. Three-dimensional distribution diagrams (a) and cross section lines of equal fractions (b) for the PbTM$_4^{2+}$ complex
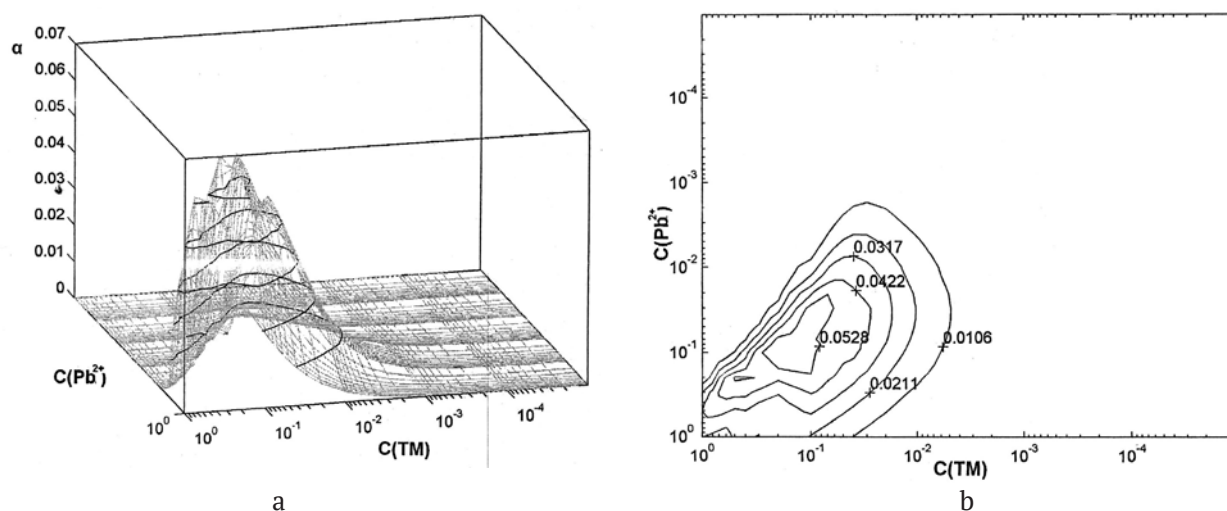
Fig. 2. Three-dimensional distribution diagrams (a) and cross section lines of equal fractions (b) for the PbTMCl$^+$ complex

Condensed Matter and Interphases / Конденсированные среды и межфазные границы   2021;23(4): 543–547

V. N. Semenov et al.   Complexation processes in "PbCl$_2$-N2H$_4$CS" aqueous solutions...
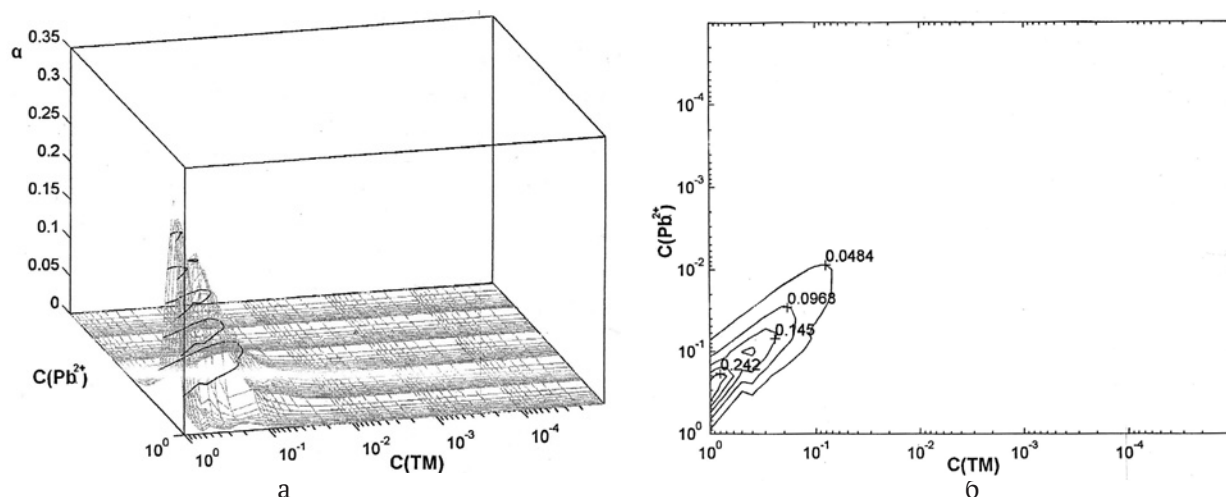
Fig. 3. Three-dimensional distribution diagrams (a) and cross section lines of equal fractions (b) for the PbT-M$_3$Cl$^+$ complex
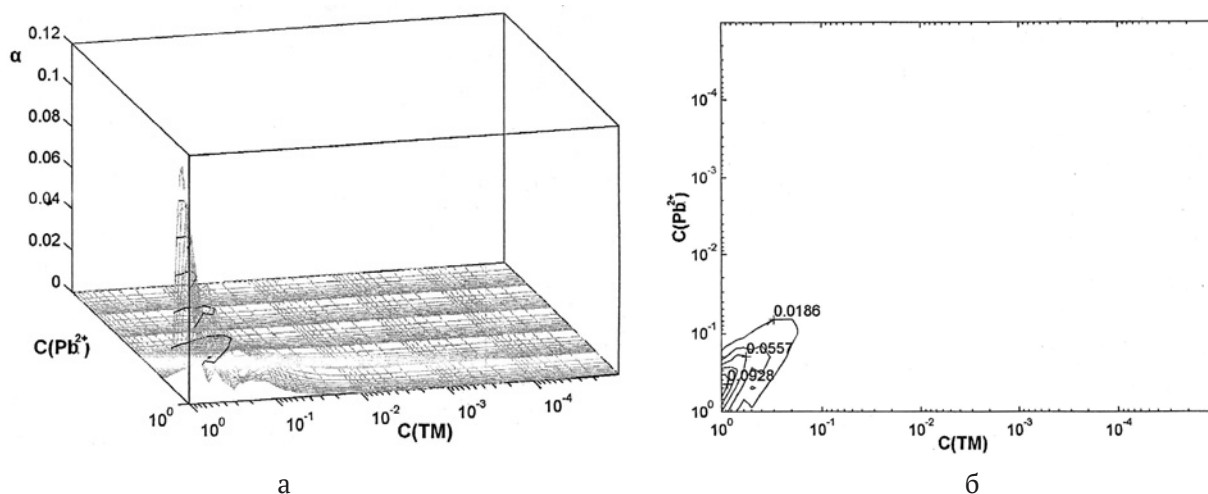
Fig. 4. Three-dimensional distribution diagrams (a) and cross section lines of equal fractions (b) for the PbT-M$_2$Cl$_2$ complex

Table 2. Formation of thiourea complexes depending on the concentration of thiourea

C_{TM}	Fractions of complexes							Total fraction of TM complexes
	PbTM$_4^{2+}$	PbTM$_3^{2+}$	PbTM$_2^{2+}$	PbTM^{2+}	PbTMCl$^+$	PbTM$_2$Cl$^+$	PbTM$_3$Cl$^+$	
0.02	0.12	0.0001	0.003	0.03	0.04	0.007	0.001	0.2
0.04	0.14	0.01	0.007	0.04	0.04	0.01	0.001	0.25
0.06	0.17	0.02	0.01	0.04	0.045	0.02	0.04	0.35
0.08	0.33	0.03	0.01	0.02	0.05	0.02	0.05	0.51
0.1	0.5	0.04	0.01	0.03	0.04	0.02	0.07	0.71

for four times excess it was 0.5, for five times excess it was 0.7. In the complexation process, thiourea, which is an ambidentate ligand, is coordinated through a sulphur atom. As a result of the thermal destruction of TCC, lead sulphide is the main solid-phase product. Thus, the process of obtaining PbS proceeds through the stage of the formation of the thiourea complex. X-ray phase analysis indicated the precipitation of lead sulphide with a cubic structure [9]. It should be noted that the fraction of aqua and chloride complexes (0.6) was quite high (Table 1); therefore, the concentration intervals $C_{TM} = 1 \cdot 10^{-5} - 1 \cdot 10^{-1}$ and $C_{PbCl_2} = 1 \cdot 10^{-5} - 5 \cdot 10^{-2}$ M/l are unsuitable for the deposition of PbS films.

Condensed Matter and Interphases / Конденсированные среды и межфазные границы   2021;23(4): 543–547

V. N. Semenov et al.   Complexation processes in "PbCl$_2$-N2H$_4$CS" aqueous solutions...

3. Conclusions

Based on diagrams and cross section lines of equal fractions for "PbCl$_2$–N$_2$H$_4$CS" aqueous solutions the areas of dominance of various complex forms formed in the process of complexation were determined. It was shown that the following complex forms dominate in the solution: $Pb(H_2O)_n^{2+}$, $PbTM_4^{2+}$, $PbCl^+$, $PbCl_2$ and $PbTM_3Cl^+$. The maximum fraction of homoligand TCC increases in the series $PbTM_2^{2+} < PbTM_3^{2+} < PbTM^{2+} < PbTM_4^{2+}$, for the mixed ligand $PbTMCl_3^- \lessgtr PbTM_2Cl^+ < PbTM_2Cl_2 < PbTM_3Cl^+$. These thiourea coordination compounds are precursors for the deposition of lead sulphide films, and with an increase in the concentration of N_2H_4CS in the initial solution, their fraction increases sharply.

Author contributions

Semenov V. N. – scientific leadership, research concept, methodology development, text writing, final conclusions. Volkov V. V. – modelling using Newton – Raphson method. Pereslytskikh N. V. – plotting three-dimensional distribution diagrams, review writing and text editing.

Conflict of interests

The authors declare that they have no known competing financial interests or personal relationships that could have influenced the work reported in this paper.

References

1. Sermakasheva N. L., Novikov G. F., Shulga Yu. M., Semenov V. N. Microwave photoconduction and photodielectric effect in thin PbS films prepared from thiocarbamide coordination compounds. *Semiconductors*. 2004;38(4): 380–386. https://doi.org/10.1134/1.1734662

2. Mohsen Cheraghizade, Ramin Yousefi, Farid Jamali-Sheini, Abdolhossein Sa'aedi. Comparative study of Raman properties of various lead sulfide morphologies. *Majlesi Journal of Telecommunication Devices*. 2013;2(1): 163–166. Available at: http://journals.iaumajlesi.ac.ir/td/index/index.php/td/article/view/90

3. Sadovnikov S. I., Gusev A. I., Rempel' A. A. *Poluprovodnikovye nanostruktury sul'fidov svintsa, kadmiya i serebra* [Semiconductor nanostructures of lead, cadmium and silver sulfides]. Moscow: Fizmalit Publ.; 2018. 464 p. (In Russ.)

4. Naumov A. V., Semenov V. N., Averbakh E. M. Tiomochevinnye koordinatsionnye soedineniya v protsessakh sinteza sul'fidov metallov [Thiourea coordination compounds in the synthesis of metal sulfides]. *Khimicheskaya promyshlennost'*. 2003;80(2): 17–26. Available at: https://elibrary.ru/item.asp?id=23712470 (In Russ.)

5. Ugai Ya. A., Semenov V. N., Shamsheeva I. L. Thermal decomposition of dichlorodithioureacadmium (II) *Russian Journal of General Chemistry*. 1986;56(9): 1945–1950. Available at: https://elibrary.ru/item.asp?id=28890314 (In Russ., abstract in Eng.)

6. Semenov V. N., Ovechkina N. M., Volkov V. V. The distributing diagrams of complex form in aqueous solution "PbCl$_2$-N$_2$H$_4$CS". *Proceedings of Voronezh State University. Series: Chemistry. Biology. Pharmacy.* 2009;2: 59–63. Available at: https://elibrary.ru/item.asp?id=12992204 (In Russ., abstract in Eng.)

7. Malozemov V. N., Tamasyan G. Sh. On the direction of the steepest descent. *Vestnik of St Petersburg University. Applied Mathematics. Computer Science. Control Processes.* 2019;15(4): 489–501. https://doi.org/10.21638/11702/spbu10.2019.406 (In Russ., abstract in Eng.)

8. Volkov A. I., Zharskii I. M. *Bol'shoi khimicheskii spravochnik* [Large chemical reference book]. Moscow: Sovremennaya shkola Publ.; 2005. 608 p.

9. Semenov V. N., Ovechkina N M. Formation of SnS, SnS$_2$, and PbS films from thiourea coordination compounds. *Russian Journal of Applied Chemistry*. 2011;84: 2033–2039. https://doi.org/10.1134/S1070427211120032

Information about the authors

Victor N. Semenov, DSc in Chemistry, Professor, Head of the Department of General and Inorganic Chemistry, Voronezh State University, Voronezh, Russian Federation; e-mail: semenov@chem.vsu.ru. ORCID iD: https://orcid.org/0000-0002-4247-5667.

Vitaly V. Volkov, Ph.D. in Physics and Mathematics, Associate Professor, Department of Structural Mechanics, Voronezh State Technical University, Voronezh, Russian Federation; e-mail: kotlac@yandex.ru.

Natalia V. Pereslytskikh, Master's degree student, Department of General and Inorganic Chemistry, Voronezh State University, Voronezh, Russian Federation; e-mail: deanery@chem.vsu.ru.

Original articles

Synthesis, structure, and photo-Fenton activity of PrFeO₃-TiO₂ mesoporous nanocomposites

A. S. Seroglazova[1,2]✉, M. I. Chebanenko[2], V. I. Popkov[2]

[1]*Saint-Petersburg State Institute of Technology,
26 Moskovsky pr., Saint Petersburg 190013, Russian Federation*

[2]*Ioffe Institute,
26 Politekhnicheskaya str., Saint Petersburg 194021, Russian Federation*

Abstract

Porous nanocomposites based on $PrFeO_3$-TiO_2 were synthesized using the glycine-nitrate combustion method with different values of mass content of TiO_2 (0–7.5 %) and subsequent heat treatment in air. The results of X-ray phase analysis and Raman spectroscopy confirmed the presence of ultradispersed TiO_2, structurally close to that of anatase. The morphology, specific surface area, and porous structure of the obtained powders were characterized by scanning electron microscopy and adsorption-structural analysis, the results of which showed that the samples had a foam-like mesoporous structure. The specific surface area and the average pore size were in the ranges of 7.6–17.8 m^2/g and 7.2–15.2 nm, respectively, and varied depending on the TiO_2 content. The optical properties of the nanocomposites were studied by UV-visible diffuse reflection spectroscopy, the energy of the band gap was calculated as 2.11–2.26 eV. The photocatalytic activity of $PrFeO_3$-TiO_2 nanocomposites was investigated in the process of photo-Fenton-like degradation of methyl violet under the action of visible light. It was shown that the maximum reaction rate constant was 0.095 min^{-1}, which is ten times higher than the value for the known orthoferrite-based analogs. The obtained photocatalysts were also characterized by their high cyclic stability. Based on the studies carried out, the obtained porous $PrFeO_3$-TiO_2 nanocomposites can be considered to be a promising basis for photocatalysts applied in advanced oxidative processes of aqueous media purification from organic pollutants.

Keywords: Solution-combustion synthesis; Praseodymium orthoferrite; Titanium Oxide; Nanocomposites; Photocatalysts; Fenton-like reactions

✉ Anna S. Seroglazova, e-mail: annaseroglazova@yandex.ru

Condensed Matter and Interphases / Конденсированные среды и межфазные границы   2021;23(4): 548–560

A. S. Seroglazova et al.   Synthesis, structure, and photo-Fenton activity of PrFeO$_3$-TiO$_2$...

1. Introduction

Most industries for the manufacture of plastics, fabrics, paper, and rubber use various dyes and organic substances, leading not only to environmental pollution but also to the development of various diseases in humans, since they are often carcinogenic and/or highly toxic compounds. Traditional methods of removing organic dyes such as adsorption, filtration, ozonizing filtration, electrochemistry, used in modern industries, are quite effective, but still do not achieve a complete decomposition of the organic dyes due to their complex aromatic structure and resistance to various environmental factors, including oxidation. Therefore, there is an urgent need for the development of an alternative, for example, photocatalytic methods of water purification using environmentally friendly photocatalysts, which make it possible to effectively destroy toxic organic substances under the action of visible light.

Orthoferrites are complex oxides based on rare earth elements (REE) and iron with the general chemical formula of RFeO$_3$ (R = Sc, Y, Ln), having a distorted perovskite-like structure with the Pbnm/Pnma space group [1–4]. Recently, there has been an increased interest in the study of REE orthoferrites due to their unique physical and chemical properties, which opens a wide range of possibilities for their practical application as a basis for new functional materials [5–8]. In addition, the structural, electromagnetic, and catalytic properties of REE orthoferrites make it possible to use them in the production of ceramics, magnetic devices, gas sensors, and magnetically controlled photocatalysts [9–11].

Earlier, various methods of synthesis were used to obtain nanocrystalline orthoferrites of rare earth elements: microwave, hydrothermal, sol-gel, co-precipitation, and others [1,12–15]. Most of these methods are labor-intensive and energy-consuming and do not always allow the control of such important parameters as particle size, shape, morphology, and structure, which determine the functional properties of REE orthoferrites. However, as was shown earlier in works [16–18], the solution combustion mthod is free from these drawbacks and allows varying the porous structure of nanoparticle aggregates, and thereby controlling the functional properties of the obtained materials based on REE orthoferrites. The two-stage synthesis of REE orthoferrites with the amorphous combustion products and their further thermal treatment to obtain pure product is particularly promising. Powders obtained by this method are characterized by their porous structure, foamy morphology, and developed surface. The latter is an important factor in the development of photocatalytic materials [19].

Among the most promising photocatalysts based on REE orthoferrites, PrFeO$_3$ stands out, which has an unusually high activity under the action of visible light [20]. Interest in such materials is caused by the possibility of their participation in heterogeneous Fenton-like processes occurring in an aqueous-organic solution. The mechanism of Fenton-like oxidation consists of the formation of powerful oxidizing hydroxyl radicals (OH$^\bullet$) during the reversible transition from Fe^{2+} to Fe^{3+} under the action of visible light, which makes it possible to achieve the highly efficient decomposition and oxidation of organic pollutants [21–23]. Despite the high catalytic activity, reverse recombination processes significantly impair the photocatalytic activity of such materials, including PrFeO$_3$. As reported in [19], the reverse recombination processes can be suppressed through the creation of a heterojunction structure during the transition from PrFeO$_3$ to a composite based on it. For several simple oxides, it has been shown that an improvement in the photocatalytic properties can be achieved by adding a second component, due to the presence of which the transfer of charge carriers becomes possible immediately after the formation of an electron-hole pair under the action of irradiation [24–28]. Thus, the transition to heterostructures based on nanocomposites of rare-earth elements and other oxides is one of the most effective strategies for suppressing electron-hole recombination. In the presented work, TiO$_2$ was chosen to improve the photocatalytic characteristics of PrFeO$_3$, which, according to modern concepts, should lead to a drop in recombination. In addition, TiO$_2$ is an active, stable, and environmentally friendly photocatalyst in the near-UV region with a strong oxidizing ability [29–31]. Interest in studying its catalytic properties when paired with PrFeO$_3$ is also associated with the relatively large band

Condensed Matter and Interphases / Конденсированные среды и межфазные границы   2021;23(4): 548–560

A. S. Seroglazova et al.   Synthesis, structure, and photo-Fenton activity of PrFeO₃-TiO₂…

gap of TiO_2 and the high intrinsic generation of electron-hole pairs.

This paper is dedicated to obtaining $PrFeO_3$-TiO_2 nanocomposite materials by the method of solution combustion with different values of TiO_2 content (0-7.5 wt%). The obtained samples were studied using a wide range of physicochemical methods of analysis, allowing a detailed study of their structure, morphology, magnetic and optical properties, etc. Photocatalytic properties were studied using the example of Fenton-like oxidation of methyl violet (MV) under the action of visible light. The data obtained were compared with the results of photocatalytic studies of pure $PrFeO_3$ and other REE orthoferrites. $PrFeO_3$-TiO_2 nanocomposite materials demonstrated a significant increase in the efficiency of MV photocatalytic oxidation. Thus, the obtained powders can be used in modern advanced oxidative processes for the purification of contaminated aqueous media.

2. Materials and methods

2.1. Preparation of the titanyl nitrate ($TiO(NO_3)_2$) solution

The synthesis of nanocomposite powders based on $PrFeO_3$-TiO_2 included the preliminary preparation of titanyl nitrate $TiO(NO_3)_2$ from titanium tetrachloride $TiCl_4$ by hydrolysis. For this, distilled water was added to 20 ml of $TiCl_4$ with constant stirring until a white precipitate of $TiO(OH)_2$ was formed, followed by its complete dissolution in concentrated nitric acid (HNO_3).

2.2. Synthesis of $PrFeO_3$-TiO_2 nanocomposites

$PrFeO_3$-TiO_2 nanocomposites were prepared by the solution combustion method. To prepare the reaction mixture, we used the nitrates of the corresponding metals, $Pr(NO_3)_3 \cdot 6H_2O$ and $Fe(NO_3)_3 \cdot 9H_2O$. Glycine with a glycine-nitrate ratio G/N = 2.0 was used as a fuel.

During the synthesis, iron (III) and praseodymium nitrates, as well as glycine, were dissolved in a small amount of distilled water, followed by the addition of a titanyl nitrate solution $TiO(NO_3)_2$. The resulting reaction mixture was stirred until the nitrates and glycine were completely dissolved. The reaction solution prepared in this way was heated in a sand bath until the water evaporated and the reaction

mixture ignited. As a result, porous brown powders were formed. Similarly, pure $PrFeO_3$ was synthesized, as well as a series of $PrFeO_3$-TiO_2 nanocomposite powders with different mass ratios of $PrFeO_3$:TiO_2 = 100:0, 97.5:2.5, 95:5, and 92.5:7.5%, which were then heat-treated at 700 °C for 1 hour in the air to remove unreacted impurities and form crystalline praseodymium orthoferrite from amorphous combustion products.

2.3. Physico-chemical characterization

The elemental composition and morphology of the synthesized samples were studied by energy-dispersive X-ray spectroscopy (EDS) and scanning electron microscopy (SEM) using a Tescan Vega 3 SBH scanning electron microscope.

To determine the phase composition of the samples, X-ray phase analysis was carried out on a Rigaku SmartLab X-ray powder diffractometer in the range of Bragg angles (2θ) from 20° to 60°. Qualitative X-ray phase analysis was performed using the ICSD database. Based on the broadening of the X-ray diffraction lines, the average crystallite size was calculated using the Scherrer formula:

$$D = \frac{k\lambda}{\beta\cos\theta}$$

where k – shape factor, equal to 0.94; λ – X-ray wavelength (Cu$K\alpha$ = 0.15406 nm); β – line broadening at half the maximum in radians; θ – Bragg's angle in radians.

The structural features of the nanocomposites were studied using Raman spectroscopy (excitation wavelength λ = 532 nm) on a SINTERRA Raman microscope.

The specific surface of the samples, pore volume, and pore size distribution were determined by adsorption-structural analysis (ASA) using a Micromeritics ASAP 2020. Sorption-desorption isotherms were obtained at a liquid nitrogen temperature of 77 K.

Diffuse reflectance spectra (DRS) were measured with an Avaspec-ULS2048 spectrometer equipped with an AvaSphere-30-Refl integrating sphere.

2.4. Photocatalytic measurements

The photocatalytic activity of the synthesized samples was estimated during the photocatalytic

Condensed Matter and Interphases / Конденсированные среды и межфазные границы   2021;23(4): 548–560

A. S. Seroglazova et al.   Synthesis, structure, and photo-Fenton activity of PrFeO₃-TiO₂...

degradation of methyl violet (MV) under the action of visible light. The dye concentration was measured using a Shimadzu UV1600 spectrophotometer. Two 100W xenon lamps with a UV filter of $\lambda \geqslant 420$ nm were used as a light source. The oxidation process was carried out in an experimental setup in the form of an insulated box, which included a 50 ml beaker, a magnetic stirrer, and lamps.

The first part of the experiment consisted in determining the most efficient catalyst among the samples $PrFeO_3$, $PrFeO_3$-TiO_2 2.5%, $PrFeO_3$-TiO_2 5%, $PrFeO_3$-TiO_2 7.5%. For this, colloidal solutions of the corresponding nanopowders with a concentration of 0.5 g/L were preliminarily prepared. Then, 12.5 ml of a colloidal solution containing the catalyst, 0.6 ml of methyl violet (C = 1 g/L) and 6 ml of hydrogen peroxide (C = 1 mol/L), and 5.9 ml of distilled water were added to each of the four cuvettes. The final concentrations of these components in the resulting 25 ml volume were 0.25 g/L, 0.0232 g/L, and 0.24 mol/L, respectively. Before the start of the photocatalytic experiment, the solutions were stirred in the dark for 30 minutes to establish adsorption equilibrium. After this time, the solutions were irradiated with visible light with continuous stirring for 15 minutes. Then, 5 ml samples were taken from each solution to determine the concentration of the dye. Methyl violet removal efficiency was evaluated using the formula:

$$\text{Rem. Eff.} = \frac{C_0 - C}{C_0} \cdot 100\,\%,$$

where C_0 – initial dye concentration, C – final dye concentration after Fenton-like oxidation.

After the determination of the most active photocatalyst ($PrFeO_3$-TiO_2 5%), the corresponding kinetic parameters of the photo-Fenton-like oxidation of methyl violet were studied. For this, 25 ml of a solution containing 12.5 ml of catalyst (C = 0.25 g/L), 1.2 ml of methyl violet (C = 0.0464 g/L), 6 ml of H_2O_2 (C = 0.24 mol/L), and 4.1 ml of H_2O were prepared. With constant stirring, the solution was irradiated for 15 minutes with a sample taken every 3 minutes to obtain the dependence of the efficiency of dye removal on the duration of irradiation.

In the final part of the experiment, the cyclic activity of the nanocomposite photocatalyst

$PrFeO_3$-TiO_2 5% was studied. As in the second experiment, a solution was prepared with the same concentrations of catalyst, dye, and hydrogen peroxide, which was irradiated for 15 minutes with constant stirring with sampling every 3 minutes. After 15 minutes, the final concentration of the decolorized dye was measured. Based on the obtained values of the final concentration MV, add the required volume of the dye to the initial solution so that its concentration becomes the same (C = 0.0464 g/L). Then this procedure was repeated.

3. Results and discussion

3.1. Energy-dispersive X-ray spectroscopy and element mapping

The results of X-ray energy dispersive spectroscopy showed that the powder synthesized without the addition of titanyl nitrate $TiO(NO_3)_2$ contains 3 main elements Pr, Fe, and O with the ratio Pr:Fe = 49.9:50.1 at%. Thus, the obtained sample corresponds in chemical composition to pure praseodymium orthoferrite (Fig. 1a). Powders synthesized with the addition of $TiO(NO_3)_2$, in terms of the ratio of key elements (Pr and Fe), also correspond to praseodymium orthoferrite within deviations of 0.1-0.6 at%, and additionally, contain titanium in the amount specified during the synthesis.

For the sample with the highest TiO_2 content (7.5%), energy dispersive elemental mapping was additionally carried out (Fig. 1 b-f). According to the multi-element image (Fig. 1b), the obtained sample is characterized by a uniform distribution of the key elements Ti, Fe, O, and Pr. Single-element images (Fig. 1 c-f) confirm the absence of regions enriched in individual chemical elements in the sample.

3.2. Powder X-ray diffraction

To determine the phase composition of the synthesized samples, powder X-ray diffraction was carried out, the results of which are shown in Fig. 2a. According to the obtained X-ray diffraction patterns, the reference sample (TiO_2-0%) is a phase-pure crystalline praseodymium orthoferrite with an orthorhombic structure. The position of the diffraction lines and their intensity are fully consistent with the known data on the structure of $PrFeO_3$ (JCPDS No: 18-9725).

Condensed Matter and Interphases / Конденсированные среды и межфазные границы   2021;23(4): 548–560

A. S. Seroglazova et al.   Synthesis, structure, and photo-Fenton activity of PrFeO$_3$-TiO$_2$...
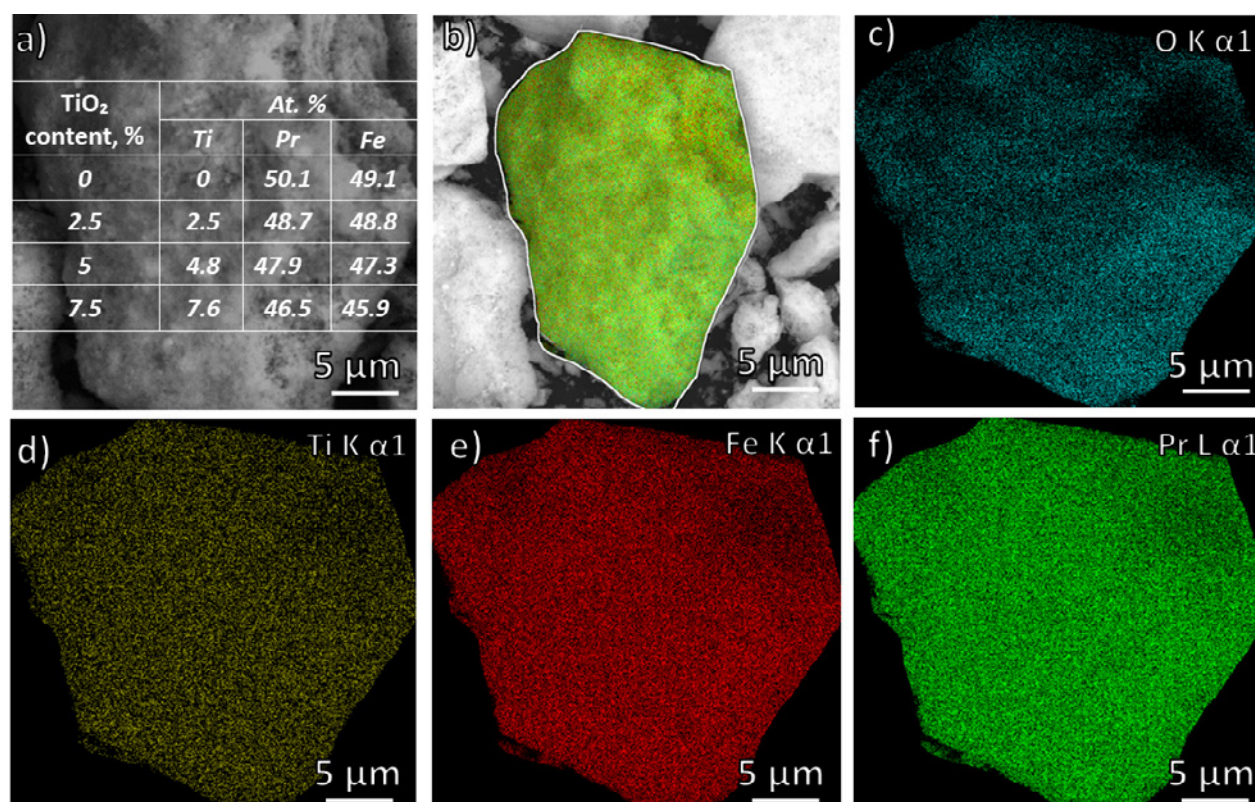
Fig. 1. EDS results (a) and EDS multi-element (a) and single element (c – O, d – Ti, e – Fe, f – Pr) mapping of the PrFeO$_3$-TiO$_2$-7.5% sample

The observed X-ray reflections of the samples with 2.5%, 5%, and 7.5% TiO$_2$ content also relate to orthorhombic praseodymium orthoferrite. The most intense PrFeO$_3$ X-ray diffraction lines do not have a noticeable shift, which indicates the absence of titanium being incorporated into the structure of praseodymium orthoferrite and the separate existence of the corresponding TiO$_2$ and PrFeO$_3$ phases. However, it should be noted, that there are no additional reflections in all diffractograms that could be attributed to other structural forms of TiO$_2$, which indirectly indicates its presence in an amorphous or ultradispersed (with crystallite sizes less than 5 nm) state. An increase in the TiO$_2$ content in this nanocomposite from 2.5% to 7.5% leads to a noticeable broadening of the PrFeO$_3$ diffraction lines (Fig. 2b), which indicates a decrease in the crystallite size in the series TiO$_2$-0 > TiO$_2$-2.5 > TiO$_2$-5 > TiO$_2$-7.5. The calculation of the average crystallite size of praseodymium orthoferrite confirms its decrease in this series from 47.2 nm (pure PrFeO$_3$) to 28.5 nm (TiO$_2$ content of 7.5%) (Fig. 2c). As previously shown in [25,26], such

a decrease in the crystallite size is associated with the effect of the second TiO$_2$ phase on the mass transfer processes, which complicates the recrystallization of praseodymium orthoferrite during the thermal treatment of solution combustion products.

3.3. Raman spectroscopy

To study the structural features of the TiO$_2$ and PrFeO$_3$ phases in the obtained nanocomposites, Raman spectroscopy was performed (Fig. 3). The results of the study showed the presence of combination modes belonging to titanium oxide with an anatase structure with the space group D4h19 (1$_4$/amd) [32]. The most intense peak of the Raman scattering of TiO$_2$ at 145 cm^{-1} corresponds to the E$_g$ mode. The less intense is at 197 cm^{-1} and is attributed also to the E$_g$ mode. The other modes A$_g$ – 285.8 cm^{-1}, B$_{3g}$ – 330.6 cm^{-1}, B$_{2g}$ – 428 cm^{-1}, A$_g$ - 447.8 cm^{-1}, B$_{3g}$ – 647.9 cm^{-1} confirm the formation of the PrFeO$_3$ phase with the space group Pbnm [33].

The data obtained indicate the co-existence of two separate phases: orthorhombic PrFeO$_3$

Condensed Matter and Interphases / Конденсированные среды и межфазные границы   2021;23(4): 548–560

A. S. Seroglazova et al.   Synthesis, structure, and photo-Fenton activity of PrFeO$_3$-TiO$_2$...
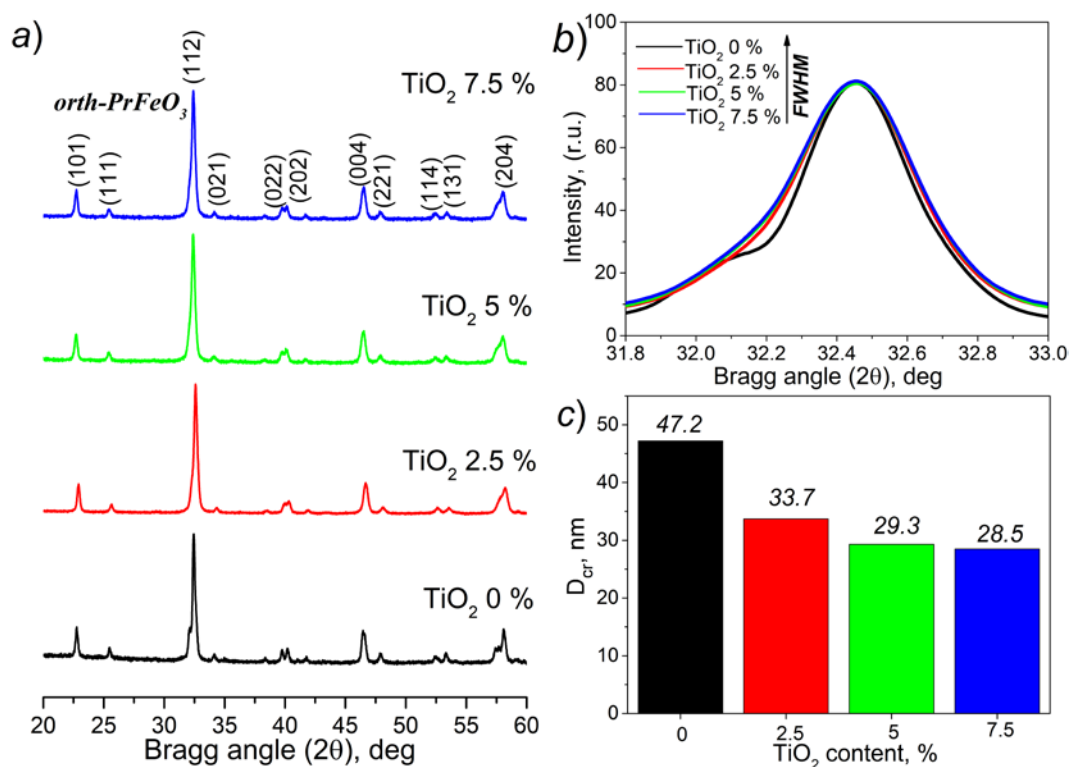
Fig. 2. PXRD patterns of the PrFeO$_3$-TiO$_2$ (0–7.5%) samples (a); FWHM of main (112) X-ray reflex of PrFeO$_3$ as a function of the TiO$_2$ content (b); average crystallite size of PrFeO$_3$ (c)
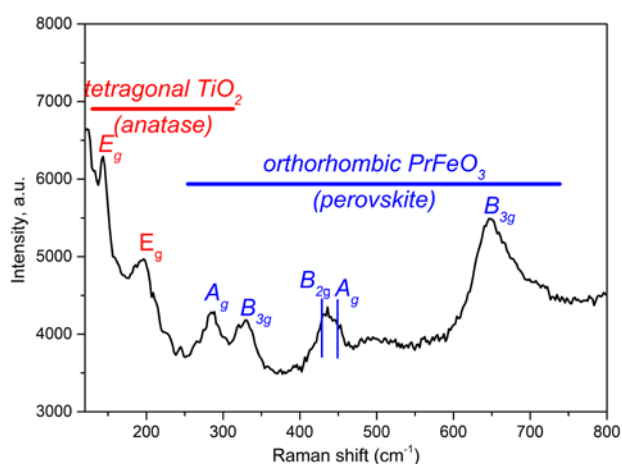
Fig. 3. Raman spectrum of the PrFeO$_3$–TiO$_2$-7.5% nanocomposite

with a perovskite structure and tetragonal TiO$_2$ with an anatase structure, which indicates the successful synthesis of the nanocomposite. Comparing these data with the results of powder X-ray diffraction, it should be concluded that TiO$_2$ in this nanocomposite occurs in the form of ultrafine nanoparticles characterized by weak crystallinity with structural motives of anatase.

3.4. Scanning electron microscopy

The morphology of the synthesized PrFeO$_3$ and PrFeO$_3$–TiO$_2$ samples was studied by the SEM method, the results of which are presented in Fig. 4. For all the samples presented, a highly porous microstructure with a developed surface and foamy morphology is observed, which is typical for oxides of powders obtained by solution combustion [3, 18, 34, 35]. The formation of a developed porous structure is associated with the abundant release of gaseous products (CO, CO$_2$, N$_2$, NO$_2$, etc.) during the redox combustion of a glycine-nitrate mixture.

It should be noted that with an increase in the proportion of TiO$_2$ in the composition of the PrFeO$_3$–TiO$_2$ composite, a visual increase in the average pore size is observed, and their size distribution becomes less uniform. Thus, in a sample with 7.5% TiO$_2$ content, pores with a size of several microns are observed, while pure PrFeO$_3$ is characterized mainly by submicron pores. In all the cases, no individual nanocrystals are observed; they are strongly aggregated into large formations (more than ten microns in size) and occupy the interpore space of the composites.

Condensed Matter and Interphases / Конденсированные среды и межфазные границы   2021;23(4): 548–560

A. S. Seroglazova et al.   Synthesis, structure, and photo-Fenton activity of $PrFeO_3$-TiO_2...
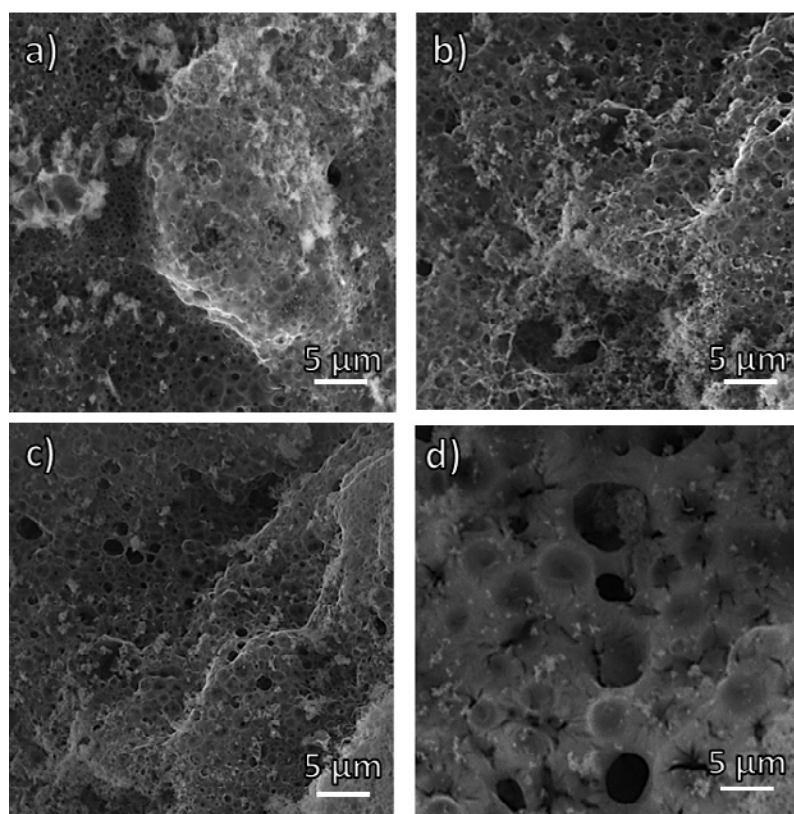
Fig. 4. SEM images of the $PrFeO_3$–TiO_2 nanocomposites synthesized at 0 (a), 2.5 (b), 5 (c) and 7.5 (d) % of TiO_2 content

3.5. Low-temperature nitrogen adsorption-desorption

A more detailed study of the fine porous structure of powders based on $PrFeO_3$ and TiO_2, as well as the determination of their specific surface area, was carried out using adsorption-structural analysis during the low-temperature (77 K) adsorption-desorption of nitrogen, the results of which are presented in Fig. 5.

According to the results obtained, all isotherms are of type II, and the hysteresis loops are of type H3, which indicates a developed meso- and macroporous structure of the obtained nanopowders with a wide pore distribution. For a pure $PrFeO_3$ sample, the smallest area of the hysteresis loop is observed, suggesting relatively low micro- and mesoporosity [29]. For samples containing the anatase TiO_2 phase, the area of the hysteresis loops increases with an increase in the TiO_2 content, which confirms an increase in porosity in this series. Based on this, it can be concluded that the addition of TiO_2 to $PrFeO_3$ facilitates pore formation in the composite at the stage of solution combustion of the glycine-nitrate reaction mixture.

The average pore size and specific surface area of the obtained nanocomposite powders were determined by the BJH and BET methods, respectively. According to the data presented in the inset in Fig. 5, the pure $PrFeO_3$ sample has the smallest pore size (7.2 nm) and a specific surface area of 7.6 m^2/g. For samples with variable TiO_2 content, the pore size and specific surface area increase in the following sequence: 5% > 7.5% > 2.5%. For TiO_2-2.5, these values were 10.3 nm and 13 m^2/g, for TiO_2-5 they were 15.2 nm and 17.8 m^2/g, and for TiO_2-7.5 they were 11.2 nm and 17.7 m^2/g. Earlier, it was shown [25] that, in similar cases, an increase in the average pore size and specific surface area while transforming into the composite could be associated with both suppressions of the growth of crystals of the main phase ($PrFeO_3$) and a higher specific surface area of the secondary phase (TiO_2), the portion of which is growing. However, with an increase in the second fraction content to 7.5%, the growth of the specific surface area and the average pore size stops, which is explained by the intensification of aggregation processes and the blocking of some of the pores by TiO_2 particles [36].

Condensed Matter and Interphases / Конденсированные среды и межфазные границы   2021;23(4): 548–560

A. S. Seroglazova et al.   Synthesis, structure, and photo-Fenton activity of PrFeO$_3$-TiO$_2$...
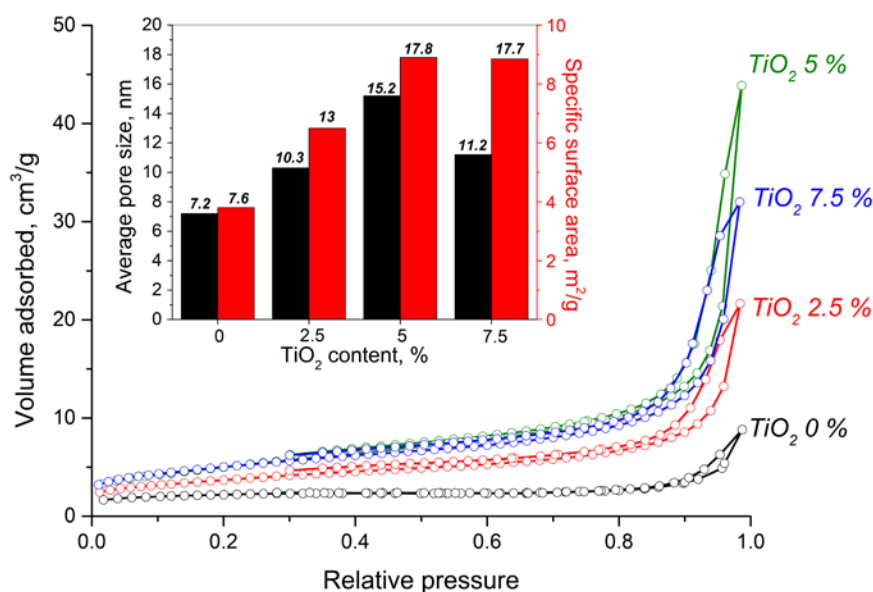
Fig. 5. N$_2$ adsorption-desorption isotherms of PrFeO$_3$-TiO$_2$ nanocomposites depending on the TiO$_2$ content. The inset shows the specific surface area and average pore size of the samples

3.6. UV-visible diffusion reflectance spectroscopy

To determine the edge of the optical absorption band and the band gap of the obtained PrFeO$_3$-TiO$_2$ nanocomposite powders, as well as pure PrFeO$_3$, diffusion reflection spectroscopy (DRS) in the UV-visible region was carried out (Fig. 6).

According to the DRS presented in Fig. 6a, the prepared samples are characterized by a broad absorption band from 500 to 800 nm, corresponding to the visible region of radiation. The edge of the absorption band for pure PrFeO$_3$ is in the region of slightly longer wavelengths than for PrFeO$_3$-TiO$_2$ nanocomposites and slowly decreases in the following sequence: TiO$_2$-5% > TiO$_2$-7.5% > TiO$_2$-2.5%.

To determine the band gap, Tauc plots were plotted using the transformation to the Kubelka-Munk function for the optical absorption spectra of the samples (Fig. 6b). The values of the band gap were determined from the tangent lines of the dependences concerning the photon energy [27, 37]. For pure praseodymium orthoferrite, the band gap was 2.11 eV, which is in good agreement with the results of previous studies [10, 38]. For the samples containing the anatase phase, an insignificant increase in the band gap values from 2.11 eV to 2.26 eV was observed; however, this delta is within the analysis error and the method for determining this value. Since in the case of the incorporation of titanium into the structure of

praseodymium orthoferrite, a significant change in the value of E_g would be observed, and in our case, it can be neglected, the results obtained are in good agreement with the data of PXRD and Raman spectroscopy, once again confirming the co-existence of the PrFeO$_3$ and TiO$_2$ phases in the nanocomposite in the form of separate phases.

3.7. Fenton-like catalytic activity analysis

Based on the results of SEM, adsorption-structural analysis, and DRS, it was concluded that the obtained PrFeO$_3$ and PrFeO$_3$–TiO$_2$ powders could be promising photocatalysts. Therefore, their functional properties were investigated in the photocatalytic process of Fenton-like oxidation of methyl violet under the action of visible light. The results of these studies are shown in Fig. 7.

Fig. 7a contains the typical absorption spectra of a methyl violet solution after a survey photocatalytic test with PrFeO$_3$ and PrFeO$_3$–TiO$_2$ nanopowders. It follows from these results that the PrFeO$_3$-TiO$_2$-5% sample has the highest catalytic activity, for which, according to the results of low-temperature adsorption analysis, the highest values of the specific surface area and average pore size (17.8 m^2/g and 15.2 nm) have been established. A higher activity, in this case, is achieved due to higher accessibility of the surface, the increased total number of active centers, easier access of reagents, and removal

Condensed Matter and Interphases / Конденсированные среды и межфазные границы   2021;23(4): 548–560

A. S. Seroglazova et al.   Synthesis, structure, and photo-Fenton activity of PrFeO₃-TiO₂...
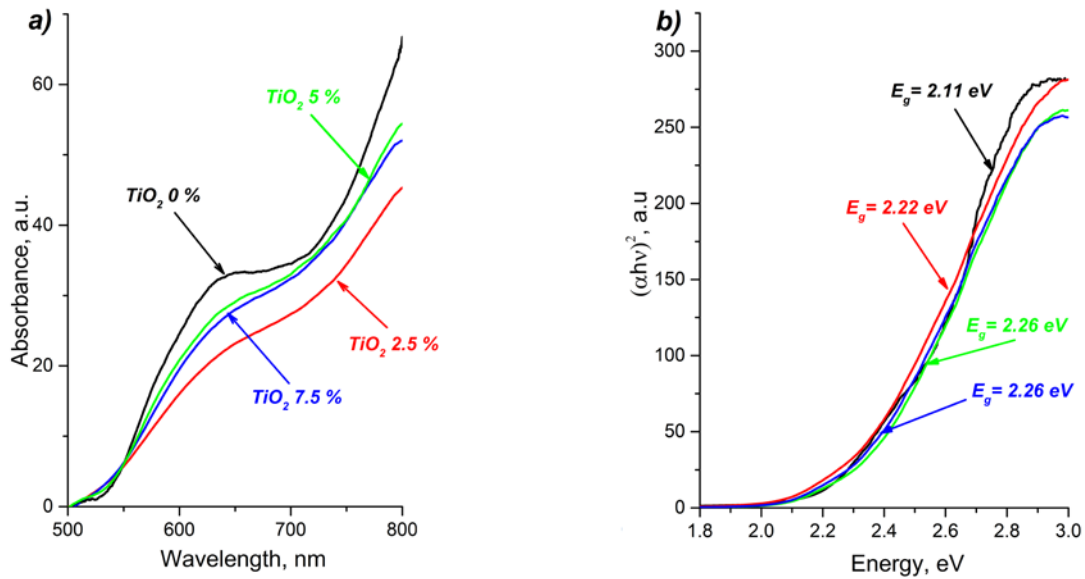
Fig. 6. UV-visible diffusion reflectance spectra of PrFeO₃ and PrFeO₃–TiO₂ samples (a) and corresponding Tauc plots (b)

of reaction products from the pore structure of the nanocomposite [23–25]. However, the nanocomposite photocatalyst PrFeO₃–TiO₂-7.5%, which has a higher specific surface area and average pore size (17.7 m²/g and 11.2 nm) compared to the PrFeO₃ and PrFeO₃–TiO₂-2.5% samples, exhibits the lowest photocatalytic activity among them. In this case, a decrease in the efficiency of dye removal may be associated

with a decrease in the efficiency of radiation absorption by photoactive PrFeO₃ due to its shielding by TiO₂ particles located on the surface of large PrFeO₃ particles (Fig. 8). Nevertheless, the process of generation of oxidative radicals from water molecules (H₂O → ·OH) during the photo-Fenton-like reaction (Fig. 8) can be suppressed, which was previously reported [21, 39]. In this case, an increase in the photocatalytic
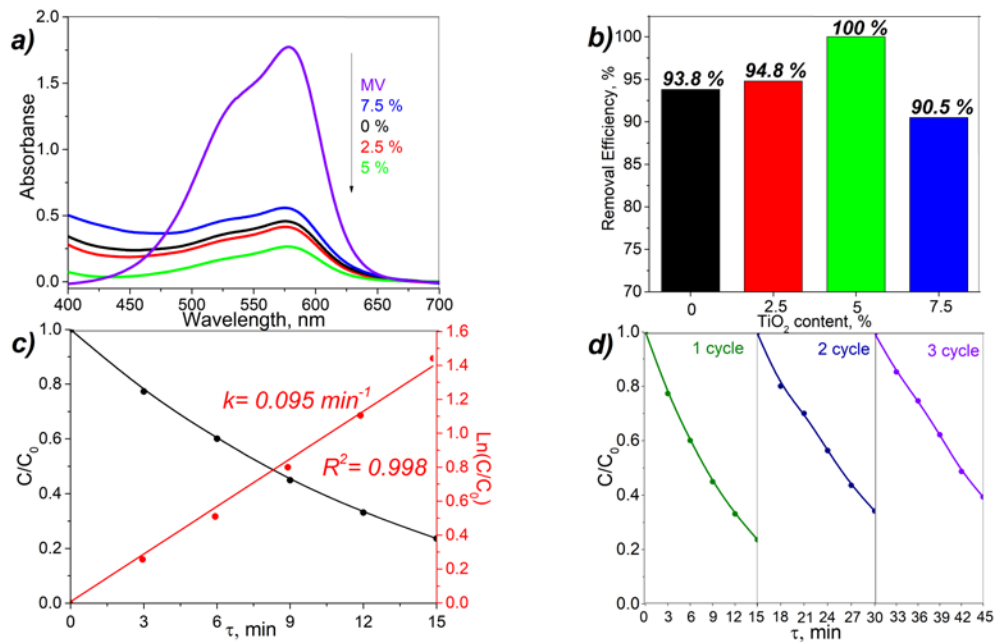
Fig. 7. UV-visible absorption spectra of MV dye during photo-Fenton-like oxidation (a); removal efficiency of PrFeO₃ and PrFeO₃-TiO₂ nanopowders depending on the TiO₂ content (b); MV concentration and kinetic curves of the PrFeO₃-TiO₂-5% sample (c)

Condensed Matter and Interphases / Конденсированные среды и межфазные границы   2021;23(4): 548–560

A. S. Seroglazova et al.   Synthesis, structure, and photo-Fenton activity of PrFeO$_3$-TiO$_2$...

activity of nanopowders based on praseodymium orthoferrite and the addition of titanium dioxide is provided by the formation of a heterojunction, which allows charge carriers to transfer to the second phase and thereby reduce the negative effect of reverse recombination of electron-hole pairs [19]. Thus, the catalytic activity of the samples decreases in the sequence TiO$_2$-5% > TiO$_2$-2.5% > TiO$_2$-0% > TiO$_2$-7.5% and the optimum positive effect of the introduction of TiO$_2$ on the photocatalytic activity of the nanocomposite is observed in the TiO$_2$-5% sample.

For the PrFeO$_3$–TiO$_2$-5% sample, providing 100% MV photodegradation under previously indicated experimental conditions, kinetic studies were carried out and the results obtained are presented in Fig. 7c. As the irradiation time of the solution increases, the relative concentration of the dye naturally decreases, and the kinetic dependence corresponds to the pseudo-first-order of the reaction. The rate constant of this process was calculated based on the linearization of the kinetic dependence in logarithmic coordinates and amounted to 0.095 min^{-1}. When comparing the results obtained with the results of photocatalytic tests of other nanocrystalline orthoferrites (Table 1), it was shown that the PrFeO$_3$–TiO$_2$-5% sample is superior to the best analogs known.

A prerequisite for the further practical application of photocatalysts is their high stability and cyclic reproducibility of results. The study of the cyclic photodegradation of the MV dye by visible light in the presence of PrFeO$_3$-TiO$_2$-5% was carried out under the same conditions as the kinetic study. The results of the cyclic stability experiment (Fig. 7d) indicate that after three cycles of the methyl violet
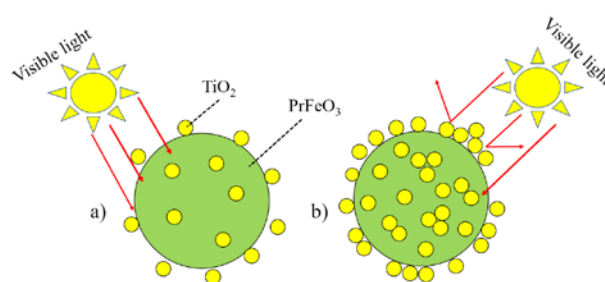
Fig. 8. Schematic representation of PrFeO$_3$ shielding effect by TiO$_2$ particles upon absorption of visible light by the nanocomposite with low (a) and high (b) TiO$_2$ content

photodegradation process, there is only a slight loss of photocatalytic activity, which confirms its high stability of functioning under the selected conditions. This insignificant decrease in photocatalytic activity may be due to the physical loss of the catalyst during its separation from the initial solution. The amount of catalytic testing results makes it possible to consider PrFeO$_3$–TiO$_2$ nanocomposite powders as a promising basis for the processes of photo-Fenton-like oxidation of organic pollutants in aqueous media.

4. Conclusion

In the current study, the method of glycine-nitrate combustion followed by heat treatment in the air has been successfully applied to obtain nanocomposite porous materials based on PrFeO$_3$–TiO$_2$ with a variable mass content of TiO$_2$ (0-7.5%). It is shown that the obtained powders contain nanocrystals of orthorhombic PrFeO$_3$ and an ultradispersed TiO$_2$ phase with an anatase structure. It is revealed that the TiO$_2$ content has a significant effect on the average crystallite size, the specific surface area, and the average pore volume of the samples, which at the considered

Table 1. Photocatalytic characteristics comparison of the PrFeO$_3$–TiO$_2$-5% nanocomposite photocatalyst with other orthoferrite-based photocatalysts described in the literature

№	Photocatalyst	Synthesis method	Band gap, eV	Lamp	Pollutant	K, min^{-1}	Ref.
1	EuFeO$_3$ nanoparticles	Sol-gel	2.22	Xenon	Rhodamine B	0.002	[23]
2	YbFeO$_3$ nanopowder	Solution-combustion	2.05	LED	Methyl violet	0.004	[19]
3	BiFeO$_3$ nanopowder	Sol-gel	2.21	Sunlight	Mordant blue	0.009	[40]
4	PrFeO$_3$-TiO$_2$-5% nanocomposite	Solution-combustion	2.22	Xenon	Methyl violet	0.095	This work

Condensed Matter and Interphases / Конденсированные среды и межфазные границы   2021;23(4): 548–560

A. S. Seroglazova et al.   Synthesis, structure, and photo-Fenton activity of PrFeO$_3$-TiO$_2$...

concentrations suppresses the growth of PrFeO$_3$ nanocrystals and increases the total porosity of the nanocomposite. The amount of added TiO$_2$ has practically no effect on the band gap values, which confirms the formation of PrFeO$_3$-TiO$_2$ composite consisting of two independent phases. The photocatalytic activity of the synthesized nanocomposite samples has been studied in Fenton-like oxidation of methyl violet. The optimal TiO$_2$ content in the nanocomposite is 5 wt%, which ensures the 100% removal of methyl violet from an aqueous solution. Compared to pure catalysts based on other orthoferrites, the PrFeO$_3$-TiO$_2$ nanocomposites obtained in this work exhibit higher photocatalytic activity. Thus, the resulting nanopowders are promising photocatalysts for modern wastewater treatment processes.

Author contribution

All authors made an equivalent contribution to the preparation of the publication.

Conflict of interests

The authors declare that they have no known competing financial interests or personal relationships that could have influenced the work reported in this paper.

References

1. Zhou Z., Guo L., Yang H., Liu Q., Ye F. Hydrothermal synthesis and magnetic properties of multiferroic rare-earth orthoferrites. *Journal of Alloys and Compounds*. 2014;583: 21–31. https://doi.org/10.1016/j.jallcom.2013.08.129

2. Lü X., Xie J., Shu H., Liu J., Yin C., Lin J. Microwave-assisted synthesis of nanocrystalline YFeO$_3$ and study of its photoactivity. *Materials Science and Engineering B: Solid-State Materials for Advanced Technology*. 2007;138(3): 289–292. https://doi.org/10.1016/j.mseb.2007.01.003

3. Martinson K. D., Ivanov V. A., Chebanenko M. I., Panchuk V. V., Semenov V. G., Popkov V. I. Facile combustion synthesis of TbFeO$_3$ nanocrystals with hexagonal and orthorhombic structure. *Nanosystems: Physics, Chemistry, Mathematics*. 2019;10(6): 694–700. https://doi.org/10.17586/2220-8054-2019-10-6-694-700

4. Ding J., Lü X., Shu H., Xie J., Zhang H. Microwave-assisted synthesis of perovskite ReFeO$_3$ (Re: La, Sm, Eu, Gd) photocatalyst. *Materials Science and Engineering B: Solid-State Materials for Advanced Technology*. 2010;171(1-3): 31–34. https://doi.org/10.1016/j.mseb.2010.03.050

5. Nguyen A. T., Nguyen N. T., Mittova I. Y., Perov N. S., Mittova V. O., Hoang T. C., Nguyen V. M., Nguyen V. H., Pham V., Bui X. V. Crystal structure, optical and magnetic properties of PrFeO$_3$ nanoparticles prepared by modified co-precipitation method. *Processing and Application of Ceramics*. 2020;14(4): 355-361. https://doi.org/10.2298/PAC2004355N

6. Akbashev A. R., Semisalova A. S., Perov N. S., Kaul A. R. Weak ferromagnetism in hexagonal orthoferrites RFeO$_3$ (R = Lu, Er-Tb). *Applied Physics Letters*. 2011;99(12): 2011–2014. https://doi.org/10.1063/1.3643043

7. Tugova E., Yastrebov S., Karpov O., Smith R. NdFeO$_3$ nanocrystals under glycine nitrate combustion formation. *Journal of Crystal Growth*. 2017;467: 88–92. https://doi.org/10.1016/j.jcrysgro.2017.03.022

8. Martinson K. D., Kondrashkova I. S., Omarov S. O., Sladkovskiy D. A., Kiselev A. S., Kiseleva T. Y., Popkov V. I. Magnetically recoverable catalyst based on porous nanocrystalline HoFeO$_3$ for processes of n-hexane conversion. *Advanced Powder Technology*. 2020;31(1): 402–408. https://doi.org/10.1016/j.apt.2019.10.033

9. Nguyen A. T., Nguyen V. Y., Mittova I. Ya., Mittova V. O., Viryutina E. L., Hoang C. Ch. T., Nguyen Tr. L. T., Bui X. V., Do T. H. Synthesis and magnetic properties of PrFeO$_3$ nanopowders by the co-precipitation method using ethanol. *Nanosystems: Physics, Chemistry, Mathematics*. 2020;11(4): 468–473. https://doi.org/10.17586/2220-8054-2020-11-4-468-473

10. Li L., Zhang M., Tian P., Gu W., Wang X. Synergistic photocatalytic activity of LnFeO$_3$ (Ln=Pr, Y) perovskites under visible light illumination. *Ceramics International*. 2014;40(9): 13813–13817. https://doi.org/10.1016/j.ceramint.2014.05.097

11. Freeman E., Kumar S., Thomas S. R., Pickering H., Fermin D. J., Eslava S. PrFeO$_3$ photocathodes prepared through spray pyrolysis. *ChemElectroChem*. 2020;7(6): 1365–1372. https://doi.org/10.1002/celc.201902005

12. Tang P., Xie X., Chen H., Lv C., Ding Y. Synthesis of nanoparticulate PrFeO$_3$ by sol-gel method and its visible-light photocatalytic activity. *Ferroelectrics*. 2019;546(1): 181–187. https://doi.org/10.1080/00150193.2019.1592470

13. Qin C., Li Z., Chen G., Zhao Y., Lin T. Fabrication and visible-light photocatalytic behavior of perovskite praseodymium ferrite porous nanotubes. *Journal of Power Sources*. 2015;285: 178–184. https://doi.org/10.1016/j.jpowsour.2015.03.096

14. Thirumalairajan S., Girija K., Ganesh I., Mangalaraj D., Viswanathan C., Balamurugan A., Ponpandian N. Controlled synthesis of perovskite LaFeO$_3$ microsphere composed of nanoparticles via self-as-

Condensed Matter and Interphases / Конденсированные среды и межфазные границы   2021;23(4): 548–560

A. S. Seroglazova et al.   Synthesis, structure, and photo-Fenton activity of PrFeO$_3$-TiO$_2$...

sembly process and their associated photocatalytic activity. *Chemical Engineering Journal*. 2012;209: 420–428. https://doi.org/10.1016/j.cej.2012.08.012

15. Rusevova K., Köferstein R., Rosell M., Richnow H. H., Kopinke F. D., Georgi A. LaFeO$_3$ and BiFeO$_3$ perovskites as nanocatalysts for contaminant degradation in heterogeneous Fenton-like reactions. *Chemical Engineering Journal*. 2014;239: 322–331. https://doi.org/10.1016/j.cej.2013.11.025

16. Kondrashkova I. S., Martinson K. D., Zakharova N. V., Popkov V. I. Synthesis of nanocrystalline HoFeO$_3$ photocatalyst via heat treatment of products of glycine-nitrate combustion. *Russian Journal of General Chemistry*. 2018;88(12): 2465–2471. https://doi.org/10.1134/S1070363218120022

17. Wen W., Wu J. M. Nanomaterials via solution combustion synthesis: A step nearer to controllability. *RSC Advances*. 2014;4(101): 58090–58100. https://doi.org/10.1039/c4ra10145f

18. Popkov V. I., Martinson K. D., Kondrashkova I. S., Enikeeva M. O., Nevedomskiy V. N., Panchuk V. V., Semenov V. G., Volkov M. P., Pleshakov I. V. SCS-assisted production of EuFeO$_3$ core-shell nanoparticles: formation process, structural features and magnetic behavior. *Journal of Alloys and Compounds*. 2021;859: 157812. https://doi.org/10.1016/j.jallcom.2020.157812

19. Tikhanova S. M., Lebedev L. A., Martinson K. D., Chebanenko M. I., Buryanenko I. V., Semenov V. G., Nevedomskiy V. N., Popkov V. I. Synthesis of novel heterojunction h-YbFeO$_3$/o-YbFeO$_3$ photocatalyst with enhanced Fenton-like activity under visible-light. *New Journal of Chemistry*. 2021;45(3): 1541–1550. https://doi.org/10.1039/D0NJ04895J

20. Mir F. A., Sharma S. K., Kumar R. Magnetizations and magneto-transport properties of Ni-doped PrFeO$_3$ thin films. *Chinese Physics B*. 2014;23(4): 048101. https://doi.org/10.1088/1674-1056/23/4/048101

21. Rehman F., Sayed M., Khan J. A., Shah L. A., Shah N. S., Khan H. M., Khattak R. Degradation of crystal violet dye by fenton and photo-fenton oxidation processes. *Zeitschrift Fur Physikalische Chemie*. 2018;232(12): 1771–1786. https://doi.org/10.1515/zpch-2017-1099

22. . Luo W, Zhu L., Wang N., Tang H., Cao M., She Y. Efficient removal of organic pollutants with magnetic nanoscaled BiFeO$_3$ as a reusable heterogeneous Fenton-like catalyst. *Environmental Science and Technology*. 2010;44(5): 1786–1791. https://doi.org/10.1021/es903390g

23. Ju L., Chen Z., Fang L., Dong W., Zheng F., Shen M. Sol-gel synthesis and photo-Fenton-like catalytic activity of EuFeO$_3$ nanoparticles. *Journal of the American Ceramic Society*. 2011;94(10): 3418–3424. https://doi.org/10.1111/j.1551-2916.2011.04522.x

24. Shi S., Xu J., Li L. Preparation and photocatalytic activity of ZnO nanorods and ZnO/Cu$_2$O nanocomposites. *Main Group Chemistry*. 2017;16(1): 47–55. https://doi.org/10.3233/MGC-160224

25. Kim J. Y., Kang S. H., Kim H. S., Sung Y. E. Preparation of highly ordered mesoporous Al$_2$O$_3$/TiO$_2$ and its application in dye-sensitized solar cells. *Langmuir*. 2010;26(4): 2864–2870. https://doi.org/10.1021/la902931w

26. Cam T. S., Vishnevskaya T. A., Omarov S. O., Nevedomskiy V. N., Popkov V. I.,Urea–nitrate combustion synthesis of CuO/CeO$_2$ nanocatalysts toward low-temperature oxidation of CO: the effect of Red/Ox ratio. *Journal of Materials Science*. 2020;55(26): 11891–11906. https://doi.org/10.1007/s10853-020-04857-3

27. Faisal M., Harraz F. A., Ismail A. A., El-Toni A. M., Al-Sayari S. A., Al-Hajry A., Al-Assiri M. S. Novel mesoporous NiO/TiO$_2$ nanocomposites with enhanced photocatalytic activity under visible light illumination. *Ceramics International*. 2018;44(6): 7047–7056. https://doi.org/10.1016/j.ceramint.2018.01.140

28. Mu J., Chen B., Zhang M., Guo Z., Zhang P., Zhang Z., Sun Y., Shao C., Liu Y. Enhancement of the visible-light photocatalytic activity of In$_2$O$_3$-TiO$_2$ nanofiber heteroarchitectures. *ACS Applied Materials & Interfaces*. 2012;4(1): 424–430. https://doi.org/10.1021/am201499r

29. Yu H., Yu J., Cheng B. Photocatalytic activity of the calcined H-titanate nanowires for photocatalytic oxidation of acetone in air. *Chemosphere*. 2007;66(11): 2050–2057. https://doi.org/10.1016/j.chemosphere.2006.09.080

30. Boulbar E. Le, Millon E., Cachoncinlle C., Hakim B., Ntsoenzok E. Optical properties of rare-earth-doped TiO$_2$ anatase and rutile thin films grown by pulsed-laser deposition. *Thin Solid Films*. 2013;553: 13–16. https://doi.org/10.1016/j.tsf.2013.11.032

31. Ismail A. A., Bahnemann D. W. Mesoporous titania photocatalysts: Preparation, characterization and reaction mechanisms. *Journal of Materials Chemistry*. 2011;21(32): 11686–11707. https://doi.org/10.1039/c1jm10407a

32. Yadav H. M., Kolekar T. V., Barge A. S., Thorat N. D., Delekar S. D., Kim B. M., Kim B. J., Kim J. S. Enhanced visible-light photocatalytic activity of Cr^{3+}-doped anatase TiO$_2$ nanoparticles synthesized by sol-gel method. *Journal of Materials Science: Materials in Electronics*. 2015;27(1): 526-534. https://doi.org/10.1007/s10854-015-3785-6

33. Rozenberg G. K., Pasternak M. P., Xu W. M., Dubrovinsky L. S., Carlson S., Taylor R. D. Consequences of pressure-instigated spin crossover in RFeO$_3$ perovskites; a volume collapse with no symmetry modification. *Europhysics Letters*. 2005;71(2): 228–234. https://doi.org/10.1209/epl/i2005-10071-9

Condensed Matter and Interphases / Конденсированные среды и межфазные границы   2021;23(4): 548–560

A. S. Seroglazova et al.   Synthesis, structure, and photo-Fenton activity of PrFeO$_3$-TiO$_2$...

34. Kotlovanova N. E., Matveeva A. N., Omarov S. O., Sokolov V. V., Akbaeva D. N., Popkov V. I. Formation and acid-base surface properties of highly dispersed η-Al$_2$O$_3$ nanopowders. *Inorganic Materials*. 2018;54(4): 392–400. https://doi.org/10.1134/S0020168518040052

35. Khaliullin S. M., Zhuravlev V. D., Ermakova L. V., Buldakova L. Y., Yanchenko M. Y., Porotnikova N. M. Solution combustion synthesis of ZnO using binary fuel (glycine + citric acid). *International Journal of Self-Propagating High-Temperature Synthesis*. 2019;28(4): 226–232. https://doi.org/10.3103/S1061386219040058

36. Ismail A. A., Robben L., Bahnemann D. W. Study of the efficiency of UV and visible-light photocatalytic oxidation of methanol on mesoporous RuO$_2$-TiO$_2$ nanocomposites. *ChemPhysChem*. 2011;12(5): 982–991. https://doi.org/10.1002/cphc.201000936

37. Peymani-Motlagh S. M., Sobhani-Nasab A., Rostami M., Sobati H., Eghbali-Arani M., Fasihi-Ramandi M., Ganjali M. R., Rahimi-Nasrabadi M. Assessing the magnetic, cytotoxic and photocatalytic influence of incorporating Yb^{3+} or Pr^{3+} ions in cobalt-nickel ferrite. *Journal of Materials Science: Materials in Electronics*. 2019;30(7): 6902–6909. https://doi.org/10.1007/s10854-019-01005-9

38. Abdellahi M., Abhari A. S., Bahmanpour M. Preparation and characterization of orthoferrite PrFeO$_3$ nanoceramic. *Ceramics International*. 2016;42(4): 4637–4641. https://doi.org/10.1016/j.ceramint.2015.12.027

39. Goldstein S., Meyerstein D. Comments: on the mechanism of the Fenton-like reaction. *Accounts of Chemical Research*. 1999;32(7): 547–550. https://doi.org/10.1021/ar9800789

40. Ćirković J., Radojković A., Luković Golić D., Tasić N., Čizmić M., Branković G., Branković Z. Visible-light photocatalytic degradation of Mordant Blue 9 by single-phase BiFeO$_3$ nanoparticles. *Journal of Environmental Chemical Engineering*. 2021;9(1): 104587. https://doi.org/10.1016/j.jece.2020.104587

Information about the authors

Anna S. Seroglazova, student at the Departament of Physical Chemistry, Saint Petersburg State Technological Institute (University), Russian Federation. Laboratory assistent, Ioffe Physical-Technical Institute of the Russian Academy of Sciences, Russian Federation; e-mail: annaseroglazova@yandex.ru. ORCID: https://orcid.org/0000-0002-3304-9068.

Maria I. Chebanenko, Junior Researcher at the Laboratory of Materials and Processes of Hydrogen Energy, Ioffe Physical-Technical Institute of the Russian Academy of Sciences, Russian Federation; e-mail: m_chebanenko@list.ru. ORCID: https://orcid.org/0000-0002-1461-579X.

Vadim I. Popkov, PhD in Chemistry, Senior Research Fellow, Head of the Laboratory of Materials and Processes of Hydrogen Energy, Ioffe Physical-Technical Institute of the Russian Academy of Sciences, Russian Federation; e-mail: vip-07@yandex.ru. ORCID: https://orcid.org/0000-0002-8450-4278.

Original articles

Pd–Pb nanoscale films as surface modifiers of Pd,Cu alloy membranes used for hydrogen ultrapurification

A. A. Skrynnikov[1], A. I. Fedoseeva[1], N. B. Morozova[1✉], A. I. Dontsov[2,3], A. V. Vvedensky[1], O. A. Kozaderov[1]

[1]*Voronezh State University,*
1 Universitetskaya pl., Voronezh 394018, Russian Federation

[2]*Baikov Institute of Metallurgy and Materials Science, Russian Academy of Sciences,*
9 Leninsky pr., Moscow 119334, Russian Federation

[3]*Voronezh State Technical University,*
84 ul. 20-Letiya Oktyabrya, Voronezh 394006, Russian Federation

Abstract

The purpose of the article is to reveal the role of the thickness of the layer of the lead-palladium alloy deposited on a copper-palladium membrane in the processes of cathodic injection and the anodic extraction of atomic hydrogen.

The objects of the study were ~ 4 μm thick copper-palladium film electrodes obtained by magnetron sputtering of a target with a composition of 56 at. % Cu and 44 at. % Pd. The studies were carried out by cyclic voltammetry and double step anodic-cathodic chronoamperometry in a deaerated 0.1 M H_2SO_4 aqueous solution. The calculation of the parameters of hydrogen permeability for samples of finite thickness was carried out by mathematical modelling.

Cathodic injection and anodic extraction of atomic hydrogen were used to study the effect of the surface modification of the foil membrane of a Pd-Cu solid solution on the diffusion and kinetic parameters of hydrogen permeability.

It was found that even a small addition of Pd-Pb (a 2 nm thick film) leads to a decrease in the concentration of atomic hydrogen and the diffusion coefficient in the foil. With an increase in the thickness of the coating there is an increase in the diffusion parameters of the hydrogen injection and extraction processes. However, the hydrogen permeability does not reach the level of the unmodified alloy. The main kinetic parameter, the hydrogen extraction rate constant, changes nonlinearly with an increase in the thickness of the coating.

Keywords: Pd-Cu and Pd-Pb solid solutions, Film electrodes, Cathodic injection and anodic extraction of atomic hydrogen, Hydrogen permeability

✉ Natalia B. Morozova, e-mail: mnb@chem.vsu.ru

Condensed Matter and Interphases / Конденсированные среды и межфазные границы   2021;23(4): 561–569

A. A. Skrynnikov et al.   Pd–Pb nanoscale films as surface modifiers of Pd,Cu alloy membranes...

1. Introduction

Currently, there is increasing demand for high-purity hydrogen (~ 99.999 wt%), which is used, for example, in low-temperature fuel cells with a polymer membrane electrolyte [1]. The most promising materials for hydrogen purification are metal membranes made of palladium or palladium-based binary alloys, which are characterised by a higher selectivity as compared to polymers [2]. In addition, palladium alloys have a rather rare combination of properties such as strength and ductility, high specific hydrogen permeability, low hydrogen dilatation, and increased corrosion resistance in corrosive gas media [3].

The disadvantages of pure palladium include, first of all, hydrogen embrittlement, the presence of the α-Pd–H ↔ β-Pd–H phase transition, and a susceptibility to catalytic poisoning [4]. To eliminate these disadvantages, pure palladium is alloyed with other metals. Homogeneous Pd-Cu alloys are of particular interest, since they reduce the cost of the membrane material due to the reduced Pd content. Moreover, the palladium-enriched fcc phase of the solid solution increases the resistance of Pd-Cu alloys to the H_2S surface poisoning [1].

One of the most acceptable methods of obtaining membranes for hydrogen purification is magnetron sputtering of the target of the corresponding composition [5–7]. In particular, the mechanical strength of an ordered Pd-Cu solid solution obtained by magnetron sputtering is noticeably higher than the mechanical strength of palladium. Therefore, such alloy can be recommended to be used in the form of a thin foil to manufacture membranes for hydrogen ultrapurification.

It is also important that, according to various research data, the catalytic efficiency of palladium in electrooxidation processes can be significantly improved by lead doping [8, 9].

High strength and ductility is a necessary combination of properties for foils of membrane elements for hydrogen ultrapurification [5]. A Pd–Pb solid solution (5 at% Pb) obtained by magnetron sputtering is formed by discrete generation with a further growth of islands and their coalescence. An average thickness of the coating of ~10 nm allows achieving the labyrinthine morphology of the surface.

Reports of studies conducted using Pd,Pb-alloys in the hydrogen evolution reaction are extremely limited. Most of them are devoted to the study of the catalytic properties of the alloys of this system in the reactions of electrooxidation [10–12], organic synthesis [13], and in quantum-chemical studies [14]. Increasing the selectivity of catalysts used in industrial processes is also important in terms of improving the production technologies.

The purpose of this work is to identify the role of the thickness of the lead-palladium alloy layer sprayed on the copper-palladium membrane in the processes of cathodic injection and anodic extraction of atomic hydrogen.

2. Experimental

The studies were carried out using copper-palladium film electrodes with a thickness of ~ 4 μm obtained by magnetron spluttering of the target with a composition of 56 at% Cu and 44 at% Pd. A coating with a thickness of 2 to 10 nm was applied to the surface of the electrodes by magnetron spraying of the target with a composition of 95 at% Pd and 5 at% Pb. The spluttering was carried out in the Ar (10^{-1} Pa) medium, the initial vacuum was 10^{-3} Pa. The growth rate was 4 nm/s. The power of the magnetron in the growth process of the foil of the Pd–Cu solid solution was 750–790 W, whereas for the coating of the Pd–Pb solid solution it was 630–650 W. To assess the coating structure of the Pd–Pb solid solution, the coating was simultaneously applied to the surface of the foil and to the surface of the synthetic mica. The structure was investigated by transmission electron microscopy (TEM) (Carl Zeiss Libra 120, Germany[*]).

Electrochemical measurements were conducted in a three-electrode glass cell with a help of an IPC-Compact potentiostat using the methods of cyclic voltammetry and double step anodic-cathodic chronoamperometry in a deaerated aqueous solution of 0.1 M H_2SO_4 [15]. The potentials were recalculated relative to the standard hydrogen electrode.

The working electrode was made of spectrally pure graphite. The samples of films were applied to its surface with the help of conductive graphite adhesive.

Condensed Matter and Interphases / Конденсированные среды и межфазные границы   2021;23(4): 561–569

A. A. Skrynnikov et al.   Pd–Pb nanoscale films as surface modifiers of Pd,Cu alloy membranes...

To remove the traces of surface oxides which form on alloys even in deaerated solutions, prior to obtaining voltammogrammes, the electrode was kept for 500 s at a constant potential of E_{pp} = 0.40 V, at which the electrode drew a weak cathodic current (at a level of $-1 \div -5$ μA). The values of E_{pp} were chosen so that $E_{pp} < E(0)$ and the duration of pretreatment was determined by the transition of the cathodic current to a steady state value.

The forward and reverse potentiodynamic $i,E(t)$-curves were obtained at the potential scan rate of dE/dt = 5 mV/s. Cyclic voltammetric curves were limited by potentials corresponding to the evolution of hydrogen (E_c = −0.15) and oxygen (E_a = 1.55 V). Cyclic voltammogrammes for all electrodes were obtained starting with the potential E_{pp} in the cathodic region till the appearance of a noticeable cathodic current of hydrogen reduction. Then the direction of the potential scanning was changed and the potential returned to the value E_{pp}.

Before receiving each double step anodic-cathodic i,t-curve, a prepolarisation potential of E_{pp} = 0.40 V was applied to the working electrode for 500 s. The curve corresponding to the cathode current transient was obtained at the cathode hydrogenation potential of E_c = −0.15 V, which was the same for all tested samples. The hydrogenation time t_c varied within the range of 1−10 s. After that, the ionisation potential of atomic hydrogen E_p^a was applied to the electrode. E_p^a was preliminarily found from the anodic peaks on the cyclic voltammogramme corresponding to each sample to take into account the inhomogeneity of the surfaces of the samples after their modifications. The current transient was recorded until it reached a constant value, which usually occurred within ~ 500 s. After that, without turning off the cell and without removing the electrode from it, the prepolarisation potential E_{pp} was again applied to it and the procedure was repeated with a sequential increase in the hydrogenation time.

It is important that at a hydrogenation time of less than 10 s, no palladium hydrides were formed, and the hydrogen concentration in the alloy (Pd/H) calculated from experimental data for a hydrogenation period of 10 s did not exceed 0.02 and remained at the level of the a-phase of the Pd-H solid solution.

It should be noted that the results were only processed using the data for cathode current transient corresponding to t_c = 10 s. The hydrogen permeability parameters for the samples of finite thickness were calculated using the method of mathematical modelling [17].

3. Results and discussion

Fig. 1 shows TEM images of a Pd-Pb alloy coating with a thickness of 5 (a) and 10 nm (b).

The 5 nm thick coating consists of individual Pd−Pb island fragments. An increase in the coating thickness to 10 nm leads to the fusion of nanoscale islands and the formation of a labyrinthine morphology.

Typical cyclic voltammogrammes obtained for a thin PdCu electrode without its modification and with a Pd−Pb coating of various thicknesses are shown in Fig. 2.
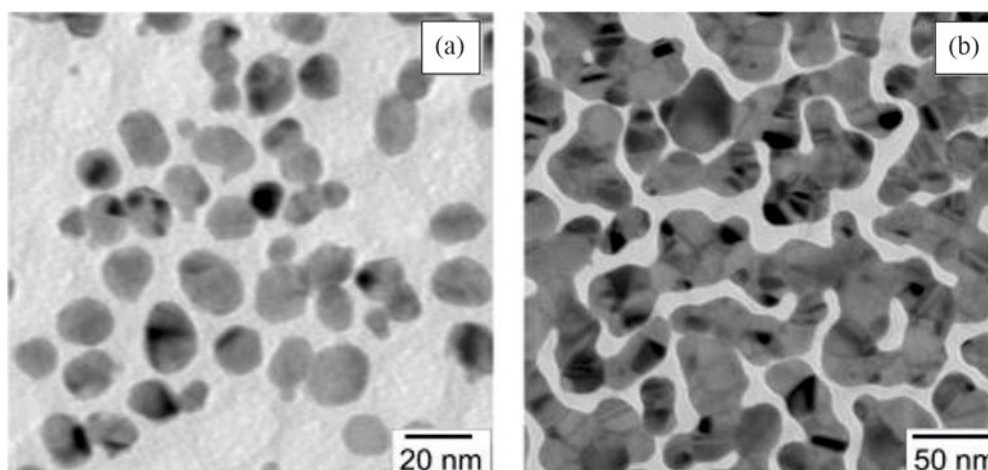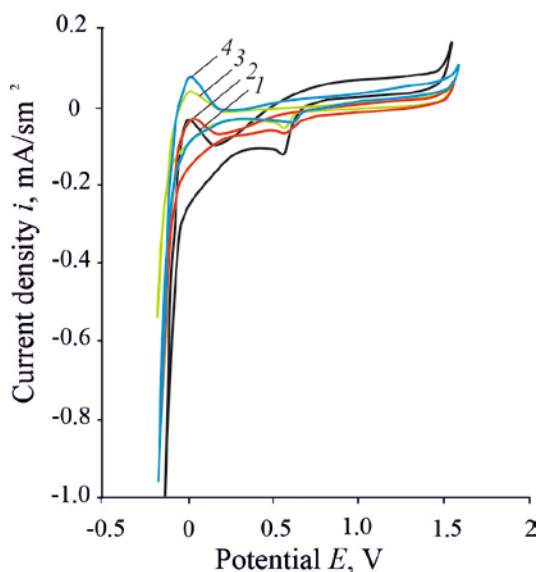

Fig. 1. TEM images of Pd-Pb alloy films (5 at. % Pb) with a thickness of 5 nm (a) and 10 nm (b) [5]

Condensed Matter and Interphases / Конденсированные среды и межфазные границы   2021;23(4): 561–569

A. A. Skrynnikov et al.   Pd–Pb nanoscale films as surface modifiers of Pd,Cu alloy membranes...

Fig. 2. Cyclic voltammogrammes for the initial foil samples of the Pd-Cu solid solution (*1*) and after applying a Pd-Pb coatings of various thicknesses *L*: 2 (*2*); 5 (*3*); 10 nm (*4*)

At the potential of $E \approx 0.00$ V, an ionisation peak of atomic hydrogen appears on the anodic branch of the curve. In case of unmodified PdCu electrode, the ionisation peak is located within the region of negative currents. However, the appearance of even a thin (~ 2 nm) coating of the Pd–Pb solid solution has a noticeable effect on the ionisation of atomic hydrogen, which is expressed in a slight decrease and broadening of the anodic peak.

For the unmodified foil sample within the potential range of 0.75-1.25 V, there is a small indistinct peak, which can be associated with the oxidation of palladium according to the equation

$Pd + H_2O \leftrightarrow PdO + 2H^+ + 2\ e^-$

or

$Pd + 2H_2O \leftrightarrow Pd\ (OH)_2 + 2H^+ + 2\ e^- \dots$

The equilibrium potential for both reactions is $E_{eq} = 0.825$ V [16]. Surface oxides of neither copper nor lead form in the studied solution (pH ~ 1.2). For other samples, such a peak is not typical, which can be attributed to the fact that the surface is blocked by island nanoscale Pd-Pb fragments. At a potential of ~ 0.60 V, the cathodic branch of the curve shows a clear peak of the reduction of oxidised palladium.

The stepped anodic-cathodic chronoamperogrammes obtained for all studied samples

are shown in Fig. 3. With an increase in the hydrogenation time t_c there is a gradual increase in the rate of hydrogen ionisation. The character of the current transient in both anodic and cathodic chronoamperogrammes for all samples remains unchanged, which indicates that the mechanism of the hydrogen injection and extraction processes is still present. It should be noted that for all studied samples, the main anodic current transient occurs within 20 seconds.

With an increase in the thickness of the nanoscale coating, there is an increase in the ionisation and injection rate of atomic hydrogen. Moreover, a sample with a coating thickness of $L = 10$ nm is characterised by the maximum rate of the process at $t_c = 10$ s.

Thus, a Pd–Pb coating even 2 nm thick has a noticeable effect on the kinetics of the process. This is reflected in an increase in the injection and extraction rate of atomic hydrogen with an increase of the thickness of the coating.

As follows from the modelling data of the hydrogenation of film samples [17], the cathode current transient at potentiostatic polarisation of the electrode is described by the equation:

$$i_c(t;\eta_c) = i_c^\infty(\eta_c) + \frac{F\overleftarrow{k}\left[c_{\bar{H}}^s(\eta_c) - c_{\bar{H}}^e\right]}{\left(1 + \frac{\overleftarrow{k}L}{2D}\right)} \cdot \exp\left[-\frac{\overleftarrow{k}t}{\left(1 + \frac{\overleftarrow{k}L}{2D}\right)L}\right]. \quad (1)$$

Here, i_c^∞ is the maximum cathodic current, D is the coefficient of solid-phase diffusion of atomic hydrogen, L is the thickness of the film sample, $\overleftarrow{k}$ is the rate constant for the atomic hydrogen extraction, $\Delta c_{\bar{H}} = [c_{\bar{H}}^s(\eta_c) - c_{\bar{H}}^e]$ is a change in the concentration of atomic hydrogen $\bar{H}$ located in the subsurface region of the alloy, $c_{\bar{H}}^s$ is the molar concentration $\bar{H}$ in the near-surface layer of the membrane, and $c_{\bar{H}}^s$ is the equilibrium concentration of atomic hydrogen in a metal sample.

After a series of transformations, equation (1) for the case of $\frac{\overleftarrow{k}L}{2D} \ll 1$, when the process of atomic hydrogen introduction into the film is significantly inhibited, has a simpler form:

$$\ln[i_c(t;\eta_c) - i_c^\infty(\eta_c)] = \ln[F\overleftarrow{k}[c_{\bar{H}}^s(\eta_c) - c_{\bar{H}}^e] - \frac{\overleftarrow{k}t}{L}. \quad (2)$$

Condensed Matter and Interphases / Конденсированные среды и межфазные границы   2021;23(4): 561–569

A. A. Skrynnikov et al.   Pd–Pb nanoscale films as surface modifiers of Pd,Cu alloy membranes...
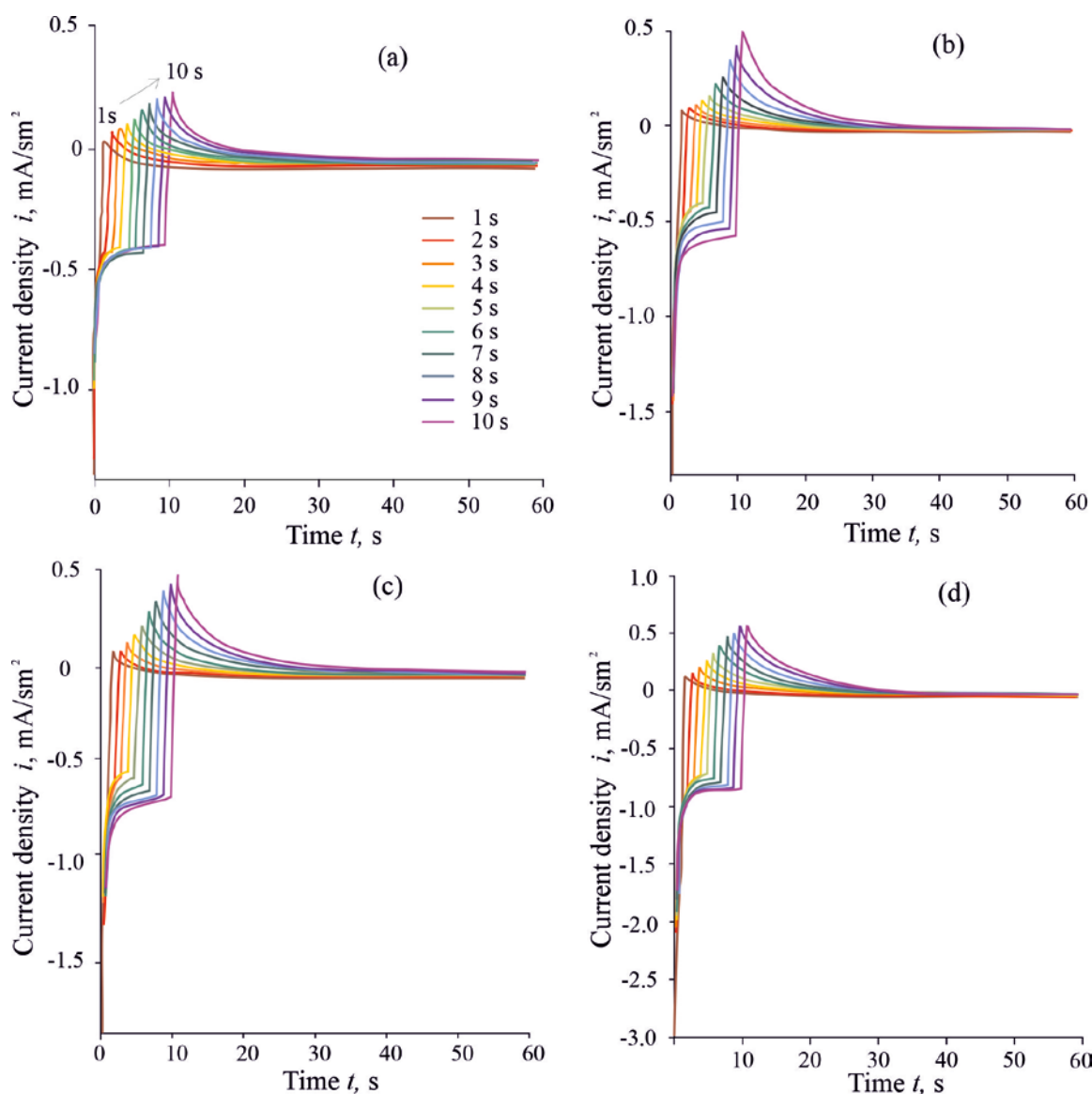
Fig. 3. Cathodic-anodic chronoamperogrammes for foil samples of the Pd-Cu solid solution: uncoated (a), with a Pd-Pb coating with a thickness of: 2(b), 5(c) 10 nm (d)

This equation corresponds to a rather short, up to 4 s, duration of the current transient and corresponds to the regime of mixed diffusion-phase-boundary kinetics. For the case when $\dfrac{\overleftarrow{k}L}{2D} \gg 1$, as well as in the case of diffusion kinetics of the atomic hydrogen injection, equation (2) is transformed:

$$\ln[i_c(t;\eta_c) - i_c^\infty(\eta_c)] = \ln\left[\frac{2FD}{L}[c_{\overline{H}}^s(\eta_c) - c_{\overline{H}}^e]\right] - \frac{2Dt}{L^2} \quad (3)$$

According to (2) and (3), it is possible to straighten the cathodic chronoamperogramme in the criteria coordinates $\ln[i_c(t;\eta_c) - i_c^\infty(\eta_c)] - t$.

The linearised chronoamperogrammes were used to calculate the main parameters of the hydrogen permeability of the modified Pd-Cu samples, which are shown in Fig. 4. Since the studied samples were only used once in the experiment, the relief of the foil surface slightly differed from experiment to experiment, which resulted in rather high values of the confidence intervals for the obtained parameters.

Fig. 4c shows the hydrogen permeability coefficients K_D for all studied samples which were calculated by the formula:

$$K_D = D^{1/2}\Delta c_{\overline{H}}. \quad (4)$$

Condensed Matter and Interphases / Конденсированные среды и межфазные границы   2021;23(4): 561–569

A. A. Skrynnikov et al.   Pd–Pb nanoscale films as surface modifiers of Pd,Cu alloy membranes...
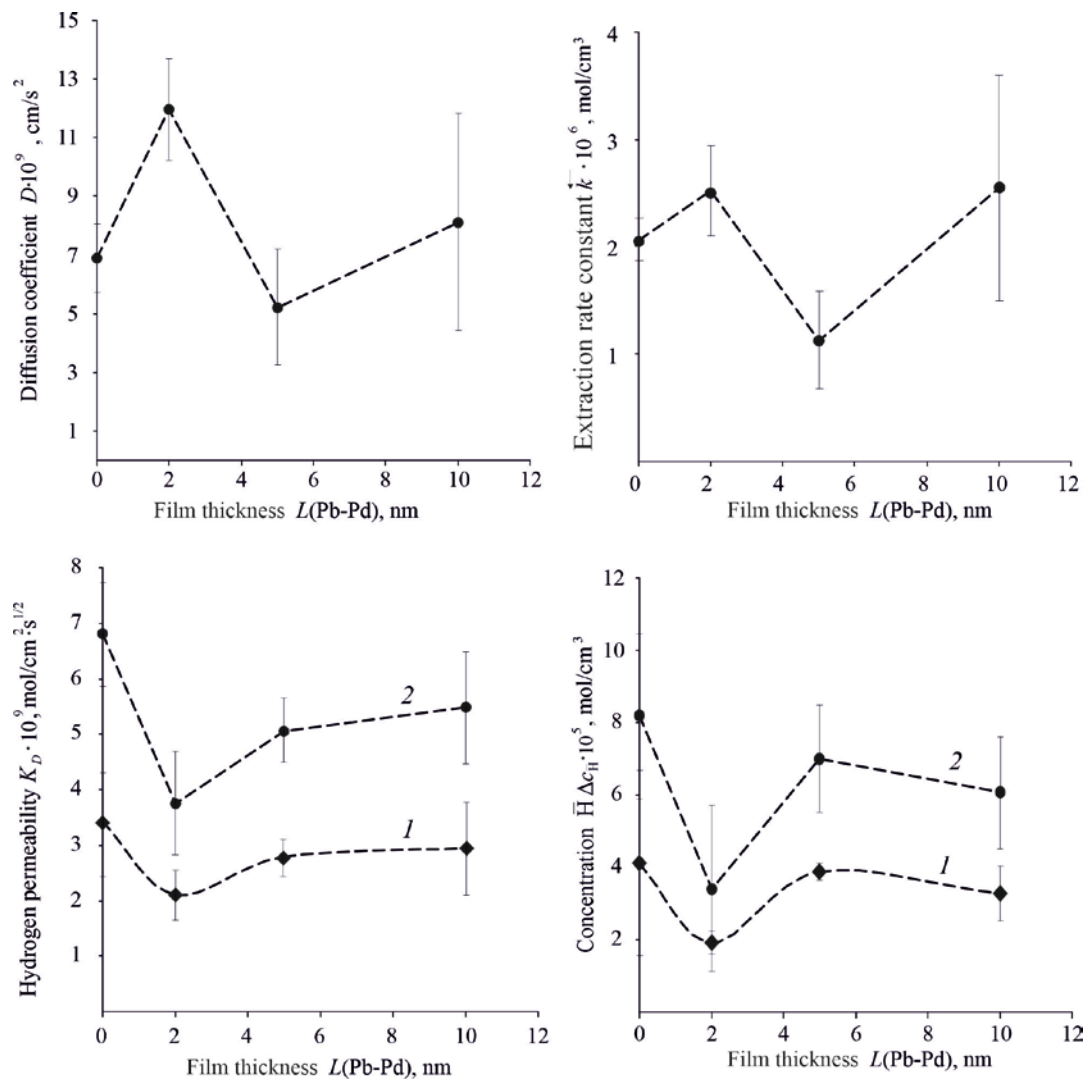
Fig. 4. Dependences of the diffusion and kinetic characteristics of the hydrogenation process on the thickness of the Pd–Pb alloy coating obtained under the modes of diffusion (*1*) and mixed (*2*) polarisation

It is convenient to use this coefficient when it is impossible to find the diffusion coefficients separately, as well as for comparison with the values of hydrogen permeability found by other methods.

The analysis of the obtained data revealed that there is an ambiguous effect of the coating thickness on the parameters of hydrogen permeability. Even with a coating thickness of ~ 2 nm, there is a significant increase in the diffusion coefficient D compared to the unmodified alloy. A further increase in the thickness of nanoscale coatings L was accompanied by a decrease in D. However, an increase in the soundness of coatings at a thickness of 10 nm demonstrated a slight increase in the diffusion coefficient. The nature

of the dependence of the rate constant for the extraction $\overleftarrow{k}$ on L is similar to the dependence of the diffusion coefficient.

The opposite effect is observed for the dependence of the change in the concentration of atomic hydrogen $\Delta c_{\overline{H}}$ on the coating thickness. It should be noted that these values were calculated taking into account different kinetic regimes of the process of atomic hydrogen injection. It is logical to assume that the quantities $\Delta c_{\overline{H}}$ corresponding to the initial time are rather small, whereas with an increase in the injection time, an increasing amount of H can penetrate into the metal membrane.

Of considerable interest is the dependence of the hydrogen permeability coefficient on L

Condensed Matter and Interphases / Конденсированные среды и межфазные границы   2021;23(4): 561–569

A. A. Skrynnikov et al.   Pd–Pb nanoscale films as surface modifiers of Pd,Cu alloy membranes...

(Fig. 4c). According to (4), the largest contribution to the K_D value is made by the value $\Delta c_{\bar{H}}$. It can be concluded that, regardless of the implemented mode of atomic hydrogen injection into the foil, the modification of the foil surface with a Pd–Pb solid solution generally reduces its hydrogen permeability. At the same time, with an increase in the thickness of the coatings, the hydrogen permeability increases, although it does not reach the value for the unmodified sample. It is assumed that the Pd–Pb coating blocks the active centres of hydrogen sorption on the surface of the Pd–Cu substrate without creating new catalytically active centres if the coating thickness is 2 nm.

According to [17], the complete anodic current transient is described by the equation

$$i_a(t) = i_a^{\infty} + \frac{2FD}{L}\left[c_{\bar{H}}^s(\eta_c) - c_{\bar{H}}^e\right] \times$$
$$\times \left(\exp\left(-\frac{\pi^2 D(t-t_c)}{4L^2}\right) - \exp\left(-\frac{\pi^2 D(2t-t_c)}{4L^2}\right)\right), \quad (5)$$

which is linearised at sufficiently noticeable values of t comparable with t_c:

$$\ln\left(\frac{i_a(t) - i_a^{\infty}}{i_a(t_c) - i_a^{\infty}}\right) \approx -\frac{\pi^2 D(t-t_c)}{4L^2}, \quad (6)$$

which allows using graphical processing to calculate D. Further, using the obtained value for D the graphical linearisation of the complete equation (5) presented in a logarithmic form is carried out:

$$\ln[i_a(t) - i_a^{\infty}] = \ln\left(\frac{2FD}{L}\left[c_{\bar{H}}^s(\eta_c) - c_{\bar{H}}^e\right]\right) +$$
$$+\ln\left(\exp\left(-\frac{\pi^2 D(t-t_c)}{4L^2}\right) - \exp\left(-\frac{\pi^2 D(2t-t_c)}{4L^2}\right)\right). \quad (7)$$

It should be noted that equation (7) is valid within the framework of a very general model of mixed solid-phase diffusion kinetics which occurs at sufficiently long (> 20 s) times of the process.

The analysis of the parameter values calculated by the anodic current transients (Table 1) allows us to conclude that with an increase in the film thickness there is a decrease in both the diffusion coefficients and the concentration of atomic hydrogen in the alloy.

Nevertheless, the hydrogen concentration and the hydrogen permeability coefficient for the sample with a coating thickness of 10 nm is higher as compared to other samples. It can be assumed that an increase in the surface area of the substrate has a definite effect on the hydrogen permeability. In particular, the parameters calculated by the anodic current transients D turned out to be somewhat lower than those found by cathodic chronoamperogrammes. The latter can be explained by the dilatation effect of the crystal lattice of Pd alloys [18], as well as by the irreversible sorption of atomic hydrogen by the bulk of the solid phase [19].

4. Conclusions

Surface modification of the Pd,Cu-alloy (56 at% Cu and 44 at% Pd) with nanoscale island films of the Pd-Pb alloy has a rather noticeable effect on the parameters of hydrogen permeability. In particular, with an increase in the average thickness of the Pd,Pb film, there is an increase both in the injection and ionisation rate of atomic hydrogen.

Even a small addition of Pd–Pb (2 nm thick film) leads to a decrease in both the concentration of atomic hydrogen in the Cu–Pd alloy and the diffusion coefficient K_D.

As the thickness of the Pd,Pb film increases on the surface of the Pd–Cu alloy substrate, there is an increase in the diffusion parameters of the H injection and extraction processes. However, the hydrogen permeability does not reach the level of the unmodified alloy. The main kinetic parameter, the hydrogen extraction rate constant, changes nonlinearly with an increase in the thickness of the coating.

Table 1. Characteristics of anodic extraction of hydrogen into film samples of the Pd-Cu solid solution with different thicknesses (*L*) of the modifying Pd–Pb layer

L, nm	$D \times 10^9$, cm²/s	$\Delta c_{\bar{H}} \times 10^5$, mol/cm³	$K_D \times 10^9$, mol/cm²s¹/²
0	4.83 ± 1.89	8.13 ± 3.79	5.65
2	3.90 ± 0.41	4.95 ± 1.25	3.10
5	2.31 ± 1.04	3.29 ± 2.26	1.58
10	0.85 ± 0.43	17.54 ± 10.59	5.11

Condensed Matter and Interphases / Конденсированные среды и межфазные границы   2021;23(4): 561–569

A. A. Skrynnikov et al.   Pd–Pb nanoscale films as surface modifiers of Pd,Cu alloy membranes...

More reliable data about the kinetics of the hydrogenation process can be obtained by processing cathodic chronoamperogrammes that are not complicated by the phenomena of dilatation and irreversible sorption of hydrogen.

Author contributions

All authors made an equivalent contribution to the preparation of the publication.

Conflict of interests

The authors declare that they have no known competing financial interests or personal relationships that could have influenced the work reported in this paper.

References

1. Al-Mufachi N. A., Steinberger-Wilckens R. Influence of temperature and pressure on surface modified Pd-Cu alloy foils for hydrogen purification applications. *Thin Solid Films*. 2018;646: 83–91. https://doi.org/10.1016/j.tsf.2017.11.032

2. Akamatsu T., Kume Y., Komiay K., Yukawa H., Morinaga M., Yamaguchi S. Electrochemical method for measuring hydrogen permeability through metals. *Journal of Alloys and Compounds*. 2005;393: 302–306. https://doi.org/10.1016/j.jallcom.2004.10.007

3. Gorbunov S. V., Kannykin S. V., Penkina T. N., Roshan N. R., Chustov E. M., Burkhanov G. S. Palladium-lead alloys for the purification of hydrogen-containing gas mixtures and the separation of hydrogen from them. *Russian Metallurgy (Metally)*. 2017;2017(1): 54–59. https://doi.org/10.1134/S0036029517010050

4. Endo N., Furukawa Y., Goshome K., Yaegashi S., Mashiko K., Tetsuhiko M. Characterization of mechanical strength and hydrogen permeability of a Pd-Cu alloy film prepared by one-step electroplating for hydrogen separation and membrane reactors. *International Journal of Hydrogen Energy*. 2019;44(16): 8290–8297. https://doi.org/10.1016/j.ijhydene.2019.01.089

5. Gorbunov S. V. Dontsov A. I., Sinetskaya D. A Structure and orientation changes in the growth process of solid solution films Pd-5 (at%)Pb. *Materials Science*. 2019;5: 10–13. https://doi.org/10.31044/1684-579x-2019-0-5-10-13

6. Ievlev V. M., Solntsev K. A., Dontsov A. I., Maksimenko A. A., Kannykin S. V. Hydrogen permeability of thin condensed Pd–Cu foil: Dependence on temperature and phase composition. *Technical Physics*. 2016;61(3): 467–469. https://doi.org/10.1134/s1063784216030105

7. Ievlev V. M., Maksimenko A. A., Kannykin S. V., Belonogov E. K., Volodina M. S., Roshan N. R. Structure and mechanical properties of the condensed foil of Pd-Cu solid solution. *Kondensirovannye sredy i mezhfaznye granitsy = Condensed Matter and Interphases*. 2016;18(4): 521–529. Available at: https://elibrary.ru/item.asp?id=27474855 (In Russ., abstract in Eng.)

8. Wang Y., Nguyen T. S., Liu X. W., Wang X. Novel palladium–lead (Pd–Pb/C) bimetallic catalysts for electrooxidation of ethanol in alkaline media. *Journal of Power Sources*. 2010;195(9): 2619–2622. https://doi.org/10.1016/j.jpowsour.2009.11.072

9. Diao Y. Y., Yan R. Y., Zhang S. J., Yang P., Li Z. X., Wang L., Dong H. F. Effects of Pb and Mg doping in Al_2O_3-supported Pd catalyst on direct oxidative esterification of aldehydes with alcohols to esters. *Journal of Molecular Catalysis A: Chemical*. 2009;303: 35–42. https://doi.org/10.1016/j.molcata.2008.12.023

10. Anderson J. A., Richard J. M., Wells P. K. Pd catalysed hexyne hydrogenation modified by Bi and by Pb. *Journal of Catalysis*. 2009;261(2): 208–216. https://doi.org/10.1016/j.jcat.2008.11.023

11. Xingwen Y., Peter G.P. Novel Pd–Pb/C bimetallic catalysts for direct formic acid fuel cells. *Journal of Power Sources*. 2009;192(2): 279–284. https://doi.org/10.1016/j.jpowsour.2009.03.036

12. Faroppa M. L., Muscia J. J., Chiossoab M. E., Caggianoa C. G., Bideberripebc H. P., Garacia Fierro J. L., Siri G. J., Casella M. L. Oxidation of glycerol with H_2O_2 on Pb-promoted Pd/Г-Al_2O_3 catalysts. *Chinese Journal of Catalysis*. 2016;37(11): 1982–1990. https://doi.org/10.1016/S1872-2067(16)62531-7

13. Khawar A., Aslam Z., Zahir A., Akbar I., Abbas A. Synthesis of Femur extracted hydroxyapatite reinforced nanocomposite and its application for Pb (II) ions abatement from aqueous phase. *International Journal Biological Macromolecules*. 2019;122: 667–676. https://doi.org/10.1016/j.ijbiomac.2018.10.223

14. Wei L., Yao X., Tian X., Cao M., Chen W., She Y., Zhang, S. DFT investigation of the effects of doped Pb atoms on Pd_n clusters ($13 \leqslant n \leqslant 116$). *Computational and Theoretical Chemistry*. 2011;966(1-3): 375–382. https://doi.org/10.1016/j.comptc.2011.03.041

15. Morozova N. B., Vvedenskii A. V., Beredina I. P. Katodic injection, anodic extraction and hydrogen diffusion in metallurgic Cu, Pd and Ag, Pd-alloys. I. Theoretical model. *Kondensirovannye sredy i mezhfaznye granitsy = Condensed Matter and Interphases*. 2014;16(2): 178–188. Available at: https://elibrary.ru/item.asp?id=21785796 (In Russ., abstract in Eng.)

16. Abiyev R. Sh., et al. *Novyy spravochnik khimika i tekhnologa. Elektrodnyye protsessy. Khimicheskaya kinetika i diffuziya. Kolloidnaya khimiya* [A new reference book of a chemist and technologist. Electrode processes. Chemical kinetics and diffusion.

Condensed Matter and Interphases / Конденсированные среды и межфазные границы   2021;23(4): 561–569

A. A. Skrynnikov et al.   Pd–Pb nanoscale films as surface modifiers of Pd,Cu alloy membranes...

Colloidal chemistry]. St. Petersburg: Mir i Semia Publ.; 2004. 837 p. (In Russ.)

17. Morozova N. B., Vvedenskii A. V., Maksimenko A. A., Dontsov A. I. Thin layer multicycle cathodic-anodic chronoamperometry of atomic hydrogen injection-extraction into metals with regard to the stage of phase boundary exchange. *Russian Journal of Electrochemistry*. 2018;54(4): 344–354. https://doi.org/10.1134/s1023193518040067

18. Barlag H., Opara L., Züchner H. Hydrogen diffusion in palladium based f.c.c. alloys. *Journal of Alloys and Compounds*. 2002;330-332: 434–437. https://doi.org/10.1016/S0925-8388(01)01459-1

19. Morozova N. B., Vvedenskii A. V. Cathodic injection, anodic extraction and hydrogen diffusion in metallurgical Cu, Pd- and Ag, Pd-alloys. III. Accounting irreversible hydrogen sorption. *Kondensirovannye sredy i mezhfaznye granitsy = Condensed Matter and Interphases*. 2016;18(1): 81–90. Available at: https://elibrary.ru/item.asp?id=25946624(In Russ., abstract in Eng.)

Information about the authors

Alexander A. Skrynnikov, 5th year student, Voronezh State University, Voronezh, Russian Federation; e-mail: aleks-skrynnikov@yandex.ru

Anastasia I Fedoseeva, 3rd year postgraduate student, Department of Physical Chemistry, Voronezh State University, Voronezh, Russian Federation; e-mail: Kanamepsp@yandex.ru. ORCID iD: https://orcid.org/0000-0002-6041-7460.

Natalia B. Morozova, PhD in Chemistry, Associate Professor, Department of Physical Chemistry, Voronezh State University, Voronezh, Russian Federation; e-mail: mnb@chem.vsu.ru. ORCID iD: https://orcid.org/0000-0003-40116510.

Alexey I. Dontsov, Ph.D. in Physics and Mathematics, Associate Professor, Department of Physics, Voronezh State Technical University, Voronezh, Russian Federation; senior researcher, Baikov Institute of Metallurgy and Materials Science, Russian Academy of Sciences, Moscow, Russian Federation; e-mail: dontalex@mail.ru. ORCID iD: https://orcid.org/0000-0002-3645-1626.

Aleksander V. Vvedenskii, DSc in Chemistry, Professor, Professor at the Department of Physical Chemistry, Voronezh State University, Voronezh, Russian Federation; e-mail: alvved@chem.vsu.ru. ORCID iD: https://orcid.org/0000-0003-2210-5543.

Oleg A. Kozaderov, DSc in Chemistry, Associate Professor, Head of the Department of Physical Chemistry, Faculty of Chemistry, Voronezh State University, Voronezh, Russian Federation; e-mail: ok@chem.vsu.ru. ORCID iD: https://orcid.org/0000-0002-0249-9517.

Condensed Matter and Interphases

Original articles

Synthesis of chitosan and *N*-vinylimidazole graft-copolymers and the properties of their aqueous solutions

A. V. Sorokin[1,2], M. G. Kholyavka[1,3], M. S. Lavlinskaya[2] ✉

[1]Voronezh State University,
1 Universitetskaya pl., Voronezh 394018, Russian Federation

[2]Voronezh State University of Engineering Technologies,
19 Prospekt Revolutsii, 394036 Voronezh, Russian Federation

[3]Sevastopol State University
33 Universitetskaya ul., Sevastopol 299053, Russian Federation

Abstract

The aim of this work is to synthesise chitosan and *N*-vinylimidazole graft-copolymers of various compositions and to study the properties of their aqueous solutions.

Chitosan and N-vinylimidazole graft-copolymers were obtained by solution polymerisation in the presence of a ceric ammonium nitrate redox initiator. The synthesised graft copolymers were characterised by FTIR to determine their compositions and the grafted side chains of poly-*N*-vinylimidazole were characterised by gel permeation chromatography to determine their molecular wights and polydispersity indices. It was established that the obtained products are characterised by high values of yield and grafting efficiency and low values of the polydispersity index. It was found that when the content of the *N*-vinylimidazole links is above 57 wt%, the synthesised graft copolymers are water-soluble. Aqueous solutions of the obtained copolymers were characterised using dynamic light scattering, transmission electron microscopy, and laser Doppler microelectrophoresis. The study showed that macromolecules of graft copolymers in aqueous solutions have stimuli-sensitive properties with respect to the medium reaction and at a concentration above 10^{-2} wt% are characterised by a tendency to self-association forming core-crown aggregates, the geometry of which depends on the molecular masses of the grafted chains. Associates of macromolecules in solutions are characterised by positive values of the electrokinetic potential, the values of which also depend on the medium reaction. Thus, it was found that the ceric ammonium nitrate initiator allows obtaining chitosan and *N*-vinylimidazole graft-copolymers showing stimuli-sensitive properties in aqueous solutions and prone to self-association at concentrations above 10^{-2} wt%.

Keywords: Graft copolymers, Aqueous solutions of polymers, Stimuli sensitivity, chitosan, *N* -vinylimidazole

✉ Maria S. Lavlinskaya, e-mail: maria.lavlinskaya@gmail.com

Condensed Matter and Interphases / Конденсированные среды и межфазные границы   2021;23(4): 570–577

A. V. Sorokin et al.   Synthesis of chitosan and N-vinylimidazole graft-copolymers…

1. Introduction

Currently, more and more research are being focused on polymeric materials of natural origin. One of the most popular materials of that kind is chitosan. This poly-β-glycoside is a linear copolymer of *D*-glucosamine and *N*-acetyl-*D*-glucosamine binded by 1,4-β-glycosidic linkages [1]. Chitosan is obtained by alkaline deacetylation of chitin, a natural polysaccharide that forms the shells of crustaceans and insects. It is also present in fungi bodies [2]. Due to the widespread renewable sources of raw materials for the production of chitosan, it is the second most common biopolymer, which has a number of properties of practical significance. They include low toxicity, biocompatibility, and intrinsic biological activity, which allow using chitosan for biomedical purposes [1, 3]. For example, some sources provide extensive information on the use of chitosan-based macromolecules of various architecture as a carrier of biologically active substances and medicinal products for oral [4] and transdermal delivery [5]. It can also be used to create innovative dressing and wound covering materials [6–7], in tissue engineering [8–9], etc.

Like many materials of natural origin, chitosan has a number of features that make it difficult to work with it. The properties of polymers are largely determined by their molecular weight (MW). Therefore, chitosan with a MW over 20,000 is insoluble in water, and at higher values of MW, it is characterised by the ability to dissolve in aqueous solutions of monohydric acids due to protonation of the free amino group of glucosamine links [1, 3]. These factors can limit the possibilities of using chitosan. In this regard, it is advisable to modify its macromolecules by expanding the pH range of polymer dissolution in aqueous media.

One of the most promising forms of the polysaccharide modification is graft copolymerisation, which does not require strict conditions or expensive reagents [10–11]. By varying the frequency of side chain grafting in the resulting graft copolymers, it is possible to change the conformation of their polymer macromolecules in aqueous solutions. Thus, it is possible to form hard macromolecular brushes or soft statistical coils, as well as to change the ability of macromolecules to form conjugates with various low and high molecular weight compounds [12–13]. In addition, the introduction of side chains with functional substituents also increases the ability of graft copolymers to interact with various substances [14–15].

A promising comonomer for the preparation of chitosan graft copolymers is *N*-vinylimidazole. The azole cycle in its composition is characterised by a high complex-forming potential due to its ability be involved in acid-base and stacking interactions, as well as to form hydrogen bonds [16]. Moreover, its homopolymer, poly-*N*-vinylimidazole, is water-soluble in a wide range of concentrations and has its own physiological activity: it can act as a catalyst, and, like chitosan, is antibacterially active [17-19]. The combination of these properties suggests that chitosan and *N*-vinylimidazole graft copolymers will be promising materials for, for example, biomedical applications.

Therefore, the aim of this work is to synthesise chitosan and *N*-vinylimidazole graft-copolymers of various compositions and to study the properties of their aqueous solutions.

2. Experimental

We used chitosan (Cht) with a molecular mass of 600×10^3 and the degree of deacetylation of 0.85; a commercial monomer *N*-vinylimidazole (VI), all of them produced by Sigma Aldrich, Germany. The polymer was used without additional purification, the monomer was distilled in vacuum immediately before use (T_{bp} = 78–79 °C/11 mmHg; n_D^{20} = 1.5338). Ceric ammonium nitrate (CAN) (Acros Organics, USA) was used without additional purification as the initiator of the radical process.

Graft copolymers were prepared by solution polymerisation with redox initiation use. A weighed portion of chitosan (0.5 g) was placed in 100 ml of a 2% acetic acid solution and kept at room temperature until the polysaccharide was completely dissolved. Then, the calculated amount of monomer and initiator was added to the mixture (Table 1) and the mixture was left at a temperature of 25 ± 2 °C for 8 hours. The resulting graft copolymer was isolated by precipitation in acetone, after which it was dissolved in water, filtered off, the filtrate was dialysed against distilled water through a cellophane membrane

Condensed Matter and Interphases / Конденсированные среды и межфазные границы   2021;23(4): 570–577

A. V. Sorokin et al.   Synthesis of chitosan and N-vinylimidazole graft-copolymers...

Таблица 1. Условия синтеза графт-сополимеров

No	Cht, g	2 % CH₃COOH, ml	VI, ml	CAN, g	Yield, %
1	0.5	100	0.1	0.06	52
2	0.5	100	0.5	0.10	61
3	0.5	100	1.0	0.15	69
4	0.5	100	1.5	0.20	76

with a pore size of 12 kDa for 7 days, after which it was freeze-dried to a constant weight. The product yield was 52 – 76 %.

The molecular weights of the grafted side chains and the polydispersity index (PDI) were determined by gel permeation chromatography according to the method described in [14].

The grafting efficiency (GE) was calculated using the following formula [14]:

$$GE = \frac{m_2 - m_1}{m_1} \cdot 100,$$

where m_1 and m_2 are the respective masses of the original chitosan and the purified dried graft copolymer in grams.

The compositions of the obtained copolymers were determined by FTIR. The spectra were recorded by a Bruker Vertex 70 instrument (Bruker Optics, Germany) by a FTIR ATR method in the frequency range of 500–4000 cm⁻¹. The composition was calculated from the ratio of the areas of absorption bands at 1591 and 1420 cm⁻¹ related to the vibrations of the primary chitosan amino group and the -C=N-bond of the azole cycle, respectively.

The properties of aqueous solutions of the synthesised graft copolymers with various concentrations of the synthesised graft copolymers were studied by the method of dynamic light scattering using a Malvern ZetaSizer Nano apparatus (Malvern Instruments, Great Britain) equipped with a He-Ne laser with a power of 25 mW and a wavelength of λ = 632.8 nm. The data were recorded at an angle of 90° at 25 °C in cuvettes equipped with a gold electrode, the measurement cycle time was 120 seconds, the number of cycles was between 3–6 and was determined automatically.

The particle shape of graft copolymers in aqueous solutions was determined by transmission electron microscopy using a Libra
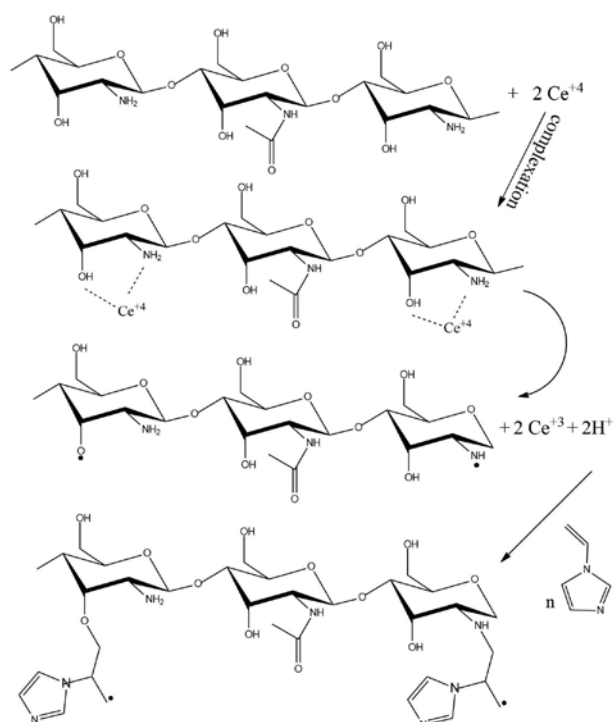
120 apparatus (Carl Zeiss, Germany). Before recording, the polymer solution was applied dropwise onto a formvar-coated copper plate and dried in an air stream.

3. Results and discussion

Chitosan graft copolymers with different contents of *N*-vinylimidazole were obtained by solution radical polymerisation with redox initiation using ceric ammonium nitrate. It is well known that depending on the synthesis conditions it is possible to obtain copolymers of polysaccharides with different architectures. The most important factors influencing the structure of the formed macromolecules are the temperature and the nature of the initiator. In thermal conditions above 50 °C and in the presence of initiators characterised by high values of redox potentials, there are primarily reactions of the formation of block copolymers of polyglycosides or homopolymers of the used comonomers [10]. Therefore, to obtain the graft-copolymer architecture, the synthesis was carried out at room temperature in the presence of ceric ammonium nitrate, the transition potential of which Ce^{+4}/Ce^{+3} was lower than commonly used persulphates or permanganates.

The mechanism of the reaction for the formation of the graft copolymer can be represented as follows (Scheme 1): the cerium (IV) ion interacts with the amino or hydroxyl groups of chitosan forming a complex compound. This results in the removal of a hydrogen atom from the pyranose cycle substituent, the formation of radicals on oxygen or nitrogen atoms, and the reduction of cerium to the Ce (III) state. The radicals formed on the polyglycoside chain interact with the monomers forming a new macroradical. Subsequent similar interactions lead to the chain growth. The chain termination is possible due to the recombination with another active centre or through reactions of chain transfer to other components [15].

The structure of the resulting products was confirmed using FTIR (Fig. 1). The chitosan IR spectrum contains the following characteristic absorption bands: 1024–1150 cm⁻¹ related to skeletal vibrations of the pyranose cycle and the C-O-C fragment, a series of bands at 1262, 1320, 1375, and 2870 cm⁻¹ corresponding to

Condensed Matter and Interphases / Конденсированные среды и межфазные границы   2021;23(4): 570–577

A. V. Sorokin et al.   Synthesis of chitosan and N-vinylimidazole graft-copolymers...

Scheme 1. Possible mechanism for the graft copolymer formation

deformation vibrations of methyl and methylene groups of the polysaccharide cyclic fragment, at 1647 cm⁻¹, stretching vibrations of the C=O group of *N*-acetyl-*D*-glucosamine residues, at 1591 cm⁻¹ vibrations of the primary amino group; and a broad absorption band at 3357 cm⁻¹ related to the vibrations of OH groups of water molecules associated with polymer macromolecules [20]. The IR spectrum of the graft copolymer contains the above-mentioned bands, and in addition, new ones appear at 2914 cm⁻¹ corresponding to the vibrations of the azole cycle and a band at 1420 cm⁻¹ corresponding to the vibrations of the -C=N- bond of the side substituent of the grafted poly-*N*-vinylimidazole chain.

The most important factor determining the properties of a macromolecule of any structure is its molecular weight. It is assumed that during
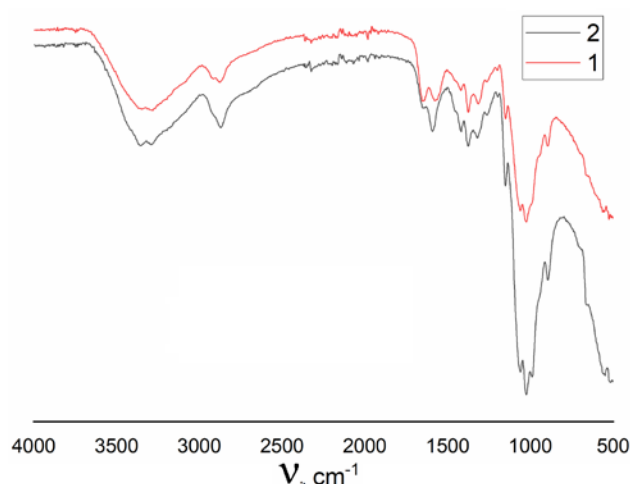
Fig. 1. FTIR spectra: (*1*) chitosan, (*2*) chitosan with *N*-vinylimidazole graft copolymer

the reaction of the graft copolymer formation, the molecular weight of the original chitosan does not change. Therefore, we studied the side chains of poly-*N*-vinylimidazole (PVI) isolated as a result of acid destruction of the polyglycoside chains. The results of the molecular weights are presented in Table 2. As expected, with an increase in the monomer content in the initial polymerisation mixture, there is an increase in the molecular weights of the grafted chains. However, under the same conditions, there is an insignificant decrease in the value of the grafting efficiency. This is due to an increase in the total viscosity of the reaction mixture and, as a consequence, an increase in the number of side processes, including the VI homopolymerisation. Separately, it is worth discussing the values of the polydispersity index (PDI) of side chains obtained as a result of the study: they are low enough for a free-radical process, which also indicates that the initiator for the synthesis of graft copolymers was well-chosen.

The compositions of the obtained copolymers calculated using the FTIR data are given in Table 2. As can be seen from the presented values,

Table 2. Characteristics of the synthesised graft copolymers

No	PVI content, wt%	GE, %	PVI grafted chains			Water-solubility	D_h^1, nm	ζ^1, mV	c^*, wt%
			M_W	M_N	PDI				
1	17	68	7 269	5 679	1.28	–	–	–	–
2	42	56	16 835	12 754	1.32	–	–	–	–
3	57	49	19 907	15 432	1.29	+	139	17.3	0.02
4	74	42	22 064	16 843	1.31	+	158	20.1	0.03

^{1} – 1 % solution in distilled water (pH = 5.6)

Condensed Matter and Interphases / Конденсированные среды и межфазные границы   2021;23(4): 570–577

A. V. Sorokin et al.   Synthesis of chitosan and N-vinylimidazole graft-copolymers...

with an increase in the *N*-vinylimidazole content in the polymerisation mixture the number of its links in the final copolymer increases. Poly-*N*-vinylimidazole, unlike chitosan, is a water-soluble polymer. Therefore, it is the number of PVI links in the macromolecules that determines the copolymer's ability to dissolve in water. It was found that samples containing less than 57 wt% of PVI are insoluble in water, however, they dissolve in acidic solutions with a pH < 6.5. Further research was only conducted with water-soluble copolymers.

The dynamic light scattering (DLS) method was used to determine the values of the hydrodynamic diameters, D_h, and particles of copolymers in 1% aqueous solutions. It was found that the systems under consideration are characterised by a narrow unimodal distribution of particles by sizes with the values of D_h within the range of 139–158 nm (Table 2). Using these values, it can be concluded that the particles of the synthesised graft copolymers in aqueous solutions are aggregates of several macromolecular chains.

Previous studies show that aggregates of polysaccharide macromolecules in aqueous solutions can have a geometry other than spherical [14]. In this case, it might be incorrect to use the method of dynamic light scattering to determine the size of such particles. Therefore, to study solutions of graft copolymers, we also used the method of transmission electron microscopy (TEM) (Fig. 2). The values of the particle sizes in the solution obtained by various methods correlate with each other. However, it should be noted that with a change in the molecular weights of the
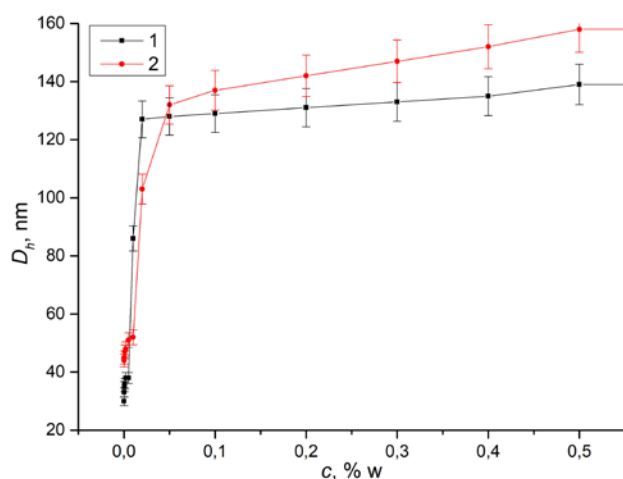
grafted PVI chains, the geometry of the multi-chain aggregate also changes: with an increase in the molecular mass and the percentage of the grafted PVI chains, the shape of the aggregates changes and becomes less elongated and oval (which is more characteristic of polysaccharides) and becomes spherical. Moreover, the aggregates of both types have a pronounced structure with a dense core surrounded by a looser crown.

Given the tendency of macromolecules of water-soluble polysaccharides and poly-*N*-vinylimidazole to self-aggregation, it is of interest to determine the critical overlap coil concentration (COCC), *c**, in water. For this, the dynamic light scattering method was used to determine the hydrodynamic diameters of particles in the concentration range of 10^{-4} – 0.5 wt%. The results of the study are shown in Fig. 3. As can be seen from the obtained data (Table 2), the COCC values increase with a growth in the molecular weights of the final modified polysaccharide, which is consistent with previously published data [21].

Another important characteristic for polymer solutions is the surface charge of particles, which is determined by the electrokinetic potential (ζ). To determine it, the laser Doppler microelectrophoresis method was used. All synthesised water-soluble graft copolymers are characterised by a positive value of the electrokinetic potential, which is due to the influence of nitrogen atoms of the side substituents of both the polysaccharide and the grafted side chains. It should be noted that with an increase in the molecular weight of the
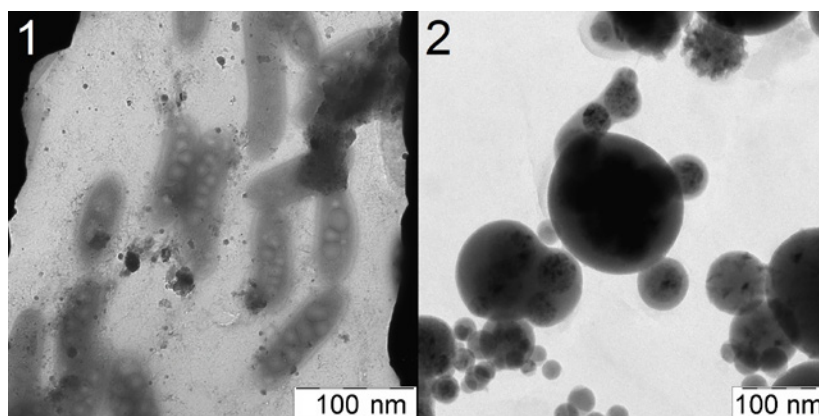
Fig. 2. TEM images of copolymer particles: (*1*) copolymer containing 17 wt% of VI; (*2*) copolymer containing 57 wt% of VI

Condensed Matter and Interphases / Конденсированные среды и межфазные границы   2021;23(4): 570–577

A. V. Sorokin et al.   Synthesis of chitosan and N-vinylimidazole graft-copolymers...
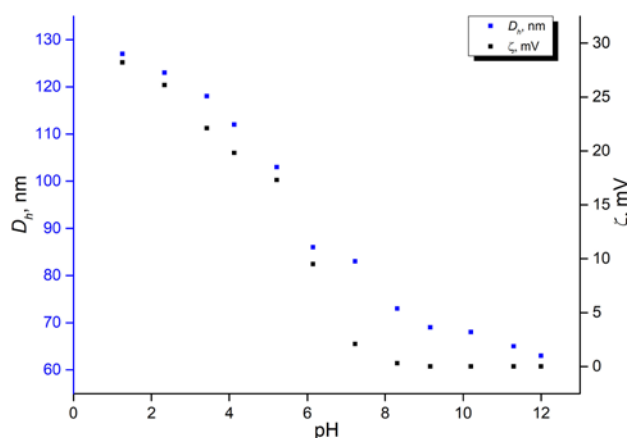

Fig. 3. Dependences of the particle sizes of the copolymer in solution on their concentration: (*1*) copolymer containing 57 wt% of VI; (*2*) copolymer containing 74 wt% of VI

Fig. 4. Dependences of the particle size of the copolymer and the electrokinetic potential on the medium reaction

grafted chains and the percentage of azole links in the macromolecules of graft copolymers, the value of the electrokinetic potential increases insignificantly.

It is well known that azole cycles are capable of acid-base interactions. Therefore, their introduction into macromolecules can make them stimuli-sensitive. We studied the dependence of the particle size on the medium reaction for a copolymer containing 57 wt% of PVI units at a concentration below the COCC, 10^{-3} wt% (Fig. 4). It was found that with an increase in the pH value, the values of the hydrodynamic diameter of the particles decrease in the range at pH < 8, after which their size remains practically unchanged. The study of the dependence of the change in the values of the electrokinetic potential from the pH value showed the following: at pH < 7, the particles of graft copolymers are characterised by positive values of the zeta potential, and with an increase in pH values, the particles lose their charge. Thus, the synthesised graft copolymers are stimuli-sensitive macromolecules that change their sizes and charges depending on external conditions.

4. Conclusion

Thus, we successfully synthesised chitosan and *N*-vinylimidazole graft copolymers with relatively high values of yields and grafting efficiency. The content of azole links above 57 wt% ensures the water solubility of polymers. Depending on the

concentration of graft copolymers, the particles of copolymers in solutions can be both in the form of single coils or multi-chain aggregates, the geometry of which depends on the grafting efficiency. It was found that regardless of the form of macromolecules in the solution, they are characterised by positive values of electrokinetic potential. However, with a change in pH, graft copolymers can change the size and charge of the particles in the solution. Thus, the obtained stimuli-sensitive polymers may be of interest for biomedical applications.

Conflict of interests

The authors declare that they have no known competing financial interests or personal relationships that could have influenced the work reported in this paper.

Author contributions

All authors made an equivalent contribution to the preparation of the publication.

References

1. Jayakumar R., Prabaharan M., Muzzarelli R. (Eds.). Chitosan for biomaterials I. *In: Advances in Polymer Science*. Berlin – Heidelberg: Springer-Verlag; 2011. 236 p. https://doi.org/10.1007/978-3-642-23114-8

2. Kou S., Peters L. M., Mucalo M. R. Chitosan: A review of sources and preparation methods. *International Journal of Biological Macromolecules*. 2021;169: 85–94. https://doi.org/10.1016/j.ijbiomac.2020.12.005

Condensed Matter and Interphases / Конденсированные среды и межфазные границы   2021;23(4): 570–577

A. V. Sorokin et al.   Synthesis of chitosan and N-vinylimidazole graft-copolymers...

3. Jennings J. A., Bumgardner J. B. (Eds.). Woodhead Publishing Series in Biomaterials. *In: Chitosan based biomaterials. Volume 1: Fundamentals*. Duxford; 2017. 325 p. https://doi.org/10.1016/b978-0-08-100230-8.09002-6

4. Lang X., Wang T., Sun M., Chen X., Liu Y. Advances and applications of chitosan-based nanomaterials as oral delivery carriers: A review. *International Journal of Biological Macromolecules*. 2020;154: 433–445. https://doi.org/10.1016/j.ijbiomac.2020.03.148

5. Sivasankarapillai V. S., Das S. S., Sabir F., Sundaramahalingam M. A., Colmenares J. C., Prasannakumar S., Rajan M., Rahdar A., Kyzas G. Z. Progress in natural polymer engineered biomaterials for transdermal drug delivery systems. *Materials Today Chemistry*. 2021;19: 100382. https://doi.org/10.1016/j.mtchem.2020.100382

6. Ueno H., Mori T., Fujinaga T. Topical formulations and wound healing applications of chitosan. *Advanced Drug Delivery Reviews*. 2001;52(2): 105–115. https://doi.org/10.1016/S0169-409X(01)00189-2

7. Patrulea V., Ostafe V., Borchard G., Jordan O. Chitosan as a starting material for wound healing applications. *European Journal of Pharmaceutics and Biopharmaceutics, Part B*. 2015;97: 417–426. https://doi.org/10.1016/j.ejpb.2015.08.004

8. Pita-López M. L., Fletes-Vargas G., Espinosa-Andrews H., Rodríguez-Rodríguez R. Physically cross-linked chitosan-based hydrogels for tissue engineering applications: A state-of-the-art review. *European Polymer Journal*. 2021;45: 110176. https://doi.org/10.1016/j.eurpolymj.2020.110176

9. Madni A., Kousar R., Naeem N., Wahid F. Recent advancements in applications of chitosan-based biomaterials for skin tissue engineering. *Journal of Bioresources and Bioproducts*. 2021;6(1): 11–25. https://doi.org/10.1016/j.jobab.2021.01.002

10. Berlin Ad. A., Kislenko V. N. Kinetics and mechanism of radical graft polymerization of monomers onto polysaccharides. *Progress in Polymer Science*. 1992;17(5): 765–825. https://doi.org/10.1016/0079-6700(92)90010-V

11. Sanchez-Salvador J. L., Balea A., Monte M. C., Negro C., Blanco A. Chitosan grafted/cross-linked with biodegradable polymers: A review. *International Journal of Biological Macromolecules*. 2021;178: 325–343. https://doi.org/10.1016/j.ijbiomac.2021.02.200

12. Lee H., Pietrasik J., Sheiko S. S., Matyjaszewski K. Stimuli-responsive molecular brushes. *Progress in Polymer Science*. 2010;35 (1-2): 24–44. https://doi.org/10.1016/j.progpolymsci.2009.11.002

13. Yan J., Bockstaller M. R., Matyjaszewski K. Brush-modified materials: Control of molecular architecture, assembly behavior, properties and applications. *Progress in Polymer Science*. 2020;100: 101180. https://doi.org/10.1016/j.progpolymsci.2019.101180

14. Kuznetsov V. A., Sorokin A. V., Lavlinskaya M. S., Sinelnikov A. A., Bykovskiy D. V. Graft copolymers of carboxymethyl cellulose with N-vinylimidazole: synthesis and application for drug delivery. *Polymer Bulletin*. 2019;76: 4929–4949. https://doi.org/10.1007/s00289-018-2635-0

15. Sorokin A. V., Kuznetsov V. A., Lavlinskaya M. S. Synthesis of graft copolymers of carboxymethyl cellulose and N,N-dimethylaminoethyl methacrylate and their study as Paclitaxel carriers. *Polymer Bulletin*. 2021;78: 2975–2992. https://doi.org/10.1007/s00289-020-03250-z

16. Broekema R. J. Durville P. F. M., Reedijk J., Smit J. A. The coordination chemistry of N-vinylimidazole. *Transition Metal Chemistry*. 1982;7: 25–28. https://doi.org/10.1007/BF00623803

17. Kodama H., Miyajima T., Tabuchi H. A calorimetric study of the acid dissociation of the conjugate acids of poly(N-vinylimidazole) and polyallylamine. *Colloid and Polymer Science*. 2000;278: 1–7. https://doi.org/10.1007/s003960050001

18. Na C. K., Park G. Y., Park H. Polypropylene surface with antibacterial property by photografting 1-vinylimidazole and subsequent chemical modification. *Korean Journal of Chemical Engineering*. 2018;35: 1748–1755. https://doi.org/10.1007/s11814-018-0080-2

19. Camacho-Cruz L. A., Velazco-Medel M. A., Parra-Delgado H., Bucio E. Functionalization of cotton gauzes with poly(N-vinylimidazole) and quaternized poly(N-vinylimidazole) with gamma radiation to produce medical devices with pH-buffering and antimicrobial properties. *Cellulose*. 2021;28: 3279–3294. https://doi.org/10.1007/s10570-021-03725-w

20. Dimzon I. K. D., Knepper T. P. Degree of deacetylation of chitosan by infrared spectroscopy and partial least squares. *International Journal of Biological Macromolecules*, 2015:72: 939–945. https://doi.org/10.1016/j.ijbiomac.2014.09.050

21. Chattopadhyay D. P., Inamdar M. S. Aqueous behavior of chitosan. *International Journal of Polymer Science*. 2010;2010: 939536. https://doi.org/10.1155/2010/939536

Information about the authors

Andrey V. Sorokin , postgraduate student at the Polymer Science and Colloid Chemistry Department, research assistant at the Department of Biophysics and Biotechnology, Voronezh State University; research assistant at the Laboratory of Metagenomics and Food Biotechnologies, Voronezh State University of Engineering Technologies, Voronezh, Russian Federation; e-mail: andrew.v.sorokin@gmail.com; ORCID ID: https://orcid.org/0000-0001-5268-9557.

Marina G. Kholyavka, DSc in Biology, Associate

Condensed Matter and Interphases / Конденсированные среды и межфазные границы   2021;23(4): 570–577

A. V. Sorokin et al.   Synthesis of chitosan and N-vinylimidazole graft-copolymers...

Professor, Professor at the Department of Biophysics and Biotechnology, researcher at the Department of Biochemistry and Cell Physiology, Voronezh State University, Voronezh, Russian Federation; Professor at the Department of Physics; leading researcher at the Core Research Centre "Molecular Structure of Matter", Sevastopol State University, Sevastopol, Russian Federation; e-mail: holyavka@rambler.ru; ORCID ID: https://orcid.org/0000-0002-1390-4119.

Maria S. Lavlinskaya, PhD in Chemistry, researcher at the Department of Biophysics and Biotechnology, Voronezh State University, Voronezh, Russian Federation; researcher at the Laboratory of Metagenomics and Food Biotechnologies, Voronezh State University of Engineering Technologies, Voronezh, Russian Federation; e-mail: maria.lavlinskaya@gmail.com; ORCID ID: https://orcid.org/0000-0001-9058-027X.

Translated by Irina Charychanskaya
Edited and proofread by Simon Cox

Original articles

Synthesis and properties of nanosized ZnO/wood composite

E. V. Tomina[1,2✉], A. A. Pavlenko[2], A. I. Dmitrenkov[1], S. A. Neminushchaya[1]

[1]*Voronezh State University of Forestry and Technologies named after G. F. Morozov,
8 Timiryazeva ul., Voronezh 394087, Russian Federation*

[2]*Voronezh State University,
1 Universitetskaya pl., Voronezh 394018, Russian Federation*

Abstract

The aim of the study was to synthesise a ZnO/silver birch wood (*Bétula péndula*) nanocomposite and evaluate its physical and mechanical properties in comparison with an unmodified natural polymer.

Using the sol-gel method, we synthesised almost spherical impurity-free zinc oxide nanoparticles with a predominant particle size of about 20 nm. Amorphous hydrated $Zn(OH)_2$ was impregnated into the wood material at the gel formation stage. It resulted in the reaction of zinc hydroxide decomposition with the formation of ZnO nanoparticles in the wood as a nanoreactor.

The hydrophobic properties of the surface of ZnO/silver birch wood nanocomposite improved significantly (the contact angle of wetting doubled). Its moisture and water resistance decreased (2-5 times and 30%, respectively). The nanocomposite also showed less swelling in the radial (8-10 times) and tangential (2.6-10 times) directions in comparison with natural wood.

Keywords: Zinc oxide, Sol-gel synthesis, Nanoparticles, Silver birch wood (*Bétula péndula*), Impregnation, Modification

✉ Elena V. Tomina, e-mail: tomina-e-v@yandex.ru

Condensed Matter and Interphases / Конденсированные среды и межфазные границы   2021;23(4): 578–584

E. V. Tomina et al.   Synthesis and properties of nanosized ZnO/wood composite

1. Introduction

Nanocomposites containing nanosized ZnO are currently a large group of in-demand materials for a variety of applications. This is due to the unique combination of their properties, the availability of raw materials, and the possibility of creating economical and environmentally friendly industries [1]. The synthesis and study of the properties of nanocomposites based on polymers is one of the priority areas due to the wide variety of functional properties of such nanomaterials. There are two main ways to synthesise polymer nanocomposites: via physical mixing of polymers and nanostructured materials by mechanical milling and diffusion in liquid or gas using ultrasonic treatment, etc. [2, 3], and by the synthesis of nanoparticles in a polymer matrix as a result of chemical reactions [4].

Nanosized zinc oxide is used as a sulphur vulcanisation activator for natural and synthetic rubbers, and as a vulcanising agent for some elastomers containing functional groups such as -Cl, -COOH, etc. [5, 6]. Compared to bulk material of the same composition, zinc oxide nanoparticles increase the rate of vulcanisation and improve the mechanical properties of the samples. When synthesising composites, it is important to establish a correlation between the synthesis conditions, the content of the composite, and its physico-chemical and performance characteristics [7].

Wood is a renewable, natural polymer material. Currently, scientists are working on improving the properties of wood by impregnating it with various compositions that are combustible, toxic (carcinogenic), change the colour of wood, or have a pungent and persistent odour, a limited lifetime, flammable, etc. There is also a promising alternative approach: the synthesis of nature-like nanocomposites with improved functional properties based on low-value wood. The capillary-porous structure of wood can act as an excellent matrix for the impregnation of nanoparticles or their synthesis in wood as in a nanoreactor. Modifying natural wood with nanosized zinc, titanium, or magnesium oxide particles gives the wood surface super-hydrophobic properties and increases its bio-resistance [8–11].

The aim of the work was to synthesise a ZnO/silver birch nanocomposite and to evaluate its physical and mechanical properties compared to the unmodified wood.

2. Experimental

To synthesise zinc oxide, we used one of the "soft chemistry" methods, the sol-gel method. It allowed us to produce nanomaterials with a narrow particle-size distribution at relatively low temperatures. As a precursor, we used zinc nitrate $Zn(NO_3)_2 \cdot 6H_2O$ (chemically pure grade, GOST 5106-77). A 20% NaOH solution (GOST R 55064-2012) was used as the precipitant. First, a 0.5 M solution of $Zn(NO_3)_2$ was introduced drop by drop to the boiling water. After the salt had been added, we boiled the mixture for a few more minutes until a sol was formed. The resulting sol was cooled to room temperature, then a solution of sodium hydroxide was added in the amount necessary for complete precipitation of Zn^{2+} cations. The resulting gel was stirred for some time.

To characterise the zinc oxide nanoparticles, the gel was separated using a vacuum filter, washed with distilled water, and dried at room temperature until a stable weight. The gel was then annealed in air at 240 °C for 2 h. To study the phase composition of the powder, we used X-ray diffraction (XRD, Empyrean B.V. X-ray diffractometer with a Cu anode (λ = 1.54060 nm)). The scanning was performed within a range of angles 2θ = 0–80° with a step of 0.1. The size of the coherent scattering regions (CSRs) in zinc oxide samples was calculated based on the XRD data using the Scherrer formula (1):

$$D_{hkl} = \frac{k \cdot \lambda}{\beta_{hkl} \cdot \cos\theta} \qquad (1)$$

where D_{hkl} is the average particle size, Å, k is the correction factor (k = 0.9 for spherical particles), λ is the X-ray tube wavelength, θ is the position of the peak maximum in degrees, and β_{hkl} is the intrinsic physical broadening of the diffraction maximum in radians.

The size and morphology of the synthesised powder particles were determined by transmission electron microscopy (TEM, CarlZeiss Libra-120 transmission electron microscope).

To study the effect of zinc oxide nanoparticles on the properties of a natural polymer material,

Condensed Matter and Interphases / Конденсированные среды и межфазные границы   2021;23(4): 578–584

E. V. Tomina et al.   Synthesis and properties of nanosized ZnO/wood composite

we chose samples of silver birch wood (*Bétula péndula*) from the experimental forestry of Voronezh State University of Forestry and Technologies named after G. F. Morozov. This birch is one of the most common hardwoods growing in the Russian Federation. For the synthesis of the ZnO/wood nanocomposite, silver birch (*Bétula péndula*) samples, pre-dried at 103 °C, were placed in the gel for 30 min, then dried in a desiccator for 6 h at 110 °C.

To determine their moisture absorption qualities, the nanocomposite samples were dried to an absolutely dry state according to the requirements of GOST 16483.7-71 and weighed with an error of not more than 0.001 g on ACZET CY-64 analytical scales. Distilled water was poured on the bottom of the desiccator, the samples were placed on the desiccator platform on their sides so that they did not touch each other and the walls of the desiccator. The samples were kept in a closed desiccator at 20 ± 2 °C. The first weighing of the samples was performed one day after placing them in the desiccator, subsequent measurements were performed after 2, 3, 6, 9, 13, 20, and 30 days. The percentage of moisture absorbed (*W*) was calculated with an accuracy of 0.1 % using formula (2).

$$W = \frac{m_n - m_1}{m_1} \cdot 100\,\%, \tag{2}$$

where m_1 is the weight of the absolutely dry sample in grams; and m_n is the weight of the sample weighed after *n* days from the time when it was first placed in the desiccator in grams.

To determine their water absorption, the nanocomposite samples were dried at 103 °C in weighing bottles until absolutely dry and placed to the bottom of the desiccator with distilled water, so that the samples were completely covered with water. The amount of water absorbed was calculated using formula (2). The samples were weighed after 1, 3, 10, and 30 days.

The samples used to determine water absorption were removed from the desiccator after a certain period of time. Their parameters were measured in the tangential and radial directions using a micrometer with an accuracy of 0.01 mm. Then, the radial and tangential swelling values were determined by formulas (3 and 4).

$$a_t = \frac{L_{t\max} - L_{t\min}}{L_{t\min}} \times 100\,\%, \tag{3}$$

$$a_R = \frac{L_{R\max} - L_{R\min}}{L_{R\min}} \cdot 100\,\%, \tag{4}$$

where $L_{t\max}$, $L_{R\max}$ are the dimensions of the sample in the tangential and radial directions respectively after soaking in water for 1, 3, 10, and 30 days; $L_{t\min}$, $L_{R\min}$ are the dimensions of the absolutely dry sample in the tangential and radial directions respectively.

The contact angle of wetting of the ZnO/ silver birch wood (*Bétula péndula*) nanocomposite samples with distilled water was measured by the sessile drop method using a goniometer and the HIview 10 software. The liquid was applied to the wood surface using a 0.01 ml microsyringe. Images were made with a handheld camera of the Digital Microscope (Ruihoge, China) and recorded for 1, 30, and 60 seconds.

3. Results and discussion

According to [12, 13], zinc oxide powders synthesised in neutral or weak acid media (pH = 6, 7) are amorphous, which is probably due to the suppression of zinc nitrate hydrolysis under these conditions. As we know from [14], the sol-gel synthesis of ZnO nanopowder at pH = 9 promotes the formation of crystalline samples. Indeed, the X-ray pattern (JCPDS, card 36-1451) showed the narrow high intensity reflections corresponding to zinc oxide. They indicate the synthesis of ZnO nanocrystals (Fig. 1). A noticeable background level may be due to the presence of a certain fraction of the amorphous phase of zinc oxide. The average CSR value of zinc oxide particles, calculated by the Scherrer formula, is 22 ± 2 nm (Table 1).

Table 1. The average CSR of the synthesised ZnO sample

The CSR diameter of the particles, nm	D_1	D_2	D_3	D_{cp}
ZnO	19±3	20±2	26±1	22±2

The TEM results are consistent with the XRD data (Fig. 2). TEM images show that the zinc oxide particles synthesised by the sol-gel method are almost spherical. The particle size of the predominant fraction does not exceed 20
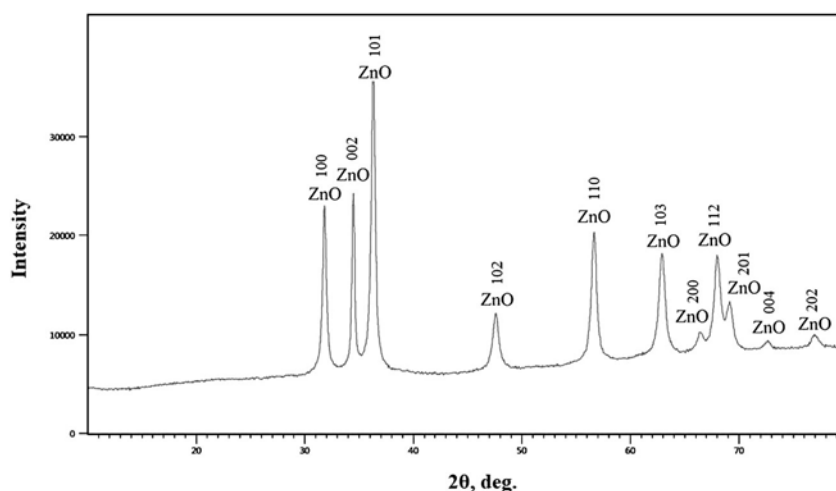
Condensed Matter and Interphases / Конденсированные среды и межфазные границы   2021;23(4): 578–584

E. V. Tomina et al.   Synthesis and properties of nanosized ZnO/wood composite

Fig. 1. Diffraction pattern of the ZnO sample synthesised via sol-gel method using NaOH as a precipitant

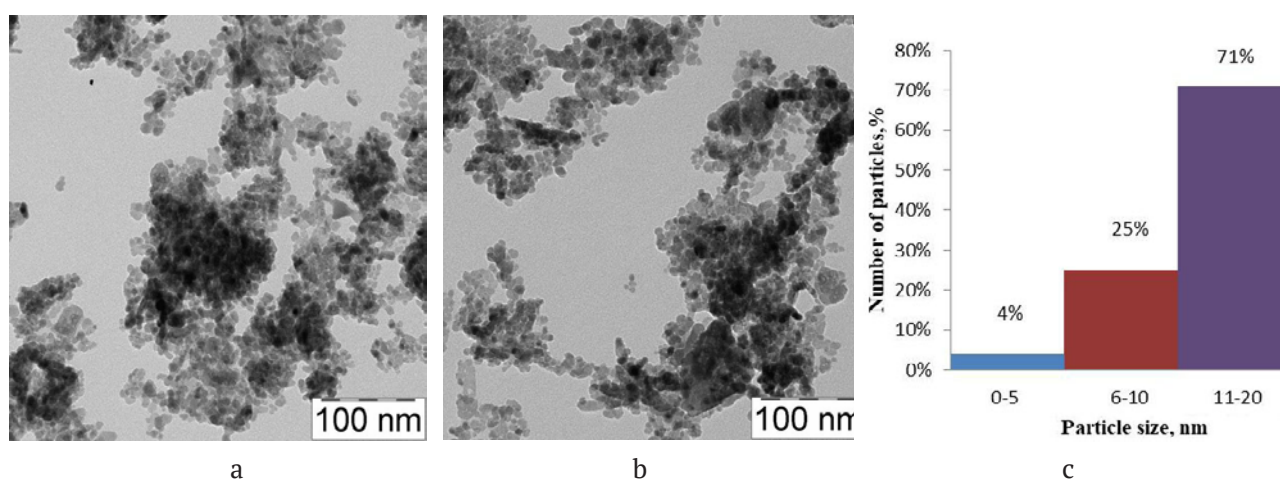a   b   c

Fig. 2. TEM images of ZnO in the gel layer – a), b), and c) – ZnO particle size distribution histogram

nm, the degree of agglomeration is low, and the size of agglomerates is less than 150 nm. The sizes and morphological features of zinc oxide nanoparticles suggest their free penetration into silver birch (*Bétula péndula*) samples through the conductive elements of wood, vessels (diameter from 0.02 to 0.5 mm).

The gel formed after the introduction of a precipitant during the synthesis of ZnO is a loose amorphous zinc hydroxide with a variable water content. This gel enters the wood through conducting vessels. The presence of water molecules facilitates the penetration of $Zn(OH)_2$ into the cavities of the wood, as wood is highly hydrophilic. When heated to 373 K and higher, zinc hydroxide begins to lose water, which is accompanied by decomposition into zinc oxide [15]. A number of studies on the synthesis of zinc oxide nanoforms confirm this temperature

range of hydroxide decomposition [16, 17]. Thus, the size and morphological features of zinc oxide nanoparticles are largely determined by the size and shape of the silver birch wood cavities (*Bétula péndula*) filled with hydrated $Zn(OH)_2$ gel. The retention of heated ZnO nanoparticles in wood vessels and capillaries is facilitated by the interaction of the polar reactive O-ZnO surface with functional groups of wood components (e.g., OH-groups of cellulose). This interaction results in the formation of hydrogen bonds [18].

Analysis of the values of the contact angle of water on the surfaces of natural birch and the ZnO/silver birch wood (*Bétula péndula*) nanocomposite (Table 2) showed that the introduction of zinc oxide nanoparticles into the wood vessels significantly increased the hydrophobic properties of the surface (the contact angle increased more than twofold).

Condensed Matter and Interphases / Конденсированные среды и межфазные границы   2021;23(4): 578–584

E. V. Tomina et al.   Synthesis and properties of nanosized ZnO/wood composite

Table 2. The contact angle of birch wood and ZnO/wood nanocomposite

Sample composition	The contact angle after 20 seconds, deg.
Birch wood	30
ZnO/wood nanocomposite	75

Filling the wood cavities with nanosized zinc oxide significantly reduced moisture and water absorption in the birch wood. After 1 day of the experiment, the moisture absorption (Fig. 3A) of the ZnO/silver birch wood (*Bétula péndula*) nanocomposite was 2.5 %, compared with 12.1 % for natural birch wood. After 30 days this parameter increases to 12.5 % for the composite and to 26 % for natural birch wood. Thus, impregnating zinc oxide nanoparticles in the natural polymer reduced its moisture absorption by almost 5 times after 1 day of testing. This effect decreased over time, but was still pronounced (the moisture absorption of the nanocomposite was half that of birch wood). The water absorption (Fig. 3B) of silver birch wood (*Bétula péndula*) doped with nanosized zinc oxide was 30 % less after one day of testing compared to natural wood (diagram 1). After 30 days of testing, the effectiveness of ZnO hardly diminished and the water absorption of the composite remained 30% lower than that of untreated birch wood (*Bétula péndula*).

Doping birch wood with zinc oxide nanoparticles reduced the swelling in both the radial (Fig. 3C)

and tangential (Fig. 3D) directions. After 1 day in water, the swelling of ZnO/silver birch wood (*Bétula péndula*) nanocomposite was practically 10 times lower in both radial and tangential directions compared to untreated birch wood. After 30 days of testing for water resistance, the swelling improvement of the doped wood decreased slightly and reached 8 times in the tangential direction and 2.6 times in the radial direction.

4. Conclusions

Using the sol-gel method with sodium hydroxide as precipitant, we synthesised zinc oxide nanoparticles with predominant size of about 20 nm and almost spherical shape (TEM data) at relatively low temperatures. Amorphous hydrated $Zn(OH)_2$ was impregnated into the wood material at the gel formation stage. It resulted in the reaction of zinc hydroxide decomposition with the formation of ZnO nanoparticles in the wood as a nanoreactor. The hydrophobic properties of the surface of ZnO/silver birch (*Bétula péndula*) wood nanocomposite improved significantly (the contact angle doubled). Its moisture and water resistance decreased (2–5 times and 30 %, respectively). The nanocomposite also showed less swelling in the radial (8-10 times) and tangential (2.6–10 times) directions in comparison with natural wood.

Author contributions

All authors made an equivalent contribution to the preparation of the publication.
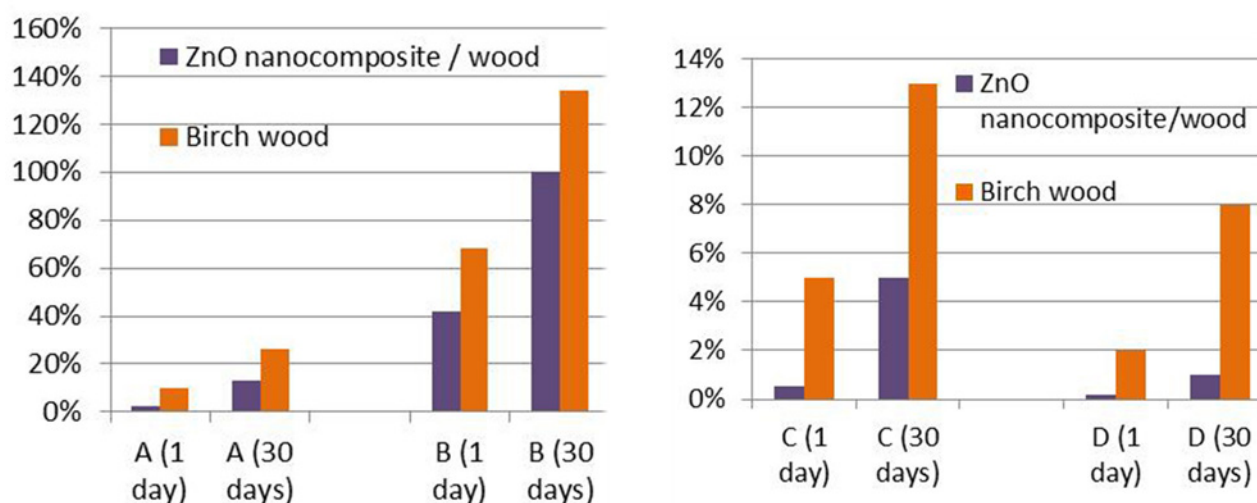
Fig. 3. Moisture absorption (A), water absorption (B), swelling in the radial (C) and tangential (D) directions of birch wood after 1 and 30 days of testing (%)

Condensed Matter and Interphases / Конденсированные среды и межфазные границы   2021;23(4): 578–584

E. V. Tomina et al.   Synthesis and properties of nanosized ZnO/wood composite

Conflict of interests

The authors declare that they have no known competing financial interests or personal relationships that could have influenced the work reported in this paper.

References

1. Sunandan B., Joydeep D. Hydrothermal growth of ZnO nanostructures. *Science and Technology of Advanced Materials*. 2009;10(1): 1–18. https://doi.org/10.1088/1468-6996/10/1/013001

2. Yang Y., Li Y.-Q., Fu S.-Y., Xiao H.-M. Transparent and light-emitting epoxy nanocomposites containing ZnO quantum dots as encapsulating materials for solid state lighting. *Journal of Physical Chemistry C*. 2008; 112 (28): 10553–10558. https://doi.org/10.1021/jp802111q

3. Dong Y., Chaudhary D., Ploumis C., Lau K. T. Correlation of mechanical performance and morphological structures of epoxy micro/nanoparticulate composites. *Composites Part A: Applied Science and Manufacturing*. 2011;42(10): 1483–1492. https://doi.org/10.1016/j.compositesa.2011.06.015

4. Nebukina E. G., Khokhlov E. M., Zaporozhets M. A., Vitukhnovskii A. G., Gubin S. P. A comparative study of the structural and spectral characteristics of ZnO nanoparticles dispersed in isopropanol and polyethylene. *Inorganic Materials*. 2011;47(2): 143–147. https://doi.org/10.1134/S0020168511020117

5. Demir M. M., Koynov K., Akbey Ü., Bubeck C., Park I., Lieberwirth I., Wegner G. Optical properties of composites of PMMA and surface-modified zincite nanoparticles. *Macromolecules*. 2007;40(4): 1089–1100. https://doi.org/10.1021/ma062184t

6. Galimova E. M., Dorozhkin V. P., Kochnev A. M. Vliyanie mekhanoaktivirovannykh oksida tsinka i difenilguanidina na kinetiku sernoi vulkanizatsii izoprenovogo kauchuka [Influence of mechanically activated zinc oxide and diphenylguanidine on the kinetics of sulphur vulcanisation of isoprene rubber]. *Bulletin of Kazan Technological University*. 2011; (19): 144–147. Available at: https://www.elibrary.ru/item.asp?id=17062989 (In Russ.)

7. Tsang S., Avdeeva A. V., Muradova A. G., Yurtov E. V. Poluchenie nanosterzhnei oksida tsinka khimicheskimi zhidkofaznymi metodami [Preparation of zinc oxide nanorods by chemical liquid-phase methods]. *Khimicheskaya Tekhnologiya*. 2014;15(12): 715–722. Available at: https://www.elibrary.ru/item.asp?id=22662585 (In Russ.)

8. Lulu X., Ye X., Baokang D., Zhangning Ye., Chunde J., Qingfeng S., Xiaohong Yu. Insitu anchoring of Fe_3O_4/ZIF-67 dodecahedrons in highly compressible wood aerogel with excellent microwave absorption properties. *Materials & Design*. 2019;182(15): 108006. https://doi.org/10.1016/j.matdes.2019.108006

9. Cai T., Shen X., Huang E., Yan Y., Shen X., Wang, F., ... Sun Q. Ag nanoparticles supported on MgAl-LDH decorated wood veneer with enhanced flame retardancy, water repellency and antimicrobial activity. *Colloids and Surfaces A: Physicochemical and Engineering Aspects*. 2020;598(5): 124878. https://doi.org/10.1016/j.colsurfa.2020.124878

10. Holy S., Temiz A., Köse Demirel G., Aslan M., Mohamad Amini M. H. Physical properties, thermal and fungal resistance of Scots pine wood treated with nano-clay and several metal-oxides nanoparticles. *Wood Material Science and Engineering*. 2020;16(1): 1–10. https://doi.org/10.1080/17480272.2020.1836023

11. Qiu Z., Xiao Z., Gao L., Li J., Wang H., Wang Y., Xie Y. Transparent wood bearing a shielding effect to infrared heat and ultraviolet via incorporation of modified antimony-doped tin oxide nanoparticles. *Composites Science and Technology*. 2019;172(1): 43–48. https://doi.org/10.1016/j.compscitech.2019.01.005

12. Alias S. S., Ismail A. B., Mohamad A. A. Effect of pH on ZnO nanoparticle properties synthesized by sol–gel centrifugation. *Journal of Alloys and Compounds*. 2010;499(2): 231–237. https://doi.org/10.1016/j.jallcom.2010.03.174

13. Rani S., Suri P., Shishodia P. K., Mehra R. M. Synthesis of nanocrystalline ZnO powder via sol-gel route for dye-sensitized solar cells. *Solar Energy Materials & Solar Cells*. 2008;92(12): 1639–1645. https://doi.org/10.1016/j.solmat.2008.07.015

14. Karpova S. S., Moshnikov V. A., Myakin S. V., Kolovangina E. S. Surface functional composition and sensor properties of ZnO, Fe_2O_3, and $ZnFe_2O_4$. *Semiconductors*. 2013;47(3): 392–395. https://doi.org/10.1134/S1063782613030123

15. Lidin R. A., Molochko V. A., Andreeva L. L. *Khimicheskie svoistva neorganicheskikh veshchestv*

Condensed Matter and Interphases / Конденсированные среды и межфазные границы   2021;23(4): 578–584

E. V. Tomina et al.   Synthesis and properties of nanosized ZnO/wood composite

[Chemical properties of inorganic substances]. Moscow: Koloss Publ.; 2006. 480 p. (In Russ.)

16. Qu X., Jia D. Synthesis of octahedral ZnO mesoscale superstructures via thermal decomposing octahedral zinc hydroxide precursors. *Journal of Crystal Growth.* 2009;311(4): 1223–1228. https://doi.org/10.1016/j.jcrysgro.2008.11.079

17. Zhu Y., Zhou Y. Preparation of pure ZnO nanoparticles by a simple solid-state reaction method. *Applied Physics A.* 2008; 92 (2): 275–278. https://doi.org/10.1007/s00339-008-4533-z

18. Vrublevskaya V. I., Matusevich V. O., Kuznetsova V. V. Substantiation of the interaction mechanism of wood components and water. *Bulletin of Higher Educational Institutions. Lesnoi Zhurnal (Forestry Journal).* 2017;3(357): 152–163. https://doi.org/10.17238/issn0536-1036.2017.3.152

Information about the authors

Elena V. Tomina, DSc in Chemistry, Associate Professor, Head of the Department of Chemistry, Morozov Voronezh State University of Forestry and Technologies, Voronezh, Russian Federation; e-mail: tomina-e-v@yandex.ru. ORCID iD: https://orcid.org/0000-0002-5222-0756.

Anna A. Pavlenko, 1st year master's degree student, Voronezh State University, Voronezh, Russian Federation; e-mail: pavlenko-a-a@mail.ru. ORCID iD: https://orcid.org/0000-0003-4899-609X.

Aleksandr I. Dmitrenkov, PhD in Technical Sciences, Morozov Voronezh State University of Forestry and Technologies, Voronezh, Russian Federation; e-mail: dmitrenkov2109@mail.ru. ORCID: https://orcid.org/0000-0001-9296-1762.

Sofiya A. Neminushchaya, student, Morozov Voronezh State University of Forestry and Technologies, Voronezh, Russian Federation; e-mail: nem.sofi@bk.ru ORCID: https://orcid.org/0000-0003-2203-3324.

Translated by Anastasiia Ananeva
Edited and proofread by Simon Cox

Original articles

Hydrothermal assisted conventional sol-gel method for synthesis of bioactive glass 70S30C

Ta Anh Tuan[1], Elena V. Guseva[1], Nguyen Anh Tien[2], Ha Tuan Anh[3], Bui Xuan Vuong[4], Le Hong Phuc[5]✉, Nguyen Quan Hien[5], Bui Thi Hoa[6,7], Nguyen Viet Long[8]

[1]Faculty of Chemical Technologies, Kazan National Research Technological University,
68 ul. K. Marksa, Kazan 420015, Tatarstan, Russian Federation

[2]Faculty of Chemistry, Ho Chi Minh City University of Education,
280 An Dương Vương str., Ward 4, District 5, Ho Chi Minh City, Vietnam

[3]Thu Dau Mot University,
6 Tran Van On str., Phu Hoa Ward, Thu Dau Mot City, Binh Duong Province 820000, Viet Nam

[4]Faculty of Pedagogy in Natural Sciences, Sai Gon University,
Ho Chi Minh City, Vietnam

[5]Institute of Applied Mechanics and Informatics,
291 Dien Bien Phu str., District 03, Ho Chi Minh City 700000, Vietnam

[6]Institute of Theoretical and Applied Research, Duy Tan University,
Hanoi 100000, Vietnam

[7]Faculty of Natural Sciences, Duy Tan University,
Da Nang 550000, Vietnam

[8]Department of Electronics and Telecommunication, Sai Gon University,
Ho Chi Minh City 700000, Vietnam

Abstract

Bioactive glasses (Bioglasses) are widely synthesized by the conventional sol-gel method consisting of two main steps for sol and gel formation. However, the conversion from sol to gel requires a long time (5–7 days). In this study, the hydrothermal system was used to quickly synthesize the bioactive glass by reducing the conversion time from sol to gel. The hydrothermal assisted conventional sol-gel method was applied for synthesis of the bioactive glass $70SiO_2$–$30CaO$ (mol%) (noted as 70S30C). The synthetic glass was investigated by the physical-chemical techniques. The ''in vitro'' experiments in SBF (Simulated Body Fluid) solution was also performed to evaluate the bioactivity of synthetic material. The obtained results show that the bioactive glass 70S30C was successfully elaborated by using the hydrothermal assisted conventional sol-gel method. The consuming time was reduced compared to the conventional method. The physical-chemical characterization confirmed that the synthetic glass is amorphous material with mesoporous structure consisting of interconnected particles. The specific surface area, pore volume and average pore diameter of synthetic glass were 142.8 m^2/g, 0.52 cm^3/g, and 19.1 nm, respectively. Furthermore, synthetic bioactive glass exhibited interesting bioactivity when immersed in simulated body fluid (SBF) solution for 1 days and good biocompatibility when cultured in cellular media.

Keywords: Bioactive glass, Hydrothermal assisted sol-gel, Bioactivity, in vitro, Cell viability

✉ Le Hong Phuc, e-mail: lhphuc76@yahoo.com

Condensed Matter and Interphases / Конденсированные среды и межфазные границы   2021;23(4): 585–593

Ta Anh Tuan et al.   Hydrothermal assisted conventional sol-gel method for synthesis of bioactive glass...

1. Introduction

In the past fifty years, bioactive glasses (bioglasses) have been developed and applied as artificial bone materials used as components in dental filling, implants, and bone grafting in orthopedic surgery to restore and repair damaged and diseased bones [1–2]. Their bioactivity is shown by the formation of a new layer of hydroxyapatite $Ca_{10}(PO_4)_6(OH)_2$ (HA) on the surfaces when they are implanted in defective and broken bone positions in the human body. The HA mineral is the inorganic component of human bone, so it is an interconnected linkage connecting the artificial graft made from bioglass and natural bone, through which the missing and broken bones are repaired and filled [3–5].

The first bioglass with the composition of $45SiO_2–24.5CaO–24.5Na_2O–6P_2O_5$ (wt%) (Denoted as 45S5) was discovered in 1969 by Larry Hench [6]. After this invention, many bioglass systems with different components such as 46S6, 58S, 55S, 70S30C, S53P4, etc. were studied, synthesized, and applied [1–2].

There are two main methods for bioglass synthesis. The first one is melting of precursors at high temperatures (melting method). The method can quickly prepare glass systems in large quantities. However, it requires synthesis processes at high temperatures (above 1350 °C) where volatile components such as P_2O_5 can be escaped, resulting in deviations in the composition of synthetic bioglasses; obtained materials often have low values of specific surface area [7]. The second one is to synthesize glass systems in solution undergoing sol- and gel-forming processes (sol-gel method). This process overcomes the disadvantages of melting method because it is performed at lower temperatures; resulting glass systems with larger values of specific surface area, leading to higher activity [8–9]. However, the sol-gel method requires long times for synthesis because the conversion from sol to gel usually takes from a few days to one week. Therefore, the modified sol-gel processes to shorten the synthesis times will be effective for the preparation of bioglass materials. On the other hand, variable synthesis processes can bring new properties of synthetic glass systems.

The purpose of this work is to synthesize the bioglass $70SiO_2–30CaO$ (mol%) by using the hydrothermal assisted sol-gel method, in which the synthesis time was greatly shortened. The physic-chemical characterizations and bioactivity of synthetic bioglass were investigated.

2. Experimental

2.1. Synthesis of bioactive glass

The bioglass $70SiO_2–30CaO$ (mol%) selected in this study is well-known and reported in the previous studies, in which it was synthesized by the sol-gel method [7–10]. The main precursors for the synthesis of bioglass included tetraethyl orthosilicate $Si(OCH_2CH_3)_4$ (TEOS, ⩾ 99.0%, Sigma-Aldrich), calcium nitrate tetrahydrate $Ca(NO_3)_2.4H_2O$ (CNT, ⩾ 98%, Merck). Hydrothermal assisted sol-gel method for bioglass synthesis is described as below. Firstly, 29.2 g of TEOS and 14.2 g of CNT were added in 25.2 g of distilled water. The molar ratio of H_2O/TEOS was selected as 10. The pH of mixture was adjusted to a value of 1.5 by adding 1M HNO_3 solution. The sol was formed after stirring for 1 hour at room temperature (32.2 °C). Next, the formed sol was put into a Teflon-lined stainless steel system, which was then heated in an oven at 150 C for 12 hours. After that, the resulting gel dried at 150 °C for 24 hours. Finally, the bioglass was obtained by sintering dried gel at 700 °C for 3 hours. To examine the phase evolution, the other samples of dried gel were heated at 800 and 1000 °C at the same times as above. The hydrothermal assisted sol-gel synthesis is briefly described in Fig. 1. It is worthy to mention that the consuming time of bioglass synthesis in this study was significantly shortened compared to the conventional sol-gel process [7, 10].

2.2. ''In vitro'' test in SBF solution

The bioactivity of synthetic bioglass was investigated by ''in vitro'' experiment according to Kokubo's method [11]. The glass material is immersed in simulate body fluid (SBF) solution at a stirring rate of 100 rpm and a temperature of 37 °C for 1, 2, 7, 10, and 15 days. The simulated body fluid (SBF) solution with inorganic ionic components similar to human blood, is synthesized in laboratory. The composition of simulated body fluid (SBF) solution is presented in the Table 1. After immersion in simulated body fluid (SBF) solution, the hydroxyapatite (HA) layer
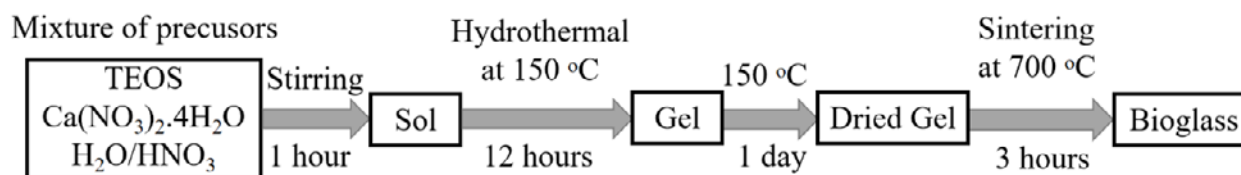
Condensed Matter and Interphases / Конденсированные среды и межфазные границы   2021;23(4): 585–593

Ta Anh Tuan et al.   Hydrothermal assisted conventional sol-gel method for synthesis of bioactive glass...

Fig. 1. Flow chart of hydrothermal assisted sol-gel synthesis of bioglass 70S

Table 1. Ionic concentration of SBF solution (mmol/L)

Composition	Na^+	K^+	Ca^{2+}	Mg^{2+}	Cl^-	HCO_3^-	HPO_4^{2-}
SBF	142.0	5.0	2.5	1.5	148.0	4.2	1.0
Plasma	142.0	5.0	2.5	1.5	103.0	27.0	1.0

will form on the surface of glass material if it is biologically active.

2.3. "In vitro" in cellular medium

"In vitro" tests were performed in according with the protocols reported by T. Mosmann [12]. The used culture environment was standard medium DMEM (Sigma Chemical Co., St. Louis, MO) consisting of 15 mM HEPES, 2 mM L-glutamine, 10% FBS (Fetal Bovine Serum), 100 UI/mL penicillin and 100 µg/mL streptomycin. Osteoblast-like $SaOS_2$ and endothelial-like Eahy926 were cultivated in DMEM at 37 °C in a humidified incubator with 5% CO_2 and 95% humidity.

The cytotoxicity was determined by using the colorimetric MTT assay [13]. The MTT (3-(4,5-Dimethylthiazol-2-yl)-2,5-diphenyl-tetrazolium bromide, a yellow tetrazole) is reduced to purple formazan in the mitochondria of living cells. The absorbance of this colored solution can be quantified by measuring at a certain wavelength (usually between 500 and 600 nm) by a spectrophotometer. The absorption maximum is dependent on the solvent employed. This reduction takes place only when mitochondrial reductase enzymes are active, and therefore conversion can be directly related to the number of living cells.
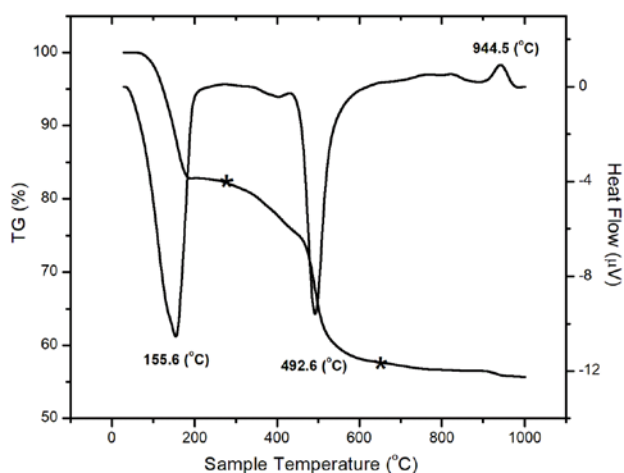
2.4. Physico-chemical characterization

The thermal properties of as-sintering bioglass were investigated by a Thermogravimetry-Differential Scanning Calorimetry (TG-DSC, SETERAM, LABSYS Evo). Powder sample was placed in a platinum crucible and then heated

from room temperature to 1000 °C at a ratio of 10 K.min⁻¹ in dried air. From this analysis, the suitable temperature for the stabilization of synthetic bioglass was chosen. The specific surface area, pore size, and pore volume of synthetic bioglass were measured by N_2 adsorption/desorption using a micromeritics porosimeter (Quantachrome Instruments). The specific surface area was calculated using the Brunauer-Emmett-Teller (BET) method. The pore size and pore volume were derived from the desorption branch of the isotherm curve using the Barrett-Joyner-Halanda (BJH) technique. The morphology of the synthetic glass was observed by a Field Emission Scanning Electron Microscopy (FE-SEM, S-4800, Japan). The phase composition of the synthetic samples was investigated using X-ray powder diffraction (XRD, D8-Advance) with Cu-K_α radiation (λ = 1.5406Å). The samples were scanned in the range from 5 to 80° (2θ) with a step of 0.02°. The composition of synthetic glass was determined by X-ray fluorescence technique (PHILIPS, PW2400). The pH and Si, Ca, P concentration behaviors versus immersion times were determined by using the pH meter and inductively coupled plasma optical emission spectrometry (ICP-OES) (ICP 2060) method.

3. Results and discussion

3.1. Characterization of synthetic bioactive glass

TG-DSC curves of dried gel are represented in Fig. 2. Two mass-loss intervals were identified in the ranges of 30 – 279 °C and 279–658 °C. The first mass-loss with an endothermic peak at 155.6 °C, which is attributed to the removal of water [14].
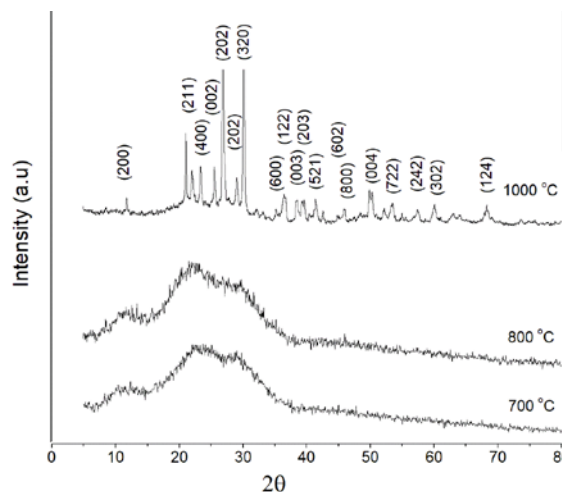
Condensed Matter and Interphases / Конденсированные среды и межфазные границы   2021;23(4): 585–593

Ta Anh Tuan et al.   Hydrothermal assisted conventional sol-gel method for synthesis of bioactive glass...

Fig. 2. TG-DSC analysis of as-sintering bioactive glass

Fig. 3. XRD diagrams of sample heated at 700, 800 and 1000 °C

The second one with an endothermic peak at 492.6 °C is characteristic of the decomposition of NO_3^- groups [10]. An exothermic peak without the mass loss at 944.5 °C is related to the crystallization of $CaSiO_3$ phase [10, 14]. From the thermal analysis, the suitable temperature for calcination was identified 700 °C, where nitrates groups are completely removed.

Fig. 3 represents the XRD patterns of sample heated at 700, 800 and 1000 °C. The XRD diagram of synthetic bioactive glass obtained at 700 °C showed some broad diffraction halos, characteristic of the amorphous material. Thus, the bioactive glass $70SiO_2$–$30CaO$ prepared by hydrothermal assisted sol-gel method still keeps the nature of glass like it was synthesized by the conventional sol-gel method [10, 14]. The composition of synthetic bioglass was analyzed using X-ray fluorescent spectroscopy (XRF). Compared to the calculated composition, the synthetic bioglas represents a moderate difference in composition (Table 2). This difference is explained by the amorphous structure of the synthetic bioglass, which leads to the uneven distribution of Ca, P, and O elements in the network of synthetic bioglass. The XRD diagram of sample heated at 1000 °C confirmed the crystallization of $CaSiO_3$ phase according to the TG-DSC analysis.

Table 2. The composition of bioglass $70SiO_2$–$30CaO$

Constituent (mol %)	SiO_2	CaO
Nominal	70	30
Analyzed	73.6	26.4

Textural and morphology of synthetic bioglass were investigated by N_2 adsorption/desorption and FE-SEM analyses (Fig. 4). The isotherm of synthetic bioglass shows type IV according to IUPAC nomenclature, typical of mesoporous material with the pore diameter in the range of 2–50 nm (Fig. 4a) [15–17]. The hysteresis loop is type H_2, given by complex pore structure in which network effect is important. The steep desorption branch can be attributed to pore-blocking or percolation in a narrow range of pore necks [16]. From the adsorption branch of isotherm curve, the pore size distribution and pore volume for synthetic bioglass were obtained by using the BJH model. The textural properties of synthetic bioglass are summarized in the table 3. The textural values of bioglass synthesized by the green synthesis are quite similar to those achieved for the bioglass with the same composition prepared by the conventional sol-gel method [10]. The morphology examination of synthetic bioglass was investigated by FE-SEM analysis. The observation shows obvious aggregations consisting of small particles, which were interconnected to form the mesoporous structure of the synthetic bioglass (Fig. 4b). According to the references, the Ca^{2+} immobilization onto the surface of silica particles modifies their surface chemistry, resulting in particle aggregation [18-19]. Under the effect of hydrothermal reaction, the Ca^{2+} ions could diffuse and act as strong cross-linkers between the silica particles, leading to highly aggregated particles.
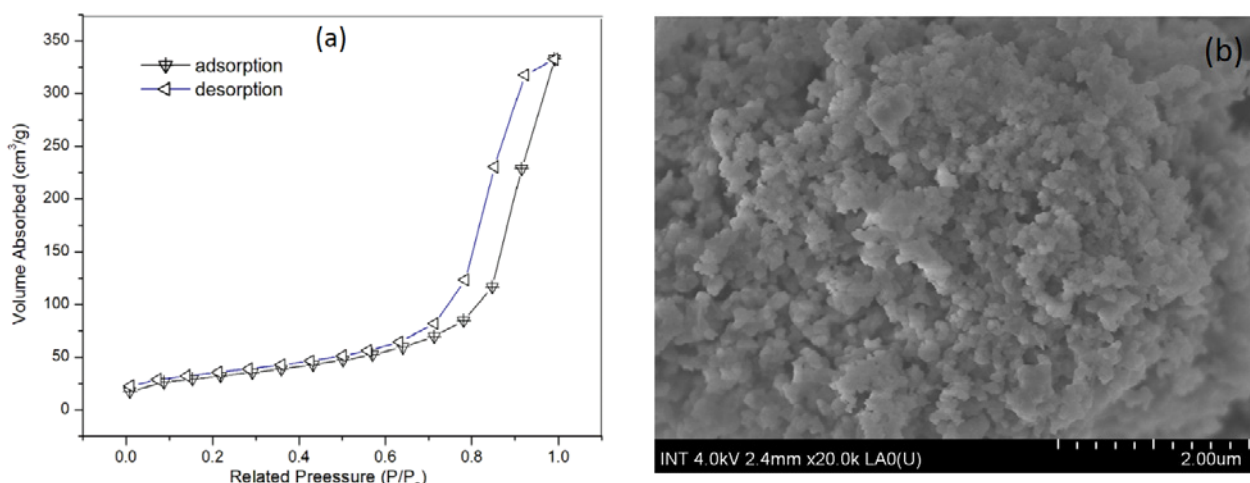
Condensed Matter and Interphases / Конденсированные среды и межфазные границы   2021;23(4): 585–593

Ta Anh Tuan et al.   Hydrothermal assisted conventional sol-gel method for synthesis of bioactive glass...

Fig. 4. a) N_2 adsorption/desorption isotherm and b) FE-SEM image of synthetic bioactive glass

Table 3. Nitrogen adsorption/desorption characterization of bioactive glass $70SiO_2–30CaO$

Sample	Specific Surface Area (m^2/g)	Total Pore Volume (cm^3/g)	Average Pore Diameter (nm)
$70SiO_2–30CaO$	142.8	0.52	19.1

3.2. Bio-mineralization

Fig. 5 represents the XRD diffractograms of synthetic bioactive glass after immersion in simulated body fluid (SBF) solution for 1, 2 and 7 days. The apatite mineral was confirmed by the well-defined appearance of two hydroxyapatite (HA) peaks at about 26° (002) and 32° (211) (JCPDS: 09432). This obtained result is similar to previous research for the same bioactive glass synthesized by the conventional sol-gel method and highlights the bioactivity of bioactive glass prepared by the hydrothermal assisted sol-gel method in this study [10, 14].

Fig. 6 shows the FE-SEM images of bioactive glass after different days in SBF. The formation of new HA was identified by a new crystalline layer, covering on the surfaces of glass samples after immersion in comparison with the sample before immersion presented in Fig. 4b.

3.3. Degradation of bioactive glass in SBF

The ionic behaviors in simulated body fluid (SBF) solution as a function of immersion time were represented in Fig. 7. The ionic changes are related to the surface reactions between the bioactive glass and the SBF solution [6, 20].

A significant increase of pH value was observed during the first seven days of immersion.

This observation corresponds to the quick ion exchange of Ca^{2+} out of the bioactive glass and H^+ in the SBF solution as the following reaction:

$$(-Si-O-Si-O-)Ca^{2+} + H^+ \rightarrow$$
$$\rightarrow -Si-O-Si-OH + Ca^{2+} \tag{1}$$
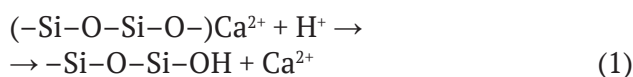
The H^+ consumption in reaction 1 lead to an increasing pH value. After that, the pH value was almost constant due to the end of reaction 1.

The release of Si element is due to the dissolution of glass network in SBF solution by
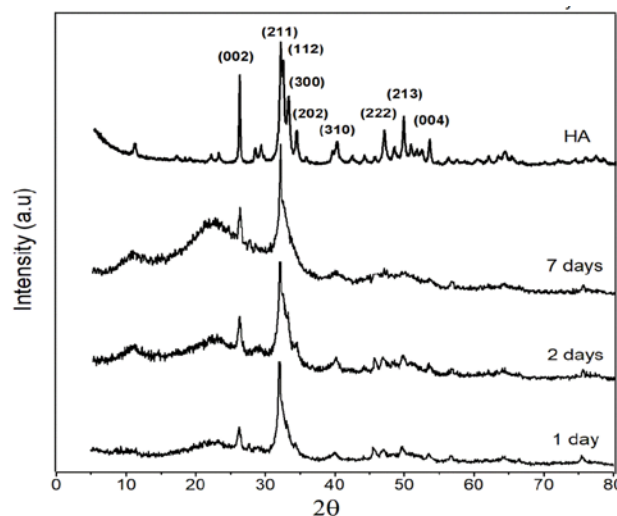

Fig. 5. XRD diagram of bioactive glass after immersion in SBF for 1, 2 and 7 days
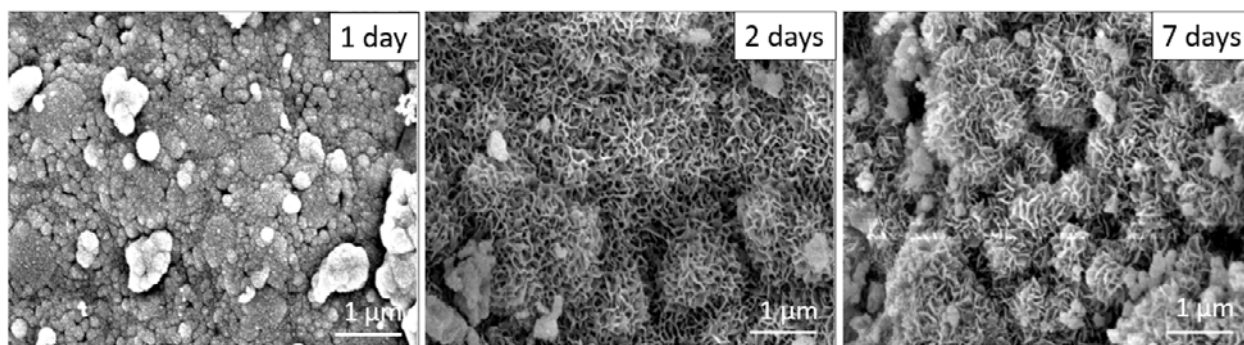
Condensed Matter and Interphases / Конденсированные среды и межфазные границы   2021;23(4): 585–593

Ta Anh Tuan et al.   Hydrothermal assisted conventional sol-gel method for synthesis of bioactive glass...

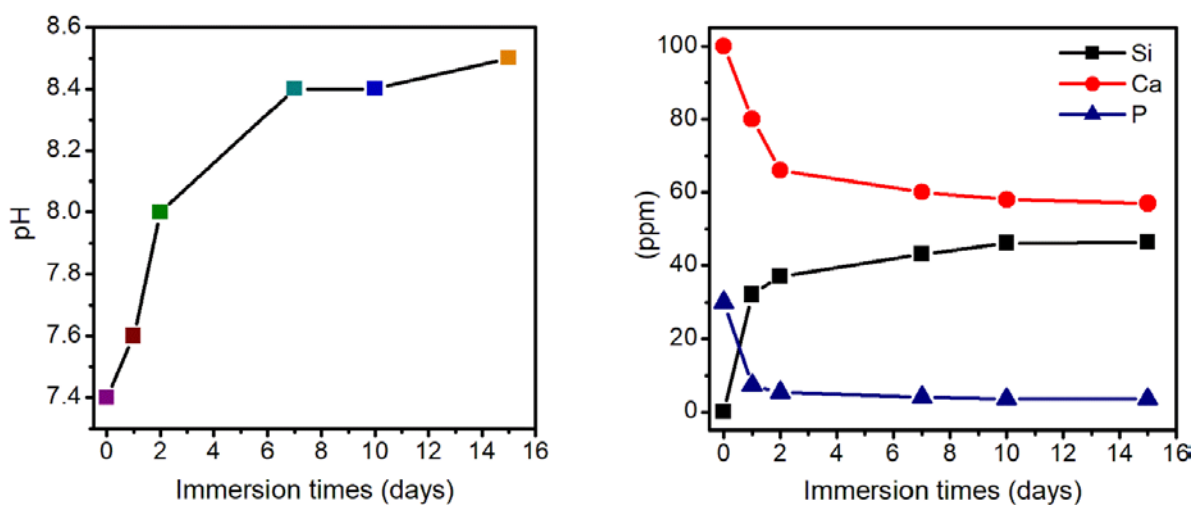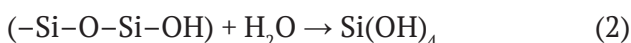**Fig. 6**. FE-SEM images of bioactive glass after immersion in SBF for 1, 2 and 7 days

Fig. 7. Ionic concentrations of the SBF solution during ''in vitro'' experiment

breaking covalent bonds –Si–O–Si–OH following the reaction 2:

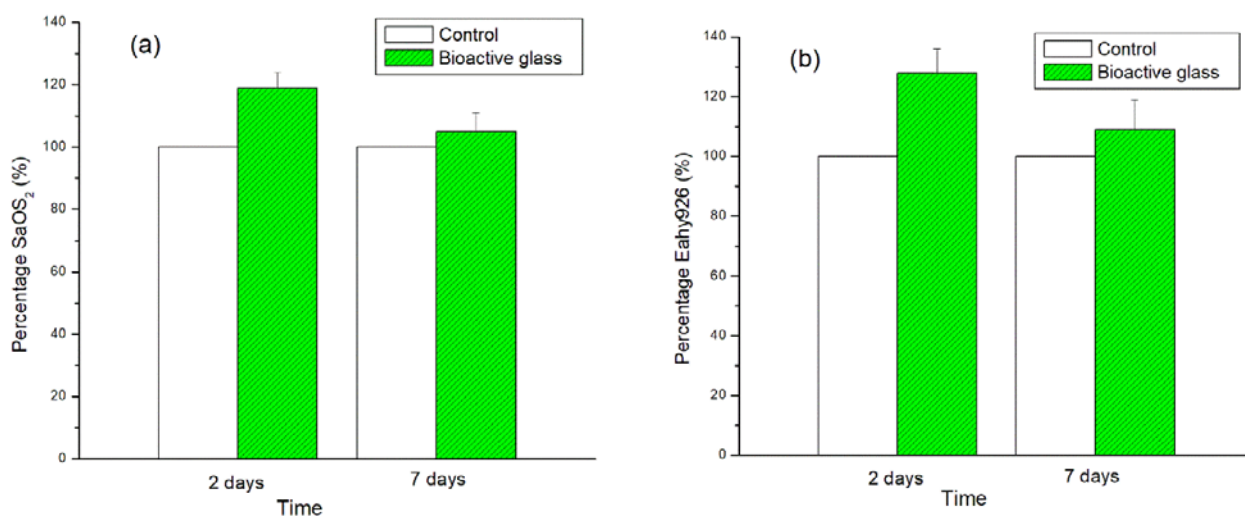$$(-Si-O-Si-OH) + H_2O \rightarrow Si(OH)_4 \tag{2}$$

The Si concentration increased strongly during seven days of immersion, followed by the saturation in which the re-polymerization of silicic acid $Si(OH)_4$ occurs to form SiO_2 silica layer on the surface of the glass sample.

The presence of Ca and P in simulated body fluid (SBF) solution related to two sources. The first one was the Ca, P components available in initial solution. The second one was the Ca, P amounts released by the reaction of glass with SBF solution. Following the reaction 1, the Ca concentration in the SBF solution increases. However, a significant decrease in Ca component was identified during the whole immersion time. A similar observation was also identified for P amount. The decrease in Ca and P components

was related to their consumption to precipitate the apatite layer on glass surface. The obvious consumption of Ca and P for the first two days of immersion in SBF confirmed the high bioactivity of synthetic bioactive glass. After 2 days of immersion, the Ca, P concentrations were almost stable while the pH value increased until 7 days. This phenomenon can be explained by the continuous degradation of bio-glass under reaction 1, simultaneously with the association of Ca and P components to form the HA layer on the surface of glass sample. The obtained result is consistent with the above analysis by the XRD, in which the HA layer was formed after 1 and 2 days of immersion.

3.4. Cell viability

The cell viabilities in the conditioned media of bioactive glass $70SiO_2–30CaO$ are represented in Fig. 8. After 2 days of culture, the cell viabilities

Condensed Matter and Interphases / Конденсированные среды и межфазные границы   2021;23(4): 585–593

Ta Anh Tuan et al.   Hydrothermal assisted conventional sol-gel method for synthesis of bioactive glass...

Fig. 8. Cell culturing viabilities on the bioactive glass after 2 and 7 days: (a) for osteoblast-like $SaOS_2$ and (b) for endothelial-like Eahy926

were 119 and 128% for osteoblast-like $SaOS_2$ and endothelial-like Eahy926, respectively. The viability of cells without contact with bioactive glass was fixed as control (100%). These obtained results confirmed the biocompatibility of synthetic bioactive glass with these two culturing cells. After 7 days, a decrease of Osteoblast-like $SaOS_2$ and endothelial-like Eahy926 viabilities was registered. That needs the renewal of culturing media. According to the standard ISO 10993-5 (Biological evaluation of medical devices – Part 5: Test for cytotoxicity, in vitro methods), the cell viability is expressed as a percentage relative to the control, set as 100% [21]. If the average cell viability of the tested samples is less than 70%, the material is cytotoxic. Following this standard, the bioactive glass $70SiO_2$-$30CaO$ synthesized by hydrothermal assisted sol-gel method showed the absence of toxicity in comparison with the control sample. The synthetic bioactive glass in this study may find the potential applications as bone substitutes.

4. Conclusions

The bioactive glass $70SiO_2$–$30CaO$ (mol%) was successfully prepared by hydrothermal assisted sol-gel method. The obtained glass is totally amorphous material and has a mesoporous structure. The in vitro assay in simulated body fluid (SBF) solution confirmed interesting bioactivity of synthetic glass by the formation of apatite phase after only one day of immersion in simulated body fluid (SBF) solution. The in vitro test in presence of cell culture confirmed good biocompatibility of synthetic bioactive glass. Especially, the synthetic processing is simple, short time-consuming in comparison with conventional sol-gel method.

Contribution of the authors

Ta Anh Tuan – Experiment, Analysis, Writing – original draft, Final conclusions. Elena V. Guseva – Investigation, Writing – review & editing. Nguyen Anh Tien – Investigation, Writing – review & editing. Ha Tuan Anh – Experiment, Investigation. Bui Xuan Vuong – Writing – review & editing. Le Hong Phuc – Experiment, Analysis. Nguyen Quan Hien – Experiment, Analysis. Bui Thi Hoa – Experiment, Analysis, Writing – review & editing. Nguyen Viet Long – Experiment, Analysis, Writing – original draft, Final conclusions.

Conflict of interests

The authors declare that they have no known competing financial interests or personal relationships that could have influenced the work reported in this paper.

References

1. Fernandez de Grado G., Keller L., Idoux-Gillet Y., Wagner Q., Musset A.-M., Benkirane-Jessel N., Bone substitutes: a review of their characteristics, clinical use, and perspectives for large bone defects management, *Journal of Tissue Engineering.* 2018;9: 1–18. https://doi.org/10.1177/2041731418776819

Condensed Matter and Interphases / Конденсированные среды и межфазные границы   2021;23(4): 585–593

Ta Anh Tuan et al.   Hydrothermal assisted conventional sol-gel method for synthesis of bioactive glass...

2. Winker T., Sass F. A., Duda G. N., Schmidt-Bleek K. A review of biomaterials in bone defect healing, remaining shortcomings and future opportunities for bone tissue engineering. *Bone & Joint Research.* 2018;7(3): 232–243. https://doi.org/10.1302/2046-3758.73.BJR-2017-0270.R1

3. Oudadesse H., Dietrich E., Bui X. V., Gal Y. L., Pellen P., Cathelineau G. Enhancement of cells proliferation and control of bioactivity of strontium doped glass. *Applied Surface Science.* 2011;257(20): 8587–8593. https://doi.org/10.1016/j.apsusc.2011.05.022

4. Bui X. V., Dang T. H. Bioactive glass 58S prepared using an innovation sol-gel process. *Processing and Application of Ceramics.* 2019;13(1):98–103. https://doi.org/10.2298/PAC1901098B

5. Letaïef N., Lucas-Girot A., Oudadesse H., Meleard P., Pott T., Jelassi J., Dorbez-Sridi R. Effect of aging temperature on the structure, pore morphology and bioactivity of new sol-gel synthesized bioglass. *Journal of Non-Crystalline Solids.* 2014;402(15): 194–199. https://doi.org/10.1016/j.jnoncrysol.2014.06.005

6. Hench L. L., The story of bioglass. *Journal of Materials Science: Materials in Medicine.* 2006;17(11): 967–978. https://doi.org/10.1007/s10856-006-0432-z

7. Jones J. R. Review of bioactive glass: from Hench to hybrids. *Acta Biomaterialia.* 2013;9(1): 4457–4486. https://doi.org/10.1016/j.actbio.2012.08.023

8. Sepulveda S., Jones J. R., Hench L. L. L. Characterization of melt-derived 45S5 and sol-gel-derived 58S bioactive glasses. *Journal of Biomedical Materials Research.* 2001;58(6): 734–740. https://doi.org/10.1002/jbm.10026

9. Owens G. J., Singh R. K., Foroutan F., Alqaysi M., Han C. M., Mahapatra C., Kim H. W., Knowles J. C. Sol-gel based materials for biomedical applications. *Progress in Materials Science.* 2016;77: 1–79. https://doi.org/10.1016/j.pmatsci.2015.12.001

10. Martínez A., Izquierdo-Barba I., Vallet-Regí M. Bioactivity of a CaO-SiO_2 binary glasses system. *Chemistry of Materials.* 2000;12(10): 3080–3088. https://doi.org/10.1021/cm001107o

11. Kokubo T., Takadama H. How useful is SBF in predicting in vivo bone bioactivity. *Biomaterials.* 2006;27(15): 2907–2915. https://doi.org/10.1016/j.biomaterials.2006.01.017

12. Mosmann T. Rapid colorimetric assay for cellular growth and survival: application to proliferation and cytotoxicity assays. *Journal of Immunological Methods.* 1983;65:55–63. https://doi.org/10.1016/0022-1759(83)90303-4

13. Tolosa L., Donato M. T., Lechón M. J. G. General cytotoxicity assessment by means of the MTT assay. *Methods in Molecular Biology.* 2015;1250: 333–348. https://doi.org/10.1007/978-1-4939-2074-7_26

14. Saravanapavan P., Hench L. L. Mesoporous calcium silicate glasses. I. Synthesis. *Journal of Non-Crystalline Solids.* 2003;318(1-2): 1–13. https://doi.org/10.1016/S0022-3093(02)01864-1

15. Valliant E. M., Turdean-Ionescu C. A., Hanna J. V., Smith M. E., Jones J. R. Role of pH and temperature on silica network formation and calcium incorporation into sol–gel derived bioactive glasses. *Journal of Materials Chemistry.* 2012;22: 1613–1619. https://doi.org/10.1039/C1JM13225C

16. Thommes M. Physical adsorption characterization of nanoporous materials. *Chemie Ingenieur Technik.* 2010;82(7): 1059–1073. https://doi.org/10.1002/cite.201000064

17. Thommes M., Kaneko K., Neimark A. V., Olivier J. P., Rodriguez-Reinoso F., Rouquerol J., Sing K. S. W. Physisorption of gases, with special reference to the evaluation of surface area and pore size distribution. *Pure and Applied Chemistry.* 2015;87(9,10): 1–19. https://doi.org/10.1515/pac-2014-1117

18. Zheng K., Boccaccini A. R. Sol-gel processing of bioactive glass nanoparticles: A review. *Advances in Colloid and Interface Science.* 2017;249: 363–373. https://doi.org/10.1016/j.cis.2017.03.008

19. Xavier K., Charlotte V., Jean-Marie N. Deeper insights into a bioactive glass nanoparticle synthesis protocol to control its morphology, dispersibility, and composition. *ACS. Omega.* 2019;4(3): 5768–5775. https://doi.org/10.1021/acsomega.8b03598

20. Galarraga-Vinueza M. E., Mesquita-Guimaraes J., Magini R. S., Souza J. C. M., Fredel M. C., Boccaccini, A. R. Mesoporous bioactive glass embedding propolis and cranberry antibiofilm compounds. *Journal of Biomedical Materials Research Part A.* 2018;106(6): 1614–1625. https://doi.org/10.1002/jbm.a.36352

21. Standard ISO 10993-5, Biological evaluation of medical devices Part 5: Test for in vitro cytotoxicity. 2009.

Information about the authors

Ta Anh Tuan, PhD student, Faculty of Chemical Technologies, Kazan National Research Technological University, Kazan, Tatarstan, Russian Federation; email: taanhtuan84pt@hpu2.edu.vn. ORCID iD: https://orcid.org/0000-0002-7254-1637.

Elena V. Guseva, PhD in Chemistry, Associate Professor, Faculty of Chemical Technologies, Kazan National Research Technological University, Kazan, Tatarstan, Russian Federation; email: leylaha@mail.ru. ORCID iD: https://orcid.org/0000-0002-2367-8012.

Nguyen Anh Tien, PhD in Chemistry, Associate Professor, Chief of General and Inorganic Chemistry Department, Ho Chi Minh City University of Education, Vietnam; e-mail: tienna@hcmue.edu.vn. ORCID iD: http://orcid.org/0000-0002-4396-0349.

Ha Tuan Anh, Thu Dau Mot University, Thu Dau Mot City, Vietnam; e-mail: anhht@tdmu.edu.vn. ORCID iD: https://orcid.org/0000-0002-1067-0863.

Condensed Matter and Interphases / Конденсированные среды и межфазные границы   2021;23(4): 585–593

Ta Anh Tuan et al.   Hydrothermal assisted conventional sol-gel method for synthesis of bioactive glass...

Bui Xuan Vuong, Associate Professor, Faculty of Natural Sciences, Sai Gon University, Ho Chi Minh City, Vietnam; e-mail: bxvuong@sgu.edu.vn. ORCID iD: https://orcid.org/0000-0002-3757-1099.

Le Hong Phuc, Institute of Applied Mechanics and Informatics, Ho Chi Minh City, Vietnam; e-mail: lhphuc@hcmip.vast.vn. ORCID iD: https://orcid.org/0000-0003-2353-7495.

Nguyen Quan Hien, Ho Chi Minh City Institute of Physics, Vietnam Academy of Science and Technology, Ho Chi Minh City, Vietnam; e-mail: quanhiengv@yahoo.com.vn. ORCID iD: https://orcid.org/0000-0002-5814-6745.

Bui Thi Hoa, Institute of Theoretical and Applied Research, Duy Tan University, Hanoi, Vietnam; Faculty of Natural Sciences, Duy Tan University, Da Nang, Vietnam; e-mail: buithihoa2@duytan.edu.vn. ORCID iD: https://orcid.org/0000-0003-0274-3716.

Nguyen Viet Long, Department of Electronics and Telecommunication, Sai Gon University, Ho Chi Minh City, Vietnam; e-mail: nguyenviet_long@yahoo.com. ORCID iD: https://orcid.org/0000-0003-0129-9879.

Condensed Matter and Interphases

Kondensirovannye Sredy i Mezhfaznye Granitsy
https://journals.vsu.ru/kcmf/

Original articles

Phase formation in the Ag_2MoO_4–Rb_2MoO_4–$Hf(MoO_4)_2$ system

Yu. L. Tushinova[1,2]✉, B. G. Bazarov[1,2], E. V. Kovtunets[1], J. G. Bazarova[1]

[1]*Baikal Institute of Nature Management, Siberian Branch of the Russian Academy of Sciences,*
6 ul. Sakhyanovoy, Ulan-Ude 670047, Republic of Buryatia, Russian Federation

[2] *Banzarov Buryat State University,*
24a ul. Smolina, Ulan-Ude 670000, Republic of Buryatia, Russian Federation

Abstract

Systematic studies of the subsolidus structure of ternary molybdate systems allow expanding the representation of ternary molybdates. In this paper we studied the solid phase interaction in the Ag_2MoO_4–Rb_2MoO_4–$Hf(MoO_4)_2$ system for the first time using X-ray phase analysis.

To determine the quasi-binary sections, we use the method of "intersecting cuts". It helped to reveal the formation of new $Rb_5Ag_{1/3}Hf_{5/3}(MoO_4)_6$ and $Rb_3AgHf_2(MoO_4)_6$ phases. We also determined their thermal characteristics using differential scanning calorimetry. The ternary molybdate $Rb_5Ag_{1/3}Hf_{5/3}(MoO_4)_6$ crystallised in the trigonal syngony with the following unit cell parameters: $a = 10.7117(1)$, $c = 38.5464(5)$ Å (space group R3c, Z = 6). The Ag_2MoO_4–Rb_2MoO_4–$Hf(MoO_4)_2$ system is characterised by the existence of ten quasi-binary cross sections.

The experimental data obtained in this work complement the information on phase equilibria in condensed ternary systems containing molybdates of tetravalent elements and two different monovalent elements. This provides opportunities for the combination of the compositions of ternary molybdates due to cationic substitutions, which will allow controlling their properties.

Keywords: Phase diagram, Triangulation, Solid-state synthesis, Ternary molybdate, Silver molybdate, Rubidium molybdate, Hafnium molybdate, X-ray diffraction analysis

✉ Yunna L. Tushinova, e-mail: tushinova@binm.ru

Condensed Matter and Interphases / Конденсированные среды и межфазные границы   2021;23(4): 594–599

Yu. L. Tushinova et al.   Phase formation in the Ag$_2$MoO$_4$–Rb$_2$MoO$_4$–Hf(MoO$_4$)$_2$ system

1. Introduction

The study of phase equilibria in multicomponent systems is one of the methods of searching for new complex oxide compounds. In recent decades, molybdates with various combinations of cationic composition have been obtained as a result of the study of ternary molybdate systems [1–4]. This class of substances is still being actively expanded [5–9]. It should be noted that the studies of the properties of the identified ternary molybdates show that their application is promising. For example, the high values of ion conductivity of silver-bearing compounds obtained in [10, 11] allowed classifying them as superionic conductors.

A systematic study of phase equilibria allows obtaining more complete information on the interaction of components and the number of the formed phases, and identifying the general patterns of phase formation in the future. For instance, ternary molybdate systems containing molybdate of a tetravalent element, zirconium or hafnium, as one of the components, were studied in detail in [12–16]. The goal of this work was to study the phase formation in the Ag$_2$MoO$_4$–Rb$_2$MoO$_4$–Hf(MoO$_4$)$_2$ system in the subsolidus region.

2. Experimental

We used the following industrial reagents: Rb$_2$CO$_3$ (extra pure grade), HfO$_2$ (chemically pure grade), AgNO$_3$ (analytical reagent grade), and MoO$_3$ (analytical reagent grade).

To obtain the initial molybdates from stoichiometric mixtures of the corresponding reagents, we used the method of solid-phase synthesis. Stepped annealing of the samples was conducted in a muffle furnace, and the samples were repeatedly ground in an agate mortar in an ethyl alcohol medium. Silver molybdate was obtained with a synthesis temperature of 200–450 °C, the total duration of annealing was 150 hours. Medium rubidium and hafnium molybdates were synthesised in the range of 400–550 °C (rubidium molybdate) and 400–750 °C (hafnium molybdate) for 80–100 hours.

Ternary molybdates with the compositions Rb$_5$Ag$_{1/3}$Hf$_{5/3}$(MoO$_4$)$_6$ and Rb$_3$AgHf$_2$(MoO$_4$)$_6$ were synthesised from stoichiometric amounts of the reaction mixtures of Ag$_2$MoO$_4$, Rb$_2$MoO$_4$, and Hf(MoO$_4$)$_2$. The annealing was conducted in the temperature range 290–500 °C with an increase in temperature with steps of 30 °C and repeated grinding of the samples. The time of annealing was 60 hours.

The phase equilibria in the ternary system were studied using the method of "intersecting cuts" [17]. The interaction in the subsolidus area was studied using X-ray and had two stages. During the first stage, we determined the phase composition of the intersection points of all possible cuts connecting the compositions of the components and intermediate phases of the faceting elements. During the second stage, we also studied individual quasi-binary sections of the system and some compositions from the three-phase regions. The achievement of equilibrium was proved by the stabilisation of the phase composition of the samples after several sequential annealings and the mutual consistency of the phase composition allowing triangulating the systems.

X-ray phase analysis (XPA) was performed on a Bruker D8 Advance automatic powder diffractometer (Cu$K\alpha$ radiation, scanning step 0.01°). The ICDD PDF-2 database was used to analyse the X-ray patterns.

We used the Le Bail method and the TOPAS 4.2 software to process the experimental data and specify the unit cell parameters of the Rb$_5$Ag$_{1/3}$Hf$_{5/3}$(MoO$_4$)$_6$ compound.

Thermal analysis was conducted on an STA 449 F1 Jupiter synchronous thermal analyser manufactured by NETZSCH. The samples were scanned in platinum crucibles in an argon atmosphere with heating and cooling at a rate of 10 °C/min. The weight of the samples was 17–20 mg.

3. Results and discussion

Phase equilibria in the Ag$_2$MoO$_4$–Rb$_2$MoO$_4$–Hf(MoO$_4$)$_2$ system were studied taking into account the previous publications on binary faceting systems.

One compound with the AgRb$_3$(MoO$_4$)$_2$ composition which melts at 435 °C was formed in the Ag$_2$MoO$_4$–Rb$_2$MoO$_4$ binary system [19]. During crystallisation from a solution, single crystals were obtained in a melt, and their composition was determined when decoding the structure

Condensed Matter and Interphases / Конденсированные среды и межфазные границы   2021;23(4): 594–599

Yu. L. Tushinova et al.   Phase formation in the Ag_2MoO_4–Rb_2MoO_4–$Hf(MoO_4)_2$ system

as $Ag_{1.19}Rb_{2.81}(MoO_4)_2$ [20]. It should be noted a single-phase sample of this composition cannot be synthesised using the method of solid-phase reactions. And the discovered crystal composition is probably limited in terms of silver content and can only be obtained from melt. It was shown that the $Ag_{1+x}Rb_{3-x}(MoO_4)_2$ samples with $0 \leqslant x \leqslant 0.10$, which is about 2 mol. %, were single-phase only at limiting subsolidus temperatures [20].

The Rb_2MoO_4–$Hf(MoO_4)_2$ binary system is characterised by the presence of two compounds with the $Rb_8Hf(MoO_4)_6$ and $Rb_2Hf(MoO_4)_3$ compositions with melting temperatures of 655 and 650 °C respectively [21, 22].

We established that one $AgRb_2(MoO_4)_2$ compound was formed in the Ag_2MoO_4–$Hf(MoO_4)_2$ binary system and melted incongruently at 570 °C [23].

When synthesizing double molybdates, we focused on the conditions of their obtaining and melting temperatures mentioned in previous publications.

The formation of new $Rb_5Ag_{1/3}Hf_{5/3}(MoO_4)_6$ – S_1 and $Rb_3AgHf_2(MoO_4)_6$ – S_2 phases was identified when studying phase equilibria in the subsolidus region. It should be noted that reflections of the new S_1 phase were observed on the X-ray patterns of the samples of the supposed section of $AgRb_3(MoO_4)_2$–$Rb_2Hf(MoO_4)_3$.

The phase relationships at 430 °C in the triple silver-rubidium-hafnium molybdate system are characterised by the following quasi-binary sections: $AgRb_3(MoO_4)_2$–$Rb_8Hf(MoO_4)_6$, Ag_2MoO_4–$Rb_8Hf(MoO_4)_6$, Ag_2MoO_4–$Rb_5Ag_{1/3}Hf_{5/3}(MoO_4)_6$, Ag_2MoO_4–$Rb_3AgHf_2(MoO_4)_6$, $Hf(MoO_4)_2$–$Rb_3AgHf_2(MoO_4)_6$, $Ag_2Hf(MoO_4)_3$–$Rb_3AgHf_2(MoO_4)_6$, $Hf(MoO_4)_2$–$Rb_5Ag_{1/3}Hf_{5/3}(MoO_4)_6$, $Rb_2Hf(MoO_4)_3$–$Rb_5Ag_{1/3}Hf_{5/3}(MoO_4)_6$, $Rb_8Hf(MoO_4)_6$–$Rb_5Ag_{1/3}Hf_{5/3}(MoO_4)_6$, $Rb_5Ag_{1/3}Hf_{5/3}(MoO_4)_6$–$Rb_3AgHf_2(MoO_4)_6$ (Fig. 1). As for the studied conditions, there were no sections radiating from the apex of the triangle where rubidium molybdate was located. Thus, the studied system was divided into nine secondary triangles by ten quasi-binary sections.

Comparing the results with those obtained previously in [24], we should mention some similarity with the phase diagram of the Li_2MoO_4–Rb_2MoO_4–$Hf(MoO_4)_2$ system despite significant

differences in the faceting elements. For example, a $RbLiMoO_4$ composition was observed in the Li_2MoO_4–Rb_2MoO_4 binary system, while an intermediate phase in the Li_2MoO_4–$Hf(MoO_4)_2$ system has a rather extended homogeneity range. The similarity was found during the triangulation of the Li_2MoO_4–Rb_2MoO_4–$Hf(MoO_4)_2$ system when a part of the stable sections was radiating from the apex of the concentration triangle where lithium molybdates were located. In our case, the sections with the participation of silver molybdate were stable. And in both phase diagrams, there were no stable sections radiating from the apex of the triangle, where rubidium molybdate was located. The differences were observed in the amount of triple molybdates. Triple molybdates with the $Rb_5Me_{1/3}Hf_{5/3}(MoO_4)_6$ and $Rb_3MeHf_2(MoO_4)_6$ (Me = Li, Ag) compositions were found in both systems. However, unlike the lithium system, there was no compound similar to the $RbLiHf(MoO_4)_3$ composition formed in the system with silver molybdate.

The compounds with the similar composition $Me_3Me'Hf_2(MoO_4)_6$ were obtained with Me = Na, K, Tl, Rb, and Me' = Li [16]. They were classified using three structure types of binary molybdates. Triple molybdates $Me_3LiHf_2(MoO_4)_6$ (Me = K, Rb) are isostructural to $KAl(MoO_4)_2$, while $Na_3LiHf_2(MoO_4)_6$ molybdate is isostructural to $NaIn(MoO_4)_2$. The diffraction pattern of $Tl_3LiHf_2(MoO_4)_6$ was indexed with the assumption of the formation of a superstructure of the rhombic $KIn(MoO_4)_2$ with a tripling of the
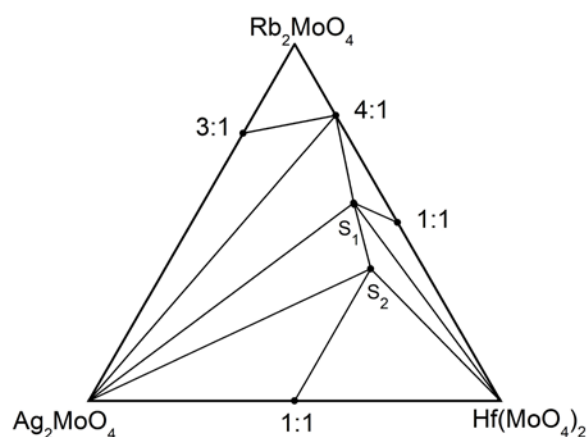

Fig. 1. Phase equilibria in the Ag_2MoO_4–Rb_2MoO_4–$Hf(MoO_4)_2$ system in the subsolidus region (400–430 °C): S_1 – $Rb_5Ag_{1/3}Hf_{5/3}(MoO_4)_6$, S_2 – $Rb_3AgHf_2(MoO_4)_6$

Condensed Matter and Interphases / Конденсированные среды и межфазные границы   2021;23(4): 594–599

Yu. L. Tushinova et al.   Phase formation in the $Ag_2MoO_4–Rb_2MoO_4–Hf(MoO_4)_2$ system

smallest parameter c. In our case, we still have not found a structural analogue for the phase. Apparently, the change of the cationic composition leads to the formation of a different structure. One endothermic effect corresponding to melting was observed on the DSC curve for the $Rb_5AgHf_2(MoO_4)_6$ sample (Fig. 2). However, the results of X-ray phase analysis of the cooled melt allowed making the assumption that melting has an incongruent nature.

According to X-ray phase analysis, the synthesised $Rb_5Ag_{1/3}Hf_{5/3}(MoO_4)_6$ ternary molybdate was isostructural to the previously studied $Rb_5Li_{1/3}Hf_{5/3}(MoO_4)_6$ which crystallised in the trigonal syngony (space group R3c, Z = 6), and its structure was determined in [24]. The base of the crystal structure is a skeletal mixed plane of $(Hf, Li)O_6$ octahedrons and MoO_4 tetrahedrons. The atoms of rubidium are located in large voids of this plane. All the reflections of the $Rb_5Ag_{1/3}Hf_{5/3}(MoO_4)_6$ compound on an X-ray pattern were satisfactorily indexed based on the assumption of the isostructurality of $Rb_5Li_{1/3}Hf_{5/3}(MoO_4)_6$ [24]. The results of the specification using the Le-Baile method are presented in Table 1, and calculated and experimental X-ray diffraction patterns with difference curves are shown in Figure 3. According to the results of differential scanning calorimetry, the compound melted at 597 °C.

Table 1. Crystallographic characteristics and parameters of unit cell specification of the $Rb_5Ag_{1/3}Hf_{5/3}(MoO_4)_6$ compound using Le-Baile method

Compound	$Rb_5Ag_{1/3}Hf_{5/3}(MoO_4)_6$
Space group	$R3c$
a, Å	10.7117 (1)
c, Å	38.5464 (5)
V, Å³	3830.27 (9)
2θ-interval, °	8–100
R_{wp}, %	4.10
R_p, %	3.26
R_{exp}, %	2.15
χ^2	1.90
R_B, %	0.46

Therefore, a new compound was added to the series of the compounds with the $Me_5(Li_{1/3}Hf_{5/3})(MoO_4)_6$ (Me = K, Rb, Tl) composition [16]. All
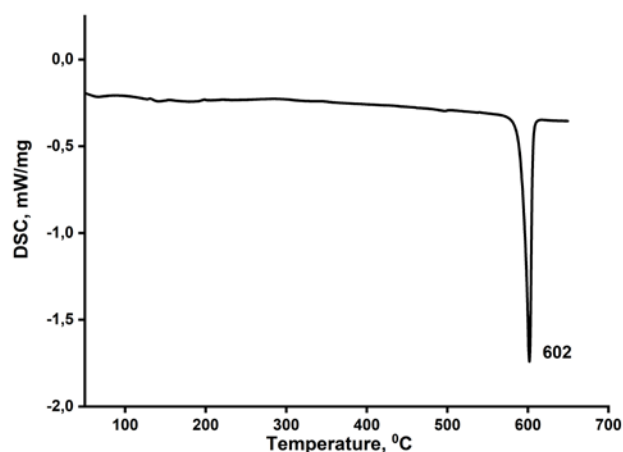
Fig. 2. DSC curve for the $Rb_5AgHf_2(MoO_4)_6$ sample
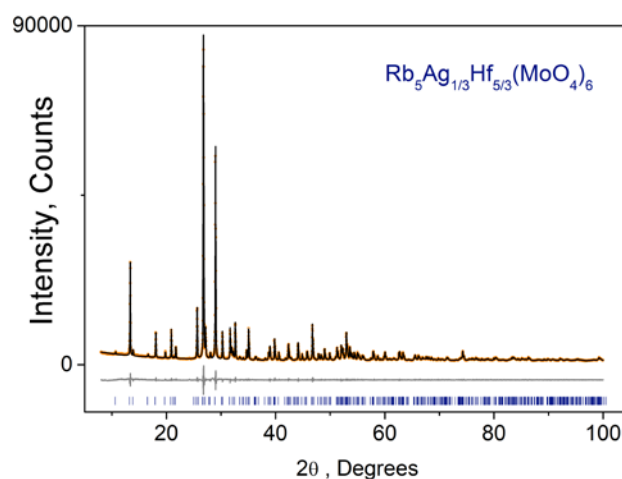
Fig. 3. Experimental (circles), calculated (line), difference, and dashed X-ray diffraction patterns of $Rb_5Ag_{1/3}Hf_{5/3}(MoO_4)_6$

these triple molybdates have already been included in a rather large group of isostructural compounds whose structure was first solved for the $K_5(Mg_{0.5}Zr_{1.5})(MoO_4)_6$ compound [25]. All the above-mentioned compounds have cage structures built from isolated MO_6 octahedrons and XO_4 tetrahedrons which differ in the nature of the mutual arrangement of the polyhedrons. As a result, various numbers of cavities of different shapes and isomorphic substitutions were formed.

4. Conclusion

Thus, the phase equilibria in the subsolidus region of the $Ag_2MoO_4–Rb_2MoO_4–Hf(MoO_4)_2$ system were studied for the first time, the formation of new triple molybdates was identified, and the system was triangulated.

Condensed Matter and Interphases / Конденсированные среды и межфазные границы   2021;23(4): 594–599

Yu. L. Tushinova et al.   Phase formation in the Ag_2MoO_4–Rb_2MoO_4–$Hf(MoO_4)_2$ system

Author contributions

All authors made an equivalent contribution to the preparation of the publication.

Conflict of interests

The authors declare that they have no known competing financial interests or personal relationships that could have influenced the work reported in this paper.

References

1. Kozhevnikova N. M., Mokhosoev M. V. *Trojnye molibdaty* [Triple molybdates]. Ulan-Udje: Izdatel'stvo Burjatskogo gosuniversiteta Publ.; 2000. 298 p. (In Russ.)

2. Khaikina G. E., Solodovnikov S. F., Basovich O. M., Solodovnikova Z. A., Kadyrova Y. M., Savina A. A., Zolotova E. S., Yudin V. N., Spiridonova T. S. Triple molybdates one-, one - and three(two)valence metals. *Chimica Techno Acta*. 2015;(2)4: 356–372. https://doi.org/10.15826/chimtech.2015.2.4.032

3. Dridi W., Zid M. F. Crystal Structure of New One-Dimensional Triple Molybdate $Na_2K_2Cu(MoO_4)_3$. *Journal of Structural Chemistry*. 2018;59: 1128–1132. https://doi.org/10.1134/S0022476618050153

4. Bazarova J. G., Chimitova O. D., Grossman V. G., Bazarov B. G., Tushinova Yu. L. Regularities of trigonal triple molybdates formation $M_5LnHf(MoO_4)_6$ in the systems M_2MoO_4–$Ln_2(MoO_4)_3$–$Hf(MoO_4)_2$ (M=K, Tl, Rb; Ln=La–Lu). *Uspehi sovremennogo estestvoznanija*. 2016;10: 14–19. Available at: https://www.elibrary.ru/item.asp?id=27179218 (In Russ., abstract in Eng)

5. Spiridonova T. S., Savina A. A., Kadyrova Yu. M., Belykh E. P., Khaikina E. G. New compounds $Li_3Ba_2Bi_3(XO_4)_8$ (X = Mo, W): synthesis and properties. *Kondensirovannye sredy i mezhfaznye granitsy = Condensed Matter and Interphases*. 2021;23(1): 73–80. https://doi.org/10.17308/kcmf.2021.23/3306

6. Gulyaeva O. A., Solodovnikova Z. A., Solodovnikov S. F., Yudin V. N., Zolotova E. S., Komarov V. Yu. Subsolidus phase relations and structures of solid solutions in the systems K_2MoO_4–Na_2MoO_4–$MMoO_4$ (M = Mn, Zn). *Journal of Solid State Chemistry*. 2019;272: 148–156. https://doi.org/10.1016/j.jssc.2019.02.010

7. Vats B. G., Shafeeq M., Kesari S. Triple molybdates and tungstates scheelite structures: Effect of cations on structure, band-gap and photoluminescence properties. *Journal of Alloys and Compounds*. 2021;865: 158818. https://doi.org/10.1016/j.jallcom.2021.158818

8. Kozhevnikova N. M., Batueva S. Y. Erbium-doped upconversion phosphor in the Li_2MoO_4–$BaMoO_4$–$Y_2(MoO_4)_3$ system. *Inorganic Materials*. 2020;56(3): 286–291. https://doi.org/10.1134/S0020168520030085

9. Logvinova A. V., Bazarov B. G., Bazarova J. G. Obtaining iron (III) – containing triple molybdate $K_5FeZr(MoO_4)_6$ by sol-gel technology. *Kondensirovannye sredy i mezhfaznye granitsy = Condensed Matter and Interphases*. 2020;22(3): 353-359. https://doi.org/10.17308/kcmf.2020.22/2966

10. Spiridonova T. S., Savina A. A., Kadyrova Y. M., Khaikina E. G., Solodovnikov S. F., Solodovnikova Z. A., Yudin V. N., Stefanovich S. Y. New triple molybdate $Rb_2AgIn(MoO_4)_3$: synthesis, framework crystal structure and ion-transport behaviour. *Acta Crystallographica. Section C, Structural Chemistry*. 2018;74(12): 1603–1609. https://doi.org/10.1107/s2053229618014717

11. Kotova I. Yu., Solodovnikov S. F., Solodovnikova Z. A., Belov D. A., Stefanovich S. Yu., Savina A. A., Khaikina E. G. New series of triple molybdates $AgA_3R(MoO_4)_5$ (A=Mg, R=Cr, Fe; A=Mn, R=Al, Cr, Fe, Sc, In) with framework structures and mobile silver ion sublattices. *Journal of Solid State Chemistry*. 2016;238: 121–128. https://doi.org/10.1016/j.jssc.2016.03.003

12. Bazarova J. G., Tushinova Yu. L., Grossman V. G., Bazarova Ts. T., Bazarov B. G., Kurbatov R. V. Phase relations in the Me_2MoO_4–$In_2(MoO_4)_3$–$Hf(MoO_4)_2$, where Me=Li, K, Tl, Rb, Cs. *Chimica Techno Acta*. 2018;5(3): 126–131. https://doi.org/10.15826/chimtech.2018.5.3.01

13. Grossman V. G., Bazarova J. G., Bazarov B. G., Molokeev M. S. New triple molybdate $K_5ScHf(MoO_4)_6$: synthesis, properties, structure and phase equilibria in the M_2MoO_4–$Sc_2(MoO_4)_3$–$Hf(MoO_4)_2$ (M = Li, K) systems. *Journal of Solid State Chemistry*. 2020;283: 121143. https://doi.org/10.1016/j.jssc.2019.121143

14. Tsyrenova G. D., Solodovnikov S. F., Popova N. N., Solodovnikova Z. A., Pavlova E. T., Naumov D. Yu., Lazoryak B. I. Phase equilibria in the Cs_2MoO_4–$ZnMoO_4$–$Zr(MoO_4)_2$ system, Crystal structures and properties of new triple molybdates $Cs_2ZnZr(MoO_4)_4$ and $Cs_2ZnZr_2(MoO_4)_6$. *Journal of Physics and Chemistry of Solids*. 2015;81: 93–99. https://doi.org/10.1016/j.jpcs.2015.01.015

15. Dorzhieva S. G., Bazarov B. G., Bazarova J. G. New molybdates in the Rb_2MoO_4–$M^I_2MoO_4$–$Zr(MoO_4)_2$ (M^I – Na, K) systems as promising ion-conducting materials. *Letters on Materials*. 2019;9(1): 17–21. https://doi.org/10.22226/2410-3535-2019-1-17-21

16. Balsanova L. V. *Troinye molibdaty litiya, odnovalentnykh metallov i gafniya* [Ternary molybdates of lithium, monovalent metals and hafnium], Cand. chem. sci. diss. Abstr. Irkutsk: Izdatel'stvo Buryatskogo gosuniversiteta; 2004. 23 p. Avalaible at: https://viewer.rusneb.ru/ru/rsl01002728973?page=1&rotate=0&theme=white (In Russ.)

17. Zaharov A. M. *Diagrammy sostojanija dvojnyh i trojnyh system* [State diagrams of double and triple systems]. Moscow: Metallurgija Publ.; 1978. 296 p. (In Russ.)

Condensed Matter and Interphases / Конденсированные среды и межфазные границы   2021;23(4): 594–599

Yu. L. Tushinova et al.   Phase formation in the Ag_2MoO_4–Rb_2MoO_4–$Hf(MoO_4)_2$ system

18. Bruker AXS TOPAS V4: General profile and structure analysis software for powder diffraction data. *User's Manual*. Bruker AXS, Karlsruhe, Germany. 2008.

19. Kadyrova Yu. M., Solodovnikov S. F., Solodovnikova Z. A., Basovich O. M., Spiridonova T. S., Khajkina E. G. New silver-rubidium double molybdate. *Vestnik Burjatskogo gosudarstvennogo universiteta*. 2015;(3): 21–25. Available at: https://www.elibrary.ru/item.asp?id=23233676 (In Russ., abstract in Eng.)

20. Spiridonova T. S., Solodovnikov S. F., Kadyrova Yu. M., Solodovnikova Z. A., Savina A. A., Khaikina E. G. Double molybdates of silver and monovalent metals. *Kondensirovannye sredy i mezhfaznye granitsy = Condensed Matter and Interphases*. 2021;23(3): 421–431. https://doi.org/10.17308/kcmf.2021.23/3527

21. Bazarov B. G., Chimitova O. D., Klevtsova R. F., Tushinova Yu. L., Glinskaya L. A., Bazarova Zh. G. Crystal structure of a new ternary molybdate in the Rb_2MoO_4-$Eu_2(MoO_4)_3$-$Hf(MoO_4)_2$ system. *Journal of Structural Chemistry*. 2008;49: 53–57. https://doi.org/10.1007/s10947-008-0008-5

22. Zolotova E. S., Sergey F. Solodovnikov S. F., Solodovnikova Z. A., Vasiliy N. Yudin V. N., Uvarov N. F., Sukhikh A. S. Selection of alkali polymolybdates as fluxes for crystallization of double molybdates of alkali metals, zirconium or hafnium, revisited crystal structures of $K_2Mo_2O_7$, $K_2Mo_3O_{10}$, $Rb_2Mo_3O_{10}$ and ionic conductivity of $A_2Mo_2O_7$ and $A_2Mo_3O_{10}$ (A = K, Rb, Cs). *Journal of Physics and Chemistry of Solids*. 2021;154: 110054. https://doi.org/10.1016/j.jpcs.2021.110054

23. Bazarova J. G., Tushinova Y. L., Bazarov B. G. Phase equilibria in systems Ag_2MoO_4–$Ln_2(MoO_4)_3$–$Hf(MoO_4)_2$, Ln = Nd, Gd, Tb, Dy. *BSU bulletin. Chemistry. Physics*. 2018;(4): 8–12. https://doi.org/10.18101/2306-2363-2018-4-8-12 (In Russ., abstract in Eng.)

24. Solodovnikov S. F., Zolotova E. S., Balsanova L. V., Bazarov B. G., Bazarova Zh. G. Phase formation in the Rb_2MoO_4–Li_2MoO_4–$Hf(MoO_4)_2$ system and the crystal structure of $Rb_5(Li_{1/3}Hf_{5/3})(MoO_4)_6$. *Russian Journal of Inorganic Chemistry*. 2003;48(7): 1084–1088. Available at: https://www.elibrary.ru/item.asp?id=13434803

25. Klevtsova R. F., Bazarova Zh. G., Glinskaya L. A., Alekseev V. I., Arkhincheeva S. I., Bazarov B. G., Klevtsov P. V., Fedorov K. N. Sintez troinykh molibdatov kaliya, magniya, tsirkoniya i kristallicheskaya struktura [Synthesis of ternary molybdates of potassium, magnesium, zirconium and crystal structure $K_5(Mg_{0.5}Zr_{1.5})(MoO_4)_6$]. *Journal of Structural Chemistry*. 1994;35(3): 286. Available at: https://jsc.niic.nsc.ru/article/16603/ https://jsc.niic.nsc.ru/article/16603/ (In Russ.)

Information about the authors

Yunna L. Tushinova, PhD in Chemistry, Researcher Fellow, Laboratory of Oxide Systems, Baikal Institute of Nature Management, Siberian Branch of the Russian Academy of Sciences (BINM SB RAS), Ulan-Ude, Russian Federation; e-mail: tushinova@binm.ru. ORCID iD: https://orcid.org/0000-0003-1032-8854.

Bair G. Bazarov, DSc in Physics and Mathematics, Leading Researcher, Laboratory of Oxide Systems Baikal Institute of Nature Management, Siberian Branch of the Russian Academy of Sciences (BINM SB RAS), Associate Professor at the Department of Inorganic and Organic chemistry, Banzarov Buryat State University, Ulan-Ude, Russian Federation; e-mail: bazbg@rambler.ru. ORCID iD: https://orcid.org/0000-0003-1712-6964.

Evgeniy V. Kovtunets, Postgraduate Student, Junior Researcher, Laboratory of Oxide Systems, Baikal Institute of Nature Management, Siberian Branch of the Russian Academy of Sciences, Ulan-Ude, Russian Federation; e-mail: kovtunets@binm.ru. ORCID iD: https://orcid.org/0000-0003-1301-1983.

Jibzema G. Bazarova, DSc in Chemistry, Chief Scientist Laboratory of Oxide Systems, Baikal Institute of Nature Management, Siberian Branch of the Russian Academy of Sciences, Ulan-Ude, Russian Federation; e-mail jbaz@binm.ru. ORCID iD: https://orcid.org/0000-0002-1231-0116.

Translated by Marina Strepetova
Edited and proofread by Simon Cox

Condensed Matter and Interphases

Original articles

Optical and magnetic properties of orthoferrite NdFeO$_3$ nanomaterials synthesized by simple co-precipitation method

Pham Thi Hong Duyen[1], Nguyen Anh Tien[2]✉

^{1}Thu Dau Mot University,
Thu Dau Mot City, Binh Duong Province, 590000, Vietnam

^{2}Ho Chi Minh City University of Education,
Ho Chi Minh City 700000, Vietnam

Abstract

In this work, orthoferrite NdFeO$_3$ nanomaterials with particle sizes 20-40 nm have been successfully synthesized via a simple co-precipitation method through the hydrolysis of Nd (III) and Fe (III) cations in hot water with 5% NaOH as a precipitating agent. Single-phase NdFeO$_3$ was generated after calcination of the as-prepared powder at 700, 800, and 900 °C for 1 hour. The UV-Vis spectra at room temperature presented strong absorption in the UV-Vis regions (λ = 200–400 nm and 400–600 nm) with small band gap energy (E_g = 2.2÷2.5 eV). The obtained NdFeO$_3$ nanomaterials exhibited a hard ferromagnetic behavior with high coercivity (H_c = 600–1600 Oe).

Keywords: NdFeO$_3$, Nanomaterial, Co-precipitation, Optical and Magnetic properties

✉ Nguyen Anh Tien, e-mail: tienna@hcmue.edu.vn

Condensed Matter and Interphases / Конденсированные среды и межфазные границы   2021;23(4): 600–606

Pham Thi Hong Duyen et al.   Optical and magnetic properties of orthoferrite NdFeO₃ nanomaterials...

1. Introduction

The characteristic structure and properties of nanomaterials in general, and $RFeO_3$ rare-earth orthoferrite nanomaterials in particular, depend on several different factors such as particle size and morphology, crystal size, the distribution of the cations in the crystal lattice, the content of doping elements and also the preparation method [1–5]. Nano-sized rare earth orthoferrites $RFeO_3$ (R = La, Y, Nd, Pr, Ho, ...) have been studied and applied in many fields such as photocatalysis for the decomposition of toxic organic waste [6–7], electrodes for solid oxide fuel cells [8], gas sensor materials [9], photomagnetic and electromagnetic devices [10–11], etc. The rare earth orthoferrites $NdFeO_3$ is amongst the materials of interest to research. The structural and optical properties, magnetic properties or electrical properties of orthoferrite neodymium were previously studies [12–15], showing promising for application in As (V) adsorption [16].

$NdFeO_3$ nanomaterials have been synthesized by various methods such as high-temperature mechanosynthesis [14–15], sol-gel or gel-combustion [16, 17–18], hydrothermal or co-precipitation with surfactants [12–13]. In our previous report [19], based on the thermal behavior of the hydroxides of Fe (III), Nd (III) and their mixture (molar ratio Fe^{3+}/Nd^{3+} = 1/1), the appropriate annealing temperature for the formation of single phase perovskite was determined and $NdFeO_3$ nano particles of < 50 nm were synthesized by co-precipitation method (without any surfactant). By this simple co-precipitation method, our group has successfully prepared a series of rare earth orthoferrite such as $PrFeO_3$ [20], $HoFeO_3$ [21–22], [$LaFeO_3$ [23] or [$YFeO_3$ [24–25] and studied their structural and optical, magnetic properties. However, in [19], the optical and magnetic properties of $NdFeO_3$ nano materials have yet to be reported.

Follow-up to the work in [19], the aim of this paper is to study the characteristic optical and magnetic properties of $NdFeO_3$ orthoferrite nanomaterial synthesized by simple co-precipitation method without any surfactants.

2. Experimental and methods

$NdFeO_3$ orthoferrite nano powder was prepared by co-precipitation method according to [19]. 50 mL aqueous solution of the mixture of two salts $Nd(NO_3)_3 \cdot 6H_2O$ and $Fe(NO_3)_3 \cdot 9H_2O$ (molar ratio of 1/1) was added dropwise to 400 mL boiling water on a stirring hot plate ($t° > 95 °C$), resulting in a reddish-brown sol. Slowly adding the solution of Fe (III) and Nd (III) salts into water at high temperature helped speed up the hydrolysis of metal cations and restrict the particle size of resulting $NdFeO_3$ particles, as proven previously for the synthesis of $HoFeO_3$ and $YFeO_3$ nano orthoferrite [22, 24]. Next, NaOH 5% solution was added dropwise to the system until all the cations Nd^{3+} and Fe^{3+} were completely precipitated (phenolphthalein paper turned pink). The obtained mixture was kept stirring for another 60 minutes, settled for 20 minutes, then vacuum filtered and washed with water until pH ~ 7.0. After drying at room temperature (for 5–7 days), the precipitate was ground with porcelain mortar and pestle into a yellowish-brown fine powder (precursor for $NdFeO_3$). The precursor was then annealed at 700, 800 or 900 °C for 1h to study the formation of single phase orthorhombic $NdFeO_3$.

Powder X-ray diffraction analysis (PXRD) of the $NdFeO_3$ samples was carried out using a D8-ADVANCE X-ray diffractometer (Bruker, Bremen, Germany) with CuK_α radiation, $\lambda = 0.154184$ nm, angle range of $2\theta = 10–80°$, and scan rate of 0.02 °/s. Average crystal size (D_{XRD}, nm) of the $Nd_{1-x}Sr_xFeO_3$ samples was calculated by Debye-Scherrer formula, lattice parameters (a, b, c, V) were calculated according to [13]. The morphology of the samples was determined by transmission electron microscopy (TEM) using a Joel JEM-1400 microscope (Jeol Ldt., Tokyo, Japan).

The UV-Vis absorption spectra of the $NdFeO_3$ nanomaterials were studied on a UV-Visible spectrophotometer (UV-Vis, JASCO V-550, Japan). The optical energy gap (E_g, eV) of the samples was calculated according to [22]. Magnetic characteristics of nanopowders, including the coercive force (H_c, Oe), remanent magnetization (M_r, emu·g⁻¹) and saturation magnetization (M_s, emu·g⁻¹), were investigated at room temperature using a vibrating magnetometer (VSM, MICROSENE EV 11, Japan) with a maximum magnetic field of ± 20 kOe.

Condensed Matter and Interphases / Конденсированные среды и межфазные границы   2021;23(4): 600–606

Pham Thi Hong Duyen et al.   Optical and magnetic properties of orthoferrite NdFeO₃ nanomaterials...

3. Results and discussion

Fig. 1 shows the PXRD patterns of the precursor for $NdFeO_3$ nano orthoferrite after annealed at 700, 800 or 900 °C for 1 hour. All three samples exhibited single phase $NdFeO_3$ orthoferrite with orthorhombic structure, Pbnm (62) space group.

The observable peaks match well with the standard pattern of $NdFeO_3$ (JCPDS: 01-074-1473). When the annealing temperature increased, the degree of crystallinity (I, a.u), lattice cell volume (V, Å^3) and average $NdFeO_3$ crystal size according to Debye–Scherrer formula also increased (Table 1).

The morphology of the material $NdFeO_3$ after annealing at 800 °C for 1h was studied by transmission electron microscopy (Fig. 2), showing particles with the size varying from 20-40 nm and clear boundaries. However, the aggregation was significant because the attraction between those magnetic particles inhibited the scattering of the samples for TEM study.

The UV-Vis spectra at room temperature of the $NdFeO_3$ materials annealed at different temperatures (700, 800 or 900 °C for 1h) show strong absorption in the UV (~ 200-400 nm) and visible regions (~ 400-600 nm) (Fig. 3a). In the UV range, the absorption of the materials tends to decrease when rising the annealing temperature (increment of crystal size). However, there were no remarkable variations in the absorption in
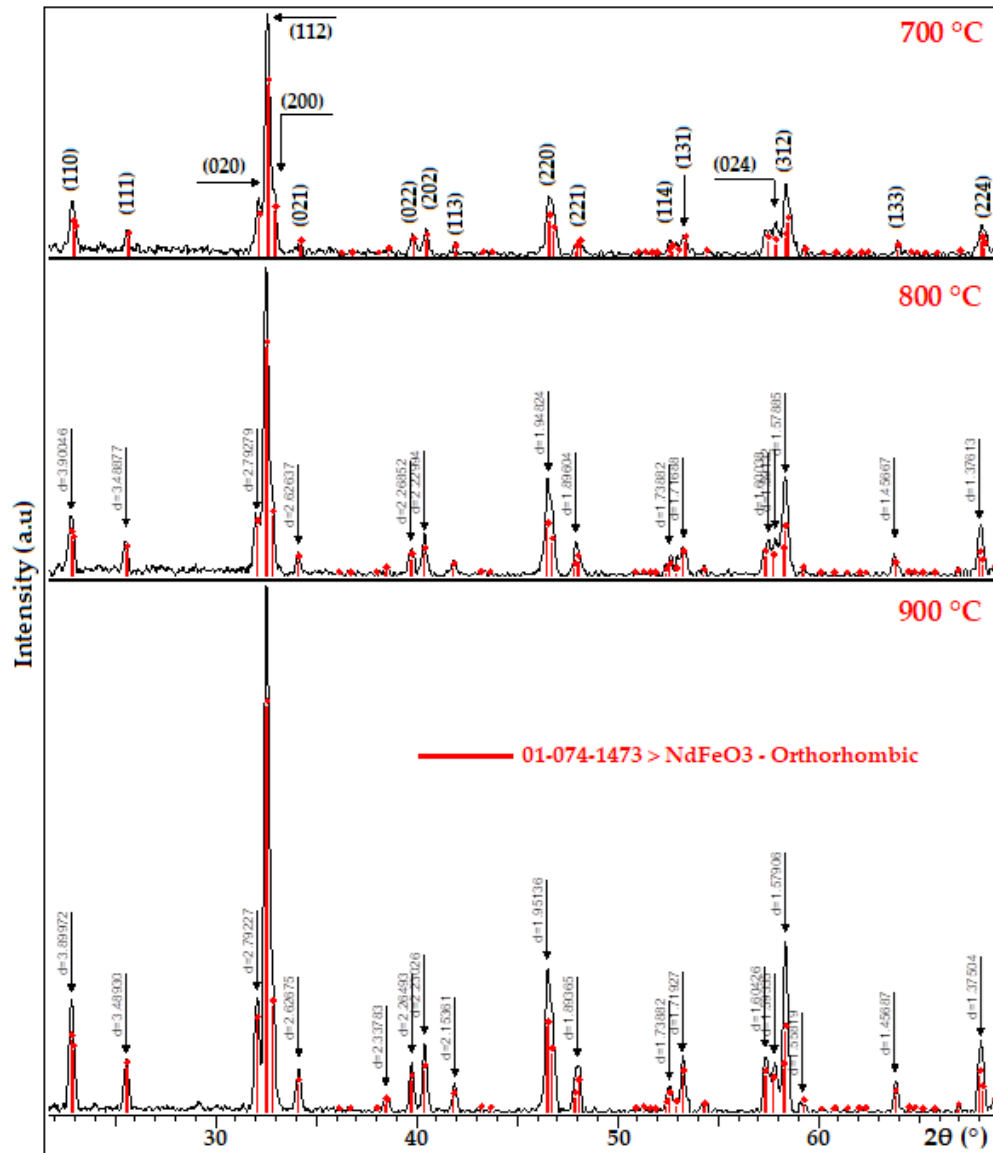
Fig. 1. XRD patterns of $NdFeO_3$ formed at 700, 800 and 900 °C for 1h

Condensed Matter and Interphases / Конденсированные среды и межфазные границы 2021;23(4): 600–606

Pham Thi Hong Duyen et al.   Optical and magnetic properties of orthoferrite NdFeO$_3$ nanomaterials...

Table 1. Structural characteristics of crystalline NdFeO$_3$ nanoparticles annealed at 700, 800 and 900 °C for 1 h

NdFeO$_3$	I, (a.u.)	d, (Å)	D, (nm)	Lattice constants, (Å)			V, Å^3
				a	b	c	
700 °C	120.29	2.75320	24.41	5.4417	5.6747	7.7727	240.02
800 °C	157.82	2.75322	25.37	5.4522	5.6827	7.7967	241.57
900 °C	269.33	2.75210	29.13	5.4573	5.6963	7.8154	242.95

the visible region for NdFeO$_3$ nanomaterials with different annealing temperature, thus showing the stability of the absorption of the materials at the wave length of λ ~ 750 nm. This can be originated from the minor amount of NdFeO$_3$ hexagonal phase (h-NdFeO$_3$) which has very indistinguishable PXRD peaks from those of orthorhombic phase (o-NdFeO$_3$). The increase in the absorption of the hexagonal phase in the visible region was also reported previously for the materials containing the o-YbFeO$_3$/h-YbFeO$_3$ mixture [26]. The existence of o-NdFeO$_3$ and h-NdFeO$_3$ in the samples is in good consistence with the band gap values (E_g, eV) showing in Fig. 3b. The band gap of NdFeO$_3$ nanomaterials varied from 2.2 eV to 2.5 eV (Table 2), remarkably lower than that of NdFeO$_3$ orthoferrite in earlier work [26] with E_g = 4.3 eV and HoFeO$_3$ with E_g = 3.39 eV) [11] prepared by solid-state reaction method. The E_g value of NdFeO$_3$ nanomaterials in this work is comparable with HoFeO$_3$ orthoferrite (E_g = 2.1–2.6 eV) in our previous study [22]. This low band gap of NdFeO$_3$ nanomaterials is
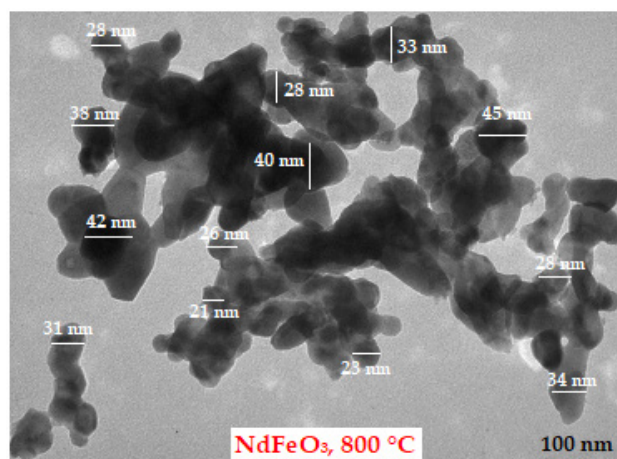
Fig. 2. TEM image of the NdFeO$_3$ nanoparticles annealed at 800 °C for 1 h

favorable for the application as photocatalysts to decompose toxic organic substances for environmental remediation [6–7, 21, 27].

From the *M-H* curves at room temperature (300 K) of the YFeO$_3$ samples annealed at 700, 800 and 900 °C, saturation magnetization
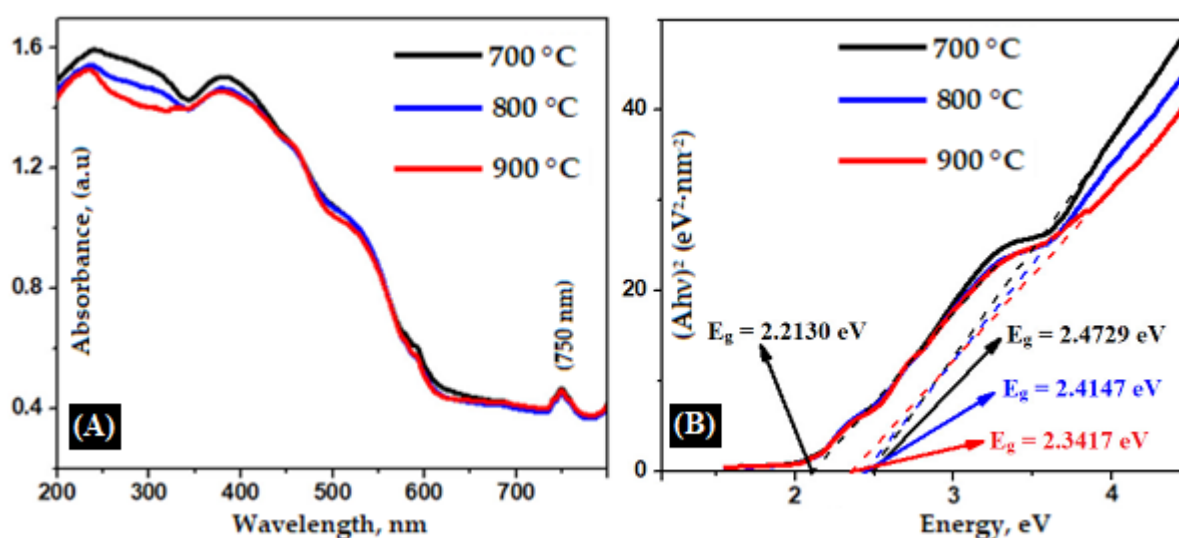
Fig. 3. (A) Room-temperature optical absorbance spectrum of the NdFeO$_3$ samples; (B) Tauc plot of (Ahv)^2 as a function of photon energy for NdFeO$_3$ nanoparticles annealed at 700, 800 and 900 °C for 1 h

Condensed Matter and Interphases / Конденсированные среды и межфазные границы   2021;23(4): 600–606

Pham Thi Hong Duyen et al.   Optical and magnetic properties of orthoferrite NdFeO₃ nanomaterials...

Table 2. Optical and magnetic characteristics of $NdFeO_3$ nanoparticles annealed at 700, 800 and 900 °C for 1 h

Samples	E_g, (eV)	H_c, (Oe)	M_r, emu·g⁻¹	M_s, emu·g⁻¹
NdFeO₃, 700 °C	2.2130–2.4729	1620.66	$7.7 \cdot 10^{-2}$	0.81
NdFeO₃, 800 °C	2.2130–2.4147	1453.30	$7.5 \cdot 10^{-2}$	1.01
NdFeO₃, 900 °C	2.2130–2.3417	590.17	$4.9 \cdot 10^{-2}$	1.47

(M_s) continued increasing in the magnetic field $H = \pm 20000$ Oe (the saturation was not reached). When the annealing temperature increased, the coercivity (H_c, Oe) and remanent magnetization (M_r, emu·g⁻¹) decreased, while he saturation magnetization (M_s, emu·g⁻¹) increased (Table 2). As the annealing temperature rose, the crystallinity of the materials also increased, the crystals became more stable, and thus the crystal anisotropy decrease, resulting in a drop in the value of M_r and H_c and an increment in M_s [28–29]. With a high coercivity ($H_c \gg 100$ Oe), the obtained NdFeO₃ orthoferrite nanomaterials can be classified as hard magnetic materials that can be applied for the manufacture of permanent magnet or magnetic tape.

4. Conclusions

NdFeO₃ orthoferrite nanomaterials were successfully synthesized by simple co-precipitation method via the hydrolysis of neodymium (III) and iron (III) cations in boiling water. Single-phase NdFeO₃ can be obtained after annealing the precursor at 700, 800 or 900 °C for 1h, having the crystal size of 25–30 nm, particle size of 20–40 nm and lattice cell volume of 240–243 Å³. The synthesized NdFeO₃ nanomaterials exhibited low band gap value (2.2–2.5 eV), and hard magnetic properties with high coercivity ($H_c \gg 100$ Oe), thus have great potential in photocatalysis for the decomposition of toxic organic waste and can be recovered easily by rare-earth magnetics.

Contribution of the authors

The authors contributed equally to this article.

Conflict of interests

The authors maintain that they have no conflict of interest to be described in this communication.
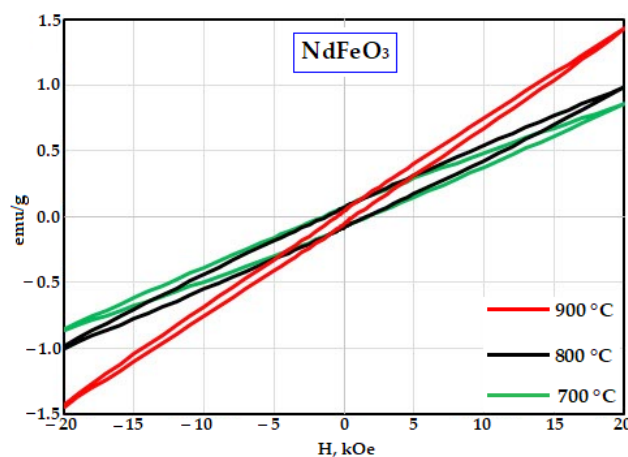
Fig. 4. Room-temperature magnetic hysteresis loops of as-prepared NdFeO₃ nanoparticles annealed at 700, 800 and 900 °C for 1h

References:

1. Kopeychenko E. I., Mittova I. Ya., Perov N. S., Nguyen A. T., Mittova V. O., Alekhina Yu. A., Pham V. Synthesis, composition and magnetic properties of cadmium-doped lanthanum ferrite nanopowders. *Inorganic Materials*. 2021;57(4): 367–371. https://doi.org/10.1134/S0020168521040075

2. Popkov V. I., Tugova E. A., Bachina A. K., Almjasheva O. V. The formation of nanocrystalline orthoferrites of rare-earth elements XFeO₃ (X = Y, La, Gd) via heat treatment of co-precipitated hydroxides. *Russian Journal of General Chemistry*. 2017;87: 2516–2524. https://doi.org/10.1134/S1070363217110020

3. Wang Z. Q., Lan Y. S., Zeng Z. Y., Chen X. R., Chen Q. F. Magnetic structures and optical properties of rare-earth orthoferrites RFeO₃ (R = Ho, Er, Tm and Lu). *Solid State Communications*. 2019;288: 10–17. https://doi.org/10.1016/j.ssc.2018.11.004

4. Berezhnaya M. V., Perov N. S., Almjasheva O. V., Mittova V. O., Nguyen A. T., Mittova I. Ya., Druzhinina L. V., Alechina Yu. A. Synthesis and magnetic properties of barium-doped nanocrystal lanthanum orthoferrite. *Russian Journal of General Chemistry*. 2019;89(3): 480–485. https://doi.org/10.1134/S1070363219030198

Condensed Matter and Interphases / Конденсированные среды и межфазные границы   2021;23(4): 600–606

Pham Thi Hong Duyen et al.   Optical and magnetic properties of orthoferrite NdFeO$_3$ nanomaterials...

5. Berezhnaya M. V., Al'myasheva O. V., Mittova V. O., Nguyen A. T., Mittova I. Ya. Sol-gel synthesis and properties of Y$_{1-x}$Ba$_x$FeO$_3$ nanocrystals. *Russian Journal of General Chemistry*. 2018;88(4): 626–631. https://doi.org/10.1134/S1070363218040035

6. Kondrashkova I. S., Martinson K. D., Zakharova N. V., Popkov V. I. Synthesis of nanocrystalline HoFeO$_3$ photocatalyst via heat treatment of products of glycine-nitrate combustion. *Russian Journal of General Chemistry*. 2018;88: 2465–2471. https://doi.org/10.1134/S1070363218120022

7. Oemar U., Ang P., Hidajat K, Kawi S. Promotional effect of Fe on perovskite LaNi$_x$Fe$_{1-x}$O$_3$ catalyst for hydrogen production via steam reforming of toluene. *International Journal of Hydrogen Energy*. 2013;38(14): 5525–5534. https://doi.org/10.1016/j.ijhydene.2013.02.083

8. Knurova M. V., Mittova I. Ya., Perov N. S., Al'myasheva O. V., Nguyen A. T., Mittova V. O., Bessalova V. V., Viryutina E. L. Effect of the degree of doping on the size and magnetic properties of nanocrystals La$_{1-x}$Zn$_x$FeO$_3$ synthesized by the sol – gel method. *Russian Journal of Inorganic Chemistry*. 2017;62(3): 281–287. https://doi.org/10.1134/S0036023617030081

9. Thu D. T. A., Giang H. T., Manh D. H., Toan N. N. Study on the preparation of gas sensing material LaFeO$_3$ by sol-gel method using citrate ion as ligand and used in ethanol sensor. *VNU Journal of Science: Natural Sciences and Technology*. 2010;26: 36–43. Available at: https://js.vnu.edu.vn/NST/article/view/1955

10. Sasikala C., Durairaj N., Baskaran I., Sathyaseelan B., Henini M. Transition metal titanium (Ti) doped LaFeO$_3$ nanoparticles for enhanced optical structure and magnetic properties. *Journal of Alloys and Compounds*. 2017;712: 870–877. https://dx.doi.org/10.1016/j.jallcom.2017.04.133

11. Habib Z., Majid K., Ikram M., Sultan K. Influence of Ni substitution at B-site for Fe^{3+} ions on morphological, optical, and magnetic properties of HoFeO$_3$ ceramics. *Applied of Physics A*. 2016; 122(5): 550. https://doi.org/10.1007/s00339-016-0082-z

12. Zhou Z., Guo L., Yang H., Liu Q., Ye F. Hydrothermal synthesis and magnetic properties of multiferroic rare-earth orthoferrites. *Journal of Alloys and Compouds*. 2014;583: 21–31. https://doi.org/10.1016/j.jallcom.2013.08.129

13. Khorasani-Motlagh M., Noroozifar M., Yousefi M., Jahani Sh. Chemical synthesis and characterization of perovskite NdFeO$_3$ nanocrystals via a co-precipitation method. *International Journal of Nanoscience and Nanotechnology*. 2013; 9(1): 7–14. Available at: http://www.ijnnonline.net/article_3874.html

14. Zharvan V., Kamaruddin Y. N., Samnur S., Sujiono E. H. The effect of molar ratio on crystal structure and morphology of Nd$_{1+x}$FeO$_3$ (x = 0.1, 0.2 and 0.3) oxide alloy material synthesized by solid state reaction method. *IOP Conference Series: Materials Science and Engineering*. 2017;202: 012072. https://doi.org/10.1088/1757-899X/202/1/012072

15. Vera Serna P., García Campos C., Sánchez De Jesús F., Bolarín Miró A. M., Juanico Lorán J. A., Longwell J. Mechanosynthesis, crystal structure and magnetic characterization of neodymium orthoferrite. *Materials Research*. 2016;19(2): 389-393. https://doi.org/10.1590/1980-5373-MR-2015-0214

16. Luu M. D., Dao N. N., Nguyen D. V., Pham N. C., Vu T. N., Doan T. D. A new perovskite-type NdFeO$_3$ adsorbent: synthesis, characterization, and As(V) adsorption. *Advances in Natural Sciences: Nanoscience and Nanotechnology*. 2016;7(2): 15–25. Available at: https://ans.ac.vn/index.php/oms/article/view/498

17. Tugova E., Yastrebov S., Karpov O., Smith R. NdFeO$_3$ nanocrystals under glycine nitrate combustion formation. *Journal of Crystals Growth*. 2017;467: 88–92. https://doi.org/10.1016/j.jcrysgro.2017.03.022

18. Babu P. R., Babu R. Starch assisted sol-gel synthesis and characterization of NdFeO$_3$. *International Journal of ChemTech Research*. 2016;9(4): 364–369.

19. Nguyen A. T., Pham V., Pham L. T., Nguyen T. T. L., Mittova I. Ya., Mittova V. O., Vo N. L., Nguyen T. B. T., Bui X. V., Viryutina E. L. Simple synthesis of NdFeO$_3$ by the co-precipitation method based on a study of thermal behaviors of Fe (III) and Nd (III) hydroxides. *Crystals*. 2020;10: 219. https://doi.org/10.3390/cryst10030219

20. Nguyen A. T., Nguyen N. T, Mittova I. Ya., Perov N. S., Mittova V. O., Hoang T. C. C., Nguyen V. M., Nguyen V. H., Pham V., Bui X. V. Crystal structure, optical and magnetic properties of PrFeO$_3$ nanoparticles prepared by modified co-precipitaiton method. *Processing and Application of Ceramics*. 2020;14(4): 355–361. https://doi.org/10.2298/PAC2004355N

21. Nguyen A. T., Nguyen T. T. L., Bui X. V., Nguyen T. H. D., Lieu D. H., Le T. M. L., Pham V. Optical and magnetic properties of HoFeO$_3$ nanocrystals prepared by a simple co-precipitation method using ethanol. *Journal of Alloys and Compounds*. 2020;834: 155098. https://doi.org/10.1016/j.jallcom.2020.155098

22. Nguyen A. T., Nguyen T. T. L., Bui X. V. Influence of the synthitic conditions on the crystal structure, magnetic and optical properties of holmium orthoferrite nanoparticles. *Journal of Materials Science: Materials in Electronics*. 2021;32: 19010–19019. https://doi.org/10.1007/s10854-021-06415-2

23. Nguyen A. T., Pham N. T. V., Le T. H., Chau H. D., Mittova V. O., Nguyen T. T. L., Dinh A. D., Hao T. V. N., Mittova I. Ya. Crystal structure and magnetic properties

Condensed Matter and Interphases / Конденсированные среды и межфазные границы   2021;23(4): 600–606

Pham Thi Hong Duyen et al.   Optical and magnetic properties of orthoferrite NdFeO$_3$ nanomaterials...

of LaFe$_{1-x}$Ni$_x$O$_3$ nanomaterials prepared via a simple co-precipitation method. *Ceramics International*. 2019;45: 21768–21772. https://doi.org/10.1016/j.ceramint.2019.07.178

24. Nguyen A. T., Pham N. T. V., Nguyen T. T. L., Mittova V. O., Vo Q. M., Berezhnaya M. V., Mittova I. Ya., Do T. H., Chau H. D. Crystal structure and magnetic properties of perovskite YFe$_{1-x}$Mn$_x$O$_3$ nanopowders synthesized by co-precipitation method. *Solid State Sciences*. 2019;96: 105922. https://doi.org/10.1016/j.solidstatesciences.2019.06.011

25. Nguyen A. T., Pham V., Chau H. D., Mittova V. O., Mittova I. Ya., Kopeychenko E. L., Nguyen T. T. L., Bui X. V., Nguyen T. P.A. Effect of Ni substitution on phase transition, crystal structure and magnetic properties of nanostructured YFeO$_3$ perovskite. *Journal of Molecule Structure*. 2020;1215: 128293. https://doi.org/10.1016/j.molstruc.2020.128293

26. Tikhanova S. M., Lebedev L. A., Martinson K. D., Chebanenko M. I., Buryanenko I. V., Semenov V. G., Popkov V. I. Synthesis of novel heterojunction h-YbFeO$_3$/o-YbFeO$_3$ photocatalyst with enhanced fenton-like activity under visible-light. *New Journal of Chemistry*. 2021;45(3):1541–1550. https://doi.org/10.1039/D0NJ04895J

27. Mir S. A., Ikram M., Asokan K. Effect of Ni doping on optical, electrical and magnetic properties of Nd orthoferitte. *Journal of Physics: Conference Series*. 2014;534: 012017. https://doi.org/10.1088.1742-6596/534/1/012017

28. Cullity B. D., Graham C. D. *Introduction to magnetic materials*, 2nd ed. Canada: John Wiley & Sons, Inc., Publication; 2009. http://doi.org/10.1002/9780470386323

29. Hien T. D., Tai L. T. *Magnetism and magnetic materials*. Bach Khoa Publishing House. Ha Noi; 2016. (in Vietnamese).

Information about the authors

Pham Thi Hong Duyen, Master in Chemistry, Lecturer of Institute of Applied Technology, Thu Dau Mot University, Binh Duong Province, Vietnam; e-mail: duyenpth@tdmu.edu.vn. ORCID iD: https://orcid.org/0000-0002-7350-0634

Anh Tien Nguyen, PhD in Chemistry, Chief of Inorganic Chemistry Department, Ho Chi Minh City University of Education, Vietnam; e-mail: tienna@hcmue.edu.vn. ORCID iD: https://orcid.org/0000-0002-4396-0349

Original articles

Investigation of the deposition of calcium fluoride nanoparticles on the chips of CaF$_2$ single crystals

P. P. Fedorov[1] ✉, **M. N. Mayakova**[1], **R. V. Gaynutdinov**[2], **N. Yu. Tabachkova**[1], **G. A. Komandin**[1],
A. E. Baranchikov[3], **E. V. Chernova**[1], **S. V. Kuznetsov**[1], **V. K. Ivanov**[3], **V. V. Osiko** [1]

[1]*Prokhorov General Physics Institute of the Russian Academy of Sciences,
38 Vavilova str., Moscow, 119991 Russian Federation*

[2]*Shubnikov Institute of Crystallography, Federal Scientific Research Centre Crystallography and Photonics,
Russian Academy of Sciences,
59 Leninskii pr., Moscow, 119991 Russian Federation*

[3]*Kurnakov Institute of General and Inorganic Chemistry, Russian Academy of Sciences,
31 Leninskii pr., Moscow, 119071 Russian Federation*

Abstract

The deposition of calcium fluoride nanoparticles on single crystal chips of calcium fluoride was studied. CaF$_2$ nanoparticles were synthesized by co-precipitation from aqueous nitrate solutions using hydrofluoric acid as a fluorinating agent at a batch system. The prepared samples were examined by atomic force microscopy, scanning electron microscopy, transmission electron microscopy and optical transmission. There is an inhomogeneous coating of the substrate surface with submicron particles of about 100–150 nm in size, which are clusters of nanoparticles of 15-20 nm in size. The initial nanoparticles coherently grow on the surface of the crystal substrate. Heat treatment of the substrate-deposited layer composite at 600 °C leads to the coalescence of submicron particles and the formation of a porous layer of a complex structure.

Keywords: Fluorite, Single crystals, Nanoparticles, Co-precipitation, Mechanism of oriented attachment growth

For citation: Fedorov P. P., Mayakova M. N., Gaynutdinov R. V., Tabachkova N. Yu., Komandin G. A., Baranchikov A. E., Chernova E. V., Kuznetsov S. V., Ivanov V. K., Osiko V. V. Investigation of the deposition of calcium fluoride nanoparticles on the chips of CaF$_2$ single crystals. *Kondensirovannye sredy i mezhfaznye granitsy = Condensed Matter and Interphases.* 2021;23 (4): 607–613. https://doi.org/10.17308/kcmf.2021.23/3681

Для цитирования: Федоров П. П., Маякова М. Н., Гайнутдинов Р. В., Табачкова Н. Ю., Командин Г. А., Баранчиков А. Е., Чернова Е. В., Кузнецов С. В., Иванов В. К., Осико В. В. Исследование осаждения наночастиц фторида кальция на сколах монокристаллов фторида кальция. *Конденсированные среды и межфазные границы.* 2021;23(4): 607–613. https://doi.org/10.17308/kcmf.2021.23/3681

✉ Pavel P. Fedorov, e-mail: ppfedorov@yandex.ru

Condensed Matter and Interphases / Конденсированные среды и межфазные границы   2021;23(4): 607–613

P. P. Fedorov et al.   Investigation of the deposition of calcium fluoride nanoparticles on the chips...

1. Introduction

In recent years, a paradigm change (correction) has taken place in the science of crystal growth: the totality of experimental data reliably indicates that in many cases the growth of crystals in laboratories, in industry, in nature, including in living organisms, is not carried out by attaching of atoms or ions from the environmental medium to the surface of a growing crystal, it proceeds by the oriented attachment of nano-, micro-, or volumetric particles [1–3]. Research on nonclassical crystal growth by the oriented attachment of particles is a "hot topic" of modern materials science [4–14].

One of the main scenarios for nonclassical growth consists of the oriented attachment of small crystalline particles to the surface of a large crystal [15]. The consideration of the possibility of creating surface crystalline layers on a single-crystal substrate in this way is promising.

The aim of this study was the investigation of the deposition of calcium fluoride nanoparticles on chips of calcium fluoride single crystals. The design of experiments was similar to the classic experiment of Shaskolskaya and Shubnikov in 1933 [2, 16] (deposition of small alum crystals on the face of a large alum crystal) with a change in the crystallized substance (calcium fluoride is practically insoluble in water, unlike alum) and particle scale.

2. Experimental

High-purity fluorite single crystals (Hellma, Germany) were split by cleavage by a specially designed manual guillotine [17]. The chip orientation {111} corresponded to the exit of the third-order symmetry axis. The thickness of the plates was about 2 mm. Atomic force microscopy showed that the surface is atomically smooth and contains steps (Fig. 1).

CaF_2 nanoparticles were synthesized by coprecipitation from aqueous solutions [18] in the batch system. The main parts of the synthesis system were: a polypropylene reactor, a magnetic stirrer, and feed dispensers for initial substances. Hydrofluoric acid was used as a fluorinating agent. Calcium nitrate $Ca(NO_3)_2 \cdot 4H_2O$ (LANHIT, Russia, 99.99 wt. %), neodymium nitrate $Nd(NO_3)_3 \cdot 6H_2O$ (LANHIT, Russia, 99.99 wt. %), hydrofluoric acid (extra pure grade 27-5) were used as initial substances. Precipitation at room temperature was carried out by the dropwise addition of a calcium nitrate solution (C_N = 0.5 M) into a solution of hydrofluoric acid (C_f = 5 M) with vigorous stirring with a magnetic stirrer. The colloidal solution was formed as a result of a chemical reaction. The precipitate formed from colloidal solution and then was washed with bidistilled water.

The high specific electrical conductivity of colloidal solutions, which is ~ 3 mS/cm, makes it impossible to experimentally determine their zeta potentials.

A single crystal plate of calcium fluoride was placed horizontally and completely immersed in a colloidal solution (mother solution or wash water with a precipitated reaction product). The plates were placed in the solution one by one: for 1 hour directly during the synthesis process, for a day after the end of precipitation, for 14 days after twice washing the precipitate from the mother solution with bidistilled water. Washes were carried out until the diphenylamine reaction to nitrate ions was negative.
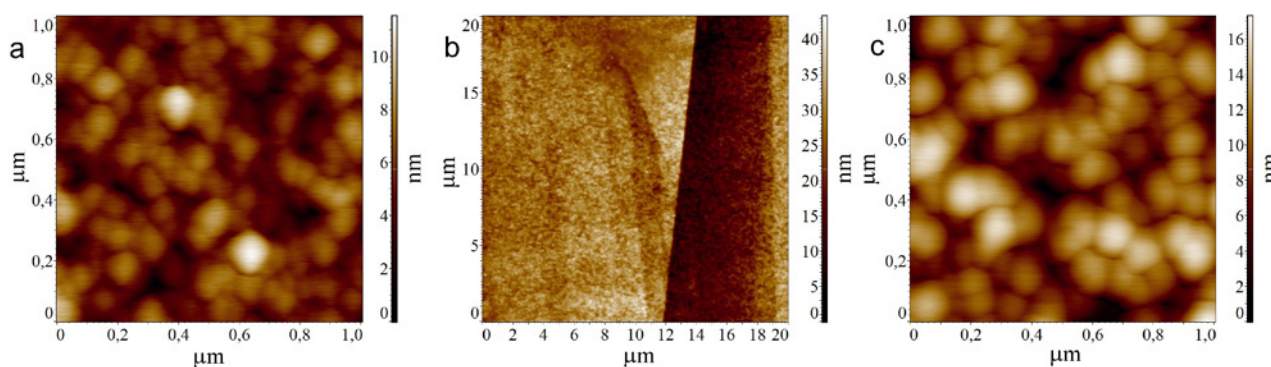
Fig. 1. AFM images of sample No. 1 (a) – precipitation, 1 hour, No. 4 (b, c) – precipitation from the mother solution, exposure for 1 day. A step in the chip is visible on the substrate surface

Condensed Matter and Interphases / Конденсированные среды и межфазные границы   2021;23(4): 607–613

P. P. Fedorov et al.   Investigation of the deposition of calcium fluoride nanoparticles on the chips...

The obtained samples were investigated by atomic force microscopy (AFM), scanning electron microscopy (SEM), transmission electron microscopy (TEM), and optical transmission.

Surface relief of CaF_2 single crystal with deposited nanoparticles was studied using AFM. Measurements were carried out using a scanning probe microscope Ntegra Prima (NT-MDT Spectrum Instruments, Russia) in tapping mode. The silicon cantilevers used (Tipsnano, Estonia) are characterised by the following parameters: resonant frequency f ~ 37 kHz, tip radius R ~ 10 nm and stiffness constant k ~ 0.65 N/m. All experiments on the study of the surface of the samples were carried out under the controlled conditions of the TRACKPORE ROOM-05 measuring complex (class 5 ISO (100), humidity 40 rel. % ± 1% and temperature 24 ± 0.05 °C).

For scanning electron microscopy (SEM) and energy dispersive X-ray spectroscopy (EDX), a Carl Zeiss NVision 40 electron microscope (Zeiss, Germany) was used in a high vacuum mode at an accelerating voltage of 20 kV (LaB_6 cathode). Images were formed with a backscattered electron detector (BSE) and a secondary electron detector (SE).

For structural studies, a high-resolution JEM 2100 transmission electron microscope (JEOL, Japan) was used. The JEM 2100 microscope has a spatial resolution of 2.3 Å (point-to-point) and 1.4 Å (lines), a maximum accelerating voltage of 200 kV. The LaB_6 cathode was used as a source of electrons. When obtaining a high-resolution image, an objective lens diaphragm with the diameter of 40 μm was used, which allowed passing a sufficient number of diffracted beams through the optical system of the microscope. For spatial coherence, a condenser lens diaphragm with a diameter of 50 μm was used. The average beam diameter for obtaining images was approximately 100 nm (3 Spot size). Survey images were obtained at low magnifications (5,000–20,000). For a more detailed study of the structure and observation of traces of atomic planes, a direct magnification of 400,000–600,000 was used.

For the investigation of particles on a substrate, samples were prepared in cross section. In order to cut the workpiece from the starting material, ultrasonic cutting was used; the cutting tool was an empty tube with an inner diameter of 3 mm. Cutting was carried out by excitation of the lead zirconate titanate (PZT) crystals at 26 kHz. The cutting medium was a boron carbide abrasive suspension. Ion etching was performed using a PIPS II system (Precision Ion Polishing System, Gatan) at an accelerating voltage of 3 keV.

The optical transmission of fluorite single crystals, both pure and deposited by layers, was investigated in the IR and terahertz ranges. Measurements were performed using a Bruker IFS113v (IR FT) Fourier spectrometer and a time-domain spectrometer (TDS) described in [19]. Transmission spectra were obtained in the transparency regions of the material in the THz and mid-IR ranges. In the region of high absorption, the reflectance spectra were measured. Reflection spectra were normalized versus a silver mirror reference with a radiation incidence angle of not higher than 6°. All measurements were performed at a temperature of 20 °C. The resolution in IR range was 2 cm⁻¹, in the THz range – 0.2 cm⁻¹.

3. Results and discussion

Typical AFM data are shown in Figs. 1–3. They slightly varied from experiment to experiment. In general, an inhomogeneous coating of the substrate surface with submicron particles with a size of about 100–150 nm was observed. Particle faceting was not revealed by AFM. The observed pattern is similar to the agglomeration of particles in samples of natural silicites, specifically samples of flints and chalcedony [20].

For a sample prepared by deposition with exposure time of 1 h (sample No. 1, Fig. 1a), formations with a size of 40–150 nm were characteristic. When the time of exposure in mother solution was increased up to 24 h (sample No. 4), a significant increase in the size of the formations (70–150 nm) was not observed, however, the general compaction of agglomerates and clearer boundaries between individual formations were noted.

In clusters of particles, agglomerated triangular formations corresponding to the symmetry of the substrate of micron sizes were visible (Fig. 2). SEM data were more informative (Fig. 3). These data allowed visualization of initial small (about 15–20 nm) faceted nanoparticles

Condensed Matter and Interphases / Конденсированные среды и межфазные границы   2021;23(4): 607–613

P. P. Fedorov et al.   Investigation of the deposition of calcium fluoride nanoparticles on the chips...
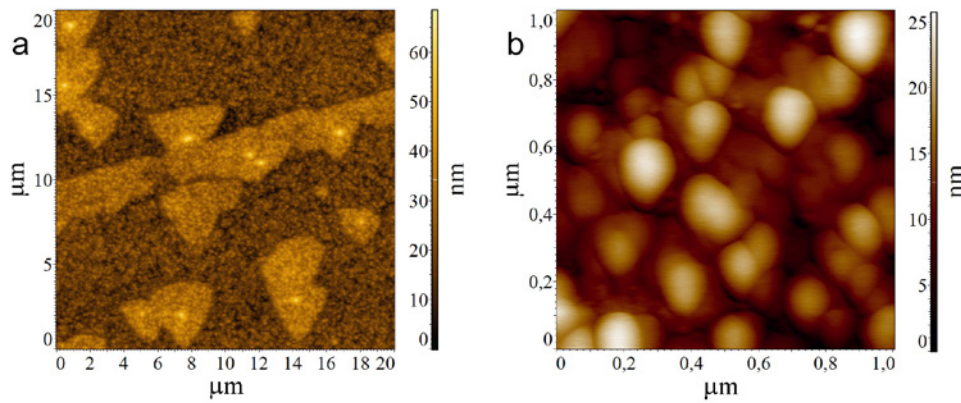
Fig. 2. AFM image of sample No. 7, precipitation from the washing solution, exposure for 2 weeks
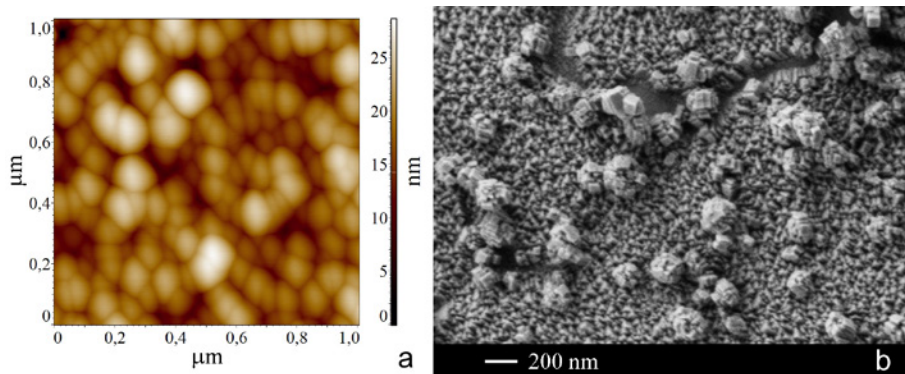
Fig. 3. Atomic force (left shot) and scanning electron microscopes (right shot) images. Sample No. 6, mother solution, exposure for 1 day

located on the substrate and mutually oriented. Submicron formations had clusters of these nanoparticles.

Transmission electron microscopy data (Fig. 4) indicated a coherent growth of fluorite nanoparticles precipitated on a single-crystal substrate. The crystallographic planes of the particles, precipitated on fluorite single crystal had a continuation into the substrate. In addition, the particles of the second deposition layer also retained their orientation relative to the particles of the first layer.

These results confirm the data of the classical experiment of Shubnikov and Shaskolskaya [2, 16] on the oriented growth of small particles during their deposition on the surface of a large crystal.

The optical transmission spectrum of a fluorite plate with deposited fluorite particles contains absorption lines in the regions of 1450–1730 and 2850–2930 cm^{-1} corresponding to vibrations of water molecules and hydroxyl species (Fig. 5). This is natural, since adsorbed water forms tightly bound layers on the surface of

fluorite nanoparticles prepared by precipitation from an aqueous solution.

The heat treatment of a fluorite single crystal substrate with a precipitated layer of CaF_2 at 600 °C was performed. Atomic force microscopy images of the formed layers are shown in Fig. 6. As expected, the attachment growth of the initial particles deposited on the substrate surface with
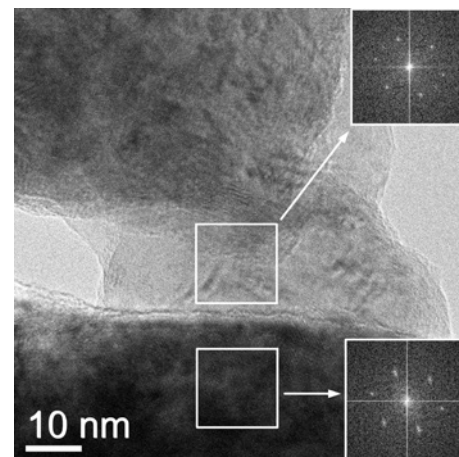
Fig. 4. TEM micrograph, sample No. 1, series "a"

Condensed Matter and Interphases / Конденсированные среды и межфазные границы   2021;23(4): 607–613

P. P. Fedorov et al.   Investigation of the deposition of calcium fluoride nanoparticles on the chips...
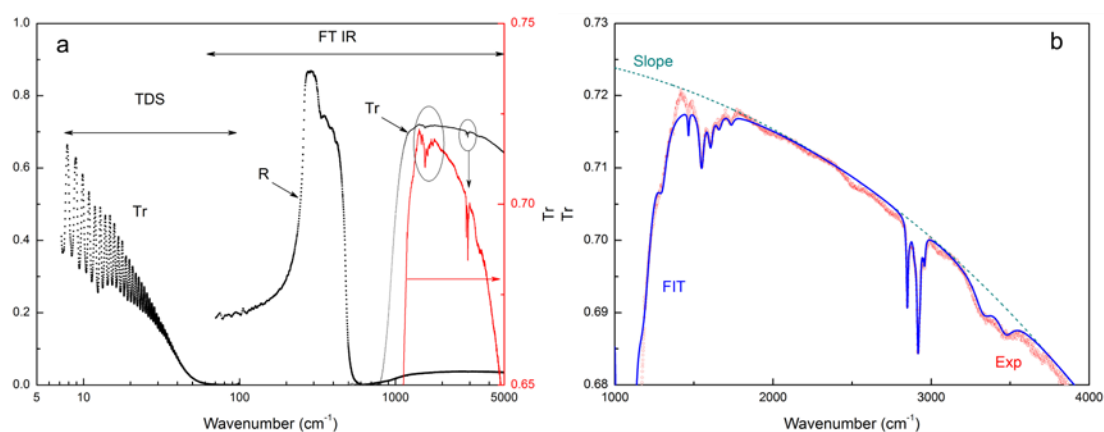
Fig. 5. Optical transmission and reflection of a fluorite plate with deposited nanoparticles in the visible, IR and THz ranges
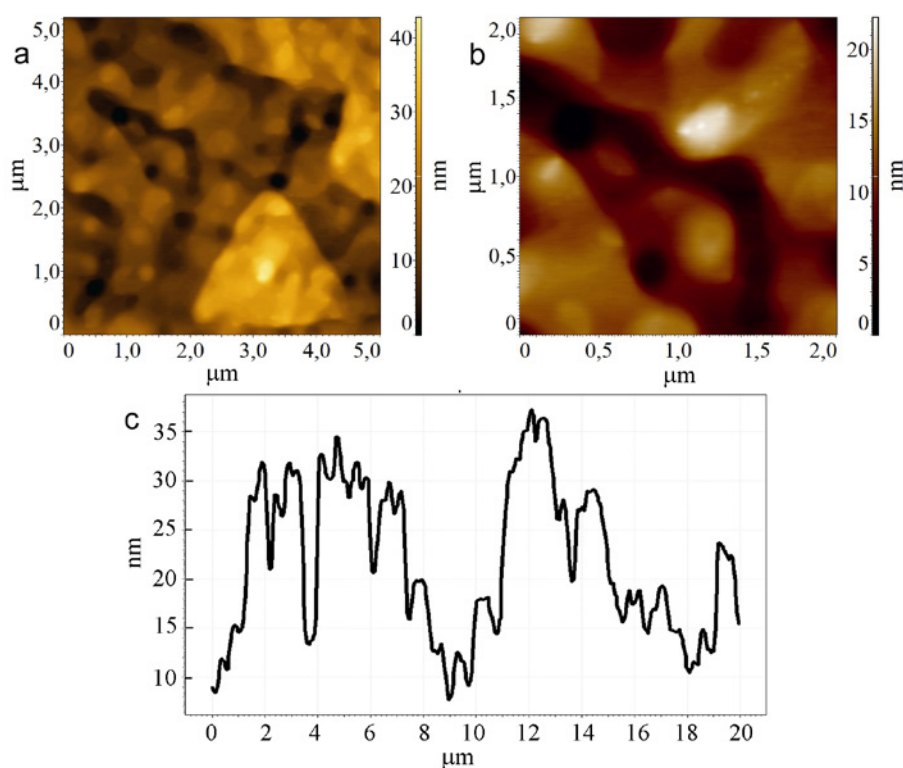
Fig. 6. AFM image of the surface of sample No. 7 annealed at 600 ° C for 1 hour (a, b) and the profile of the formed surface (c)

the formation of a single continuous agglomerate of complex topology was observed. The formation of the layer did not finish. The profile of the layer is complex, with strong height differences at the level of 10–30 nm (Fig. 6c).

4. Conclusions

Thus, the deposition of fluorite nanoparticles on the surface of a CaF$_2$ single crystal is oriented with a coherent attachment growth to the surface of the single crystal (Fig. 4). However, the formation of associates of nanoparticles in the initial colloidal solution promotes the chaotic deposition of submicron particles on the substrate surface (Figs. 1–3). The structure formed during the deposition process after heat treatment creates a nanoarchitecture of complex topology. This circumstance prevents the formation of a homogeneous monolithic film suitable for use in photonics on the surface of a single-crystalline substrate. However, this structure of the deposited film can be attractive, for example, for the creation of catalysts.

Condensed Matter and Interphases / Конденсированные среды и межфазные границы   2021;23(4): 607–613

P. P. Fedorov et al.   Investigation of the deposition of calcium fluoride nanoparticles on the chips...

Authors contributions

Fedorov P. P. – planning research, writing the article. Mayakova M. N. – carrying out syntheses. Gaynutdinov R. V. – studies by means of atomic force microscopy. Tabachkova N. Yu. – studies by means of transmission electron microscopy. Komandin G. A. – carrying out optical measurements. Baranchikov A. E. – studies by means of scanning electron microscopy. Chernova E. V. – the design of figures, the text, and related materials. Kuznetsov S. V. – discussion of the results. Ivanov V. K. – discussion of the results. Osiko V.V. – the idea of experiments, discussion of the results.

Conflict of interests

The authors declare that they have no known competing financial interests or personal relationships that could have influenced the work reported in this paper.

References

1. Colfen H., Antonietti M. *Mesocrystals and nonclassical crystallization*. John Wiley & Sons, Ltd: Chichester; 2008. https://doi.org/10.1002/9780470994603

2. Ivanov V.K., Fedorov P.P., Baranchikov A.Y., Osiko V.V. Oriented attachment of particles: 100 years of investigations of non-classical crystal growth. *Russian Chemical Reviews*. 2014;83(12): 1204–1222. https://doi.org/10.1070/RCR4453

3. De Yoreo J. J., Gilbert P. U. P. A., Sommerdijk N. A. J. M., Penn R. L., Whitelam S., Joester D., Zhang H., Rimer J. D., Navrotsky A., Banfield J. F., Wallace A. F., Miehel F. M., Meldrum F. C., Cölfen H., Dove P. M. Crystallization by particle attachment in synthetic, biogenic, and geologic environments. *Science*. 2015;349(6247): aaa6760-1–aaa6760-8. https://doi.org/10.1126/science.aaa6760

4. Garsio-Romero E., Suares M. A structure-based argument for non-classical crystal growth in natural clay minerals. *Mineralogical Magazine.* 2018;82: 171. https://doi.org/10.1180/minmag.2017.081.031

5. Sushko M. L. Understanding the driving forces for crystal growth by oriented attachment through theory and simulations. *Journal of Materials Research.* 2019;34: 2914–2927 https://doi.org/10.1557/jmr.2019.151

6. Fedorov P. P., Osiko V. V. Relationship between the faceting of crystals and their formation mechanism. *Doklady Physics.* 2019;64(9): 353–355. https://doi.org/10.1134/S1028335819090076

7. Neira-Carrillo A., Vásquez-Quitral P., Sánchez M., Farhadi-Khouzani M., Aguilar-Bolados H., Yazdani-Pedram M., Cölfen H. Functionalized multiwalled CNTs in classical and nonclassical CaCO$_3$ crystallization. *Nanomaterials.* 2019;9(8): 1169. https://doi.org/10.3390/nano9081169

8. Witts B. D., Clode P. L., Patel N. H., Schroder-Turk G. E. Natures's functional nanomaterials: Growth or self-assembly? *MRS Bulletin.* 1919;44(2): 106–112. https://doi.org/10.1557/mrs.2019.21

9. Zhou W. Reversed crystal growth. *Crystals.* 2019;9:7. https://doi.org/10.3390/cryst9010007

10. Liu Y., Geng H., Qin X., Yang Y., Zeng Z., Chen S., ... Kawazoe Y. Oriented attachment revised: Does a chemical reaction occur? *Matter.* 2019;1(3): 390–704. https://doi.org/10.1016/j.matt.2019.05.001

11. Colfen H. Nonclassical nucleation and crystallization. *Crystals.* 2020;10(2): 61. https://doi.org/10.3390/cryst10020061

12. Bard A. B., Zhou X., Xia X., Zhu G., Lim M. B., Kim S. M., ... Pauzauskie P. J. A mechanistic inderstanding of non-classical crystal growth in hydrothermally synthezied sodium yttrium fluoride nanowires. *Chemistry of Materials.* 2020;32(7): 2753–2763. https://doi.org/10.1021/acs.chemmater.9b04076

13. Mu Z., Tang R., Liu Z. Construction of inorganic bulks through coalescence of particle precurcor. *Nanomaterials.* 2021;11(1): 241. https://doi.org/10.3390/nano11010241

14. Mashiach R., Weissman H., Avram L., Houben L., Brontvein O., Lavie A., Arunacalam V., Leskes M., Rybtchinski B., Bar-Shir A. In situ NMR reveals real-time nanocrystal growth evolution via monomer-attachment or particle-coalescence. *Nature Communications.* 2021;12(1): 229. https://doi.org/10.1038/s41467-020-20512-6

15. Fedorov P. P., Ivanov V. K., Osiko V. V. Basic features and crystal growth scenarios based on the mechanism of oriented attachment growth of nanoparticles. *Doklady Physics.* 2015;60(11): 483–485. https://doi.org/10.1134/S1028335815110105

16. Shubnikov A. V. *Kak rastut kristally* [*How crystals grow*]. Moscow–Leningrad: Publ. AN SSSR; 1935. 176 p. (In Russ.)

17. Maslov V. A., Chernova E. V., Fedorov P. P. Search for flux media for crystallization of epitaxial fluorite layers. *Crystallography Reports*. 2020;65(4): 647 652. https://doi.org/10.1134/S106377452004015X

18. Fedorov P. P., Kuznetsov S. V., Mayakova M. N., Voronov V. V., Ermakov R. P., Baranchikov A. E., Osiko V. V. Coprecipitation from aqueous solutions to prepare binary fluorides. *Russian Journal of Inorganic Chemistry*. 2011;56(10): 1525–1531. https://doi.org/10.1134/S003602361110007X

19. Komandin G. A., Gavdush A. A., Goncharov Y. G., Porodinkov O. E., Nozdrin V. S., Chuchupal S. V., Spektor I. E. Electrodynamical characteristics of α-lactose monohydrate in the terahertz range. *Optics*

Condensed Matter and Interphases / Конденсированные среды и межфазные границы   2021;23(4): 607–613

P. P. Fedorov et al.   Investigation of the deposition of calcium fluoride nanoparticles on the chips...

and Spectroscopy. 2019;126(5):514–522. https://doi.org/10.1134/S0030400X1905014X

20. Gaynutdinov R., Voronov V. V., Chernova E. V., Maslov V. A., Mayakova M. N., Chislov A. S., Novikov I. A., Fedorov P. P. Flints as nanostructured chalcedons. *Journal of Surface Investigation: X-ray, Synchrotron and Neutron Techniques.* 2020;14(4):762–770. https://doi.org/10.1134/S1027451020040084

Information about the authors

Pavel P. Fedorov, DSc in Chemistry, Professor, Chief Researcher, Prokhorov General Physics Institute of the Russian Academy of Sciences, Moscow, Russian Federation; e-mail: ppfedorov@yandex.ru. ORCID iD: https://orcid.org/0000-0002-2918-3926.

*Maria N. Mayakova***, PhD in Chemistry, Researcher of the Laboratory of Technology of Nanomaterials for Photonics, Department of Nanotechnologies at the Research Center for Laser Materials and Technologies, Prokhorov General Physics Institute of the Russian Academy of Science, Moscow, Russian Federation; e-mail: mayakova@lst.gpi.ru. https://orcid.org/0000-0003-0713-5357.

Radmir V. Gaynutdinov, PhD in Physics and Mathematics Senior Research, Crystallography and Photonics Federal Research Center of the Russian Academy of Science, Moscow, Russian Federation; e-mail: rgaynutdinov@gmail.com. ORCID iD: https://orcid.org/0000-0002-5384-4026.

Natalia Yu. Tabachkova, PhD in Physics and Mathematics, Senior Research, Prokhorov General Physics Institute of the Russian Academy of Science, Moscow, Russian Federation; e-mail: ntabachkova@gmail.com. ORCID iD: https://orcid.org/0000-0002-0169-5014.

Gennadiy A. Komandin, DSc in Physics and Mathematics, Leading Researcher, Prokhorov General Physics Institute of the Russian Academy of Science, Moscow, Russian Federation; e-mail: gakomandin@mail.ru. ORCID iD: https://orcid.org/0000-0003-1101-8225.

Alexander E. Baranchikov, PhD in Chemistry, Head of the Laboratory for the Synthesis of Advanced Materials and Minerals Processing, Kurnakov Institute of General and Inorganic Chemistry of the Russian Academy of Sciences, Moscow, Russian Federation; e-mail: a.baranchikov@yandex.ru. ORCID iD: https://orcid.org/0000-0002-2378-7446.

Elena V. Chernova, Junior Researcher of the Laboratory of Technology of Nanomaterials for Photonics, Department of Nanotechnologies at the Research Center for Laser Materials and Technologies. Prokhorov General Physics Institute of the Russian Academy of Science, Moscow, Russian Federation; e-mail: e-chernova@yandex.ru. ORCID iD: https://orcid.org/0000-0001-7401-5019.

Sergey V. Kuznetsov, PhD in Chemistry, Head of the Laboratory of Technology of Nanomaterials for Photonics, Department of Nanotechnologies at the Research Center for Laser Materials and Technologies. A. M. Prokhorov General Physics Institute of the Russian Academy of Science, Moscow, Russian Federation; e-mail: kouznetzovsv@gmail.com. ORCID iD: https://orcid.org/0000-0002-7669-1106.

Vladimir K. Ivanov, DSc in Chemistry, Corresponding member of the Russian Academy of Sciences, Director of Kurnakov Institute of General and Inorganic Chemistry of the Russian Academy of Sciences, Moscow, Russian Federation; e-mail: van@igic.ras.ru. ORCID iD: https://orcid.org/0000-0003-2343-2140.

Vyacheslav V. Osiko (1932-2019), Academician of the Russian Academy of Sciences, Head of Department of Nanotechnologies at the Research Center for Laser Materials and Technologies, Prokhorov General Physics Institute of the Russian Academy of Science, Moscow, Russian Federation; ORCID iD: https://orcid.org/0000-0002-3338-6187.

Translated by Valentina Mittova
Edited and proofread by Simon Cox

Original articles

New nanocomposites for deep water deoxygenation

T. E. Fertikova[1], S. V. Fertikov[2], E. M. Isaeva[2], V. A. Krysanov[2], T. A. Kravchenko[2]✉

[1]*Voronezh State Medical University named after N. N. Burdenko,
10 Universitetskaya pl., Voronezh 394036, Russian Federation*

[2]*Voronezh State University,
1 Universitetskaya pl., Voronezh 394018, Russian Federation*

Abstract

New metal-polymer nanocomposites for deep water deoxygenation have been obtained and studied. A macro- and monoporous sulphocation exchanger with a nanometer pore size was used as the polymer matrix, and the metal was nanodispersed copper deposited in the pores of the matrix. A specific feature of the studied nanocomposites is their sodium ionic form, which eliminates the possibility of the formation of soluble copper oxidation products. The established linear dependence of the copper capacity on the number of cycles of ion-exchange saturation - chemical deposition shows that the process of metal deposition into the pores of the matrix does not have significant obstacles during 10 cycles and contributes to the production of high-capacity samples.

The high efficiency and duration of the life cycle of high-capacity copper ion exchanger nanocomposites have been shown. Experimental studies of water deoxygenation in column-type apparatus with a nanocomposite nozzle were confirmed by a theoretical analysis of the process dynamics. Experimental data and theoretical calculations showed the deep level of water deoxygenation had practically unchanged values of pH and electrical conductivity. Residual oxygen can be controlled and does not exceed 3 μg/l (ppb).

The hygienic and economic substantiation of the expediency of using the obtained nanocomposites is provided. The necessity of using modern nanocomposite metal-polymer materials for deep water deoxygenation circulating in technological systems was analysed. When using this innovation, the metal components of the distribution facilities will be protected from corrosion and, therefore, the hygienic requirements for the water quality of centralised drinking water supply systems will be ensured. Deep chemical water deoxygenation using copper ion-exchange polymer nanocomposites in sodium form allows solving the problem of the corrosion resistance of metals, ensuring that water meets hygienic requirements on a large scale.

The competitive advantage of the considered water deoxygenation system in comparison with the known systems is the rejection of the use of precious metals-catalysts (palladium, platinum), pure hydrogen, and complex design solutions. The proposed new nanocomposite installation for water deoxygenation is characterised by its ease of use and can be built into a filter system for water purification.

SWOT analysis of the advantages and disadvantages of the proposed method of water deoxygenation showed that its main advantages are the high oxygen capacity of the nanocomposite, low residual oxygen content (3 ppb (μg/l)) in the water, and ease of operation of the deoxygenator. Calculations of the economic efficiency of the nanocomposite have been carried out. The breakeven point is reached when producing only ~100 l of nanocomposite and a volume of sales ~1,600,000 roubles, above which a profit can be obtained. The payback period for an investment of ~15,000,000 roubles is rather short and will not exceed 2 years.

Keywords: Metal-polymer nanocomposites, Water deoxygenation, Hygiene requirements, Economic efficiency

✉ Tamara A. Kravchenko, e-mail: krav280937@yandex.ru

Condensed Matter and Interphases / Конденсированные среды и межфазные границы   2021;23(4): 614–625

T. E. Fertikova et al.   New nanocomposites for deep water deoxygenation

1. Introduction

The content of molecular oxygen in water to the level required for modern technological processes can be reduced, using traditional methods of deoxygenation: physical, chemical, electrochemical and sorption. It seems expedient to develop and introduce into the practice of water treatment an innovative method of deep water deoxygenation using new nanocomposite metal-polymer materials and evaluate their hygienic and economic efficiency. The proposed approach to water deoxygenation is based on the reduction of oxygen by nanoparticles of reactive metals deposited in porous ion-exchange matrices, with the retention of oxidation products in them.

Metal-polymer nanocomposites are three-dimensional polymer chains of highly porous materials, consisting of a polymer framework, metal nanoparticles, and, as a rule, fixed ionogenic groups and counterions. It is preferable to use macroporous structures with pore sizes up to 100 nm. In macropores, metal nanoparticles (about 10–30 nm) occupy separate areas, localizing near ionogenic groups on the walls and in the volume of macropores. Ion exchange is reversible, due to which multiple depositions of metal into nanopores is possible [1–4]. The size of the metal particles can be controlled [5]. Nanocomposite materials, the outer and inner surfaces of which are open to highly efficient sorption, chemical, and electrochemical processes are obtained [6–10]. The metal in the ion-exchange matrix can be in the form of highly dispersed particles (usually, nanoparticles) in a zero-valent state or be a part of oxides, poorly soluble hydroxides, simple and complex salts, fixed in a polymer matrix. Due to the fact that metal-ion exchanger nanocomposites are capable of simultaneously electron (redox) and ion exchange reactions, they are called electron ion exchangers and belong to the class of redoxites.

Nanocomposite materials based on polymer matrices and precious metals allow reducing the oxygen content in water to the level required for modern technological processes. The achieved high level of control over the properties of nanoparticles synthesised in various matrices clearly indicates good prospects for the use of nanocomposite materials in solving the problem of the deep removal of oxygen from water [11–15]. However, unlike noble metals and pure hydrogen used for these purposes, reactive metals (copper, iron, etc.) in ion-exchange matrices can be more widespread for water deoxygenation [16–18].

The aim of this study was the production of new copper-ion exchange nanocomposites (NC) and the investigation of these NCs for deep water deoxygenation, including the substantiation of the feasibility of their use from a hygienic and economic perspective.

2. Experimental

In order to achieve this aim, metal ($Cu°$) – sulphocation exchanger (Lewatit K2620) nanocomposites were used. The determination of the content of the metal component was carried out using complexometric titration, the size of metal particles was investigated using scanning electron microscopy (SEM) and X-ray diffraction analysis (XRD), and the composition of grains was determined using energy dispersive X-ray spectroscopy (EDS). The dynamics of water deoxygenation by granular layers of nanocomposites was studied.

The Lewatit K2620 (Germany) sulphocation exchanger, which is a strongly acidic macroporous resin based on cross-linked polystyrene with a spherical shape of granules, containing sulfonic acids, served as an ion-exchange matrix for the preparation of metal-containing NC [19]. It is characterised by its monoporosity. The pore size is strictly fixed (41 nm). The high ion exchange capacity (1.86 meq/cm^3) and the optimal grain radius (0.028 cm) promoted the deposition of metal nanoparticles and the conduction of target process. The high degree of crosslinking in combination with the compact structure of the

Condensed Matter and Interphases / Конденсированные среды и межфазные границы   2021;23(4): 614–625

T. E. Fertikova et al.   New nanocomposites for deep water deoxygenation

granule ensured the chemical and mechanical stability of this material. Metal-containing nanocomposites based on the Lewatit K2620 have a significant adjustable metal capacity.

The synthesis of NC containing dispersed copper can be considered as being the process of ion-exchange saturation of fixed polymer groups with copper from a solution followed by its chemical reduction [7]. A feature of the synthesis in comparison with [20] is the production of NC in the sodium form ensuring the formation of oxide products of copper oxidation with oxygen in the future

$$2[R-SO_3^-]H^+ + Cu^{2+} \rightarrow [R-SO_3^-]_2 Cu^{2+} + 2H^+, \quad (1)$$

$$[R-SO_3^-]_2 Cu^{2+} \xrightarrow{\text{Red+OH}^-} [R-SO_3^- Na^+]_2 \cdot Cu^0. \quad (2)$$
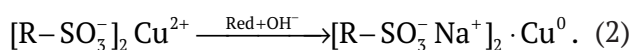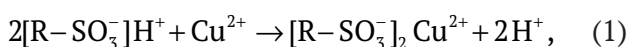
The number of processing cycles regulates the amount of metallic copper in the ion exchanger (from 1 to 10 and more meq/cm³).

The capacities for metallic copper, the size of copper particles, and the elemental composition of NC were determined. Metal capacity is the main parameter determining the quantitative content of metal in a nanocomposite. In order to determine the amount of copper in NC, the metal was transferred to a soluble state and then its concentration in the solution was analysed.

The particle size of the dispersed metal was determined by X-ray phase analysis and using a JSM 6380LV scanning electron microscope (Japan). For X-ray analysis, copper-containing nanocomposite granules (1 cm³) was placed in a metal cuvette. In the studied range of diffraction angles, the polymer matrix did not increase the background of X-ray patterns and did not produce its own peaks. X-ray diffraction patterns were obtained using a Thermo ARL X-TRA diffractometer (Switzerland) with MoK_α-radiation, in the range of angles $2\theta = 15–40°$ in scan mode by points with a step of 0.05° and an accumulation time of 3 seconds. Copper powder was used as a reference.

Scanning electron microscopy (SEM) is one of the most widely used methods for the diagnostics of nanomaterials and nanostructures. SEM is a method for analysing the surface structure of micro-objects, based on the interaction of an electron beam with compound, designed for obtaining an image of the surface of an object with a high spatial resolution (several nanometers), providing information about the composition, structure and some other properties of near-surface layers.

The determination of the elemental composition of the sample was carried out using energy dispersive analysis. The method is based on the registration of characteristic X-ray radiation excited by an electron beam. The samples for the energy dispersive analysis were grain sections prepared for SEM. The spectra were recorded using an INCA Energy-250 scanning electron microscope attachment (Great Britain).

For the investigation of the dynamics of oxygen uptake, the installation was designed (Fig. 1), consisting of a direct-flow column *1* filled with a layer of granular nanocomposite *2,* through which water with an oxygen concentration equal to atmospheric concentration was passed. This was achieved by a long preliminary and simultaneous (during the experiment) aeration of the water layer at the inlet. The flow rate of a of the molecular oxygen solution in distilled water was controlled by a flow meter *6*.

The concentration of the oxidant was recorded with an AKPM-01 oxygen analyser (Russia), which was protected from external electromagnetic fields
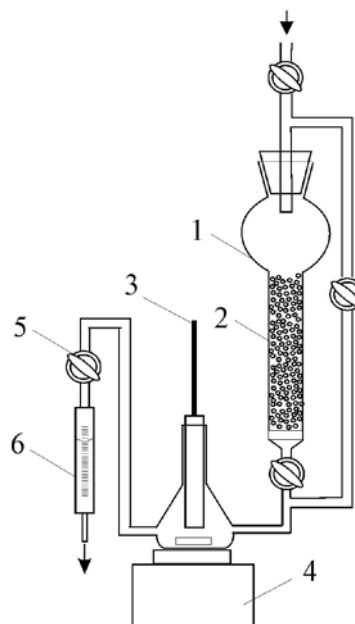
Fig. 1. Diagram of the installation for studying the dynamics of oxygen absorption by the NC layer: *1* - column, *2* – granular layer, *3* - oxygen meter, *4* - magnetic stirrer, *5* - adjustable tap, *6* - water flow meter

Condensed Matter and Interphases / Конденсированные среды и межфазные границы   2021;23(4): 614–625

T. E. Fertikova et al.   New nanocomposites for deep water deoxygenation

by a metal mesh. The maximum permissible error of the analyser in the concentration range of 0–2,000 µg/l and 2–20 mg/l, is ±(2.5+0.025*A) and ±0.025*A, respectively, where A is the readings of the oxygen meter in the selected unit of measurement. Oxygen meter sensor *3* was hermetically attached to a vessel, the water in which was stirred with a magnetic stirrer *4*, which allowed to consider it as an ideal mixing reactor. The individual elements of the installation were interconnected with polypropylene hoses, which minimised the passage of oxygen into the system. After the deoxygenating column, a mixed-bed polisher (MBP) was installed, which trapped impurity particles that could be washed out by passing water. All experiments were carried out at room temperature and under atmospheric pressure.

Simultaneously with the registration of the dynamic output curves of oxygen absorption, the pH and electrical conductivity of the filtered water were monitored. The pH value of water was determined using an ANION-4100 ionomer (Russia). An aqueous sample with a volume of 5 µL for spectral analysis was taken with a micropipette. The values of the electrical conductivity of water were recorded using a Cond 7110 conductometer (Germany). All solutions were prepared using distilled water with a specific electronic conductivity of $5 \cdot 10^{-4}$ S/m at 20 °C.

3. Results and discussion

3.1. Physical and chemical properties of synthesised Cu°·Lewatit K2620 nanocomposites

Cu°·Lewatit K2620(Na⁺) nanocomposites with varying copper content were obtained. The dependence of the NC capacity for copper on the number of deposition cycles was obtained (Fig. 2). The capacity increased linearly with the number of fittings. From the linear dependence, it follows that the process of deposition of metallic copper into the pores of NC did not have significant obstacles during 10 deposition cycles.

The rather small particle sizes calculated from the XRD results allowed us to conclude that the globules revealed on SEM micrographs were associates with a size of 100-200 nm, consisting of smaller structures with a size of about 10-30 nm. According to the data of energy dispersive analysis, it was found that the obtained NC with a capacity for copper of 9.80±0.01 meq/cm³
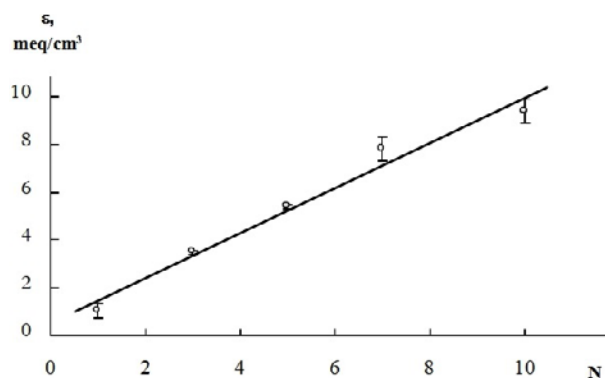
Fig. 2. Dependence of the capacity ε of the Cu°·Lewatit K2620 nanocomposite on the number of N deposition cycles

contained ~18 wt% of copper with predominant localization in the near-surface parts of the grain (Table 1).

Thus, Cu°·Lewatit K2620(Na⁺) nanocomposites with a high capacity for the metal component were obtained and characterised.

3.2. Chemical water deoxygenation

The process of chemical water deoxygenation was investigated. The experiment was carried out in two column-type deoxygenators connected in series (Fig. 1) for 150 h. The dimensions of the first deoxygenator were determined by the need to fix the changing digital values on the oxygen sensor for recording of data over time. The height of the first column was $L = 42 \cdot 10^{-2}$ m, section $S = 1.2 \cdot 10^{-4}$ m², the capacity of the NC was $\varepsilon_{Cu^0} = 6.68 \pm 0.08$ meq/cm³ with the number of deposition cycles $N = 7$. Water saturated with atmospheric oxygen was supplied to the deoxygenating unit at a rate $u = 0.33$ cm/s, which was regulated by a pump. The volumetric flow rate

Table 1. The elemental composition of the nanocomposite Cu°·Lewatit K2620 (Na⁺) with a capacity of 9.80±0.01 meq/cm³ depending on the radial distribution over the grain R/R_0, R_0 is the grain radius

Ele-ment	Weight %			Average weight %
	$R/R_0 = 0$	$R/R_0 = 0.5$	$R/R_0 = 1$	
Cu	5.13	13.97	34.09	17.73±16.79
C	38.06	35.57	37.87	37.17±1.57
O	17.55	14.46	11.69	14.63±3.32
Na	7.14	5.65	3.36	5.38±2.15
S	8.68	6.94	4.05	6.56±2.65

Condensed Matter and Interphases / Конденсированные среды и межфазные границы   2021;23(4): 614–625

T. E. Fertikova et al.   New nanocomposites for deep water deoxygenation

was accordingly u = 0.40 cm³/s (1.43·10⁻³ m³/h). The water passing through the first deoxygenator entered the second deoxygenator, which further purified the water at the outlet. The total height of this filter was L = 28.5·10⁻² m, filter section S = 6.83·10⁻⁴ m², water flow rate u = 0.058 cm/s, the volumetric flow rate, respectively, was u = 0.40 cm³/s (1.43·10⁻³ m³/h), the capacity of the nanocomposite was ε_{Cu^0} = 9.38±0.01 meq/cm³ with the number of deposition cycles N = 10.

The results are presented in Table 2. As can be seen, the oxygen concentration in the water at the outlet of the first deoxygenator significantly decreased from 4 - 6 mg/l to 0.1 - 0.3 mg/l and after the second filter reached 0.00 mg/l with practically unchanged pH and electrical conductivity of water. Fluctuations in concentration (Fig. 3) were most likely caused by periodic stoppages of the experiment and the associated suction of oxygen

Table 2. Experimental data on the reduction of oxygen dissolved in water at the outlet of the first and second deoxygenators with granular layers of Cu⁰Lewatit (Na⁺) nanocomposite

Time, h	O₂ concentration in the water at the inlet C_0, mg/l	O₂ concentration in the water after the first layer C_1, mg/l	O₂ concentration in the water after the second layer C_2, mg/l	Water pH at outlet	Water conductivity at the outlet æ, mS/cm
0	4.22	3.22	4.60	6.9	1.9
5	4.66	0.08	0.12	7.1	2.2
10	4.70	0.08	0.06	7.7	2.3
15	4.70	0.17	0.00	7.6	1.7
20	4.82	0.08	0.00	7.4	1.8
30	4.88	0.30	0.01	7.0	2.2
40	4.78	0.09	0.03	7.4	1.9
50	4.68	0.19	0.08	7.1	1.7
60	4.80	0.34	0.03	6.8	1.7
70	5.19	0.23	0.03	6.7	1.8
80	5.43	0.43	0.00	7.0	2.0
90	5.53	0.17	0.01	7.1	2.1
100	5.55	0.05	0.03	6.9	2.0
110	5.31	0.47	0.00	7.1	2.5
120	5.76	0.09	0.00	7.3	2.3
130	5.77	0.67	0.00	7.2	2.2
140	5.80	0.66	0.00	7.0	2.0
150	5.75	0.51	0.00	7.1	2.1

through the connecting hoses. The amount of absorbed oxygen naturally increased with time in both deoxygenators.

The theoretical analysis of the dynamics of oxygen uptake on the first and second deoxygenators was carried out using a software product (Mathcad), based on a mathematical model of external and internal diffusion and a staged oxidation reaction [21]. The data used for the calculation are shown in Table 3. The theoretical dependence of the relative concentration of oxygen in water at the outlet of the 1st deoxygenator is shown in Fig. 4. The dependence shows after what time of the experiment the oxygen concentration will decrease from C_0 = 5.0 mg/l to C_1 = 0.3 mg/l and will reach C_{lim} = C_1/C_0 = 0.06. The service life of the first deoxygenator was 152 h, which is consistent with the experiment and allows theoretical estimates of a longer life cycle of the nanocomposite in the second deoxygenator.
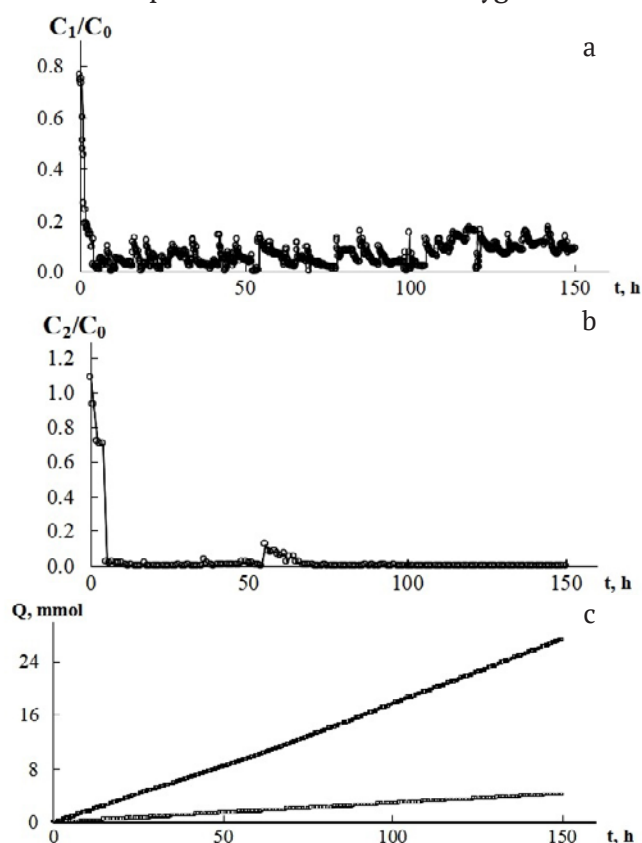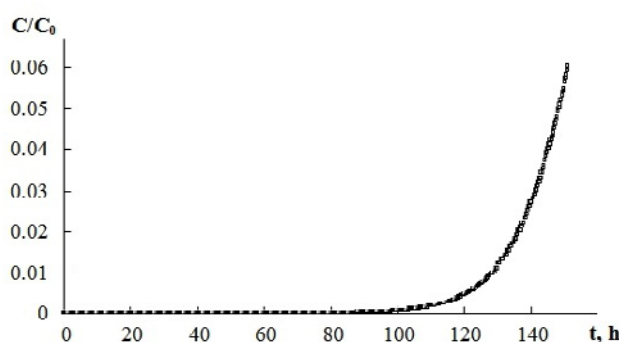

Fig. 3. Kinetic dependences of the relative oxygen concentration at the outlet after the first deoxygenator C_1/C_0 (*a*), after the second deoxygenator C_2/C_0 (*b*), the amount of Q (*c*) absorbed oxygen from the water after the first (*1*) and second (*2*) deoxygenators
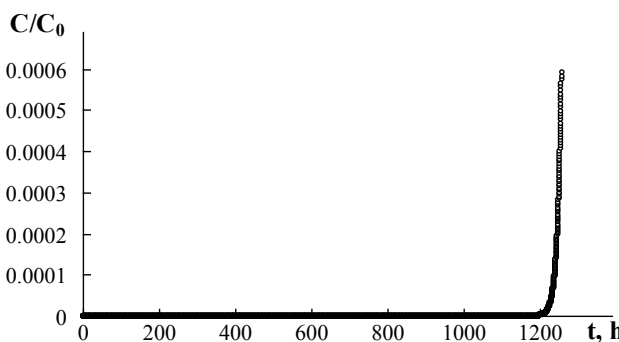
Condensed Matter and Interphases / Конденсированные среды и межфазные границы   2021;23(4): 614–625

T. E. Fertikova et al.   New nanocomposites for deep water deoxygenation

Table 3. Technological characteristics of the water deoxygenation plant

Chemical deoxygenator No. 1	
1. Grain layer height L, m	0.42
2. Sectional area of the layer S, m^2	$1.2 \cdot 10^{-4}$
3. The radius of the nanocomposite grains R_0, m	$2.8 \cdot 10^{-4}$
4. Loading volume of nanocomposite in one column, m^3	$50.4 \cdot 10^{-6}$
5. Grain filling ratio of the column, χ	0.70
6. Ion-exchange capacity of NC for hydrogen per bulk volume, meq/cm^3	1.86
7. Capacity ε_{Cu^0} for copper per bulk volume, meq/cm^3 (mol/l)	6.68 ± 0.08 (1.67)
8. Water flow rate l/h (cm/s)	1.43 (0.33)
9. Oxygen concentration in water at the inlet to the first deoxygenator C_0, mg/l (mol/l)	5.01 ± 0.39 ($1.56 \cdot 10^{-4}$)
10. Oxygen concentration in water at the outlet of the first deoxygenator $C(L)$, mg/l (mol/l)	0.30 ($0.9 \cdot 10^{-5}$)
11. Deoxygenator service life, theoretically calculated, h	126
Chemical deoxygenator No. 2	
1. Grain layer height L, m	0.285
2. Sectional area of the layer S, m^2	$6.83 \cdot 10^{-4}$
3. The radius of the nanocomposite grains R_0, m	$2.8 \cdot 10^{-4}$
4. Loading volume of nanocomposite in one column, m^3	$198 \cdot 10^{-6}$
5. Grain filling ratio of the column, χ	0.70
6. Ion-exchange capacity of NC for hydrogen per bulk volume, meq/cm^3	1.86
7. Capacity ε_{Cu^0} for copper per bulk volume, meq/cm^3 (mol/l)	1.43 (0.058)
8. Water flow rate l/h (cm/s)	9.38 ± 0.01 (2.37)
9. Oxygen concentration in water at the inlet to the first deoxygenator C_0, mg/l (mol/l)	5.01 ± 0.39 ($1.56 \cdot 10^{-4}$)
10. Oxygen concentration in water at the outlet of the first deoxygenator $C(L)$, mg/l (mol/l)	0.003 ($0.9 \cdot 10^{-7}$)
11. Deoxygenator service life, theoretically calculated, h	1258

Fig. 4. Theoretical dependence on the time of the relative concentration C/C_0 of oxygen dissolved in water at the outlet of the 1st deoxygenator

Fig. 5. Theoretical dependence on the time of the relative concentration C/C_0 of oxygen dissolved in water at the outlet of the 2nd deoxygenator

The theoretical dependence of the relative concentration of oxygen in water at the outlet from the second deoxygenator is shown in Fig. 5. The dependence shows after what time of the experiment the oxygen concentration will change from $C_0 = 5.0$ mg/l to $C_1 = 0.003$ mg/l and will reach $C_{lim} = C_2/C_0 = 0.0006$. Since the operating time of the first deoxygenator is relatively short, after 152 h only the second deoxygenator remained in operation. However, due to the different column parameters, the water flow rate, and also the higher capacity of the NR for copper, the second deoxygenator gives a low oxygen concentration (up to 0.003 mg/l) for a significant period of operation (1,258 h).

The main result achieved (Table 4) indicates that the first deoxygenator deoxygenates water by 94% within 152 h. Then the concentration in it will increase and will soon reach the initial one, i.e. the first deoxygenator will stop deoxygenating the water, and the entire load will be on the second deoxygenator, the operating time of which will be ~ 1,260 h and can be adjusted by the size of the column commensurate with the wear of all filters in the purification system. The degree of deoxygenation will be 99.99%, residual oxygen will be 0.003 mg/l (3 ppb).

A copper-ion-exchange nanocomposite was used in the sodium ionic form, in which the process of oxygen absorption occurs to solid-phase oxides of mono- and bivalent copper, which is clearly recorded on the cuts of NC grains. The processes take place along sequential routes without the participation of sodium counterions

Condensed Matter and Interphases / Конденсированные среды и межфазные границы   2021;23(4): 614–625

T. E. Fertikova et al.   New nanocomposites for deep water deoxygenation

Table 4. Results of laboratory tests of the deoxygenators

Deoxygenator	O_2 concentration at the inlet C_0, mg/l	O_2 concentration at the outlet C, mg/l	C/C_0	Experiment time t_{exp}, h	Theoretically calculated time of continuous operation t, h	$\frac{C_0 - C}{C_0}$, %
1	5.01±0.39	0.30	0.06	150	152	94.01
2	5.01±0.39	0.003	0.0006	150	1258	99.99

$$4\,Cu + 4\,OH^- = 2\,Cu_2O + 2\,H_2O + 4\,e^-,$$
$$O_2 + 2\,H_2O + 4\,e^- = 4\,OH^- \qquad (3)$$

and

$$2\,Cu_2O + 4\,OH^- = 4\,CuO + 2\,H_2O + 4\,e^-,$$
$$O_2 + 2\,H_2O + 4\,e^- = 4\,OH^-. \qquad (4)$$

General scheme

$$Cu + O_2 \rightarrow Cu_2O \rightarrow CuO \qquad (5)$$
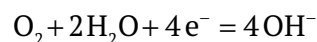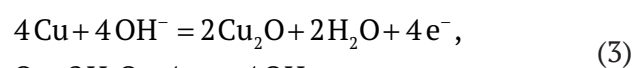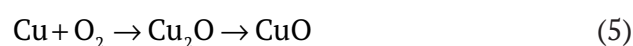
shows the path of chemical water deoxygenation due to the oxidation of copper nanoparticles deposited in the pores of the ion-exchange matrix in the sodium form.

Thus, the deep removal of corrosive dissolved oxygen ensures that the water meets hygienic requirements (Appendix 1). The economic efficiency of the life cycle of a new nanocomposite material is considered in Appendix 2.

Appendix 1

Hygienic aspect
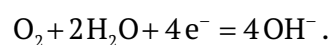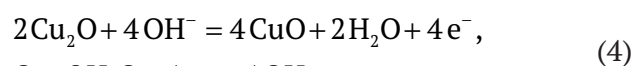
The quality of drinking water is an environmental factor that largely determines the health and standard of living of the population. Improving the quality of drinking water is a priority designated by the Decree of the President of the Russian Federation "On national objectives and strategic aims for the development of the Russian Federation until 2024". As part of the implementation of the federal project «Clean Water» Rospotrebnadzor in 2019 developed and approved Methodological Recommendations MR 2.1.4.0143-19 «Methodology for assessing the quality improvement of drinking water supplied to centralised water supply systems.»

According to reports [22, 23] on the state of the sanitary and epidemiological well-being of the population in the Russian Federation and, in particular, based on the example of the Voronezh region, positive dynamics in water quality from centralised water supply sources and distribution facilities were noted.

The share of centralised drinking water supply sources in Russia that do not meet sanitary and epidemiological requirements decreased in 2019 compared to 2012 (the growth rate is −5.27%) and amounted to 14.93%. In the Voronezh Region, all sources of centralised drinking water supply met sanitary and epidemiological requirements in 2019. The share of the population of Russia and the Voronezh Region provided with quality drinking water from centralised water supply systems was 85.5 and 88.3%, respectively.

According to data on the state of water from centralised water supply sources in Russia [22], the proportion of water samples that do not meet the requirements for sanitary and chemical indicators decreased during 2012–2019 from 28.63 to 25.71% (by 2.92%), for microbiological indicators it decreased from 5.47 to 4.12% (by 1.35%). The share of water samples from the distribution facilities that do not meet the standards for sanitary and chemical indicators decreased from 16.68 to 12.38% (by 4.3%), for microbiological ones it decreased from 4.45 to 2.68% (by 1.77%).

As part of the implementation of the federal project «Clean Water» within the territory of the Voronezh Region, there is a state program «Provision of high-quality housing and communal services for the population of the Voronezh Region» (for the period until 2025). Water supplied to the population for drinking needs must meet hygienic requirements, which are formulated in the Sanitary Rules and Norms "Drinking Water. Hygienic requirements for the quality of water from centralised drinking water supply systems. Quality control" (SanPiN 2.1.4.1074-01), introduced in 26.09.2001. A positive trend was revealed by the analysis of data on the quality of drinking water from centralised water supply sources in the Voronezh region [23]: the proportion of water samples that do not meet hygienic requirements for sanitary and chemical indicators decreased from 44.4 to 36.0%, in terms of microbiological indicators it decreased from 2.0 to 1.6% over the period 2012-2020. In the distribution facilities of the centralised water supply of the region, the proportion of drinking water samples that do not meet hygienic standards in terms of sanitary and chemical indicators decreased from 28.0 to 12.7%, in terms of microbiological indicators it decreased from 1.7 to 0.8%.

Despite the positive dynamics, in the Voronezh region there is water of low quality due to both natural (increased content of iron, manganese, boron, hardness salts) and man-made factors (anthropogenic pollution of groundwater; high deterioration of water supply networks). The solution to this problem requires environmentally oriented management methods; technical improvement, repair and replacement of treatment facilities, distribution facilities and, finally, introduction of more advanced innovative methods of water treatment, in particular, the use of nanocomposite metal-polymer materials for deep water deoxygenation. The latter is very important, since dissolved oxygen contained in water is an impurity competing and corrosive agent, damaging equipment and pipelines, causing significant damage to metals and alloys, and reducing the quality of water supplied to the population [24, 25]. As a result, heavy metals such as iron, zinc, copper, and others appear in drinking water, which have a toxic effect on the human body. Iron and manganese, found in high concentrations in drinking water, cause allergic reactions, skin and subcutaneous tissue diseases, and

Condensed Matter and Interphases / Конденсированные среды и межфазные границы   2021;23(4): 614–625

T. E. Fertikova et al.   New nanocomposites for deep water deoxygenation

increase the risk of blood diseases. In addition, the presence of molecular oxygen in water intended for the manufacture of pharmaceutical dosage forms is undesirable.

The result of deep deoxygenation of water achieved in this study using an innovative technology based on modern metal-ion-exchange nanocomposites provides a solution to these problems.

Appendix 2
Economic efficiency of the life cycle of
a new nanocomposite material

For the calculation of the economic efficiency of a new nanocomposite material, SWOT analysis was used as an analysis of a business in the context of a market environment. It consisted of a study of the advantages and disadvantages to the business, in addition, it determines the possibilities for the successful functioning of the organization under current and forecast market conditions [26].

After analysing the advantages and disadvantages (Tables 5 and 6), we can conclude that the main competitive advantages are:

– high oxygen content;
– low residual oxygen content (3 ppb (μg/l));
– and ease of use of the filter.

It is also necessary to create such favourable conditions that would allow the further development of an innovative project and increase its competitiveness. It is necessary to cope with such risks as the lack of investors (to present the

project in a way that it will interest potential consumers).

At the beginning of the development of the release of new products, the production process is characterised by high costs of labour, material, and other resources. As the number of manufactured products increases, the technological process is stabilised, technological and other shortcomings are eliminated, and production links are established. During this period, various technical and organizational measures are actively carried out, which reduce the destabilizing influence of factors in the process of the release of new products. As a result, the technically required values of resource consumption are established, the costs are gradually reduced and reach the required value at the level of technically justified norms.

We will calculate the cost of the material (Table 7). The laboratory will be able to produce 200 litres of the material per month. Therefore, 2,400 litres per year. The price also includes control of the properties of the obtained products and conditioning (preparation of an ion-exchange basis for the introduction of metal).

Property control involves the following analyses:
– analysis for the amount of copper in the sample; it should be performed 3 times, i.e. the total cost increases by 900 roubles;
– acidity analysis; it should be performed 12 times, i.e. the total cost will increase by 600 roubles;
– analysis for copper ions; one analysis costs 50 roubles; it should be performed 12 times, i.e. 600 roubles.

Table 5. Consumer advantages of the development in comparison with analogues

Property	Traps for removing oxygen from chromatographic columns (Cheminst) [27]	Catalysts containing palladium (Lanxess) [28]	The proposed nanocomposite, containing copper
The use of additional reagents	No	Requires a constant hydrogen supply	No
Application area	For chromatography only	Wide range of applications	Wide range of applications
Regeneration	Not regenerated	Not required	Regeneration is only required after the entire filter has been used up
Deoxygenation depth	1 ppb (μg/l)	< 20 ppb (μg/l)	3 ppb (μg/l)
Lifetime without regeneration	–	5 years	5 years

Table 6. Strategic planning (SWOT analysis)

Strengths and weaknesses	Opportunities and threats
Strengths: – a material that can be used for water deoxygenation filters has been developed; – oxygen is removed using sorbents; – deep cleaning, product purity, simplicity; – high oxygen sorption capacity; – high service life (5 years); – ease of filter regeneration; – high motivation for the rapid achievement of commercial success; –application in many areas.	Opportunities: – is able to deeply deoxygenate water without precious metals and pure hydrogen; – it is able to retain its properties and characteristics for several years under a layer of water; – creation of favourable conditions for the development of an innovative project; – increasing competitiveness.
Weaknesses: – the need for regeneration of the sorbent; – lack of funds for promotion.	Threats: – financial instability (possible changes in taxation, inflation); – lack of investors; – inflexible response to the market situation; –immunity to innovations.

Condensed Matter and Interphases / Конденсированные среды и межфазные границы   2021;23(4): 614–625

T. E. Fertikova et al.   New nanocomposites for deep water deoxygenation

Table 7. Cost of reagents for 1 litre of NC

Reagent	Price + VAT (20%), Roubles/kg	Place of purchase	Required amount, kg	Cost of goods + customs duties (25%), rub.
Cation exchanger Lewatit K-2620	490	Lanxess	1	610
Cation exchanger KU-2*8	144	Vekton	0.5	79
Anionite AV-17-8	336	Vekton	0.5	185
Sulphuric acid, reagent grade	94	Vekton	1	113
Sodium hydroxide, reagent grade	180	Vekton	1,25	248
Copper sulphate pentahydrate, pure grade	580	Vekton	4	2552
Sodium dithionite, Germany	852	Vekton	3	2811
Total				6596

Reagents and work on treating the starting material for the synthesis of the filler is estimated at 550 roubles. The material production requires equipment - special columns made only to order. They can be made of clear plastic or glass. Two columns are required. The cost of one column is 9,000 roubles. Their useful life is 5 years.

The equipment is capable of producing 200 litres per month. In the linear method, accrual of depreciation is performed by equal instalments over the entire useful life of fixed assets. Depreciation rate (H_{dep}) is calculated as a percentage of the original (reinstatement) value of the property [29]:

$$H_{dep} = (1/n) \cdot 100\% \qquad (6)$$

where n – useful life of the equipment (months or years).

Depreciation rate: 1/(5*12) * 100% = 1.66666 %/month.

The cost of two columns is 2 * 9,000 = 18,000 roubles.

Monthly depreciation: 18,000*1.66666%/100% = = 300 roubles/month.

Amount for the year of depreciation: 300 * 12 = = 3,600 roubles/year.

Linear method:
– at the end of the 1st year: 18,000 – 3,600 = 14,400 roubles;
– at the end of the 2nd year: 14400 – 3,600 = 10,800 roubles;
– at the end of the 3rd year: 10800 – 3,600 = 7,200 roubles;
– at the end of the 4th year: 7200 – 3,600 = 3,600 roubles;
– at the end of the 5th year: 3,600 – 3,600 = 0.

The rent of premises will be also required. Cost of 1 sq. meter is 400 roubles. The premises of 20 sq. meters is required. Therefore, 400 * 20 = 8,000 roubles. [30]. Two workers will be required. The salary of one worker is 20,000 roubles per month.

Social security contributions include [31]:
– contributions to the Social Insurance Fund (2.9%) – 1,160 roubles;
– contributions to the Pension Fund (22%) – 8,800 roubles;
– contributions to the Federal Compulsory Medical Insurance Fund (5.1%) - 2,040 roubles.

Total deductions for the unified social tax (UST) amount to 11,000 roubles. Thus, the wages of production workers are 51,000 roubles (Table 8).

For technical and industrial goods sold to the population, a surcharge of no more than 25% is applied (12,403*25/100 = = 3,101 roubles). Thus, the price of material for 1 litre will be 15,504 roubles.

In order to sell the fillers, a small business enterprise in the form of IP should be registered. It will cost 3,500 roubles. The first batch will be a trial run. Possible risks in the implementation of the project are equipment stoppage, financial crisis, and lack of funding. Potential consumers are companies producing equipment for water and waste water treatment: GIDROTECH, Bayer, Creminst, National Water Resources, Kontur-Aqua, and others.

It is necessary to calculate the minimum volume of production at which the costs will be offset by income, and with the production and sale of each subsequent unit of production, the enterprise begins to make a profit. Therefore, you need to determine the breakeven point.

200 litres will be produced per month.
Fixed costs:
– depreciation (RUB 300);
– rental of premises (8,000 roubles);
– salary (51,000 roubles);
– VAT (RUB 396,400);
– commission (190,800 roubles).

Therefore, the planned fixed costs are 646,500 roubles per month.
Variable costs:
– raw materials and supplies (6,596 roubles);
– quality control (2,100 roubles);
– air conditioning (550 roubles).

Therefore, the planned variable costs will be 9,246 roubles per 1 litre (hence, 1,849,200 roubles per month).

The breakeven point in monetary terms is the minimum amount of income at which all costs are fully paid off [32]:

$$BEP = \frac{Zfix}{(B - Zvar)} * B, \qquad (7)$$

where BEP – breakeven point; Z_{fix} – the amount of fixed costs per month; Z_{var} – the amount of variable costs per month; B – revenues from sales:

$$BEP = \frac{646500}{(3100800 - 1849200)} * 3100800 =$$

$$= \frac{646500}{1251600} * 3100800 = 1601683 \text{ roubles.}$$

This is the minimum amount of income at which all costs are fully paid off.

Condensed Matter and Interphases / Конденсированные среды и межфазные границы   2021;23(4): 614–625

T. E. Fertikova et al.   New nanocomposites for deep water deoxygenation

Table 8. Total cost of production for 1 litre of NC

Name of cost elements	Price in rub.
Depreciation	1.5
Material costs	6,596
Wages of production workers with accruals	255
Other expenses	
Premises for rent	40
Property control	2,100
Conditioning	550
Total	9,541
VAT 20%	1,982
Commission 10%	954
Total	12,477

Breakeven point in units of production:

$$BEP = \frac{TFC}{P - VC}, \qquad (8)$$

where TFC - the amount of fixed costs; VC - the variable costs per unit of production; R - unit cost.

$$BEP = \frac{646500}{15504 - 9246} = \frac{646500}{6258} = 103 \text{ l}.$$

This is the minimum amount of products at which the income from the sale of this product will completely cover all the costs of its production (Fig. 6).

The breakeven point is reached at 103 litres of products and sales of 1,601,683 roubles.

We will calculate the planned volume of product sales and profit for the month:

Price × Volume = Variable unit costs × Volume + Fixed costs + + Profit:

15,504×200 = 9,246×200 + 646,500 + Profit

3,100,800 = 1,849,200 + 646,500 + Profit

Profit = RUB 605,500 per month.

Planned sales volume = 3,100,800 roubles

Payback period = Investment / (Annual net profit + Annual depreciation) = 14,539,200/(605,500×12 + 3600) = 2 years, i.e. it has a relatively short duration.

The fact that the used nanocomposite can be regenerated and reintroduced into production should be taken into account.

4. Conclusions

New copper-ion-exchange nanocomposites in the sodium ionic form were obtained by ion-exchange saturation and chemical deposition. These nanocomposites are characterised by a narrow range of sizes of base metal particles and capable of reducing oxygen dissolved in water with the formation of solid-phase oxidation products. The cyclic process of ion exchange saturation - chemical deposition leads to a linear
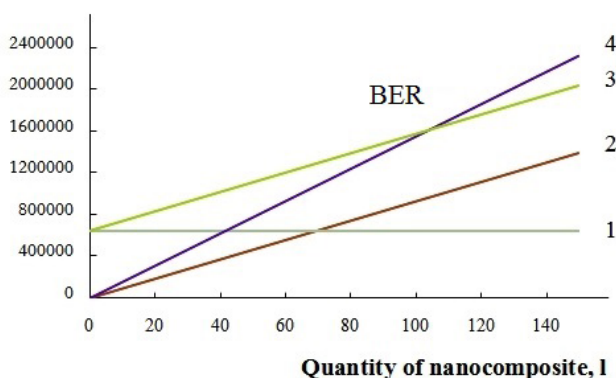
Fig. 6. The dependence of the cost on the amount of nanocomposite. *1* - fixed costs, *2* - variable costs, *3* - total costs, *4* - income, BEP - breakeven point

dependence of the copper capacity on the number of cycles and allows obtaining high-capacity samples.

Experimental data on the dynamics of oxygen absorption by granular layers of columnar nanocomposites have been obtained. The correspondence of the experimental output curves with curves theoretically calculated according to the previously proposed mathematical model of dynamics, based on external and internal diffusion and a sequential chemical oxidation reaction, has been established. The experiment and calculation show the attainability of a deep level of water deoxygenation with practically unchanged pH and electrical conductivity values. Residual oxygen can be controlled and does not exceed 3 μg/l (ppb).

The hygienic and economic substantiation of the expediency of using the obtained nanocomposites is provided. Deep chemical water deoxygenation using copper-ion-exchange nanocomposites in sodium form allow solving the problem of the corrosion resistance of metals, ensuring the compliance of water with hygienic requirements on a large scale.

The competitive advantage of the considered water deoxygenation system in comparison with the known systems is the rejection of the use of precious metals-catalysts (palladium, platinum), pure hydrogen, and complex design solutions. The proposed new nanocomposite installation for water deoxygenation is characterised by its ease of use and can be built into a filter system for water

Condensed Matter and Interphases / Конденсированные среды и межфазные границы   2021;23(4): 614–625

T. E. Fertikova et al.   New nanocomposites for deep water deoxygenation

purification. The breakeven point is achieved with the production of ~100 litres of nanocomposite and a sales volume of ~1,600,000 roubles, above which a profit can be obtained. The payback period for an investment of ~15,000,000 roubles is rather short and will not exceed 2 years.

Author contributions

All authors made an equivalent contribution to the preparation of the publication.

Conflict of interests

The authors declare that they have no known competing financial interests or personal relationships that could have influenced the work reported in this paper.

References

1. Kravchenko T. A. Poverkhnostnaya okislitel'no-vosstanovitel'naya reaktsiya v sorbtsionnykh protsessakh [Surface redox reaction in sorption processes]. *Kondensirovannye sredy i mezhfaznye granitsy = Condensed Matter and Interphases*. 1999;1(1): 10–20. Kravchenko T. A. 1999;1(1): 10-20. Available at: https://www.elibrary.ru/item.asp?id=26781449 (In Russ.)

2. Zagorodni A. A. Electroseparation with ion exchange materials. In: *Ion exchange materials*. Amsterdam: Elsevier; 2007. pp. 351–376. https://doi.org/10.1016/b978-008044552-6/50018-6

3. Kravchenko T. A., Polyanskiy L. N., Krysanov V. A., Zelensky E. S., Kalinichev A. I., Hoell W. H. Chemical precipitation of copper from copper-zink solutions onto selective sorbents. *Hydrometalurgy*. 2009;95(1-2): 141–144. https://doi.org/10.1016/j.hydromet.2008.05.027

4. Kravchenko T. A., Chayka M. Yu., Konev D. V., Polyansky L. N., Krysanov V. A. The influence of the ion-exchange groups nature and the degree of chemical activation by silver on the process of copper electrodeposition into the ion exchanger. *Electrochimica Acta*. 2007;53(2): 330–336. https://doi.org/10.1016/j.electacta.2007.04.003

5. Zolotukhina E. V., Kravchenko T. A. Synthesis and kinetics of growth of metal nanoparticles inside ion-exchange polymers. *Electrochimica Acta*. 2011;56(10): 3597–3604. https://doi.org/10.1016/j.electacta.2010.12.019

6. Kravchenko T. A., Aristov I. V. Kinetics and dynamics of redox sorption. In: *Ion Exchange. Highlights of Russian Science*. D. Muraviev, V. Gorshkov, A. Warshawsky (eds.). New York-Basel: M. Dekker; 2000. pp. 691–764. https://doi.org/10.1201/9780203908341.ch11

7. Kravchenko T. A., Polyansky L. N., Kalinichev A. I., Konev D. V. *Nanokompozity metall-ionoobmennik* [Nanocomposites metal-ion exchanger]. Moscow: Nauka Publ.; 2009. 391 p. (In Russ.)

8. Kravchenko T. A., Zolotukhina E. V. Chaika M. Yu., Yaroslavtsev A. B. *Elektrokhimiya nanokompozitov metall-ionoobmennik* [Electrochemistry of nanocomposites metal-ion exchanger]. Moscow: Nauka Publ.; 2013. 365 p. (In Russ.)

9. Kravchenko T. A., Khorolskaya S. V., Polyanskiy L. N., Kipriyanova E. S. Investigation of the mass transfer process in metal-ion-exchanger nanocomposites. In: *Nanocomposites: synsesis, characterization and application*. X. Wang (ed.). N.Y.: Nova Science Publishers; 2013. pp. 329–348.

10. Sakardina E. A., Kravchenko T. A., Zolotukhina E. V., Vorotyntsev M. A. Silver/ion exchanger nanocomposites as low-temperature redox-catalysts for methanal oxidation. *Electrochimica Acta*. 2015;179: 364–371. https://doi.org/10.1016/j.electacta.2015.03.227

11. Dorfner K. *Ion exchangers*. Berlin and New-York: Walter de Gruyter; 1991. 1494 p. https://doi.org/10.1515/9783110862430

12. Volkov V. V., Kravchenko T. A, Roldughin V. I. Metal nanoparticles in catalytic polymer membranes and ion-exchange systems for advanced purification of water from molecular oxygen. *Russian Chemical Reviews*. 2013;82(5): 465–482. https://doi.org/10.1070/RC2013v082n05ABEH004325

13. Lebedeva V. I., Petrova I. V, Volkov V. V., Tereshchenko G. F., Shkol'nikov E. I, Plyasova L. M., Kochubey D. I., Vaart R. Van Der, Soest-Verecammen E. L. J. Van, Gryaznov V. M. Porous Pd-containing polypropylene membranes for catalytic water deoxygenation. *Kinetics and Catalysis*. 2006;47(6): 867–872. https://doi.org/10.1134/S0023158406060097

14. Kirpikov D. A., Pykhteev O. Yu., Kharitonova E. Yu., Tsapko Yu. V., Chistyakov I. V., Gursky V. S. Ustroistvo dlya elektrokhimicheskoi deoksigenatsii vysokochistoi vody. *Opisanie izobreteniya k patentu [Device for electrochemical deoxygenation of high-purity water. Description of the invention to the patent]*. Application: 2012114642/05, 12.04.2012. Published: 10.10.2013. Byul. No. 28. (In Russ.)

15. Yasnev I. M., Gursky V. S., Dombrovsky A. P., Vishnyakova N. B. The UD VVCH-500 modular system for deoxygenation of high-purity water. *Technologies for ensuring the life cycle*. 2017;(2): 71–75. Available at: https://www.elibrary.ru/item.asp?id=29847926 (In Russ., abstract in Eng.)

16. Selvaraju T., Ramaraj R. Nanostructured copper particles-incorporated Nafion-modified electrode for oxygen reduction. *Pramana*. 2005;65(4): 713–722. https://doi.org/10.1007/bf03010459

Condensed Matter and Interphases / Конденсированные среды и межфазные границы   2021;23(4): 614–625

T. E. Fertikova et al.   New nanocomposites for deep water deoxygenation

17. Du C., Gao X., Chen W. Recent developments in copper-based, non-noble metal electrocatalysts for the oxygen reduction reaction. *Chinese Journal of Catalysis.* 2016;37: 1049–1061. https://doi.org/10.1016/S1872-2067(15)61059-2

18. Wolf I. V., Romanov A. V. Deep desalination and deoxygenation of water using ionites and an iron-hydrosakis electron-ion exchanger. *Sorbtsionnye i Khromatograficheskie Protsessy.* 2006;6(6): 1318–1326. (In Russ.)

19. *Product Information about Lewatit K 2620.* Available at: https://lanxess.com/en/Products-and-Solutions/Products/l/LEWATIT--K-2620

20. Krysanov V. A., Plotnikova N. V., Kravchenko T. A. Nanostrukturnyi kompozit dlya glubokogo udaleniya kisloroda iz vody [Nanostructured composite for deep removal of oxygen from water]. *Utility model patent RU 172 363 U1.* Application 201640241b dated 12.10.2016. Published on 05.07.2017. Byul. No. 19. (In Russ.)

21. Kravchenko T. A., Vakhnin D. D., Chumakova A. V., Konev D. V. Electrodynamic model of oxygen redox sorption by metal-containing nanocomposites. *Nanotechnologies in Russia.* 2019;14(11-12): 523–530. https://doi.org/10.1134/S1995078019060090

22. *On the state of sanitary and epidemiological well-being of the population in the Russian Federation in 2019: State report.* Moscow: Federal Service for Supervision of Consumer Rights Protection and Human Well-being; 2020. 299 p. (In Russ.)

23. *The report "On the state of sanitary and epidemiological welfare of the population in the Voronezh region in 2020".* Voronezh: Department of the Federal Service for Supervision of Consumer Rights Protection and Human Welfare in the Voronezh Region; 2021. 193 p. (In Russ.)

24. Muravyev A. G. *Rukovodstvo po opredeleniyu pokazatelei kachestva vody polevymi metodami* [Guidelines for determining water quality indicators by field methods]. St. Petersburg: "Krismas+" Publ.; 2009. 248 p. (In Russ.)

25. Belikov S. E. *Spravochnik dlya professionalov. Vodopodgotovka* [Handbook for professionals]. Water treatment. Moscow: Aqua-Term Publ.; 2007. 240 p. (In Russ.)

26. Azoev G. L. *Konkurentsiya: analiz, strategiya i praktika* [Competition: analysis, strategy and practice]. Moscow: Center for Economics and Marketing Publ.; 2012. 257 p. (In Russ.)

27. The official website of the company «Cheminst». Available at: https://www.cheminst.ru

28. The official website of the company «Lanxess». Available at: https://lanxess.com/en/Products-and-Solutions/Products/l/LEWATIT--K-3433

29. Treshchevsky Yu. I., Vertakovoy Yu. V., Pidoimo L. P. *Ekonomika i organizatsiya proizvodstva* [Economics and organization of production: textbook]. Moscow: INFRA-M Publ.; 2014. 381 p. (In Russ.)

30. The official website of the real estate agency «Transfer». Available at: https://transfert-vrn.ru

31. The Tax Code of the Russian Federation (part two) of 05.08.2000 N 117-FZ (as amended on 20.04.2021) (with amendments and additions, intro. effective from 20.05.2021). Article 425. Insurance premium rates. (In Russ.)

32. Vasina A. A. *Doiti do tochki… bezubytochnosti* [Reach the point… break-even]. An electronic article. 2008. Available at: https://www.cfin.ru/finanalysis/math/break_even_point.shtml

Information about the authors

Tatyana E. Fertikova, PhD in Medicine, Associate Professor of the Department of General Hygiene, Voronezh State Medical University, Voronezh, Russian Federation; e-mail: tefertikova@vrngmu.ru. ORCID iD: https: //orcid.org/0000-0002-4370-9197.

Sergey V. Fertikov, Student of the Department of Economics and Management of Organizations, Voronezh State University, Voronezh, Russian Federation; e-mail: fertikov.sergei@yandex.ru. ORCID iD: https://orcid.org/0000-0003-0382-8236.

Ekaterina M. Isaeva, PhD in Economic, Associate Professor of the Department of Economics and Management of Organizations, Voronezh State University, Voronezh, Russian Federation; e-mail: ek-isaeva@yandex.ru. ORCID iD: https://orcid.org/0000-0002-0428-037.

Vyacheslav A. Krysanov, PhD in Chemistry, Associate Professor of the Department of Physical Chemistry, Voronezh State University, Voronezh, Russian Federation; e-mail: krysanov@chem.vsu.ru. ORCID iD: https://orcid.org/0000-0002-6580-1939.

Tamara A. Kravchenko, DSc in Chemistry, Professor of the Department of Physical Chemistry, Voronezh State University, Voronezh, Russian Federation; e-mail: krav2809837@yandex.ru. ORCID iD: https://orcid.org/0000-0001-9214-7357.

Original articles

Experimental study and mathematical modelling of self-oscillation at the electrode-magnetic fluid interface in an electric field

V. S. Chekanov[1] ✉, E. V. Kirillova[2], A. V. Kovalenko[3], E. N. Diskaeva[4]

[1]*North-Caucasus Federal University,
1 Pushkina ul., Stavropol 355017, Russian Federation*

[2]*RheinMain University of Applied Sciences*

18 Kurt-Schumacher-Ring, Wiesbaden 65197, Germany

[3]*Kuban State University,
149 Stavropolskaya ul., Krasnodar 350040, Russian Federation*

[4]*MIREA – Russian Technological University,
8 Kulakova pr., Stavropol 355000, Russian Federation*

Abstract

The article describes a mathematical model of self-oscillation in the form of a boundary value problem for a nonlinear system of partial differential equations, with a numerical solution. The numerical results were compared to the experimental data to confirm the adequacy of the model. The model uses the classical system of differential equations of material balance, Nernst-Planck and Poisson equations without simplifications or fitting parameters. The aim of the article was to study the parameters of concentration self-oscillation in a layer of the dispersed phase particles of magnetic fluid at the interface with an electrode in an electric field. For this purpose, we developed a mathematical model, the consistency of which was confirmed by the corresponding physical mechanism.

As a result of numerical experiments, we found the critical value of the potential jump after which self-oscillation began. We also determined the oscillation growth period and other characteristics of the process. We developed software called AutoWave01 with an intuitive user interface and advanced functionality for the study of self-oscillation in a thin layer of magnetic colloid.

Keywords: Magnetic fluid, Interface, Near-electrode layer, Electric field, Self-oscillation, Mathematical model.

✉ Vladimir S. Chekanov, e-mail: oranjejam@mail.ru

Condensed Matter and Interphases / Конденсированные среды и межфазные границы   2021;23(4): 626–636

V. S. Chekanov et al.   Experimental study and mathematical modelling of self-oscillation...

1. Introduction

Colloidal solutions of magnetic composite materials, later called "magnetic fluids", were synthesised in the 1960s, and they still attract the attention of both experimenters and theorists [1, 2].

Magnetic fluids (MF) are ultradispersed stable colloids of ferro- or ferrimagnetic single-domain particles dispersed in various fluids and exhibiting intense Brownian motion. Small particles of metals such as iron, cobalt, nickel, gadolinium, and their various ferrites and ferromagnetic oxides are used as the dispersed phase. Surfactants are used as stabilisers in order to prevent coagulation of the colloidal solution, which would be unavoidable due to magnetic dipole-dipole and Van der Waals interactions, and to avoid the subsequent particle aggregation. When adsorbed on the surface of microcrystalline dispersed particles, the surfactants form a protective coating, which is a kind of a structural mechanical barrier. The average size of the dispersed particles is d_{av} ~ 10 nm, so the MFs do not stratify and remain homogeneous practically indefinitely.

Dielectric fluid-based MFs have unique electrical and magneto-optical properties related, among other things, to near-surface phenomena. One of these properties of the MFs is their ability to form dense layers at the interface with the electrode in an electric field. These layers consist of the dispersed phase particles with a protective coating. These layers have a significant effect on the macroscopic properties of the colloidal system. They play a major role in obtaining materials with defined properties. This phenomenon is used in the field of indicating instruments [3–5].

Self-organisation was observed in the near-electrode layer and studied, which was self-oscillation and its distributed analogue, autowaves [6].

A magnetic fluid is a unique experimental medium, because the self-oscillation process can not only be observed and studied indefinitely in this medium, but it can also be controlled by means of the electric field.

Mathematical modelling of the self-oscillation process can make it possible to determine its fundamental laws and describe the state of the process at any point in space at any point of time.

In this study, we proposed a mathematical model for the self-oscillation of the MF particle concentration. The model is based on a dynamical approach: the processes occurring in the system are defined by partial differential equations describing the laws of conservation of matter and charge. The model does not include any fitting parameters. The relevant chemical reactions are considered by its boundary conditions.

2. Experimental

For the experiment, we used a magnetic fluid of the magnetite in kerosene type. The volume concentration of the solid phase was calculated based on the density of the magnetic fluid. For the MF with a density of $\rho = 1.14$ kg/m³, the concentration of the solid phase was 3.4 vol%. The volume concentration of magnetite was calculated from the density values of the magnetic fluid, the dispersion medium (kerosene), and the dispersed phase (magnetite) by the formula:

$$\varphi_T = \frac{\rho_{MF} - \rho_O}{\rho_T - \rho_O},$$

where ρ_{MF}, ρ_O, and ρ_T are the density values of the magnetic fluid, kerosene, and magnetite. The density of the MF was determined by the weight method using the buoyant force acting on a brass measuring cylinder immersed in the fluid. The value was calculated by the formula:

$$\rho = \frac{P_1 - P_2}{gV},$$

where P_1 is the cylinder weight in air; P_2 is the cylinder weight in fluid; V is the volume of the cylinder; and g is the gravitational acceleration.

The cylinder was weighed on a VLR-200 analytical balance. The error in determining the density ρ was ~ 0.1 %.

The relative dielectric constant of the fluid was $\mu = 2$, its specific conductivity was $Ã = 3,8 \cdot 10^{-7}$ Ohm·m⁻¹. To determine the dielectric constant and conductivity, we measured the resistance and capacity of the cell containing the MF using an LCR-821 LCR Meter (at a frequency of 1000 Hz). Then we calculated the conductivity σ and the dielectric constant ε. The average particle size of magnetite was ~ 10 nm, the protective coating consisting of oleic acid molecules was ~1.5 nm thick [7, 8].

Condensed Matter and Interphases / Конденсированные среды и межфазные границы   2021;23(4): 626–636

V. S. Chekanov et al.   Experimental study and mathematical modelling of self-oscillation...

In order to determine the change in reflectivity (reflection coefficient, following the terminology in [9]) of the conductive electrode-magnetic fluid interface in the electric field, we used the experimental unit shown in Fig. 1. The unit was a plane-parallel cell consisting of two electrodes. One of the electrodes was made of glass with a conductive transparent coating (ITO). A glass prism was placed on the cell surface to avoid the illumination. The magnetic fluid was placed between the electrodes. A beam with a diameter of 2 mm, produced by a laser light source ($\lambda = 650$ nm), was incident on the face of the prism adhered to glass with immersion liquid, so that the angle of incidence on the glass surface was 45 degrees. The beams reflected from the prism-glass interface and from the conductive coating - MF layer were spatially separated (5 mm). To level the parasitic illumination of the photodiodes, a diaphragm with an aperture of ~ 1 mm was placed in front of polaroid 7. The laser and polaroid could rotate relative to the beam. The polarisation plane of polaroid 10 coincides with the polarisation plane of the laser beam. The polaroid served to reduce the depolarised component of the laser light. Rotating the laser and the polaroid ensured that the s-component (TE wave) was perpendicular to the plane of incidence. The light was reduced by rotating polaroid 7 to make the photodiode operate in linear mode. The surface area of the electrodes was $S = 36 \times 30$ mm^2, the
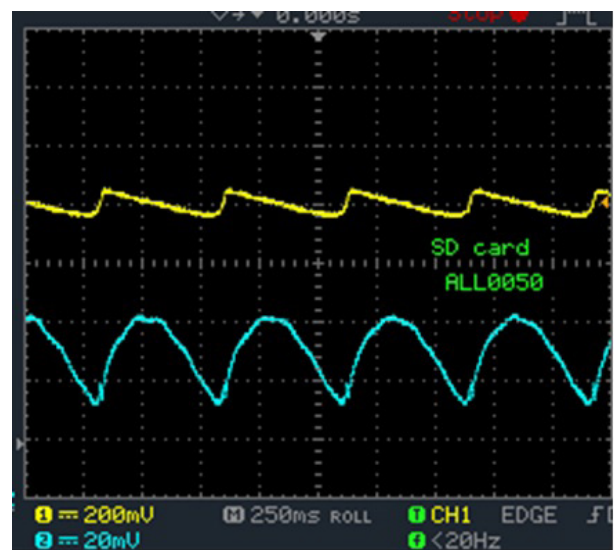
thickness of the magnetic fluid layer was 250 µm. In our experiments, we used glass samples with an ITO conductive coating (manufactured by OOO Poltekh, St. Petersburg).

The experimental technique was as follows: voltage U was applied to the electrodes and, due to electrophoresis, 100-200 nm thick dense layers were formed. The layers consisted of magnetite particles. The glass with the ITO conductive coating was illuminated by a monochromatic light source. The beam was reflected from two surfaces: glass-conductive coating and conductive coating-magnetic fluid. It interfered, passed through diaphragm 6 and polaroid 7, and hit the FD-256 photodiode, The photodiode was connected to the input of a GDS-71022 dual beam oscilloscope. Since the photodiode operates in linear mode, the voltage at the oscilloscope is directly proportional to the intensity of the reflected beams (reflection coefficient).

When the jump in potential between the electrodes reached the critical value φ_{crit}, we observed a periodic change in the intensity of the reflected beam (Fig. 2, beam 2), which was due to a change in the thickness of the near-electrode dense layer.

When the cell surface was illuminated by light with a wide wavelength spectrum, the change in thickness of the layer was accompanied by a periodic colour change of the electrode surface from green to crimson. The green colour of the

Fig. 1. Layout of the experimental unit for measuring reflection coefficient at the electrode-magnetic fluid interface: *1* – magnetic fluid; *2* – foil-clad paper-based laminate plate; *3, 11* – polystyrene insulation pads; *4* – glass with conductive transparent coating; *5* – right isosceles prism; *6* – diaphragm; *7, 10* – polaroids; *8* – photodiode; *9* – laser light source; and *12* – electrodes

Fig. 2. Auto oscillation of the current (*1*) and optical signal (*2*) in the cell with the magnetic fluid. The oscillation period is $T \approx 0.5$ s, the potential jump is $\Delta\varphi = 5$ B

Condensed Matter and Interphases / Конденсированные среды и межфазные границы   2021;23(4): 626–636

V. S. Chekanov et al.   Experimental study and mathematical modelling of self-oscillation...

surface corresponded to the reflection spectrum in the absence of a particle layer, and the crimson colour corresponded to the maximum thickness of the near-surface particle layer. We interpreted the periodic colour change of the surface or the periodic change in the intensity of the reflected light (Fig. 2, beam 2) as self-oscillation of the particle concentration. The electro-optical effect involves a change in the spectrum of reflected light (when illuminated by white light) or its intensity (when illuminated by monochromatic light) due to a thin near-surface layer of a magnetic fluid changing in an electric field. It is called electro-optical interference [10].

2.1. Physical model of particle self-oscillation in the cell with a magnetic fluid

General characteristics of the electrical conductivity of a magnetic fluid. The electrical conductivity of a magnetic fluid is due to several mechanisms. First of all, it is related to impurity ions, their concentration depends on the quality of washing the dispersed magnetite after co-precipitation during the MF preparation process:

$FeCl_2 \cdot 4H_2O + 2FeCl_3 \cdot 6H_2O + 8NH_4OH \leftrightarrow$
$\leftrightarrow Fe_3O_4\downarrow + 8NH_4Cl + 20H_2O.$

Due to the incomplete dissociation of the salt, the fluid also contains ionic complexes: ionic pairs and triplets [11, 12].

The second type of conductivity is due to contact processes on the electrode surfaces. They are called injection processes [11–14]. In high voltage fields with a medium intensity of about 10^6 V/m, electrochemical injection develops. It causes electrohydrodynamic effects in both liquid dielectrics and magnetic fluids [14].

In addition to ionic conduction, charge transfer in a magnetic fluid can be carried out by magnetic particles (MPs) [16].

Space charge formation in a magnetic fluid in an electric field. In an electric field, a space charge is formed at the electrodes in a magnetic fluid. Many specific effects are associated with it [17–19], including the autowave process. The mechanism of space charge formation in a liquid dielectric under the action of an electric field in the vicinity of conductive surfaces was described in detail. In [13, 19], there is an expression for determining the thickness of the near-electrode layer of the space charge:

$$\delta \sim E_0 \frac{FD^{\pm}}{RT} \tau_M \sim \frac{\varepsilon_0 \varepsilon E_0 (b_1 + b_2)}{\sigma}, \qquad (1)$$

where τ_M is the Maxwell-Wagner relaxation time, $D^{\pm}$ is the ion diffusion coefficient, E_0 is the field intensity at the interface of the non-equilibrium dissociation-recombination reaction zone, b_1, b_2 are the mobility values of positive and negative ions, F is the Faraday constant, T is the temperature, R is the molar gas constant, σ is the ohmic conduction, ε is the dielectric permittivity, and μ_0 is the vacuum permittivity.

Ratio (1) shows that the thickness of the space charge layer can be estimated as the distance travelled by the ion during the relaxation time. That is why the effect of electrification is greater the lower the electrical conductivity of the liquid, and therefore the longer the Maxwell-Wagner relaxation time. It was shown in [13] that the repulsion of similarly charged ions at the electrodes causes an imbalance in the dissociation-recombination reaction of impurity ions. It results in the formation of a space charge.

Let us consider the layout of the magnetic fluid cell (Figure 3). The electric field transports anions (cations) from the near-cathode (near-anode) region. Since the cathode (anode) does not provide anions (cations), the cathode (anode) region is depleted of anions (cations), resulting in a cathode (anode) region with a positive (negative) charge.
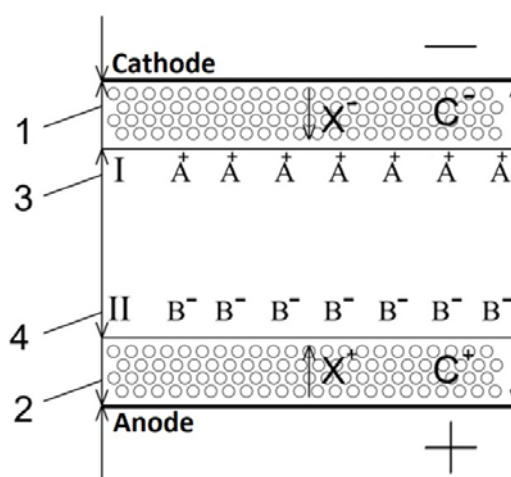
Fig. 3. Layout of the cell containing the magnetic fluid: *1, 2* – dense near-electrode layers of magnetic particles; *3, 4* – the regions of the space charge; A^+ and A^- – impurity ions; C^+ and C^- – charged particles of the magnetic fluid; and X^+, X^- – injected ions

Condensed Matter and Interphases / Конденсированные среды и межфазные границы   2021;23(4): 626–636

V. S. Chekanov et al.   Experimental study and mathematical modelling of self-oscillation…

The size of the localisation region of the space charge in a magnetite-in-kerosene fluid was estimated using the following parameters: the concentration of magnetite was 3.4 vol% and the specific conductivity was $\sigma \approx 10^{-7}$ Ohm^{-1}m^{-1}. The calculation showed that the width of the regions of space charge is $\delta \sim 4 \cdot 10^{-7}$ m, when the potential jump between the electrodes is $\Delta\varphi = 5$ V, the distance between the electrodes is $d = 5 \cdot 10^{-5}$ m, and the mobility of the impurity ions is $b_1 \approx b_2 \approx 10^{-8}$ m^{2}V^{-1}s^{-1} [13]. The value of the electric field intensity in the near-electrode region varies according to the Poisson equation due to the presence of a space charge with a density of ρ [21].

According to [22], characteristic time of formation of a space charge in a fluid with a medium magnetite concentration (3.4 vol%) for kerosene-based samples is about 0.05 s. To estimate the space charge formation time in an electric field, the migration polarisation of magnetite particles should be taken into account. In our case the migration polarisation can be described in the framework of Maxwell-Wagner theory. The Maxwell-Wagner polarisation time (2) is much shorter than the space charge formation time:

$$\tau_M \sim \frac{\varepsilon_0 \varepsilon}{\sigma} \sim \frac{2 \cdot 8.85 \cdot 10^{-12}}{10^{-7}} \sim 1.7 \cdot 10^{-4} \text{ s.} \qquad (2)$$

A space charge also occurs at the surface of the dispersed particle. The region of the space charge around the particle is located in that part of the fluid where the ion, resulting from the dissociation of the impurity at the surface of the particle, keeps moving, without recombination.

Concentration self-oscillation in a magnetic fluid. In the absence of an electric field, magnetic fluid particles are not charged [22]. In the field $\vec{E}$, the particles are charged and acquire an induced dipole moment p. As a result of the polarisation $\vec{f}_E = (\vec{p}\nabla)\vec{E}$ and the Coulomb $\vec{f}_q = q\vec{E}$ forces, the particles begin to move towards the corresponding electrode, forming a concentrated layer of particles. At the same time, the surface of the cell containing the MF changes its colour. Once a dense near-electrode layer is formed as a result of the contact of the magnetic particles with the electrode surface, the oleic acid molecules surrounding the particle begin

to interact with the electrode. For example, the reaction releases negative ions X^- at the cathode, which have almost zero mobility in the dense electrode layer, causing the cathode to charge. When the Coulomb repulsive energy of the layer U_q exceeds the attraction energy U_{im}, the layer becomes unstable. The particles change their charge and begin to move towards the opposite electrode. This way the concentration wave occurs. When the particles reach the region of space charge II (Fig. 3), they start moving in the opposite direction. Self-oscillation of the groups of magnetic particles was visualised by electrically controlled interference [10], based on periodic colour changes of the surface of the cell with magnetic fluid and the oscillations of the optical signal (Fig. 2). A dense near-electrode layer of particles was also formed on the opposite electrode (anode). Due to near-electrode reactions, X^+ ions were formed, which resulted in the second concentration wave moving towards the first.

Assuming that all particles in the magnetic fluid have the same size, electric charge, and equal electrophoretic mobility b. Then in the stationary electric field $\vec{E}$ the velocity of the particle is: $v = b(\vec{E}, \vec{n})$, where $\vec{n}$ is the direction of the particle motion.

The particle mobility $b = 5 \cdot 10^{-9}$ m^{2}V^{-1}s^{-1} was determined using the formula from [21]. Then the velocity of the particle in the cell is $v = 5 \cdot 10^{-4}$ m·s^{-1}.

On the other hand, based on the equality of the electrostatic force and the viscous frictional force, we can determine that:

$$q\vec{E} = 3\pi d\eta \cdot \vec{v}, \qquad (3)$$

where $d = 10^{-8}$ m is the particle diameter, $\eta = 1.5 \cdot 10^{-3}$ Pa·s is the dynamic viscosity of the dispersion medium, $\vec{E}$ is the intensity of the electric field, and the charge of the particle q is equal to the charge of the electron [22]. According to our experimental data, the period of self-oscillation is ~ 1 s. It is how long it takes the particle to leave the electrode and return.

For $t = 0.5$ s, the particle covers a distance of $\approx 5 \cdot 10^{-5}$ m, that is, the distance to the opposite electrode. Thus, when the potential jump is $\Delta\varphi = 5$, there is a periodic movement of particles from one electrode to the other.

Condensed Matter and Interphases / Конденсированные среды и межфазные границы   2021;23(4): 626–636

V. S. Chekanov et al.   Experimental study and mathematical modelling of self-oscillation...

Let us explain why the observed concentration oscillation is auto-oscillation. Self-oscillation is a non-damped oscillation in a dissipative dynamical system with nonlinear feedback. It is maintained by the energy of a constant, i.e. non-periodic, external influence [23]. In the laboratory experiments conducted, the source of this constant (non-periodic) influence is a jump in potential at the electrodes. The capacity of the near-electrode layer C serves as the nonlinear regulator. It regulates the accumulation of charge in the layer. In [24] it was shown that due to the formation of a pre-electrode layer, the cell containing the magnetic fluid was a capacitor of variable capacity. The charge in the near-electrode layer is accumulated during the time t_1. Then, after reaching the critical voltage at the electrodes U_{crit}, the layer changes its charge during the time t_1. This way, the constant impact is converted into a variable impact. The oscillating element of the system is the concentration of magnetic particles. The oscillation of the concentration is carried out via a feedback mechanism. It is represented by the layer resistance, which decreases sharply at U_{crit}. The energy dissipation in a self-oscillating system is compensated by the energy supplied to it from a constant voltage source, so that the oscillation is not damped.

2.2. A one-dimensional mathematical model of the oscillation process

We developed a simplified mathematical model of self-oscillation which allowed us to determine the dependence of the process characteristics on the initial parameters of the problem. For example, how the process depends on the potential jump between the electrodes $\Delta\varphi$, geometrical dimensions, etc. The proposed model considers the transfer of only positively and negatively charged magnetic particles with concentrations C_1, C_2 and fluxes j_1, j_2, and the potential jump $\Delta\varphi$ without taking into account chemical reactions. The influence of impurity and injection ions is taken into account indirectly by the boundary conditions. The basic idea of the model is to investigate the possibility of oscillation due to the change of charge of the MF particles near electrodes or in the regions of localised space charges.

We took $x = 0$ and $x = H$ as the conditional points where the MF particles are charged. In

certain cases there can be an anode and a cathode. The initial conditions are $C_1(0, x) = C_{10}(x)$ and $C_2(0, x) = C_{20}(x)$. The initial distribution of the neutral MF particles with a known concentration is determined by diffusion [25]. At the initial moment of time $t = 0$, the MF particles are charged in the electric field. Near the point of $x = H$ the MF particles are charged negatively, and near the point of $x = 0$ they are charged positively. In the electric field, negatively charged magnetic particles move towards the anode and positively charged particles move towards the cathode. Thus, dense layers are formed at the electrodes.

We used a one-dimensional nonlinear mathematical model with the classical system of differential equations of material balance, Nernst–Planck and Poisson [26-29] without simplifications or fitting parameters:

$$\frac{\partial C_i}{\partial t} = -\frac{\partial j_i}{\partial x}, i = 1, 2, \tag{4}$$

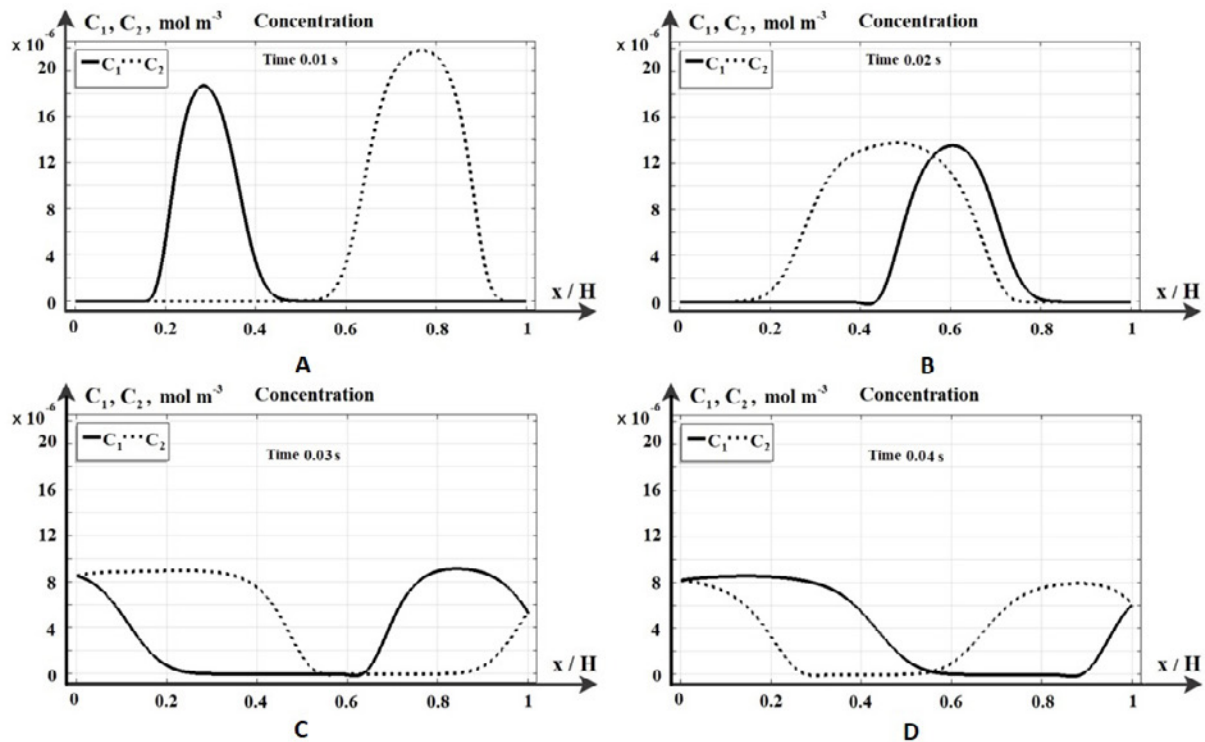$$j_i = -\frac{F}{RT_0} z_i D_i C_i \frac{d\varphi}{dx} - D_i \frac{dC_i}{dx}, i=1, 2, \tag{5}$$

$$\frac{d^2\varphi}{dx^2} = -\frac{F}{\varepsilon_r}(z_1 C_1 + z_2 C_2), \tag{6}$$

where C_i, j_i are the concentrations and fluxes of the charged MF particles, z_i are the charge numbers, φ is the potential, ε_r is the dielectric permittivity of the magnetic fluid, F is the Faraday constant, D_i are the diffusion coefficients of the charged MF particles, T_0 is the temperature, and R is the molar gas constant.

Our 1D model of self-oscillation of particles in a magnetic fluid considers two types of charged magnetic particles. So, the process of the charge change and corresponding oscillation take place from one to the other region of the space charge.

Assume that the process of the charge change of a wave of charged MF particles occurs gradually at the points $x = 0$ and $x = H$ as the charged particles approach them. For example, negatively charged particles at the point $x = 0$ receive a positive charge and become positively charged, while positively charged MF particles (if any) reach the point $x = H$ and become negatively charged (Figure 4b). Note that the charge change process is described by the boundary conditions at $x = 0$ (7) and at $x = H$ (8), the potential jump $\Delta\varphi$ is determined by (9).

Condensed Matter and Interphases / Конденсированные среды и межфазные границы   2021;23(4): 626–636

V. S. Chekanov et al.   Experimental study and mathematical modelling of self-oscillation...

Fig. 4. Concentration distribution of positively (C_1) and negatively (C_2) charged MF particles at: a) t = 0.01 s, b) t = 0.02 s, c) t = 0.03 s, and d) t = 0.04 s

$$\left(-\frac{F}{RT_0}D_1C_2\frac{d\varphi}{dx}-D_1\frac{dC_2}{dx}\right)\Bigg|_{x=0}=j_{1A},$$

$$\left(\frac{F}{RT_0}D_2C_1\frac{d\varphi}{dx}-D_2\frac{dC_1}{dx}\right)\Bigg|_{x=0}=j_{2A},$$ (7)

$$-\left(-\frac{F}{RT_0}D_1C_2\frac{d\varphi}{dx}-D_1\frac{dC_2}{dx}\right)\Bigg|_{x=H}=j_{1K},$$

$$-\left(\frac{F}{RT_0}D_2C_1\frac{d\varphi}{dx}-D_2\frac{dC_1}{dx}\right)\Bigg|_{x=H}=j_{2K},$$ (8)

$$\varphi(t,0)=\Delta\varphi,\varphi(t,H)=0,$$ (9)

where $j_{1A}, j_{2A}, j_{1K}, j_{2K}$ are the fluxes of overcharged particles at anode and cathode.

The initial conditions ($t = 0$) determine the initial state of the system. Its further evolution is determined by the equations and boundary conditions. Since thin near-surface layers are formed at both electrodes, we assumed that at the initial moment of time the MF particles are concentrated at each of the electrodes (10):

$$C_1(0,x)=C_{10}(x), C_2(0,x)=C_{20}(x)$$ (10)

As will be shown below, this initial state results in two concentration waves moving towards each

other. The waves then interact with each other. For the change in potential, we defined the initial condition as a linear function (11):

$$\varphi(0,x)=\varphi_0(x)=\frac{H-x}{H}\Delta\varphi.$$ (11)

Function (11) corresponds to condition (10) and Ohm's law at $t = 0$.

3. Numerical results and discussion

Numerical study was carried out with the following problem parameters: electrode spacing $H = 5\cdot10^{-5}$ m, calculation for $t\in[0,10]$ seconds with a sample of 0.01 s. Mesh parameters: 20,000 elements. The potential jump $\Delta\varphi$ was studied in the range of 1 to 20 V. In our calculations we adopted the initial distribution of magnetic particle concentration corresponding to the experimental data:

$C_1(0,x) = C_2(0,x) = 3.4$ vol%.

The finite element method in the Comsol Multiphysics modelling environment was used to numerically solve the boundary value problem of the mathematical model.

The volume concentration of magnetite particles, expressed in mol/m³, was:

Condensed Matter and Interphases / Конденсированные среды и межфазные границы   2021;23(4): 626–636

V. S. Chekanov et al.   Experimental study and mathematical modelling of self-oscillation...

$C = 0.73593 \cdot 10^{-3}$ mol/m³,

$C_1(0,x) = C_{10}(x) = 0.0074 \cdot e^{-x(0/01 \cdot H)}$ mol/m³,

$C_2(0,x) = C_{20}(x) = 0.0074 \cdot e^{-(H-x/(0/01 \cdot H))}$ mol/m³.

According to these initial conditions, the MF particles were initially distributed quite densely near the electrodes, i.e., a near-surface layer had already been formed.

3.1. Numerical analysis results for two concentration waves

Fig. 4a shows the initial concentration distribution of the particles $C_1(t,x)$ and $C_2(t,x)$. At the initial moment of time they are charged positively at the coordinate $x = 0$ or negatively at $x = H$. The positively charged MF particles begin to move towards $x = H$, and the negatively charged magnetic particles move towards $x = 0$ (Fig. 4b). The dotted line (C_2) shows the negatively charged magnetic particles moving to the positively charged electrode (anode). The solid line (C_1) shows the positively charged magnetic particles moving to the negatively charged electrode (cathode). Initially, two concentration waves with different amplitude parameters moved towards each other. Their amplitudes then gradually became equal (Fig. 4d). Once the concentration waves reached the corresponding electrodes, the particles changed their charges. Then the cycle was repeated.

At t = 0.05 s (Fig. 5a) a front of positively charged magnetic particles was formed. When
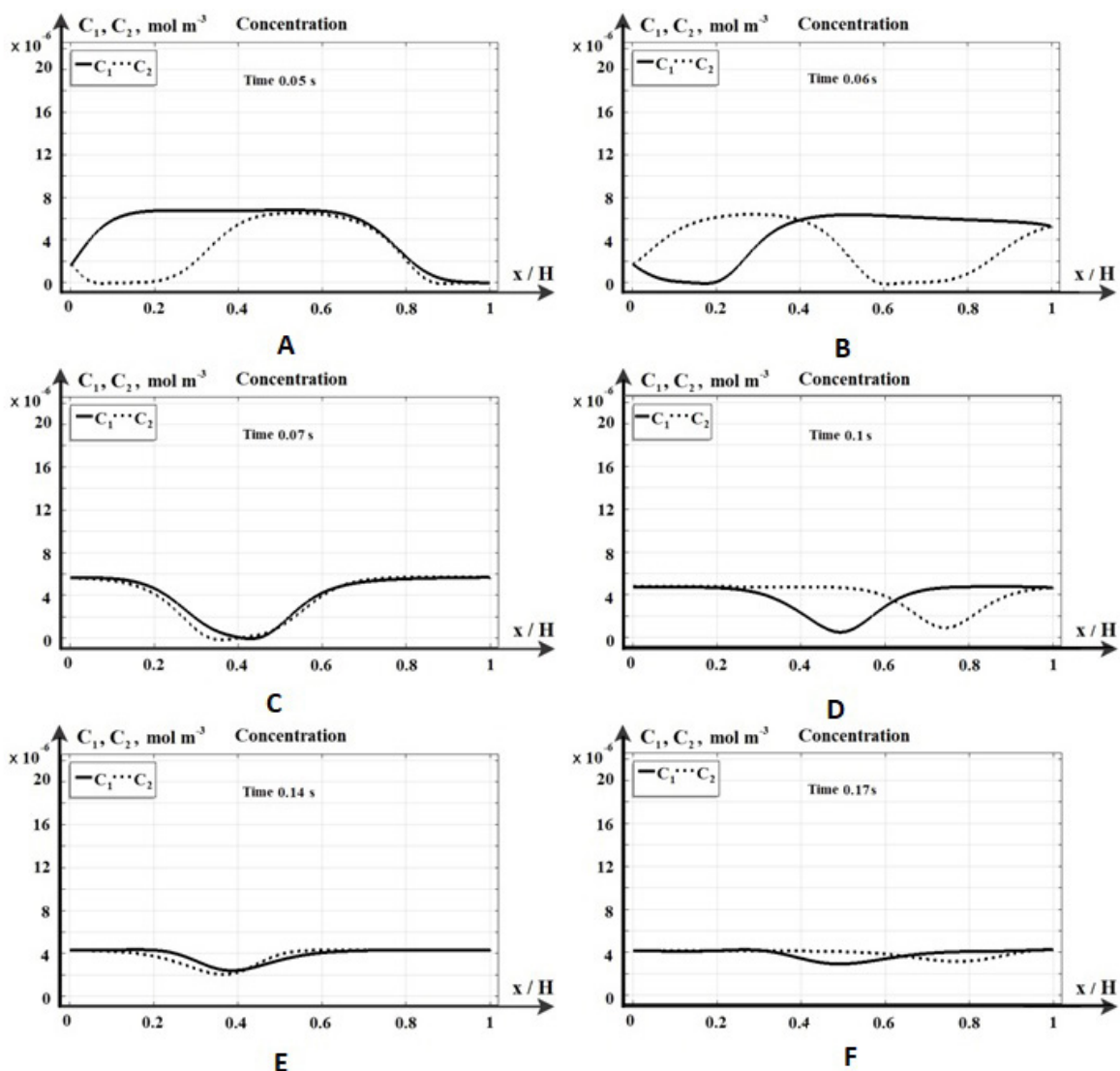
Fig. 5. Concentration distribution of positively (C_1) and negatively (C_2) charged MF particles at: a) $t = 0.05$ s, b) $t = 0.06$ s, c) $t = 0.07$ s, d) $t = 0.1$ s, e) $t = 0.14$ s, and f) $t = 0.17$ s

Condensed Matter and Interphases / Конденсированные среды и межфазные границы   2021;23(4): 626–636

V. S. Chekanov et al.   Experimental study and mathematical modelling of self-oscillation...

one cycle ended (Fig. 5b), the next cycle began (Fig. 5c), etc. At $t = 0.14$ s and $t = 0.17$s (Fig. 5e, f), the number of positively and negatively charged particles became almost constant. At a time of 0.29 s (Fig. 6A) the wave of positively charged magnetic particles was moving towards the cathode, and the wave of negatively charged particles was moving towards the anode. At $t = 0.33$ s (Fig. 6b) the wave at the anode reached its maximum. Then (Fig. 6B) it began to recede.

Thus, the particles move from one electrode to the other and back. They change their charge at the electrodes.

3.2. Comparative analysis of the numerical and laboratory experiments

The analysis revealed that the oscillation period in the numerical experiment varies from 0.5 to 0.6 s, which is consistent with the experimental data. The numerical study was carried out for different values of the potential jump $\Delta\varphi$ in the range from 1 to 20 V. It was determined that the larger the potential jump, the smaller the oscillation period, which was also confirmed experimentally. Moreover, it should be noted that the smaller the potential jump, the more the diffusion process prevails over electromigration, thus suppressing the auto-oscillation process.

We saw that when the potential jump was less than 3 V, concentration waves were not formed in computer simulations and were not observed experimentally. Different charge numbers of the particles from ±1 to ±4 were considered. It was determined that the larger the charge value, the more chaotic the motion and waveform became.

3.3. Software development

We developed software called AutoWave01 with an intuitive user interface and advanced functionality for the study of self-oscillation in a thin layer of magnetic colloid. Using AutoWave01 significantly reduces the cost of expensive experiments. It provides preliminary analysis to find the optimum parameters and all results can be stored in a convenient format.

4. Conclusion

In this study, we carried out mathematical and computer 1D simulations of self-oscillation of particles in magnetic fluids, which are fully consistent with the laboratory experiment at a qualitative level. When the voltage on the electrodes increases to a certain threshold value U_{crit}, oscillation of the particles of the dispersed phase occurs between the electrodes. This phenomenon is related to the charging of the particles and the change in charge. Our model has a predictive value: it can be used to determine the critical value of the potential jump, to find the oscillation growth period and other characteristics of the process.

Authors contributions

All authors made an equivalent contribution to the preparation of the publication.

Conflict of interests

The authors declare that they have no known competing financial interests or personal relationships that could have influenced the work reported in this paper.
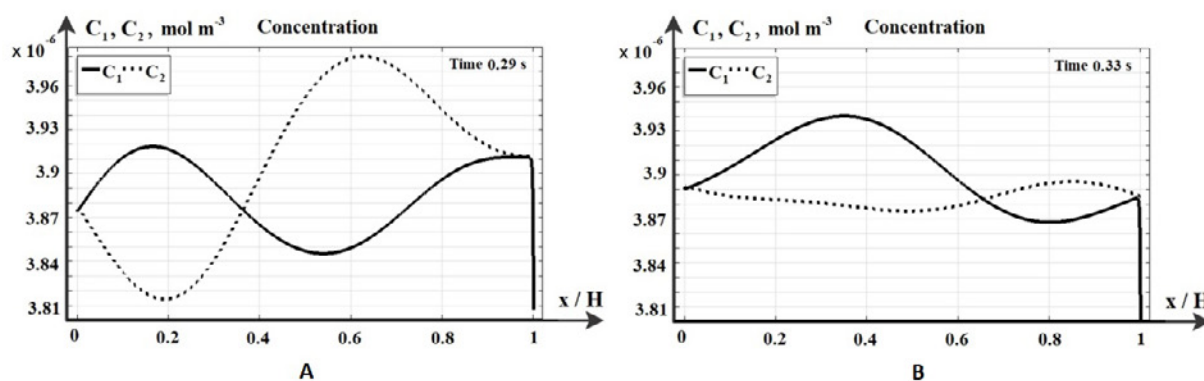
Fig. 6. Concentration distribution of positively (C_1) and negatively (C_2) charged MF particles at a) $t = 0.29$ s, b) $t = 0.33$ s (enlarged scale)

Condensed Matter and Interphases / Конденсированные среды и межфазные границы   2021;23(4): 626–636

V. S. Chekanov et al.   Experimental study and mathematical modelling of self-oscillation...

References

1. Muradova A. G., Sharapaev A. I., Zaytseva M. P., Kuznetsova S. A., Yurtov E. V. Nanostructured iron oxides. *Advances in Chemistry and Chemical Technology*. 2019; 1 (211): 77–78. Available at: https://www.elibrary.ru/item.asp?id=38098384 (In Russ., abstract in Eng.)

2. Zakinyan A. Electrical conductivity of inverse magnetic fluid emulsion. *Magnetohydrodynamics*. 2018;54(1-2):163–166. https://doi.org/10.22364/mhd.54.1-2.29

3. Chekanov V. V., Kandaurova N. V., Rakhmanina Yu. A., Chekanov V. S. *Indikator ul'trazvuka 2* [Ultrasound indicator 2]. Patent RF, no. 2446384, 2012. Publ. 27.03.2012, bull. no. 9.

4. Chekanov V. V., Kandaurova N. V., Rakhmanina Yu. A., Chekanov V. S. *Indikator teplovogo izlucheniya* [Heat radiation indicator]. Patent RF, no. 2446422, 2012. Publ. 27.03.2012, bull. no. 9.

5. Chekanov V. V., Kandaurova N. V., Rakhmanina Yu. A., Chekanov V. S. *Indikator raznosti potentsialov* [Potential difference indicator]. Patent RF, no. 2449382, 2012. Publ. 27.04.2012, bull. no. 12.

6. Chekanov V. V., Kandaurova N. V., Chekanov V. S. Observation of the autowave process in the near-electrode layer of the magnetic fluid. Spiral waves formation mechanism. *Journal of Molecular Liquids*. 2018; 272: 828–833. https://doi.org/10.1016/j.molliq.2018.10.073

7. Shliomis M. I. Magnetic fluids. *Uspekhi Fizicheskih Nauk*. 1974; 112 (3): 427. https://doi.org/10.3367/ufnr.0112.197403b.0427

8. Rosenzweig R. E. *Ferrohydrodynamics*. Cambridge University Press; 1985. 344 p.

9. Born M., Wolf E. *Principles of optics*. Pergamon Press; 1959. 803 p.

10. Chekanov V. V., Kandaurova N. V. Chekanov V. S., Romantsev V. V. Application of electrically controlled interference to observe the autowave process in the near-electrode layer of a magnetic fluid and in an electroprojectible color filter. *Journal of Optical Technology*. 2019; 86 (1): 21–26. https://doi.org/10.17586/1023-5086-2019-86-01-21-26

11. Zhakin A. I. Ionic conductivity and complexation in liquid dielectrics. *Uspekhi Fizicheskih Nauk*. 2003; 173 (1): 51–68. https://doi.org/10.3367/ufnr.0173.200301c.0051 (In Russ.)

12. Zhakin A. I. *Kinetika agregirovaniya v nepolyarnykh zhidkikh dielektrikakh*. [Aggregation kinetics in non-polar liquid dielectrics.] *Elektronnaya obrabotka materialov (Electronic Processing of Materials)*. 2015; 51 (4): 49–60. https://eom.ifa.md/en/journal/shortview/1206 (In Russ., abstract in Eng.)

13. Zhakin A. I. Near-electrode and transient processes in liquid dielectrics. *Uspekhi Fizicheskih Nauk*. 2006; 176 (3): 279–310. https://doi.org/10.3367/ufnr.0176.200603d.0289

14. Zhakin A. I. Electrohydrodynamics. *Uspekhi Fizicheskih Nauk*. 2012; 55 (5): 465–488. https://doi.org/10.3367/ufne.0182.201205b.0495

15. Stishkov Yu. K., Bogdanov D. V. Effect of nonequilibrium near-electrode layers on the structure of EHD flows in the three-ions model of a dielectric liquid. *Technical Physics*. 2017; 62(8): 1156–1162. https://doi.org/10.1134/s1063784217080266

16. Kozhevnikov V. M., Larionov Yu. A., Demin M. S. Charge transfer and accumulation in a layer of a magnetodielectric colloid with nanosized particles. *Vestnik Severo-Kavkazskogo Federalnogo Universiteta (Newsletter of North-Caucasus Federal University)*. 2008; 3: 46-50. Available at: https://www.elibrary.ru/item.asp?id=11674845 (In Russ., abstract in Eng.)

17. Kolesnikova A., Zakinyan A. Rotating magnetic field induced structure formation in a magnetic fluid emulsion. *Magnetohydrodynamics*. 2018;54(1-2): 45–48. https://doi.org/10.22364/mhd.54.1-2.8

18. Kuz'ko A. E., Chekanov V. S. Anisotropy of magnetic fluid conductivity in constant magnetic fields. *Surface Engineering and Applied Electrochemistry*. 2020; 56 (6): 727–733. https://doi.org/10.3103/S1068375520060095

19. Kozhevnikov V. M., Larionov Y. A., Chuenkova I. Y. Features of electrical properties in a structured thin magnetic fluid layer. *Magnetohydrodynamics*. 2018;54(1-2): 55–59. https://doi.org/10.22364/mhd.54.1-2.10

20. Dukhin S. S., Estrela L'opis V. R., Zholkovskii E. K. *Elektropoverkhnostnye yavleniya i elektrofil'trovanie* [Electrosurface phenomena and electrofiltration]. Kiev: Naukova dumka Publ.; 1985. 288 p. (In Russ.)

21. Erin K. V. Study of the kinetics of space charge formation in colloidal magnetic nanoparticles in liquid dielectrics. *Surface Engineering and Applied Electrochemistry*. 2017; 53 (4): 327–332. https://doi.org/10.3103/S1068375517040044

22. Erin K. V. An electro-optical study of electrophoresis of colloidal magnetite particles in kerosene in the field of near-electrode volume charge. *Colloid Journal*. 2015; 77 (1): 20–24. https://doi.org/10.1134/s1061933x15010068

23. Vavilin V. A. *Avtokolebaniya v zhidkofaznykh khimicheskikh sistemakh* [Self-oscillations in liquid-phase chemical systems]. *Priroda*. 2000; 5: 19–24. Available at: https://www.elibrary.ru/item.asp?id=35128874 (In Russ.)

24. Chekanov V. V., Kandaurova N. V., Chekanov V. S. Effect of a nearsurface nanolayer formation on the magnetic fluid electrical properties. *Acta Technica*. 2018; 63 (4): 555–562.

25. Chekanov V. S., Kovalenko A. V., Diskaeva E. N., Kirillova, E. V. Mathematical modeling of autowave process in a thin layer of magnetic colloid. *Ecological Bulletin of Research Centers of the Black Sea Economic*

Condensed Matter and Interphases / Конденсированные среды и межфазные границы   2021;23(4): 626–636

V. S. Chekanov et al.   Experimental study and mathematical modelling of self-oscillation...

Cooperation. 2020; 17 (4): 57–67. https://doi.org/10.31429/vestnik-17-4-57-67

26. Urtenov M. K., Uzdenova A. M., Kovalenko A. V. Nikonenko V. V., Pismenskaya N. D., Vasil'eva V. I., Pourcelly G. Basic mathematical model of overlimiting transfer enhanced by electroconvection in flow-through electrodialysis membrane cells. *Journal of Membrane Science.* 2013; 447: 190–202. https://doi.org/10.1016/j.memsci.2013.07.033

27. Nikonenko V. V., Vasil'eva V. I., Akberova E. M., Uzdenova A. M., Urtenov M. K., Kovalenko A. V., Pismenskaya N. D., Mareev S. A., Pourcelly G. Competition between diffusion and electroconvection at an ion-selective surface in intensive current regimes. *Advances in Colloid and Interface Science.* 2016; 235: 233–246. https://doi.org/10.1016/j.cis.2016.06.014

28. Gudza V. A., Pismenskiy A. V., Urtenov M. K., Shkorkina I. V., Chubyr N. O., Kovalenko A. V. The influence of water dissociation/recombination on transport of binary salt in diffusion layer near ion exchange membrane. *Journal of Advanced Research in Dynamical and Control Systems.* 2020; 12 (4): 923–935. https://doi.org/10.5373/JARDCS/V12SP4/20201563

29. Kovalenko A. V., Yzdenova A. M., Sukhinov A. I., Chubyr N. O., Urtenov M. Kh. Simulation of galvanic dynamic mode in membrane hydrocleaning systems taking into account space charge. *AIP Conference Proceedings.* 2019; 2188 (1): 050021. https://doi.org/10.1063/1.5138448

Information about the authors

Vladimir S. Chekanov, PhD in Technical Sciences, Associate Professor at the Department of Information Systems and Technologies, North-Caucasus Federal University, Stavropol, Russian Federation; e-mail: oranjejam@mail.ru. ORCID iD: https://orcid.org/0000-0002-2680-2883.

Evgeniya V. Kirillova, PhD in Physics and Mathematics, Professor at the RheinMain University of Applied Sciences in Wiesbaden, Germany; e-mail: kirillova@web.de. ORCID iD: https://orcid.org/0000-0002-6797-0920.

Anna V. Kovalenko, DSc in Physics and Mathematics, Associate Professor, Head of the Department of Data Analysis and Artificial Intelligence, Kuban State University, Krasnodar, Russian Federation; e-mail: Savanna-05@mail.ru. ORCID iD: https://orcid.org/0000-0002-3991-3953.

Elena N. Diskaeva, PhD in Physics and Mathematics, Associate Professor at the Department of Industrial Technologies, Branch of "MIREA – Russian Technological University" in Stavropol, Stavropol, Russian Federation; e-mail: diskaevapes@mail.ru. ORCID iD: https://orcid.org/0000-0002-5185-6023.

Original articles

Semiconductor metal oxide sensor for hydrogen sulphide operating under non-stationary temperature conditions

A. V. Shaposhnik[1] ✉, **A. A. Zvyagin**[1], **O. V. Dyakonova**[1], **S. V. Ryabtsev**[2], **D. A. Ghareeb**[2]

[1]*Voronezh State Agrarian University,*
1 Michurina ul., Voronezh 394087, Russian Federation

[2]*Voronezh State University,*
1 Universitetskaya pl., Voronezh 394018, Russian Federation

Abstract

The aim of the work was to create a selective gas sensor for hydrogen sulphide. As a result of adding ammonia to the zinc acetate solution, centrifuging the obtained zinc hydroxide and subsequent calcination, a polydisperse zinc oxide powder with a grain size of 5–50 nm was obtained. The material was characterized using X-ray phase analysis and transmission electron microscopy. Subsequently, silver nitrate and terpeniol were added to the zinc oxide nanopowder to form a paste. The gas-sensitive material was obtained by applying the resulting paste on a special dielectric substrate and subsequent calcination, as a result of which the terpeniol burned out, and the silver nitrate turned into an oxide (the mass fraction of the silver was 3%). A non-stationary temperature mode for the operation of the sensor was selected, in which, after rapid heating of the sensor to 450 °C (2 seconds), slow (13 seconds) cooling to 100 °C occurred. Each subsequent heating-cooling cycle with a total period of 15 seconds began immediately after the end of the previous cycle. The use of an unsteady temperature mode in combination with the selection of the composition of the gas-sensitive layer made it possible to obtain a response of 200 for a hydrogen sulphide concentration of 1 ppm. Along with an increase in sensitivity, a significant increase in selectivity was also observed. The cross-sensitivity for the determination of hydrogen sulphide and other reducing gases (CO, NH_3, H_2) was more than three orders of magnitude. Thus, this sensor can be used to detect hydrogen sulphide even in the presence of interfering components. The use of highly selective sensors in the tasks of qualitative and quantitative analysis can significantly simplify the calibration in comparison with "electronic nose" devices. Devices based on highly selective sensors do not require the use of mathematical methods for processing multidimensional data arrays.

Keywords: Sensitivity; MOX sensor; Temperature modulation; Qualitative analysis; Quantitative analysis

✉ Alexey V. Shaposhnik, e-mail: avshaposhnik@gmail.com

Condensed Matter and Interphases / Конденсированные среды и межфазные границы 2021;23(4): 637–643

A. V. Shaposhnik et al. Semiconductor metal oxide sensor for hydrogen sulphide…

1. Introduction

Due to their high sensitivity, compactness, and low cost, semiconductor gas sensors are often used in the determination of toxic and flammable substances, however, the area of their possible use is limited by insufficient selectivity [1]. There are two approaches to the solution of this problem. The first of them is associated with the use of a matrix of low-selective sensors in multisensor "electronic nose" devices. In this case, mathematical processing of the obtained multidimensional data arrays can lead to the solution of problems of qualitative and quantitative analysis. The disadvantages of this approach are the complexity and laboriousness of device calibration, the laboriousness of recalibration when replacing even one sensor, the difficulty of mathematical processing, which requires significant computing resources. The second approach involves the creation of selective sensors, the cross-sensitivity of which to interfering components is rather low.

It is known that the determination of hydrogen sulphide by semiconductor metal oxide sensors is characterized by a higher selectivity compared to the determination of other gases. This is due to the fact that the sorption of hydrogen sulphide on the surface of metal oxides can lead to the reversible transformation of some oxides into sulphides with high electrical conductivity and/or a different conductivity type, and this process can make an additional significant contribution to the sensor response. For example, the addition of copper oxide (+2) leads to a change in the composition of the gas-sensitive layer during the sorption of hydrogen sulphide [2, 3], the transformation of semiconductors with the *p*-type conductivity, copper oxide, into a sulphide with high electrical conductivity.

The most common material for hydrogen sulphide sensors is tin dioxide with the addition of copper oxide (+2). High sensitivity and selectivity were shown, in particular, for SnO_2 nanofibers coated with CuO obtained by electrospinning [4, 5]. Sensors for H_2S based on SnO_2 nanowires coated with CuO nanoparticles were obtained [6, 7], the mechanism of the sensory response of thin films SnO_2:CuO obtained by thermal sputtering to hydrogen sulphide was investigated [8]. A gas-sensitive material based on hollow nanospheres coated with CuO was successfully used for the determination of hydrogen sulphide in medical diagnostics. [9] The multilayer SnO_2–CuO structure showed a response of more than four orders of magnitude to 20 ppm H_2S combined with a low response time [10]. The influence of the interdiffusion of SnO_2 and CuO nanoparticles on the sensory properties to hydrogen sulphide was considered [11]. The sensory properties of thin-layer nanostructures based on CuO/SnO_2 were also investigated [12]. However, the most common method for obtaining SnO_2/CuO nanocomposites is the sol-gel process [13].

Along with the addition of copper oxide, sensors with the addition of silver are used for the determination of hydrogen sulphide. As well as copper oxide, silver oxide is able to reversibly transform into silver sulphide with high electrical conductivity. The transition of silver oxide into sulphide makes a large contribution to the analytical signal of the sensor [14, 15]. The addition of silver to nanocrystalline SnO_2 increases the response to hydrogen sulphide [16–18].

Pure SnO_2 [19] and SnO_2 with the addition of platinum [20] or fullerenes [21] were used for the determination of hydrogen sulphide.

In some cases, copper oxide was not an additive to other metal oxide materials, but the basis of the sensor, for example, a highly sensitive sensor was obtained based on palladium-doped "nanoflowers" from CuO [22]. The sensory properties of unsintered copper oxide (+2) nanowires were investigated [23].

For the determination of hydrogen sulphide, such traditional materials as, for example, zinc oxide without special additives have been successfully used [24]. The addition of copper oxide (+2) to zinc oxide usually increases the sensitivity to hydrogen sulphide [25–29]. Examples illustrating the influence of the composition of the gas-sensitive layer on the magnitude of response of the sensor to hydrogen sulphide are shown in Table 1.

It is known that the transition from ordinary stationary temperature modes to non-stationary modes often leads to a very significant increase in the sensitivity [22, 32, 33]. As we demonstrated in our study, the use of non-stationary temperature modes also contributes to an increase in the selectivity of the analysis of hydrogen sulphide.

Condensed Matter and Interphases / Конденсированные среды и межфазные границы   2021;23(4): 637–643

A. V. Shaposhnik et al.   Semiconductor metal oxide sensor for hydrogen sulphide...

Table 1. The properties of different sensor materials in relation to hydrogen sulphide

Sensor material	Receiving method	Concentration H$_2$S (ppm)	Response	Working temperature (°C)	Ref.
SnO$_2$	Impregnation of biomatrix with precursor solution followed by annealing	1	~ 5	92	[19]
SnO$_2$/CuO nanofibers	Electrospinning	1	23	200	[5]
SnO$_2$/CuO	Ultrasonic spray pyrolysis	1	78	300	[9]
CuO/Pd	Precipitation from solution (sol-gel process)	1	63.8	80/300 (pulse mode)	[22]
ZnO/Ag	Precipitation from solution (sol-gel process)	1	193	100/450 (pulse mode)	This work
Fe$_2$O$_3$	Thermal oxidation of iron film	10	~ 5	250	[30]
CaCu$_3$Ti$_4$O$_{12}$/Ag	Precipitation from solution (sol-gel process)	10	~ 100	250	[31]
ZnO/Ag	Precipitation from solution (sol-gel process)	10	905	100/450 (pulse mode)	This work

2. Experimental

2.1. Synthesis and characterisation of gas sensitive material

An aqueous solution of ammonia (w = 25%) was added dropwise to an aqueous solution of zinc acetate (chemically pure grade) acidified with acetic acid (pH = 5) to pH = 8 for the formation of sol and peptization of the resulting zinc oxide hydrate suspension:

$$Zn(CH_3COO)_2 + 2NH_3 + 2H_2O \rightarrow$$
$$\rightarrow Zn(OH)_2\downarrow + 2CH_3COONH_4. \qquad (1)$$
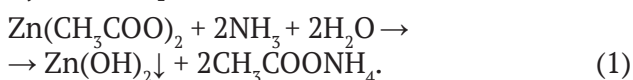
Ammonia was added with continuous stirring, the reaction mixture was cooled to a temperature of 20 °C. The resulting zinc hydroxide sol was precipitated by centrifugation, dried at 80 °C for 8 h, and calcined, resulting in the formation of zinc oxide nanoparticles:

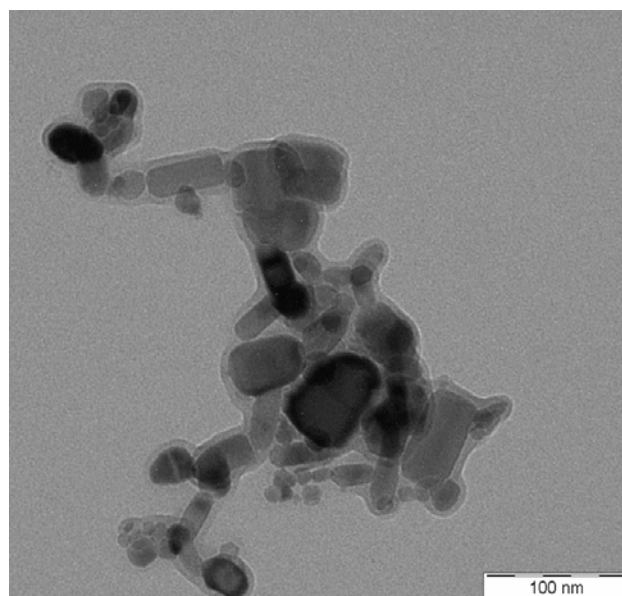$$Zn(OH)_2 \rightarrow ZnO + H_2O \qquad (2)$$

Calcination was performed for 8 hours at temperatures of 300 °C (sample 1), 400 °C (sample 2), 500 °C (sample 3), 600 °C (sample 4). The composition and structure of zinc oxide powder were investigated using transmission electron microscopy (Fig. 1) and X-ray phase analysis (Fig. 2). The main phase for all ZnO samples has a hexagonal syngony, while individual reflections of samples 3 and 4 may belong to the ZnO phase of the cubic modification.

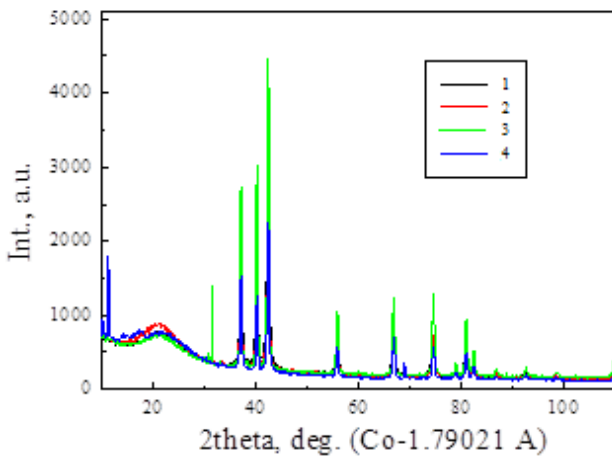Subsequently, the zinc oxide powder was treated with a solution of silver nitrate, dried, and then terpeniol was added to the powder as a bonding agent. The resulting paste was applied to a dielectric substrate made of aluminium oxide with special platinum electrodes for measuring electrical conductivity and with a platinum heater. The substrate with the applied paste was calcined to a temperature of 750 °C, as a result bonding agent burned out, and a ZnO gel with the addition of silver was formed.

2.2. Measurement of sensory characteristics

For the investigation of the sensory properties of the obtained materials, calibration gas mixtures "hydrogen sulphide in synthetic air"
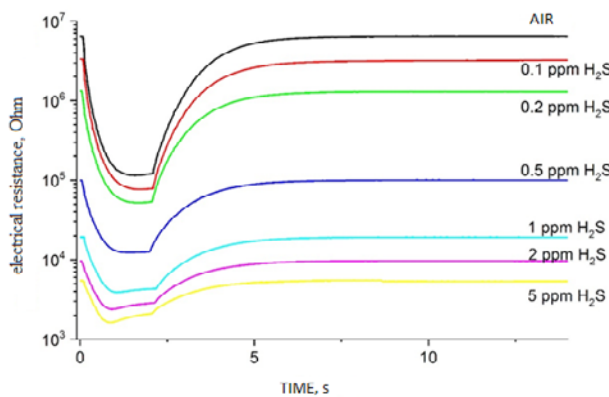

Fig. 1. Transmission electron microscopy image of a zinc oxide nanopowder

Condensed Matter and Interphases / Конденсированные среды и межфазные границы   2021;23(4): 637–643

A. V. Shaposhnik et al.   Semiconductor metal oxide sensor for hydrogen sulphide...

Fig. 2. X-ray diffraction. Sample *1* of zinc oxide nano-powder was calcined at 300 °C, sample *2* – at 400 °C, sample *3* – at 500 °C, sample *4* – at 600 °C

with concentrations of 10 and 200 ppm, diluted with synthetic air were used. The total flow rate was 250 ml/min. The sensor in a TO-8 metal case was placed in a stainless-steel chamber. The temperature of the sensor was set using a special electronic device based on the temperature coefficient of resistance of the heater known from preliminary measurements.

The electrical resistance of the gas-sensitive layer was determined using a special electronic device with a frequency of up to 40 Hz and recorded as a computer file. The duration of each measurement cycle was 15 seconds, of which heating from 100 to 450 °C was performed for 2 seconds, and the cooling from 450 to 100 °C was performed for the following 13 seconds. The heating-cooling cycles followed each other

without interruption. The measurement results obtained in the first five cycles were discarded. For quantitative analysis, only one out of the 575 points of the cycle was used, corresponding to a time of 14.95 seconds after the start of the cycle.
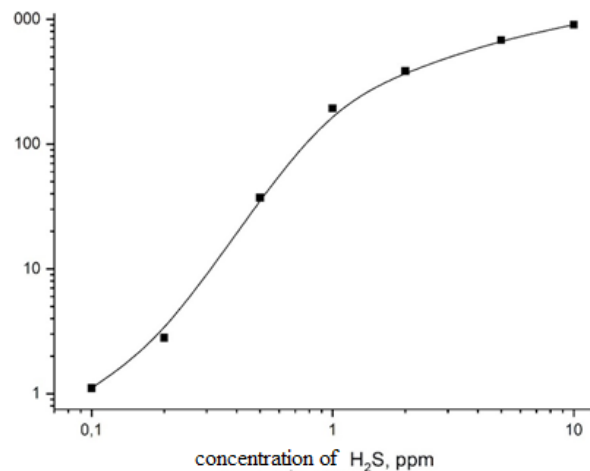
The response S was calculated as the ratio of electrical resistance R_0 in air to electrical resistance R_g in the investigated gaseous medium:

$$S = R_0/R_g. \tag{3}$$

3. Results and discussion

The dependence of the electrical resistance of the ZnO-Ag sensor on time during one measurement cycle for different hydrogen sulphide concentrations is shown in Fig. 3. As can be seen from Fig. 3, an increase in the concentration of hydrogen sulphide led not only to a significant increase in the response, but the shape of the curves also changed.

The calibration dependence for determination of hydrogen sulphide concentration with a ZnO-Ag sensor in non-stationary temperature mode is shown in Fig. 4. The transition from a constant temperature to a non-stationary mode led not only to an increase in the response to hydrogen sulphide, but also increased the selectivity of the analysis. The cross-sensitivities of SnO_2-Ag sensor to hydrogen sulphide/carbon monoxide, hydrogen sulphide/hydrogen, hydrogen sulphide/ammonia are shown in Table 2. As can be seen from Table 2, a ZnO-Ag sensor operating in non-stationary mode can be considered highly selective, since its responses to the same concentration of hydrogen sulphide and other

Fig. 3. Electrical resistance of ZnO-Ag sensor in hydrogen sulphide as a function of H_2S concentration under non-stationary temperature condition during one measurement cycle

Fig. 4. Calibration curve of the sensor ZnO-Ag at the determination of hydrogen sulphide concentrations

Condensed Matter and Interphases / Конденсированные среды и межфазные границы   2021;23(4): 637–643

A. V. Shaposhnik et al.   Semiconductor metal oxide sensor for hydrogen sulphide...
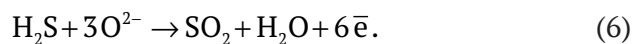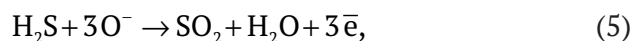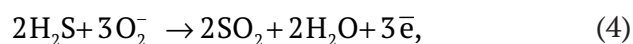
Table 2. Responses of sensor ZnO + Ag

Response to 10 ppm H_2S	Response to 10 ppm CO	Response to 10 ppm NH_3	Response to 10 ppm H_2
905	0.21	0.44	0.87

reducing gases differ by more than 3 orders of magnitude.

Under stationary temperature modes, the cross-sensitivity of the determination of hydrogen sulphide and other reducing gases (hydrogen, carbon monoxide, ammonia) was one and a half orders of magnitude; when switching to non-stationary mode, the cross-sensitivity exceeded three orders of magnitude (Table 2). One of the reasons for the increased sensitivity and selectivity in the determination of hydrogen sulphide is the time separation of the sorption of the gas analyte and the catalytic activity of the gas-sensitive layer. Pulsed temperature mode allows the catalyst to be activated before desorption of the gas analyte occurs [33]. This effect seems to play an important role, but it is not the only one effect. The sensor response largely depends on the total concentration of charge carriers. In the case of the same action of the gas analyte, the sensory response will be the higher, the fewer charge carriers were present in the semiconductor before the gas analyte was introduced. The unsteady temperature mode allows increasing the resistance of the metal oxide nanomaterial in the air due to the efficient sorption of oxygen. Various forms of chemisorbed oxygen play an important role in the interaction with hydrogen sulphide:

$$2H_2S + 3O_2^- \rightarrow 2SO_2 + 2H_2O + 3\overline{e}, \qquad (4)$$

$$H_2S + 3O^- \rightarrow SO_2 + H_2O + 3\overline{e}, \qquad (5)$$

$$H_2S + 3O^{2-} \rightarrow SO_2 + H_2O + 6\overline{e}. \qquad (6)$$

At low temperatures (for example, at room temperature), chemisorbed oxygen is predominantly in the form O_2^-, therefore, the reaction channel (4) prevails. At temperatures slightly exceeding 200 °C, chemisorbed oxygen transforms into the form O^-, and channel (5) prevails. A further increase in temperature (400 °C and above) leads to the reaction through channel (6). However, the redox mechanism of the interaction of hydrogen sulphide with the semiconductor surface (4–6) does not allow the

selective determination of reducing gases, since similar interaction mechanisms occur on the surface during the chemisorption of hydrogen, carbon monoxide, ammonia, ethanol, and so on.

Sensors based on metal oxides with silver additives exhibit some selectivity to hydrogen sulphide even when they operate with a stationary temperature. This is due to the processes of reversible transformation of silver oxide into sulphide, which has a low electrical resistance, and therefore this transition makes a significant contribution to the donor sensory response:

$$Ag_2O + H_2S \rightarrow Ag_2S + H_2O. \qquad (7)$$
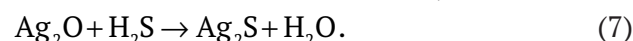
Process (7) is exothermic, and at low temperatures the equilibrium shifts towards the formation of silver sulphide. At high temperatures, an endothermic process (8) of the formation of silver oxide occurs [17]:

$$2Ag_2S + 3O_2 \rightarrow 2Ag_2O + 2SO_2. \qquad (8)$$
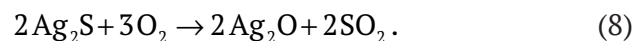
4. Conclusions

In our study, we investigated the sensory characteristics of the material obtained by adding silver oxide (3% by weight) to the ZnO nanopowder in relation to hydrogen sulphide and other reducing gases (H_2, CO, NH_3). The sensor was obtained using the classic sol-gel technology. The main task of the study was comparison of the characteristics of the sensor in two modes: with a stationary temperature and with temperature modulation. It was shown that the use of a mode in which the sensor quickly heated up to 450 °C (2 seconds) and then cooled down to 100 °C (13 seconds), led not only to a significant increase in sensitivity, but also to a noticeable increase in selectivity. The cross-sensitivity in the determination of hydrogen sulphide and in the determination of other reducing gases (hydrogen, carbon monoxide, ammonia) was approximately three orders of magnitude, which makes this sensor highly selective.

Thus, a sensor based on ZnO–Ag when operating in a pulsed temperature mode has a high selectivity and can be used to determine hydrogen sulphide in the presence of interfering components, as well as in mixtures of hydrogen sulphide with other target gases.

Authors contributions

All authors made an equivalent contribution to the preparation of the publication.

Condensed Matter and Interphases / Конденсированные среды и межфазные границы   2021;23(4): 637–643

A. V. Shaposhnik et al.   Semiconductor metal oxide sensor for hydrogen sulphide...

Conflict of interests

The authors declare that they have no known competing financial interests or personal relationships that could have influenced the work reported in this paper.

References

1. Yamazoe N. New approaches for improving semiconductor gas sensors. *Sensors and Actuators B: Chemical*. 1991;5(1–4): 7–19. https://doi.org/10.1016/0925-4005(91)80213-4

2. Maekawa T., Tamaki J., Miura N., Yamazoe N. Sensing behavior of CuO-loaded SnO_2 element for H_2S detection. *Chemistry Letters*. 1991;20(4): 575–578. https://doi.org/10.1246/cl.1991.575

3. Tamaki J., Maekawa T., Miura N., Yamazoe, N. CuO-SnO_2 element for highly sensitive and selective detection of H_2S. *Sensors and Actuators B: Chemical*. 1992;9(3): 197–203. https://doi.org/10.1016/0925-4005(92)80216-k

4. Choi S.-W., Zhang J., Akash K., Kim S. S. H_2S sensing performance of electrospun CuO-loaded SnO_2 nanofibers. *Sensors and Actuators B: Chemical*. 2012;169: 54–60. https://doi.org/10.1016/j.snb.2012.02.054

5. Zhao Y., He X., Li J., Gao X., Jia J. Porous CuO/SnO_2 composite nanofibers fabricated by electrospinning and their H_2S sensing properties. *Sensors and Actuators B: Chemical*. 2012;165(1): 82–87. https://doi.org/10.1016/j.snb.2012.02.020

6. Shao F., Hoffmann M. W. G., Prades J. D., Zamani R., Arbiol J., Morante J. R., ... Hernández-Ramírez F. Heterostructured *p*-CuO (nanoparticle)/*n*-SnO_2 (nanowire) devices for selective H_2S detection. *Sensors and Actuators B: Chemical*. 2013;181: 130–135. https://doi.org/10.1016/j.snb.2013.01.067

7. Hwang I.-S., Choi J.-K., Kim S.-J., Dong K.-Y., Kwon J.-H., Ju B.-K., Lee J.-H. Enhanced H_2S sensing characteristics of SnO_2 nanowires functionalized with CuO. *Sensors and Actuators B: Chemical*. 2009;142(1): 105–110. https://doi.org/10.1016/j.snb.2009.07.052

8. Katti V. R., Debnath A. K., Muthe K. P., Kaur M., Dua A. K., Gadkari S. C., ... Sahni V. C. Mechanism of drifts in H_2S sensing properties of SnO_2:CuO composite thin film sensors prepared by thermal evaporation. *Sensors and Actuators B: Chemical*. 2003; 96(1–2): 245–252. https://doi.org/10.1016/s0925-4005(03)00532-x

9. Choi K.-I., Kim H.-J., Kang Y. C., Lee J.-H. Ultraselective and ultrasensitive detection of H_2S in highly humid atmosphere using CuO-loaded SnO_2 hollow spheres for real-time diagnosis of halitosis. *Sensors and Actuators B: Chemical*. 2014;194: 371–376. https://doi.org/10.1016/j.snb.2013.12.111

10. Verma M. K., Gupta V. A highly sensitive SnO_2-CuO multilayered sensor structure for detection of H_2S gas. *Sensors and Actuators B: Chemical*. 2012;166–167: 378–385. https://doi.org/10.1016/j.snb.2012.02.076

11. Vasiliev R. B., Rumyantseva M. N., Podguzova S. E., Ryzhikov A. S., Ryabova L. I., Gaskov A. M. Effect of interdiffusion on electrical and gas sensor properties of CuO/SnO_2 heterostructure. *Materials Science and Engineering: B*. 1999;57(3): 241–246. https://doi.org/10.1016/s0921-5107(98)00432-2

12. Vasiliev R., Rumyantseva M., Yakovlev N., Gaskov A. CuO/SnO_2 thin film heterostructures as chemical sensors to H_2S. *Sensors and Actuators B: Chemical*. 1998;50(3): 186–193. https://doi.org/10.1016/s0925-4005(98)00235-4

13. Malyshev V. V., Pislyakov A. V. SnO_2-based thick-film-resistive sensor for H_2S detection in the concentration range of 1-10 mg m^{-3}. *Sensors and Actuators B: Chemical*. 1998;47(1–3): 181–188. https://doi.org/10.1016/S0925-4005(98)00021-5

14. Lantto V., Mizsei J. H_2S monitoring as an air pollutant with silver-doped SnO_2 thin-film sensors. *Sensors and Actuators B: Chemical*. 1991;5(1–4): 21–25. https://doi.org/10.1016/0925-4005(91)80214-5

15. Harkoma-Mattila A., Rantala T. S., Lantto V., Leppävuori, S. Sensitivity and selectivity of doped SnO_2 thick-film sensors to H_2S in the constant- and pulsed-temperature modes. *Sensors and Actuators B: Chemical*. 1992;6(1–3): 248–252. https://doi.org/10.1016/0925-4005(92)80063-4

16. Gong J., Chen Q., Lian M.-R., Liu N.-C., Stevenson R. G., Adami F. Micromachined nanocrystalline silver doped SnO_2 H_2S sensor. *Sensors and Actuators B: Chemical*. 2006;114(1): 32–39. https://doi.org/10.1016/j.snb.2005.04.035

17. Ngoc T. M., Duy N. V., Hung C. M., Hoa N. D., Nguyen H., Tonezzer M., Hieu N. V. Self-heated Ag-decorated SnO_2 nanowires with low power consumption used as a predictive virtual multisensor for H_2S-selective sensing. *Analytica Chimica Acta*. 2019;1069: 108–116. https://doi.org/10.1016/j.aca.2019.04.020

18. Kolhe P. S., Koinkar P. M., Maiti N., Sonawane K. M. Synthesis of Ag doped SnO_2 thin films for the evaluation of H_2S gas sensing properties. *Physica B: Condensed Matter*. 2017;524: 90–96. https://doi.org/10.1016/j.physb.2017.07.056

19. Song B.-Y., Zhang M., Teng Y., Zhang X.-F., Deng Z.-P., Huo L.-H., Gao S. Highly selective ppb-level H_2S sensor for spendable detection of exhaled biomarker and pork freshness at low temperature: Mesoporous SnO_2 hierarchical architectures derived from waste scallion root. *Sensors and Actuators B: Chemical*. 2020;307: 127662. https://doi.org/10.1016/j.snb.2020.127662

20. Sberveglieri G., Groppelli S., Nelli P., Perego C., Valdré G., Camanzi A. Detection of sub-ppm H_2S

Condensed Matter and Interphases / Конденсированные среды и межфазные границы   2021;23(4): 637–643

A. V. Shaposhnik et al.   Semiconductor metal oxide sensor for hydrogen sulphide...

concentrations by means of SnO_2(Pt) thin films, grown by the RGTO technique. *Sensors and Actuators B: Chemical*. 1993;15(1–3): 86–89. https://doi.org/10.1016/0925-4005(93)85032-6

21. Keshtkar S., Rashidi A., Kooti M., Askarieh M., Pourhashem S., Ghasemy E., Izadi N. A novel highly sensitive and selective H_2S gas sensor at low temperatures based on SnO_2 quantum dots-C60 nanohybrid: Experimental and theory study. *Talanta*. 2018;88: 531–539. https://doi.org/10.1016/j.talanta.2018.05.099

22. Hu X., Zhu Z., Chen C., Wen T., Zhao X., Xie L. Highly sensitive H_2S gas sensors based on Pd-doped CuO nanoflowers with low operating temperature. S*ensors and Actuators B: Chemical*. 2017;253: 809–817. https://doi.org/10.1016/j.snb.2017.06.183

23. Hu Q., Zhang W., Wang X., Wang Q., Huang B., Li Y., … Zhang Z. Binder-free CuO nanoneedle arrays based tube-type sensor for H_2S gas sensing. *Sensors and Actuators B: Chemical*. 2021;326: 128993. https://doi.org/10.1016/j.snb.2020.128993

24. Diao K., Zhou M., Zhang J., Tang Y., Wang S., Cui X. High response to H_2S gas with facile synthesized hierarchical ZnO microstructures. *Sensors and Actuators B: Chemical*. 2015;219: 30–37. https://doi.org/10.1016/j.snb.2015.04.116

25. Kim S.-J., Na C. W., Hwang I.-S., Lee J.-H. One-pot hydrothermal synthesis of CuO-ZnO composite hollow spheres for selective H_2S detection. *Sensors and Actuators B: Chemical*. 2012;168: 83–89. https://doi.org/10.1016/j.snb.2012.01.045

26. Na H.-B., Zhang X.-F., Zhang M., Deng Z.-P., Cheng X.-L., Huo L.-H., Gao S. A fast response/recovery ppb-level H_2S gas sensor based on porous CuO/ZnO heterostructural tubule via confined effect of absorbent cotton. *Sensors and Actuators B: Chemical*. 2019;297: 126816. https://doi.org/10.1016/j.snb.2019.126816

27. Wang L., Kang Y., Wang Y., Zhu B., Zhang S., Huang W., Wang S. CuO nanoparticle decorated ZnO nanorod sensor for low-temperature H 2S detection. *Mater. Sci. Eng. C*. 2012;32(7): 2079–2085. https://doi.org/10.1016/j.msec.2012.05.042

28. Shewale P. S., Yun K. S. Synthesis and characterization of Cu-doped ZnO/RGO nanocomposites for room-temperature H_2S gas sensor. *Journal of Alloys and Compounds*. 2020;837: 155527. https://doi.org/10.1016/j.jallcom.2020.155527

29. Wang X., Li S., Xie L., Li X., Lin D., Zhu Z. Low-temperature and highly sensitivity H_2S gas sensor based on ZnO/CuO composite derived from bimetal

metal-organic frameworks. *Ceramics International*. 2020;46(10): 15858–15866. https://doi.org/10.1016/j.ceramint.2020.03.133

30. Balouria V., Kumar A., Samanta S., Singh A., Debnath A. K., Mahajan A., … Gupta S. K. Nano-crystalline Fe_2O_3 thin films for ppm level detection of H_2S. *Sensors and Actuators B: Chemical*. 2013;181: 471–478. https://doi.org/10.1016/j.snb.2013.02.013

31. Natkaeo A., Phokharatkul D., Hodak J. H., Wisitsoraat A., Hodak S. K. Highly selective sub–10 ppm H_2S gas sensors based on Ag-doped $CaCu_3Ti_4O_{12}$ films. *Sensors and Actuators B: Chemical*. 2018;260: 571–580. https://doi.org/10.1016/j.snb.2017.12.134

32. Liang X., Kim T.-H., Yoon J.-W., Kwak C.-H., Lee J.-H. Ultrasensitive and ultraselective detection of H_2S using electrospun CuO-loaded In_2O_3 nanofiber sensors assisted by pulse heating. *Sensors and Actuators B: Chemical*. 2015;209: 934–942. https://doi.org/10.1016/j.snb.2014.11.130

33. Shaposhnik A., Moskalev P., Sizask E., Ryabtsev S., Vasiliev A. Selective detection of hydrogen sulfide and methane by a single MOX-sensor. *Sensors*. 2019;19(5): 1135. https://doi.org/10.3390/s19051135

Information about the authors

Alexey V. Shaposhnik, DSc in Chemistry, Professor at the Department of Chemistry, Voronezh State Agrarian University, Voronezh, Russian Federation; e-mail: avshaposhnik@gmail.com. ORCID iD: https://orcid.org/0000-0002-1214-2730.

Alexey A. Zviagin, PhD in Chemistry, Docent at the Department of Chemistry, Voronezh State Agrarian University, Voronezh, Russian Federation; e-mail: a.a.zviagin@rambler.ru. ORCID iD: http://orcid.org/0000-0002-9299-6639.

Olga V. Dyakonova, PhD in Chemistry, Docent at the Department of Chemistry, Voronezh State Agrarian University, Voronezh, Russian Federation e-mail: dyakol@yandex.ru.

Stanislav V. Ryabtsev, DSc in Physics and Mathematics, Head of the Laboratory, Voronezh State University, Voronezh, Russian Federation; e-mail: raybtsev@niif.vsu.ru. ORCID iD: https://orcid.org/0000-0001-7635-8162.

Dina Ghareeb, postgraduate student, Voronezh State University, Voronezh State University, Voronezh, Russian Federation; e-mail: raybtsev@niif.vsu.ru ORCID iD: https://orcid.org/0000-0002-8794-2791.
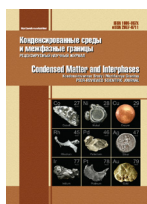
Original articles

Dps protein localization studies in nanostructured silicon matrix by scanning electron microscopy

E. V. Parinova[1] ✉, S. S. Antipov[1,2], V. Sivakov[3], I. S. Kakuliia[1], S. Yu. Trebunskikh[1], E. A. Belikov[1], S. Yu. Turishchev[1]

[1]*Voronezh State University,*
Universitetskaya pl., 1, Voronezh 394018, Russian Federation

[2]*Immanuel Kant Baltic Federal University,*
ul. Universitetskaya, 2, Kaliningrad, 236041 Russian Federation

[3]*Leibniz Institute of Photonic Technology,*
9 Albert Einstein str., Jena 07745, Germany

Abstract

The present work is related to the microscopic studies of the morphology of the planar and inner part of silicon nanowires arrays before and after immobilization with a natural nanomaterial, Dps protein of bacterial origin.

Silicon nanowires were formed by metal-assisted wet chemical etching. To obtain the recombinant protein, *Escherichia coli* cells were used as excretion strain and purification were carried out using chromatography. The combination of silicon nanowires with protein molecules was carried out by layering at laboratory conditions followed by drying under air. The resulting hybrid material was studied by high-resolution scanning electron microscopy. Studies of the developed surface of the nanowires array were carried out before and after combining with the bioculture. The initial arrays of silicon wires have a sharp boundaries in the planar part and in the depth of the array, transition layers are not observed. The diameter of the silicon nanowires is about 100 nm, the height is over a micrometer, while the distances between the nanowires are several hundred of nanometers. The pores formed in this way are available for filling with protein during the immobilization of protein.

The effectiveness of using the scanning electron microscopy to study the surface morphology of the hybrid material "silicon wires – bacterial protein Dps" has been demonstrated. It is shown that the pores with an extremely developed surface can be combined with a bio-material by deposition deep into cavities. The protein molecules can easily penetrate through whole porous wires matrix array. The obtained results demonstrate the possibility of efficient immobilization of nanoscaled Dps protein molecules into an accessible and controllably developed surface of silicon nanowires.

Keywords: Silicon wires, Developed surface, Ferritin-like Dps protein, Scanning electron microscopy, Combination

✉ Elena V. Parinova, e-mail: parinova@phys.vsu.ru

Condensed Matter and Interphases / Конденсированные среды и межфазные границы   2021;23(4): 644–648

E. V. Parinova et al.   Dps protein localization studies in nanostructured silicon matrix...

1. Introduction

Arrays of Silicon Nanowires (Si-NW) are a well-known material, including nanomaterials, whose formation technologies are well developed [1]. Si-NW traditionally attracts the attention of researchers as a material with important properties: visible photoluminescence at room temperature [2] or the possibility of use in hydrogen generation issues [3]. However, the most important property of this material is a simple and economical technology of reproducible formation in combination with an extremely developed surface [4], which is available for activation when combined with numerous functional materials, including nano-biomaterials of natural origin. With this approach to using the available surface of silicon wires arrays of controlled morphology, the issues of the general possibility of combining with the necessary material are the issue of a great interest.

Dps protein (DNA-binding protein of starving cells) of *Escherichia coli* (*E. coli*) bacteria is a representative of bacterial ferritins [5]. The shell size of the bacterial Dps protein is about 9 nm. The protein part includes 12 identical subunits with a homo-dodecamer structure [5, 6]. Dps protein molecules are able to accumulate (deposition) inorganic nanoparticles of the iron-oxygen system [7] inside a hollow part with a diameter of up to 5 nm [7, 8]. Thus, ferritin Dps is a potential container of natural origin, which can be used for the accumulation, storage and targeted delivery of nanomaterials. Previously, synchrotron X-ray absorption near edge fine structure spectroscopy showed a complex composite-like composition of a nanoparticle, which is formed from the oxidation products of Fe^{2+} ions in the ferroxidase centers of natural Dps molecules isolated from *E.coli* bacteria grown aerobically [9]. Moreover, the possibility of forming one-dimensional structures of Dps molecules has been shown by cryo-electron microscopy [5, 8].

Finally, it should be noted that the Scanning Electron Microscopy (SEM) method is one of the most popular in the diagnosis of a large variety of objects, including nanoscale structures and biomaterials. The capabilities of the method make it possible to study the morphology features for objects of various origins with high lateral resolution. However, the question of the SEM technique applicability for the precision study of hybrid nano-biomaterials requires experimental verification due to the complex composition and structure of such objects.

Thus, the issue of presented study is related to the possibility of combining Si-NW silicon wires arrays with natural nanomaterial bacterial protein Dps. This is relevant, from the point of view, for the development and application of hybrid materials – combining inorganic structures with desired properties with functional nanomaterials of natural origin. This work is devoted to the application of high-resolution scanning electron microscopy to study structures formed as a result of combining arrays of silicon wires with bacterial protein Dps.

2. Experimental

To obtain Si-NW arrays, the metal-assisted wet chemical etching was used [2, 10]. Standard substrates of n-type crystalline silicon (resistivity of ~ 1–5 Ω/cm were rinsed in a 2% solution of HF for 10 sec. Further, silver nanoparticles were deposited on the surface as a result of immersion of purified Si substrates in $AgNO_3$ (0.01 M) and HF (5M) solution for 30 sec. The next step was etching in 30% H_2O_2 and HF (5M) solution for 180 sec, followed by rinsing in 65% HNO_3 solution (to remove silver nanoparticles) with additional rinsing in water for 10 minutes. The structures formed were dried in the air in ambient conditions.

Recombinant Dps protein was obtained using *Escherichia coli* BL21*(DE3) cells as producers. *E.coli* cells were transformed by the pGEM_dps plasmid. The paper [5] provides detailed information about protein biosynthesis and its subsequent isolation and purification. The solution of protein molecules had a concentration of 2 mg/ml in the initial buffer of 10 mM NaCl, 50 mM tris-HCl (pH 8.0) and 0.1 mM EDTA.

Protein molecules were deposited on the surface of formed and previously studied Si-NW arrays by layering 10 ml solution. After that, the resulting structure was dried in ambient conditions, rinsed in deionized water (by pulling) in order to remove residual salts and dried again under the same conditions.

The surfaces morphology of the initial Si-NW array and the hybrid structure based on

Condensed Matter and Interphases / Конденсированные среды и межфазные границы   2021;23(4): 644–648

E. V. Parinova et al.   Dps protein localization studies in nanostructured silicon matrix...

it with layered protein, as well as the sections were studied by SEM. The Carl Zeiss ULTRA 55 microscope was used (secondary electrons registration) with low accelerating voltages of 2, 3 and 5 kV, necessary for working with bio-structures.

The Image J software package was used to estimate the areas occupied by the Si wires, cavities and filling the arrays with molecular culture.

3. Results and discussion

Fig. 1 shows the morphology of the initial surface of Si-NW arrays. The largest wide cavities V1–V6, which were formed as a result of etching, were noted. The width of such pores is up to 737 nm. At the same time, pores with a width of less than 100 nm are observed.

It should be noted that the edges of the wires arrays are sharp, while the arrays themselves have morphological features with sizes less than 50 nm as a result of local etching processes not stimulated by silver nanoparticles [2, 10]. There are no noticeable morphologically transitional layers in the initial array of Si-NW. To estimate the areas in the lateral projection that were taken into account in the calculation are indicated: 1 – the surface of the wires arrays, including the pores side parts available for observation, 2 – cavities (pores). The ratio of the areas of type 1 and type 2 areas is 48 to 52%.

Fig. 2 shows the results of Si-NW arrays combining with Dps protein after drying in
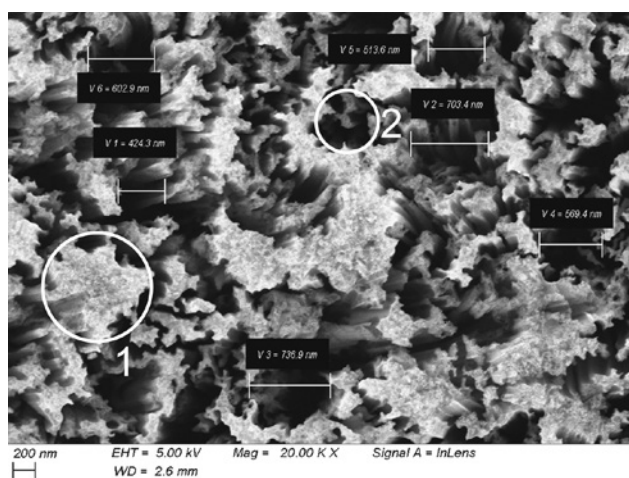
Fig. 1. Morphology of the silicon wires array initial surface. The sizes of cavities (pores) of the largest width are underlined
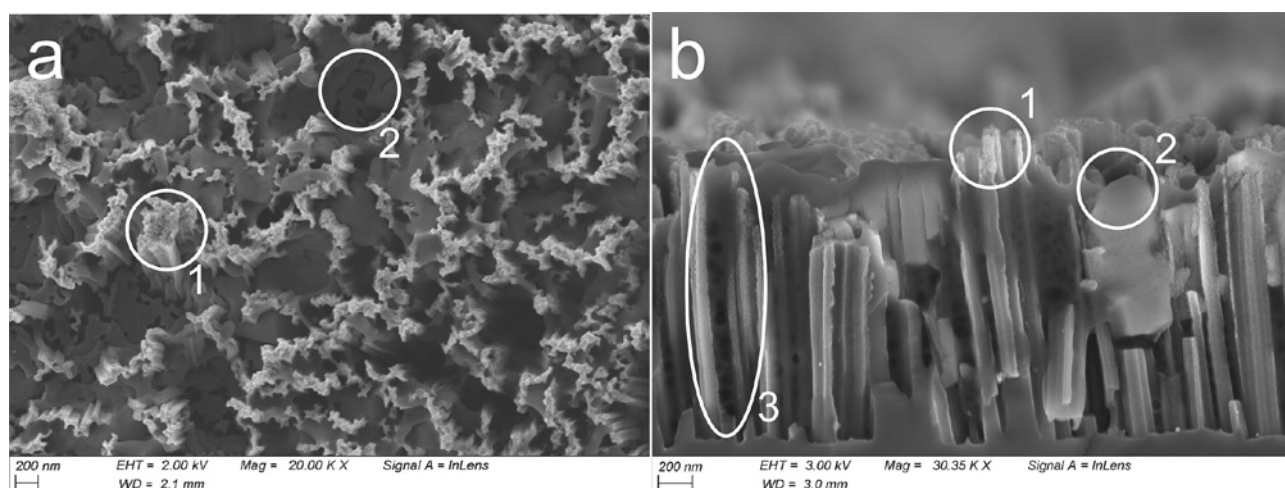
laboratory conditions. Before discussing the result of the combination, let us pay attention to the section of the hybrid structure (Fig. 2b) that gives the morphology of individual wires and their height as a whole. Note that the lateral surfaces of the wires are morphologically similar to the surface of the wires arrays. This is especially noticeable for areas of non-etched surface (for example, see the highlighted area 1 in Fig. 1). The height of almost vertical wires is more than a micrometer (Fig. 2b). Consequently, the depth of the cavities (pores) available for filling with protein molecules exceeds a micrometer. At the same time, individual wires, which, on the other hand, we can consider as the walls of cavities (pores) are uniform.

The small accelerating voltages used for registration (shown in the figures) were sufficient to form images (Fig. 2) of the morphology of hybrid bio-structures of sufficient sharpness and degree of detailing.

In Fig. 2 it is clearly visible that the cavities between the wires of the Si-NW array are filled with protein. Areas 1 (as in Fig. 1) mark the surface of non-etched areas, including those not covered with deposited molecular culture. At the same time, areas 2 clearly contain morphologically pronounced areas corresponding to the residual volumes of the molecular culture, which are located in the cavities after drying the hybrid structures in the laboratory and vacuuming in the microscope working chamber. In fact, the material that fills the pores is morphologically more homogeneous than the surface (walls) of Si-NW and is located precisely in the cavities available for deposition (combining). In Fig. 2b area 3 is additionally marked confirming the fact that the entire volume of the pore is filled with the molecular culture. The ratio of unfilled surface areas (1) and protein coating (2) is estimated as 30% and 70% of the total area of the microscopic surface image. This fact confirms the success of the first time combination of the nano-biomaterial of the molecular culture of the Dps protein with the available developed surface of the silicon wires array.

4. Conclusions

For the first time, a combination of a nano-biomaterial as the Dps protein molecular

Condensed Matter and Interphases / Конденсированные среды и межфазные границы   2021;23(4): 644–648

E. V. Parinova et al.   Dps protein localization studies in nanostructured silicon matrix...

Fig. 2. Morphology of (a) – the surface and (b) – the inner part (section) of the silicon wires array after combining with the Dps protein

culture with an accessible developed surface of a silicon wires array was performed. It has been shown by high-resolution scanning electron microscopy that ferritin Dps molecules can successfully penetrate into the submicron size pores, successfully filling them and covering the silicon wires array highly developed surface as a whole. Suggested approach can be used for the functionalization of the Si wires arrays surface by using ferritin molecules as nanometer-sized containers for targeted delivery of materials tasks and the formation of functional hybrid nano-biomaterials in general.

Conflict of interests

The authors declare that they have no known competing financial interests or personal relationships that could have influenced the work reported in this paper.

Author contributions

All authors made an equivalent contribution to the preparation of the publication.

References

1. Xiao Yu, Yuchen Wang, Hong Zhou, Yanxiang Liu, Yi Wang, Tie Li, Yuelin Wang. Top-down fabricated silicon-nanowire-based field-effect transistor device on a (111) silicon wafer. *Small*. 2013;9(4): 525–530. https://doi.org/10.1002/smll.201201599

2. Sivakov V. A., Voigt F., Berger A., Bauer G. and Christiansen S. H. Roughness of silicon nanowire sidewalls and room temperature photoluminescence. *Phys. Rev. B*. 2010;82: 125446. https://doi.org/10.1103/PhysRevB.82.125446

3. Ming T., Turishchev S., Schleusener A., Parinova E., Koyuda D., Chuvenkova O., Schulz M., Dietzek B., Sivakov V. Silicon suboxides as driving force for efficient light enhanced hydrogen generation on silicon nanowires. *Small*. 2021;17: 2007650. https://doi.org/10.1002/smll.202007650

4. Ravi P. Srivastava, Dahl-Young Khang. Structuring of Si into multiple scales by metal-assisted chemical etching. *Advanced Materials*. 2021;33(47): 2005932. https://doi.org/10.1002/adma.202005932

5. Almiron M., Link A. J., Furlong D., Kolter R. A novel DNA-binding protein with regulatory and protective roles in starved Escherichia coli. *Genes & Development*. 1992;6: 2646-2654. https://doi.org/10.1101/gad.6.12b.2646

6. Dubrovin E. V., Dadinova L. A., Petoukhov M. V., Soshinskaya E. Yu., Mozhaev A. A., Klinov D. V., Schaffer T. E., Shtykova E. V., Batishchev O. V. Spatial organization of Dps and DNA–Dps complexes, *Journal of Molecular Biology*. 2021;433(10): 166930. https://doi.org/10.1016/j.jmb.2021.166930

7. Antipov S., Turishchev S., Purtov Yu., Shvyreva U., Sinelnikov A., Semov Yu., Preobrazhenskaya E., Berezhnoy A., Shusharina N., Novolokina N., Vakhtel V, Artyukhov V., Ozoline J. The oligomeric form of the escherichia coli Dps protein depends on the availability of iron ions. *Molecules*. 2017;22(11): 1904. https://doi.org/10.3390/molecules22111904

8. Antipov S. S., Pichkur E. B., Praslova N. V., Preobrazhenskaya E. V., Usoltseva D. S., Belikov E. A., Chuvenkova O. A., Presnyakov M. Yu., Artyukhov V. G., Ozoline O. N., Turishchev S. Yu. High resolution cryogenic transmission electron microscopy study of Escherichia coli Dps protein: first direct observation in quasinative state. *Results in Physics*. 2018;11: 926-928. https://doi.org/10.1016/j.rinp.2018.10.059

9. Turishchev S. Yu., Antipov S. S., Novolokina N. V., Chuvenkova O. A., Melekhov V. V., Ovsyannikov R.,

Condensed Matter and Interphases / Конденсированные среды и межфазные границы   2021;23(4): 644–648

E. V. Parinova et al.   Dps protein localization studies in nanostructured silicon matrix...

Senkovskii B. V., Timchenko A. A., Ozoline O. N., Domashevskaya E. P. A soft X-ray synchrotron study of the charge state of iron ions in the ferrihydrite core of the ferritin Dps protein in Escherichia coli. *Biophysics*. 2016;61(5): 705-710. https://doi.org/10.1134/S0006350916050286

10. Huang Z., Shimizu T., Senz S., Zhang Z., Zhang X., Lee, W., ... Gösele U. Ordered arrays of vertically aligned [110] silicon nanowires by suppressing the crystallographically preferred <100> etching directions. *Nano Letters*. 2009;9(7): 2519–2525. https://doi.org/10.1021/nl803558n

Information about the authors

Elena V. Parinova, PhD in Physics and Mathematics, Researcher of the Joint Laboratory "Electronic Structure of Solids", Voronezh State University, Voronezh, Russian Federation; e-mail: parinova@phys.vsu.ru. ORCID iD: https://orcid.org/0000-0003-2817-3547

Sergey S. Antipov, DSc in Biology, Associate Professor, Biophysics and Biotechnology Department, Voronezh State University, Voronezh, Russian Federation; e-mail: ss.antipov@gmail.com

Vladimir Sivakov, PhD, Deputy Head, Leibniz Institute of Photonic Technology, Jena, Germany; e-mail: vladimir.sivakov@leibniz-ipht.de. ORCID iD: https://orcid.org/0000-0002-3272-501X.

Iuliia S. Kakuliia, Leading Engineer of General Physics Department, Voronezh State University, Voronezh, Russian Federation; e-mail: kakuliia@phys.vsu.ru

Sergey Yu. Trebunskikh, PhD in Physics and Mathematics, Researcher of the joint laboratory "Electronic Structure of Solids", Voronezh State University, Voronezh, Russian Federation; e-mail: tsu@phys.vsu.ru

Evgeny A. Belikov, Engineer of the Joint Laboratory "Electronic Structure of Solids", Voronezh State University, Voronezh, Russian Federation; e-mail: tsu@phys.vsu.ru

Sergey Yu. Turishchev, Dr. Sci. (Phys.-Math.), Associate Professor, Acting Head of the General Physics Department, Voronezh State University, Voronezh, Russia; e-mail: tsu@phys.vsu.ru. ORCID iD: https://orcid.org/0000-0003-3320-1979

Translated by Sergey Turishchev